LABORATORY
FOR
HYDROSPHERIC PROCESSES

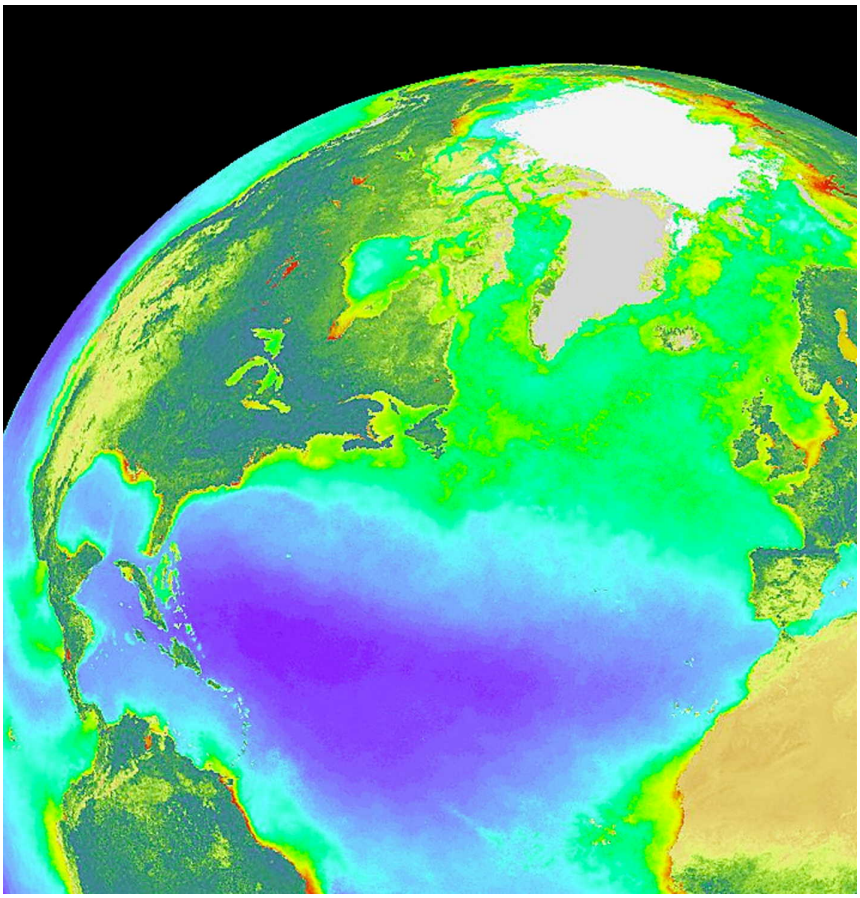

RESEARCH PUBLICATIONS
2002

NATIONAL AERONAUTICS AND SPACE ADMINISTRATION
GODDARD SPACE FLIGHT CENTER
GREENBELT, MARYLAND 20771
301-614-5671

Cover Figure Caption

Global measurements with SeaWiFS have provided an unprecedented, single-sensor, multi-year data set of biospheric plant biomass. Behrenfeld et al. (2002) used these data to quantify changes in ocean and land photosynthesis during a strong El Nino to La Nina transition as captured by SeaWiFS during its first 3 years of operation. The SeaWiFS data represent a starting point from which MODIS and follow-on missions will contribute toward building a sustained climatological global data set enabling similar analyses of biospheric change over longer and longer time periods.

This cover figure is from the Laboratory's Peer Award for best publication for calendar year 2001, **Michael J. Behrenfeld**, James T. Randerson, **Charles R. McClain**, **Gene C. Feldman**, Sietso O. Los, Compton J. Tucker, Paul G. Falkowski, Christopher B. Field, Robert Frouin, **Wayne E. Esaias**, Dorota D. Kolber, Nathan H. Pollack, Biospheric Primary Production During an ENSO Transition, *Science*, 291, 2594-2597, (includes cover figure).

Laboratory for Hydrospheric Processes 2002 Publications

This document is a compilation of publications of the Goddard Space Flight Center Laboratory for Hydrospheric Processes for calendar year 2002. Each two-page entry is a cut-and-pasted extraction from a 2002 published journal article, book chapter, symposium or conference proceeding, or technical memorandum. This provides a quick, inexpensive way to communicate our research. If you wish further information, or a reprint, please contact the author of the article or the publisher. There are two sections, the first consisting of 61 journal articles and book chapters which are arranged according to the science priorities of NASA's Earth Science Enterprise:

Ecosystem Productivity and the Global Carbon Cycle
Climate Variability and Prediction
Sensors/Algorithm Development *
Modeling and Remote Sensing Techniques. *

A second section, consisting of 62 other contributions (e.g. conference/symposium proceedings and technical memoranda) provides additional scientific information to the outside community.

This document was initiated within the Earth Sciences Directorate at NASA/Goddard Space Flight Center to provide internal communication. We anticipate it will prove useful to visitors and other people interested in our research. This is our ninth annual document.

The Laboratory for Hydrospheric Processes is one of the major elements of the Earth Sciences Directorate at NASA's Goddard Space Flight Center. Scientific investigations within the Division range from theoretical to experimental research dealing with oceanic, hydrologic, and cryospheric sciences. The Laboratory currently has a staff of 61 civil servants and approximately 182 visiting scientist, postdoctoral fellows, and contractors. At various times throughout the year, the Laboratory hosts additional personnel through NASA and Goddard sponsored enrichment programs for high school, undergraduate and graduate students, and high school and university faculty. For further information see our web site at http://neptune.gsfc.nasa.gov.

I would like to express my appreciation to O. Williams, M. Gover, S. Coleman-Turner, and J. Ormsby for their efforts in compiling, formatting, and editing each of the papers and to those individuals (W. Gregg, S. Hakkinen, J. Wang, and M. Owe) that took of their time to prepare the respective summaries preceding each science priority.

Dr. Peter H. Hildebrand, Chief
Laboratory for Hydrospheric Processes
Code 970
NASA Goddard Space Flight Center
Greenbelt, MD 20771

* These group titles were added to provide a logical place for other studies that are done within the Division that do not readily fall within the five science priorities.

Laboratory for Hydrospheric Processes Best Publication Awards

Each year, as part of our Peer Award process, the Laboratory selects an article and presents the author or authors an award to honor their publication efforts during the previous year. Listed below are the previous winners since we began compiling the Laboratories' publications in a booklet similar to this beginning with calendar year 1993.

1993

Robert J. Gurney, **James L. Foster**, and **Claire L. Parkinson**, *Atlas of satellite observations related to global change*, Cambridge University Press.

1994

Kevin Arrigo, Impact of ozone depletion on phytoplankton growth in the Southern Ocean: large-scale and temporal variability, *Marine Ecology Progress Series*, **114**, 1-12.

1995

William B. Krabill, Robert H. Thomas, Chreston F. Martin, **Robert N. Swift**, and **Earl B. Frederick**, Accuracy of airborne laser altimetry over the Greenland ice sheet, *International Journal of Remote Sensing*, **16**(7), 1211-1222.

1996

Norden E. Huang, **Steven R. Long**, and Zheng Shen, The mechanism for frequency downshift in nonlinear wave evolution. *Advances in Applied Mechanics*, **32**, Eds. Hutchinson and Wu, Academic Press, 60-117 plus figures.

1997

None awarded

1998

Robert Bindshcadler, Monitoring ice sheet behavior from space. Reviews of Geophys., 36 (1), 79-104, Future of thre west Antarctic ice sheet, *Science*, **282**, 428-429, and Changes in the west Antarctic ice sheet since 1963 from declassified satellite photography, *Science*, **279**, 689-692.

1999

William Krabill, **Earl Frederick**, **Serdar Manizade**, Creston Martin, John Sonntag**, Robert Swift**, **Robert Thomas**, **C. Wayne Wright**, and **James Yungel**, Rapid thinning of parts of the southern Greenland ice sheet, *Science*, **283**, 1522-1524.

2000

Randal D. Koster, J. J. Suarez, and M. Heiser, 2000: Variance and predictability of precipitation at seasonal-to-interannual timescales. *J. Hydrometeor*., **1**, 26-46.

2001

Michael J. Behrenfeld, James T. Randerson, **Charles R. McClain**, **Gene C. Feldman**, Sietso O. Los, Compton J. Tucker, Paul G. Falkowski, Christopher B. Field, Robert Frouin, **Wayne E. Esaias**, Dorota D. Kolber, Nathan H. Pollack, Biospheric Primary Production During an ENSO Transition, *Science*, **291**, 2594-2597, (includes cover figure).

Journal Papers and Book Chapters

ECOSYSTEM PRODUCTIVITY AND THE GLOBAL CARBON CYCLE

A diverse set of publications arises from Ecosystem Productivity and the Global Carbon Cycle for 2002. Papers range from new physiologically based photosynthetic modeling, to ship surveys, to global decadal trends.

Behrenfeld et al. provide new parameterizations based on light acclimation and nutrients to improve primary production models, and also outline a summary of the analysis of global scale primary production.

In the Antarctic, Arrigo et al. documented the potential effects of an iceberg on ecosystem dynamics. They found the iceberg reduced primary production more than 40% below normal and altered the abundance and behavior of upper trophic level organisms.

Atkinson et al described ecosystem of physical dynamics in the coastal waters off Chile. Their observations utilized in situ sampling and satellite data to describe spatial variability in relation to upwelling, river runoff, intrusion of eddies, mixing and heating.

A longer set of cruise observations by Barlow et al in the Atlantic Ocean were used to characterize phytoplankton pigment characteristics. These pigments are indicative of ecosystem functionality, and indicated major changes across the various physical/biogeochemical regimes encountered in the greater North Atlantic.

Finally, Gregg and Conkright used a reanalysis of historical ocean color data to observe a six percent decline in global chlorophyll concentrations from the early 1980's to the present. Larger declines were observed at the high latitudes, while low latitudes indicated an increase. The changes have major implications for the global carbon cycle and climate change.

Ecological impact of a large Antarctic iceberg

Kevin R. Arrigo,[1] Gert L. van Dijken,[1] David G. Ainley,[2] Mark A. Fahnestock,[3] and Thorsten Markus[4]

Received 1 October 2001; accepted 20 December 2001; published 6 April 2002.

[1] Satellite imagery has been used to document for the first time the potential for large icebergs to substantially alter the dynamics of a marine ecosystem. The B-15 iceberg (~10,000 km^2), which calved off the Ross Ice Shelf in the biologically productive southwestern Ross Sea, Antarctica, restricted the normal drift of pack ice, resulting in heavier spring/summer pack ice cover than previously recorded. Extensive ice cover reduced both the area suitable for phytoplankton growth and the length of the algal growing season. Consequently, primary productivity throughout the region was >40% below normal, which changed both the abundance and behavior of upper trophic level organisms. *INDEX TERMS:* 1827 Hydrology: Glaciology (1863); 4207 Oceanography: General Arctic and Antarctic oceanography; 4275 Oceanography: General: Remote sensing and electromagnetic processes (0689)

1. Introduction

[2] Polar ice sheets and associated ice shelves are important indicators of climate change, responding to elevated temperatures with increased melt, accelerated motion, and/or increased iceberg calving [*Skvarca et al.*, 1999; *Scambos et al.*, 2000]. The calving of large tabular icebergs in the Antarctic has likely increased since the Last Glacial Maximum accompanying the formation of the Ross Ice Shelf [*Conway et al.*, 1999], with recent calving rates for large (>18.5 km) icebergs of 4.4 per year (iceberg tracking data obtained from the National Ice Center show that between 1978 and 2001, Antarctic ice sheets calved an average 4.4 icebergs larger than 18.5 km in length annually). Consequences of these calving events for marine ecosystems remain largely unexplored. Fortunately, the huge iceberg B-15 (at 295 km in length and up to 40 km in width is one of the largest icebergs ever observed), which calved off the Ross Ice Shelf in March 2000, is providing insights.

[3] The southwestern Ross Sea (Figure 1) is one of the most biologically productive regions of the Southern Ocean [*Smith and Gordon*, 1997; *Arrigo et al.*, 1998a]. Located on the Antarctic continental shelf, it owes its biological richness to the annual formation of the Ross Sea polynya, a region of diminished sea ice cover in the midst of heavy pack ice north of the Ross Ice Shelf. The Ross Sea polynya is formed by the strong, persistent katabatic winds that move sea ice offshore during winter, generally to the northwest [*Bromwich et al.*, 1992]. Come springtime, a large area of open water forms in this region as winds clear away the remaining sea ice. The resulting exposure of surface waters to sunlight is followed by a profuse growth of phytoplankton [*Arrigo et al.*, 1998b]. Concentrations of chlorophyll *a* (Chl *a*) in these blooms typically exceed 5 mg m^{-3} over an area of >100,000 km^2 (Figures 2a and 2b) [*Arrigo et al.*, 1998b; *Arrigo et al.*, 2000], compared to <0.05 mg m^{-3} in low productivity central ocean gyres. As a result of its high productivity, the Ross Sea supports large populations of upper-trophic level organisms, such as marine mammals and birds [*Ainley et al.*, 1984; *Kooyman and Burns*, 1999; *Kasamatsu et al.*, 1998]. Indeed, 25% and 30% of the world populations of the circumpolar Emperor (*Aptenodytes forsteri*) and Adélie penguins (*Pygoscelis adeliae*), respectively, nest at colonies in the Ross Sea [*Woehler*, 1993], which has a coastline <10% of the Antarctic continental margin.

2. Methods

[4] Sea ice distributions were computed from daily Special Sensor Microwave Imager (SSM/I) imagery obtained from the EOS Distributed Active Archive Center (DAAC) at the National Snow and Ice Data Center, University of Colorado, Boulder, CO. Images were processed to 6.25 km resolution using the algorithm of *Markus and Burns* [1995], and used to calculate open water areas. All satellite imagery were mapped to a common polar-stereographic projection using the Interactive Data Language (IDL, Research Systems, Inc.). Sea-viewing Wide Field-of-view Sensor (SeaWiFS) data were obtained from the Goddard Earth Sciences Data and Information Services Center, DAAC. Chl *a* concentrations were derived from SeaWiFS Level 2 data (4 km resolution) and processed using the NASA SeaDAS image processing software and OC4v4 algorithm. Validation studies for the Ross Sea show that SeaWiFS surface Chl *a* retrievals are within ±15% of in situ observations [*Arrigo et al.*, unpublished]. Multi-day (<1 week) Chl *a* composites were constructed to reduce loss due to cloud cover. Primary productivity was calculated from SeaWiFS data using the algorithm of *Arrigo et al.* [1998a]. Iceberg positions were projected using MODerate resolution Imaging Spectrometer (MODIS) band 1 (620–670 nm, 0.25 km resolution) imagery except for images where the sun was below the horizon; then the thermal infrared band 24 (4.433–4.498 μm, 1 km resolution) imagery were used. MODIS data were obtained from the Goddard Earth Sciences Data and Information Services Center, DAAC.

[5] At three penguin colonies on Ross Island (Cape Royds, Bird, and Crozier), stomach samples were taken from 3–5 adult penguins each week for five weeks, 25 December to ca. 22 January. Adults were forced to regurgitate stomach contents using the water-off loading technique: filling them with warm water, then turning them upside down in a plastic bucket.

3. Results and Discussion

[6] Satellite imagery from a variety of platforms show that on March 2000, the iceberg B-15 (iceberg numbers are assigned by the National Ice Center, Suitland, MD, USA) calved from the eastern portion of the Ross Ice Shelf (Figure 1). Almost immediately after calving, B-15 began to fragment, and at the present time, there are at least nine separate sections, denoted B-15A through B-15I, drifting in and around the western Ross Sea. By far the largest of these are B-15A and B-15B. Tracking the movement of the icebergs using imagery from MODIS shows that B-15A (~6,400 km^2) drifted westward along the front of the Ross Ice

[1]Department of Geophysics, Stanford University, Stanford, CA 94305-2215, USA.
[2]H. T. Harvey & Associates, San Jose, CA 95118, USA.
[3]ESSIC, University of Maryland, College Park, MD 20742-2465, USA.
[4]NASA Goddard Space Flight Center-University of Maryland Baltimore County Joint Center for Earth Systems Technology (NASA/GSFC-UMBC JCET), Greenbelt, MD 20771, USA.

Copyright 2002 by the American Geophysical Union.
0094-8276/02/2001GL014160$05.00

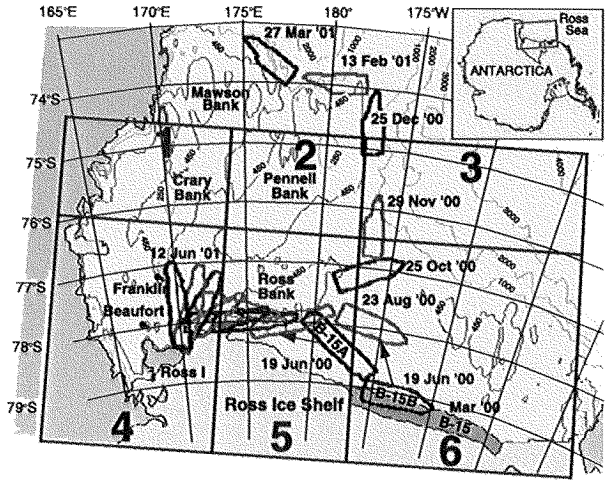

Figure 1. Map of the southwestern Ross Sea showing changes in the position of the B-15 iceberg and the location of the 6 regions referred to in the text. The sequential drift paths taken by B-15A and B-15B as determined from MODIS data are also shown. B-15A moved into its current position by edging past the Ross Bank but is now too large to move westward.

Shelf, likely guided by bathymetry and a narrow coastal current [*Keys et al.*, 1990] and is currently grounded near Ross Island at the face of the Ross Ice Shelf (Figure 1). B-15B first drifted to the north along the eastern edge of the Ross and Pennell banks and then moved west along the northern margin of the Pennell and Mawson Banks (Figure 1). It is now located near Cape Adare, over 1000 km from its original location. Like B-15A, however, other smaller icebergs (e.g. B-15C) remain grounded within the southwestern Ross Sea.

[7] In November 2000, nine months after the initial calving event, the pieces of B-15 were still in the southwestern Ross Sea, forming a barrier that greatly restricted the typical northwest drift pattern of pack ice (Figure 2c). As a result, sea ice concentrations measured using the SSM/I remained unusually heavy throughout November and early December 2000 (compare Figures 2a and 2b with 2c), the time when the southwestern Ross Sea normally shifts from being predominantly ice-covered to ice-free [*Arrigo et al.*, 2000]. As late as mid-December 2000, large amounts of sea ice remained piled up on the southeast side of the line of icebergs (Figure 2c), restricting the expansion of open water.

[8] Changes in the seasonal dynamics of sea ice cover brought about by the presence of B-15 are exemplified in an SSM/I time series for Region 5 (Figure 1), an area of the Ross Sea that was moderately impacted by B-15 (Figure 3a). During the spring of typical years (e.g. 1998–1999 and 1999–2000), sea ice cover in Region 5 diminishes rapidly, and from the beginning of December to early March, these waters are more than 80% ice-free. In contrast, the presence of the B-15 iceberg during 2000–2001 dramatically reduced the rate of ice advection, resulting in a 2-month delay in the time to reach maximum open water area. In fact, all regions of the southwestern Ross Sea experienced fewer days with <50% ice cover in 2000–2001, compared to the normal sea ice pattern represented by the 1998–2000 time period (Table 1). In the three regions adjacent to the Ross Ice Shelf (Figure 1), the number of days with sea ice concentrations below 50% was reduced by 37–48% in 2000–2001, and Region 3 did not become ice-free all year.

[9] The heavy sea ice conditions of 2000–2001 caused by the presence of the B-15 iceberg had a dramatic effect on phytoplankton populations throughout the southwestern Ross Sea. In ordinary years, phytoplankton begin to bloom in mid-November (Figure 3b), just as the area of open water and the availability of light begins to increase (Figure 3a). Imagery from the Sea-viewing Wide Field-of-view Sensor (SeaWiFS) shows that typically, Chl *a* concentrations in the Ross Sea increase rapidly, as do calculated rates of primary production (Figure 3c), eventually peaking in late December. After blooming for approximately six weeks, phytoplankton growth rates begin to diminish. At this time, loss processes such as grazing and sinking exceed rates of growth, causing Chl *a* abundance and primary production to decline steadily.

[10] SeaWiFS imagery reveals, however, that the normal phytoplankton dynamics in the Ross Sea were markedly altered during 2000–2001, most probably a direct result of the effects of the B-15 iceberg. Diminished light availability due to the high concentrations of sea ice present throughout the southwestern Ross Sea in the austral spring and summer resulted in a dramatic delay in the initiation of the phytoplankton bloom in some regions and no bloom at all in others. In Region 5, the phytoplankton bloom was delayed by approximately two months due to abnormally extensive sea ice cover. As a result of the reduced length of the growing season, peak Chl *a* concentrations in this region reached only about 50% of normal values (Figure 3b). Unlike most years when the decline of the phytoplankton bloom is precipitated well in advance of ice freeze-up, the rapid drop in Chl *a* and primary production observed in many regions (e.g. Region 5) in 2000–2001 (Figures 3b and 3c) was due to a reduced ice-free growth season (Figure 3a).

[11] The extensive sea ice cover and delayed phytoplankton bloom in 2000–2001 resulted in a substantial drop in the annual phytoplankton production estimated for all regions of the Ross Sea, the severity of which varied spatially. The effect was most extreme in Region 3, where unusually high sea ice cover and an extremely short growing season (Table 1) reduced annual primary production by 95% (Table 1). Annual production in Regions 4 (dominated by diatoms), 5 and 6, where blooms of the alga *Phaeocystis antarctica* are generally the most intense [*Arrigo et al.*, 1998b; *Arrigo et al.*, 2000], was diminished by 32%, 44%, and 35%, respectively in 2000–2001.

Table 1. Regional Differences in Length of Growing Season[a] and Annual Primary Production in the Southwestern Ross Sea in 1998–1999, 1999–2000, and 2000–2001 by Region

Region	1998–1999		1999–2000		2000–2001		% Change[b]	
	Growing Season (Days)	Primary Production (Tg C)	Growing Season (Days)	Primary Production (Tg C)	Growing Season (Days)	Primary Production (Tg C)	Growing Season	Primary Production
1	83	4.9	91	4.9	80	3.0	−8	−40
2	105	5.1	121	5.5	112	3.7	−1	−31
3	59	2.5	81	4.5	0	0.2	−100	−95
4	77	6.0	76	6.9	48	4.4	−37	−32
5	118	9.5	107	10	59	5.5	−48	−44
6	88	13	93	19	54	10	−39	−35
All		41		51		27		−41

Regions are shown in Figure 1.
[a]Defined as the number of continuous days with <50% sea ice cover.
[b]% Change was calculated as the difference between 2000–2001 and the mean of 1998–1999 and 1999–2000.

Oceanographic observations in Chilean coastal waters between Valdivia and Concepción

Larry P. Atkinson,[1] Arnoldo Valle-Levinson,[1] Dante Figueroa,[2] Ricardo De Pol-Holz,[2] Victor A. Gallardo,[2] Wolfgang Schneider,[2] Jose L. Blanco,[1] and Mike Schmidt[3]

Received 23 May 2001; revised 29 November 2001; accepted 11 December 2001; published 25 July 2002.

[1] The physical oceanography of the biologically productive coastal waters of central Chile (36° to 40°S) is relatively unknown. In December 1998 we made a short exploratory cruise between Valdivia (40°S) and Concepción (37.8°S) taking temperature, salinity, oxygen, and current velocity profiles. Coincident sea surface temperature and color measurements were obtained by satellite. The results showed an area dominated by wind-induced coastal upwelling, river runoff, intrusion of offshore eddies, mixing, and heating. Upwelling centers were found over the shelf at three locations: inshore of Mocha Island, off Valdivia, and off Lavapie Point. At these centers, equatorial subsurface water (ESSW) intrudes into the coastal waters, sometimes affecting the surface waters. Since ESSW has characteristically low-oxygen and high-salinity values, it is easily detected. Off Valdivia, runoff imparts stratification, while farther north, solar heating and reduced mixing may facilitate stratification. In some areas, even strong winds would not destroy the stratification imparted by the advection of buoyancy that occurs during the upwelling process. Strong equatorward currents (>1 m s^{-1}) in the form of an upwelling jet were found off Lavapie Point. This is also the location of an intruding anticyclone. Elsewhere, currents were mainly northward but highly variable because of intrusions from offshore eddies. The sea surface temperature and ocean color images show a complex field of onshore and offshore intrusions combined with the effects of mixing on chlorophyll concentrations. The residence time of upwelled water on the shelf is estimated to be less than 1 week. *INDEX TERMS:* 4279 Oceanography: General: Upwelling and convergences; 4516 Oceanography: Physical: Eastern boundary currents; 4528 Oceanography: Physical: Fronts and jets; *KEYWORDS:* Upwelling; wind; water circulation; eddies; central Chile coast

1. Introduction

[2] The coastal waters of Chile are unique because a combination of meteorological and oceanographic processes and geography has created one of the world's most biologically productive ocean areas. The coast extends in a nearly north/south direction over 40° of latitude (not including the Antarctic) bordered by the Andes to the east and the Peru-Chile Trench to the west. Thus Chilean coastal waters lie between two of the highest relief features on Earth. Over this vast latitudinal range, climatic conditions vary from arid to subantarctic with upwelling winds off northern Chile, downwelling winds off southern Chile, and strong westerlies and considerable variability between. Rainfall toward the north is in some places nonexistent, while farther south it is quite high. The extremely high productivity of the Chilean coastal waters is attributable to upwelling of nutrient rich Peru-Chile Undercurrent water [*Strub et al.*, 1998] and processes that maintain biological populations in the shallow coastal waters.

[3] In December 1998 we made an exploratory cruise along the coast between Valdivia (40°S) and Concepción (37.8°S). This region is noted for its extremely high biological productivity that sometimes provides 4% of the world's fish catch. Our preliminary results, based on a unique but sparse data set, show the structure of currents, upwelling centers, and low-salinity water along the coast and the relationship to satellite-derived SST and chlorophyll.

2. Regional Setting

[4] The region studied has a broad shelf that gradually narrows to the north at Lavapie Point (Figure 1). The shelf is about 50 km wide south of Tucapel Point with Mocha Island lying on the outer shelf marking the widest and shallowest part of the shelf. North of Tucapel Point the shelf narrows to about 10 km then starts to widen again at Lavapie Point. The broad and shallow Gulf of Arauco lies northeast of Lavapie Point. The Gulf of Arauco is a large embayment with Santa Maria Island lying offshore inline with the coast to the south. The Bio Bio River flows into the northern end of the Gulf, and the submarine canyon associated with the Bio Bio River crosses the shelf west of its present mouth.

[5] It is important to note two geographic features that affect the wind field. The first feature is change in coastline direction at Lavapie Point. South of Lavapie Point the coastline trends toward 355°T, while north of Lavapie Point

[1]Old Dominion University, Norfolk, Virginia, USA.
[2]University of Concepción, Concepción, Chile.
[3]Goddard Space Flight Center, NASA, Greenbelt, Maryland,

the shore trends toward 20°T. The Gulf of Arauco itself represents a large-scale equatorward facing embayment in the 20°T trending coast. Response to upwelling winds depends on the changing trends of the general bathymetry that follows the shoreline. The changing shoreline direction and diverging isobaths at Lavapie Point would induce upwelling in a northward flowing current [*Arthur*, 1965; *Blanton et al.*, 1981].

[6] The coastal wind field may also be affected by the presence of a coastal range of mountains extending from Concepción southward to the latitude of Mocha Island: the Cordillera de Nahuelbuta. North and south of the Cordillera de Nahuelbuta the coastal range is relatively low in relief. However, maximum heights in the range reach over 1000 m. These heights may cause intensified winds in the adjacent coastal waters.

[7] River flow into the region consists of the Bio Bio River (36.8°S) to the north and the Imperial River (38.8°S), Tolten River (39.2°S), Queule River (39.6°S), and the Calle Calle River (39.8°S) to the south. The previously mentioned cordillera blocks westward flowing rivers in the central part of the region. The total flow in the region from 37° to 40°S is about 3100 $m^3 s^{-1}$ or 100 $km^3 yr^{-1}$ [*Davila et al.*, 2000]. This amount of flow is not large but would be expected to produce areas of low salinity and coastal currents for a few tens of kilometers around the river mouths during the rainy winter season and early summer when the snow melts. South of 40°S the river flow increases significantly relative to flow to the north.

[8] The water mass and general circulation characteristics off central Chile were recently summarized [*Strub et al.*, 1998], so we will keep the review here to a minimum. Wind-driven coastal upwelling is the dominant process in the area during the summer. The cold, salty, nutrient-rich, oxygen-poor equatorial subsurface water (ESSW) flowing southward in the Peru-Chile Undercurrent upwells across the shelf and often intrudes to the coast [*Gunther*, 1936; *Silva and Neshyba*, 1979].

[9] Satellite-derived sea surface temperature imagery [*Cáceres*, 1992] shows filaments and offshore eddies in the region. Offshore anticyclonic eddies are most often found north of Lavapie Point. Offshore-flowing filaments are concentrated in the region just north of Mocha Island and off the Gulf of Arauco. Our data show that offshore and onshore flow affects the inshore waters that we sampled.

3. Methods

[10] In this section we review the methods used and sources of data. The observations were made from the R/V *Kay Kay* operated by the Universidad de Concepción. Between 8 and 11 December 1998 the ship was taken along a path up the coast in a pattern dictated by the schedule and weather (Figure 1). Courses were laid out to sample the coastal current, upwelling centers, and other features of the region. Along the route, continuous current profiles were made with acoustic Doppler current profiler (ADCP) and conductivity-temperature-depth (CTD) casts were made at the end points of each zigzag leg.

[11] Mean monthly upwelling winds were obtained from the NOAA Pacific Fisheries Environmental Laboratory in Monterey, California. We used data from the 36°S node. Coastal winds were obtained from a station at Lavapie Point maintained by the Department of Physics of the Atmosphere and Ocean at the University of Concepción. There are no other wind observations in the region's coastal waters for this time period. Sea surface temperature data were from advanced very high resolution radiometer for 9 December 1998. Images for 10 and 11 December were contaminated with clouds but suggested surface warming consistent with the decreasing upwelling wind speeds. A SeaWifs image from 9 December 1998 was processed using the most recent algorithms for coastal waters.

[12] An RD Instruments Workhorse (300 kHz) ADCP was used to make the current velocity profiles. The ADCP was mounted on a 1.2-m-long catamaran towed several meters to the side of the ship. Raw data were averaged over 90 s and 1-m bins. Bottom tracking was always on, and navigation was by GPS. The data were not detided as the onshore offshore cruise track created nodes similar to tidal nodes if any were present. This was the first time an ADCP was used in this region of Chile.

[13] Temperature, oxygen and salinity profiles were made with a SeaBird 19 CTD. All data where processed using SeaBird software.

4. Results

[14] In this section the results of the observations and other ancillary data are described. First the winds and remotely sensed data are presented, followed by the subsurface observations.

[15] The mean monthly upwelling index (Figure 2a) was very high in late 1998 relative to other years. The short-term record (Figure 2b) shows that the upwelling during the year started in July 1998 and had reached very high values by December. It is clear that our sampling took place during a period of steadily increasing upwelling on the monthly scale. Data from Lavapie Point (Figure 3) indicate a pulse of strong upwelling winds late on 9 December then two smaller events on 10–11 December. The consistent wind stresses over 0.1 N m^{-2} no doubt led to the upwelling we observed, and the decreasing stress on the 10 and 11 December would have caused a decrease in wind-induced upwelling. It should be noted that the cruise was toward the end of an El Niño period and at the beginning of a La Niña.

6. Conclusions

[45] Our limited observations between Valdivia and Concepción during upwelling wind conditions suggest a coastal area strongly influenced by both local upwelling centers and the presence of offshore eddies. That, combined with the influx of runoff into some parts of the region and variations in heating and mixing, creates variations in stratification.

[46] This unique combination of forces and geography result in a complex physical oceanographic situation that apparently results in extremely high biological productivity. Regions such as this one are excellent examples of how carbon, fixed in a coastal upwelling system, is exported offshore. The highly productive fisheries suggest that much of the primary production makes its way to higher trophic levels, but it eventually must be deposited in slope and trench sediments. Examination of those sediments might yield new insights into coastal upwelling and carbon sequestration processes.

[47] The similarities and differences between this region and the California upwelling regions are striking. It seems that comparative studies would be enlightening.

PERGAMON

Deep-Sea Research I 47 (2002) 637–660

DEEP-SEA RESEARCH
PART I

www.elsevier.com/locate/dsr

Phytoplankton pigment and absorption characteristics along meridional transects in the Atlantic Ocean

R.G. Barlow[a,*], J. Aiken[b], P.M. Holligan[c], D.G. Cummings[b], S. Maritorena[d], S. Hooker[e]

[a] *Marine and Coastal Management, Private Bag X2, Rogge Bay 8012, Cape Town, South Africa*
[b] *Plymouth Marine Laboratory, Prospect Place, West Hoe, Plymouth PL1 3DH, UK*
[c] *Southampton Oceanography Centre, Empress Dock, Southampton SO14 3ZH, UK*
[d] *ICESS, University of California, Santa Barbara, CA, USA*
[e] *NASA Goddard Space Flight Centre, Greenbelt, MD 20771, USA*

Received 22 January 2001; received in revised form 12 September 2001; accepted 15 October 2001

Abstract

Pigment patterns and associated absorption properties of phytoplankton were investigated in the euphotic zone along two meridional transects in the Atlantic Ocean, between the UK and the Falkland Islands, and between South Africa and the UK. Total chlorophyll *a* (TChla = MVChla + DVChla + chlorophyllide *a*) concentrations and the biomarker pigments for diatoms (fucoxanthin), nanoflagellates and cyanobacteria (zeaxanthin) appeared to have similar distribution patterns in the spring and in the autumn in the temperate NE Atlantic and the northern oligotrophic gyre. Divinyl chlorophyll *a* levels (prochlorophytes) were greater in spring at the deep chlorophyll maximum in the oligotrophic gyre, however. Marked seasonal differences were observed in the NW African upwelling region. TChla concentrations were twice as high in the upper mixed layer in the spring, with the community dominated by diatoms and prymnesiophytes (19′-hexanoyloxyfucoxanthin). A layered structure was prevalent in the autumn where cyanobacteria, diatoms and prymnesiophytes were located in the upper water column and diatoms and mixed nanoflagellates at the sub-surface maximum. In the South Atlantic, the Benguela upwelling ecosystem and the Brazil-Falklands Current Confluence Zone (BFCCZ) were the most productive regions with the TChla levels being twice as high in the Benguela. Diatoms dominated the Benguela system, while nanoflagellates were the most ubiquitous group in the BFCCZ. Pigment concentrations were greater along the eastern boundary of the southern oligotrophic gyre and distributed at shallower depths. Deep chlorophyll maxima were a feature of the western boundary oligotrophic waters, and cyanobacteria tended to dominate the upper water column along both transects with a mixed group of nanoflagellates at the chlorophyll maximum.

Absorption coefficients were estimated from spectra reconstructed from pigment data. Although absorption was greater in the productive areas, the TChla-specific coefficients were higher in oligotrophic regions. In communities that were dominated by diatoms or nanoflagellates, pigment absorption was generally uniform with depth and attenuating irradiance, with TChla being the major absorbing pigment at 440 nm and photosynthetic carotenoids (PSC) at 490 nm. Absorption by chlorophyll *c* and photoprotective carotenoids (PPC) was much lower. Populations where cyanobacteria were prevalent were characterized by high PPC absorption, particularly at 490 nm, throughout most of the euphotic zone. The data suggested that the effect of pigments on the variability of phytoplankton absorption was due primarily to the variations in absorption by PPC. © 2002 Elsevier Science Ltd. All rights reserved.

1. Introduction

Spatially extensive investigations have been coordinated within the UK Atlantic Meridional Transect (AMT) programme with the purpose of improving our knowledge of biogeochemical processes, ecosystem dynamics and food webs across basin scales in the Atlantic Ocean (Aiken et al., 2000). One of the goals of the programme has been to examine and characterize the properties of biogeochemical provinces (Longhurst et al., 1995), and an objective method was developed to determine the boundaries of physical provinces (Hooker et al., 2000). Another objective has been to conduct ground-truthing measurements of optical and pigment parameters for the validation and calibration of SeaWiFS ocean colour data (Hooker and McClain, 2000). In this regard, the surface distribution pattern of pigments for

transects between the UK and the Falkland Islands was discussed by Gibb et al. (2000), and Barlow et al. (in press) have examined the bio-optical properties of surface pigments in relation to ocean colour data of absorption and back scattering for a transect between South Africa and the UK. Observations of the variability in the vertical distribution of phytoplankton pigments and associated absorption properties across Atlantic basins, however, have not yet been reported.

Total chlorophyll *a* (TChla), defined as the sum of MVChla, DVChla and chlorophyllide *a*, is used as a surrogate marker for the abundance of phytoplankton in the oceans, but other accessory pigments that can be identified and quantified by liquid chromatography (Jeffrey et al., 1997) provide chemotaxonomic information on the range of phytoplankton groups that make up the community structure in the Atlantic (Barlow et al., 1993, in press; Bidigare et al., 1990a; Gibb et al., 2000). The major role of chlorophyll *a* is to absorb light for photosynthesis, but there is also a range of pigments, such as, chlorophylls *b* and *c* plus a variety of carotenoids, that have a significant function in extending the light-harvesting spectrum in the phytoplankton, thus ensuring optimal absorption efficiencies (Kirk, 1994). Other carotenoids, however, serve to protect microalgal cells against the effects of high irradiances, which may damage the photosynthetic apparatus, and these pigments may be termed photoprotective carotenoids (PPC) (Kirk, 1994).

4. Discussion

4.1. Phytoplankton communities

The AMT cruises were essentially confined to investigating only the autumn and spring seasons in the Atlantic because of the logistical programme of the research vessel (Aiken et al., 2000). During AMT-3 (September–October 1996), it was autumn in the North Atlantic and spring in the south; for AMT-6 (May–June 1998), it was autumn in the South Atlantic and spring in the north. Thus, for the NE Atlantic, the two seasons can be compared because the cruise tracks were similar (Fig. 1). The cruise tracks in the southern hemisphere were on opposite sides of the South Atlantic basin, and therefore, the communities along the eastern and western boundaries could be compared, even though the observations were made in different seasons.

The phytoplankton in the temperate NE Atlantic and the northern oligotrophic gyre appeared to have similar characteristics for both the autumn and spring seasons. TChla levels were similar (Figs. 2 and 3) as well as the distribution pattern for diatoms (Fuc) and nanoflagellates (Hex + But + All + Chlb). Dinoflagellates (Per) were detected only in the upper water column on the European shelf during autumn (Fig. 2), but were virtually undetectable in the spring (Fig. 3). The cyanobacterial pattern (Zea) also appeared to be similar for both seasons, although the concentrations of divinyl chlorophyll *a* (prochlorophytes) were greater in the spring (AMT-6) at the deep chlorophyll maxima in the oligotrophic gyre (Figs. 2 and 3). The selected vertical profiles confirmed the observations of the contoured data, but provided more detail on subtle differences. The profiles for 49.68°N and 48.45°N indicated a more diverse nanoflagellate community in the temperate NE Atlantic during autumn (AMT-3) compared to the spring (AMT-6), with chlorophyll *b* being significant in autumn but not in the spring (Figs. 4 and 7). At 29.49°N and 28.68°N, both communities displayed a layered structure, typical of oligotrophic communities, where cyanobacteria (Zea) and prymnesiophytes (Hex) dominated the upper 80–100 m, and a group of mixed flagellates were abundant at the chlorophyll maximum and below (Figs. 4 and 7). Chlorophyll *b* was most prominent at the deep maximum during both seasons, and this was due to the increased synthesis of divinyl chlorophyll *b* in prochlorophyte cells at depth to maximize their absorption of low intensity blue light (Fig. 7, 28.68°N).

These observations are consistent with other studies in the North Atlantic. Bidigare et al. (1990a) and Barlow et al. (1993) reported diatom dominance during spring bloom investigations that were conducted early in the season, followed by a succession to nanoflagellates when key nutrients declined. The temperate NE Atlantic in June 1998 corresponded to the end of bloom conditions, so nanoflagellates were the dominant organisms. The phytoplankton pattern in the northern oligotrophic region appears to be consistent during all seasons, because a similar layering structure of pigments has been demonstrated in North Atlantic oligotrophic waters by Claustre and Marty (1995), Babin et al. (1996), Lazzara et al. (1996) and Goericke (1998). Barlow et al. (in press) and Gibb et al. (2000) estimated the contribution of divinyl chlorophyll *a* to TChla in the northern gyre can be up to 50% in surface waters, indicating the importance of prochlorophytes. Divinyl chlorophyll *a* concentrations in this study were greater at the subsurface maximum than at the surface, but accounted for similar proportions at 37–53% for AMT-3 and 31–50% for AMT-6.

Phytoplankton Productivity

Carbon Assimilation in Marine and Freshwater Ecosystems

Edited by

Peter J. le B. Williams,* David N. Thomas* and Colin S. Reynolds**

*School of Ocean Sciences, University of Wales, Bangor, UK
**Centre for Ecology and Hydrology, Windermere, UK

Blackwell
Science

Chapter 7

Assessment of Primary Production at the Global Scale

Michael J. Behrenfeld, Wayne E. Esaias and Kevin R. Turpie

7.1 Introduction

Since the evolution of the first photosynthetic organisms some 3.8 billion years before present (Schopf, 1983), photoautotrophic organisms and the communities they support have continuously altered the chemical composition of the oceans and, through exchange across the air–sea interface, influenced the composition of the overlying atmosphere. Variations in the concentration of radiatively sensitive gases in the atmosphere (e.g. CO_2, CH_4), in turn, influence global climate and consequently ocean circulation, stratification, and the transport of dust to remote ocean regions. These physical forcings govern spatio–temporal variability in phytoplankton distributions through the direct effect of temperature on growth and through their secondary influence on factors such as mixed-layer light availability and the distribution of macro- and micro-nutrients. Perhaps beyond any other observations, satellite measurements of global phytoplankton pigment concentrations have most clearly demonstrated this dependence of ocean productivity on physical processes.

Biogeochemical cycles in the oceans are clearly not in steady state (Falkowski *et al.*, 1998). Biological responses to global perturbations in the physical environment are delayed by the buffering effects of ecosystem complexity. An urgency to characterise such physical–biological feedbacks developed during the final decades of the twentieth century due to escalating public and scientific concerns that environmental impacts of human activities were transitioning from the local to the global scale. At the forefront of these emergent global issues is the potential for a change in climate resulting from rising atmospheric concentrations of carbon dioxide and other 'greenhouse' gases. Unquestionably, sequestration of CO_2 by the photosynthetic biosphere (land and oceans) will play a critical role in future climate trends, but quantifying this CO_2 exchange and its temporal sign remains an uncertainty in global climate models (GCMs).

The most accurately constrained carbon fluxes in GCMs are the release from fossil fuel combustion (presently, $5.5 \pm 0.5 \times 10^{15}$ g C y^{-1} = 5.5 petagrams (Pg) y^{-1}) and atmospheric CO_2 accumulation (3.3 ± 0.2 Pg C y^{-1}). Less well quantified is the

terrestrial carbon source from land-use change and deforestation, estimated at 1.6 ± 1.0 Pg C y^{-1} (Sarmiento and Wofsy, 1999). Thus, of the 7.1 Pg C released annually, 3.3 Pg C y^{-1} are retained in the atmosphere and the remaining 3.8 Pg C are removed both abiotically and through photosynthetic fixation. Based on ≈ 2 million measurements of the partial pressure of CO_2 over the oceans (pCO_2) collected across 25 years, the annual oceanic sink for CO_2 has been estimated at 2.0 ± 0.8 Pg C (Sarmiento and Wofsy, 1999). Balancing the global CO_2 budget thus requires an additional sink of 1.8 ± 1.6 Pg C y^{-1}. This 'missing sink' is assumed to involve the biosphere and likely entails both oceanic and terrestrial components. Partitioning of the unaccounted carbon between the land and oceans is difficult, however, because it represents less than 2% of biospheric net primary production, estimated at 111–117 Pg C y^{-1} (Behrenfeld *et al.* 2001a).

7.6 Summary

Primary productivity models, when coupled with time-varying global measurements of phytoplankton biomass, provide critical information for detecting changes in oceanic carbon fluxes. Such models are also beneficial for assessing ecological responses to regional changes in nutrient loading and may provide estimates of biologically mediated long-term carbon sinks if linked to secondary models of export production. The foundation of both aquatic and terrestrial NPP models is similar and, in the simplest terms, can be described as equating NPP to the product of plant biomass and light utilisation efficiency. From this basic relationship, a wide variety of phytoplankton productivity models have developed. At the categorical level, these models differ with respect to the presumed importance of resolving the time, depth, and spectral dependence of photosynthesis. Within each model category, differences largely centre around the specific treatment of the photosynthesis–irradiance relationship and in the characterisation of the underwater light field.

In this chapter, we have attempted to describe the relationship between various NPP models and the assumptions required to progress from fully expanded WRMs to the very simple DIMs. We have argued that all global estimates of NPP are critically dependent on the approach employed for modelling light-saturated photosynthesis and demonstrated this conclusion using two temperature-dependent models and a new light-nutrient model. This later model produces ΣNPP estimates comparable with local-scale, daily ^{14}C-uptake results. Although the model was applied to global satellite C_{sat} data using a simple DIM formulation, its description at the level of chlorophyll synthesis and Calvin cycle reactions is ideally suited for application in a WRM. The primary advantage of using a spectrally resolved model will be the improved estimates of mixed-layer acclimation irradiances, which are a primary forcing factor for variability in P^b_{max}.

Over the 50 year history of productivity modelling, significant advances have been made toward assessing global-scale phytoplankton photosynthesis. Noteworthy accomplishments include the development of variable P^b_{max} models; characterisation of the underwater light field; description of vertical variability in phytoplankton biomass distributions, and the development of remote sensing capabilities that now provide global measurements of near-surface chlorophyll every two days. These achievements notwithstanding, we hope our discussion has impressed upon the reader the need for further improvements in primary productivity modelling. These improvements will require laboratory, field, computational and remote sensing components, all of which represent exciting challenges for future research programmes.

Vol. 228: 103–117, 2002 | MARINE ECOLOGY PROGRESS SERIES Mar Ecol Prog Ser | Published March 6

Photoacclimation and nutrient-based model of light-saturated photosynthesis for quantifying oceanic primary production

Michael J. Behrenfeld[1,*], Emilio Marañón[2], David A. Siegel[3], Stanford B. Hooker[1]

[1]National Aeronautics and Space Administration, Goddard Space Flight Center, Code 971, Building 33, Greenbelt, Maryland 20771, USA
[2]Departamento de Ecología y Biología Animal, Universidad de Vigo, 36200 Vigo, Spain
[3]Institute for Computational Earth System Science, University of California Santa Barbara, Santa Barbara, California 93106-3060, USA

ABSTRACT: Availability of remotely sensed phytoplankton biomass fields has greatly advanced primary production modeling efforts. However, conversion of near-surface chlorophyll concentrations to carbon fixation rates has been hindered by uncertainties in modeling light-saturated photosynthesis (P^{b}_{max}). Here, we introduce a physiologically-based model for P^{b}_{max} that focuses on the effects of photoacclimation and nutrient limitation on relative changes in cellular chlorophyll and CO_2 fixation capacities. This 'PhotoAcc' model describes P^{b}_{max} as a function of light level at the bottom of the mixed layer or at the depth of interest below the mixed layer. Nutrient status is assessed from the relationship between mixed layer and nutricline depths. Temperature is assumed to have no direct influence on P^{b}_{max} above 5°C. The PhotoAcc model was parameterized using photosynthesis-irradiance observations made from extended transects across the Atlantic Ocean. Model performance was validated independently using time-series observations from the Sargasso Sea. The PhotoAcc model accounted for 70 to 80% of the variance in light-saturated photosynthesis. Previously described temperature-dependent models did not account for a significant fraction of the variance in P^{b}_{max} for our test data sets.

KEY WORDS: Photosynthesis · Modeling · Primary production

INTRODUCTION

Photosynthesis is a fundamental process of nearly all known ecosystems, such that the level of photoautotrophic carbon fixation supported by a given environment broadly dictates the local biomass of subsequent trophic levels and the biogeochemical exchange of elements between systems. Models of biospheric primary production have been greatly aided by global-scale satellite observations (Field et al. 1998), but conversion of measured plant biomass to net photosynthesis has remained problematic. Whereas terrestrial productivity models suffer from a lack of observational data for parameterization and testing (Field et al. 1998), high-sensitivity measurements of net primary production in aquatic systems have been routine since the introduction of the ^{14}C method by Steemann Nielsen (1952).

Analyses of vertical profiles of phytoplankton photosynthesis revealed early on that, when normalized to depth-specific chlorophyll concentrations, primary production can be modeled to first order simply as a function of subsurface irradiance (Ryther 1956, Ryther & Yentsch 1957, Talling 1957). A variety of analytical expressions have consequently been developed de-

scribing this relationship between vertical light attenuation and chlorophyll-normalized carbon fixation (reviewed by Platt & Sathyendranath 1993, Behrenfeld & Falkowski 1997b). Such models can account for most of the observed variance in depth-integrated photosynthesis (ΣPP), particularly when measurements encompass a wide phytoplankton biomass range, provided model input includes measured values for: (1) the vertical distribution of chlorophyll, (2) the downwelling attenuation coefficient (K_d) for photosynthetically active radiation (PAR), and (3) the maximum carbon fixation rate per unit of chlorophyll (P^b_{opt}) (Behrenfeld & Falkowski 1997a,b).

For over 40 yr, developments in phytoplankton primary production models have focused on refining characterizations of the above 3 critical water-column features, with clearly the greatest achievements realized in the description of the underwater light field (e.g. Platt & Sathyendranath 1988, Morel 1991, Antoine et al. 1996). Progress has also been made in predicting vertical profiles of chlorophyll (Platt & Sathyendranath 1988, Morel & Berthon 1989), but models of P^b_{opt} have remained rudimentary and inconsistent (Behrenfeld & Falkowski 1997b). The importance of accurate P^b_{opt} estimates cannot be overstated, especially when model performance is evaluated by comparison with point-source field observations. For globally representative data sets, phytoplankton biomass alone accounts for <40% of ΣPP variability, while inclusion of measured P^b_{opt} values can account for >80% of the variance in ΣPP (Balch & Byrne 1994, Behrenfeld & Falkowski 1997a). In oligotrophic regions where the range in chlorophyll concentration is further constrained, accurate estimates of P^b_{opt} are even more critical (Banse & Yong 1990, Siegel et al. 2000).

The function of P^b_{opt} models is to capture spatial and temporal changes in assimilation efficiencies (i.e. carbon fixed per unit of chlorophyll) resulting from physiological acclimation to environmental variability. Currently, the 2 principal approaches for estimating P^b_{opt} in regional- to global-scale models are: (1) to assign fixed, climatological values to biogeographical provinces (Longhurst 1995, Longhurst et al. 1995), and (2) to define predictive relationships between P^b_{opt} and 1 or more environmental variables (e.g. temperature, nutrient concentration) (Megard 1972, Balch et al. 1992, Antoine et al. 1996, Behrenfeld & Falkowski 1997a). Both techniques have advantages, but differ in their intended application. For example, the first approach furnishes broad-scale average values for designated regions and is not intended to accurately reproduce the much finer scale physiological variability in ^{14}C-uptake rates corresponding to a given day, depth and location. As for the second approach, an effective model should, ideally, provide P^b_{opt} estimates comparable at this point-source scale of field measurements, but a successful model of this genre has not yet been described.

Here we introduce a model, belonging to this second category, that captures P^b_{opt} variability in natural phytoplankton assemblages. The model largely focuses on changes in P^b_{opt} resulting from photoacclimation and is thus referred to as the 'PhotoAcc Model', although a nutrient-dependence is also prescribed. In the following section, we describe the conceptual basis and underlying equations of the PhotoAcc model, the field data used for model parameterization and testing, and our approach to assessing nutrient status and photoacclimation irradiances. Model limitations, directions for expansion, and potential avenues for global implementation are addressed in the section 'Discussion'.

DISCUSSION

The importance of effectively modeling light-saturated photosynthesis at the difficult local scale of daily primary production measurements has been recognized for over 40 yr (Ryther 1956, Ryther & Yentsch 1957). The most common approach to this problem has been to describe P^b_{opt} as a function of temperature. Such models capture only a fraction of the observed variability in P^b_{opt}, because temperature is weakly correlated with causative environmental forcing factors. In contrast, the PhotoAcc model attempts to explicitly describe primary causative relationships at the level of chlorophyll synthesis and changes in the Calvin cycle capacity. With this approach, the model effectively reproduced spatial and temporal variability in light-saturated photosynthesis for the AMT and BATS studies. These field programs do not, however, fully encompass global nutrient, light, and temperature conditions. In the following sections, we evaluate the predictions and hypotheses of the PhotoAcc model, discuss potential alterations to account for additional growth constraints, and propose avenues for global implementation.

Decadal changes in global ocean chlorophyll

Watson W. Gregg
Laboratory for Hydrospheric Processes, NASA/Goddard Space Flight Center, Greenbelt, Maryland, USA

Margarita E. Conkright
Ocean Climate Laboratory, NOAA/National Oceanographic Data Center, Silver Spring, Maryland, USA

Received 8 January 2002; accepted 24 April 2002; published 7 August 2002.

[1] The global ocean chlorophyll archive produced by the CZCS was revised using compatible algorithms with SeaWiFS. Both archives were then blended with in situ data to reduce residual errors. This methodology permitted a quantitative comparison of decadal changes in global ocean chlorophyll from the CZCS (1979–1986) and SeaWiFS (1997–2000) records. Global spatial distributions and seasonal variability of ocean chlorophyll were similar, but global means decreased over the two observational segments. Major changes were observed regionally: chlorophyll concentrations decreased in the northern high latitudes while chlorophyll in the low latitudes increased. Mid-ocean gyres exhibited limited changes. The overall spatial and seasonal similarity of the two data records suggests that the changes are due to natural variability. These results provide evidence of how the Earth's climate may be changing and how ocean biota respond. *INDEX TERMS:* 1620 Global Change: Climate dynamics (3309); 4805 Oceanography: Biological and Chemical: Biogeochemical cycles (1615); 4215 Oceanography: General: Climate and interannual variability (3309); 1635 Global Change: Oceans (4203); 4275 Oceanography: General: Remote sensing and electromagnetic processes (0689)

1. Introduction

[2] The Sea-viewing Wide Field-of-view Sensor (SeaWiFS) has produced the first multi-year time series of global ocean chlorophyll observations since the demise of the Coastal Zone Color Scanner (CZCS) in 1986. Global observations from 1997–2000 by SeaWiFS combined with observations from 1979–1986 by the CZCS should in principle provide an opportunity to observe decadal changes in global ocean chlorophyll. However, incompatibilities between algorithms have so far precluded quantitative analysis. We have developed and applied compatible processing methods for the CZCS [*Gregg et al.*, 2002], using recent advances in atmospheric correction and consistent bio-optical algorithms to enhance the CZCS archive to comparable quality with SeaWiFS. Even with careful application of modern methodologies, there remain residual errors deriving from assumptions of atmospheric and oceanic optical behavior. We applied blending methodologies [*Gregg and Conkright*, 2001], where in situ data observations are merged with the satellite data, to reduce residual errors. These re-analyzed, blended data records provide maximum compatibility and permit, for the first time, a quantitative analysis of the changes in global ocean chlorophyll from the early-to-mid 1980's to the present.

2. Methods

[3] Reanalyzed CZCS chlorophyll data (Jan 1979–Jun 1986) [*Gregg et al.*, 2002] and Version 3 SeaWiFS data (Sep 1997–Dec 2000) were averaged to produce seasonal means at 1° spatial resolution, and were then blended with in situ chlorophyll data [*Gregg and Conkright*, 2001]. In statistical analyses of these data sets, we excluded comparisons in the North Pacific, North Atlantic, and Antarctic basins poleward of 40° in local autumn and winter, because of sparse sampling by the CZCS. These were the only places and times when the lower density sampling of the CZCS was important in the comparison. Basin and global means were areally-weighted for both satellite data sets and only co-located observations were used, to further minimize problems associated with low sampling density by the CZCS. Coastal observations (where bottom depth $\leq$200 m) were excluded from the analysis.

[4] Sea surface temperature (SST) and surface mean wind stress data were obtained from the NOAA/National Center for Environmental Prediction (NCEP) Reanalysis Project. The data were averaged over the two observational segments corresponding to the CZCS and SeaWiFS. Only data co-located with the ocean color data were used in the means.

3. Global and Basin Scale Decadal Changes in Blended Ocean Chlorophyll

[5] Blended satellite/in situ observations indicated that global ocean chlorophyll has decreased since the CZCS data record (Table 1). The decreases ranged from about 9% in autumn (Oct–Dec) to nearly 11% in summer (Jul–Sep). No significant change was observed in winter (Jan–Mar) or spring (Apr–Jun). Seasonal temporal patterns between the blended satellite chlorophyll records were similar, indicating a global maximum in spring/summer and a minimum in winter/autumn. The annual mean global change was −6.1% from the early 1980's to the present.

[6] Much of the global decrease was due to changes in the high latitudes (Figure 1). Blended SeaWiFS data were more than 10% lower than blended CZCS in the North Pacific and Atlantic basins in summer (Figure 1). The southern mid-ocean basins, South Indian, South Pacific, and South Atlantic, all exhibited significant decreases in blended chlorophyll in spring and summer, to nearly 28% in the South Pacific.

Table 1. Global ocean chlorophyll concentrations (mg m^{-}) and standard deviations from the blended CZCS record (1979–1986) and the modern blended SeaWiFS record (1997–2000), and the percent change (SeaWiFS-CZCS). *An asterisk indicates statistical significance at P < 0.05.

	Winter (Jan–Mar)	Spring (Apr–Jun)	Summer (Jul–Sep)	Autumn (Oct–Dec)
CZCS	0.232±0.359	0.250±0.402	0.288±0.431	0.242±0.412
SeaWiFS	0.225±0.309	0.245±0.375	0.257±0.347	0.221±0.296
% difference	−2.8	−2.1	−10.7*	−8.6*

compatibility. The analysis of the two chlorophyll records indicated large similarity in the global spatial distributions and seasonal variability. This included the extent and spatial structure of the mid-ocean gyres, the equatorial upwelling regions, and the bloom-recede dynamics of the high latitudes. There were also many decadal changes indicated in the analysis of the archives. Global chlorophyll concentrations indicated a decrease from the CZCS record to the present, of about −6%. Larger reductions occurred in the northern high latitudes. Conversely, chlorophyll in the low

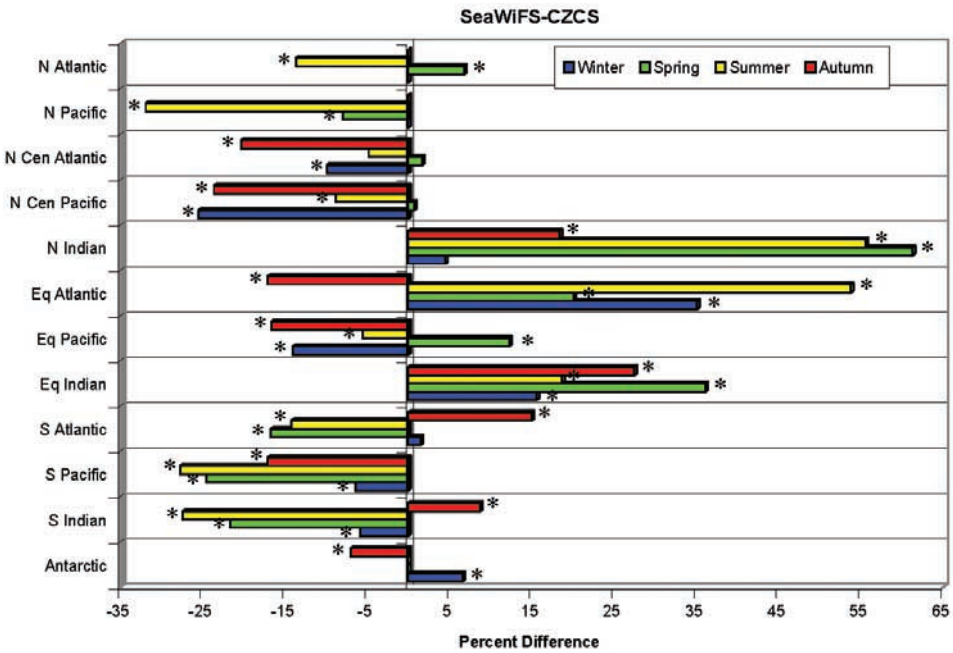

Figure 1. Seasonal differences between blended SeaWiFS and blended CZCS chlorophyll in the 12 major oceanographic basins [*Gregg et al.*, 2002]. Equatorial basins are between −10° and 10° latitude, the North Pacific and North Atlantic are north of 40°, and Antarctic is south of −40°. The other basins fall within these limits. Differences are expressed as blended SeaWiFS-blended CZCS. An asterisk indicates the difference is statistically significant at P < 0.05.

[7] The low latitude oceanographic basins, in contrast, generally exhibited an increase in chlorophyll from the CZCS period (Figure 1). Three of these basins (North Indian, Equatorial Indian, Equatorial Atlantic) showed major increases for the blended SeaWiFS. An exception was the equatorial Pacific in winter, summer, and autumn.

5. Summary

[17] The CZCS global ocean chlorophyll archive was reanalyzed using compatible atmospheric correction and bio-optical algorithms with SeaWiFS. This permitted, for the first time, a quantitative comparison of the decadal trends in global ocean chlorophyll from 1979- mid-1986 to the present (Sep 1997–Dec 2000). Blending of both archives with available coincident in situ data improved the residual errors of each data record and provided further latitudes increased. Mid-ocean gyres exhibited limited changes. These results may indicate facets of climate change, some of which may be related to regional oscillation behavior such as the PDO and ENSO. Some of the decadal changes can be attributed to observed changes in SST or meteorological forcing, but some cannot. We believe that this reanalysis of the CZCS and SeaWiFS archives enables identification of some aspects of decadal change, and provides a marker of how the Earth's climate may be changing and how ocean biota respond.

CLIMATE VARIABILITY AND PREDICTION

Climate variability and prediction is a central scientific theme within NASA's Earth Science Program. To understand climate variability, an integrated program of observations and modeling of air-sea-ice interactions and their feedbacks are required. The following professional papers for the year 2002 by the NASA researchers have spanned the entire globe with special focus on the poles as harbingers of climate change.

The Greenland and Antarctic ice sheets with their massive ice sheets are of especial interest for climate change and societal impact. Bindschadler and Bentley note that the West Antarctic ice sheet contains more than three million cubic kilometers of fresh water. Previously it had been thought that this ice sheet was in a stage of rapid collapse which could raise global sea level five meters with major societal effect. However, it now appears that the ice sheet is shrinking more slowly than originally suspected and thus a sea level rise of half a meter during the next century is more likely, still a fact for planners to anticipate. Obviously temperature in the Antarctic region will be crucial for prediction of ice melt. Shuman and Comiso have studied data from in situ weather stations with AVRR and SSM/I satellite data to determine how best to use NASA satellite to observe regional small temperature changes. This study has enabled an improved understanding of the three available data sets. At present, the thermal infrared data provide the only spatially detailed temperature distributions in Antarctica, but contain data gaps due to intermittent cloud cover. The passive-microwave data have the potential to provide spatially detailed, continuous and gap-free temperature distributions; however calibrations with weather station data requires more work.

Sea ice is an indicator of global change as its extent and volume reflect temperature changes in both the surface and water column. Zwally et al. analyzed passive microwave observations to study the variability of Antarctic sea ice from 1979 to 1998. They show that in recent decades the sea ice cover has varied significantly from year to year with some anomalies persisting for periods of 3-5 years. Over the 20 year study period, the entire sea ice pack increased about 11,180 km2. The largest increase was in the autumn ice cover, but there was significant regional variability. Parkinson in a related study analyzed the length of the southern sea ice season for the same time period showing an overall lengthening of the sea ice season with significant spatial variability. Specifically, most of the Ross Sea ice cover has undergone a lengthening of the season; whereas most of the Amundson Sea ice cover and almost all the Bellinghausen Sea ice cover has undergone a shortening of the sea ice season, and the Weddell Sea is mixed. Two papers by Kwok and Comiso analyzed the spatial patterns of temperature over both the Antarctic continent and the adjacent ocean. Their data revealed a 17-year (1982-1998) cooling over the continent and a warming of the sea-ice zone, but moderate changes over the oceans. As expected the warming of the seas is in regions where sea ice is shrinking as noted by Parkinson. Kwok and Comiso relate the effects of the Southern Hemisphere Annular Mode (SAM) and the extra-polar Southern Oscillation (SO) on surface temperature through regression analysis. Positive polarities of the SAM are associated with cold anomalies over most of Antarctic, with the most notable exception of the Antarctic Peninsula. Positive temperature anomalies and the ice edge retreat in the Pacific sector are shown to be associated with El-Nino episodes.

The Arctic Ocean is the smallest of the Earth's oceans and unlike Antarctica is surrounded by land-masses. Its temperature, salinity and ice cover have all undergone changes in the past several decades. As Parkinson notes it is uncertain whether these reflect long-term changes or oscillations within the system. Parkinson and Cavalieri have documented 2.7 km2 per decade reduction in sea ice extent from satellite passive-microwave data (1979-1999). These negative trends are statistically significant at a 99% confidence level. Comiso in two papers made use of simultaneous satellite sea-ice concentration and surface data to gain insight into the changing Arctic climate. In general sea ice extent has been declining at a rate 2.3% per decade while surface temperature has increased by 0.4 K per decade. If this continues, it means that the multi-year sea ice will disappear during this century.

To extract significant information from varied climate data, Vinnikov et al have developed a new statistical approach to analyze climatic data that explicitly accepts the idea that long-term climatic records contain trends in means, variances, covariances and other moments of statistical distribution of meteorological variables. This approach will provide better analysis of past climate change and climatic model output of existing data.

Another statistical approach was presented by Chen et al. to address the feasibility of using collocated wind speed and significant wave height measurements from simultaneous scatterometer and altimeter to observe the spatial and seasonal pattern of dominant swell and wind waves in the world's oceans. Knowledge of these parameters on a global basis is generally poor. Based on this method they found swell dominance in the eastern tropical areas of the Pacific, the Atlantic and Indian Oceans; wave growth areas are the northwest Pacific, Atlantic, the Southern Ocean and Mediterranean.

On a more local scale and closer to GSFC, Foster describes the recent spate of tornados in Maryland in comparison to previous occurrences of extreme weather events. These are attributed to an energetic cold front acting as a triggering mechanism for tornado formation when a large area of moisture is surging north from the Gulf of Mexico and a vigorous jet stream is positioned overhead.

On Thin Ice?

BY ROBERT A. BINDSCHADLER AND CHARLES R. BENTLEY

Twelve thousand years ago, as the earth emerged from the last ice age,

vast armadas of *Titanic*-size icebergs invaded the North Atlantic. Purged vigorously from the enormous ice sheets that smothered half of North America and Europe at the time, those icebergs displaced enough water to raise global sea level more than a meter a year for decades.

As the frozen north melted, the ice gripping the planet's southernmost continent remained essentially intact and now represents 90 percent of the earth's solid water. But dozens of scientific studies conducted over the past 30 years have warned that the ice blanketing West Antarctica—the part lying mainly in the Western Hemisphere—could repeat the dramatic acts of its northern cousins. Holding more than three million cubic kilometers of freshwater in its frozen clutches, this ice sheet would raise global sea level five meters (about 16 feet) if it were to disintegrate completely, swamping myriad coastal lowlands and forcing many of their two billion inhabitants to retreat inland.

Most Antarctic scientists have long concurred that the continent's ice has shrunk in the past, contributing to a rise in sea level that continued even after the northern ice sheets were gone. The experts also agree that the ice covering the eastern side of the continent is remarkably stable relative to that in West Antarctica, where critical differences in the underlying terrain make it inherently more erratic. But until quite recently, they disagreed over the likelihood of a catastrophic breakup of the western ice sheet in the near future. Many, including one of us (Bindschadler), worried that streams of ice flowing from the continent's interior toward the Ross Sea might undermine the sheet's integrity, leading to its total collapse in a few centuries or less. Others (including Bentley) pointed to the sheet's recent persistence, concluding that the sheet is reasonably stable.

For a time it seemed the debate might never be resolved. Agreement was hampered by scant data and the challenge of studying a continent shrouded half the year in frigid darkness. In addition, although areas of the ice sheet have drained quickly in the past, it is difficult to determine whether changes in the size or speed of the ice seen today are a reflection of normal variability or the start of a dangerous trend. In the past few years, though, a variety of field and laboratory studies have yielded a growing consensus on the forces controlling West Antarctica's future, leading experts in both camps to conclude that the ice streams pointing toward the Ross Sea are not currently as threatening as some of us had feared.

We remain puzzled, however, over the ice sheet's ultimate fate. New studies have revealed thinning ice in a long-neglected sector of West Antarctica, suggesting that a destructive process other than ice streams is operating there. And another region—the peninsula that forms Antarctica's northernmost arm—has recently experienced warmer summer temperatures that are almost certainly the reason behind an ongoing breakup of ice along its coasts.

Around the world temperatures have risen gradually since the end of the last ice age, but the trend has accelerated markedly since the mid-1990s with the increase of heat-trapping greenhouse gases in the atmosphere. So far the peninsula seems to be the only part of Antarctica where this recent climate trend has left its mark; average temperatures elsewhere have risen less or even cooled slightly in the past 50 years. Researchers are now scrambling to determine whether global warming is poised to gain a broader foothold at the bottom of the world.

Overview/*Antarctic Ice*

- For nearly three decades, numerous Antarctic experts warned that West Antarctica's ice sheet is in the midst of a rapid disintegration that could raise global sea level five meters in a few centuries or less.
- Many of those researchers now think that the ice sheet is shrinking much more slowly than they originally suspected and that sea level is more likely to rise half a meter or less in the next century.
- That consensus is not without its caveats. The ice sheet's poorly understood Amundsen sector now appears to be shrinking faster than previously thought.
- Global warming, which has so far played a negligible role in West Antarctica's fate, is bound to wield greater influence in the future.

Early Alarms

INDICATIONS THAT the West Antarctic ice sheet might be in the midst of a vanishing act first began cropping up about 30 years ago. In 1974 Johannes Weert-

PAST, PRESENT AND FUTURE?

ANTARCTICA'S THICK BLANKET OF ICE (*below*) has been contracting, mostly gradually but sometimes swiftly, since the height of the last ice age, 20,000 years ago. The greatest reduction has occurred in West Antarctica, where the ice sheet is considerably more fragile than its counterpart in the east. Because the western sheet has changed quickly in the past, scientists have been unsure whether recent dramatic ice losses reflect normal variability or the start of an ominous trend toward total collapse. In the wake of a catastrophic collapse, rapidly rising seas would flood coastal communities around the world. *—R.A.B. and C.R.B.*

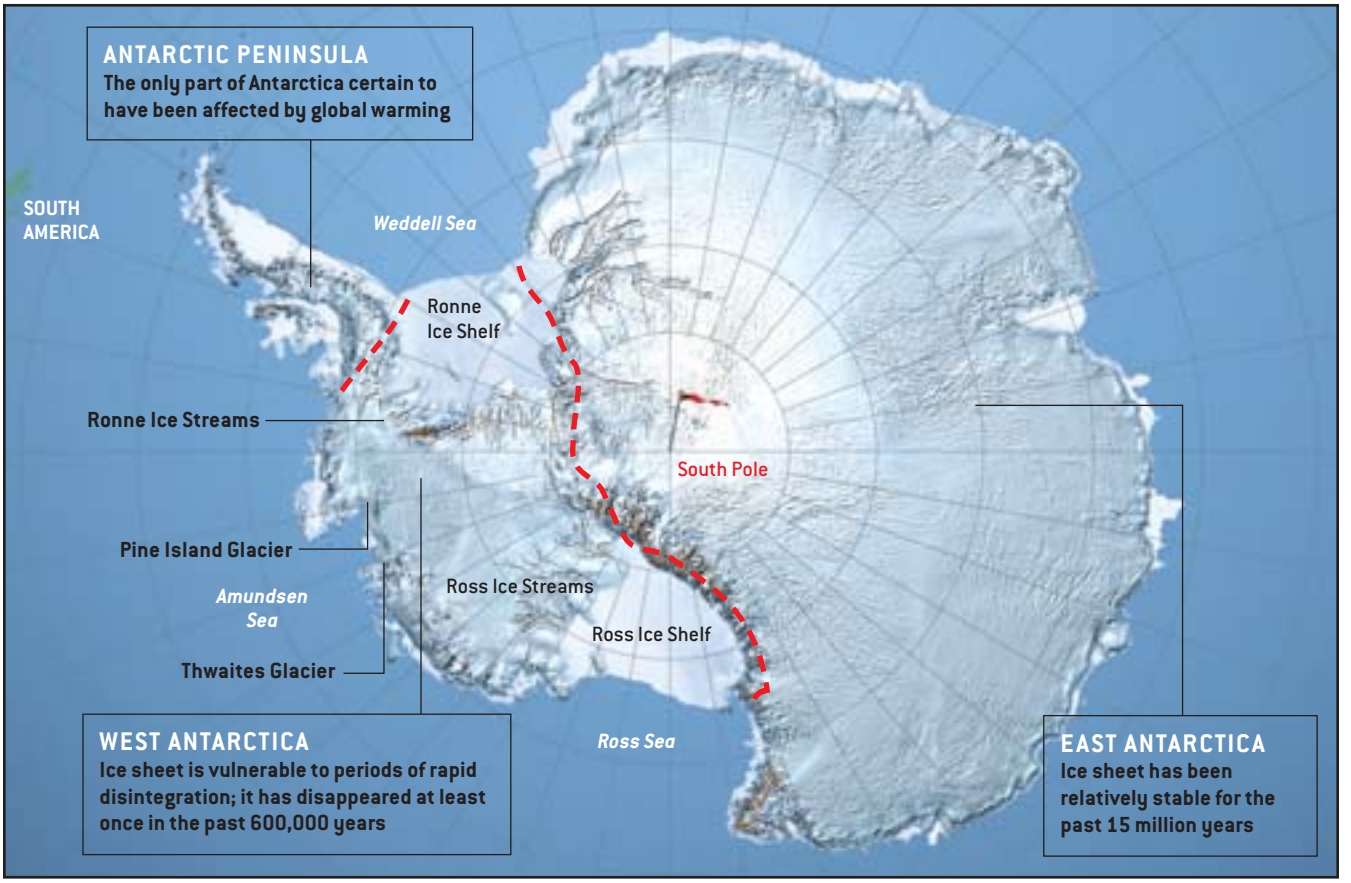

SHEDDING AND SHRINKING

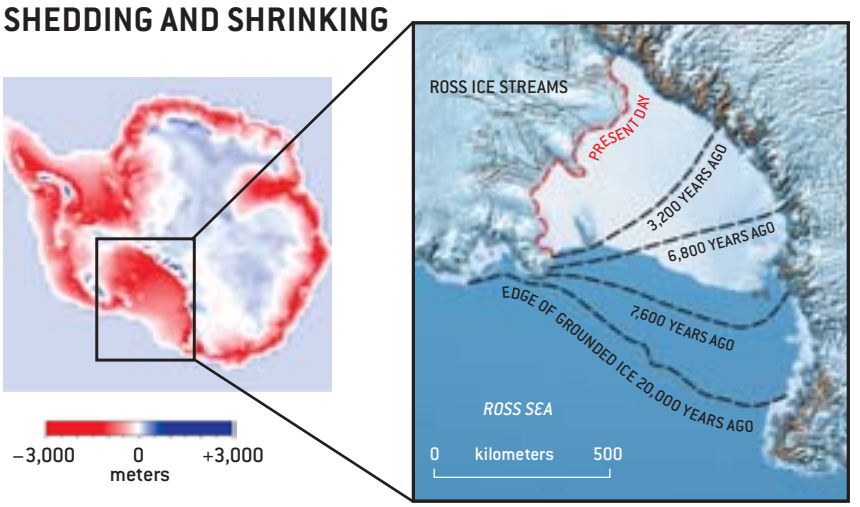

CHANGE IN ICE THICKNESS since the last ice age (*above left*) translates into a loss (*red*) of about 5.3 million cubic kilometers, much of it from West Antarctica. The ice sheet's grounded edge, that reaching the seafloor, has shrunk particularly rapidly in the Ross Sea (*detail, right*) over the past 7,000 years, retreating some 700 kilometers inland.

THE WORST-CASE SCENARIO

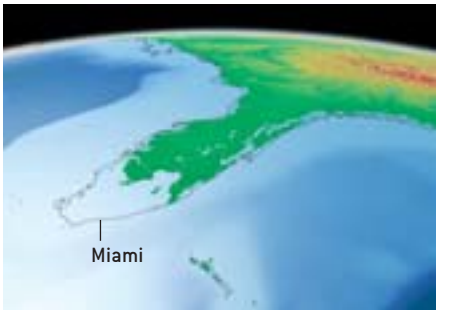

COMPLETE COLLAPSE of West Antarctica's ice sheet would raise sea level five meters. Among the casualties would be southern Florida (*above*), where about a third of the famous peninsula would disappear underwater. Today West Antarctica contributes about 10 percent of the average sea-level rise of two millimeters a year.

DAVID FIERSTEIN (*main Antarctica map and Ross Ice Shelf map*); ROBERT A. BINDSCHADLER (*ice thickness map*); WILLIAM F. HAXBY (*Florida map*)

A Global View of Swell and Wind Sea Climate in the Ocean by Satellite Altimeter and Scatterometer

GE CHEN

Ocean Remote Sensing Institute, Ocean University of Qingdao, Qingdao, China

BERTRAND CHAPRON AND ROBERT EZRATY

Département d'Océanographie Spatiale, Centre de Brest, IFREMER, Plouzane, France

DOUGLAS VANDEMARK

Wallops Flight Facility, NASA Goddard Space Flight Center, Wallops Island, Virginia

(Manuscript received 8 August 2001, in final form 18 February 2002)

ABSTRACT

Numerous case reports and regional studies on swell and wind sea events have been documented during the past century. The global picture of these common oceanic phenomena, however, is still incomplete in many aspects. This paper presents a feasibility study of using collocated wind speed and significant wave height measurements from simultaneous satellite scatterometer and altimeter sources to observe the spatial and seasonal pattern of dominant swell and wind wave zones in the world's oceans. Two energy-related normalized indices are proposed, on the basis of which global statistics of swell/wind sea probabilities and intensities are obtained. It is found that three well-defined tongue-shaped zones of swell dominance, termed ''swell pools,'' are located in the eastern tropical areas of the Pacific, the Atlantic, and the Indian Oceans, respectively. Regions of intensive wave growth are observed in the northwest Pacific, the northwest Atlantic, the Southern Ocean, and the Mediterranean Sea. Seasonality is distinct for the climate of both swell and wind sea, notably the large-scale northward bending of the swell pools in boreal summer, and the dramatic shift of wave-growing extent from a summer low to an autumn high. The results of this study may serve as a useful reference for a variety of activities, such as ocean wave modeling, satellite algorithm validation, coastal engineering, and ship routing, when information on swell and wind sea conditions is needed.

1. Introduction

Waves are one of the most fundamental and ubiquitous phenomena present at the air–sea interface. Since the spectrum of ocean waves is continuous and infinite, they are likely to cover a wide range of frequency and wavelength. The dominant portion of the wave spectrum in terms of energy is known to be associated with gravity waves whose period ranges from 1 to 30 s [see, e.g., Figs. 1.2–1 of Kinsman (1965)]. Therefore it comes as no surprise that a majority of ocean wave studies are devoted to gravity waves.

Two main classes of gravity waves exist in the ocean, namely, the so-called wind wave (or wind sea when emphasizing its state) and swell. The former refers to young waves under growth or in equilibrium with local wind, while the latter is defined as waves generated elsewhere and propagating over large distances. As a rule of thumb, a period of 10 s may be taken as separating swell from wind wave (Kinsman 1965). Because of the different dynamics involved, studies on swell and wind wave usually have different motivations and concerns. Swell is of increasing concern because of its potentially destructive consequences on coastal structures and sea-going activities (Mettlach et al. 1994). For example, in October 1987 nine elementary school children were drowned by the sudden arrival of a typhoon-generated swell hitting the Mau-Pi-Tou coast of Taiwan (Liang 1990). On the other hand, wind wave with a fetch up to an equilibrium state is of particular importance for the development and verification of wave models. Many previous studies, both theoretical and experimental, have been carried out in this regard (e.g., Pierson and Moskowitz 1964; Hasselmann et al. 1973; Hasselmann et al. 1988; Kahma 1981; Ewing and Laing 1987; Ebuchi et al. 1992).

In view of the different natures and impacts of swell and wind sea, a global knowledge of each individual process in terms of its frequency of occurrence and associated energy is highly desirable. This can be quickly understood by examining the prerequisites of the two categories of studies outlined above. Analysis of swell energy and prediction of its propagation would obviously benefit from a zero-wind condition. On the other hand, a wind-wave-related investigation always seeks an ideal sea state with no swell presence, especially when time and site have to be determined or selected for a field experiment. Despite their different dynamics,

Corresponding author address: Dr. Ge Chen, Ocean Remote Sensing Institute, Ocean University of Qingdao, 5 Yushan Road, Qingdao 266003, China.
E-mail: gechen@public.qd.sd.cn

swell and wind sea often overlap in wave characteristics. Moreover, they are usually a complex mixture at a given location. This sometimes makes it difficult to separate the two phenomena in real observations. In this study, taking the advantage of the newly available simultaneous measurements from National Aeronautics and Space Administration (NASA) satellite sensors, the TOPEX altimeter and the NSCAT and QuikSCAT (hereinafter abbreviated as QSCAT) scatterometers, an energy-based scheme is proposed to estimate the respective degree of swell and wind wave for each collocation site (section 2), on the basis of which global maps of swell and wind sea climate are produced and analyzed (sections 3 and 4). Finally, major swell and wind wave zones in the world's oceans are discussed and summarized (section 5).

2. Data and scheme

a. Wind–wave relation

According to wave forecasting models, sea surface wind speed and significant wave height follow a monotonical relationship under a growing sea up to the fully developed stage. This final stage is usually reached when the phase velocity corresponding to the dominant peak wave slightly exceeds the wind speed. The significant wave heights for fully developed seas were proposed by various authors, for example, Sverdrup and Munk (1947), Neumann (see Kinsman 1965), Pierson and Moskowitz (1964), Ewing and Laing (1987), and Hasselmann et al. (1988). Among these relationships, the Wave Model (WAM)-derived expression is found to have an intermediate overall growth rate for wind speed ranging from 0 to 30 m s^{-1} (see Pierson 1991), and is therefore chosen for our analysis.

Based on the WAM model (Hasselmann et al. 1988), the wind–wave relation for fully developed seas can be expressed as

$$H = 1.614 \times 10^{-2} U^2 \qquad (0 \le U \le 7.5 \text{ m s}^{-1}) \tag{1a}$$

$$H = 10^{-2} U^2 + 8.134 \times 10^{-4} U^3 \qquad (7.5 \text{ m s}^{-1} < U \le 50 \text{ m s}^{-1}), \tag{1b}$$

where U (in m s^{-1}) is the wind speed at 10-m height, and H (in m) is the significant wave height (Pierson 1991). A graphic illustration of Eq. (1) is shown in Fig. 1 (the thick curve), along with coincident measurements of wind speed from NSCAT/QSCAT and significant wave height from TOPEX (see section 2b). The Pierson and Moskowitz (1964) and the Ewing and Laing (1987) wind–wave relations are also included in Fig. 1 for reference. A direct implication of this graph is that the fully developed relationship may be used as a dividing line for sea state maturity: Measurements lying below the curve are mostly from a growing sea, while those above the curve are probably swell dominated. Of course this inference is not supposed to be valid in an absolute sense due to the complexity of the wind wave–swell coupling. But it is expected to give a meaningful classification of the two regimes from a statistical point of view.

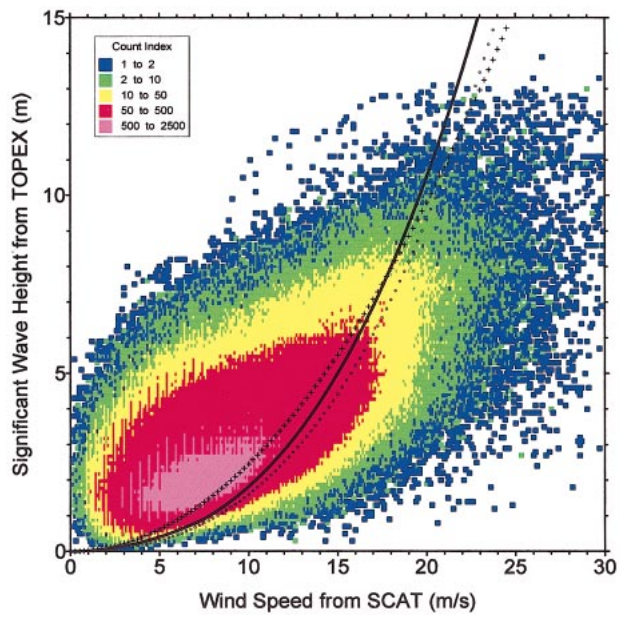

FIG. 1. A scatter diagram of sea surface wind speed and significant wave height based on the collocated TOPEX/NSCAT and TOPEX/QSCAT datasets. The wind speeds are extracted from NSCAT and QSCAT, and the significant wave heights are extracted from TOPEX. The color legend depicts data density. Also overlaid are the theoretical relations between wind speed and significant wave height for fully developed seas according to Hasselmann et al. (1988) (the WAM model), Pierson and Moskowitz (1964), and Ewing and Laing (1987), as depicted by the solid line, the crosses, and the circles, respectively.

5. Summary

Knowledge on the global structure of swell and wind sea probabilities in a climatological sense is believed to be generally poor to date. This study represents the first of its kind toward a better understanding of these important parameters. It has benefited from the availability of simultaneous multisatellite missions, which provide independent measurements of wind speed and significant wave height with unprecedented accuracy. Using the two energy-based indices proposed in this study, the global distribution and seasonal variation of swell and wind sea climate of the ocean is investigated. As a summary, the identified major swell pools (in red) and wind wave zones (in blue) in the world's oceans are indicated in Fig. 7. Given the reasonable results obtained in this study and their general consistency with available field observations and model predictions, the proposed scheme appears to be effective and efficient in characterizing the global swell and wind sea climate. Further exploration based on this feasibility study with longer duration of collocation dataset (which can be readily achievable by incorporating simultaneous TOPEX/ERS measurements as well as other forthcoming concurrent altimeter/scatterometer missions) will undoubtedly lead to a more realistic and more complete description of the swell and wind sea conditions in the ocean, in particular their interannual variabilities on a decadal timescale.

A rapidly declining perennial sea ice cover in the Arctic

Josefino C. Comiso

Laboratory for Hydrospheric Processes, NASA Goddard Space Flight Center, Greenbelt, Maryland, USA

Received 11 June 2002; revised 13 August 2002; accepted 28 August 2002; published 18 October 2002.

[1] The perennial sea ice cover in the Arctic is shown to be declining at −9% per decade using satellite data from 1978 to 2000. A sustained decline at this rate would mean the disappearance of the multiyear ice cover during this century and drastic changes in the Arctic climate system. An apparent increase in the fraction of second year ice in the 1990s is also inferred suggesting an overall thinning of the ice cover. Surface ice temperatures derived from satellite data are negatively correlated with perennial ice area and are shown to be increasing at the rate of 1.2 K per decade. The latter implies longer melt periods and therefore decreasing ice volume in the more recent years. *INDEX TERMS:* 4207 Oceanography: General: Arctic and Antarctic oceanography; 4215 Oceanography: General: Climate and interannual variability (3309); 1635 Global Change: Oceans (4203); 1640 Global Change: Remote sensing. **Citation:** Comiso, J. C., A rapidly declining perennial sea ice cover in the Arctic, *Geophys. Res. Lett.*, *29*(20), 1956, doi:10.1029/2002GL015650, 2002.

1. Introduction

[2] The Arctic sea ice cover has been noted as basically impenetrable because of the dominant presence of the perennial ice cover that consists mainly of multiyear ice, the average thickness of which is about 3–4 meters [*Wadhams and Comiso*, 1992]. The thick multiyear ice floes are the major components of the current Arctic sea ice cover. Their presence during the peak of summer makes a big difference in the ocean-ice-albedo feedback because of their vast extent and high albedo. They survive the summer melt mainly because of a strongly stratified Arctic Ocean that is in part responsible for the scarcity of convection in the region [*Aagard and Carmack*, 1994]. A study of the perennial ice cover is of immense practical importance because of the potential impact not only on climate but also on the environment and ecology of the system and in light of recent reports of ice retreat [*Bjorgo et al.*, 1997; *Parkinson et al.*, 1999] and ice thinning [*Rothrock et al.*, 1999; *Wadhams and Davis*, 2000].

[3] In this paper, the state of the perennial sea ice cover is studied using satellite passive microwave data from 1978 through 2000. The multiyear ice cover has been inferred from passive microwave data in winter using a technique that assumes that the signature is spatially stable during this period [*Johannessen et al.*, 1999]. However, previous studies have indicated large regional variations in the passive microwave signature [*Grenfell*, 1992] causing substantial biases in the derived fraction of multiyear ice within the pack [*Kwok et al.*, 1996]. The key to a more accurate quantification of the multiyear ice cover is through the use of data during minimum extent since at this time, the seasonal sea ice cover has basically melted and what is left is what we call the perennial ice cover consisting mainly of multiyear ice floes [*Comiso*, 1990]. These data are also easier to quantify and interpret since no ice classification is needed.

2. Spatial Variability in the Perennial Sea Ice Cover

[4] To provide an overview about interannual variations in the spatial distribution of the perennial ice cover, color-coded ice concentration maps during the summer ice minimum from 1979 to 2000 are shown in Figure 1. The ice concentration maps were derived from satellite passive microwave data using the Bootstrap Algorithm as described in *Comiso et al.* [1997]. Slight adjustments were made to ensure that the data set is temporally consistent using a procedure similar to that used in *Parkinson et al.* [1999]. The day of minimum extent for each year is determined through the use of seven-day running mean data of ice extents. The running mean is used to maximize the chance that what is chosen is the date of real minima and not what might be the result of a temporary compaction due to wind forcing. The dates are mainly in the second or third week of September (Figure 1) and are found to be consistent within a few days with those of ice area minimum.

[5] The images in Figure 1 provide a means to quantitatively identify the relative location and concentration of multiyear ice floes at the end of each ice season. The open water area (blue) around the pack is shown to vary considerably from one year to the next. The circular black areas in the middle are areas not covered by the satellite sensors but are usually highly consolidated. The general location of the perennial sea ice cover changes from one year to another and depends on many factors, the most important of which is the ice drift which has been shown to be strongly influenced by atmospheric circulation [*Thorndike and Colony*, 1982]. The latter can be in cyclonic mode in which the ice is normally advected to the west causing large open water areas in the east (e.g., Laptev and Kara Seas) and relatively small open areas in the west (e.g., Beaufort Sea and Chukchi Seas) or in anti-cyclonic mode in which the opposite scenario occurs. Examination of the images in Figure 1 also indicates that the open water areas are generally larger in the 1990s than in the 1980s.

[6] To better illustrate the changes from one decade to another, Figure 2a shows the average of the ice concentration minimum maps from 1979 to 1989 while Figure 2b shows the corresponding average from 1990 to 2000. It is apparent that the size of the ice cover in the latter period is smaller than that of the earlier one and that much of the changes occurred around the ice margin. The changes from

Copyright 2002 by the American Geophysical Union.
0094-8276/02/2002GL015650$05.00

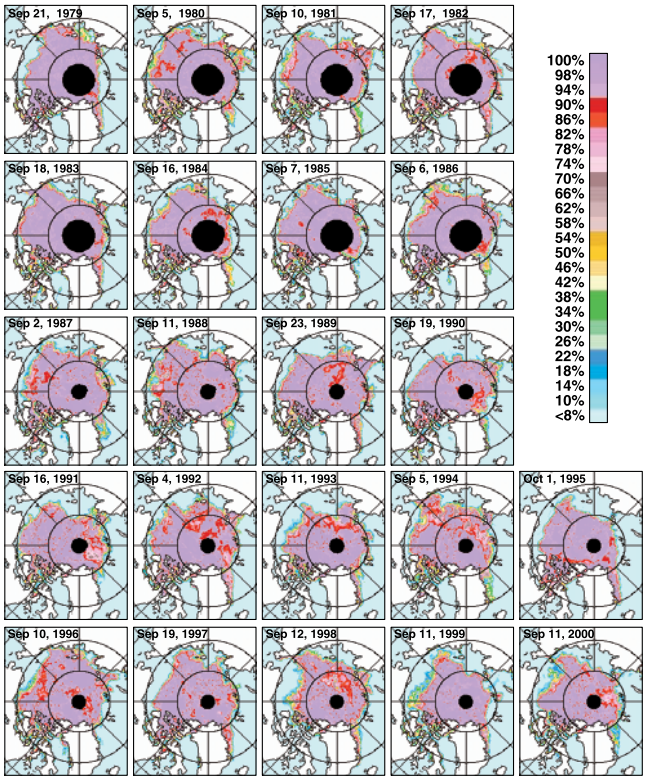

Figure 1. Color-coded daily ice concentration maps in the Arctic during ice extent minima for each year from 1979 to 2000. Each map represents the state of the perennial ice cover at the end of the ice season.

one decade to another are better quantified in the difference map (Figure 2c) between the two ice concentration maps. This map shows the magnitude and location of the changes with the negative changes represented by yellows, oranges, purples and reds while positive changes are in grays, greens, and blues. The interdecadal change is surprisingly large and intriguing with the net negative changes in extent and ice area being 5.1×10^5 km^2 (6.3%) and 6.9×10^5 km^2 (11.0%), respectively, during the 22-year period. The biggest change occurred in the western area (Beaufort and Chukchi Seas) while considerable changes are also apparent in the eastern region (Siberian, Laptev and Kara Seas). To get an idea how the ice cover may look like 5 decades from now, the decadal change as reflected in Figure 2c (but shifted towards the north) is applied to the data in Figure 2b and subsequent projections, normalized such that the change is about 10% per decade. The projected perennial ice cover for the decade of the 2050s is shown in Figure 2d. Although the technique is crude and the assumption of a linear decline is likely incorrect, Figure 2d provides a means to assess how the perennial ice cover could look like if the decline persists. It is important to note that the Arctic is governed by complex processes including a positive ice-ocean-atmosphere feedback and decadal as well as interdecadal variability including that associated with the Arctic Oscillation (AO) as described by [*Thompson and Wallace*, 1998]. A simple regression analysis of AO indices with the perennial ice area indicates that the relationship between these two variables is relatively weak with the correlation coefficient being only 0.20. The link is likely stronger if continuous ice cover data are analyzed in conjunction with the AO but such study is not within the scope of this paper.

4. Discussion and Conclusions

[13] The area of the Arctic perennial sea ice cover is shown to be declining at a relatively fast rate of 8.9 ± 2.0% per decade. A decadal change of 10% is also inferred from the difference of 11-year averages of ice minima data. If such a rate of decline persists for a few more decades, the perennial sea ice cover will likely disappear within this century. The decline is unlikely linear because of positive feedback effects between ice, ocean, and the atmosphere Furthermore, a positive trend in the ice temperature of about 1.2 K per decade is observed leading to earlier onset of melt and delayed onset of freeze up that in turn causes further thinning and retreat of the perennial ice cover.

[14] The implications of such a disappearance of the perennial ice cover are many and can be profound. It would mean a different albedo for the Arctic during the peak of solar insolation in summer and therefore a drastically differ ent ice-ocean-atmosphere feedback. It would mean a much larger influx of solar radiation into the Arctic Ocean thereby changing the characteristics of the mixed layer and the stratification of the ocean. The seasonality and character istics of the ice cover in the region would be very different. The climate, the productivity, and biota in the region will change tremendously while the region becomes more accessible to human activities.

[15] The Arctic system is however a complex system controlled by many variables and influenced by unpredictable events (e.g., volcanic eruptions). There are also periodic cycles, such as the Arctic Oscillation [*Thomson and Wallace*, 1998], the North Atlantic Oscillation [*Mysak and Venegas*, 1998] and the Pacific Decadal Oscillation [*Chao et al.*, 2000] the effects of which need to be considered. The associated decadal and inter-decadal changes in pressure and atmospheric circulation could cause a decadal variability in the ice cover that could lead to a reversal in the current trend. Nevertheless, because of the magnitude in the observed rate of decline and associated feedback effects, a near term recovery is likely needed to avoid an irreversible change in the Arctic ice cover and its environment.

Annals of Glaciology 34 2002
© International Glaciological Society

Correlation and trend studies of the sea-ice cover and surface temperatures in the Arctic

JOSEFINO C. COMISO
Laboratory for Hydrospheric Processes, NASA Goddard Space Flight Center, Code 971, Greenbelt, MD 20771, U.S.A.

ABSTRACT. Co-registered and continuous satellite data of sea-ice concentrations and surface ice temperatures from 1981 to 2000 are analyzed to evaluate relationships between these two critical climate parameters and what they reveal in tandem about the changing Arctic environment. During the 19 year period, the Arctic ice extent and actual ice area are shown to be declining at a rate of $-2.0 \pm 0.3\%$ dec^{-1} and $-3.1 \pm 0.4\%$ dec^{-1}, respectively, while the surface ice temperature has been increasing at 0.4 ± 0.2 K dec^{-1}, where dec is decade. The extent and area of the perennial ice cover, estimated from summer minimum values, have been declining at a much faster rate of $-6.7 \pm 2.4\%$ dec^{-1} and $-8.3 \pm 2.4\%$ dec^{-1}, respectively, while the surface ice temperature has been increasing at 0.9 ± 0.6 K dec^{-1}. This unusual rate of decline is accompanied by a very variable summer ice cover in the 1990s compared to the 1980s, suggesting increases in the fraction of the relatively thin second-year, and hence a thinning in the perennial, ice cover during the last two decades. Yearly anomaly maps show that the ice-concentration anomalies are predominantly positive in the 1980s and negative in the 1990s, while surface temperature anomalies were mainly negative in the 1980s and positive in the 1990s. The yearly ice-concentration and surface temperature anomalies are highly correlated, indicating a strong link especially in the seasonal region and around the periphery of the perennial ice cover. The surface temperature anomalies also reveal the spatial scope of each warming (or cooling) phenomenon that usually extends beyond the boundaries of the sea-ice cover.

INTRODUCTION

The Arctic region is of particular interest because it is expected to provide early signals associated with a potential change in climate (Budyko, 1966; Manabe and others, 1992; Alley, 1995). Because of observed global warming, especially in the second half of the 1990s (Jones and others, 1999), it is important to know how such increases in temperature are reflected in the Arctic. Recent reports show that the sea-ice cover has been retreating by about -3% dec^{-1} (Bjørgo and others, 1997; Parkinson and others, 1999), while submarine sonar data show a thinning by >1 m in deep-water portions of the Arctic (Rothrock and others, 1999; Wadhams and Davis, 2000) over a period of 4 dec, where dec is decade. The Arctic climate system is, however, a very complex system affected by periodic atmospheric phenomena, like the North Atlantic and Arctic Oscillations (Mysak, 1999), and unexpected changes in ice-cover dynamics. Accurate interpretation of observed Arctic changes thus requires a better understanding of Arctic processes.

The key objective of this study is to make simultaneous use of satellite sea-ice concentration and surface temperature data to gain insight into the changing Arctic climate. Co-registered datasets of these two geophysical variables are examined to obtain a better understanding of how the various components of the climate system interact and how they act in concert to influence the system. Previous studies on the variability and trends of the Arctic sea-ice cover have been carried out using solely satellite passive-microwave data or submarine sonar data. In this study, trends and spatial changes in the ice cover are analyzed in conjunction with trends and changes in surface temperatures. Anomalies in ice concentration and surface temperatures are examined on a year-to-year basis, and relationships between these two variables are evaluated. The results are also used to gain insight into the observed changes in the Arctic, interpret trends in the total ice cover and its surface temperature, and better understand the status of the perennial sea-ice cover.

VARIABILITY AND TREND OF THE SEA-ICE COVER

Although a slightly longer time series for sea-ice cover is available, the time period used in this study is 1981–99 since this is the period for which coincident and continuous infrared and passive-microwave satellite data are available. The procedure for deriving ice concentration from satellite passive-microwave data has been described before (Comiso and others, 1997) and will not be repeated here. The error associated with the ice-concentration data is about 5–15% under dry surface conditions, and increases when the surface becomes wet as the snow melts in spring and when melt ponds are formed over ice floes in the summer. In this study, the ice concentrations are derived using the Bootstrap algorithm as described in Comiso and others (1997). The values and trends may therefore be slightly different from those reported elsewhere (Bjørgo and others 1997; Parkinson and others, 1999) even for identical periods.

Ice-concentration maps are used to derive monthly ice extent, actual ice area and average ice concentrations within the pack, as done previously (Comiso and others, 1997; Parkinson and others, 1999). These are in turn used to calculate anomalies in monthly ice extent, actual ice area and ice concentration by subtracting the 19 year climatological

averages created for each of the 12 months of the year. The anomalies in ice extent, ice area and ice concentration for each month from August 1981 through July 2000, which are also used for trend studies, are shown in Figure 1. Yearly averages were also calculated for analysis of the yearly variability and associated trend. The yearly averaging was done from August of one year to July the following year to be able to compare yearly differences between different ice seasons, instead of different annual averages that would extend from the middle of one ice season to the middle of another.

The plot of ice-extent anomalies (Fig. 1a) shows significant variability, with a standard deviation of 0.33×10^6 km^2. Simple linear regression of the data yielded a trend of $-246\,000 \pm 40\,000$ km^2 dec^{-1}, or $-2.04 \pm 0.33\%$ dec^{-1}. This is significantly less than the -2.8% dec^{-1} reported by Parkinson and others (1999), but the latter was for a slightly different time period (i.e. 1978–96) and a different ice dataset was used (i.e. Team algorithm as described in Comiso and others, 1997), as indicated earlier. Anomalously low values occurred in 1989, 1990, 1993, 1995 and 1998, while an anomalously high value is apparent in 1996. The regression results from the yearly data yielded $-2.04 \pm 0.56\%$ dec^{-1} the result of which is almost the same as the monthly anomaly data but with higher error.

The variability in the anomalies in actual ice area (Fig. 1b) is comparable to that of ice extent, with a standard deviation of 0.33×10^6 km^2. However, the trend in ice area is significantly larger at $-336\,000 \pm 36\,000$ km^2 dec^{-1}, or $-3.11 \pm 0.33\%$ dec^{-1}. This is more in line with previous reports for the 1978–96 period. The yearly averages yielded similar trends but larger error at $-3.12 \pm 0.51\%$ dec^{-1}.

The difference between the ice-extent and ice-area trends stems mainly from a net negative trend in ice concentration (Fig. 1c), estimated at $-1.16 \pm 0.12\%$ dec^{-1}. The change in estimated ice concentration may not be entirely due to a change in true ice concentration since it could also be linked to a change in the areal coverage of melt ponding. To test this possibility, a similar analysis was conducted that excluded the summer months (June–August). The results yielded a trend in ice concentration of $-1.09 \pm 0.14\%$ dec^{-1}, which is similar to that with the summer months included. This implies that the impact of changes in melt-ponded area on the trend results is not significant. However, excluding the summer months significantly reduced the trends in ice extent and area to $-1.47 \pm 0.14\%$ dec^{-1} and $-2.47 \pm 0.37\%$ dec^{-1}, respectively. This suggests that the trends in the ice cover during the summer, especially during minima, may be high as indicated later.

The distributions for the yearly average extent and area in Figure 1 exhibit a periodic cycle with a period of about 5 years. Such periodicity is intriguing in light of a possible correlation with many important processes, such as the Arctic Oscillation. The effect is not so apparent in the monthly anomalies. However, a detailed study of this phenomenon is beyond the scope of this paper.

DISCUSSION AND CONCLUSIONS

Co-registered satellite ice-concentration and surface-temperature data for the period 1981–2000 have been assembled and analyzed, and this study shows that simultaneous observation of the two parameters provides useful knowledge about the changing Arctic. Ice-concentration data provide physical characterization of sea-ice spatial distributions, while surface temperatures provide information about the thermal state of the ice surface. Each dataset provides independent evaluation of the changing state of the Arctic, but together they provide a more complete characterization.

A general assessment from the monthly and yearly data shows that ice extent has been declining at a rate of 2.3% dec^{-1} while surface temperature has increased by 0.4 K dec^{-1}. This rate of decline is smaller than the 2.8% dec^{-1} previously reported, but that value was for a different period (1978–96) and a different ice-concentration algorithm was utilized to generate the ice dataset.

The yearly anomalies in both ice concentration and temperature provide new insights into the changing Arctic ice environment. They provide year-to-year changes in good spatial detail of sea-ice distributions, and specific locations and magnitude of large positive and negative anomalies. The data show that positive anomalies in ice concentrations predominate in the 1980s, while the reverse is true in the 1990s. This indicates that the ice cover has been declining. Similarly, negative anomalies in surface temperatures were dominant in the 1980s, while positive anomalies were more frequent in the 1990s. This shows that while the ice cover is declining, the surface temperature is rising, indicating a close linkage of the two variables.

The yearly temperature-anomaly maps provide useful information that is not available from the sea-ice-cover data. These maps show that there are large anomalies in the Arctic that extend beyond the sea-ice margins. They allow quantification of the scope of these anomalies which are apparently driven by atmospheric patterns. The coherence of the spatial distribution of the anomalies of ice concentration and surface temperature is quite good, and quantitative analysis shows high negative correlation of the two variables, especially in the seasonal ice regions where the anomalies are abnormally high. It is also apparent that there were some years when the anomaly patterns were exceptionally high, such as 1998, which is regarded as the warmest year in the 20th century. High positive anomalies are indeed evident in the 1997/98 and 1998/99 ice seasons, but they are confined primarily to the Beaufort Sea and North America, while slight cooling occurred in Russia and the Kara Sea.

To better understand the current state of the Arctic ice cover, a good quantification of the variability of the perennial ice cover is required, derived from analysis of the extents and areas of the ice cover during summer minimum. Results show that the Arctic summer ice extent and area have been declining at a rate of $-6.7 \pm 2.4\%$ dec^{-1} and $-8.3 \pm 2.4\%$ dec^{-1}, respectively, while the average September surface temperature values increased by 0.9 ± 0.6 K dec^{-1}. The rate of decline in the perennial ice cover is more than twice the rate of decrease in total sea-ice cover. The rate of increase in surface temperature in September is also surprisingly high and more than double that for all seasons. These are significant results since they pertain to the perennial ice cover which is directly connected to the ice-thickness distribution. In addition, the minimum extent shows higher yearly fluctuations in the 1990s than in the 1980s. Even without a trend, such a phenomenon would cause a change in the overall composition of the different ice types, and favors increases in the fraction of the thinner, younger ice cover (e.g. second-year ice), compared with the older, thicker ice types. The large fluctuation in the areal coverage of the perennial ice cover may thus be accompanied by a decrease in ice thickness.

WEATHER MAGAZINE

May/June ISSUE, 2002

Abstract

A state that ranks 42nd in size, Maryland has taken an inordinate number of tornado hits--two of them deadly. On Sep 24, 2001, an F3 twister took the lives of two students as it ripped through the University of Maryland at College Park. On Apr 28, 2002, an F4 tornado killed five people and devastated the town of La Plata. During the first half of May 2002, three different twisters and several downbursts pounded various parts of the state.

MAY HIGHLIGHT

Twisters Claw Maryland

by James Foster

JAMES FOSTER is a lifelong Maryland resident and a climatologist in the Hydrological Sciences Branch at NASA's Goddard Space Flight Center in Greenbelt, Maryland.

Many of us can recall our grandparents regaling us with stories about what the weather was like when they were growing up. Gramps would say something like, "Back in '32, the winter was so long that I had to put snowshoes on both me and the mule to plow the north 40."

We listened in amazement and wondered what it must have been like back then. Sometimes you've got to wonder if it really was that much worse. Chances are, Gramps was remembering a cluster of bad weather events that made the extremes seem even more extreme.

Take the past couple of years in Maryland, for example. A state that ranks 42nd in size, Maryland has taken an inordinate number of tornado hits—two of them deadly. Almost a year ago, on September 24, 2001, an F3 twister took the lives of two students as it ripped through the University of Maryland at College Park.

And this past spring, on April 28, an F4 tornado killed five people and devastated the town of La Plata, 30 miles south of Washington, D.C. If that wasn't bad enough, during the first half of May, three different twisters and several downbursts pounded various parts of the state.

Maryland residents have become more attuned to just how dangerous tornadoes can be and are taking tornado warnings more seriously, sometimes to the point of dramatically overreacting. In fact, about a week after the La Plata tornado occurred, an adjacent county closed schools when a tornado watch was issued.

The La Plata tornado was a product of a supercell thunderstorm that formed ahead of a cold front pushing east across the Ohio Valley. April 28 was warm and very humid across the mid-Atlantic. Dew points in Washington, D.C., were in the low 70s (°F), and temperatures rose to the upper 70s once the sun emerged after heavy morning rain. Wet ground, moist air, and warm temperatures helped to fuel the development of afternoon thunderstorms. Moreover, the jet stream, positioned over the mid-Atlantic region, acted to intensify the developing storms.

An energetic cold front can act as a triggering mechanism for tornado formation if a large area of moisture is surging north from the Gulf of Mexico and if a vigorous jet stream is positioned overhead. Because of the very unstable atmosphere, the National Weather Service issued tornado watches and severe thunderstorm warnings well before the first funnel cloud was sighted.

Even by "Tornado Alley" standards, the La Plata tornado was big. After demolishing La Plata, it hit Prince Frederick, Maryland, and then hopscotched across the Chesapeake Bay onto Maryland's Eastern Shore. The storm cell associated with the deadly La Plata tornado persisted all the way from the Appalachians to the Atlantic Ocean.

Maryland's most deadly tornado disaster also occurred near La Plata 76 years ago when a schoolhouse was demolished and more than a dozen children were killed.

While little Maryland has recently been battered by a number of unwelcome twisters, most of the rest of the country has dodged them. In fact, for the last two years and thus far this year, the number of reported tornadoes nationwide has been below the 30-year mean.

So, why then has Maryland had to deal with more than its share of tornadoes? Basically, it's just by chance that the cast of meteorological characters that must appear on stage at the same time to produce the fiercest winds on Earth has done so with some regularity in Maryland. The show is usually seen in the southern Plains and the Midwest, but over the past year, it went on the road to the east. As always, the reviews were dreadful. The bottom line is that Maryland needn't worry about becoming a new "Tornado Alley," though it may have seemed so recently.

Nonetheless, I suppose in 50 years, today's kids will be telling their grandchildren what it was like when they were young sprouts. "Back in '02, you didn't even have to till your fields in the spring; the twisters came so thick and fast, you'd just wait for one of them to plow up the ground for you."

An aerial view of the 10-mile swath that the tornado left behind in La Plata, Maryland, in late April. The remains of La Plata appear at the left, where the tornado path crossed the north-to-south Route 301.
COURTESY OF EO-1 SCIENCE TEAM, NASA GODDARD SPACE FLIGHT CENTER

Southern Ocean Climate and Sea Ice Anomalies Associated with the Southern Oscillation

R. KWOK

Jet Propulsion Laboratory, California Institute of Technology, Pasadena, California

J. C. COMISO

NASA Goddard Space Flight Center, Greenbelt, Maryland

(Manuscript received 5 February 2001, in final form 7 August 2001)

ABSTRACT

The anomalies in the climate and sea ice cover of the Southern Ocean and their relationships with the Southern Oscillation (SO) are investigated using a 17-yr dataset from 1982 to 1998. The polar climate anomalies are correlated with the Southern Oscillation index (SOI) and the composites of these anomalies are examined under the positive (SOI > 0), neutral ($0 >$ SOI > -1), and negative (SOI < -1) phases of SOI. The climate dataset consists of sea level pressure, wind, surface air temperature, and sea surface temperature fields, while the sea ice dataset describes its extent, concentration, motion, and surface temperature. The analysis depicts, for the first time, the spatial variability in the relationship of the above variables with the SOI. The strongest correlation between the SOI and the polar climate anomalies are found in the Bellingshausen, Amundsen, and Ross Seas. The composite fields reveal anomalies that are organized in distinct large-scale spatial patterns with opposing polarities at the two extremes of SOI, and suggest oscillations that are closely linked to the SO. Within these sectors, positive (negative) phases of the SOI are generally associated with lower (higher) sea level pressure, cooler (warmer) surface air temperature, and cooler (warmer) sea surface temperature in these sectors. Associations between these climate anomalies and the behavior of the Antarctic sea ice cover are evident. Recent anomalies in the sea ice cover that are clearly associated with the SOI include the following: the record decrease in the sea ice extent in the Bellingshausen Sea from mid-1988 to early 1991; the relationship between Ross Sea SST and the ENSO signal, and reduced sea ice concentration in the Ross Sea; and the shortening of the ice season in the eastern Ross Sea, Amundsen Sea, far western Weddell Sea and lengthening of the ice season in the western Ross Sea, Bellinghausen Sea, and central Weddell Sea gyre during the period 1988–94. Four ENSO episodes over the last 17 years contributed to a negative mean in the SOI (-0.5). In each of these episodes, significant retreats in ice cover of the Bellingshausen and Amundsen Seas were observed showing a unique association of this region of the Antarctic with the Southern Oscillation.

1. Introduction

The Southern Oscillation (SO) refers to the seesaw in the surface pressure anomalies between the Indian Ocean–Australian region and the southeastern tropical Pacific on a seasonal and interannual timescale. The large-scale character of the SO in the Tropics and subtropics in the Southern Hemisphere is well known (Philander and Rasmusson 1985). The SO has a signature that extends to the mid- and high latitudes in the Southern Hemisphere in the winter and summer. The high-latitude signature of the SO has associated anomalies over the Antarctic sea ice cover. Understanding these links between the SO and Antarctic sea ice cover are important due to the sensitivity of sea ice to anomalies in climate forcing as sea ice interacts with the global climate over a broad range of spatial and temporal scales (Schlesinger and Mitchell 1985; Manabe et al. 1991). Sea ice albedo feedback involves changes in the climatological area of the ice cover and adjustments in the poleward heat transport by the atmosphere, in addition to changes in the thickness, albedo, and temperature of ice within the Antarctic ice pack. The ocean structure and circulation are affected during sea ice growth, as salt is rejected to the underlying ocean increasing its density and leading sometimes to deep ocean convection and bottom water formation. Equatorward transport of ice results in a net flux of freshwater and negative heat. Thus, anomalies in these polar processes have complex consequences in the global climate.

Many studies have analyzed the recent behavior of the Antarctic ice extent and have suggested connections between sea ice extent and the Southern Oscillation (Carleton 1988; Jacobs and Comiso 1993; Simmonds and Jacka 1995; Gloersen 1995; Ledley and Huang 1997; Jacobs and Comiso 1997; Watkins and Simmonds 2000). Using a 10-yr dataset (1985–94), White and Peterson (1996) found coupled anomalies that propagate eastward with the Antarctic Circumpolar Current during a period of 4–5 years (wavenumber 2) and taking 8–10 years to encircle Antarctica. It was suggested that this Antarctic Circumpolar Wave (ACW) is associated with ENSO-related activities in the equatorial Pacific, possibly through an atmospheric teleconnection with higher southern latitudes. Peterson and White (1998), in a case study, show ENSO can be a possible source of the interannual anomalies for sustaining the ACW in the western subtropical South Pacific. Parkinson (1998) also

Corresponding author address: Dr. R. Kwok, Jet Propulsion Laboratory, California Institute of Technology, 4800 Oak Grove Dr., Pasadena, CA 91109.
E-mail: ron.kwok@jpl.nasa.gov

suggests that the lengthening/shortening sea ice season might be related to the variability of the ACW. Bonekamp et al. (1999) in an examination of the European Centre for Medium-Range Weather Forecasts (ECMWF) Atmospheric Reanalysis dataset from 1979 to 1994, however, did not find eastward propagating anomalies suggestive of an ACW prior to 1984. For that time period at least, a two-regime structure with and without the presence of ACW was indicated. Yuan and Martinson (2000) explored possible relationships between the record of Antarctic sea ice extent between 1978 and 1996 and global climate variability. Their analyses show a strong link of the sea ice edge anomalies in the Amundsen, Bellingshausen, and Weddell Seas to extrapolar climate. In a recent article, Venegas et al. (2001) found coupled oscillations in Antarctic sea ice and atmosphere in the South Pacific sector.

The objective of this study is to explore the spatial details in the teleconnections between SO and the anomalies in the Southern Ocean climate and in particular the anomalies of the Antarctic sea ice cover. Our approach is to analyze the linear correlation of the Southern Oscillation index (SOI) with the polar climate anomalies, and to examine the composites of these anomalies during three phases of the SOI that we define as SOI > 0, $0 >$ SOI > -1, and SOI < -1, and henceforth will be referred to as the positive, neutral, and negative phases. The datasets used here span a 17-yr period from 1982 to 1998. Our study takes advantage of new data on ice motion and ice surface temperature derived from passive microwave imagery and the National Oceanic and Atmospheric Administration's (NOAA) Advanced Very High Resolution Radiometer (AVHRR) data. Rather than having to restrict our study area to the ice edge region, as was done previously (White and Peterson 1996), this dataset allows a more detailed examination of the spatial signatures of the climate and sea ice anomalies.

The paper is composed of five sections. Section 2 describes the climate and sea ice datasets used in our analysis. Section 3 presents the spatial pattern of correlation between the Southern Ocean climate anomalies and the SOI, and the composite patterns of the climate and sea ice anomalies associated with three phases of the SOI over 17 years. We discuss our results in the context of previous work in section 4. The paper is summarized in the last section.

5. Conclusions

The spatial signature of the climate and sea ice anomalies in the Southern Ocean associated with the Southern Oscillation are revealed in the correlation patterns and the composite fields. The correlation maps and lag-correlation plots show features of the spatial and temporal relationships between these anomalies and the index of Southern Oscillation, while the composite maps show the dominant spatial signature of the anomalies during the three phases of SOI. On a large scale, these anomalies are organized in coherent patterns and assume opposite polarities during the two extremes of SOI. Also, these anomalies covary with the Southern Oscillation and oscillate at approximately the same frequency. Association with ENSO-related activities in the equatorial Pacific is clearly indicated.

Overall, the climate anomalies in the Amundsen, Bellingshausen, and Weddell Sea sectors of the Antarctic polar ocean show the strongest link to the Southern Oscillation. Within these sectors, the climate anomalies show the highest correlation with the SOI and the composite patterns show the most intense and localized climate and sea ice anomalies associated with the extremes of SOI. Positive (negative) phases of the SOI are generally associated with lower (higher) sea level pressure, cooler (warmer) surface air temperature, and cooler (warmer) sea surface temperature in these sectors. Outside these sectors, the anomalies are not as distinct.

Linkages between the SOI, the climate anomalies, and the sea ice extent, concentration, motion, and ice surface temperature are also evident. The sea ice cover anomalies are located within the same sectors as those with the dominant climate anomalies. During the positive (negative) phase of SOI, positive (negative) anomalies of the SIE are located between 180° and 130°W in the Ross and Amundsen Seas, negative (positive) anomalies can be found between 100°W and 10°E in Bellingshausen and Weddell Seas, and, smaller positive (negative) anomalies are found in the sector between 10° and 50°E.

The physical mechanisms by which these polar processes are linked to the Southern Oscillation are complex and beyond the scope of this study. However, the identified relationships may be useful as diagnostic tools for climate models and for the eventual understanding of the underlying mechanisms of these associations. The composite fields presented can be used as an indicator of the general condition of the Antarctic ice cover during different phase of the Southern Oscillation as measured by the SOI. We have used these fields to explain, in a broad sense, the large-scale trends and anomalies (reported in recent literature) in the sea ice extent and the length of the ice seasons over the past 20 years. These composite fields are weighted by four strong ENSO episodes over the last 17 years. As a result, these warm events have probably weighted the sea ice and climate anomalies towards the patterns associated with the negative extremes of the SO index. Data of monthly anomalies of ice extent, ice area, and concentration in the Bellingshausen–Amundsen Sea sector (Fig. 9) show that the ice cover in the region is still declining while those in other regions appear to be increasing slightly. In fact, the mean trend of the Antarctic sea ice edge is close to zero over the period. Recession of the ice edge in the Bellingshausen–Amundsen Sea sector is compensated by expansion in the Weddell Sea and western Ross Sea sectors. Our analysis shows that spatially, the Pacific sector is different from other Antarctic regions in that it is influenced by climate anomalies with strong associations with the Southern Oscillation. The results suggest that the Bellingshausen–Amundsen Sea area is unique in its close association with the Southern Oscillation.

Spatial patterns of variability in Antarctic surface temperature: Connections to the Southern Hemisphere Annular Mode and the Southern Oscillation

Ron Kwok
Jet Propulsion Laboratory, California Institute of Technology, Pasadena, California, USA

Josefino C. Comiso
Goddard Space Flight Center, Greenbelt, Maryland, USA

Received 1 May 2002; revised 7 June 2002; accepted 14 June 2002; published 31 July 2002.

[1] The 17-year (1982–1998) trend in surface temperature shows a general cooling over the Antarctic continent, warming of the sea ice zone, with moderate changes over the oceans. Warming of the peripheral seas is associated with negative trends in the regional sea ice extent. Effects of the Southern Hemisphere Annular Mode (SAM) and the extrapolar Southern Oscillation (SO) on surface temperature are quantified through regression analysis. Positive polarities of the SAM are associated with cold anomalies over most of Antarctica, with the most notable exception of the Antarctic Peninsula. Positive temperature anomalies and ice edge retreat in the Pacific sector are associated with El-Niño episodes. Over the past two decades, the drift towards high polarity in the SAM and negative polarity in the SO indices couple to produce a spatial pattern with warmer temperatures in the Antarctic Peninsula and peripheral seas, and cooler temperatures over much of East Antarctica. *INDEX TERMS:* 3309 Meteorology and Atmospheric Dynamics: Climatology (1620)

1. Introduction

[2] While global temperatures rose by 0.3°C between 1978–1997 [*Jones et al.*, 1999], the spatial distribution of this trend is certainly not uniform. During the last 20 years, pronounced warming of the Antarctic Peninsula [*King and Harangozo*, 1998] has been contrasted by reported cooling at a number of weather stations on the coast and plateau of East and West Antarctica [*Comiso*, 2000]. Recently, the analysis of *Doran et al.* [2002] suggests a net cooling of the Antarctic continent between 1966 and 2000. Over approximately the same period, the warming trend of 0.09°C/yr (1980–1999) at Faraday Station at the northern tip of the Antarctic Peninsula can be compared to the cooling trends of 0.07°C/yr (1986–2000) at the McMurdo Dry Valleys and 0.05°C/yr at the South Pole (1980–1999).

[3] Surface temperature (ST) anomalies of the Antarctic are related to anomalies in atmospheric and ocean circulation, and the sea ice cover. A new 17–year (1982–1998) ST dataset [*Comiso*, 2000] allows us to identify the characteristic spatial patterns of variability in the Antarctic ST field and their relation to large-scale circulation patterns. In this paper, we explore the linear effects of the SAM and the SO on the ST fields of the Antarctic. The SAM describes a predominantly zonally symmetric pattern and is characterized by sea-saws of atmospheric mass between the polar caps regions poleward of 60°S and the surrounding zonal ring centered along ~45°S, as manifested in the leading empirical orthogonal functions (EOFs) of the 850-hPa geopotential height field [*Thompson and Wallace*, 2002a]. This annular mode is also related to strong perturbations in temperature and total ozone column over the polar caps during the stratosphere's active season. Linkages between the well known SO, and the climate and sea ice anomalies of the Southern Ocean have been described by *Kwok and Comiso* [2002]. The SO plays a role in the regional pattern of Antarctic climate changes over the past 20-years. Here, the SO is discussed in the context of potential interactions between the two modes of atmospheric variability.

2. Data Sets and Circulation Indices

[4] The monthly ST fields used in this study are derived from AVHRR (A Very High Resolution Radiometer) infrared data. The dataset, on a 6.25 km grid, covers ocean and ice south of 50°S. STs at skin depth are generally close estimates of near surface air temperatures (SATs). In the extreme these temperatures maybe cooler by several degrees, compared to near SATs, under conditions with stable stratification over ice surfaces. As infrared observations of the surface are available only during cloud-free conditions, the temperatures may not properly reflect the monthly mean. When compared to monthly station data, the cloud-free averages are cooler than the true monthly mean by ~0.5 K. Details of the retrieval procedure and evaluation of the dataset can be found in *Comiso* [2000]. Uncertainties in the retrievals are estimated to be generally less than 3 K over ice-covered surfaces and less than 1 K over open ocean. The data are mapped onto the polar stereographic projection used in SSM/I (Special Sensor Microwave/Imager) data. Monthly anomaly ST fields are produced by removing the monthly climatology at each sample location.

[5] Indices of the SAM are those derived by *Thompson and Wallace* [2002a]. These are coefficients of the leading mode in the EOF expansion of the monthly 850-hPa geopotential height field, from 20–90S, [1958–1997] from the NCEP/NCAR Reanalysis [*Kalnay et al.*, 1996]. This mode explains ~27% of the variance of the monthly mean fields poleward of 20°S. The monthly SO indices used in this

Copyright 2002 by the American Geophysical Union.
0094-8276/02/2002GL015415$05.00

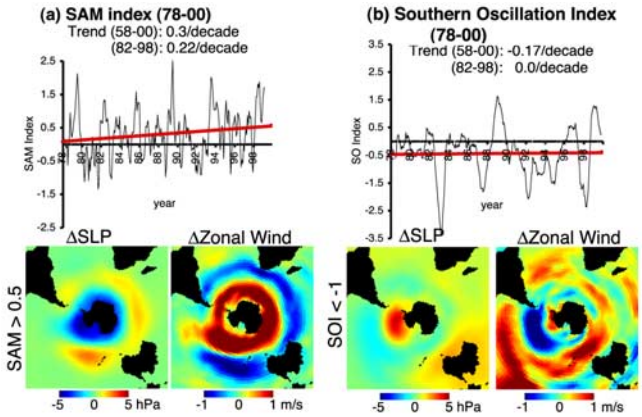

Figure 1. The indices of the SAM and the SO from 1978–2000, and the composites of SLP and zonal wind anomalies associated with their positive polarities (SAM index > 0.5; SO index < −1) of the indices. The SLP and wind anomalies are derived from NCEP/NCAR analyses. The trends (1958–2000) in the indices are also shown. The 17-year trend is shown in red.

study are those of the Climate Analysis Center. The time series of the two indices and the mean SLP and wind anomaly patterns associated with the positive polarity of the SAM and negative polarity of the SO indices are shown in Figure 1. The most striking features associated with the positive polarity of the SAM index are the lowered SLP within the circumpolar trough, enhancement of the westerlies north of 70°S, and negative anomalies in the meridional wind west of the Antarctic Peninsula. For the positive polarity of the SO, lowered SLP is found centered over the Amundsen and Bellingshausen Seas, with corresponding meridional and zonal wind anomalies. Opposite polarities of the SAM and SO indices exhibit the same spatial patterns but with anomalies of opposite sign.

3. Results and Discussion

[6] The 17-year (1982–1998) trends of the ST and ice edge (IE) anomalies are shown in Figure 2. The most pronounced feature on the map is the warming of the sea ice zone around Antarctica. It should be emphasized that the trend over sea ice should be interpreted with care, as the retrievals over sea ice are highly variable because the STs are dependent on ice thickness and concentration. The ST of thin ice is closer to the freezing point at the bottom boundary (sea water at ∼−1.8°C) while the ST of thick ice is closer to that of the SATs. With sea ice in the 0–1 meter range, as is typical in the Southern Ocean, there could be significant contrasts between ice and air temperatures. Ice concentration anomalies are results of openings and closings of the ice cover due to gradients in ice motion. Thus, the overall trend may be potentially interpreted as expressions of lower ice concentration and/or a thinner ice cover. In the warming over the Amundsen/Bellingshausen Seas, there are no significant trends in the sea ice concentration [*Kwok and Comiso*, 2002] but observations show significant negative trends in the IE (shown in Figure 1) and decreases in the sea ice season [*Parkinson*, 1998]. Thus, the increase in ST could be partially attributable to the increase the area of thinner first year ice in winter and longer periods with open water in summer. Regions with negative trend in the IE are coincident with areas with warming. The two sectors, west of the Ross Sea and east of the Antarctic Peninsula in the Weddell Sea, showing cooling trends are coincident with positive trends in the IE.

4. Conclusions

[12] Observed changes in the ST of the Antarctic appear to be linked to variations in the extratropical SH annular mode and the extrapolar Southern Oscillation. Spatially, it is clear from Figure 2 that the SAM and SO indices do not explain the same ST variances, as the two indices are almost uncorrelated. The SAM plays an important role in the circulation pattern and the spatial temperature distribution of the Antarctic sea ice and ice sheet. In surface temperature, positive (negative) polarities of the SAM indices are associated with the positive (negative) temperature anomalies over the Antarctic Peninsula and negative (positive) temperature anomalies over much of the continent. The regions of extremes in correlation with the SO indices are found in the SST fields off the Ross Sea (negative correlation) and sector off the George V and Oakes coasts (positive correlation). Warmer (cooler) SSTs off the Ross Sea is associated with the negative (positive) polarity of SO index, with the opposite behavior found in the other region. This analysis serves to illustrate the importance of the circulation changes associated with the SAM and SO in determining the spatial pattern of surface temperature anomalies.

[13] The upward trend in the SAM index accounts partially for the observed warming over the Antarctic Peninsula during the past 17-years while the negative bias in the SO index accounts for the retreat of the ice edge in the Bellingshausen Sea west of the Antarctic Peninsula. The significant and prolonged positive trend and bias in the difference between the SAM and SO indices (positive SAM and negative SO) during the past 17-years gave rise to this regional pattern with positive ST anomaly and reduced sea ice cover. We suggest perhaps that the total observed warming of the Antarctic Peninsula can be associated with the potential coupling of the modes of atmospheric variability described by the two indices through regional positive temperature/sea ice feedback. Regardless of the cause, the changes in the circulation since the early 80s have resulted in a particular ST anomaly pattern that has amplified warming of the Antarctic Peninsula because of the interactions between ice and ocean.

[14] The source of variability of the SAM has not been established. It is interesting to note that the variability of the tropospheric SH annular mode has been shown to be related to changes in the lower stratosphere [*Thompson and Wallace*, 2000b]. The high index polarity of the SH annular mode is associated with the trend toward a cooling and strengthening of the SH stratospheric polar vortex during the stratosphere's relatively short active season in November, and ozone depletion. A causal mechanism was suggested by recent Antarctic data showing a strong cooling trend in the lower stratosphere that is consistent with recent ozone depletions [*Randel and Wu*, 1999]. However, the primary mechanism responsible for the recent trend in the SH annular mode remains to be determined.

Annals of Glaciology 34 2002
© International Glaciological Society

A 21 year record of Arctic sea-ice extents and their regional, seasonal and monthly variability and trends

CLAIRE L. PARKINSON, DONALD J. CAVALIERI
Oceans and Ice Branch/Code 971, NASA Goddard Space Flight Center, Greenbelt, MD 20771, U.S.A.

ABSTRACT. Satellite passive-microwave data have been used to calculate sea-ice extents over the period 1979–99 for the north polar sea-ice cover as a whole and for each of nine regions. Over this 21 year time period, the trend in yearly-average ice extents for the ice cover as a whole is $-32\,900 \pm 6100$ km^2 a^{-1} (-2.7 ± 0.5% per decade), indicating a statistically significant reduction in sea-ice coverage. Regionally, the reductions are greatest in the Arctic Ocean, the Kara and Barents Seas and the Seas of Okhotsk and Japan; and seasonally, the reductions are greatest in summer, for which season the 1979–99 trend in ice extents is $-41\,600 \pm 12\,900$ km^2 a^{-1} (-4.9 ± 1.5% per decade). On a monthly basis, the reductions are greatest in July and September for the north polar ice cover as a whole, in September for the Arctic Ocean, in June and July for the Kara and Barents Seas, and in April for the Seas of Okhotsk and Japan. Of the nine regions, only the Bering Sea and the Gulf of St Lawrence show positive ice-extent trends on a yearly-average basis. However, the increases in these two regions are not statistically significant. For the north polar region as a whole, and for the Arctic Ocean, the Seas of Okhotsk and Japan, and Hudson Bay, the negative trends in the yearly averages are statistically significant at a 99% confidence level.

INTRODUCTION

Sea ice is an integral component of the Arctic climate system, restricting exchanges of heat, mass and momentum between the ocean and the atmosphere, reflecting most of the solar radiation incident upon it, releasing salt to the underlying ocean during freezing and transporting fresh water Equatorward through sea-ice advection. It is also of vital importance to the ecology of the Arctic, serving as a habitat for organisms living within it, a platform for animals wandering over it and either a help or a hindrance to numerous marine plant and animal species. Hence, changes in the sea-ice cover can have many outreaching effects on other elements of the polar climate and ecological systems. Furthermore, through the interconnectedness of the climate system, major changes in the sea-ice cover could have more far-reaching effects, extending well beyond the polar regions. For instance, changes in the ice transport of cold fresh water southward in the Greenland Sea could impact the deep-water formation in the northern North Atlantic and thereby affect the "conveyor-belt" circulation that cycles through much of the global ocean.

Considerable attention has been given recently to decreases in Arctic sea-ice extents detected through analysis of satellite passive-microwave data since late 1978 (e.g. Johannessen and others, 1995; Maslanik and others, 1996; Bjørgo and others, 1997; Parkinson and others, 1999). These studies have emphasized decreases examined for the record length as a whole or for annual or seasonal averages. Here we update the annual and seasonal decreases to a 21 year record through the end of 1999, and additionally present time series and trends for each month. Results are given for the Northern Hemisphere as a whole and for each of nine regions, identified in Figure 1. Although a much longer record would be desired (if available), this 21 year period does include El Niño and La Niña episodes, positive and negative phases of the North Atlantic Oscillation and the Arctic Oscillation, and major volcanic eruptions of El Chichón, Mexico (28 March–4 April 1982), and Mount Pinatubo, Philippines (15 June 1991). Hence it provides researchers studying those phenomena with a chance to examine effects they may have had on the Arctic sea-ice cover, thereby helping to quantify the respective climate interconnections.

DATA AND METHODOLOGY

The data used in this study are satellite passive-microwave data from the Nimbus 7 Scanning Multichannel Microwave Radiometer (SMMR) and three U.S. Defense Meteorological Satellite Program (DMSP) Special Sensor Microwave/Imagers (SSM/Is). Microwave data are particularly applicable for sea-ice research because the microwave emissions of sea ice and liquid water differ significantly, thereby allowing a ready distinction between ice and water from the satellite microwave data. Complications arise from the diversity of ice surfaces and from melt ponding and snow cover on the ice, but the satellite passive-microwave data still allow a clear depiction of the overall distribution of the ice and thereby allow a calculation of ice extents (areas covered by ice of concentration at least 15%).

The SMMR was operational on an every-other-day basis for most of the period 26 October 1978 to 20 August 1987, and the sequence of SSM/Is has been operational on a daily basis for most of the period since 9 July 1987. The SMMR and SSM/I data have been used to create a consistent dataset of sea-ice concentrations (per cent areal coverages of ice) and extents through procedures described in Cavalieri and others (1999). Briefly, the method used for obtaining consistency was one of matching sea-ice extents and areas during periods of overlap

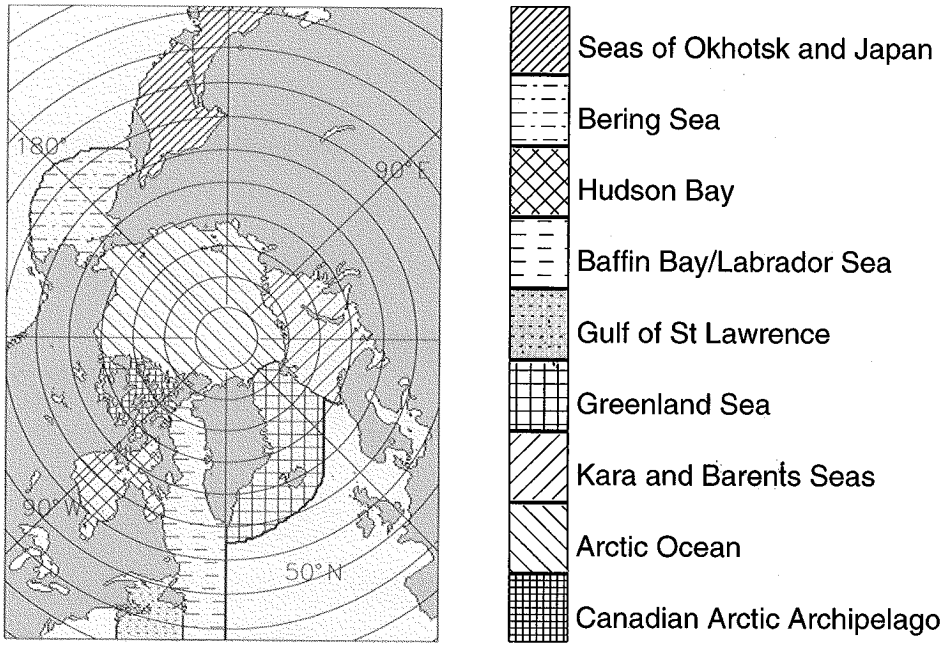

Fig. 1. Identification of the nine regions used in the analysis.

between consecutive sensors. This procedure reduced errors resulting from different sensor frequencies, footprint sizes, observation times and calibrations. While the periods of overlap were shorter than desirable, the average ice-extent differences between sensors were reduced to $<0.05\%$, and the average ice-area differences were reduced to 0.6% or less.

The ice concentrations are gridded to a resolution of approximately 25 km × 25 km (NSIDC, 1992) and are available at the U.S. National Snow and Ice Data Center (NSIDC) in Boulder, CO. The ice extents are calculated by adding the areas of all gridcells containing ice with a calculated concentration of at least 15%. This is done for each of the nine regions identified in Figure 1 and for the total.

Trends in the ice extents are determined through linear least-squares fits separately on the monthly-averaged, seasonally averaged and yearly-averaged data. The trends are calculated for each of the nine regions and the total, and in each case an estimated standard deviation of the trend (σ) is calculated following Taylor (1997). Trends are considered statistically significant in those cases where the trend magnitude exceeds 1.96σ, signifying a 95% confidence level that the slope is non-zero. Trends with magnitudes exceeding 2.58σ are considered significant at a 99% confidence level (Taylor, 1997).

DISCUSSION

Satellite technology provides a powerful resource for monitoring the Arctic sea-ice cover's distribution and extent, and we have taken advantage of this by using this technology to quantify changes in the Arctic ice cover since the late 1970s, with results presented in Table 1 and Figures 2–4 for the 21 year period 1979–99. Most notably, the ice cover as a whole has negative trends for every month, with a trend in the annual averages of $-32\,900 \pm 6100\ \mathrm{km^2\,a^{-1}}$.

Because of the sharp contrast between the microwave emissivities of liquid water and ice, the satellite passive-microwave data are particularly good at revealing the distribution of the sea-ice cover, which in turn allows calculation of the ice extent and determination of changes in ice extent. These satellite data are not as appropriate for determining changes in ice thickness, but analyses of submarine data have revealed a thinning of the ice cover (e.g. Rothrock and others, 1999) that is even more dramatic, percentage-wise, than the ice-extent reductions reported here. (However, Winsor (2001) reports that the thinning did not continue in the 1990s, at least over a limited region from north of Alaska to the North Pole.)

Of course neither the satellite data nor the submarine data can explain the causes of the sea-ice changes or predict future changes. If the decreasing ice coverage is tied most closely to an ongoing Arctic warming (Martin and others, 1997; Serreze and others, 2000) that continues, then the ice cover is likely to continue to decrease as well; but if the sea-ice changes are tied more closely to oscillatory behaviors in the climate system, such as the North Atlantic Oscillation and the Arctic Oscillation (as suggested by, e.g., Deser and others, 2000; Morison and others, 2000; Parkinson, 2000), then it is likely that there will also be fluctuations between periods of sea-ice decrease and periods of sea-ice increase.

Arctic Ocean

Claire L Parkinson
NASA Goddard Space Flight Center, Greenbelt, MD, USA

The Arctic Ocean is the smallest of the Earth's four major oceans (the Pacific, Atlantic, Indian, and Arctic), covering 14 × 10^6 km^2 located entirely within the Arctic Circle (66° 33′N). It is a major player in the climate of the north polar region, has a variable sea ice cover, and is home to a multitude of plant and animal species. Its temperature, salinity, and ice cover have all undergone changes in the past several decades, although it is uncertain whether these predominantly reflect long-term trends, oscillations within the system, or natural variability.

The Arctic Ocean is surrounded largely by the land masses of Eurasia, Greenland, and North America (Figure 1). Its principal connection to the rest of the Earth's oceans lies between Greenland and Scandinavia, where it connects to the North Atlantic. Smaller connections include the narrow (85 km wide) Bering Strait, linking it to the North Pacific, and the passageways within the Canadian Archipelago and between the Archipelago and Greenland, leading to Baffin Bay and thence to Davis Strait and the North Atlantic.

The Arctic Ocean has an unusually broad and shallow continental shelf on the Eurasian side, extending more than 1000 km northward from Scandinavia and approximately 800 km northward from Siberia. The deeper portion of the Arctic is divided by the Lomonosov Ridge into two main basins, the Canadian Basin and the smaller and deeper Eurasian Basin, which has a maximum depth exceeding 5000 m.

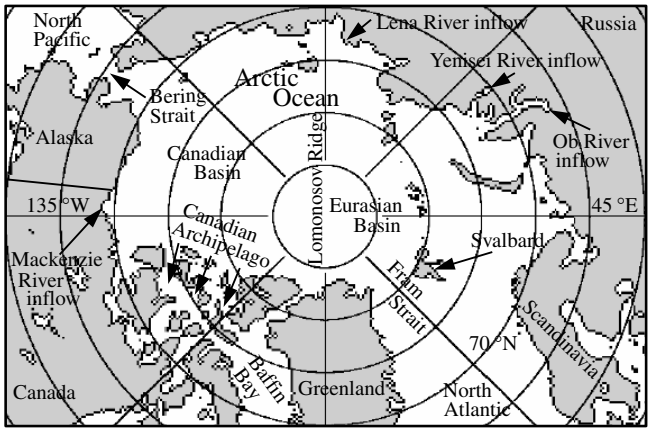

Figure 1 The Arctic Ocean and its surroundings

Water flows into the Arctic principally from the Atlantic as a warm, salty undercurrent. There are also smaller oceanic inputs through the Bering Strait and cold, freshwater inputs from many rivers, most significantly the Lena, Yenisei, and Ob rivers in Russia and the Mackenzie River in Canada. A large part of the outflow from the Arctic is through the Fram Strait between Greenland and Svalbard. Surface currents in the Arctic tend to be clockwise in the Canadian Basin, with occasional reversals to this flow, and more linear along the Transpolar Drift Stream flowing from north of Russia, across the Eurasian Basin and the vicinity of the North Pole, and out through Fram Strait (*see* **Ocean Circulation**, Volume 1).

The water inflows and outflows play a major role in the temperature and salinity structure of the Arctic (*see* **Salinity Patterns in the Ocean**, Volume 1). The warm, salty Atlantic layer from the Atlantic inflows is most prominent closest to the entrance regions but is also apparent throughout the Arctic at depths exceeding 200 m. Overlying the Atlantic layer, the Arctic surface water, in contact with the cold Arctic atmosphere and subject to the freshwater inputs from the surrounding rivers, is colder and less saline. The upper 30–50 m of the surface water tends to be fairly well mixed vertically, with temperatures near the freezing point and salinities ranging from highs exceeding 34 parts per thousand (ppt) near the North Atlantic to lows below 29 ppt near river inflows. Surface salinities in the Bering Strait are approximately 31 ppt. Vertically, salinities tend to increase with depth from the bottom of the mixed layer down to the Atlantic layer, with this vertical variation forming a prominent halocline, especially in the Eurasian Basin. The resulting stable density stratification hinders the warm Atlantic layer waters from upwelling to the surface.

Importantly, the Arctic Ocean is largely capped by a thin, broken layer of sea ice, generally less than 6 m thick and covered by snow (*see* **Sea Ice**, Volume 1). The sea ice restricts exchanges of heat, mass, and momentum between the ocean and the overlying atmosphere and, due to its high reflectivity, also tremendously restricts the input of solar radiation to the ocean. Ice covers almost all of the Arctic Ocean in winter, to an ice concentration (percent areal coverage) of at least 90%, and most of the Arctic Ocean in summer. Sea ice is considerably less saline than the ocean water from which it forms and tends to decrease in salinity over time, as more of the salt content is washed downward through the ice during periods of summer melt.

The Arctic ice cover is in constant flux, being melted by solar radiation, augmented by additional freezing, and moved by winds, waves, and currents. As ice floes separate, openings appear, called *leads* when linear and *polynyas* when large and non-linear. In contrast, when the forces acting on the ice result in floes colliding forcefully together,

the ice breaks and piles of ice rubble form. The above-water portions of these are called *ridges*, and the more massive underwater portions are called *keels*. A ridge/keel combination can have an ice thickness of 30 m or more, far exceeding the level-ice thickness.

Despite the cold temperatures, the Arctic is home to a host of plant and animal life, including algae colonizing the sea ice, sometimes at a concentration of millions in a single ice floe, and protozoans, crustaceans, and nematodes, most of which are smaller than 1 mm in length, also living in the ice and feasting upon the algae. Although biomass tends to be low under the permanent ice pack, high phytoplankton and zooplankton concentrations are frequently found in the ice-free waters. The resulting availability of food makes the ice-free waters popular for numerous species of birds and marine mammals. Amongst the larger animals, polar bears and Arctic foxes roam over the ice, and seals, walruses, and whales live in the ocean waters.

The Arctic has received considerable attention during the late 20th century and the start of the 21st century because of various changes reported to be occurring in it and the sense that these could be related to a possible global warming. Among the changes are the following:

1. A warming and spatial expansion of the Atlantic layer, at depths of 200–900 m, determined from ship-based conductivity–temperature–density (CTD) measurements in the 1990s versus data from 1950–1989 (Morison *et al.*, 2000; Serreze *et al.*, 2000).
2. A warming of the upper ocean in the Arctic's Beaufort Sea (north of Alaska) from 1975 to 1997, found from *in situ* measurements (McPhee *et al.*, 1998).
3. A considerable thinning, perhaps as high as 40%, of the Arctic sea ice cover in the second half of the 20th century, found from submarine data (Rothrock *et al.*, 1999).
4. A lesser and uneven retreat of the ice cover, averaging approximately 3% per decade between late 1978 and the end of 1996, found from satellite data (Bjørgo *et al.*, 1997; Parkinson *et al.*, 1999), and a related shortening of the length of the sea ice season throughout much of the region of the Arctic Ocean's seasonal sea ice cover, also found from satellite data (Parkinson, 2000).
5. An increase of 5.3 days per decade in the length of the melt season on the perennial ice cover, found from satellite data for 1979–1996 (Smith, 1998).
6. A decrease in the salinity of the upper 30 m of the central Beaufort Sea from 1975 to 1997, found from *in situ* measurements. This freshening of the water has been attributed largely to sea ice melt (McPhee *et al.*, 1998) and to increased runoff from the Mackenzie River (Macdonald *et al.*, 1999).
7. A mixed pattern of salinity increases and decreases through the expanse and depth of the rest of the Arctic Ocean (Morison *et al.*, 2000). This includes an increase in the salinity of the surface waters in the mid-Eurasian Basin during the 1990s, found from submarine data, and a thinning of the halocline separating the surface from the warm Atlantic layer waters (Steele and Boyd, 1998; Morison *et al.*, 2000).

In view of the highly coupled nature of the Arctic climate system, many of the changes occurring within it are likely connected. In particular, the freshening of the upper ocean in the Beaufort Sea is likely a response in part to the thinning of the ice, as ice melt adds freshwater to the upper ocean which consistently is much less saline than the ocean average. Similarly, the reduction in the sea ice cover and warming of the upper ocean are probably both connected to the Arctic surface air temperature increases reported, for instance, by Serreze *et al.* (2000).

The causes of the late-20th century changes in the Arctic system remain uncertain, although it is likely that several factors are involved. The increase in carbon dioxide and other greenhouse gases in the global atmosphere, is believed to cause atmospheric warming, although some human influences, such as the increase in particulate matter in the atmosphere, tend to offset a portion of the warming (*see* **Arctic Climate**, Volume 1). Atmospheric warming contributes to oceanic warming, sea ice melt, and upper ocean freshening, all observed in recent decades in portions of the Arctic.

Other potential influences, however, are more oscillatory in nature, such as the impacts of the North Atlantic Oscillation (NAO) and the Arctic Oscillation (AO), two major decadal-scale oscillations in atmospheric pressure patterns, or the impacts of El Niño/La Niña cycles. The NAO and AO in particular have received attention because many of the patterns of change in the ocean and ice cover of the Arctic can be explained by changes in the NAO and AO in recent decades (e.g., Parkinson *et al.*, 1999; Morison *et al.*, 2000). It remains uncertain, however, whether the changes in the NAO and AO are exclusively natural fluctuations in the climate system or are related to long-term, perhaps anthropogenically induced climate change (*see* **Arctic Oscillation**, Volume 1; **El Niño**, Volume 1; **North Atlantic Oscillation**, Volume 1).

Annals of Glaciology 34 2002
© International Glaciological Society

Trends in the length of the Southern Ocean sea-ice season, 1979–99

CLAIRE L. PARKINSON
Oceans and Ice Branch/Code 971, NASA Goddard Space Flight Center, Greenbelt, MD 20771, U.S.A.

ABSTRACT. Satellite passive-microwave data have been used to calculate and map the length of the sea-ice season throughout the Southern Ocean for each year 1979–99. Mapping the slopes of the lines of linear least-squares fit through the 21 years of resulting season-length data reveals a detailed pattern of trends in the length of the sea-ice season around the Antarctic continent. Specifically, most of the Ross Sea ice cover has, on average over the 21 years, undergone a lengthening of the sea-ice season, whereas most of the Amundsen Sea ice cover and almost the entire Bellingshausen Sea ice cover have undergone a shortening of the sea-ice season. Results for the Weddell Sea are mixed, with the northwestern portion of the sea having experienced a shortening of the sea-ice season but a substantial area in the south-central portion of the sea having experienced a lengthening of the ice season. Overall, the area of the Southern Ocean experiencing a lengthening of the sea-ice season by at least 1 day per year over the period 1979–99 is 5.6×10^6 km^2, whereas the area experiencing a shortening of the sea-ice season by at least 1 day per year is 46% less than that, at 3.0×10^6 km^2.

INTRODUCTION

The Southern Ocean (Fig. 1) sea-ice cover extends over a vast area, approximately 18×10^6 km^2, in the austral winter and experiences an enormous annual decay each spring and summer, with its coverage at the summer minimum typically reduced to $< 4 \times 10^6$ km^2 (Zwally and others, in press). The ice cover has a substantial impact on regional climate, most prominently by restricting exchanges of heat, mass and momentum between the ocean and the atmosphere and by reflecting most of the solar radiation incident on it. It also has a substantial impact on the biology of the Southern Ocean, for instance housing many species of micro-organisms, serving as a platform for penguins, seals and other animals, insulating marine life below the ice from the atmosphere, and reducing light penetration into the ocean. The reader is referred to Bentley (1984), Drewry and others (1993) and Worby and others (1996) for more on the climatological impacts of the ice and to Massom (1988), Drewry and others (1993) and Smith and others (1995) for more on the biological impacts of the ice, including the impacts on primary productivity, phytoplankton blooms, krill and breeding success in seabirds.

Until the 1970s, datasets regarding the Southern Ocean sea-ice cover tended to be sparse both temporally and spatially, due in large part to the vast area, the remoteness from most human habitations and the harshness of the in situ conditions. Fortunately, the ease of obtaining data on the ice cover changed dramatically with the advent of satellite technology. Satellite passive-microwave instrumentation in particular has allowed fairly routine monitoring of the Southern Ocean sea-ice cover since the late 1970s. In fact, the ease with which ice and water can be distinguished in passive-microwave data, due to the sharp contrast in ice and water emissivities at many microwave wavelengths, makes sea-ice coverage now amongst the most readily observed of all climate variables.

This paper takes advantage of satellite passive-microwave datasets over the 21 year period 1979–99 to report on changes in the length of the sea-ice season, defined as the number of days per year with sea-ice coverage, throughout

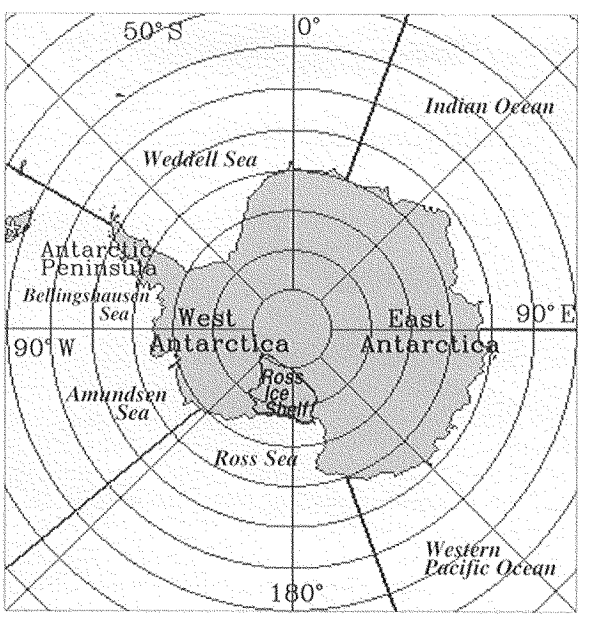

Fig. 1. Location map, including the boundaries of the five sectors into which the Southern Ocean is divided for analysis. The non-land boundaries are along the longitude lines at 20° E, 90° E, 160° E, 130° W and 60° W.

the Southern Ocean. Changes in the length of the sea-ice season not only affect the regional climate and ecology, in ways alluded to above, but also can serve as indicators of change within the broader climate system. The length of

the sea-ice season was first examined and mapped for the Southern Ocean in Parkinson (1994), where results were presented for the 8 year period 1979–86. It has subsequently been examined for the 7 year period 1988–94 by Parkinson (1998) and for the two 8 year periods 1979–86 and 1989–96 by Watkins and Simmonds (2000).

DATA AND METHODOLOGY

This study uses data from the Nimbus 7 Scanning Multichannel Microwave Radiometer (SMMR) and the Defense Meteorological Satellite Program (DMSP) Special Sensor Microwave/Imagers (SSM/Is). The SMMR instrument collected data on an every-other-day basis for most of the period 26 October 1978 to 20 August 1987, and the SSM/Is have collected data on a daily basis for most of the period since 9 July 1987. The two datasets have been used by Cavalieri and others (1999) to create a consistent set of sea-ice concentrations (areal percentages of sea ice) using an algorithm commonly termed the NASA Team algorithm. This algorithm is based on the assumption of three surface types (two ice types plus liquid water), polarization and gradient ratios calculated from three channels of the satellite data, and a weather filter. The algorithm is described in detail in Gloersen and others (1992), and the procedures for matching the SMMR and SSM/I datasets are described in Cavalieri and others (1999). The ice concentrations have spatial resolutions of approximately 55 km and are gridded to a consistent grid with gridcell size approximately 25 × 25 km (NSIDC, 1992).

The sea-ice concentration data are used here to determine the length of the sea-ice season in each year at each gridpoint, by counting the number of days with ice coverage of at least 15%. Alternative ice-concentration cut-offs of 30% and 50% have also been used, with similar patterns resulting irrespective of which cut-off is selected (e.g. next section and Parkinson, 1994). The 15% cut-off is used for the main results in this paper both because it is the standard cut-off used for the ice-extent results from the same dataset (e.g. Zwally and others, in press) and because comparison of the ice concentrations from the NASA Team algorithm with those derived from other algorithms yields a close match in distributions of ice coverage of at least 15% but some substantial differences in distributions of ice of higher concentrations (e.g. Comiso and others, 1997; Hanna, 1999; Markus and Cavalieri, 2000). The 15% results are thus considered the most robust.

The trend in the length of the sea-ice season is calculated at each ocean gridpoint as the slope of the line of linear least-squares fit through the 21 years of season-length data. The calculations are done through matrix manipulations on the 21 annual matrices of the length of the sea-ice season for the 15% ice-concentration cut-off, and are then repeated for the 30% and 50% cut-offs. For the trend calculations, each year's season lengths are linearly scaled to equivalents for a 365 day year.

In order to obtain a measure of statistical significance for the trend results, an estimated standard deviation (σ) of the 21 year trend is calculated at each gridpoint following Taylor (1997). Trends are considered statistically significant when the trend magnitude exceeds 1.96σ, signifying a 95% confidence level that the slope is non-zero. Trends that additionally meet the criterion of exceeding 2.58σ are considered statistically significant at a 99% confidence level (Taylor, 1997).

SUMMARY AND DISCUSSION

Satellite passive-microwave data have been used to determine and map the length of the sea-ice season in each year 1979–99, with results showing (a) season lengths generally decreasing outward from the coast except in regions of coastal polynyas, (b) perennial ice cover consistently in the far-western Weddell Sea and more selectively elsewhere around the continent, and (c) decidedly short ice seasons (for the high latitudes involved) off the Ross Ice Shelf (Fig. 2). Trends in the season lengths over the 1979–99 period show that: (a) most of the Ross Sea underwent a lengthening of the sea-ice season, (b) most of the Amundsen Sea and almost the entire Bellingshausen Sea underwent a shortening of the sea-ice season, (c) the Weddell Sea had a shortening of the sea-ice season in the northwest but a lengthening of the season in a substantial area of the south-central sea, and (d) around much of East Antarctica, the near-coastal region experienced a lengthening of the season, while further from the coast there was a more even mixture of areas experiencing season shortenings and those experiencing season lengthenings (Fig. 3). Integrating spatially, a much larger area of the Southern Ocean experienced an overall lengthening of the sea-ice season over the 21 years 1979–99 than experienced a shortening (Fig. 4).

These results complement results on trends in the Southern Ocean ice extent (defined as the area having sea-ice concentrations of at least 15%) found from the SMMR and SSM/I record. Analyses of the regional and hemispheric ice extents for the 16 year period 1979–94 by Stammerjohn and Smith (1997) and for the 20.2 year period from November 1978 through December 1998 by Zwally and others (in press) reveal positive ice-extent trends for the Weddell Sea, the Western Pacific Ocean, the Ross Sea and the Southern Ocean as a whole and negative ice-extent trends for the Bellingshausen and Amundsen Seas. The mapped results of the trends in the length of the sea-ice season (Fig. 3) provide a far more detailed spatial picture of the 21 year changes in the Southern Ocean than is possible when examining the ice extents, but at the same time, they provide a far less detailed temporal picture. Together, the ice-extent and season-length results show an overall increasing Southern Ocean ice cover, with the Bellingshausen and Amundsen Seas and the far-western and northwestern Weddell Sea showing instead ice-cover decreases. These results are consistent with reports of notable warming over the Antarctic Peninsula from 1978 to 1996 (King and Harangozo, 1998; Skvarca and others, 1998; both studies also include years prior to 1978) and with a tendency for air-temperature anomalies in the peninsula region to be opposite in sign to those predominating over much of the rest of the Antarctic (Rogers, 1983; Stammerjohn and Smith, 1997).

The satellite-derived Southern Ocean sea-ice results, with overall lengthening sea-ice seasons (Figs 3 and 4) and increasing ice extents (Stammerjohn and Smith, 1997; Zwally and others, in press), provide a sharp contrast with the widely publicized overall ice-cover decreases in the Arctic occurring over the same period. Many uncertainties remain, but one certainty is that the ice covers of the two hemispheres have not been fluctuating synchronously over the past two decades.

Annals of Glaciology 34 2002
© International Glaciological Society

In situ and satellite surface temperature records in Antarctica

CHRISTOPHER A. SHUMAN,[1,2] JOSEFINO C. COMISO[2]
[1]*Earth System Science Interdisciplinary Center, University of Maryland, College Park, MD 20742-2465, U.S.A.*
[2]*Oceans and Ice Branch, Laboratory for Hydrospheric Processes, NASA Goddard Space Flight Center, Code 971, Greenbelt, MD 20771, U.S.A.*

ABSTRACT. Air-temperature records (T_A) during 1992 from five inland Antarctic automatic weather station (AWS) sites were compared with the best available infrared temperatures (T_{IR}) from the Advanced Very High Resolution Radiometer (AVHRR) as well as calibrated passive-microwave temperatures (T_C) from the Special Sensor Microwave/Imager (SSM/I). Daily and monthly average T_A, T_{IR}, and T_C data indicate that each approach captures generally similar trends at each site but each approach also has limitations. AWS T_A data are considered the most accurate but represent spatially restricted areas and may have long gaps due to sensor or transmission problems. AVHRR T_{IR} data have daily variability similar to the T_A record but have numerous small gaps due to cloud cover or observation interruptions. An offset between T_A and T_{IR} (>4 K) at the South Pole site was identified that may be due to the inclusion of data with large satellite scan angles necessary to cover this area. SSM/I T_C data have the most continuity but exhibit calibration problems, a significantly damped daily response and do not cover all of Antarctica. Individual daily differences between T_A and T_{IR} as well as T_A and T_C can exceed 17 K, but all sites have mean daily differences of about 1 K or better, after compensating for the offset at South Pole, and standard deviations of <6 K. Monthly temperature differences are typically 5 K or better, with standard deviations generally <3 K. And finally, using the available data, the 1992 average temperature differences are <1 K.

INTRODUCTION

Detection of climate change involves determining a multi-year baseline for a climate parameter and then detecting variations that exceed its observed range over the baseline period. Increasing temperatures, possibly linked to global climate warming, have been detected at sites on the Antarctic Peninsula (Jacka and Budd, 1991; King, 1994; Vaughan and Doake, 1996). Further inland, at specific automatic weather stations (AWSs), data on near-surface temperature (T_A) are beginning to define a climate baseline (Shuman and Stearns, 2001). However, these data have significant gaps and may not be representative of broader regional or continental-scale patterns. Temperature fields derived from satellite infrared (Comiso, 2000) or passive-microwave sensors can provide a much more complete characterization of spatial and temporal variations in Antarctic temperature. Currently, the only spatially detailed record of surface temperature across Antarctica is provided by Advanced Very High Resolution Radiometer (AVHRR) infrared channels (T_{IR}), but they must be carefully processed to remove the effects of clouds (Comiso, 2000). Passive-microwave data from the 37 GHz channel of the Special Sensor Microwave/Imager (SSM/I) are not influenced by cloud cover and can be calibrated (T_C) at specific AWS locations (Shuman and others, 1995) or by complex radiative transfer models (Fung and Chen, 1981; Comiso and others, 1982), but cannot yet be broadly extrapolated in space and time because of still poorly understood spatial variations in the emissivity of the surface. Time series of these satellite data, if they could be used consistently, would provide the temperature data needed to identify regional and continental-scale climate change across Antarctica. This study, using recently published temperature data, analyzes in situ and satellite temperature information, and documents the advantages and limitations of each approach. The intent of this study is to use the AWS data to gain insight into the accuracy of the surface temperatures retrieved from satellite infrared and microwave sources and establish confidence limits on these data.

Table 1. Site data for inland Antarctic AWS temperature records

AWS name	*Location*	*Elevation*	*Grid*	*Start*	*Stop*
		m			
Byrd	80.01° S, 119.40° W	1530	121 196	Feb. 1980	
Clean Air	90.00° S, 120.00° W	2835		Jan. 1986	
Lettau	82.52° S, 174.45° W	55	155 206	Jan. 1986	
Lynn	74.21° S, 160.41° E	1772	182 239	Jan. 1988	Jan. 1998
Siple	75.90° S, 84.00° W	1054	97 168	Jan. 1982	Apr. 1992

Notes: This analysis is based on available 3 hourly average data taken from the University of Wisconsin server in March 1999. The grid column contains the coordinates of the 25 km SSM/I pixel covering the AWS location. There is no SSM/I coverage at the South Pole, where AWS Clean Air is located.

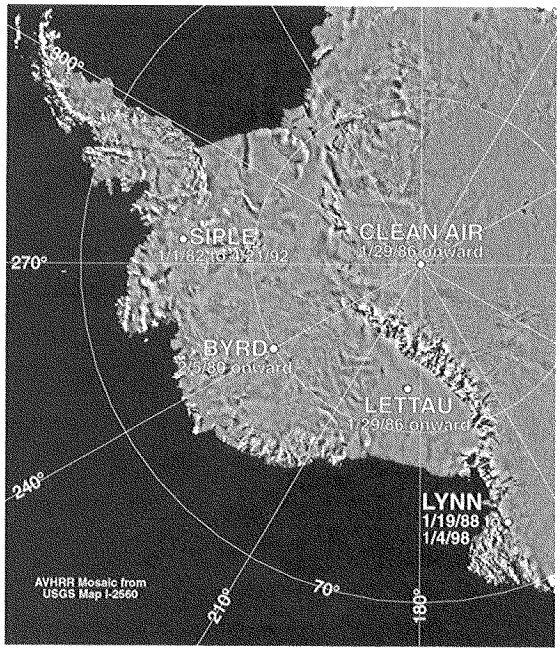

Fig. 1. The locations and dates of operation of the five inland Antarctic AWSs used in this study. Dates are mm/dd/yy.

This project used three types of temperature data from 1992 that were spatially and temporally co-registered:

(1) daily-average T_A records from five AWSs in Antarctica operated by the University of Wisconsin (see Fig. 1; Table 1);

(2) daily-average AVHRR T_{IR} data compiled and processed as described in Comiso (2000); and

(3) daily-average T_C data derived from the SSM/I datasets compiled by the U.S. National Snow and Ice Data Center (NSIDC) and calibrated as described in Shuman and Stearns (2001).

The three measurements are not exactly for the same physical parameter since the AWS measures near-surface air temperature (~2 m), the infrared sensor measures skin-depth temperature, and the passive-microwave sensor measures the average temperature of the upper surface layer. This comparative analysis will help establish how the three datasets can be used in conjunction to study the variations of an important climate parameter through time.

CONCLUSIONS

The significance of this study is that it enabled an improved understanding of three currently available Antarctic surface temperature datasets. At present, the thermal infrared data provide the only spatially detailed temperature distributions in Antarctica, but contain data gaps due to intermittent cloud cover. The passive-microwave data have the potential to provide spatially detailed, continuous and gap-free temperature distributions. However, more research is needed to correctly calibrate these data for regional changes in the radiative characteristics of the snow cover. The AWS data are the most accurate, but are the most difficult to use for large-scale scientific research because of their limited spatial coverage and gaps in the temporal series due to occasional instrument malfunction. The AWS data, however, provide the means to determine the value and the significance of both the infrared and the passive-microwave datasets.

Table 4. Difference statistics for all 1992 T_{IR} and T_C daily mean temperatures

	Byrd	*Clean Air*	*Lettau*	*Lynn*	*Siple*
Days	323	305	313	342	328
T_{IR}	245.66	226.38	246.97	238.85	248.12
T_C	247.02		246.64	237.64	247.61
$T_{IR} - T_C$	−1.36		0.33	1.21	0.52

Notes: This analysis is based on all days where there was both an AVHRR infrared temperature (T_{IR}) and a calibrated SSM/I temperature (T_C). There are no T_C data for AWS Clean Air due to the hole in SSM/I coverage at the South Pole.

These different near-surface temperature datasets are quite complementary and should enable the development of improved temperature baselines for sites in Antarctica. Although T_A data may be discontinuous, T_{IR} data can accurately fill most gaps at specific sites. Any gaps due to cloud cover in the T_{IR} record can then be filled with extrapolated T_C values, and these values also provide a reliability check on the spatially more extensive T_{IR} data. Processing requirements are significant, especially for T_{IR}, however, and detecting and removing cloud impacts and accurately calibrating these data remains a challenge. Overall, this study has demonstrated that the satellite data compare quite well in most cases, assuming that these AWS T_A data reliably represent these locations. The limited comparisons presented here certainly justify continued efforts with additional years of data at these and other sites across the Antarctic continent. Although individual day differences between in situ and satellite temperatures can be quite large, the average errors are relatively small and appear well constrained. For the thermal infrared dataset, the standard products are the monthly averages that appear to provide a realistic representation of temperature distributions around the continent. Some of the discrepancies between the methods studied here are probably due to the differing spatial and temporal resolutions of the three different methods. We also have assumed that the AWS hardware for measuring temperature is always in perfect condition, which is not guaranteed in such an adverse environment, and there may be some instances when the AWS actually provides erroneous results despite quality-control procedures. For optimal accuracy, especially at high temporal resolution, a combination of the three methods may be necessary to determine an accurate climate baseline and then evaluate potential changes that may come in the years ahead.

Analysis of seasonal cycles in climatic trends with application to satellite observations of sea ice extent

Konstantin Y. Vinnikov
Department of Meteorology, University of Maryland, College Park, Maryland, USA

Alan Robock
Department of Environmental Sciences, Rutgers University, New Brunswick, New Jersey, USA

Donald J. Cavalieri and Claire L. Parkinson
Oceans and Ice Branch, NASA Goddard Space Flight Center, Greenbelt, Maryland, USA

Received 29 November 2001; accepted 8 January 2002; published 8 May 2002.

[1] We present a new technique to study the seasonal cycle of climatic trends in the expected value, variance, and other moments of the statistical distribution. The basis of the technique is multiple linear regression, but with periodic basis functions. The technique allows us to provide comprehensive information on statistical parameters of climate for every day of an observational period. Using daily data, the technique has no problems caused by different lengths of months or the leap-year cycle. Without needing to assume the stationarity of contemporary climate, the technique allows the study of statistical parameters of climatic records of arbitrary length. We illustrate the technique with applications to trends in the satellite observed variations of sea ice extent in the Northern and Southern Hemispheres. We show that a significant part of the variability in hemispheric sea ice extents for the period 1978–1999 is related to linear trends. *INDEX TERMS:* 1620 Global Change: Climate dynamics (3309); 1866 Hydrology: Soil moisture; 3309 Meteorology and Atmospheric Dynamics: Climatology (1620); 4215 Oceanography: General: Climate and interannual variability (3309)

1. Introduction

[2] Traditional climatology uses monthly averages and statistics estimated for 30-yr time intervals. This approach, however, has well-known limitations. Monthly averages incorporate different lengths for different months and different years (leap years). Using only 12 monthly averages is a very crude approximation of the seasonal variation for many meteorological variables and produces biases in the spectrum of meteorological records. Time series for specific months are too short to estimate the parameters of the statistical distribution of monthly averages properly.

[3] Here we introduce a new statistical approach to analyzing climate data that explicitly accepts the idea that long-term climatic records may contain trends in means, variances, covariances, and other moments of the statistical distribution of meteorological variables. We also explicitly permit seasonal cycles of these trends. This approach is designed to analyze observed past climate change and climate model output, but is not designed to be used to extrapolate the trends into the future.

2. Theory

[4] We start by using daily observations instead of monthly averages. Let us denote

$$y(t) = Y(t) + y'(t); \tag{1}$$

where $y(t)$ is the observed value of y for day number t, $t = t_1, t_2, t_3, \ldots, t_n$; $Y(t)$ is the expected value of $y(t)$; and $y'(t)$ is the residual (anomaly). We can use as t the Julian day number, or choose any other specific date as the reference day ($t = 0$).

[5] A common approach in studies of the seasonal cycle is to use Fourier harmonics of the annual period to approximate the seasonal variation of the mean values of the observed data [*Anderson*, 1971; *Polyak*, 1975]. It is well known that climatic trends may be different for different seasons [*Mitchell*, 1961; *Vinnikov*, 1986; *Hansen and Lebedeff*, 1987; *Chapman and Walsh*, 1993; *Stammerjohn and Smith*, 1997; *Hansen et al.*, 1999; *Parkinson et al.*, 1999; *Jones et al.*, 1999; *Rigor et al.*, 2000; *Serreze et al.*, 2000]. Let us assume that the climatic trend in the expectation $Y(t)$ of the observed variable $y(t)$ is a periodic function of the annual period. Particularly, for a linear trend this means:

$$Y(t) = A(t) + B(t) \cdot t, \tag{2}$$

where $A(t) = A(t + T)$, $B(t) = B(t + T)$, and $T = 365.25$ days. Let us use a limited number of Fourier harmonics to approximate both periodic functions, $A(t)$ and $B(t)$:

$$Y(t) = a_0 + \sum_{k=1}^{K}\left[a_k \sin\left(\frac{2\pi kt}{T}\right) + b_k \cos\left(\frac{2\pi kt}{T}\right)\right] + \alpha_0 t + \sum_{m=1}^{M}\left[\alpha_m t \sin\left(\frac{2\pi mt}{T}\right) + \beta_m t \cos\left(\frac{2\pi mt}{T}\right)\right]. \tag{3}$$

We can estimate all the unknown multiple regression coefficients in (3) from the least squares condition:

$$\sum_{t=t_1}^{t_n}[y(t) - Y(t)]^2 = F(a_0, \ldots, a_K, b_1, \ldots, b_K, \alpha_0, \ldots, \alpha_M, \beta_1, \ldots, \beta_M) = \min. \tag{4}$$

The number of harmonics required for approximation of $A(t)$ and $B(t)$, K, and M, should be chosen from independent considerations or should be estimated from analyses of the same data.

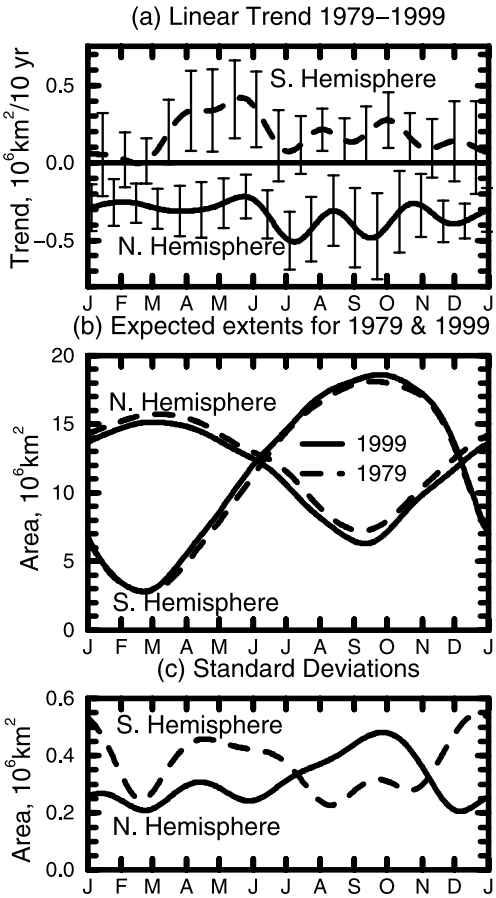

Figure 3. Sea ice extents in the Northern and Southern Hemispheres: (a) linear trend 1979–1999, (b) expected extent for years 1979 and 1999, (c) standard deviations of daily extents, 1979–1999.

4. Discussion and Conclusions

[10] Most previous analyses of trends in sea ice extents have produced statistics for monthly or yearly averages. Daily observations give us an opportunity to see additional interesting details in the same climatic records. Results of applying the new technique to sea ice extents yield the following conclusions:

4.1. Northern Hemisphere Sea Ice Extent

[11] The expected sea ice extent in the Northern Hemisphere has been decreasing during 1979–1999 for each day of the year with rates from -0.2×10^6 km^2/10 yr to -0.5×10^6 km^2/10 yr (Figures 3a and 3b). Consistently, although in less detail, *Parkinson and Cavalieri* [2002] find that monthly trends in the Northern Hemisphere ice extents have negative values for all 12 months, all with magnitudes of at least -0.23×10^6 km^2/10 yr.

[12] The expected maximum seasonal sea ice extent in 1999 was about 0.5×10^6 km^2 less than it was in 1979 (Figure 1, line (a)). This corresponds to a $\sim$0.3° latitude poleward shift of the average position of the sea ice boundary at the time of its maximum seasonal expansion.

[13] The expected minimum seasonal sea ice extent in 1999 was about 1.0×10^6 km^2 less than it was in 1979 (Figure 1, line (b)). This corresponds to a $\sim$1° latitude poleward shift of the average position of the sea ice boundary at the time of its maximum seasonal retreat.

[14] The average amplitude of the seasonal variation in sea ice extent has increased about 0.5×10^6 km^2 during the 21-year period 1979–1999, from $\sim 8.5 \times 10^6$ km^2 to $\sim 9.0 \times 10^6$ km^2 (Figure 1).

[15] Daily anomalies of sea ice extent (Figure 1) are an order of magnitude smaller than the seasonal variation of sea ice extent (about $8.5–9.0 \times 10^6$ km^2/10 yr, Figure 1).

[16] Trend-related changes during the last two decades of the 20th Century have the same order of magnitude ($0–1 \times 10^6$ km^2) as daily anomalies of sea ice extent (Figure 1).

4.2. Southern Hemisphere Sea Ice Extent

[17] The expected sea ice extent in the Southern Hemisphere has been increasing during 1979–1999 for almost every day of the year, with rates up to $\sim 0.4 \times 10^6$ km^2/10 yr (Figures 3a and 3b). This asymmetry between Northern and Southern Hemisphere sea ice variation was predicted using a climate model forced by increasing greenhouse gases [*Manabe et al.*, 1992] and then observed through satellite microwave measurements [*Cavalieri et al.*, 1997].

[18] The expected seasonally maximum sea ice extent in 1999 is about 0.5×10^6 km^2 larger than it was in 1979 (Figure 2, line (a)). There is no noticeable trend in sea ice extent at the time of its maximum seasonal retreat (Figure 2, line (b)). The average amplitude of seasonal variation in sea ice extent has increased about 0.5×10^6 km^2 during the 21-year period, from $\sim 15.3 \times 10^6$ km^2 to $\sim 15.8 \times 10^6$ km^2. Thus the seasonal amplitude of sea ice extent has increased in both hemispheres, and in both cases by about 0.5×10^6 km^2 (Figures 1 and 2).

[19] Daily anomalies of sea ice extent in the Southern Hemisphere (Figure 2) are an order of magnitude smaller than the seasonal variation of sea ice extent (Figure 3b), the same as in the Northern Hemisphere.

[20] As in the Northern Hemisphere, daily anomalies in the Southern Hemisphere are generally between -1×10^6 km^2 and 1×10^6 km^2 (Figures 1 and 2), although the 1979–1999 trends are generally smaller in magnitude, as well as being opposite in sign (Figure 3a).

4.3. Further Development of the Technique

[21] Harmonic functions may not be optimal for approximation of seasonal variations of many climatic variables. Other classes of periodic functions may be used, and empirical statistically orthogonal functions should be considered as possible alternatives to harmonic functions.

[22] In some cases, significant seasonal variations can exist in the variance of climatic indices. In such cases, it might be useful to repeat the calculations using a "weighted least squares" with weights that are inversely proportional to the estimated variance.

[23] Trend estimates for each day of a year provide information about the seasonality of trends in moments of the statistical distribution of climatic variables. The same technique can be applied to analyze time series of observed climatic indices at every specific time of a day. In the case when we have hourly meteorological observations, we can put together the estimates for every hour and receive a full picture of seasonal and diurnal cycles in climatic trends. Joint analysis of the seasonal and diurnal cycles in climatic trends will be discussed in another paper.

[24] The existing traditional practice of climatic services is based on monthly averages and a 30-year period for normals. Even for a variable with an autocorrelation time scale of 50 days, such as sea ice, this technique provides high temporal resolution depictions of the seasonal cycles of the means, anomalies, and trends (Figures 1–3). Without needing to assume the stationarity of contemporary climate, our approach allows the study of statistical parameters of climatic records of arbitrary length. This opens a new opportunity to modernize existing climate services.

Variability of Antarctic sea ice 1979–1998

H. Jay Zwally, Josefino C. Comiso, Claire L. Parkinson, Donald J. Cavalieri, and Per Gloersen

Oceans and Ice Branch, NASA Goddard Space Flight Center, Greenbelt, Maryland, USA

Received 22 November 2000; revised 23 July 2001; accepted 13 September 2001; published 16 May 2002.

[1] The principal characteristics of the variability of Antarctic sea ice cover as previously described from satellite passive microwave observations are also evident in a systematically calibrated and analyzed data set for 20.2 years (1979–1998). The total Antarctic sea ice extent (concentration >15%) increased by 11,180 ± 4190 $km^2\ yr^{-1}$ (0.98 ± 0.37% $(decade)^{-1}$). The increase in the area of sea ice within the extent boundary is similar (10,860 ± 3720 $km^2\ yr^{-1}$ and 1.26 ± 0.43% $(decade)^{-1}$). Regionally, the trends in extent are positive in the Weddel Sea (1.4 ± 0.9% $(decade)^{-1}$), Pacific Ocean (2.0 ± 1.4% $(decade)^{-1}$), and Ross (6.7 ± 1.1% $(decade)^{-1}$) sectors, slightly negative in the Indian Ocean (−1.0 ± 1.0% $(decade)^{-1}$), and strongly negative in the Bellingshausen-Amundsen Seas sector (−9.7 ± 1.5% $(decade)^{-1}$). For the entire ice pack, ice increases occur in all seasons, with the largest increase during fall. On a regional basis the trends differ season to season. During summer and fall the trends are positive or near zero in all sectors except the Bellingshausen-Amundsen Seas sector. During winter and spring the trends are negative or near zero in all sectors except the Ross Sea, which has positive trends in all seasons. Components of interannual variability with periods of about 3–5 years are regionally large but tend to counterbalance each other in the total ice pack. The interannual variability of the annual mean sea ice extent is only 1.6% overall, compared to 6–9% in each of five regional sectors. Analysis of the relation between regional sea ice extents and spatially averaged surface temperatures over the ice pack gives an overall sensitivity between winter ice cover and temperature of −0.7% change in sea ice extent per degree Kelvin. For summer some regional ice extents vary positively with temperature, and others vary negatively. The observed increase in Antarctic sea ice cover is counter to the observed decreases in the Arctic. It is also qualitatively consistent with the counterintuitive prediction of a global atmospheric-ocean model of increasing sea ice around Antarctica with climate warming due to the stabilizing effects of increased snowfall on the Southern Ocean. *INDEX TERMS:* 1620 Global Change: Climate dynamics (3309); 1635 Global Change: Oceans (4203); 1640 Global Change: Remote sensing; 4207 Oceanography: General: Arctic and Antarctic oceanography; *KEYWORDS:* sea ice, Antarctic, climate, passive microwave, Southern Ocean

1. Introduction

[2] In recent decades the Antarctic sea ice cover has varied significantly from year to year with some anomalies persisting for periods of 3–5 years [e.g., *Zwally et al.*, 1983a]. However, decadal-scale sea ice changes have been smaller and more difficult to ascertain with statistical significance. Furthermore, while the physical processes (ice-ocean-atmosphere-solar) that control the annual growth and decay of sea ice are well known, the manner in which these processes combine on decadal timescales and regional spatial scales is complex and not well determined. In particular, the interaction of the Antarctic sea ice cover with global climate change is uncertain. In one view the intuitive expectation that a smaller sea ice cover should be associated with warmer atmospheric temperatures is supported by some observations and models. For example, *Gordon and O'Farrell* [1997] modeled a decreasing Antarctic sea ice cover in a warmer climate but with a smaller rate of decrease than their modeled rate of decrease for the Arctic sea ice. Observationally, *Jacka and Budd* [1991] and *Weatherly et al.* [1991] also showed the expected negative correlation between regional-scale sea ice changes and Antarctic coastal air temperatures. In another view, at least one climate model, which included coupled ice-ocean-atmosphere interactions [*Manabe et al.*, 1992], gives the counterintuitive result that the sea ice cover would actually increase with global climate warming. The physical processes in the model that cause the predicted sea ice increase are increased precipitation with a warmer atmosphere in polar regions, more snowfall on sea ice, lower salinity in the near-surface ocean layers, more stable mixed layer and reduced heat flux to the surface, and consequently, more sea ice.

[3] Clearly, if changes in the distribution of Antarctic sea ice are expected to be indicative of global climate change, a better understanding of the nature and causes of Antarctic sea ice variability is required. In particular, we should know whether Antarctic sea ice is expected to increase or decrease with climate warming. In this paper we describe the variability of the Antarctic ice cover in detail, including the variations in regional sectors as defined by *Zwally et al.* [1983b] and *Gloersen et al.* [1992], using 20 years of well-calibrated data. We believe the characteristics of the observed sea ice variability of the Antarctic provide new insights to the interplay of the relevant physical and climatic processes on seasonal to decadal timescales. In particular, our analysis of the decadal-scale trends in sea ice by season show that the trend of increasing Antarctic sea ice cover is dominated by summer and autumn increases and that changes in the winter are near zero overall. These results are important because the dominant climatic processes controlling the distribution of sea ice around the time of the winter maximum extent are likely to be

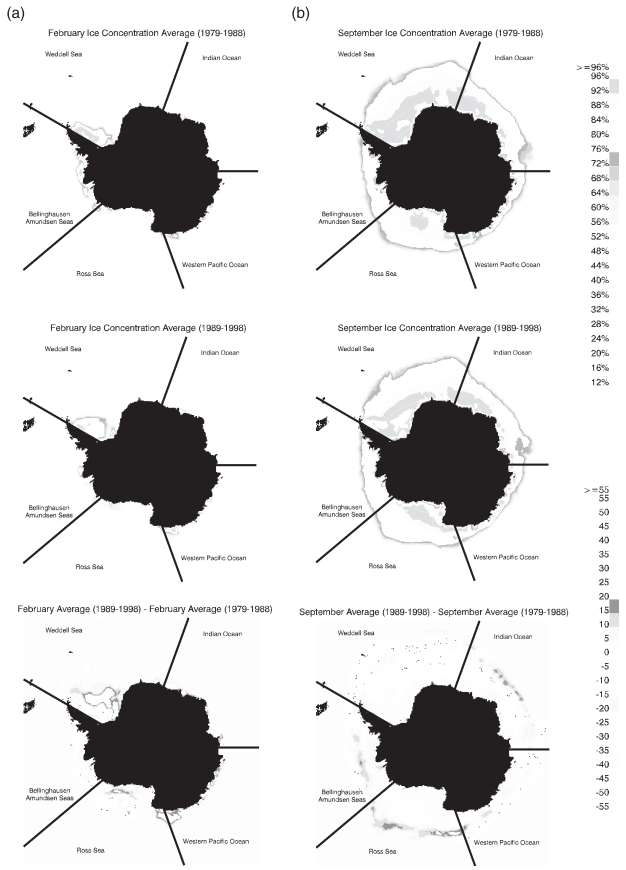

Figure 1. Average sea ice concentration maps averaged over (top) the first 10 years (1979–1988) and (middle) the second 10 years (1989–1998) and (bottom) their differences for (a) February, the month of summer minimum and (b) September, the month of winter maximum. The five regional sectors are Weddell Sea (60°W–20°E), Indian Ocean (20°–90°E), Pacific Ocean (90°–160°E), Ross Sea (160°–140°W), and Bellingshausen-Amundsen Seas (140°–60°W). See color version of this figure at back of this issue.

significantly different than those near the summer minimum. Examination of potential correlations between temperature (using new satellite estimates of surface temperature averaged over the sea ice pack) and sea ice extent shows a wintertime correlation on a regional basis, which gives an estimate of the sensitivity of sea ice cover to temperature change.

2. Background

[4] Since the advent of satellite remote sensing, the study of interannual changes in the Antarctic sea ice cover and their possible climatic significance have been the subject of numerous investigations. Initially, the use of relatively short or poorly calibrated satellite historical records caused some conflicting results regarding trends in ice extent [e.g., *Kukla*, 1978; *Kukla and Gavin*, 1981; *Zwally et al.*, 1983a]. Even with the sole use of longer and more consistent passive microwave data, the trends from analysis of the same set of satellite data have differed [*Johannessen et al.*, 1995; *Bjørgo et al.*, 1997; *Cavalieri et al.*, 1997; *Stammerjohn and Smith*, 1997]. This is partly because the satellite sensors have finite lifetimes and the time series is made up of measurements from different sensors, some of which have different footprints and characteristics than the others. Furthermore, different investigators use different ice algorithms for the retrieval of ice parameters and their own techniques for removing abnormal values in the land/ocean boundaries and the open ocean. During periods of overlap the different sensors also provide slightly different sea ice extents and actual areas, even with the same techniques. Therefore further intersensor adjustments are required to match the overlap results and obtain a uniform time series.

[5] For the period of November 1978 through December 1996, *Cavalieri et al.* [1997] found an asymmetry in the trends of decreasing Arctic sea ice extent ($-2.9 \pm 0.4\%$ (decade)$^{-1}$) and increasing Antarctic sea ice extent ($+1.3 \pm 0.2\%$ (decade)$^{-1}$). *Cavalieri et al.* [1997] also reviewed the results of previous analyses, which used essentially the same multisatellite passive microwave data set but with some different methodologies and conclusions about the apparent trends in the Antarctic sea ice. The methodologies for sea ice mapping and intersatellite calibration techniques employed by *Cavalieri et al.* [1997] to produce a data [e.g., see *Steffen et al.*, 1992].

9. Discussion and Conclusions

[51] A primary result of this analysis of the 20 years of measurements of sea ice concentration on the Southern Ocean is the $+11{,}181 \pm 4190$ km^2 yr^{-1} ($+0.98 \pm 0.37\%$ (decade)$^{-1}$) increase in sea ice extent and a very similar $+10{,}860 \pm 3720$ km^2 yr^{-1} ($+1.26 \pm 0.43\%$ (decade)$^{-1}$) increase in sea ice area. Regionally, the trends in extent are positive in the Weddell Sea ($1.4 \pm 0.9\%$ (decade)$^{-1}$), Pacific Ocean ($2.0 \pm 1.4\%$ (decade)$^{-1}$), and Ross Sea ($6.7 \pm 1.1\%$ (decade)$^{-1}$) sectors, slightly negative in the Indian Ocean ($-1.0 \pm 1.0\%$ (decade)$^{-1}$), and negative in the Bellingshausen/Amundsen Seas sector ($-9.7 \pm 1.5\%$ (decade)$^{-1}$). An overall increase in Antarctic sea ice cover, during a period when global climate appears to have been warming by 0.2 K (decade)$^{-1}$ [*Hansen et al.*, 1999], stands in marked contrast to the observed decrease in the Arctic sea ice extent of $-34{,}300 \pm 3700$ km^2 yr^{-1} ($-2.8 \pm 0.3\%$ (decade)$^{-1}$) and sea ice area of $-29{,}500 \pm 3800$ km^2 yr^{-1} ($-2.8 \pm 0.4\%$ (decade)$^{-1}$) in sea ice area [*Parkinson et al.*, 1999]. The observed decrease in the Arctic has been partially attributed to greenhouse warming through climate model simulations with increased CO_2 and aerosols [*Vinnikov et al.*, 1999]. As discussed in section 1, an increasing Antarctic sea ice cover is consistent with at least one climate model that includes coupled ice-ocean-atmosphere interactions and a doubling of CO_2 content over 80 years [*Manabe et al.*, 1992].

[52] Another main aspect of the results is the seasonality of the changes, being largest in autumn in both magnitude ($+24{,}700 \pm 17{,}500$ km^2 yr^{-1}) and percentage ($+2.5 \pm 1.8\%$ (decade)$^{-1}$) and second largest in summer ($+6700 \pm 12{,}600$ km^2 yr^{-1} and $+1.7 \pm 3.2\%$ (decade)$^{-1}$) in terms of percentage change. The changes for the winter season ($+7400 \pm 8500$ km^2 yr^{-1} and $+0.4 \pm 0.5\%$ (decade)$^{-1}$) and for spring ($+10{,}100 \pm 14{,}000$ km^2 yr^{-1} and $+0.7 \pm 1.0\%$ (decade)$^{-1}$) are small as a fractional change. On a regional basis the trends differ season to season. During summer and fall the trends are positive or near zero in all sectors except the Bellingshausen/Amundsen Seas sector. During winter and spring the trends are negative or near zero in all sectors except the Ross Sea, which has positive trends in all seasons.

[53] In the context of climate change the sensitivity of the sea ice to changes in temperature is of particular interest. Analysis of the relation between regional sea ice extents and spatially averaged surface temperatures over the ice pack gives an overall sensitivity between winter ice cover and temperature of -0.70% change in sea ice extent per degree Kelvin ($-0.11 \pm 0.09 \times 10^6$ km^2 K^{-1}). A change in the winter ice extent of 0.70% corresponds to a latitudinal change in the average position of ice edge of <10 km or a meridional change of <0.1°, which is small compared to some previous estimates [e.g., *Parkinson and Bindschadler*, 1984]. For summer some regional ice extents vary positively with temperature, and others vary negatively.

SENSORS/ALGORITHM DEVELOPMENT

The laboratory's mission enfolds the observations of many components of the hydrological budget. The rising number of satellite sensors for Earth observation presents unique challenges and opportunities for creation and/or refinement of geophysical parameter retrievals techniques. These activities are essential to the success of NASA's Earth science enterprise. One key part of Goddard's contribution to the Earth science community is the design, validation, calibration, and refinement of such techniques. There are twelve papers from the Laboratory that fall under this subtopic for calendar year 2002. The launch of Aqua satellite in May 2002 promises the new observational capability in the infrared and microwave regions, as well as the flow of additional measurements from similar sensors that already existed in Terra satellite; a paper summarizes the instrument suite of this new platform. The MODIS onboard the Terra satellite has been providing measurements of land, ocean and atmospheric parameters since 1999, and a paper gives a timely assessment of the performance of this instrument during its first year of operation. Three papers deal with various aspects of ocean color measurements. The remaining seven papers in the microwave region are related to the studies of noise-level assessment of various orbiting altimeters, the effect ionosphere on L-band sea surface salinity measurements, as well as the retrievals of water vapor, rain parameters, and water surface emissivities. The span of applications is broad and we invite the reader to thumb through these efforts and directly contact authors within the laboratory to discuss findings for future collaborations.

Is desert dust making oligotrophic waters greener?

H. Claustre,[1] A. Morel,[1] S. B. Hooker,[2] M. Babin,[1] D. Antoine,[1] K. Oubelkheir,[1] A. Bricaud,[1] K. Leblanc,[3] B. Quéguiner,[3] and S. Maritorena[4]

Received 8 September 2001; accepted 28 January 2002; published 28 May 2002.

[1] In situ optical measurements provide evidence that oligotrophic waters of the Mediterranean Sea have a greener color than would result from their phytoplankton content alone. This anomaly, detectable in low chlorophyll waters, remains unnoticed in the chlorophyll-rich waters of the nearby waters of the Moroccan upwelling zone. It is due to enhanced absorption in the blue and enhanced backscattering in the green parts of the visible spectrum likely resulting from the presence of submicron Saharan dust in suspension within the upper layer. This result implies that regional estimations of carbon fixation from ocean color images might be significantly overestimated, not only in the Mediterranean Sea, but also in other oligotrophic areas of the Northern hemisphere, subjected to desert dust deposition. *INDEX TERMS:* 4552 Oceanography: Physical: Ocean optics; 4805 Oceanography: Biological and Chemical: Biogeochemical cycles (1615); 1640 Global Change: Remote sensing

1. Introduction

[2] Brick-red or pink dust massively exported from the Sahara is at the origin of the so-called "red-rains", sporadically falling over Europe. Besides this spectacular effect, Saharan dust influences several atmospheric and marine processes, such as regional radiative budgets [*Legrand et al.*, 1992], the formation of clouds and rain [*Levin and Ganor*, 1996], the acidity of rainfall [*Loÿe-Pilot et al.*, 1986]. Dust deposition also affects sedimentary processes and the biogeochemistry of the Mediterranean Sea, including, perhaps, its productivity through iron enrichment of surface waters [*Guerzoni et al.*, 1997]. Desert dust also impacts optical properties of the atmosphere, leading to some biases in the retrieval of the chlorophyll *a* concentration (⟨Chl*a*⟩) from color images of the upper ocean [*Moulin et al.*, 2001].

[3] The possible effect of desert dust on optical properties of oceanic waters remains however unknown. Therefore, one of the objectives of the PROSOPE (French acronym for Productivity of Pelagic Oceanic Systems) cruise (Figure 1) was to examine if any peculiar optical characteristic caused by Saharan dust deposition could be detected in oligotrophic Mediterranean waters, that would bias the optical assessment (in situ or remotely) of ⟨Chl*a*⟩.

2. Methods-Background

[4] The cruise took place from 4 September to 4 October, 1999. The upwelling waters off Morocco (UPW station) were sampled over 3 days, and the MIO (Ionian Sea, eastern basin) and DYF (Ligurian Sea, western basin) stations were occupied for 5 days each. Short intermediate stations (St 1 to St 9) were sampled over 4-h periods. Optical measurements and pigment sampling were always performed around noon, within 1 h of overflight by the SeaWiFS satellite.

[5] ⟨Chl*a*⟩ was analysed according to a slightly modified version of the HPLC method described by *Vidussi et al.* [1996]. The accuracy of ⟨Chl*a*⟩ measurements (8%) was checked as part of an international intercomparison exercise (four laboratories were involved) performed on samples taken during the cruise [*Hooker et al.*, 2001].

[6] In situ spectral measurements of upwelling irradiance or radiance and downwelling irradiance were performed using three instruments: LI-1800 LICOR, Satlantic LoCNESS and Satlantic SeaFALLS.

[7] The reflectance of a water body, $R(\lambda)$, is defined as the ratio of upwelling irradiance (or radiance) to downwelling irradiance, and the spectral shape of $R(\lambda)$ define the so-called "water color". This color is indexed by the blue-to-green reflectance ratio (B/G), R(443)/R(555), which, in open-ocean (Case-1) water is essentially governed by the phytoplankton content (actually B/G decreases with increasing phytoplankton content). Therefore, algorithms have been developed that relate surface ⟨Chl*a*⟩ to B/G [*O'Reilly et al.*, 1998; *Morel and Maritorena*, 2001]. $R(\lambda)$ is approximately proportional to the ratio of the backscattering and absorption coefficients, $b_b(\lambda)/a(\lambda)$.

3. Results

[8] The PROSOPE data set spans two orders of magnitude in surface ⟨Chl*a*⟩ (0.03 to 3.75 mg m^{-3}) and about one order of magnitude in B/G (0.5 to 6.7) (Figure 2). Data collected in the upwelling (station UPW) off Morocco, are in close agreement with global algorithms (Figure 2). This is no longer the case for Mediterranean waters which look systematically greener (lower B/G) than typical oceanic waters with the same ⟨Chl*a*⟩, as already observed by *Gitelson et al.* [1996] for the eastern Mediterranean sea. As a consequence, derivation of ⟨Chl*a*⟩ from B/G measurements through conventional algorithms overestimates actual ⟨Chl*a*⟩ in Mediterranean waters by a factor exceeding 2 (Table 1).

[9] For a given ⟨Chl*a*⟩, a lower than expected B/G (Figure 2) is due to a lower than expected $b_b(440)/b_b(555)$ and/or a lower than expected a(555)/a(440). When compared to optical properties modeled for a standard ocean with similar ⟨Chl*a*⟩, PROSOPE data show two important features (Table 1): (i) the color shift is caused by both anomalous absorption and backscattering ratios (Mediterranean waters absorb more blue light and backscatter more green light than anticipated); and (ii) the particle scattering coefficients, $b_p(555)$, are anomalously high compared to those modeled for a standard ocean.

[10] Additional absorption measurements performed during the cruise permitted an inquiry into the substance(s) potentially responsible for the B/G changes. An absorption budget can be written as:

$$a(\lambda) = a_W(\lambda) + a_P(\lambda) + a_{OS}(\lambda) \quad (1)$$

[1]Laboratoire d'Océanographie de Villefranche, Villefranche-sur-mer, France.
[2]Laboratory for Hydrospheric Processes, NASA Goddard Space Flight Center, Greenbelt, MD, USA.
[3]Laboratoire d'Océanographie et de Biogéochimie, Marseille, France.
[4]Institute for Computational Earth System Science, University of California, Santa Barbara, CA, USA.

Copyright 2002 by the American Geophysical Union.
0094-8276/02/2001GL014056$05.00

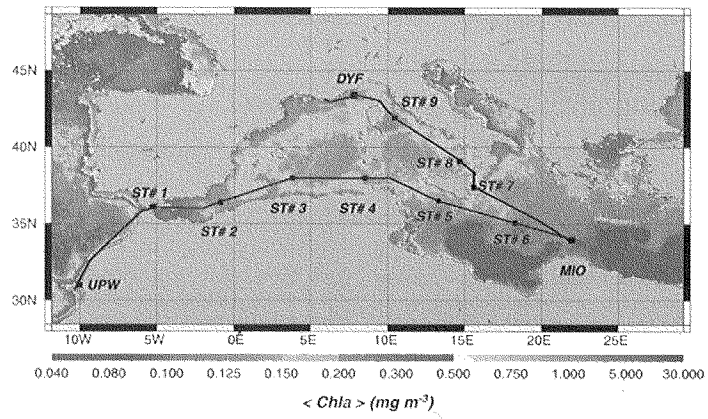

Figure 1. PROSOPE cruise track superimposed on the composite SeaWiFS image of surface ⟨Chl*a*⟩ for September 1999. This composite was derived from SeaWiFS reflectances using the OC4v4 algorithm [*O'Reilly et al.*, 1998].

where $a(\lambda)$ is the total absorption, $a_W(\lambda)$ and $a_P(\lambda)$ are the absorption by water and particles (phytoplankton, heterotrophs, and associated biogenic detritus), respectively and $a_{OS}(\lambda)$ is a residual term accounting for "other substances". The latter can be estimated by subtraction, because $a_W(\lambda)$ is known and $a(\lambda)$ and $a_P(\lambda)$ were measured.

[11] The high $a_P(440)$ values (Table 1) result primarily from the presence of non-photosynthetic carotenoids, typical of algae in oligotrophic surface waters, and, to a lesser extent, from non-algal particles. Such a pigmentation slightly decreases the ratio a(555)/a(440). In open-ocean Case-1 waters, a_{OS} is generally believed to result from the presence of colored dissolved organic matter (CDOM). However, the PROSOPE $a_{OS}(440)$ values are inappropriately high when compared to modeled $a_{CDOM}(440)$ values for standard oceanic waters. Moreover, high CDOM content is unlikely for two reasons: (i) CDOM is a by-product of biological activity, which is rather low in the Mediterranean; and (ii) CDOM is exposed to intense photo-bleaching [*Vodacek et al.*, 1997], favored by the summer vertical stratification combined with high surface irradiance. In addition, CDOM has no scattering capability able to account for the high $b_p(555)$ value as well as for the unexpectedly low $b_b(440)/b_b(555)$ ratio, also observed. The presence of bubbles could be put forward to account for the enhanced scattering coefficient [*Zhang et al.*, 1998]. It is unlikely, however, as the conditions during the cruise were exceptionally good in term of sea state and ambient wind.

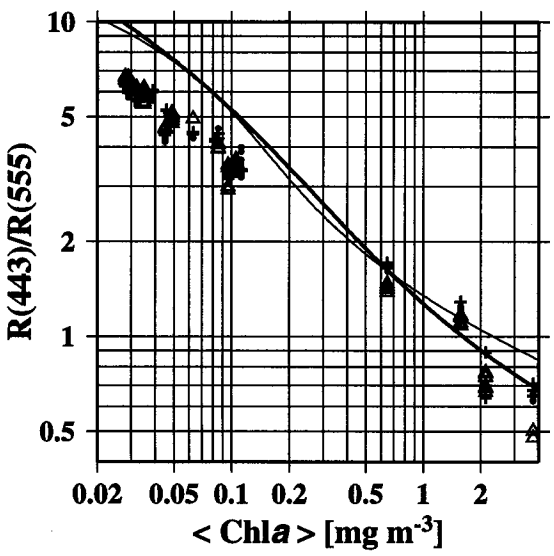

Figure 2. Relationship between surface ⟨Chl*a*⟩ and the blue-to-green reflectance ratio derived from in situ data (determined just below the surface). The ⟨Chl*a*⟩ values below 0.15 mg m^{-3} are from the Mediterranean, and values >0.6 mg m^{-3} are from the upwelling area off Morocco. The blue-to-green reflectance ratios were derived from spectral irradiance or radiance measurements performed by a LI-1800 LICOR (△), aSatlantic LoCNESS (▲) and aSatlantic SeaFALLS (+). The field data are compared to an empirical model [*O'Reilly et al.*, 1998] (algorithm OC4v4, thin line) and to a semi-analytical model [*Morel and Maritorena*, 2001] (thick line).

[12] Given that algal, non-algal particles, CDOM and bubbles are not plausible causes for concomitant decreases in both a(555)/a(440) and $b_b(440)/b_b(555)$, and for enhanced $b_p(555)$ values, "other substances" have to be found to explain the conspicuous green color shift. We suggest that submicron Saharan dust, probably smaller than 0.7 μm [*D'Almeda, and Schütz*, 1983; *Gomes et al.*, 1990], is responsible for this unexpected observation.

5. Concluding Remarks

[17] It has been shown that the presence of non-phytoplankton constituents — namely of dust — in open ocean waters with low ⟨Chl*a*⟩ can depress the in situ B/G compared to its expected value. Moreover, the remotely-sensed B/G can be even more lowered because the atmospheric correction of the blue bands is less accurate when absorbing aerosols are present in the atmosphere [*Moulin et al.*, 2001], which leads to an underevaluation of the actual B/G. This appears to be the case in oligotrophic Mediterranean waters where the ⟨Chl*a*⟩ retrieved from SeaWiFS (Figure 1) are distinctly higher than the sea truth data (Table 1). These observations suggest that regional algorithms are needed and that the dependence of ⟨Chl*a*⟩ retrieval on the proximity of desert dust sources must be systematically investigated. Given the large spatial extension of sub-tropical gyres, a proper estimation of their contribution to oceanic carbon fixation requires very accurate estimate of their surface ⟨Chl*a*⟩. A careful re-examination of their optical properties is, therefore, a prerequisite to address (and quantify) potential dust-induced bias in ⟨Chl*a*⟩ retrieval.

ELSEVIER

Remote Sensing of Environment 83 (2002)

Remote Sensing of Environment

www.elsevier.com/locate/rse

On-orbit performance of the Earth Observing System Moderate Resolution Imaging Spectroradiometer; first year of data

B. Guenther [a,*], X. Xiong [b], V.V. Salomonson [a], W.L. Barnes [a], James Young [c]

[a] *NASA's Goddard Space Flight Center, Greenbelt, MD 20771, USA*
[b] *Science Systems Applications, Inc., Suite 104, 7501 Forbes Boulevard, Seabrook, MD 20706, USA*
[c] *Raytheon, Santa Barbara Remote Sensing, Building 32, 75 Coromar Drive, Goleta, CA 93117, USA*

Received 5 April 2001; received in revised form 31 January 2002; accepted 1 March 2002

Abstract

The Moderate Resolution Imaging Spectroradiometer (MODIS) completed the first year of science data acquisition on February 24, 2000. The overall performance of the sensor and the on-board calibration systems for this first year have been very good. Several features of the performance lead to characteristics in the data set that merit special attention. These items are sometimes called data product caveats, and are described here. Uncertainty budgets for the 0.555-μm band, the 1.240-μm band and the 12.000-μm band are presented at several days throughout this first year. The uncertainty is estimated to be decreasing with time during this period, and to be near 1.8% in reflectance factor for 0.555 μm, 1.9% for the reflectance factor product for the 1.240 μm band, and 0.7% for the 12.000-μm band at nadir at the end of the first year. Degradation of the solar diffuser is 2.3% at 0.412 μm, known to an uncertainty of ± 0.5%. Solar diffuser degradation for wavelengths longer that 0.5 μm is indistinguishable from the uncertainty in trend determination for the first year. Mirror side degradation at 0.412 μm is 6 ± 0.5%, with a mirror side difference of an additional 3%. The performance present in the data at the end of year 1 provides significant encouragement that many improvements in our understanding of the Earth system performance can and will be based on MODIS data during the coming years.
© 2002 Published by Elsevier Science Inc.

1. Introduction

The Earth Observing System (EOS) was designed to provide observations that would enable better understanding on a global scale of the entire Earth system and the included processes. There was and there is urgency attached to this effort because an expanding human population is more affected by natural variability in the environment and, more importantly, has become an active participant in the evolution of the Earth system. To address questions that were both scientifically important, and relevant to resource management and sustainability policies, many sensors were designed with considerable attention to enhancing existing data bases for cloudiness, sea surface temperature, land cover, etc. Key among these sensors is the Moderate Resolution Imaging Spectroradiometer (MODIS) whose heritage comes from the NOAA Advanced High Resolution Radiometer (AVHRR), the Nimbus Coastal Zone Color Scanner (CZCS) and the Orbview-2 SeaWIFS sensor, the NOAA High-resolution Infrared Sounder (HIRS), and the Landsat Thematic Mapper. MODIS has been designed as a primary sensor to address questions related to: atmospheric variables such as cloud properties, radiative fluxes, and aerosol properties; land variables such as land cover and land use change, vegetation dynamics, surface temperature, fire occurrence, volcanic effects, and snow cover and, ocean variables such as sea surface temperature, and ocean color related to phytoplankton distribution and dynamics and photosynthetic efficiency.

MODIS was launched on the EOS Terra spacecraft on 18 December 1999. Initial engineering data was returned almost immediately, and science data was acquired first on 24 February 2000. The MODIS sensor has wide spectral range and wide spatial coverage, with 36 carefully selected bands to observe land, ocean, and atmosphere features on a global basis every 1–2 days (Table 1). The bands are distributed on four local plane assemblies (FPA), with wavelengths between 0.4 and 0.6 μm on the VIS FPA, 0.6–1.0 μm on the NIR FPA, 1.0–5.0 μm on the SW/MWIR FPA and 5.0–15.0 μm on the LWIR FPA. The MODIS measurements program is designed to provide a data set from which scientists can construct models of the Earth's global dynamics—atmospheric, oceanic and terrestrial—and predict changes. Characteristics of the MODIS are described

in Barnes, Pagano, and Salomonson (1998), and its prelaunch calibration is summarized in Guenther, Godden, Xiong, et al. (1998). The purpose of this paper is to summarize the MODIS first year performance in orbit and the resulting quality of the data.

The MODIS includes several calibration systems to provide on-orbit calibration. The early on-orbit performance of these calibration and characterization systems is provided in Section 2. The overall MODIS performance is described in Section 3. The uncertainty of the resulting radiometrically calibrated data product (Level 1B) is summarized for three bands, with the contributions of several known sensor features highlighted in that analysis. The detailed MODIS performance is described in Section 4. Actions taken to improve performance or better characterize the performance are highlighted, and cautions on how these features may be impacting the Level 1 data set are reviewed as well.

Table 1
Overall characteristics of the MODIS instrument and selected operational specifications

Primary use	Band	Bandwidth[a]	Special radiance[b]	Required SNR[c]	Primary use	Band	Bandwidth[a]	Spectral radiance[b]	Required NEΔT (K)[d]
Land/cloud/	1	620–670	21.8	128	Surface/cloud	20	3.660–3.840	0.45 (300 K)	0.05
aerosols boundaries	2	841–876	24.7	201	temperature	21	3.929–3.989	2.38 (335 K)	2
Land/cloud/	3	459–479	35.3	243		22	3.929–3.989	0.67 (300 K)	0.07
aerosols properties	4	545–565	29	228		23	4.020–4.080	0.79 (300 K)	0.07
	5	1230–1250	5.4	74	Atmospheric	24	4.433–4.498	0.17 (250 K)	0.25
	6	1628–1652	7.3	275	temperature	25	4.482–4.549	0.59 (275 K)	0.25
	7	2105–2155	1	110	Cirrus clouds	26	1.360–1.390	6	150[c]
Ocean color/	8	405–420	44.9	880	water vapor	27	6.535–6.895	1.16 (240 K)	0.25
Phytoplankton/	9	438–448	41.9	838		28	7.175–7.475	2.18 (250 K)	0.25
Biogeochemistry	10	483–493	32.1	802	Cloud properties	29	8.400–8.700	9.58 (300 K)	0.05
	11	526–536	27.9	754	Ozone	30	9.580–9.880	3.69 (250 K)	0.25
	12	546–556	21	750	Surface/cloud	31	10.780–11.280	9.55 (300 K)	0.05
	13	662–672	9.5	910	temperature	32	11.770–12.270	8.94 (300 K)	0.05
	14	673–683	8.7	1087	Cloud top altitude	33	13.185–13.485	4.52 (260 K)	0.25
	15	743–753	10.2	586		34	13.485–13.785	3.76 (250 K)	0.25
	16	862–877	6.2	516		35	13.785–14.085	3.11 (240 K)	0.25
Atmospheric	17	890–920	10	167		36	14.085–14.385	2.08 (220 K)	0.35
water vapor	18	931–941	3.6	57					
	19	915–965	15	250					

MODIS Technical Specifications
Orbit: 705 km, 10:30 a.m. descending node (Terra) or 1:30 p.m. ascending node (Aqua), sun synchronous, near-polar, circular.
Scan rate: 20.3 rpm, cross-track.
Swath dimensions: 2330 km (cross-track) by 10 km (along track at nadir).
Telescope: 17.78 cm diameter off-axis, afocal (collimated), with intermediate field stop.
Size: 1.0 × 1.6 × 1.0 m.
Weight: 228.7 kg.
Power: 162.5 W (single orbit average).
Data rate: 10.6 Mbps (peak daytime); 6.1 Mbps (orbital average).
Quantization: 12 bits.
Spatial resolution: 250 m (Bands 1–2); 500 m (Bands 3–7); 1000 m (Bands 8–36).
Design life: 6 years.

[a] Bands 1–19 are in nm; Bands 20–36 are in μm.
[b] Special radiance values are (W/m^2 μm sr).
[c] SNR = signal-to-noise ratio.
[d] NEΔT = noise-equivalent temperature difference.

5. Summary and conclusions

The completion of the first year of MODIS operations has demonstrated that the derived data products will enable significant improvements in our understanding of the Earth systems. Data sets for annual and longer-term performance likely will start near 1 November 2000. The noise charts presented in Section 3 indicate that the sensor is capable of low noise measurements at nearly all wavelengths. The sample uncertainty tables indicate that the Level 1 calibration products are expected to meet the very demanding uncertainty measurements under many geophysical conditions. On the other hand, Section 4 provides a list of areas where initial MODIS performance was different than expected, and where significant improvements were needed to allow the derived data to meet scientific expectations. Numerous improvements now are in place. Continued improvements are being sought for even better quality MODIS data. The documentation for these improvements is available from the MODIS and MCST web pages. MODIS may be the most complex instrument built and flown on a spacecraft for civilian research purposes, and the performance present in the data at the end of year 1 provides significant encouragement that many improvements in our understanding of the Earth system performance can and will be based on MODIS data during the coming years.

An Evaluation of Above- and In-Water Methods for Determining Water-Leaving Radiances

STANFORD B. HOOKER

NASA Goddard Space Flight Center, Greenbelt, Maryland

GORDANA LAZIN

Satlantic, Inc., Halifax, Nova Scotia, Canada

GIUSEPPE ZIBORDI

Joint Research Centre, Ispra, Italy

SCOTT MCLEAN

Satlantic, Inc., Halifax, Nova Scotia, Canada

(Manuscript received 30 August 2000, in final form 17 August 2001)

ABSTRACT

A high-quality dataset collected at an oceanographic tower was used to compare water-leaving radiances derived from simultaneous above- and in-water optical measurements. The former involved two different above-water systems and four different surface glint correction methods, while the latter used three different in-water sampling systems and three different methods (one system made measurements a fixed distance from the tower, 7.5 m; another at variable distances up to 29 m away; and the third was a buoy sited 50 m away). Instruments with a common calibration history were used, and to separate differences in methods from changes in instrument performance, the stability (at the 1% level) and intercalibration of the instruments (at the 2%–3% level) was performed in the field with a second generation Sea-viewing Wide Field-of-view Sensor (SeaWiFS) Quality Monitor (SQM-II). The water-leaving radiances estimated from the methods were compared to establish their performance during the field campaign, which included clear and overcast skies, Case-1 and Case-2 conditions, calm and roughened sea surface, etc. Three different analytical approaches, based on unbiased percent differences (UPDs) between the methods, were used to compare the various methods. The first used spectral averages across the 412–555-nm SeaWiFS bands (the part of the spectrum used for ocean color algorithms), the second used the ratio of the 490- and 555-nm bands, and the third used the individual (discrete) wavelengths. There were eight primary conclusions of the comparisons, which were considered within the context of the SeaWiFS 5% radiometric objectives. 1) The 5% radiometric objective was achieved for some in-water methods in Case-1 waters for all analytical approaches. 2) The 5% radiometric objective was achieved for some above-water methods in Case-2 waters for all analytical approaches, and achieved in both water types for band ratios and some discrete wavelengths. 3) The largest uncertainties were in the blue domain (412 and 443 nm). 4) A best-to-worst ranking of the in-water methods based on minimal comparison differences did not depend on the analytical approach, but a similar ranking of the above-water methods did. 5) Above- and in-water methods not specifically designed for Case-2 conditions were capable of results in keeping with those formulated for the Case-2 environment or in keeping with results achieved in Case-1 waters. 6) There was a significant difference between two above-water instruments oriented perpendicular with respect to the sun, but pointed in the same direction (best agreement) versus the opposite direction (worst agreement). 7) The overall intercomparison of all methods across Case-1 and Case-2 conditions was at the 9.1% level for the spectral averages, and at the 3.1% level for the band ratios (uncertainties other than those associated with implementing the individual methods account for 2%–4% and 1%–3% of these values, respectively). 8) A comparison with traditional regression analyses confirms the UPD conclusions.

1. Introduction and background

Spectral water-leaving radiance, $L_w(\lambda)$, is the central physical quantity for bio-optical studies in the upper ocean; whether determined from above- or in-water data, $\hat{L}_w(\lambda)$ and $\tilde{L}_w(\lambda)$, respectively, it must be accurately measured. The Sea-viewing Wide Field-of-view Sensor (SeaWiFS) Project, for example, requires $L_w(\lambda)$ uncertainties within 5% (Hooker et al. 1993b). This was shown to be achievable for in-water measurements in Case-1 waters using primarily a single methodology (Hooker and Maritorena 2000), but the uncertainty associated with multiple methods has not been well quantified. The SeaWiFS calibration and validation plan (Hooker and McClain 2000) has emphasized in-water field work because when the plan was conceived, the above-water protocols were not as mature as the in-water protocols (Mueller and Austin 1992). Although there has been steady progress in defining the proper metrology for above-water measurements, intracomparisons within a group of accepted techniques have not occurred. More importantly, intercomparisons between above- and in-water methods have also not been thoroughly investigated, although individual comparisons are available in the literature (e.g., Pinkerton et al. 1999; Toole et al. 2000).

6. Conclusions

This study used data from three different environmental conditions that covered much of the dynamic range of in situ optical measurements, but, nonetheless, it was based on a small dataset collected during three

days of measurements in the near-coastal environment. One of the three days (SDY 194) was within the parameter range established by the NRSR Workshop; the other two were not, but they were typical of the kinds of environmental conditions that can be encountered during above- and in-water radiometric field campaigns. Three in-water methods for determining water-leaving radiances from profiling (S84) and fixed-depth (P94 and P97) sampling systems were combined with four above-water methods to quantify the performance of all the methods. The removal of glint contamination from the surface measurement distinguished the above-water methods from one another and included four correction schemes: near-infrared radiance ratio (M80), Fresnel reflectance plus residual reflection (C85), modified Fresnel reflectance (S95), and near-infrared irradiance ratio (L98).

The seven methods, three different days of environmental conditions, and five sampling platforms produced a large number of performance comparisons, which were separated according to UPD analyses based on spectral averages, band ratios, and discrete wavelengths. Although each method was usually found superior to the others at some stage in the performance evaluation process, the most suitable point for overall evaluation is at the intercomparison level summarized in Tables 6–9 and Figs. 8–9. Based on these summaries, some general capabilities concerning all the methods can be discerned.

1) In terms of the 5% calibration and validation objective, and the hoped for performance to within 3%, the spectral-average approach (Table 7d) produced larger average differences (and standard deviations) than the band-ratio approach (Table 8d), which were 9.1% (5.6%) and 3.7% (1.1%), respectively. Using band ratios, the S84, P94, C85, and S95 methods produced ranges of expected differences (average plus and minus 1 standard deviation) within the 5% level, and frequently to within 3%.
2) The best results were not restricted to Case-1 or clear-sky conditions; water type was seen to be important, although other environmental parameters agreed well with the UPD levels (considered in more detail below). Consider, for example, the difficult circumstance of overcast conditions, which can be highly variable in terms of sky radiance distribution and relative (percent) variations in illumination conditions during a deployment interval. Because of the low signal levels, small absolute differences represent large relative discrepancies, but all the methods agreed very well for overcast conditions when using the data from the same instrument.
3) Above- and in-water methods not formulated for Case-2 conditions were capable of results in keeping with those achieved in Case-1 waters (e.g., Table 6). Agreement to within 5% was achieved with in-water methods in Case-1 waters for all three analytical approaches. Agreement within 5% was achieved with above-water methods in Case-2 waters for all analytical approaches, and was achieved in both water types for the band-ratio and discrete wavelength analyses (spectral averages were elevated due to large uncertainties in the blue domain).
4) For both above- and in-water methods, the largest uncertainties were usually associated with the blue part of the spectrum (412–443 nm), with the blue-green transition (490–510 nm) a local minimum, which was followed by a small increase at 555 nm (Table 9). The above-water methods that calculated the surface reflectance by assuming $\lambda_r = 0$ (M80 and L98) were spectrally dependent during Case-2, clear-sky conditions, with very large uncertainties at 412 nm (as much as 38%) and minimum uncertainties at 555 nm (less than 5%).

Note that all of the analytical approaches yielded average uncertainties across all three days and all methods below the 10% level, so for applications where this level of agreement is acceptable—for example, perhaps with large-scale bio-optical models, any of the methods are probably acceptable. It is also important to remember the regression analysis results confirm these overall conclusions (although there are small shifts in the magnitude of the uncertainties).

For the in-water methods alone, the specific details of the capabilities of the methods are as follows.

5) P94 and P97 grouped together, but S84 performed the best. Consequently, an in-water method making use of vertical profiles of the water column should be considered superior than those using sensors at a fixed depth, although good results were obtained for the latter during Case-1 conditions and for band-ratio analyses.
6) The best-to-worst ranking of the in-water methods (using the minimal range in average differences) did not depend on the analytical approach (S84, P94, and P97), but the ranking of the above-water methods did (S95, L98, C85, and M80 for the spectrally averaged approach; and C85, S95, M80, and L98 for the band-ratio approach).
7) The in-water spectral averages intracompared best during Case-1 conditions and worst during Case-2 conditions (Table 7c), which is consistent with the higher variability associated with the latter; however, the opposite result was seen with the band-ratio analysis (Table 8c).

Before considering the above-water methods separately, it is important to remember proper data filtering to remove glint spikes is an essential part of above-water methods that permit it (the C85 method does not). Although many schemes were considered in this study (section 3c), the adopted filter retained only the lowest 5% of the data, based on the reddest (780-nm) band. Similarly, data averaging was shown to needlessly and significantly degrade the quality of the above-water data because it artificially elevated the $L_T(\lambda)$ values by contaminating them with glint. Subsampling did not degrade the above-water data as significantly as averaging, but it showed that above-water sampling rates should be equal to, or greater than, 1 Hz (Fig. 7). The conclusion to be derived here is the glint field must be adequately discretized, so it can be removed by filtering.

The Effect of the Ionosphere on Remote Sensing of Sea Surface Salinity From Space: Absorption and Emission at L Band

David M. Le Vine, *Fellow, IEEE,* and Saji Abraham, *Member, IEEE*

***Abstract*—The purpose of this work is to examine the effects of Faraday rotation and attenuation/emission in the ionosphere in the context of a future remote sensing system in space to measure salinity. Sea surface salinity is important for understanding ocean circulation and for modeling energy exchange with the atmosphere. A passive microwave sensor in space operating near 1.4 GHz (L-band) could provide global coverage and complement in situ arrays being planned to provide subsurface profiles. However, the salinity signal is relatively small and changes along the propagation path can be important sources of error. It is shown that errors due to the ionosphere can be as large as several psu. The dominant source of error is Faraday rotation but emission can be important.**

***Index Terms*—Ionospheric electromagnetic propagation, microwave radiometry, ocean salinity, remote sensing.**

I. Introduction

THE SALINITY of the open ocean is important for understanding ocean circulation and for modeling energy exchange with the atmosphere. For example, salinity gradients affect mixed layer processes, which influence fluxes of heat near the surface [1]. Salinity and temperature determine water density and are important factors in large-scale ocean circulation [2]. Also, changes in salinity are primarily caused by changes in freshwater (evaporation, precipitation, melting ice, or river input). These changes are manifestations of elements of the water cycle, which are poorly known over the ocean [3].

Microwave remote sensing from space could provide the necessary temporal and spatial sampling needed to understand the role of salinity in these ocean processes [2], [4]. Changes in salinity modulate the emissivity of the surface and cause changes in emission that are sufficiently strong in the low frequency portion of the microwave spectrum to be detected with passive sensors [5], [6]. Measurements from space have been proposed [7] and salinity differences were observed from space with the L- band radiometer on SKYLAB 25 [8]. Recently, experiments with L-band radiometers on aircraft have demonstrated that salinity can be retrieved with accuracy useful for studying processes in coastal regions [9], [10].

Manuscript received June 1, 2001; revised December 13, 2001.

D. M. Le Vine is with the Microwave Sensors Branch/Code 975, Laboratory for Hydrospheric Processes, Goddard Space Flight Center, Greenbelt, MD 20771 USA (e-mail: dmlevine@priam.gsfc.nasa.gov).

S. Abraham is with the Science System and Applications, Inc., Microwave Sensors Branch/Code 975, Goddard Space Flight Center, Greenbelt, MD 20771 USA (e-mail: sabraham@synth.gsfc.nasa.gov).

Publisher Item Identifier S 0196-2892(02)04604-1.

However, measurement of sea surface salinity (SSS) in the open ocean presents a special challenge. This is so because the dynamic range of SSS in the open ocean is relatively small (about 5 K) and the requirements for a scientifically useful measurement (about 0.05 K) put a severe constraint on radiometric performance. A change of 0.05 K at L-band corresponds to a change of about 0.1 psu [7] where "psu" denotes changes measured on the practical salinity scale [11]. To put the challenge of this measurement in perspective, the dynamic range associated with changes in soil moisture is on the order of 100 K [12] and measurement requirements are 1–4 K [13].

Among the important potential sources of error at L-band is the ionosphere. The ionosphere causes a change in the direction of polarization (Faraday rotation) and because the ionosphere is lossy at L-band, there is both attenuation and emission along the signal path. As will be shown here, both phenomena can cause errors that are important for remote sensing of salinity at the 0.1-psu level of accuracy. A brief background is given in Appendices A and B to define Faraday rotation and attenuation in the ionosphere. In Section II, the magnitude of Faraday rotation and its effect on observed brightness temperature are presented. In Sections III–IV, attenuation and its effect on brightness temperature (emission) are discussed.

II. Faraday Rotation

A. Magnitude

The rotation of the polarization vector in the ionosphere is due to the change along the propagation path from surface to sensor of the phase, Ω, in (B3). Substituting (A6) into (B4) and integrating along the propagation path, s, one obtains

$$\Omega_F = \left(\frac{\pi}{c\nu^2}\right) \int \nu_p^2(s)\nu_B(s)\cos\left(\Theta_B(s)\right)\mathrm{ds} \tag{1}$$

where Ω_F is the Faraday rotation in radians and Θ_B is the angle between the direction of propagation and the Earth magnetic field [14], [15]. To simplify the many calculations needed to make a global map of Ω_F, (1) has been approximated by making the change of variables $\mathrm{ds} = \sec(\theta)\mathrm{dz}$ where z is the normal to the surface at the subsatellite point nadir and θ is the polar angle between nadir and the line of sight to the surface (incidence angle). Substituting for the plasma frequency, ν_p and electron gyro frequency, ν_B, from (A2)–(A3) and replacing B by its value at an altitude of 400 km [16], one obtains

$$\Omega_F \approx 6950\, B(400)\cos\left(\Theta_B\right)\sec(\theta)\mathrm{VTEC}. \tag{2}$$

These approximations are reasonable because B is slowly varying with altitude and because there is little curvature of the ray path. In (2), B is in tesla, Ω_F is in degrees, and VTEC $= \int N_e(z)$dz is the vertical total electron content at the sub-satellite point in total electron content units (10^{16} electrons/m^2).

It is clear from (1) and (2) that Faraday rotation depends on electron density and magnetic field and also on the orientation of the sensor with respect to the local magnetic field (i.e., on Θ_B). Examples of the effect of sensor orientation (scan pattern and look angle) can be found in [16]. For purposes of this paper, it will be assumed that the sensor looks to the right (i.e., across track in the plane perpendicular to the satellite heading). The sensor will be assumed to be in a sun-synchronous orbit with an altitude of 675 km, which is representative of orbits proposed for microwave remote sensing at L-band [4]. Faraday rotation will be computed using the International Reference Ionosphere (IRI-95) [17] to generate the necessary electron density profiles and the International Geomagnetic Reference Field (IGRF) [18] for the magnetic field.

V. Comments

Calculations have been presented here illustrating the effect of Faraday rotation and attenuation/emission from the ionosphere on passive microwave remote sensing at L-band (1.4 GHz). The motivation for this work is current interest in remote sensing of ocean salinity from space. To put the effects of the ionosphere into context, the change of brightness temperature with salinity is about 0.5 K/psu. It is clear from Figs. 2 and 3 (error due to Faraday rotation) and Tables II and III (error due to attenuation and emission) that corrections for these phenomena will have to be made to achieve salinity retrievals accurate to 0.1–0.2 psu.

The data also indicate some obvious choices for remote sensing. Clearly an optimum choice as far as minimizing errors is 6 am local time and as close to a minimum of solar activity as possible. Local time of 6 am is near the minimum in the daily cycle of the ionosphere, (Fig. 7 is an example of the diurnal variation). Remote sensing from a sun-synchronous orbit with an equatorial crossing time of 6am/6pm would provide observations near this minimum. Fig. 1 and Tables I–III illustrate the dependence on solar activity. For a fixed local time and location, Faraday rotation and emission/absorption increase roughly linearly with the solar activity (IG) index, Rz.

The studies presented here use the IRI-95 and are therefore representative of climatalogical data for the ionosphere. The IRI-95 model [17] is a good representation of mean characteristics of the ionosphere but is not a particularly good predictor of current (instantaneous) behavior [24], [25]. It may be possible to improve its ability to predict current behavior given input of local, measured parameters [26], [27]. However, without such input corrections for Faraday rotation and emission will likely have to be based on other models or techniques. (One possibility is to measure the third Stokes parameter [28].)

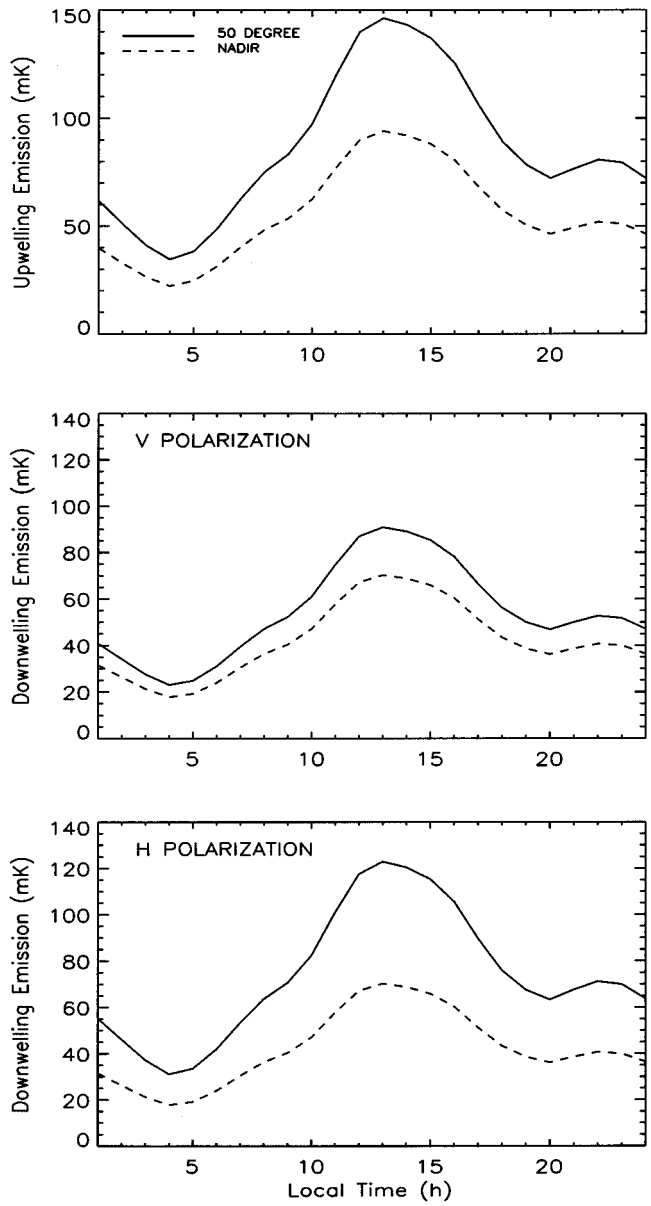

Fig. 7. Diurnal variation of upwelling (top) and downwelling emissions (vertical polarization, middle; horizontal polarization, bottom). The calculations are at 30 N, 330 E during high solar activity (June 1989). The surface is ocean with $S = 35$ psu and $T_0 = 20$ °C.

Attenuation is proportional to ν_z as in (7) which follows from the Appleton–Hartree equation and simplifications for L-band. This is a "cold" plasma approximation. In the present study, the collision frequency is taken as $\nu_z = \nu_{\text{eff}}$ (see (9)–(10)). It has been suggested that, when $\nu \gg \nu_{\text{eff}}$, as is the case at L-band, a better approximation is to use $\nu_z = 1.333\,\nu_{\text{eff}}$ [29]. Hence, it is likely that the values for emission and loss given here are underestimated. Also, the results presented here employ approximations that are reasonable at low and middle latitudes. Near the poles, additional care must be taken in the calculation of attenuation [30].

AQUA: IN ORBIT AND READY FOR THE SCIENTISTS

Claire L. Parkinson
NASA Goddard Space Flight Center

After over a decade of development, the Aqua spacecraft was finally launched on May 4, 2002, from Vandenberg Air Force Base in California. Dozens of Code 400 personnel were critical to its success; and now, as many of them move on to other projects, the core of the Aqua work passes to mission operations, data handlers, and scientists. This article presents an overview of the Aqua mission from the science perspective, emphasizing the Earth-observing instruments and science teams to the exclusion of the equally fascinating and numerous additional aspects of the mission.

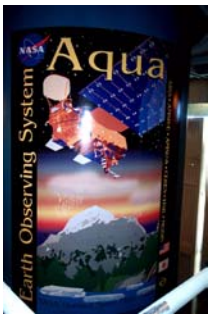

Aqua carries six distinct Earth-observing instruments, all placed on board the spacecraft in order to help scientists examine and further understand the Earth's global climate system. As the name suggests, the Aqua mission has a particular concentration on water, with Aqua scientists examining ocean surface water, evaporation from the oceans, water vapor in the atmosphere, clouds, precipitation, soil moisture, snow cover and glacial ice on land, and sea ice in the oceans. In addition to water in all its forms, scientists are also analyzing Aqua data for information on vegetation, ocean productivity, trace gases and aerosols in the atmosphere, and other elements of the Earth's climate system.

Launch of the Aqua spacecraft, May 4, 2002. (Photo by Bill Ingalls/NASA.)

AIRS/AMSU/HSB

Of the six Aqua instruments, the one with the greatest technological advances made as part of the Aqua program is the Atmospheric Infrared Sounder (AIRS). AIRS is a high-resolution sounder with 2378 channels measuring infrared radiation at wavelengths in the range 3.74-15.4 μm and four channels measuring visible/near-infrared radiation at wavelengths in the range 0.4-1.1 μm.

AIRS. (Photo courtesy of BAE Systems.)

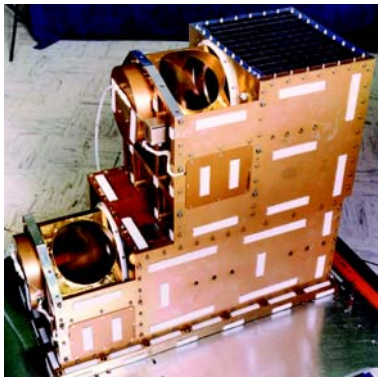

AMSU-A1. (Photo courtesy of Aerojet.)

AIRS is joined on Aqua by two micro-wave sounders: a 15-channel Advanced Microwave Sounding Unit (AMSU, consisting of two separate units, AMSU-A1 and AMSU-A2) and a four-channel Humidity Sounder for Brazil (HSB), provided by the Instituto Nacional de Pesquisas Espaciais (INPE), the Brazilian National Institute for Space Research. The AMSU and HSB are similar to instruments flying on satellites of the National Oceanic and Atmospheric Administration (NOAA) since May 1998, but when linked with the AIRS on Aqua, they become vital components of the most advanced sounding system ever flown in space: Aqua's AIRS/AMSU/HSB triplet.

The central purpose of the AIRS/AMSU/HSB combination is to obtain accurate atmospheric temperatures and humidities throughout the atmosphere, from the surface upward to an altitude of 40 km

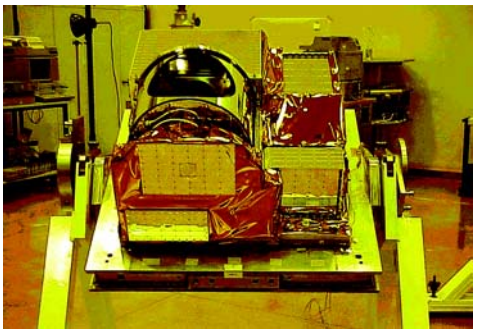

HSB. (Photo courtesy of Brazil's Instituto Nacional de Pesquisas Espaciais.)

MODIS

The other three instruments on Aqua, outside of the AIRS/AMSU/HSB sounding suite, are the Moderate Resolution Imaging Spectroradiometer (MODIS), the Clouds and the Earth's Radiant Energy System (CERES), and the Advanced Microwave Scanning Radiometer for EOS (AMSR-E). MODIS and CERES instruments are also on Terra, launched in December 1999, and are provided by NASA, while AMSR-E is new and is provided by Japan's National Space Development Agency (NASDA).

Early Data

All six Earth-observing instruments on Aqua (or seven, when counting the two CERES individually) are now operating and sending down high quality data. The first instrument to be turned on was the AMSU, on May 12, followed two days later by the HSB. Within days, the AIRS/AMSU/HSB science team had created first-light images from these data streams, mapping color-coded brightness temperatures (reflecting the radiation values received) for individual channels of data across the eastern U.S., the western U.S., and, for the HSB, Brazil. The next instrument to be turned on was NASDA's AMSR-E, with its data flow beginning on May 24. Some initial complications with the AMSR-E data were quickly solved by NASDA, who by June 1 had adjusted the automatic gain control (AGC), correcting the data flow. Days later NASDA created two global maps illustrative of the high quality data from the AMSR-E instrument, one map showing sea surface temperatures and the other showing a color-composite produced from three of the AMSR-E channels.

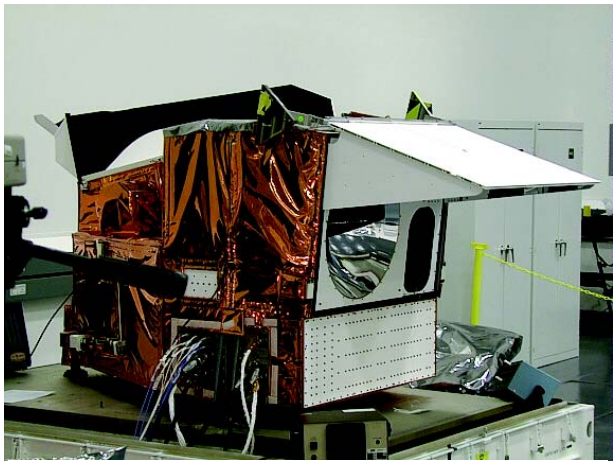

MODIS. (Photo courtesy of Raytheon.)

The AIRS visible data started flowing on May 26, and the AIRS infrared data started to flow on June 12. The CERES data started to flow on June 18, and the MODIS data started on June 24. In each case, very quickly after the instrument was turned on, the relevant science team had created first-light images illustrating the fact that the instrument is working and is obtaining high quality data. The MODIS team has indicated the clearly superior quality of the initial Aqua images versus the initial MODIS images from Terra, where there was an undesired striping; and the AIRS team, in addition to creating images, has plotted infrared spectra at individual points, establishing that every one of the 2378 infrared channels on AIRS is working.

Assessment of the Cycle-to-Cycle Noise Level of the Geosat Follow-On, TOPEX, and Poseidon Altimeters

N. TRAN

Raytheon ITSS and NASA Goddard Space Flight Center/Wallops Flight Facility, Wallops Island, Virginia

D. W. HANCOCK III AND G. S. HAYNE

NASA Goddard Space Flight Center/Wallops Flight Facility, Wallops Island, Virginia

D. W. LOCKWOOD

Raytheon ITSS and NASA Goddard Space Flight Center/Wallops Flight Facility, Wallops, Virginia

D. VANDEMARK

NASA Goddard Space Flight Center/Wallops Flight Facility, Wallops, Virginia

M. L. DRISCOLL AND R. V. SAILOR

TASC, Inc., Reading, Massachusetts

21 September 2001 and 1 April 2002

ABSTRACT

The Geodetic Satellite (Geosat) Follow-On (GFO), Ocean Topography Experiment (TOPEX), and Poseidon altimeter white-noise levels have been evaluated using a technique based on high-pass filtering of 1-Hz sea surface height time series. High-pass filtering removes the geoid and oceanography signals while revealing the random noise. This filtering technique is simpler to use than the repeat-track method, gives essentially the same results, and makes it easier to analyze much larger amounts of data to investigate subtle variations in noise levels. The new noise-level measurements provided here all show stable noise-process characteristics from cycle to cycle, with a linear dependence of the noise level upon significant wave height (SWH). The GFO altimeter noise level is estimated to be 2.5 cm for an SWH of 2 m. The Poseidon noise level is estimated at 2.0 cm for the same value of 2 m SWH. The TOPEX altimeter noise level is 1.8 cm when the dual-frequency ionospheric correction is included; when this noisy correction is not used, the level is reduced to 1.5 cm. Although the dual-frequency ionospheric correction provides an average improvement over the ''Doppler orbitography and radiopositioning integrated by satellite'' (DORIS) correction, high-frequency noise enters into the dual-frequency correction via noise from the Ku- and C-band ranges. Because the variations in ionospheric refraction are a relatively long wavelength global effect (with strong dependence on latitude), the dual-frequency ionospheric correction should be low-pass filtered before use, and this correction should not be included when estimating the high-frequency noise level of the altimeter.

1. Introduction

The Geodetic Satellite (Geosat) Follow-On (GFO) and the Ocean Topography Experiment (TOPEX)/Poseidon (T/P) missions are dedicated to the observation of the ocean surface topography from orbit using satellite-based nadir-pointing radar altimeters. The basic data are altimeter-derived sea surface heights (SSH) that are obtained by taking the difference of the satellite altitude (relative to a reference ellipsoid) as determined by precision orbit tracking and the altimeter range as determined by precise measurement of the round-trip time of flight of the radar signal. The range estimate requires environmental corrections, for example, for atmospheric propagation delays and sea-state biases. Measurements of the range in 1-s averages are generally analyzed in applications of altimeter data.

An integral part of the analysis of altimeter datasets is a quantitative evaluation of altimeter instrument noise. This is necessary for monitoring improvements in measurement systems, for projecting future capabilities, and for properly analyzing the data in oceanographic and geodetic applications. The precision of satellite radar altimeter instruments has improved since the earlier programs [the *Geodynamics Experimental Ocean Satellite* (*GEOS-3*), Seasat, and Geosat], and continuous improvements in environmental corrections (orbits, ionospheric refraction, tides, etc.) have resulted in modern altimeters (e.g., TOPEX) having absolute errors of only a few centimeters.

The largest contributions to the measured sea surface topography come from 1) geoid undulations, 2) dynamic oceanography associated with geostrophic surface currents and eddies, 3) tides, 4) the sea surface response to atmospheric pressure loading, and 5) altimeter instrument noise; not included in this list are orbit errors, which are very long in wavelength and relatively small in amplitude and which may be ignored for the purpose of this discussion. The elevation variability of the geoid signal is on the order of meters to tens of meters; the oceanographic signals are from a few centimeters to no more than 2 m; and tides in the open ocean are generally less than 1 m but can be predicted by numerical models to better than a few centimeters. The atmospheric loading or ''inverse barometer'' effect is a few centimeters, and the instrument noise is also at the few-centimeter level. One additional, but small, effect comes from ocean waves and swell. Although very obvious to mariners, waves are not a major factor in the measured sea surface topography, because each altimeter pulse illuminates a circular area on the ocean that is several kilometers in diameter, so the local waves are approximately averaged out. Actually, the averaging out is not perfect, and there is an ''electromagnetic bias'' correction proportional to significant wave height (SWH) and wind speed that should be made for the most precise uses of altimeter data (e.g., Gaspar et al. 1994).

The original analyses of satellite altimeter noise were developed in the context of geodesy, and ''noise'' was defined as any effect in the data other than the geoid signal. Noise was studied by comparing the repeatability of the data observed along colinear or repeat tracks. By differencing the data series along two repeat tracks (having a cross-track offset of no more than 1 km), the time-invariant geoid signal cancels out and a time series of random noise remains. Spectral analysis of the difference time series reveals two main components of the noise: 1) a ''colored'' noise process behaving approximately like a first-order Markov random process (this is attributable to oceanography) and 2) a lower-powered additive contribution that appears as a ''white-noise floor,'' visible as the noise spectra flatten out at high frequency (Brammer and Sailor 1980; LeSchack and Sailor 1988). The white-noise component was attributed to electronic noise in the altimeter instrument, and, indeed, the on-orbit results are generally consistent with laboratory measurements of instrument noise made before launch.

However, as this paper shows, a portion of the white-noise component can be attributed to random scattering effects from ocean waves, since the white-noise level is found to be proportional to the SWH. The repeat-track method of studying noise in altimeter data requires that repeat tracks be matched up and aligned, that environmental corrections (e.g., tides) be applied independently to each track, and that power spectra be computed from the difference segments. This is straightforward but was not easily automated to process large amounts of data. Consequently, the early studies did not apply this method to very many repeat-track pairs and did not investigate in much detail the variability in noise that might occur as a function of aging of the spacecraft or that might be due to environmental factors such as SWH. Nevertheless, the white-noise level for each altimeter was found to be fairly consistent, and the average values obtained for different altimeters are a good measure of the relative quality of those instruments. For example, *GEOS-3*, launched in 1975, had a white-noise level of about 23 cm. For Seasat in 1978 the result is 5 cm, and for Geosat in 1985 it was 3 cm (Sailor and LeSchack 1987; Sailor and Driscoll 1992). Le Traon et al. (1994) analyzed TOPEX and Poseidon spectra and estimated that the Poseidon repeat-track noise level is about 3 cm and the TOPEX repeat-track noise level is about 1.8 cm, calculated as rms. All of these numbers have been determined without consideration of the SWH. They all represent the integrated white-noise power in the frequency band from -0.5 to $+0.5$ Hz (the folding frequencies for data sampled at 1 Hz), so these noise values correspond to a 1-s average. Sailor (1993) defines the signal processing and spectral analysis techniques in detail and gives examples that confirm the validity of the noise-modeling approach that involves repeat tracks.

To summarize and conclude, the assessment of the altimeter noise by high-pass filtering 1-Hz sea surface height time series can be applied to single-frequency altimeter data such as from GFO and the French altimeter Poseidon, as well as to dual-frequency altimeter data such as from TOPEX. As pointed out in an early analysis (Driscoll and Sailor 2001), this approach to estimating the altimeter noise provides results similar to those derived from the noise spectra computed from differenced repeating ground tracks and is also in agreement with the alternate operational TOPEX Ku-band range noise estimation method as presented in this paper

This paper presents the first application of the high-pass-filtering method to multiple altimeters for determining the noise level in satellite altimeter data. This technique is found to be valuable because it allows the noise levels to be determined from individual tracks rather than from repeat tracks, facilitating time-dependent noise-level monitoring. The most obvious effect on the observed noise level is SWH, and, for all altimeters, the noise level increases linearly with increasing SWH. Other than the dependence on SWH, the noise level is very stable from cycle to cycle for GFO, TOPEX, and Poseidon. Thus, the high-pass-filtering technique will be useful for monitoring the performance of any altimeter as the satellite ages and for comparing the relative performance of different altimeters with respect to high-frequency noise.

As shown here, the effective number of independent radar return pulses directly affects altimeter range estimation precision. The new Poseidon-2 altimeters aboard the *Jason-1* satellite transmit at rates of 1800 and 300 Hz, for Ku and C band, respectively. Altimeters aboard *Envisat* operate at 1800 Hz at Ku band and 450 Hz at S band. These rates will thus set limits for both sensor's performance, as pointed out by Quartly et al. (2001).

The Dependence of Nadir Ocean Surface Emissivity on Wind Vector as Measured With Microwave Radiometer

Ngan Tran, Douglas Vandemark, Christopher S. Ruf, and Bertrand Chapron

***Abstract*—Global brightness temperature observations of TOPEX/Poseidon microwave radiometer (TMR) at 18, 21, and 37 GHz have been collocated with near-simultaneous SeaWinds wind vector data as well as with monthly sea surface temperature and salinity products. The combined data allow us to study the dependence of zenith-directed ocean surface emissivity, at each frequency, upon both wind speed and direction. Results show a clear two-branch wind speed dependence; weak and linear below 7 m·s^{-1} with an increase in sensitivity above that point. The observed emissivity also depends on the angle between the wind direction and TMR's antenna polarization orientation, providing satellite confirmation of aircraft-derived results. There is little change in these wind vector dependencies with frequency.**

***Index Terms*—Nadir ocean surface emissivity, SeaWinds wind vector, TOPEX/Poseidon microwave radiometer (TMR).**

I. Introduction

The TOPEX/Poseidon microwave radiometer (TMR) is a three-frequency radiometer operating on the TOPEX/Poseidon (T/P) satellite. It measures radiometric brightness at 18, 21, and 37 GHz in a nadir-viewing direction co-aligned with T/P radar altimeters [1]. Its primary objective is to monitor and correct for the propagation path delay of the Ku-band altimeter signal due to atmospheric water vapor and cloud liquid water [2]. For TMR, this wet tropospheric path delay is derived from the three-frequency brightness temperatures T_b as discussed in [3]. Delay is highly variable in space and time and, if uncorrected, leads to altimeter range measurement errors of 3–45 cm. TMR is designed to provide this range correction with 1.2 cm accuracy.

Most satellite altimeters are now supported by a two- or three-frequency water vapor radiometer. One issue in designing these systems is compensation for the second-order brightness temperature variations associated with changing ocean surface emission. While the wind speed dependence of zenith-directed emission is fairly well known and already characterized within path delay algorithms, it has also been shown [4] that there should be a small ΔT_b associated with wind direction change. This sensitivity comes from the fact that the thermal emission from anisotropic sea waves depends upon azimuthal (polarization at nadir) observation angle.

Several experimental studies have addressed this sensitivity to the wind vector by means of circle flights [4]–[8]. These aircraft measurements indicate a direction detection capability for nadir-looking systems as well as a potential error source for spaceborne water vapor radiometers (such as TMR) aboard altimeter platforms. Reported measurements and theoretical investigations [9]–[11] suggest that the nadir-looking radiometer directional sensitivity follows from the azimuthal anisotropy of the spatial spectrum of short-gravity and capillary waves.

The aim of this communication is to use satellite data from the TMR to document the impact of wind speed and direction on surface emissivity at 18, 21, and 37 GHz. To the authors' knowledge, the study presents the first on-orbit evidence of a wind direction dependence at nadir. This work follows similar efforts focused on the off-nadir pointing spaceborne Special Sensor Microwave/Imager (SSM/I) deployed on the Defense Meteorological Satellite Program (DMSP) missions [12], [13]. The approach is simply to observe ΔT_b variation versus the angle between TMR's linear polarization alignment and the surface wind direction. To this end, a large global data set has been compiled by combining scatterometer (SeaWinds) wind vector measurements with T/P observations at satellite crossover points over a year-long period. The extensive data set carries a broad coverage of environmental conditions and permits robust removal of the first-order atmospheric signal needed to isolate the surface emission signals with certainty. In Section II, we recall Giampaolo and Ruf's [14] approach for TMR emissivity estimation using quantities that can either be obtained directly from satellite measurements or approximated from ancillary sources with satisfactory accuracy. Section III describes the large global compilation of TMR, SeaWinds wind vector, the monthly sea surface temperature (T_s) climatological estimates, and the climatological sea surface salinity (SSS) product used in this study. Sections IV and V present, respectively, wind speed and wind direction dependencies of the sea surface emissivity as measured with TMR. Section VI provides conclusions.

VI. Conclusion

Observations presented in Sections IV and V serve to document the zenith-directed wind-induced ocean emissivity ($\Delta\epsilon$) at 18, 21, and

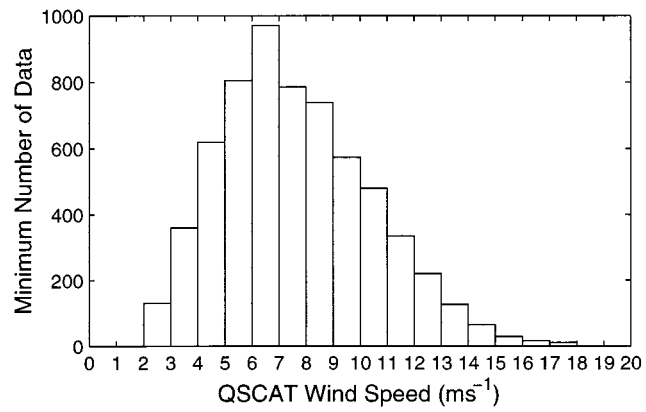

Fig. 7. Minimum number of data in a 30° azimuth angle bin for each 1 m·s^{-1} SeaWinds/QSCAT wind speed interval.

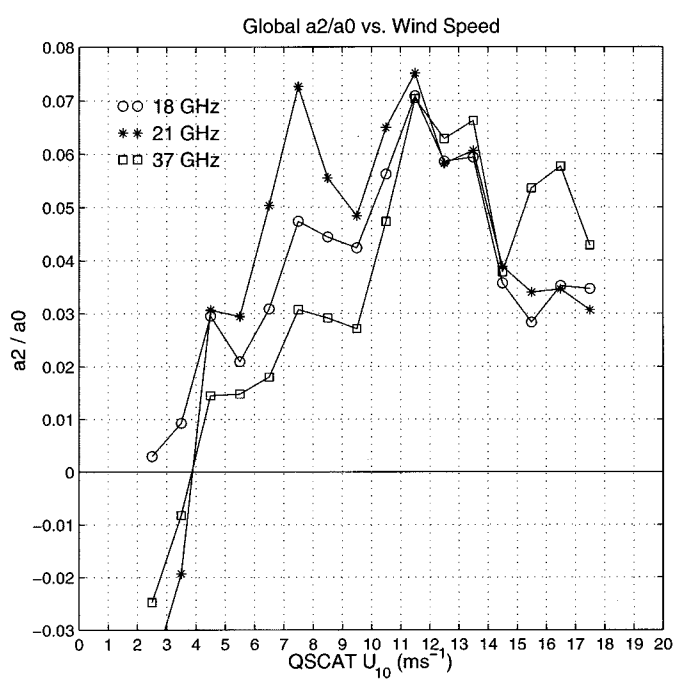

Fig. 8. Dependence of the normalized second-order harmonic $a2/a0$ on SeaWinds/QSCAT wind speed.

37 GHz. These data come from a carefully filtered combination of TOPEX radiometer and SeaWinds scatterometer data, augmented by surface temperature and salinity estimates. The nadir-detected satellite brightness temperature is shown to depend on both wind speed and direction. This study represents the first satellite confirmation of a directional sensitivity at nadir.

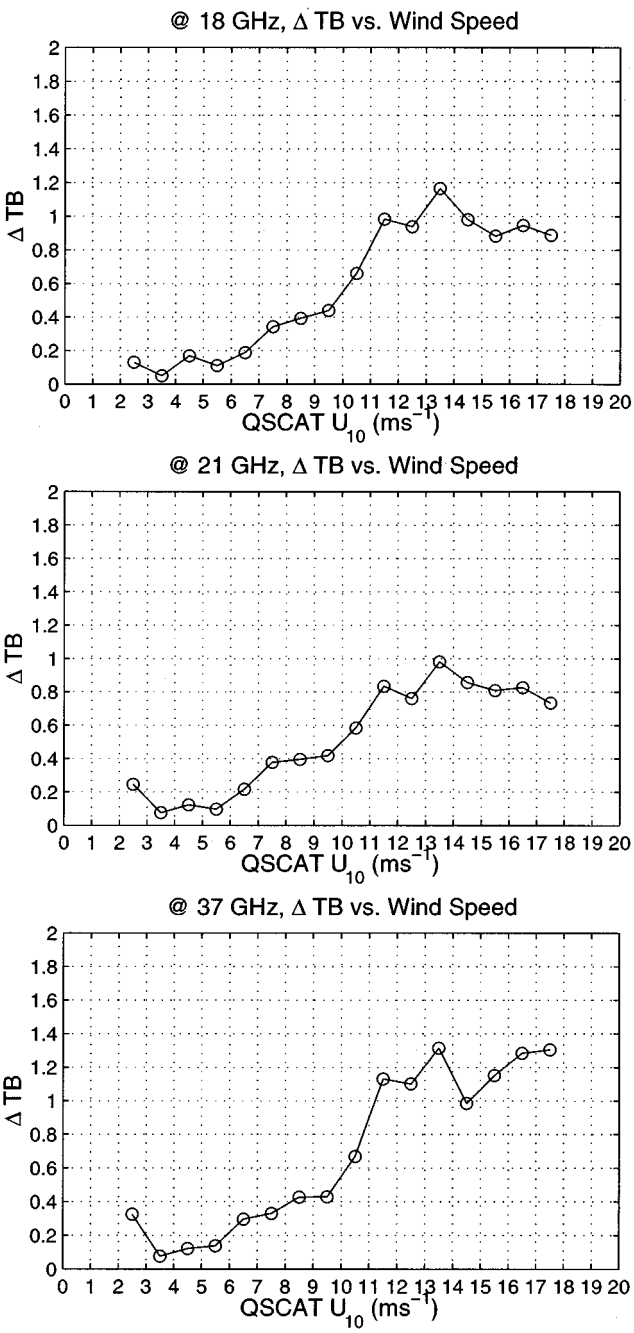

Fig. 9. Amplitude of the directional signal in term of peak-to-peak brightness temperature as a function of SeaWinds/QSCAT wind speed for the three frequencies.

The data show a clear two-branch wind speed dependence; weak and linear below 7 $m \cdot s^{-1}$ with an abrupt increase in sensitivity above that point for all TMR three frequencies. The $\Delta\epsilon$ is a factor of two to three higher above 7 $m \cdot s^{-1}$. As mentioned, the microwave emission exhibits a smaller, but measurable, dependence on wind direction. This signal is attributed to the polarized nature of the surface wave structure. The peak-to-peak brightness temperature directional signal is of the order of 1.0 K at 11.5 $m \cdot s^{-1}$. Observations vary little with frequency versus wind speed or direction. These global-average results are the product of a large data compilation and low regression uncertainties. Agreement with previous aircraft and SSM/I studies suggest high confidence in the findings.

These results are applicable in several areas. First, the data confirm the potential for a nadir-viewing wind direction sensor. Such a sensor would necessarily be a polarimetric radiometer in order to isolate the polarized emission from the largely unpolarized background signal. The globally-derived observations should also serve to complement the results derived from aircraft case studies, where all measurements are being assimilated into ocean emission models [8], [34]. Finally, the accuracy of the water vapor radiometer's altimeter path delay correction can be reassessed based on the present observations. As discussed in [35], the two frequency systems are most susceptable to an additional frequency-independent error source (such as $\Delta\epsilon$ dependence on direction). For example, the GEOSAT-follow-on (GFO) or ERS radiometers operate near 22 and 37 GHz. A first-order estimate suggests that a 0.20 cm wet path delay error (and hence sea level error) will result from a peak-to-peak directional T_b variation of 1.2 K at both 22 and 37 GHz. While this level is certainly small, ocean basins can systematically differ in their mean wind directions. Therefore, the error is not necessarily random.

A Comparison of the MIR-Estimated and Model-Calculated Fresh Water Surface Emissivities at 89, 150, and 220 GHz

James R. Wang, *Senior Member, IEEE*

***Abstract*—The airborne millimeter-wave imaging radiometer (MIR) measurements over three lakes (surface temperature ~ 273 K) in the Midwest region of the USA during February 1997 were used to estimate surface emissivities at 89, 150, and 220 GHz and the results were compared with those calculated from three different dielectric permittivity models for fresh water. The measurements were during clear and dry atmospheric conditions so that the column water vapor could be accurately retrieved and its effect on the MIR measurements predicted. The standard deviations of the estimated emissivities were found to be about 0.003, 0.004, and 0.008 for 89, 150, and 220 GHz, respectively. The errors of the estimation were calculated to be $\pm 0.005, \pm 0.006$, and ± 0.011 in the same order of frequency, respectively, based on the MIR measurement accuracy of ± 1 K in the brightness temperature range of 190–290 K.**

The estimated emissivities at normal incidence, under the assumption of a calm water surface, compare quite well with values generated by the model of Stogryn *et al.* [1]. These estimated values are slightly lower than those calculated from the model of Liebe *et al.* [2] at both 89 and 150 GHz. The estimated 89 GHz emissivity is higher than that calculated from the model of Ellison *et al.* [3]. Additionally, the retrievals using different models of atmospheric absorption as well as off-nadir measurements of the MIR are explored. The impact of these retrievals on the comparison of estimated and calculated emissivities is discussed.

***Index Terms*—Millimeter-wave radiometry, remote sensing, surface emissivity.**

I. Introduction

MICROWAVE remote sensing of atmospheric and oceanic parameters such as water vapor, clouds, precipitation, surface wind and temperature from aircraft and satellite platforms depends crucially on the knowledge of surface emissivity (or reflectivity) and therefore the dielectric permittivity of water. A number of models for the dielectric permittivity of water [1]–[4] have been formulated in the past decades to facilitate measurements of these parameters. At low frequencies $\leq$10 GHz, the complex dielectric permittivity, ε, of water and its temperature dependence appear to comply with Debye's model of single-frequency dielectric relaxation [3]–[5]. In the frequency range below 85 GHz covered by the special sensor microwave/imager (SSMI) or other satellite radiometers that were used to retrieve parameters like column water vapor clouds, and wind speed over ocean surface [6]–[8], the results of emissivity calculations based on the single-frequency model were not completely satisfactory [8]. Dual-frequency models based on new measurements have been formulated [1], [2], but these models lack extensive testing. More recently, the radiometric measurements at higher frequencies than 85 GHz have been used for studying and retrieving water vapor, clouds, and precipitation [9]–[11]. Thus, it is important to examine the adequacy of ε values derived from these models at frequencies $>$10 GHz for reliable retrievals of these atmospheric and oceanic parameters.

In this paper, we attempt to validate three recent models of dielectric permittivity for fresh water [1]–[3] from the 89–220 GHz radiometric measurements of the millimeter-wave imaging radiometer (MIR). MIR is a total power, cross-track scanning radiometer that measures radiation at the frequencies of 89, 150, $183.3 \pm 1, 183.3 \pm 3, 183.3 \pm 7$, and 220 GHz [12]. The measurement accuracy of the instrument is within ± 1 K in the temperature range of 190–290 K. Racette *et al.* [12] provided a more detailed description of the characteristics and operation of the instrument. For profiling of water vapor using the MIR measurements over a water surface, the surface temperature T_s and emissivity ξ calculated from a given dielectric permittivity model are the known parameters that are used as input for a retrieval algorithm [13]. However, when the atmosphere is relatively dry with total column water $W \leq 0.8$ g/cm^2, it is possible to estimate W with good precision, without a detailed knowledge of T_s and ξ, from the MIR measurements over a water, sea ice or land surface [14]–[16]. Then ξ and its frequency dependence are readily determined after W is estimated and T_s is independently measured. This procedure is explored in an effort to estimate ξ of a water surface at 89, 150, and 220 GHz. Estimation of both W and ξ from the MIR measurements depends on the selection of atmospheric absorption models; therefore, a brief discussion of the models of atmospheric absorption and water's dielectric permittivity is given in the next section. This is followed by a description of the MIR measurements and retrievals of W and ξ. Finally, a comparison between the estimated and calculated ξ values as well as the ensuing discussion and conclusion of the results are presented.

II. Models of Atmospheric Absorption and Dielectric Permittivity for Water

A. Atmospheric Absorption

The millimeter-wave propagation model (MPM) formulated by Liebe [17] is frequently used in radiative transfer calculations, in the microwave-millimeter-wave region of the electromagnetic spectrum, in recent years [13], [18]–[20]. More recently, Rosenkranz [21] reexamined most of the available data and formulated a new model, which was used by Westwater *et al.* [20] to compute T_b values from rawinsonde data acquired at Barrow, Alaska and compared with near concurrent measurements from ground-based radiometers during March 1999. Westwater *et al.* [20] found subtle differences between the cal-

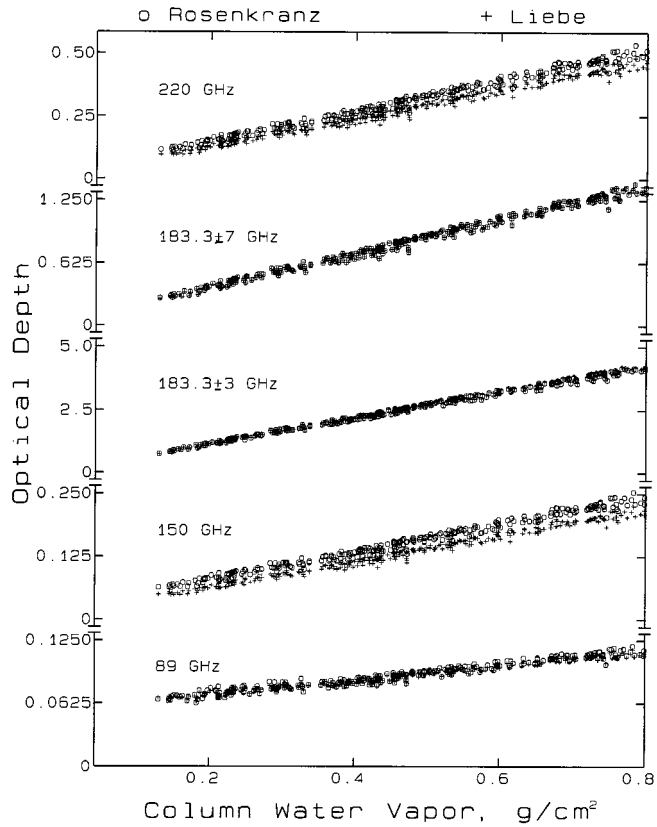

Fig. 1. Scatter plot showing the dependence of optical depth on column water vapor for several selected MIR channels. The values of optical depth are calculated based on the rawinsonde data from the Midwest USA and Alaska-Arctic regions [15].

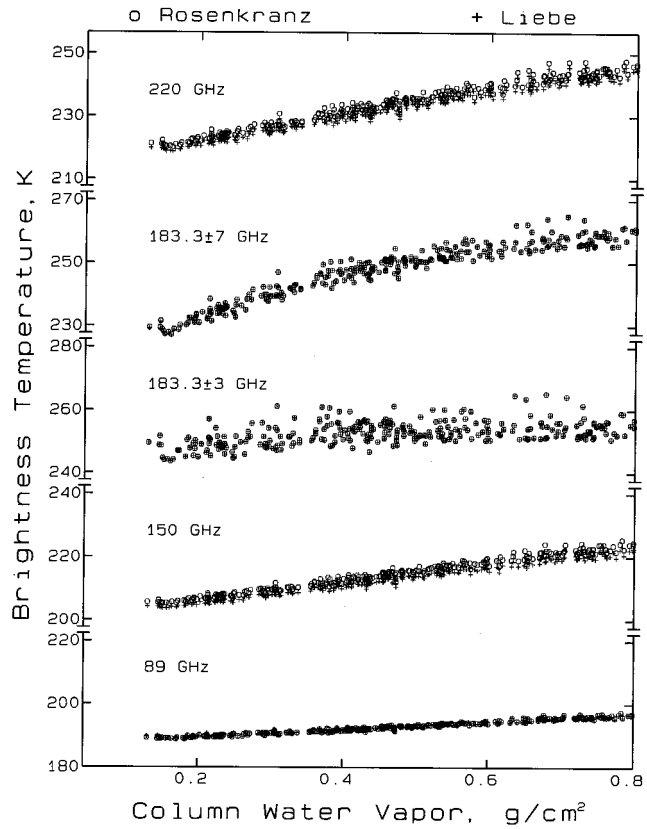

Fig. 2. Scatter plot showing the dependence of brightness temperature on column water vapor for several selected MIR channels. The calculations are based on the same rawinsonde data as in Fig. 1.

culated and measured T_b values, as well as the calculated values between the models of Liebe and Rosenkranz. To see the differences in the MIR frequency range between these two models under dry atmospheric conditions with $W \leq 0.8$ g/cm^2, we show in Figs. 1 and 2, respectively, the calculated optical depth Γ and T_b based on rawinsonde data used by Wang *et al.* [15], [16] from both WINCE and FIRE-ACE. The vertical scales from both figures are adjusted in an effort to distinctively demonstrate the variations of Γ and T_b at each frequency. In the T_b calculations, the dielectric permittivity model by Stogryn *et al.* [1] for fresh water is used to derive surface emissivity, assuming a water temperature of 274 K.

VII. Conclusion

The MIR measurements over Lake Huron, Lake Michigan, and Lake Superior under clear and dry atmospheric conditions were used to estimate surface emissivity $\xi(\nu)$ of fresh water. The estimated $\xi(\nu)$ values at $\nu = 89, 150$, and 220 GHz were compared with those calculated from three different models of dielectric permittivity [1]–[3]. Both along-track and across-track measurements were used; thus, the retrieved column water vapor W and $\xi(\nu)$ could be analyzed with respect to incidence angle (θ) up to 40°. The retrieved W values depend on θ as expected from a path length consideration. A positive gradient in W from southeast to northwest of Lake Huron during the time of the aircraft flight is revealed by the retrieval. The θ dependence of the retrieved $\xi(\nu)$ follows a pattern expected from the polarization vector of the MIR. The standard deviations of the retrieved $\xi(\nu)$ values and their frequency dependence are consistent with those estimated from statistical considerations.

The $\xi(\nu)$ values retrieved at 89, 150, and 220 GHz for fresh water are in good agreement with those calculated from the dielectric permittivity model of Stogryn *et al.* [1] in the limited temperature range near 273 K, especially if the Liebe's MPM model is used to account for the effect of atmospheric absorption [17]. When Rosenkranz's atmospheric model [21] is used the estimated $\xi(\nu)$ at 150 GHz appears low compared to all model calculations. The dielectric permittivity model of Liebe *et al.* [2] gives $\xi(\nu)$ values at both 89 and 150 GHz, which are slightly higher than the estimated values (i.e., just outside of errors based on ± 1 K measurement accuracy of the MIR). Finally, the estimated $\xi(\nu)$ values at 89 GHz are about 0.012 higher than those calculated at $T_s = 273$ K from the model of Ellison *et al.* [3] for seawater. Because the $\xi(\nu)$ values for fresh water are generally lower than those of saline water, this difference suggests a lower bound of the disagreement between estimation and calculation, unless the enhanced $\xi(89)$ can be totally accounted for by a wind-roughened surface effect. The $\xi(89)$ curve calculated from the model of Ellison *et al.* displays a milder dependence on T_s than those calculated from the other three models. It will be interesting to examine the T_s dependence of $\xi(\nu)$ and, therefore, the complex dielectric permittivity over a wider T_s range than available from the data used in this paper.

Profiling of Atmospheric Water Vapor With MIR and LASE

James R. Wang, *Senior Member, IEEE*, Paul Racette, *Member, IEEE*, M. E. Triesky, E. V. Browell, S. Ismail, and L. A. Chang

***Abstract*—Concurrent measurements of atmospheric water vapor profiles were conducted over the Atlantic Ocean on September 25, 1995 with both the millimeter-wave imaging radiometer (MIR) and lidar atmospheric sounding experiment (LASE) on board the NASA ER-2 aircraft. LASE provides high precision measurements of both aerosol backscatter and water vapor profiles; aerosol backscatter has a vertical resolution of 60 m while the water vapor profiles have a resolution of 330 m in the low-to-mid troposphere and 550 m in the upper troposphere. Therefore, LASE measurements provide an excellent resource for assessing the capabilities and limitations of MIR as a water vapor profiler. Previously, the water vapor profiles retrieved from the MIR measurements have been compared with those of rawinsonde and Raman lidar observations at point locations. The frequency and extent of the comparisons made in that fashion were largely constrained by the requirement of near coincidence in time and space. The data acquired concurrently by MIR and LASE from this ER-2 aircraft flight enable the comparison of MIR-retrieved and LASE-measured moisture profiles over a long stretch of time and space. In addition, the LASE-measured profiles of aerosol backscatter provide a resource to assess the impact of clouds on the retrieval of water vapor profiles from the MIR measurements.**

It is shown that profiles of water vapor mixing ratio retrieved from the MIR data generally conform to those measured by the LASE; however, differences in the values of mixing ratio at individual altitude levels are quite often not small. The standard deviations of these differences are found to be about $\pm 0.98, \pm 0.84, \pm 0.95, \pm 0.42$, and ± 0.06 g/kg at altitudes of 1.25, 2.75, 4.75, 7.25, and 10.25 km. It is demonstrated that a substantial portion of these differences are due to the poor vertical resolution inherent in the profile retrieval using the MIR radiometric measurements. Additionally, MIR water vapor profiling under cloudy conditions is demonstrated, and it is shown that location and height of the low-altitude clouds estimated from the retrieval process were generally consistent with those observed by the LASE. For study cases where cirrus clouds are present, retrievals from the MIR data over-estimate the mixing ratio; this over-estimate is provoked by brightness temperature decreases that occur at 183–220 GHz within these regions. Undoubtedly, the retrieval method needs an additional procedure to account for the millimeter-wave scattering by cloud ice particles so that water vapor profiling can be improved within regions where cirrus clouds are present.

***Index Terms*—Millimeter-wave radiometry, remote sensing, water vapor.**

I. Introduction

PROFILING of atmospheric water vapor using the strong absorption line at 183.3 GHz has been studied for nearly two decades [1]–[13]. Theoretically, Schaerer and Wilheit [1] explored the characteristics of this strong water vapor line by performing both forward calculations and profile retrievals over the ocean surface. The approach was extended by Wilheit [7] to retrieve water vapor profiles under both clear and cloudy conditions. Other alternative simulation studies and analyzes have been performed by Rosenkranz *et al.* [2], Kuo *et al.* [11] and Muller *et al.* [12]. Experimentally, water vapor profiles have been retrieved using radiometric measurements by the Airborne Microwave Moisture Sounder (AMMS) in the 1980s [3]–[6]. Because of its limited number of channels and poor temperature sensitivity (ΔT), the AMMS radiometric measurements could not provide robust retrievals of water vapor profiles under cloudy conditions [8]. More recently, a millimeter-wave imaging radiometer (MIR) was built and after a number of field experiments [9], [10] the radiometer was shown to provide more robust radiometric measurements than the AMMS. It contains six channels in the frequency range of 89–220 GHz and, with a comparable integration time to the AMMS, has ΔT's of <1 K at all channels [14]. The radiometric measurements from this sensor have been used to retrieve water vapor profiles under cloudy conditions with reasonable success [10]. Burns *et al.* [13] have also examined the effects of precipitation and cloud ice on these water vapor channels using measurements from the special sensor microwave/temperature-2 (SSM/T-2) on board the defense meteorological satellite program (DMSP) F-11 satellite. These theoretical and experimental efforts provide an effective demonstration of the capabilities and limitations of using the 183.3 GHz line for water vapor profiling.

The experimental results of water vapor profiling derived from the AMMS and MIR measurements were routinely compared with nearly concurrent (within ± 3 hours) rawinsonde observations at some selected locations [3], [6], [9]. Additionally, a comparison of water vapor profiles retrieved from the MIR measurements was made with ground-based Raman lidar observations at NASA's Wallops Flight Facility (WFF), Wallops Island, Virginia during the Convection and Atmospheric Moisture Experiment (CAMEX) of July–August, 1993 [9]. Reasonable agreements were found between the profiles retrieved from these AMMS and MIR measurements and those measured at the ground locations. However, these comparisons were limited to single locations and there has been no validation of the profiles retrieved from the measurements of these sounders over an extended region. During September 1995, MIR and LASE (Lidar Atmospheric Sensing Experiment) were on board the NASA ER-2 aircraft during a number of flights both over land and ocean areas in the eastern U.S. LASE measures both aerosol backscatter and water vapor mixing ratio with high accuracy and vertical resolution [15], [16]. The LASE-measured mixing ratio was compared with that measured concurrently by the ground-base Raman Lidar

and rawinsondes at WFF and an excellent agreement was found among the three different approaches [15]. These flights provide the first opportunity to validate the water vapor profiling method derived from the MIR radiometric measurements over an extended region.

VI. Conclusion

Measurements of water vapor profiles were made concurrently with LASE and MIR on board the NASA ER-2 aircraft over the Atlantic ocean on September 25, 1995. The LASE measured profiles have a vertical resolution of 330 to 550 m, depending on altitude, and, therefore, serve as an excellent standard for comparison with the lower-resolution profiles retrieved from the MIR measurements. Previously, the water vapor profiles obtained from the MIR measurements were compared only with those measured by dropsondes released from a different aircraft or by the ground-based Raman lidar and rawinsondes [9], [10]. The requirement of the approximate coincidence in time and location of these measurements essentially limited the comparison to a few selected cases. The 3-h flight of LASE and MIR described above, on the other hand, provides about 180 independent and concurrent measurements over an ocean area that includes both clear and cloudy conditions. This combined LASE and MIR data set serves as an extremely valuable resource that can be utilized to analyze and evaluate the capabilities and limitations of millimeter-wave remote sensing to profile water vapor. However, there is a deficiency related to this data set: it is obtained within a short time period over a small geographic region and, as a consequence, the range of observed variation in the moisture field of the atmosphere is rather limited.

The comparison of the MIR-retrieved profiles of water vapor mixing ratio with those measured by LASE leads to the following conclusions. First, in general the MIR-retrieved profiles correspond well with those measured by the LASE, although they could not provide the fine vertical structure reflecting the rapid changes of moisture with altitude that was observed by LASE. At individual altitude levels, the differences in the mixing ratios retrieved by the MIR and measured by LASE are not small. A substantial portion of these differences is undoubtedly caused by the poor vertical resolution of the retrieved profiles that is inherent to the inversion process. For instance, column 3 of Table I shows that, using LASE measurements as a standard, the inversion process could cause standard deviations of $\pm 0.95, \pm 0.57, \pm 0.16$, and ± 0.02 g/kg at the altitudes of 2.75, 4.75, 7.25, and 10.25 km. The retrieval results from the MIR measurements give corresponding numbers of $\pm 0.84, \pm 0.95, \pm 0.42$, and ± 0.06 g/kg at those respective altitudes; the larger numerical values at higher altitudes could be attributed to the measurement differences between the two sensors. The standard deviations were significantly smaller than those of climatological variations. Therefore, radiometric measurements at the MIR frequencies can provide water vapor profiles that are useful for studying the large-scale changes in the water vapor fields of the atmosphere.

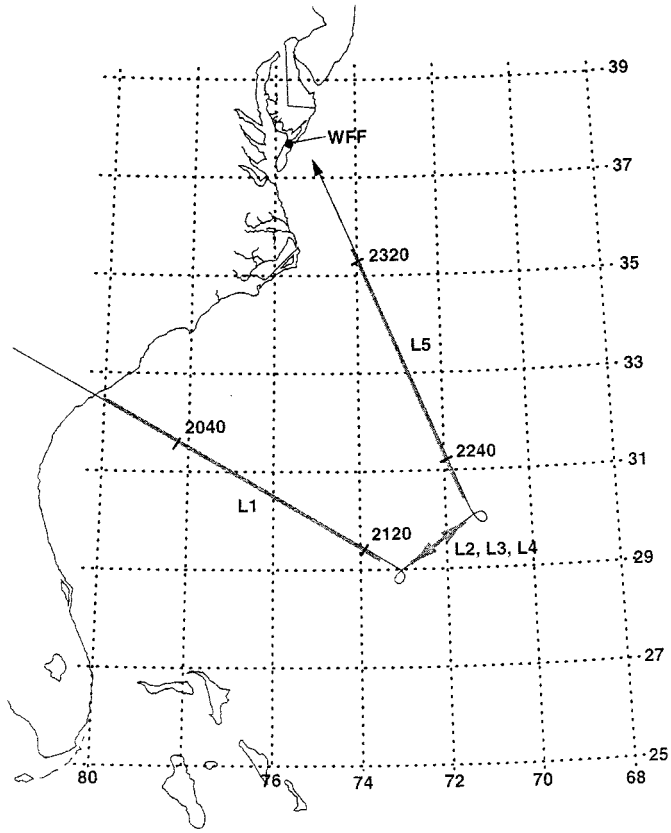

Fig. 1. Sketch showing the path of the ER-2 aircraft flight over the Atlantic Ocean on September 25, 1995. Five straight line segments are denoted by L1, L2, L3, L4, and L5. L2, L3, and L4 are repeated passes over the same region.

Next, it was shown that MIR could profile atmospheric water vapor over a region with moderate, low-altitude cloud cover. There is a close association between the locations where low-level clouds are detected by LASE and the locations where the cloud liquid water were also required as input to the MIR retrieval algorithm to reach a convergent retrieval of water vapor profiles from the MIR measurements. The cloud tops predicted by the retrieval algorithm are closely related to those observed by the LASE; however, the retrieval does experience some difficulty in areas of dense clouds where the measured 89 GHz brightness temperatures are >270 K (Fig. 3). The retrievals for these areas result in low values of mixing ratio at altitudes below the cloud tops, require cloud liquid water in excess of 0.4 kg/m^2, and are associated with poor convergent criteria ($\Delta T_b \simeq 2$–3 K) (see Fig. 4).

Finally, in the region of dense cirrus clouds where the depressions in 220 GHz brightness temperatures are clearly observed, the effect of millimeter-wave scattering by ice particles must be considered to improve retrievals of water vapor profiles. The algorithm used to retrieve water vapor profiles from the MIR measurements, as discussed above, does not currently incorporate such a procedure.

Retrievals of Column Water Vapor Using Millimeter-Wave Radiometric Measurements

James R. Wang, *Senior Member, IEEE*, Paul Racette, *Member, IEEE*, M. E. Triesky, and Will Manning

***Abstract*—The airborne millimeter-wave imaging radiometer (MIR) measurements conducted over the midwest region of the continental United States during January/February 1997 and over the Alaska–Arctic region during May 1998 are used to estimate column water vapor $W < 0.8$ g/cm^2 under a clear sky. On board the same aircraft are two other instruments, the cloud lidar system (CLS) and MODerate-resolution imaging spectrometer (MODIS) airborne simulator (MAS), which provide cloud cover information and independent measurements of W, respectively. The MIR-estimated W values are compared and found to be in very good agreement with those measured by rawinsondes at near concurrence. A close correlation is found between the MIR-estimated W and that estimated from the MAS near-IR reflectance ratios. Water surface emissivities at several MIR frequencies are obtained in the process of the W retrieval from several flights over the mid-west lakes. These estimated emissivities compared favorably with values calculated for a calm water surface, which are based on a recent dielectric permittivity model and MAS-measured surface temperatures. The results from all comparisons strongly demonstrate the soundness of the technique for estimating W.**

***Index Terms*—Millimeter-wave radiometry, remote sensing, water vapor.**

I. Introduction

MILLIMETER-WAVE radiometry with the strong absorption line of 183 GHz is normally used for profiling of water vapor, as both theoretical and experimental studies have demonstrated during the past two decades [1]–[5]. Additionally, some studies have shown that measurements near this line can be used to estimate total amount of water vapor column W for relatively dry atmospheric conditions that frequently occur in high latitude regions [6] or following a cold air outbreak [7]. Over Antarctica or the arctic region, dry-air conditions are prevalent from late fall to early spring so radiometry near 183 GHz provides an excellent resource for W estimation. Monitoring the state of atmospheric water vapor and its transport into and out of these regions is important toward our understanding the state of balance of ice sheets and its effect on global sea level [8]. Both Moore [9] and Miao [10] have selected Antarctica as their study area for estimation of W from measurements of the 183 GHz channels of the special sensor microwave/temperature-2 (SSM/T-2); however, the techniques employed by these authors are different. Moore [9] used measurements from the 183.3 $\pm$ 3 and 183.3 $\pm$ 7 GHz channels of the SSM/T-2, as well as the surface temperature derived from the European Center for Medium-range Weather Forecast (ECMWF) data source to simultaneously retrieve both W and surface reflectivity, R, using an iterative technique. Miao [10], on the other hand, used a regression approach with the SSM/T-2 measurements at 150, 183.3 $\pm$ 3, and 183.3 $\pm$ 7 GHz as inputs. R is assumed constant over the frequency range of 150–183 GHz in the latter approach.

Wang *et al.* [11] attempted to apply these techniques of Moore [9] and Miao [10] for estimation of W while using airborne MIR (Millimeter-wave Imaging Radiometer) measurements over Alaska and Arctic region on May 20, 1998 instead of the SSM/T-2 data. The flight is one of many conducted during the FIRE-ACE (First ISCCP (International Satellite Cloud Climatology Project) Regional Experiment—Arctic Cloud Experiment) field campaign that occurred from May 18–June 6, 1998. However, the thermal IR channels of the MODIS (MODerate-resolution imaging spectrometer) airborne simulator (MAS) on board the same NASA ER-2 aircraft were not functioning properly during that clear day of flight and, thus, the analysis was limited to the technique of Miao [10]. In addition to the data from the frequency group of 150, 183.3 $\pm$ 3, and 183.3 $\pm$ 7 GHz that is needed for estimation of W, MIR also provided measurements at 220 GHz; therefore, W can be estimated independently using data from the frequency group of 220, 183.3 $\pm$ 3, and 183.3 $\pm$ 7 GHz. The results from both frequency groups can then be compared. Wang *et al.* [11] analyzed the MIR data from both frequency groups and found discrepancies of various amounts in the estimated W values. They attributed these discrepancies to the unsubstantiated assumption that R (or emissivity e) is constant across the frequency ranges of 150–183 GHz and 183–220 GHz. They modified the technique by allowing a linear dependence of e on frequency over the entire frequency range of 150–220 GHz; by varying the slope of this linear dependence, estimated Ws were forced to converge to a common value. The results obtained from this modified version of the technique appeared reasonable. The estimated W values were compared with the available rawinsonde data at two locations and the differences between the estimated and measured W values were within the accuracy of the radiometric measurements. A more extensive comparison with rawinsonde data was not possible, because all other flights from that mission were made when atmospheric conditions were too moist for the retrieval technique to be applicable.

In the following we extend the previous work of Wang *et al.* [11] to the MIR data obtained from the flights over the Midwest region of the continental U.S. during the WINter cloud experiment (WINCE) [12] of January/February 1997. The techniques of both Moore [9] and Miao [10] and its modified version are described and analyzed with simulated brightness temperatures from a vast number of rawinsonde data from the Alaskan, Arctic, and Midwest regions. The technique of Moore [9] is proven inadequate for application to the MIR data. The modified version of Miao's technique [11] is used exclusively to estimate W from the MIR measurements. The estimated W values from both FIRE-ACE and WINCE are compared with those derived from rawinsonde observations. Additionally, a comparison

is made between these MIR-estimated Ws and those expected from the reflectance ratios in the near IR channels of the MAS. Finally, surface emissivities at several frequencies are estimated from a few observations over the lakes in the Midwest and compared with the calculated results, which substantiate the robustness of the retrieval technique.

V. Conclusions

Two different techniques [9], [10] developed recently for the estimation of integrated water vapor $W < 0.8$ g/cm^2 have been examined in this paper. The technique by Moore [9] utilizes the 183.3 $\pm$ 3 and 183.3 $\pm$ 7 GHz channels of the SSM/T-2 and ECMWF-derived surface temperature to estimate W and surface reflectivity R iteratively. Additionally, this approach requires as input an *a priori* optical-depth weighted effective atmospheric temperature in the equations for estimation of W and R. This latter requirement is found impractical for the data sets we obtained from the aircraft flights and therefore the technique is not explored further in the paper. The technique of Miao [10] is regression-based and uses the 150, 183.3 $\pm$ 3, and 183$\pm$ 7 GHz channels of the SSM/T-2 to estimate W over Antarctica. Equivalent surface emissivity values in the frequency range of 150–183 GHz are assumed in this approach, which, if not correct, could result in a significant error in the estimation of W [11]. MIR has an additional channel at 220 GHz that is absent from the SSM/T-2 and thus is capable of providing estimation of W with a simple linear dependence of e on frequency in the range of 150–220 GHz. Wang *et al.* [11] provided a demonstration of this modified version of Miao's technique using data from a clear-sky MIR flight over the Alaska-Arctic region on May 20, 1998. The present analysis extends that work to cover additional measurements over several different areas. Furthermore, the estimated W values are compared with those derived from the near IR channels of the MAS, as well as from a number of rawinsonde data. Additionally, as a by-product of the retrieval process, the surface emissivities at 89, 150, and 220 GHz for several lakes in the mid-west region of the continental U.S. are estimated and compared with results of calculations based on a recent dielectric permittivity model for fresh water [16].

The estimated W values are found to compare very well with those measured from the rawinsonde data for about the same time and location. On average the estimated W is about 0.02 g/cm^2 higher than the measured ground truth, which falls within the accuracy of the radiometric measurements. An increase of about 2 K in the measured brightness temperature at 150 GHz would offset this small bias [11]. The comparison between the MIR and MAS estimated W values is not exact because the estimation algorithm based on the reflectance ratios from the available near IR channels of the MAS is optimized for $W > 1$ g/cm^2 [15]. Interestingly, the variation in the scatter plot between the MIR estimated W and the MAS near IR reflectance ratios definitely show a significant correlation.

The estimated and calculated emissivities for fresh water are compared at three frequencies and over four different measurements. Except for a single case at 220 GHz, the estimated and calculated values agree very well. The small differences in the comparison can be accounted for either by considering measurement errors or inadequacy of extrapolation of the dielectric permittivity model to high frequencies. Together, the comparisons with rawinsonde data, MAS reflectance ratios, and emissivity calculations substantiate the soundness of the present regression approach for W estimation from the four-channel MIR measurements.

The technique presented here is useful for areas with relatively dry atmosphere conditions such as the Arctic region and Antarctica. However, it cannot be applied to the currently available satellite data, which are limited to three channels at 150, 183.3 $\pm$ 3, and 183.3 $\pm$ 7 GHz. Using data from these three channels alone requires an assumption of the same emissivity across the frequency range of 150–183 GHz [10], which could result in a significant error in W estimation [11]. Perhaps an improved method to better characterize surface type and, therefore, approximate frequency dependence of surface emissivity can be devised to resolve this problem. This is a nontrivial problem that remains to be pursued in future studies.

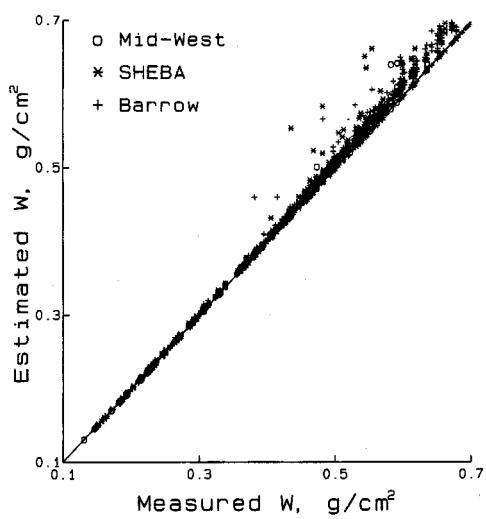

Fig. 1. Scatter plot of W values estimated from the simulated T_b(183.3 $\pm$ 3) and T_b(183.3 $\pm$ 7) and derived from the corresponding rawinsonde from Barrow, Alaska, SHEBA ship, and Mid-West. The surface emissivity is varied between 0.50–0.95 in 0.05 increments in the $T_b(\nu)$ calculations.

Autonomous Above-Water Radiance Measurements from an Offshore Platform: A Field Assessment Experiment

G. ZIBORDI

Space Applications Institute, Joint Research Centre of the European Union, Ispra, Italy

S. B. HOOKER

Laboratory for Hydrospheric Processes, NASA GSFC, Greenbelt, Maryland

J. F. BERTHON AND D. D'ALIMONTE

Space Applications Institute, Joint Research Centre of the European Union, Ispra, Italy

(Manuscript received 7 August 2000, in final form 5 June 2001)

ABSTRACT

An autonomous system for making above-water radiance measurements has been produced by adding a new measurement scenario to a CIMEL CE-318 sun photometer. The new system, called the Sea-viewing Wide Field-of-view Sensor (SeaWiFS) Photometer Revision for Incident Surface Measurement (SeaPRISM), combines the normal CE-318 capability for measuring direct sun irradiance and sky radiance, with a new capability for measuring above-water radiance for the retrieval of water-leaving radiance. The system has been extensively tested during several measurement periods over a 1-yr time frame from August 1999 to July 2000 under various sun elevations along with different atmospheric, seawater, and sea-state conditions. The field assessment of the new instrument was conducted at an oceanographic tower located in the northern Adriatic Sea within the framework of measurement campaigns aimed at supporting ocean color calibration and validation activities. Sample data at 440, 500, 670, 870, and 1020 nm were collected at azimuth and zenith angles satisfying the SeaWiFS Ocean Optics Protocols (and successive revisions) for above-water radiance measurements. Specifically, data were collected with azimuth angles of 90° with respect to the sun plane, and with nadir viewing angles of 30°, 40°, and 45° for above-water measurements and of 150°, 140°, and 135° for sky radiance measurements, respectively (the latter are needed for glint correction of the data). The intercomparison between water-leaving radiances computed from SeaPRISM measurements and those obtained from in-water optical profiles taken with the Wire-Stabilized Profiling Environmental Radiometer (WiSPER) system were performed using 113 coincident sets of measurements collected during clear-sky conditions. The SeaPRISM measurements taken at 40° and corrected for glint effects using different methods show the best agreement with WiSPER data. The intercomparisons exhibit average absolute unbiased percent differences, generally lower than 10% at 440 and 500 nm, and lower than 26% at 670 nm. The intercomparison of the water-leaving radiance ratio $L_w(440)/L_w(500)$ from SeaPRISM data taken at 40° and WiSPER data exhibits average absolute unbiased percent differences lower than 5.6%.

1. Introduction

Water-leaving radiance at wavelength λ in the visible and near-infrared parts of the solar spectrum, $L_w(\lambda)$, is the primary parameter for vicariously calibrating ocean color satellite sensors and for validating the algorithms used for estimating chlorophyll *a* concentration (Hooker and McClain 2000). Most spaceborne instruments, like the Sea-viewing Wide Field-of-view Sensor (SeaWiFS), ensure global products on a routine basis, so extensive spatial and temporal measurements of water-leaving radiance are required to satisfy the calibration and validation objectives (McClain et al. 1998).

Oceanographic cruises can ensure the collection of in-water optical profiles over large areas regardless of the water type, but they can only provide data in a restricted time frame (i.e., from days to weeks). Although shading from the deployment platform can be easily avoided through the use of free-falling profilers that can be floated away from the ship, platform stability is still required for solar reference measurements or for water-leaving radiance measurements through above-water methods. The latter feature is particularly important in the coastal environment, because small research vessels are frequently used for nearshore surveys.

In-water moored systems based on buoys, are an alternative platform when the collection of optical data at discrete depths with very good temporal resolution is needed (Clark et al. 1997). The use of moorings is best suited to clear-water regions, so biofouling effects on the submerged optical surfaces are minimized. The negative influence of waves and currents on the pointing stability of the sensors with respect to the vertical, and on the geometric alignment of the sensors with respect to the sun, must be quantified (i.e., the sensors need to be vertically oriented and outside the shadow of the buoy during data collection). Additional difficulty is the extrapolation of the subsurface upward radiance from discrete measurements taken at a few depths. This process can be significantly influenced by different seawater optical properties (e.g., caused by vertical stratification) within the depth intervals defined by the relative locations of each underwater sensor. Taken together, these elements make moored systems a difficult platform for calibration and validation activities in coastal waters, because the biofouling problem is severe, and the sea state and current structure is a strong function of daily and seasonal forcing.

5. Summary and conclusions

The intercomparison of SeaPRISM (above-water) and WiSPER (in-water) $L_w(\lambda)$ data, highlights the difficulty in minimizing glint effects in above-water radiance measurements collected during clear-sky conditions. The methods discussed in this study for the retrieval of $L_w(\lambda)$ from above-water measurements are based on the removal of sun- and sky-glint effects applying a theoretical sea surface reflectance factor $\rho(\theta)$ and three different processing schemes: (i) making use of time-averaged data (method $S95_a$); (ii) using the minimum value from a sequence of $L_T(\lambda, \theta, \phi)$ measurements as further minimization of sun-glint effects (method $S95_m$); and (iii) using time-averaged data and direct sun irradiance measurements to estimate sun-glint residuals (method S00). Recognizing that the small number of measurements collected during each SeaPRISM sea-viewing measurement sequence (three) reduces the statistical robustness of the $L_w(\lambda)$ estimates, the intercomparisons nevertheless demonstrate that with $\phi = \phi_0 + 90°$, the $S95_m$ method at $\theta = 40°$ for spectral averages give the best agreement with WiSPER data.

For the 113 matchups composing the assessment dataset, the $S95_m$ method exhibits $|\psi|$ values of 6.1%, 7.1%, and 20.5% at 440, 500, and 670 nm, respectively. The larger $|\psi|$ values at 670 nm, systematically observed for all the applied processing methods and at all values of θ, is justified by the large surface perturbations induced in the above-water measurement in the red part of the spectrum. It is important to remember the data were taken with different solar positions as well as different atmospheric and marine conditions over a 1-yr period—so the variance associated with seasonal forcing is present in the results—but all measurements were made during clear-sky conditions and for wind speed generally less than 5 m s^{-1}, that is, in near-ideal conditions. The latter would not be expected for fully operational measurements, and sampling issues raised by other investigators for above-water methods in the coastal environment (e.g., high wind speeds) would have to be considered (Toole et al. 2000).

The intercomparison of radiance ratios $L_w(440)/L_w(500)$ from SeaPRISM and WiSPER data have $|\psi|$ values ranging from 4.5% to 5.6% at $\theta = 40°$, with the best result derived from the $S95_a$ and S00 methods. The latter is an important accomplishment, in terms of using SeaPRISM for remote sensing calibration and validation activities, because it is close to the 5% SeaWiFS radiometric objectives. It is important to note the $S95_m$ method applied for radiance ratios is sufficiently close to the 5% level at $\theta = 40°$ that additional investigations into the sources of variances might render this method acceptable as well.

The analysis of the uncertainty budget (restricted to instrument overall intercalibration accuracy, tower- and self-shading, and environmental perturbations), shows a quadrature sum of the relative uncertainties generally within 4%–5% for both SeaPRISM and WiSPER radiances, with the exception of the SeaPRISM water-leaving radiance at 670 nm exceeding 12% (Table 4). The latter high value is again justified by the significant contribution of surface effects in the red part of the spectrum and is in agreement with the data shown in Table 2. This level of uncertainty accounts for approximately half of the spectral differences for the $S95_m$ method, and it is close to the band ratio differences. The former suggests some additional sources of uncertainty have not been well quantified (e.g., bidirectional effects in the spatial distribution of the in-water radiance field, differences in the above- and in-water tower perturbations, etc.), while the latter suggests that some uncertainties are cancelled or minimized by the band ratio calculation (Hooker et al. 2002).

Based on the results achieved with the SeaPRISM prototype system, the requirements for an operational, fully autonomous system can be considered:

1) a maximum number of channels, at the appropriate center wavelengths, for ocean color observations (IOCCG 1998) are needed;
2) programmable θ and ϕ angles to satisfy the testing or operational use of different measurement protocols;
3) the collection of a maximum number of sea-viewing values (per measurement sequence and per channel), to ensure statistical robustness for rejecting measurements contaminated by wave, cloud, and sun-glint effects and to maximize the signal-to-noise ratio;
4) characterization of the instrument offset during each measurement sequence; and
5) automatic data transmission through a satellite link.

There are a few restrictions with these recommendations if SeaPRISM instruments are to be used within the AERONET activity. First, AERONET requires at least six channels in keeping with WMO recommendations for aerosol and water vapor sun photometry (Frohlich and London 1986), so this leaves two channels for ocean color applications (in addition to the channels within the six for sun photometry that are useful for ocean color work). Given the present form of operational ocean color algorithms (O'Reilly et al. 1998), 443, 490, 510, and 555 nm are appropriate wavelengths to consider. Second, the amount of data that can be transmitted through the satellite link is limited, so to maximize the number of sea-viewing measurements (under most circumstances 11 should be possible), some of the data processing could be handled by the sun photometer control unit. Third, the SeaPRISM system does not include a capability for making $E_d(0^+, \lambda)$ measurements, which are needed for the computation of normalized water-leaving radiances (Gordon and Clark 1981). For the validation of satellite radiometric data and the vicarious calibration of space sensors; however, $L_w(\lambda)$ data collected at a time very close to the satellite overpass, may be used without any normalization. Different applications requiring normalized water-leaving radiances could use, during clear sky conditions, the aerosol optical thickness retrieved from the direct sun irradiance measurement and the aerosol scattering phase function derived from the sky radiance measurement as input for a theoretical computation of $E_d(0^+, \lambda)$.

MODELING AND REMOTE SENSING TECHNIQUES

The Laboratory is involved in a broad range of programs dealing with theoretical and experimental research in the oceanic, cryospheric, and hydrologic sciences. One of the Laboratory's primary missions is the development of remote sensing technologies for the purpose of modelling and retrieving the various spectral and physical properties, which define the elements of the hydrosphere. Twenty-nine papers were found to address these specific issues. The focus for these contributions is the development of remote sensing techniques for measuring quantities ranging from snow and ice sheet properties to various ocean and land surface properties. Broad categories for these research papers can be established as follows: (1) sea ice studies (2) snow and ice-sheet studies, (3) ocean surface properties, (4) land surface hydrology studies, and (5) surface topography and altimetry studies.

(1) Sea ice studies. This collection of studies included such diverse topics as estimating rainfall (Meneghini et al.; Chang et al), atmospheric moisture in its various physical states (Olson et al.; Whiteman et al., atmospheric heat profiles (Tao et al.), and a review paper by Chang which covered a variety of atmospheric parameters.

(2) Snow and ice-sheet studies. Research in this subject area included papers on snow cover extent and mapping and (Hall et al.), ice-sheet studies (Bardel et al.), and snow physics (Wergin et al.).

(3) Ocean surface properties. By far the largest category, these studies covered subjects such as sea ice monitoring (Markus et al.; Markus and Dokken; Zhao et al.), general ocean circulation (Keppenne and Rienecker; Hakkinen and Mo; Gregg), coastal zone studies (Renfrew and King; Dokken et al.) and ocean surface studies (Hoge and Lyon; Gregg et al.; Moisan et al.; Campbell et al.; Liu et al.; Wang et al.).

(4) Land surface hydrology studies. These studies reported on a variety of research aspects, including soil moisture studies (Chen et al.; Jackson et al.; Owe) data assimilation (Reichle et al.) atmospheric correction (Skofronick-Jackson), and general hydrology (Houser; Bradley et al.).

(5) Surface topography and altimetry studies. Research in these areas covered studies of sea surface altimetry studies (Vandemark et al.; Gourrion et al.) and coastal topography studies (Brock et al.).

Annals of Glaciology 34 2002
© International Glaciological Society

Synthetic aperture radar detection of the snowline on Commonwealth and Howard Glaciers, Taylor Valley, Antarctica

PATRICK BARDEL,[1] ANDREW G. FOUNTAIN,[1] DOROTHY K. HALL,[2] RON KWOK[3]
[1]*Departments of Geography and Geology, Portland State University, Portland, OR 97207, U.S.A.*
[2]*Hydrological Sciences Branch, NASA Goddard Space Flight Center, Code 974, Greenbelt, MD 20771, U.S.A.*
[3]*Jet Propulsion Laboratory, California Institute of Technology, 4800 Oak Grove Drive, Pasadena, CA 91109-8099, U.S.A.*

ABSTRACT. Synthetic aperture radar (SAR) images of Taylor Valley, Antarctica, were acquired in January 1999 in coordination with ground-based measurements to assess SAR detection of the snowline on dry polar glaciers. We expected significant penetration of the radar wave resulting in an offset of the SAR-detected snowline relative to the true snowline. Results indicated no detectable displacement of the SAR snowline. Snow depths of 15 cm over ice can be detected on the imagery. We hypothesize that the optical depth of thin snowpacks is enhanced by reflection and refraction of the radar beam by internal snow layers. The enhanced optical depth increases the volume scattering, and thereby enhances backscatter sufficiently to be detected by the SAR. Consequently, SAR imagery may be used directly to image the position of transient snowlines in dry polar regions.

INTRODUCTION

Assessing glacier change in the polar regions, particularly in the Antarctic, has been difficult because of the distance and expense involved in conducting the fieldwork. Fieldwork also limits the spatial scope of the measurements due to the logistics of surface movement. Monitoring glaciers in the polar regions is an important component of studying the effects of climatic change because the rate and magnitude of change are expected to be greatest in those regions (Serreze and others, 2000). To monitor glacial change efficiently over broad regions requires the use of remote-observation methods. Currently, remote monitoring includes airborne laser altimetry of alpine glacier altitude (Echelmeyer and others, 1997), and satellite remote sensing (Advanced Very High Resolution Radiometer and Landsat) of ice-shelf extent (Scambos and others, 1998). An important glacial feature that can be tracked on dry polar glaciers is the position of the equilibrium line.

The equilibrium line separates the zone of net mass accumulation from the zone of net mass loss (ablation) at the end of the melt season. The equilibrium-line altitude (ELA) relative to the distribution of glacier area with altitude is an important characteristic for determining the state of the glacier's mass balance (Paterson, 1994). This presumes that the gradient of mass balance with altitude is relatively constant from year to year, but the intercept is shifted. Unlike glacier-length (terminus-position) changes, the ELA is entirely controlled by climatic processes and is not influenced by the behavior of glacier flow. In contrast to temperate or subpolar glaciers, the ELA on polar glaciers is the same as the snowline because there is no melting. One of the most attractive techniques for tracking the ELA on polar glaciers is satellite synthetic aperture radar (SAR) since it covers broad areas, it images through clouds, and it is self-illuminating. These attributes are particularly useful for the cloudy coastal conditions and long polar nights common to polar marine environments. For dry-snow conditions, typical of polar glaciers, however, the SAR beam penetrates snow (Ulaby and others, 1981, 1982, 1986; Jezek and others, 1993; Lucchitta and others, 1995) and would displace the location of the ELA up-glacier. Maximum penetration in homogeneous snow is estimated to be about 20 m (Ulaby and others, 1981, 1982, 1986; Rott and Mätzler, 1987). This effect should be quite pronounced for thin snow accumulations on low-sloping surfaces, characteristics common to polar glaciers. For example, with a small mass-balance gradient with altitude, typical of polar glaciers, we would expect roughly a 2 km shift in the apparent snowline for a glacier with a 5° slope. The purpose of our study was to examine the extent of ELA displacement on a polar glacier and determine a correction for the SAR-estimated ELA.

STUDY SITE

We examined two glaciers in Taylor Valley, one of the McMurdo Dry Valleys in Antarctica (Fig. 1). This area was chosen because of ongoing glaciological investigations in the valleys on four glaciers that include measurements of mass balance, energy balances, ice velocity and ice depth. Mean annual temperature in Taylor Valley is −17°C (Clow and others, 1988), and summer temperatures have not often exceeded freezing since 1993 (unpublished information from P.T. Doran). The glaciers show little or no evidence of melt except in the lowermost fringe near the glacier terminus and along the cliff face, which forms the terminus (Lewis and others, 1995; Fountain and others, 1998). Most of the mass loss is from sublimation, which during the summer represents 40–90% of the ablation (Lewis and others, 1995).

The two glaciers we studied were Commonwealth and Howard Glaciers. In this paper we examine Commonwealth Glacier in detail, and briefly mention the results from Howard Glacier in the discussion section. Commonwealth Glacier (Fig. 2) faces south-southeast with a gentle (5°) slope.

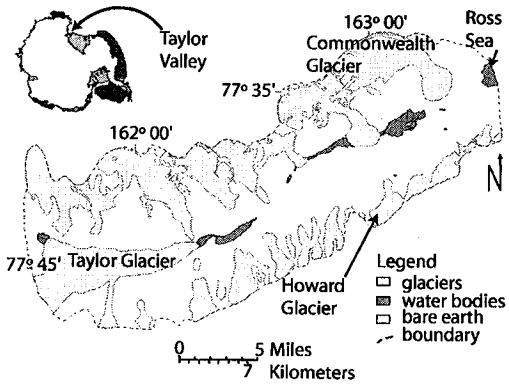

Fig. 1. Taylor Valley.

The glacier is about 2 km wide across the ELA at 350 m, with a relatively constant slope and even surface. The snow cover in the ablation zone ranges from traces to patchy, dune-like formations 4–35 cm high and covering areas of 1–20 m^2. In the accumulation zone, dry snow exists on the surface, with thin (cm or less) ice layers and hoar crystals at depth.

Methods

Mass-balance measurements are collected over the entire surface with a network of 21 stakes on Commonwealth Glacier as part of the ongoing monitoring. The stakes are typically measured twice annually, once in the spring (October–November) and once in the autumn (mid- to late January). The measurements include surface height, and snow depth if the snow covers the ice of the ablation zone. Whenever snow is present, a snow pit is dug at every stake and the snow stratigraphy is measured, including layer thickness, density and crystal shape. To supplement these measurements with precisely located measurements relative to the SAR image, we set up a transect on Commonwealth Glacier from the ablation zone, across the snowline and into the accumulation zone.

CONCLUSIONS

Glacier surfaces in Taylor Valley are generally radiometrically smooth and appear dark in the SAR image over most of the ablation zone. The snow zone images brighter because of the volume reflection from the entire depth of snow penetrated by the SAR beam. Because of the known penetration characteristics of SAR in dry snow, we expected a displacement of the SAR-inferred snowline. In contrast, the SAR-inferred and actual snowlines were very close to each other. We believe that this correspondence is due to enhanced volume reflection and can reveal the presence of snow depths of only 15 cm. Enhanced volume reflection results from layers of different densities acting as specular reflective surfaces (Ulaby and others, 1981, 1982, 1986; Mätzler and Schanda, 1984; Tsang and others, 1986). Reflection off internal layers increases the path length the beam travels (Ulaby and others, 1981, 1982, 1986), creates more opportunity to scatter in the snow and increases total reflection. Therefore thin, dry snowpacks with no internal layers will not be visible in SAR imagery.

The largest difference of backscatter between polarizations occurred in the ablation zone and reduced in the accumulation zone. On the ice surface of the ablation zone, VV polarization backscatters more than the HH polarization. In deep snow, HH backscatter increases relative to VV, and the difference in backscatter is reduced.

The corner reflectors worked very well, precisely locating the transect, adding scale and two known points to the SAR image. The reflectors were placed on smooth glacial ice, and the contrast between the dark backscatter of the ice and the brilliant reflection of the reflectors left no doubt of their locations on the image.

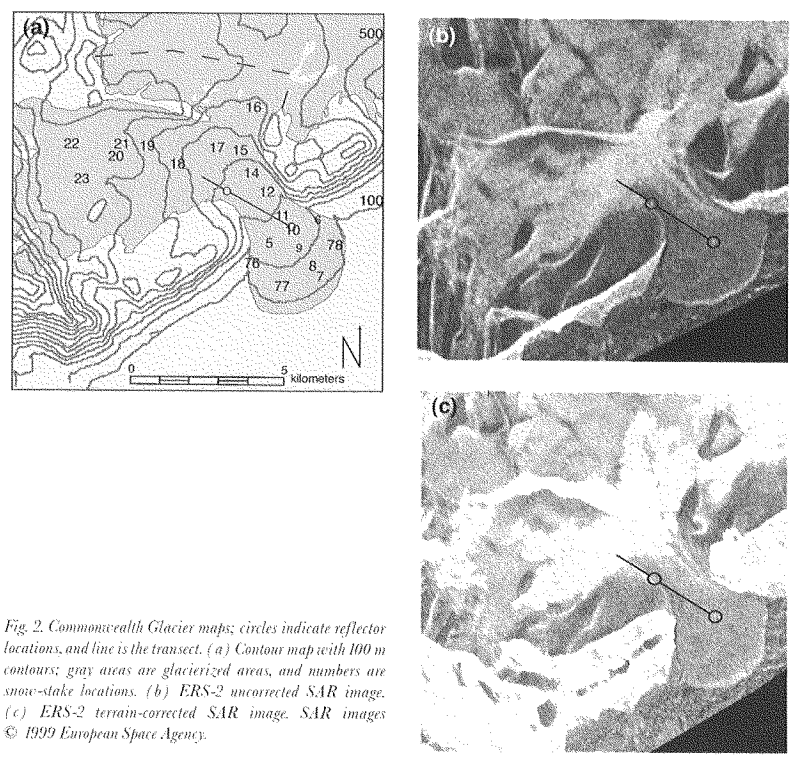

Fig. 2. Commonwealth Glacier maps; circles indicate reflector locations, and line is the transect. (a) Contour map with 100 m contours; gray areas are glacierized areas, and numbers are snow-stake locations. (b) ERS-2 uncorrected SAR image. (c) ERS-2 terrain-corrected SAR image. SAR images © 1999 European Space Agency.

JOURNAL OF THE AMERICAN WATER RESOURCES ASSOCIATION
VOL. 38, NO. 5 AMERICAN WATER RESOURCES ASSOCIATION OCTOBER 2002

RAINGAGE NETWORK DESIGN USING NEXRAD PRECIPITATION ESTIMATES[1]

A. Allen Bradley, Christa Peters-Lidard, Brian R. Nelson, James A. Smith, and C. Bryan Young[2]

ABSTRACT: A general framework is proposed for using precipitation estimates from NEXRAD weather radars in raingage network design. NEXRAD precipitation products are used to represent space time rainfall fields, which can be sampled by hypothetical raingage networks. A stochastic model is used to simulate gage observations based on the areal average precipitation for radar grid cells. The stochastic model accounts for subgrid variability of precipitation within the cell and gage measurement errors. The approach is ideally suited to raingage network design in regions with strong climatic variations in rainfall where conventional methods are sometimes lacking. A case study example involving the estimation of areal average precipitation for catchments in the Catskill Mountains illustrates the approach. The case study shows how the simulation approach can be used to quantify the effects of gage density, basin size, spatial variation of precipitation, and gage measurement error, on network estimates of areal average precipitation. Although the quality of NEXRAD precipitation products imposes limitations on their use in network design, weather radars can provide valuable information for empirical assessment of raingage network estimation errors. Still, the biggest challenge in quantifying estimation errors is understanding subgrid spatial variability. The results from the case study show that the spatial correlation of precipitation at subgrid scales (4 km and less) is difficult to quantify, especially for short sampling durations. Network estimation errors for hourly precipitation are extremely sensitive to the uncertainty in subgrid spatial variability, although for storm total accumulation, they are much less sensitive.
(KEY TERMS: network design; hydrologic sampling; precipitation measurement; NEXRAD; Catskill Mountains.)

INTRODUCTION

Raingage network design is a problem that has received considerable attention in the hydrologic literature (for a review see Bras and Rodríguez-Iturbe, 1985). An objective of raingage network design is to determine the effects of raingage sampling (both the number of gages and their locations) on the estimation uncertainty of precipitation variables or hydrologic variables computed from precipitation estimates (Bras *et al.*, 1988). This is done using either theoretical models of the rainfall process (Rodríguez-Iturbe and Mejía, 1974a; Peters-Lidard and Wood, 1994) or high resolution rainfall data from dense networks or weather radars (Huff, 1970; Seed and Austin, 1990; Fontaine, 1991).

The use of theoretical models of the rainfall process has certain advantages in raingage network design. For example, Rodríguez-Iturbe and Mejía (1974a) applied an analytical model of rainfall to derive precipitation estimation variance as a function of gage density, area of interest, correlation length scale of the rainfall process, and variance of the rainfall process. Their work considers both long-term and storm event rainfall as well as stratified (uniform) and random sampling designs. Peters-Lidard and Wood (1994) extended this approach to include events with anisotropic, time-dependent correlation structures and hierarchical clustering behavior, using a space-time stochastic model of rainfall. The use of a stochastic rainfall model in this case allowed the investigation of raingage sampling at small space (e.g., a few km) and time (e.g., minutes) scales associated with data collection for hydrologic field experiments.

Still, a limitation of using theoretical rainfall models is that space-time patterns of storm precipitation, including the initiation, growth, and dissipation of storms, are very difficult to represent with stochastic models. Usually these models assume that the statistical characteristics of precipitation do not vary in space (i.e., a stationary random field). However, cli-

[1]Paper No. 99151 of the *Journal of the American Water Resources Association*. **Discussions are open until April 1, 2003.**
[2]Respectively, Iowa Institute of Hydraulic Research and Department of Civil and Environmental Engineering, University of Iowa, Iowa City, Iowa 52242; Hydrological Sciences Branch, NASA-GSFC Code 974, Greenbelt, Maryland 20771; Iowa Institute of Hydraulic Research and Department of Civil and Environmental Engineering, University of Iowa, Iowa City, Iowa 52242; Department of Civil and Environmental Engineering, Princeton University, Princeton, New Jersey 08544; and Department of Civil and Environmental Engineering, Learned Hall, University of Kansas, Lawrence, Kansas 66045 (E-Mail/Bradley: allen-bradley@uiowa.edu).

matological variations are usually evident across large regions for precipitation sampled at both short and long time scales. For example, in regions with complex mountainous terrain, orography is known to affect precipitation formation and accumulation patterns.

The use of high resolution rainfall data in raingage network design attempts to mimic space-time patterns of observed precipitation (Huff, 1970). Of course, the data based approach is restricted to locations where high resolution data are available. With the recent deployment of the NEXRAD network of WSR-88D (Weather Surveillance Radar – 1988 Doppler) weather radars (Klazura and Imy, 1993), high resolution data are now being collected across the United States. Although there are known problems associated with NEXRAD radar rainfall estimates (Smith *et al.*, 1996a; Young *et al.*, 1999, 2000), NEXRAD observations still provide very good qualitative information on space-time patterns of precipitation that can be utilized in water resources applications.

In this paper we propose a general approach for use of NEXRAD radar rainfall data in raingage network design. The approach is similar to that of Seed and Austin (1990), which used radar data in Florida and South Africa to examine precipitation errors for gage sampling with hypothetical stratified and random networks. Specifically, radar rainfall data are used to represent the "true" rainfall fields for the region. However, the proposed approach differs in that the mismatch between the point precipitation (measured at a gage) and true areal average precipitation (for each radar grid cell) is considered using a theoretical model to represent the subgrid spatial variability of precipitation and gage measurement errors. As will be seen, the effect of subgrid spatial variability is very important for short sampling durations.

In the following sections, the proposed framework is presented using a case study for a mountainous region in New York. This case study for a region with complex terrain is a challenging application of the approach and demonstrates many issues that need to be considered in raingage network design using NEXRAD precipitation estimates.

SUMMARY AND CONCLUSION

This paper describes a general framework for using NEXRAD precipitation estimates for raingage network design. The approach is illustrated through a case study conducted for six catchments in the Catskill Mountains. Network design experiments quantified the estimation errors in areal average precipitation for the catchments for random gage network alternatives. The mismatch between point (gage) measurement and the areal average precipitation for each radar grid cell was simulated using a model that accounts for spatial variability of precipitation within the grid cell and gage measurement errors.

The case study for the Catskill region shows how the simulation approach can be used to quantify the effects of gage density, basin size, spatial variation of precipitation, and gage measurement error on network estimates of areal average precipitation. Subgrid spatial variability was found to be the most critical factor in error estimation for hourly precipitation. Average errors differed by a 100 percent or more for assumed correlation function models representing low and high subgrid variability. However, for storm total accumulation, average errors differed by around 10 to 25 percent for low and high subgrid variability cases. The high sensitivity for hourly precipitation occurs because (1) the correlation of precipitation in space is much lower, and (2) the shape of the correlation function is more difficult to estimate with available gage observations. A better understanding of small-scale spatial variability of precipitation is needed to improve quantitative estimates of network errors for short sampling durations.

The case study for the Catskill region also demonstrates the challenges in using NEXRAD precipitation estimates in a region with complex mountainous terrain. NEXRAD precipitation estimates suffered from problems due to beam blockage, ground returns, and systematic underestimation. Despite these problems, NEXRAD observations still contain valuable information on space-time patterns of storm rainfall over the region. However, to select the best storms for use in network design, we needed to focus on heavier rainfall events, carefully screen the NEXRAD data, merge estimates from multiple radars, and correct for biases with gage data. Similar efforts may be required in other regions to deal with inherent problems with NEXRAD precipitation estimates.

With conventional approaches to raingage network design, stochastic modeling is often used to simulate space-time patterns for a region. Often these models assume that precipitation fields are stationary, which severely limits their utility in large regions with complex terrain. An advantage of the proposed approach is that it uses the high resolution NEXRAD precipitation estimates to characterize space-time variations over large regions. Stochastic models of the rainfall process are applied only to simulate the mismatch between point and areal precipitation at small-scales (the size of a single radar grid cell). At this scale, the simplifying assumptions needed to model the rainfall process can still be justified. Hence, the proposed approach is ideally suited to applications in regions where significant climatic variations exists.

Journal of Coastal Research	18	1	1–13	West Palm Beach, Florida	Winter 2002

Basis and Methods of NASA Airborne Topographic Mapper Lidar Surveys for Coastal Studies

John C. Brock†, C. Wayne Wright‡, Asbury H. Sallenger§, William B. Krabill*, and Robert N. Swift††

†USGS Center for Coastal and Regional Marine Studies
600 4th Street South
St. Petersburg, FL, 33701, USA
jbrock@usgs.gov,

‡NASA Goddard Space Flight Center
Wallops Flight Facility
Wallops Island, VA 23337, USA
wright@osb.wff.nasa.gov

§USGS Center for Coastal and Regional Marine Studies
600 4th Street South
St. Petersburg, FL 33701, USA
asallenger@usgs.gov

*NASA Goddard Space Flight Center
Wallops Flight Facility
Wallops Island, VA 23337, USA
krabill@osb1.wff.nasa.gov

††EG&G, NASA Goddard Space Flight Center
Wallops Flight Facility
Wallops Island, VA 23337, USA
swift@ao15.wff.nasa.gov

ABSTRACT

BROCK, J.C.; WRIGHT, C.W.; SALLENGER, A.H.; KRABILL, W.B., and SWIFT, R.N., 2002. Basis and methods of NASA airborne topographic mapper lidar surveys for coastal studies. *Journal of Coastal Research,* 18(1), 1–13. West Palm Beach (Florida), ISSN 0749-0208.

This paper provides an overview of the basic principles of airborne laser altimetry for surveys of coastal topography, and describes the methods used in the acquisition and processing of NASA Airborne Topographic Mapper (ATM) surveys that cover much of the conterminous US coastline. This form of remote sensing, also known as "topographic lidar", has undergone extremely rapid development during the last two decades, and has the potential to contribute within a wide range of coastal scientific investigations. Various airborne laser surveying (ALS) applications that are relevant to coastal studies are being pursued by researchers in a range of Earth science disciplines. Examples include the mapping of "bald earth" land surfaces below even moderately dense vegetation in studies of geologic framework and hydrology, and determination of the vegetation canopy structure, a key variable in mapping wildlife habitats. ALS has also proven to be an excellent method for the regional mapping of geomorphic change along barrier island beaches and other sandy coasts due to storms or long-term sedimentary processes. Coastal scientists are adopting ALS as a basic method in the study of an array of additional coastal topics. ALS can provide useful information in the analysis of shoreline change, the prediction and assessment of landslides along seacliffs and headlands, examination of subsidence causing coastal land loss, and in predicting storm surge and tsunami inundation.

ADDITIONAL INDEX WORDS: *Shoreline change, airborne laser altimetry, LaserMap.*

INTRODUCTION

During the last decade, several complementary airborne remote sensing methods have matured, resulting in significant new capabilities that are enabling advances in coastal research. Topographic information, essential for regional and local geomorphologic studies, and useful in investigations of sedimentary processes, hydrology, pedogenesis, and wildlife habitats, can now be rapidly and accurately acquired at various spatial scales by airborne laser surveying (ALS) (ACKERMANN, 1999; BUFTON, 1989). Airborne laser surveying, or "topographic lidar", is a type of remote sensing generally known as "Light Detection and Ranging" (lidar) that has undergone very rapid development during the last two decades (GARVIN, 1993; FLOOD and GUTELIUS, 1997). Airborne laser surveying herein refers to airborne topographic lidar, exclusive of other lidar methods. Numerous recent studies have demonstrated that current ALS systems have the potential to contribute within a wide range of coastal scientific investigations (CARTER and SHRESTHA, 1997; FLOOD *et al.,* 1997; GUTIERREZ *et al.,* 1998; HUISING and VAESSEN, 1997; KRABILL and SWIFT, 1982; KRABILL *et al.,* 2000; SALLENGER *et al.,* 1999a; SHRESTHA and CARTER, 1998).

00027 received 5 June 2000; accepted in revision 8 June 2001.

The advent of laser scanning as a new method for the direct, high density measurement of decimeter accuracy elevation from aircraft has been enabled by the parallel development of several incorporated techniques. Kinematic differential Global Positioning System (GPS) methods now enable the positioning of light aircraft to within several centimeters (KRABILL and MARTIN, 1987). Inertial Navigation Systems (INS) or Inertial Measuring Units (IMU) can now provide three-dimensional aircraft orientation at 64-Hz within 0.1 degree, rendering aerotriangulation based on ground data points obsolete (DELOACH, 1998). Modern lightweight laser pulse transmitters can be operated at extremely high repetition rates ranging to greater than 20,000 pulses per second, and can provide ranges from a nominal 1000 m altitude with an accuracy of 1 cm or better (BUFTON, 1989).

Combined within contemporary airborne laser mapping systems, these newly emerged technologies now enable low cost geomorphic surveys at decimeter vertical accuracy and at spatial densities greater than 1 elevation measurement per square meter. Multiple-reflection ALS is uniquely well suited to the mapping of land surfaces below even moderately dense vegetation. This technique enables the creation of "bald earth" digital elevation models in forested areas for application in investigations of geologic structure and hydrology

(KRABILL *et al.*, 1984; KRAUS and PFEIFER, 1998; LOHR, 1997; RITCHIE, 1995). In addition to sub-canopy topography, topographic lidars that capture the entire time-amplitude history of the return pulse can acquire the height and vertical structure of vegetation (BLAIR *et al.*, 1999). Unlike microwave or passive optical sensors, topographic lidars that capture the full reflected pulse can provide volumetric representations of canopy structure (BLAIR *et al.*, 1994; HARDING *et al.*, 1994; LEFSKY *et al.*, 1999).

As much recent work has demonstrated, ALS is an excellent means of mapping change along barrier island beaches and other sandy coasts (CARTER and SHRESTHA, 1997; FLOOD *et al.*, 1997; GUTIERREZ *et al.*, 1998; HUISING and VAESSEN, 1997; KRABILL and SWIFT, 1982; KRABILL *et al.*, 2000; SALLENGER *et al.*, 1999a; SALLENGER *et al.*, 1999b; SALLENGER *et al.*, 1999c; SHRESTHA and CARTER, 1998). The ability of ALS to rapidly survey long, narrow strips of terrain is very valuable in this application, as beaches are very elongate, highly dynamic sedimentary environments that undergo seasonal and long-term erosion or accretion, and are also impacted by severe storms (SALLENGER *et al.*, 1999b). Closely related applications are airborne laser mapping of flood-prone coastal fluvial zones, and the use of laser bathymeters to survey benthic change driven by hurricanes (PEREIRA and WICHERSON, 1999). Wave effects on nearshore circulation, sediment transport, and littoral zone topography may be investigated through ALS observations of sea state and surface wave displacement over continental shelves (HWANG *et al.*, 1998; TSAI and GARDNER, 1982).

OBJECTIVES

The goal of this paper is to provide an overview of the methods applied within the NASA/USGS/NOAA U.S. "lower 48" coastal mapping project (SALLENGER *et al.*, 1999b) for airborne laser surveys of coastal geomorphology. The specific objectives of this paper are:

(1) to provide the basic principles that govern the acquisition of laser ranging observations for surveys of coastal topography, and
(2) to describe the topographic lidar surveying and processing methods in use by a NASA/USGS/NOAA project that has mapped most of the conterminous US coastline.

Basis of Lidar Remote Sensing

The acronym "laser" stands for "*l*ight *a*mplification by *s*timulated *e*mission of *r*adiation" and refers to devices that rely on stimulated emission to generate narrow spectral band radiation, in contrast to conventional broad spectral band spontaneous emission of radiation governed by Planck's Law. The invention of laser transmitters capable of compressing laser energy into very short, high power density single pulses enabled range-resolved measurements (MCCLUNG and HELLWARTH, 1962), analogous to microwave *radar* ranging. By timing the two-way travel time of a laser pulse reflected off a remote target, the range to the reflector can be directly determined through division by the speed of light. The acronym "lidar" (light detection and ranging), generally refers to any remote sensing system that emits laser light and detects,

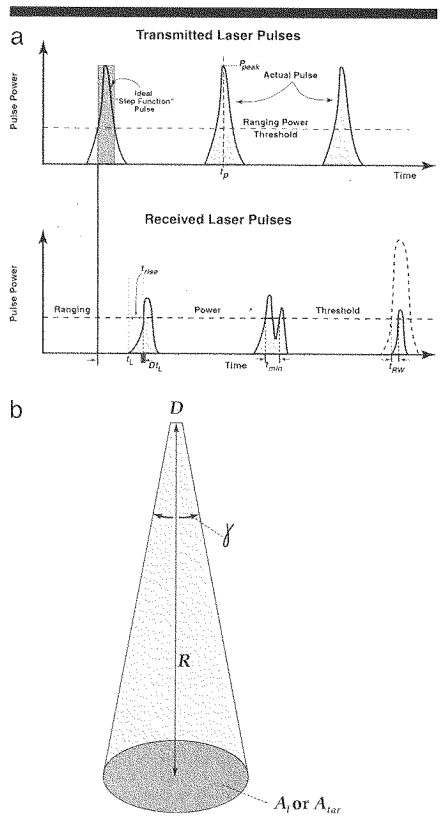

Figure 1a. Relationships between transmitted and received laser pulses (adapted from Wehr and Lohr, 1999).

Figure 1b. Geometry of a single laser shot.

ranges, or identifies remote objects based on the time-resolved sensing of light reflected or emitted through subsequent fluorescence from that object (MEASURES, 1984). By definition, lidar is a type of active remote sensing, because it incorporates an energy source to illuminate objects. Therefore, lidar differs fundamentally from passive remote sensing methods, such as multi-spectral scanning or aerial photography that rely upon reflected sunlight.

SUMMARY

Based on its capacity for carefully-timed high resolution regional surveys keyed to natural processes, ALS is becoming a fundamental tool for coastal scientists within coastal studies. This paper provides a set of basic equations that describe laser ranging, and its implementation within the airborne laser scanning of topography. A description of the processing steps used by NASA and the USGS to extract scientifically useful information from the vast number of observations that are obtained through NASA ATM surveys is provided. The multi-tiered lidar processing approach outlined here supports the geometric, reference system, and file structure transformations that are required for most coastal applications of ALS. This approach is being incorporated in a software package called LaserMap that creates lidar data products that may be directly inserted into a Geographic Information System, or used within specialized analysis programs designed to extract landscape information for coastal studies.

Comparison of algorithms for estimating ocean primary production from surface chlorophyll, temperature, and irradiance

Janet Campbell,[1] David Antoine,[2] Robert Armstrong,[3] Kevin Arrigo,[4] William Balch,[5] Richard Barber,[6] Michael Behrenfeld,[7] Robert Bidigare,[8] James Bishop,[9] Mary-Elena Carr,[10] Wayne Esaias,[7] Paul Falkowski,[11] Nicolas Hoepffner,[12] Richard Iverson,[13] Dale Kiefer,[14] Steven Lohrenz,[15] John Marra,[16] Andre Morel,[2] John Ryan,[17] Vladimir Vedernikov,[18] Kirk Waters,[19] Charles Yentsch,[5] and James Yoder[20]

Received 21 May 2001; revised 8 March 2002; accepted 8 March 2002; published 17 July 2002.

[1] Results of a single-blind round-robin comparison of satellite primary productivity algorithms are presented. The goal of the round-robin exercise was to determine the accuracy of the algorithms in predicting depth-integrated primary production from information amenable to remote sensing. Twelve algorithms, developed by 10 teams, were evaluated by comparing their ability to estimate depth-integrated daily production (IP, mg C m^{-2}) at 89 stations in geographically diverse provinces. Algorithms were furnished information about the surface chlorophyll concentration, temperature, photosynthetic available radiation, latitude, longitude, and day of the year. Algorithm results were then compared with IP estimates derived from ^{14}C uptake measurements at the same stations. Estimates from the best-performing algorithms were generally within a factor of 2 of the ^{14}C-derived estimates. Many algorithms had systematic biases that can possibly be eliminated by reparameterizing underlying relationships. The performance of the algorithms and degree of correlation with each other were independent of the algorithms' complexity. *INDEX TERMS:* 4894 Oceanography: Biological and Chemical: Instruments and techniques; 4275 Oceanography: General: Remote sensing and electromagnetic processes (0689); 4805 Oceanography: Biological and Chemical: Biogeochemical cycles (1615); 4806 Oceanography: Biological and Chemical: Carbon cycling; 4853 Oceanography: Biological and Chemical: Photosynthesis; *KEYWORDS:* primary productivity, algorithms, ocean color, remote sensing, satellite, chlorophyll

1. Introduction

[2] Global maps of the upper-ocean chlorophyll concentration are now being generated routinely by satellite ocean color sensors. These multispectral sensors are able to map the chlorophyll concentration, a measure of phytoplankton biomass, by detecting spectral shifts in upwelling radiance. As the chlorophyll concentration increases, blue light is increasingly absorbed, and thus less is scattered back into space. Although global coverage can nominally be achieved every 1–2 days, the actual temporal resolution is reduced to ~5–10 days because of cloud cover. Nevertheless, the coverage afforded by satellite remote sensing is vastly greater than that obtainable by any other means.

Table 1. Algorithm Testing Subcommittee of NASA's Ocean Primary Productivity Working Group[a]

Participant	Affiliation
Robert Armstrong	Stony Brook University
Richard T. Barber	Duke University
James Bishop	Lawrence Berkeley National Laboratory
Janet W. Campbell	University of New Hampshire
Mary-Elena Carr	Jet Propulsion Laboratory
Wayne E. Esaias	NASA Goddard Space Flight Center
Richard Iverson	Florida State University
Charles S. Yentsch	Bigelow Laboratory for Ocean Sciences

[a] These individuals were responsible for conducting the primary productivity algorithm round-robin experiment. They agreed not to participate by testing algorithms of their own.

[3] A principal use of the global ocean chlorophyll data is to estimate oceanic primary production [*Behrenfeld et al.*, 2001]. The mathematical models or procedures for estimating primary production from satellite data are known as primary productivity algorithms. In the early days of the Coastal Zone Color Scanner (CZCS), simple statistical relationships were proposed for calculating primary production from the surface chlorophyll concentration [e.g., *Smith and Baker*, 1978; *Eppley et al.*, 1985]. Such empirically derived algorithms are still considered useful when applied to annually averaged data [*Iverson et al.*, 2000], but they are not sufficiently accurate to estimate production at seasonal timescales. The surface chlorophyll concentration explains only ~30% of the variance in primary production at the scale of a single station [*Balch et al.*, 1992; *Campbell and O'Reilly*, 1988].

[4] Over the past 2 decades, scientists have sought to improve algorithms by combining the satellite-derived chlorophyll data with other remotely sensed fields, such as sea surface temperature (SST) and photosynthetic available radiation (PAR). These algorithms incorporate models

of the photosynthetic response of phytoplankton to light, temperature, and other environmental variables, and some also incorporate models of the vertical distribution of these properties within the euphotic zone [*Balch et al.*, 1989; *Morel*, 1991; *Platt and Sathyendranath*, 1993; *Howard*, 1995; *Antoine and Morel*, 1996a; *Behrenfeld and Falkowski*, 1997a; *Ondrusek et al.*, 2001]. Algorithms have been used to estimate global oceanic primary production from CZCS data [*Antoine and Morel*, 1996b; *Longhurst et al.*, 1995; *Behrenfeld and Falkowski*, 1997a; *Howard and Yoder*, 1997], and more recently from Sea-viewing Wide Field-of-view Sensor (SeaWiFS) data [*Behrenfeld et al.*, 2001]. Global maps of the average daily primary production for varying periods (weeks, months, and years) are now being produced from Moderate Resolution Imaging Spectroradiometer (MODIS) data.

[5] While many of the photosynthetic responses (to light, temperature, etc.) are commonly represented, model-based algorithms differ with respect to structure and computational complexity [*Behrenfeld and Falkowski*, 1997b]. Models may be similar in structure but require different parameters depending on whether they describe daily, hourly, or instantaneous production, and even where these aspects are similar, algorithms often yield different results because of differences in their parameterization. *Balch et al.* [1992] evaluated a variety of algorithms (both empirical and model based), using in situ productivity measurements from a large globally distributed data set, and found that they generally accounted for <50% of the variance in primary production.

[6] In January 1994 the National Aeronautics and Space Administration (NASA) convened an Ocean Primary Productivity Working Group with the goal of developing one or more "consensus" algorithms to be applied to satellite ocean color data. The working group initiated a series of round-robin experiments to evaluate and compare primary productivity algorithms. The approach was to use in situ data to test the ability of algorithms to predict depth-integrated daily production (IP, mg C m^{-2}) based on information amenable to remote sensing. It was decided to compare algorithm performances with one another and with estimates based on ^{14}C incubations.

[7] Our understanding of primary productivity in the ocean is largely based on the assimilation of inorganic carbon from ^{14}C techniques [*Longhurst et al.*, 1995], and thus it was considered appropriate to compare the algorithm estimates with ^{14}C-based estimates. However, it was recognized that the ^{14}C-based estimates are themselves subject to error [*Peterson*, 1980; *Fitzwater et al.*, 1982; *Richardson*, 1991]. The ^{14}C incubation technique measures photosynthetic carbon fixation within a confined volume of seawater, and there are no methods for absolute calibration of bottle incubations [*Balch*, 1997]. Furthermore, there is no universally accepted method for measuring and verifying vertically integrated production derived from discrete bottle measurements. Despite this fact, here we treat the ^{14}C-based estimates as "truth" and refer to the differences between algorithm-derived and ^{14}C-derived estimates as "errors." In all statistical analyses, however, the two are recognized as being subject to error.

[8] Participation in the round robin was solicited through a widely distributed "Dear Colleague" letter. A central ground rule was that the algorithms tested would be identified only by code numbers. The first round-robin experiment involved data from only 25 stations and was thus limited in scope. It was decided that a more comprehensive second round was needed. In this paper, we present results of the second round-robin experiment involving data from 89 stations with wide geographic coverage. Round two was open to all participants of round one, as well as to others who had responded positively to the initial invitation.

6. Conclusions

[45] Conclusions related to the four questions addresseed by this study are summarized as follows:

[46] 1. How do algorithm estimates of primary production derived strictly from surface information compare with estimates derived from ^{14}C incubation methods? The 12 algorithms tested varied widely in performance. The best-performing algorithms agreed with the ^{14}C-based estimates within a factor of 2. Two of these algorithms have been adapted by NASA for producing primary productivity maps with MODIS data. Most of the algorithms had significant biases causing them to differ systematically from the in situ data. A concerted effort should be made to understand the cause of the biases and to eliminate them if possible.

[47] 2. How does the error in satellite-derived chlorophyll concentration affect the accuracy of the primary productivity algorithms? The relative errors in primary productivity (Δ_{sat}) resulting from the simulated errors in surface chlorophyll concentration (Δ_B) were highly correlated with Δ_B. This fact reflects the deterministic relationship between production and chlorophyll in the underlying models. The slopes of the regressions (Δ_{sat} versus Δ_B) ranged between 0.3 and 0.8, indicating that errors in surface chlorophyll produce less-than-proportionate errors in IP.

[48] 3. Are there regional differences in the performance of algorithms? There were significant regional differences, as well as algorithm-region interactions, indicated by the ANOVA results. No one region was uniformly better or worse for all algorithms. The region with the most serious biases was the equatorial Pacific, where algorithms underestimated in situ measurements by a factor of 2.

[49] 4. How do algorithms compare with each other in terms of complexity vis-a-vis performance? Many of the algorithms were highly correlated with one another. This was not surprising, since several are based on the same models, but what was surprising was that the level of agreement had no apparent relationship to the mathematical structure or complexity of the algorithms. In some cases, complex algorithms based on depth-, time- and wavelength-resolved models were highly correlated with simpler algorithms that were time and/or depth integrated. There were distinct systematic differences between algorithms. A future effort to understand systematic differences is strongly recommended.

ELSEVIER

Remote Sensing of Environment 80 (2002)

Remote Sensing of Environment

www.elsevier.com/locate/rse

ERS SAR characterization of coastal polynyas in the Arctic and comparison with SSM/I and numerical model investigations

Sverre Thune Dokken[a,*], Peter Winsor[b], Thorsten Markus[c], Jan Askne[a], Göran Björk[b]

[a]*Department of Radio and Space Science, Chalmers University of Technology, Gothenburg, Sweden*
[b]*Department of Oceanography, Earth Sciences Centre, Göteborg University, Gothenburg, Sweden*
[c]*NASA/GSFC-UMBC JCET, Greenbelt, MD, USA*

Received 31 July 2000; received in revised form 21 June 2001; accepted 25 June 2001

Abstract

Coastal polynyas in the Arctic basin from the winter period (January to April) are characterized using ESA European Remote Sensing satellite (ERS)-1/2 Synthetic Aperture Radar (SAR) Precision (Precise Image, PRI) and Browse images. A SAR polynya algorithm is used to delineate open water, new ice, and young ice, and to define the size and shape of polynyas. In order to extract radiometric and contextual information in the ERS SAR PRI images, three different image classification routines are developed and applied. No in situ data have been available for verification of the polynya shapes and sizes, but one of the ice classification routines have been verified earlier using ground truth data. The SAR polynya algorithm is demonstrated to be able to discriminate between the polynya and the surrounding ice area for 85 analyzed cases. The results from the SAR algorithm are compared to ERS Browse images, passive microwave data (a recent Polynya Signature Simulation Method (PSSM), and the Bootstrap and the NASA Team ice concentration algorithms), and a numerical polynya model (NPM) forced by National Center for Environmental Predictions (NCEP) wind fields and air temperatures. The ERS SAR Browse images show a relatively good correlation with the ERS SAR PRI images (.88) while the Special Sensor Microwave Imager (SSM/I) Bootstrap and the NASA Team ice concentration algorithms both have low correlation coefficients (below .3). The PSSM calculates the polynya shape and size, and delineates open water and thin ice. For polynyas of all sizes it has a correlation of .69 compared to the SAR PRI images. For polynyas with widths greater than 10 km the correlation increases to .83. The NPM computes offshore coastal polynya widths, heat exchange, and ice production. Compared to SAR data, it overestimates the maximum size of the polynya by about 15% and has a correlation of .71 compared to the analyzed SAR PRI images. The polynyas in our main investigation area, located at Franz Josef Land, are found to be primarily wind driven. The surrounding large-scale ice drift and tidal currents have little effect on the polynya behavior. One overall conclusion from this investigation is that SAR images processed through the SAR polynya algorithm in combination with the NPM is a powerful tool for investigating and characterizing polynyas at various scales in the Arctic.
© 2002 Elsevier Science Inc. All rights reserved.

1. Introduction

Global climate models predict that a possible temperature rise will be amplified in the Arctic because of various feedback mechanisms associated with a strong coupling among the Arctic ice cover, the atmosphere, and the ocean (see e.g., Gloersen & Campbell, 1991; Manabe & Stouffer, 1993). Some of these feedback mechanisms are related to the intense heat transfer between ocean and atmosphere in polynyas and leads with large ice production and release of salt. The heat exchange from the ocean to the atmosphere can be two to three orders of magnitude larger in polynyas compared to the surrounding ice masses with an ice production of up to 5 m per event or some 50% of the seasonal mean in some areas (Winsor & Björk, 2000). Siberian shelf polynyas are capable to form 20–60% of the Arctic intermediate water (Martin & Cavalieri, 1989), and Arctic polynyas in general provide about 30% of the estimated salt flux necessary to maintain the cold halocline layer of the Arctic Ocean (Winsor & Björk, 2000). Knowledge of the distribution and frequency of coastal polynyas and leads is therefore important in order to understand large-scale climate processes in the Arctic Basin.

Satellite observations is the only possibility to monitor the Arctic ice cover on a basin wide scale. The detection potential of satellite sensors is, however, limited by their radiometric properties and their temporal and spatial resolution. Traditionally, satellite passive microwave sensors have been used to study polynyas because of their continuous temporal and spatial coverage (c.f. Cavalieri & Martin, 1985, 1994; Markus, Kottmeier, & Fahrbach, 1998; Martin & Cavalieri, 1989; Zwally, Comiso, & Gordon, 1985). Due to the typical size of polynya features (6 km average width, Winsor & Björk, 2000), a relatively high spatial resolution of the satellite sensor is required. The relatively coarse spatial resolution of passive microwave sensors (25–50 km) therefore strongly restricts the information that can be retrieved for polynya studies (i.e. they necessitate subpixel classification). There are means to improve the resolution of passive microwave data by

designing a special algorithm for detecting coastal polynyas such as the Polynya Signature Simulation Method (PSSM, Markus & Burns, 1995). The PSSM has an improved spatial resolution (approximately 6 km) compared to traditional methods (e.g. the Bootstrap and the NASA Team ice concentration algorithms), which increases the possibility to detect and characterize polynyas.

The active Synthetic Aperture Radar (SAR) enables high resolution imaging (25 m spatial resolution) of the geographic region of interest independent of daylight and cloud cover. However, satellites carrying this sensor (European Remote Sensing satellite, ERS-1/2) have relatively low temporal resolution and today's SARs only use one polarization and one frequency, further limiting the detection possibilities. However, Radarsat-1, and within soon, Envisat and Radarsat-2 will have improved coverage.

This article presents one of the first approaches to study polynyas in the inner Arctic Basin during the winter months (January to April). A combination of methods is presented in order to detect the size and shape of coastal polynyas. We use both atmospheric and oceanographic data sets and a numerical model in addition to satellite observations. First, we describe routines to identify polynyas in the Arctic, by (1) ERS SAR Browse images for location of polynyas in space and time and Precise Image (PRI) images for detailed study of the polynyas, (2) Special Sensor Microwave Imager (SSM/I) images using the PSSM algorithm, and (3) a numerical polynya model (NPM). A major issue described in some detail is a new wavelet-based SAR polynya algorithm that is used to identify sizes and shapes of polynyas. We investigate to what extent the NPM and the PSSM agree with the polynya characteristics from the SAR algorithm, which we consider the most accurate identification method due to, e.g., its spatial resolution. The different methods are applied for the same geographical region of interest and within the smallest possible time interval.

4. Conclusions

Automatic polynya characterization using SAR with only VV polarization is limited primarily because open water and/or an ice class can mix with each other in the backscatter and/or texture domain. However, the SAR sensor's high spatial resolution, and the SAR polynya algorithm's addition of a ''irregularity'' parameter and a wavelet-based edge detection method compensate for this weakness. The SAR polynya algorithm is shown to be competitive compared to traditional methods based solely on intensity and texture measures (cf. Fig. 7) and is able to discriminate between the polynya and the surrounding ice areas for 85 analyzed cases. The algorithm consists of three independent loops in order to reduce possible errors. One of the loops (the right loop in Fig. 3) has previously been verified with overlapping aerial photography. The high-resolution SAR images can also be visually interpreted, which enables an additional control of the algorithm's performance. The SAR polynya algorithm is suitable to serve as a reference when compared to the Polynya SSM/I signature model (Markus & Burns, 1995) and an NPM (Winsor & Björk, 2000).

The NPM-estimated average offshore width of coastal polynyas in the Arctic is about 6 km. This is too small for effective monitoring with the SSM/I Bootstrap and the NASA Team ice concentration algorithms. Results from these algorithms have traditionally been used for polynya identification and classification but they give low correlation (less than .3) with the measured SAR polynya sizes (see Fig. 8). The PSSM, however, significantly increases the applicability of the SSM/I data, given the coarse resolution of approximately 6 km. When only larger-sized polynyas (>10 km) are compared, it has a thin ice correlation coefficient of .83 compared to SAR derived young ice. When all sizes of polynyas are compared (54 cases) it has an offshore width correlation of .69 compared to the SAR (see Table 1).

Numerical modeling of polynyas is effective even at small scales and in the dynamic environment typical of coastal polynyas. SAR PRI images provides the most useful data set to validate NPMs and the use of SAR in combination with an NPM significantly contributes to characterize and to gain knowledge about the dynamics of polynyas. This SAR investigation shows that the NPM-computed polynya widths (and thereby the ice and salt productions) are overestimated by approximately 15% for areas with high polynya activity. This investigation also shows that the NPM is mostly hampered by uncertainties in the atmospheric forcing and the large-scale ice drift in the basin. The NPM-computed offshore width has a correlation of .71 compared to SAR open water/new ice for 61 analyzed cases.

Future enhancement of the SAR polynya algorithm will be to combine different image representations (e.g. curvelets and wavelets) in order to improve the delineation of young ice types inside the polynya. A further operational combination of the PSSM and the SAR methods (applicable when SAR data are not available) can enhance the distinction between different new and young ice types in the PSSM model. This distinction is very important for a better understanding of the dynamics and processes in polynyas as well as for a more accurate description of the ocean to atmosphere heat exchange.

One overall conclusion from this investigation is that SAR images processed through the SAR polynya algorithm in combination with the NPM is a powerful tool for investigating and characterizing polynyas at any scale in the Arctic.

The future development of SAR satellite imagery is promising. Forthcoming SAR satellites (Envisat and Radarsat-2) will have full polarization and increased temporal and spatial coverage that will further increase the usage of this sensor. Envisat will have the same orbit configuration as ERS (35-day repeat cycle) and a maximum available swath width of 485 km (while ERS has 100 km).

A Two-Parameter Wind Speed Algorithm for Ku-Band Altimeters

J. GOURRION

IFREMER, Département d'Océanographie Spatiale, Plouzane, France

D. VANDEMARK AND S. BAILEY

NASA Goddard Space Flight Center, Wallops Island, Virginia

B. CHAPRON

IFREMER, Département d'Océanographie Spatiale, Plouzane, France

G. P. GOMMENGINGER, P. G. CHALLENOR, AND M. A. SROKOSZ

The James Rennell Division, Southampton Oceanography Centre, Southampton, United Kingdom

(Manuscript received 5 July 2001, in final form 15 March 2002)

ABSTRACT

Globally distributed crossovers of altimeter and scatterometer observations clearly demonstrate that ocean altimeter backscatter correlates with both the near-surface wind speed and the sea state. Satellite data from TOPEX/Poseidon and NSCAT are used to develop an empirical altimeter wind speed model that attenuates the sea-state signature and improves upon the present operational altimeter wind model. The inversion is defined using a multilayer perceptron neural network with altimeter-derived backscatter and significant wave height as inputs. Comparisons between this new model and past single input routines indicates that the rms wind error is reduced by 10%–15% in tandem with the lowering of wind error residuals dependent on the sea state. Both model intercomparison and validation of the new routine are detailed, including the use of large independent data compilations that include the SeaWinds and ERS scatterometers, ECMWF wind fields, and buoy measurements. The model provides consistent improvement against these varied sources with a wind-independent bias below 0.3 m s^{-1}. The continuous form of the defined function, along with the global data used in its derivation, suggest an algorithm suitable for operational application to Ku-band altimeters. Further model improvement through wave height inclusion is limited due to an inherent multivaluedness between any single realization of the altimeter measurement pair [σ^o, H_S] and observed near-surface winds. This ambiguity indicates that H_S is a limited proxy for variable gravity wave properties that impact upon altimeter backscatter.

1. Introduction

Empirical models have been devised to improve satellite altimeter ocean wind speed retrieval using many differing numerical approaches and datasets (Brown et al. 1981; Dobson et al. 1987; Chelton and McCabe 1985; Witter and Chelton 1991; Glazman and Greysukh 1993; Young 1993; Lefèvre et al. 1994; Freilich and Challenor 1994). The global altimeter ocean wind product is mostly limited to validation and climatological usage (e.g., Young 1999) because the altimeter's nadir-pointing geometry only permits estimates of surface wind speed along a narrow ($\simeq$2 km) swath and precludes wind direction detection. However, accurate wind speed estimates are also important because they are used in the point-by-point correction of an altimeter's estimate of mean sea surface height via the electromagnetic bias algorithm. Freilich and Challenor (1994) and Glazman and Greysukh (1993) expand on these points and suggest that objective model improvement metrics should include the minimization of wind speed biases and root-mean-square error, removal of nonwind geophysical impacts such as sea state, and functional continuity (finite first derivative) such that the wind speed histogram is not distorted.

The operational altimeter wind speed product for TOPEX is derived from interpolation over the look up table known as the modified Chelton–Wentz algorithm (MCW) of Witter and Chelton (1991). This model directly maps measured Ku-band altimeter backscatter (σ^o) to the wind speed 10 m above the ocean (U_{10}). The overall bias, $\langle U_{\mathrm{err}} \rangle$, for this algorithm is suggested to be 0.48 m s^{-1} ($U_{\mathrm{err}} = U_{\mathrm{altim}} - U_{\mathrm{insitu}}$) and the root-mean-square (rms) error lies between 1.5 and 2.0 m s^{-1} (e.g., Witter and Chelton 1991; Gower 1996; Freilich and Challenor 1994; Wu 1999). Numerous studies have suggested that the form for this single parameter algorithm could be improved upon (e.g., Freilich and Challenor 1994). However, the limited amount of validation data combined with the generally small level of improvement in algorithm performance leaves MCW as the current choice for new altimeters such as the GEOSAT Follow-On (GFO) and *Jason-1*.

A goal that remains of interest for altimeter wind retrieval is the detection and correction of wind speed errors associated with longer ocean waves that are not necessarily closely coupled to the local wind field. Evidence for a sea-state effect on altimeter-derived wind has been addressed in several studies (Monaldo and

Dobson 1989; Glazman and Pilorz 1990; Glazman and Greysukh 1993; Lefèvre et al. 1994; Freilich and Challenor 1994; Hwang et al. 1998). Reported results range from substantial impacts to no impact (cf. Wu 1999). The central and unique factor here is an altimeter's coincident and accurate measure of significant wave height, H_S.

Motivation for the present study follows from compilation of a large number of TOPEX altimeter observations made coincident with National Aeronautics and Space Administration (NASA) scatterometer (NSCAT) surface wind estimates. The global coverage, fidelity, and volume of this dataset leads to a much clearer picture of H_S variation impacts upon altimeter backscatter and wind inversion over a range of wind speeds from 1 to 20 m s^{-1}. We develop two models, a forward and an inverse solution, using neural network methods to map between altimeter and scatterometer observations and incorporating a globally derived correction for sea-state impacts using the altimeter-derived H_S estimate. Numerous independent datasets containing collocation between altimeter and ancillary wind estimates are then used to evaluate a best-choice routine and its applicability for operational usage. This paper is derived from an earlier report by Gourrion et al. (2000). That effort includes wind speed models for the C-band altimeter aboard TOPEX, but the present effort concentrates solely on Ku-band model definition.

7. Summary

This study defines and validates a two-input altimeter wind speed algorithm applicable for operational use, where a Ku-band altimeter's coincident σ^o and H_S estimates are utilized in the point-to-point inversion. An analytical formulation (termed f_1) is prescribed with nine coefficients as detailed in section 4. Motivation comes from the new capability to assemble large, globally distributed and high fidelity model training sets composed of coincident satellite altimeter and scatterometer crossovers. The dataset chosen for model training and subsequent validation is a 96 000 sample compilation of TOPEX and NSCAT crossings. Limiting NSCAT usage to only higher incidence angle retrievals strengthens our assumption that the scatterometer wind product is itself free of sea-state impacts. Subsequent validations using buoy and ECMWF winds provide further support.

The empirical development is focused to define an improved and robust wind inversion that incorporates H_S into the solution. This routine should be applicable for all Ku-band altimeters such as those aboard the ERS, ENVISAT, GFO, and *Jason-1* platforms. f_1 intercomparison to past altimeter models and numerous independent validations demonstrates modest, but measurable, success in improving upon the current operational MCW model. These independent data sources include an extensive buoy compilation, the ERS scatterometer, the SeaWinds scatterometer, and the ECMWF model. The f_1 inversion ($[\sigma^o, H_S] \rightarrow [U_{10N}]$) delivers an overall rms improvement of 10–15%, 0.1 to 0.2 m s^{-1} in absolute terms. The domain for model application covers all values of H_S and wind speeds ranging from 1 to 20 m s^{-1}. Error statistics were evaluated over the range of 1–17 m s^{-1}. Wind speed bias is below 0.3 m s^{-1} throughout this range. Improvement in rms error is significant up to winds of about 12 m s^{-1} and equivalent to MCW above this point. The weighting of H_S within the model becomes negligible at these high wind levels. While wind speeds above 20 m s^{-1} are infrequent, a slight modification of f_1 that aligns the altimeter inversion with that predicted by the *QSCAT-1* model function is proposed in appendix B. Statistically, the GG2 algorithm provides similar improvement, but we recall that this classification scheme leads to point-to-point estimate discontinuities and a bi-modal wind speed distribution. TOPEX wind speed histograms, derived using f_1, provide marked improvement over the MCW result in comparison to either buoy, model or scatterometer results. This affirms the continuous nature of the network solution and its applicability for operational use. The TOPEX-generated model is also shown to work well when applied to *ERS-2* altimeter data. The model is adjusted for differing altimeters using a constant σ^o bias and is also relatively insensitive to H_S estimate errors.

Physically, one expects that H_S is a limited proxy for actual gravity wave slope variations that affect the nominal relation between the observed radar cross section and wind speed. Observations and model functions depict measurable correlations amongst the three variables $[\sigma^o, H_S, U_{\mathrm{NSCAT}}]$ but they also exhibit a multivaluedness that inhibits further wind estimate improvement in the absence of additional surface roughness information. This ambiguity leads to an increased altimeter wind speed noise if one attempts to use the forward (f_2) model for U_{10} inversion. This effect occurs even though f_2 is the most effective at removing residual error associated with H_S. Another repercussion is the inability of the f_1 model to correct altimeter wind underestimation during fetch-limited events. These events are rare within the global data set and the neural network minimization solution gives little weight (by design) to this mapping within the domain of possible outcomes.

These points emphasize that present empirical and global-mean model functions do not fully capture the scattering physics. Their application to specific case study will not dramatically improve upon results derived using the MCW model. It is clear, however, that the f_1 algorithm is a measurable improvement that can directly replace the single parameter routine. As importantly, the documented correlation between σ^o and H_S at any chosen wind speed needs to be considered within the empirical modeling of the altimeter sea state bias correction (cf. Chapron et al. 2001). Future work combining the altimeter's unique coincident measure of H_S with multifrequency σ^o (e.g., at S-, C-, Ka- and/or Ku-band) signatures is certain to bring further refinement to these geophysical inversions on both global and local scales.

PERGAMON

Deep-Sea Research II 49 (2002)

DEEP-SEA RESEARCH
PART II

www.elsevier.com/locate/dsr2

Tracking the SeaWiFS record with a coupled physical/biogeochemical/radiative model of the global oceans

Watson W. Gregg

NASA/Goddard Space Flight Center, Laboratory for Hydrospheric Processes, Greenbelt, MD 20771, USA

Accepted 16 June 2001

Abstract

The Sea-Viewing Wide Field-of-view Sensor (SeaWiFS) has observed multiple years of routine global chlorophyll observations from space. The mission was launched into a record El Niño event, which eventually gave way to one of the most intense and longest-lasting La Niña events ever recorded. The SeaWiFS chlorophyll record captured the response of ocean phytoplankton to these significant events in the tropical Indo-Pacific basins, but also indicated significant interannual variability unrelated to the El Niño/La Niña events. This included large variability in the North Atlantic and Pacific basins, in the North Central and equatorial Atlantic, and milder patterns in the North Central Pacific.

This SeaWiFS record was tracked with a coupled physical/biogeochemical/radiative model of the global oceans using near-real-time forcing data such as wind stresses, sea surface temperatures, and sea ice. This provided an opportunity to offer physically and biogeochemically meaningful explanations of the variability observed in the SeaWiFS data set, since the causal mechanisms and interrelationships of the model are completely understood.

The coupled model was able to represent the seasonal distributions of chlorophyll during the SeaWiFS era, and was capable of differentiating among the widely different processes and dynamics occurring in the global oceans. The model was also reasonably successful in representing the interannual signal, especially when it was large, such as the El Niño and La Niña events in the tropical Pacific and Indian Oceans. The model provided different phytoplankton group responses for the different events in these regions: diatoms were predominant in the tropical Pacific during the La Niña, but other groups were predominant during El Niño. The opposite condition occurred in the tropical Indian Ocean. Both situations were due to the different responses of the basins to El Niño. Interannual variability in the North Pacific was exhibited as an increase in the spring bloom in 1999 and 2000 relative to 1998. This resulted in the model from a shallower and more rapidly shoaling mixed layer, producing more average irradiance in the water column and preventing herbivore populations to keep pace with increasing phytoplankton populations. However, several aspects of the interannual cycle were not well-represented by the model. Explanations range from inherent model deficiencies, to monthly averaging of forcing fields, to biases in SeaWiFS atmospheric correction procedures.

1. Introduction

The Sea-Viewing Wide Field-of-view Sensor (SeaWiFS; McClain et al., 1998) has provided the first multi-year global chlorophyll observations from space since the Coastal Zone Color Scanner (CZCS). It represents an unprecedented data set in terms of coverage, continuity, and duration that enables us for the first time to make meaningful observations about the state of biological components in the global oceans, their spatial variability, and their medium-term (seasonal to interannual) variability. This latter point especially differentiates SeaWiFS from the two previous large-scale-coverage missions, the CZCS, which did not provide routine global coverage in its 8-year lifetime (Feldman et al., 1989), and the Ocean Color and Temperature Scanner (OCTS), which failed after nine months of on-orbit operations (Shimoda, 1999).

The comprehensive SeaWiFS data set, beginning in September 1997, provides an opportunity to observe the behavior of ocean phytoplankton in response to seasonal and interannual variability. If analysis of this record is combined with the outputs of a coupled physical/biogeochemical model whose dynamical features are completely understood, then insights may be gained into the causes of this variability, especially when the results are in agreement. Even when they are not, this combination of analysis methodologies can help us infer what processes are not incorporated into the model and their apparent importance.

4. Conclusions

The nearly 3-year SeaWiFS record from launch (September 1997) to June 2000 has given us our first comprehensive glimpse of interannual variability of ocean chlorophyll dynamics. Moreover, SeaWiFS was launched as one of the largest El Niño events was underway, and which eventually gave way to one of the largest, most intensive, and longest-lasting La Niña events ever recorded (continuing at the end of the record). The SeaWiFS chlorophyll record captured the response of ocean phytoplankton to these significant events in the tropical Indo-Pacific basins, but also indicated significant interannual variability unrelated to the El Niño/La Niña. This included large variability in the North Atlantic and Pacific basins, large variability in the North Central and equatorial Atlantic, and milder patterns in the North Central Pacific, the latter of which may be due partially to the El Niño. The Southern Hemisphere exhibited, in contrast, relatively little interannual variability during the SeaWiFS record.

We are fortunate to live in an era when global atmospheric data sets are routinely and nearly immediately available. Thus we have the opportunity to drive a coupled physical/biogeochemical/radiative model of the global oceans with actual near-real-time forcing data such as wind stresses, SSTs, shortwave radiation, and sea ice. Our only limitation is cloud cover and thickness data, which are necessary to evaluate the spectral irradiance with depth, which drives phytoplankton dynamics. Although this is a shortcoming, the availability of the other forcing data gives us an opportunity to track the SeaWiFS record with a global coupled model and attempt to provide physically and biogeochemically meaningful explanations of the variability observed in the SeaWiFS data set.

Even without cloud data, the coupled model was able to represent the seasonal distributions of chlorophyll during the SeaWiFS era, and was capable of differentiating among the widely different processes and dynamics occurring in the global oceans. The model was also reasonably successful in representing the interannual signal, especially when it was large, such as the El Niño and La Niña events in the tropical Pacific and Indian Oceans. In these two regions the model provided different phytoplankton group responses for the different events. The interannual variability in the North Pacific, which was exhibited in SeaWiFS data as an increase in the spring bloom in 1999 and 2000 relative to 1998, was represented and resulted in the model from a more rapidly shoaling mixed layer, inhibiting herbivore population development, thus preventing maximum and immediate utilization of available nutrients from winter convection. However, several aspects of the interannual cycle were not well-represented by the model. Some of which may be due to the model deficiencies of a lack of topographic and coastal influences such as the North Indian Ocean, some may be related to the lack of monthly cloud data, some may be due to riverine influences missing in the model such as the equatorial Atlantic, and finally some may be the result of biases in SeaWiFS atmospheric correction procedures such as absorbing aerosols which are common in the equatorial and mid-latitude eastern Atlantic and the North and equatorial Indian Oceans. Nevertheless, broad agreement suggests confidence in the large scale (synoptic and basin scale) processes in the model and its ability to provide plausible explanations for some the variability observed in this unique spaceborne data set.

NOAA–NASA Coastal Zone Color Scanner Reanalysis Effort

Watson W. Gregg, Margarita E. Conkright, John E. O'Reilly, Frederick S. Patt, Menghua H. Wang, James A. Yoder, and Nancy W. Casey

Satellite observations of global ocean chlorophyll span more than two decades. However, incompatibilities between processing algorithms prevent us from quantifying natural variability. We applied a comprehensive reanalysis to the Coastal Zone Color Scanner (CZCS) archive, called the National Oceanic and Atmospheric Administration and National Aeronautics and Space Administration (NOAA–NASA) CZCS reanalysis (NCR) effort. NCR consisted of (1) algorithm improvement (AI), where CZCS processing algorithms were improved with modernized atmospheric correction and bio-optical algorithms and (2) blending where *in situ* data were incorporated into the CZCS AI to minimize residual errors. Global spatial and seasonal patterns of NCR chlorophyll indicated remarkable correspondence with modern sensors, suggesting compatibility. The NCR permits quantitative analyses of interannual and interdecadal trends in global ocean chlorophyll. © 2002 Optical Society of America

OCIS codes: 010.4450, 010.1290, 280.0280.

1. Introduction

NASA and the international scientific communities have established a record of nearly continuous, high-quality global ocean color observations from space since 1996. The Ocean Color and Temperature Scanner (OCTS; November 1996–June 1997), the Sea-viewing Wide Field-of-view Sensor (SeaWiFS; September 1997–present), and the Moderate-Resolution Imaging Spectroradiometer (MODIS; September 2000–present) have provided an unprecedented view of chlorophyll dynamics on global scales by use of modern, sophisticated data processing methods. A predecessor sensor, the Coastal Zone Color Scanner (CZCS; November 1978–June 1986), utilized processing methodologies and algorithms that are outdated by modern standards. Thus the CZCS archive is severely limited for scientific analyses of interannual and interdecadal variability. This is an issue of fundamental importance to the study of global change.

In response, the National Oceanic and Atmospheric Administration (NOAA) and NASA established an effort to reanalyze the CZCS record by utilizing advances in algorithms that are shared by modern remote sensing missions. In this paper we describe the methods and results of this effort, called the NOAA–NASA CZCS Reanalysis Effort (NCR). Our methods involve the application of (1) recent algorithms to CZCS data to enhance quality and provide consistency with the modern sensors OCTS, SeaWiFS, and MODIS and (2) blending techniques[1] combining satellite data and the extensive *in situ* archives maintained by the National Oceanographic Data Center (NODC) Ocean Climate Laboratory (OCL) to minimize bias and residual error.

Our objective is to provide a high-quality blended satellite *in situ* data set that will enable a consistent view of global surface ocean chlorophyll and the primary production patterns in two observational time segments (1978–1986 and 1996–present) spanning two decades. By reconstructing the historical CZCS data set, we can gain new insights into the processes and interactions involved in producing the interannual and interdecadal chlorophyll signals.

2. Background

A. Coastal Zone Color Scanner and the Modern Ocean Color Sensors

The CZCS was a demonstration mission with two objectives: (1) to establish the technological and scientific feasibility of mapping ocean phytoplankton pigment concentrations from satellites and (2) to determine the improvements that must be made for successful follow-on ocean color missions. The CZCS amply demonstrated the first objective. It also clearly indicated deficiencies in its design and operations that required correction to meet the scientific objectives of a successor mission. In approximate order of priority, these deficiencies, or required improvements, were

(1) the need for routine, continuous global synoptic observations;
(2) better methods to characterize aerosols;
(3) the need for a dedicated calibration and validation program over the lifetime of the mission;
(4) methods to account for multiple scattering by aerosols and the interaction between scattering by molecules and aerosols;
(5) better signal-to-noise ratios (SNRs);
(6) the need to produce estimates of chlorophyll, not pigment;
(7) new information about chromophoric dissolved organic matter;
(8) the need to account for whitecap and foam reflectance; and
(9) improved pixel navigation.

All the modern global missions meet the scientific requirements for ocean color observations. They are dedicated, routine observational platforms. They contain spectral bands in the near-infrared region of the spectrum to enable improved determination of aerosol characteristics. Dedicated, high-quality *in*

situ calibration and validation activities were established before launch. Complex algorithms were developed to account for aerosol multiple scattering and interactions with molecules. SNRs were improved so that all the global missions have at least 500:1 for the visible wavelengths[2] instead of 200:1 for the CZCS.[3] All the missions produce chlorophyll distributions as the primary geophysical product. A new spectral band was included at short wavelengths (near 410 nm) to help determine the distribution and abundance of chromophoric dissolved organic matter. Whitecap and foam reflectance algorithms were developed and refined. Finally, precise navigation methods were developed prelaunch, including improved orbit determination, sensor attitude information, and geolocation algorithms.

B. Coastal Zone Color Scanner Algorithm Deficiencies

Of course, some of the deficiencies of the CZCS data set, such as sensor design and operation activities, cannot be improved after the fact. However, recent advances in our understanding of atmospheric and oceanic optical principles that affect ocean color observations can be applied to the archive. The global CZCS data archive generally available from the NASA Goddard Earth Sciences (GES) Distributed Active Archive Center (DAAC) was produced in 1989 with algorithms that were standard for the time.[4] All the subsequent algorithm improvements (AIs) are utilized in the atmospheric correction and bio-optical algorithms for the modern sensors OCTS, SeaWiFS, and MODIS and in future sensors such as the medium resolution imaging spectrometer, Global Imager, and the visible infrared imaging radiometer suite.

The CZCS archive contains eight major algorithm deficiencies compared with modern sensors: (1) calibration, (2) navigation, (3) constant aerosol type, (4) single-scattering approximation for aerosols and no Rayleigh–aerosol interaction, (5) production of pigment rather than chlorophyll, (6) lack of whitecap and foam reflectance correction, (7) lack of correction to Rayleigh scattering because of nonstandard atmospheric pressure, (8) lack of accounting for water-leaving radiance at 670 nm in high chlorophyll.

These deficiencies affect the representation of global chlorophyll and are a major reason for differences observed between the CZCS era and the modern satellite observations of chlorophyll (shown in Section 4).

C. Blending of Coastal Zone Color Scanner and *in situ* Data for Analysis of Seasonal Variability

Gregg and Conkright[1] combined the extensive archive of NOAA NODC OCL chlorophyll data (>130,000 profiles) with the global CZCS archive at the GES DAAC using the blended analysis of Reynolds[5] to improve the quality and accuracy of global chlorophyll seasonal climatologies. The blended analysis produced a dramatically different representation of global, regional, and seasonal chlorophyll distributions than the archived CZCS.[1] Generally, the CZCS appeared to underestimate chlorophyll concentrations globally by 8–35%. On regional and seasonal scales, larger underestimates were common (20–40%, and occasionally the differences exceeded 100%).

Although the blending approach appeared to have improved many of the deficiencies of the CZCS seasonal climatologies, vast areas of the ocean lacked *in situ* observations, limiting the ability of the method to correct for the deficiencies in the CZCS processing. Further improvements by use of the blended method require better CZCS data.

5. Summary and Conclusions

We revised the CZCS global ocean chlorophyll archive using compatible atmospheric correction and bio-optical algorithms with modern generation ocean color sensors, such as OCTS, SeaWiFS, and MODIS. The revision involved two components: (1) AI, where CZCS processing algorithms were improved to take advantage of recent advances in atmospheric correction and bio-optical algorithms; and (2) blending, where *in situ* data were incorporated into the final product to provide improvement of residual errors. The combination of the two components is referred to as the NOAA–NASA CZCS reanalysis effort. The results of the NCR are compared with *in situ* data and indicate major improvement from the previously available CZCS archive maintained by the NASA GES DAAC. Blending with *in situ* data produced only a 21% adjustment to the CZCS AI field, compared with a 75% percent adjustment required for the DAAC CZCS. This represented a 72% improvement. Global annual means for the NCR suggested a small overestimate of 9.7% from the CZCS AI, compared with a mean 26% underestimate for the DAAC CZCS blend. Frequency distributions of normalized water-leaving radiances at 520 and 550 nm were in close agreement with expected. Finally, observations of global spatial and seasonal patterns indicated remarkable correspondence with SeaWiFS, suggesting data set compatibility.

This revision can permit a quantitative comparison of the trends in global ocean chlorophyll from 1979–1986, when the CZCS sensor was active, to the present, beginning in 1996 with OCTS, SeaWiFS, and MODIS. The overall spatial and seasonal similarity of the data records of CZCS and SeaWiFS strongly suggests that differences are due to natural variability, although some residual effects that are due to CZCS sensor design or sampling may still exist. We believe that this reanalysis of the CZCS archives can enable identification of interannual and interdecadal change. NCR CZCS data are available through the GES DAAC.

The Low-Frequency Variability of the Tropical Atlantic Ocean

SIRPA HÄKKINEN

NASA Goddard Space Flight Center, Greenbelt, Maryland

KINGTSE C. MO

Climate Prediction Center, NOAA/NWS/NCEP, Camp Springs, Maryland

(Manuscript received 16 November 2000, in final form 7 May 2001)

ABSTRACT

Upper-ocean temperature variability in the tropical Atlantic is examined from the Comprehensive Ocean–Atmosphere Data Set (COADS) as well as from an ocean model simulation forced by COADS anomalies appended to a monthly climatology. The findings are as follows: Only the sea surface temperatures (SST) in the northern Tropics are driven by heat fluxes, while the southern tropical variability arises from wind-driven ocean circulation changes. The subsurface temperatures in the northern and southern Tropics are found to have a strong linkage to buoyancy forcing changes in the northern North Atlantic. Evidence for Kelvin-like boundary wave propagation from the high latitudes is presented from the model simulation. This extratropical influence is associated with wintertime North Atlantic oscillation (NAO) forcing and manifests itself in the northern and southern tropical temperature anomalies of the same sign at depths of 100–200 m as result of a Rossby wave propagation away from the eastern boundary in the wake of the boundary wave passage. The most apparent association of the southern tropical sea surface temperature anomalies (SSTA) arises with the anomalous cross-equatorial winds that can be related to both NAO and the remote influence from the Pacific equatorial region. These teleconnections are seasonal, so that the NAO impact on the tropical SST is the largest at midwinter but in spring and early summer the Pacific remote influence competes with NAO. However, NAO appears to have a more substantial role than the Pacific influence at low frequencies during the last 50 years. The dynamic origin of SSTA is indirectly confirmed from the SST–heat flux relationship using ocean model experiments that remove either anomalous wind stress forcing or atmospheric forcing anomalies contributing to heat exchange.

1. Introduction

Variability of the tropical Atlantic has been of wide interest due to its relationship to rainfall in the surrounding landmasses, primarily northeastern Brazil (Nordeste), Sahel, and Angola, Africa (Hastenrath 1978; Moura and Shukla 1981; Folland et al. 1986; Hirst and Hastenrath 1983). These climatic conditions are associated with a dipole of SST anomalies in the Tropics that is the second empirical orthogonal function (EOF) of SST anomalies (Hastenrath 1978; Houghton and Tourre 1992). The existence of this dipole pattern has been questioned (Houghton and Tourre 1992; Enfield and Mayer 1997; Enfield et al. 1999) because the two centers are not anticorrelated with each other at zero lag.

This work will explore the dynamical origin of the decadal variability in the tropical Atlantic Ocean. So far the studies are inconclusive as to whether the decadal variability is internal to the Tropics (Chang et al. 1997) arising from so-called wind–evaporation–SST feedback (Xie and Philander 1994), or driven remotely by the Pacific, or related to the extratropical North Atlantic, or whether a well-defined ''decadal'' signal in the Atlantic exists at all (Dommenget and Latif 2000). The study by Tourre et al. (1999) finds a tropical–extratropical oscillatory mode with a period of 11.4 yr that displays a tropical dipole as a part of a joint sea level pressure (SLP) and SST pattern. The SLP pattern associated with their decadal mode resembles the North Atlantic oscillation (NAO). Rajagopalan et al. (1998) found a significant association with NAO and tropical variability at decadal timescales, but arrived at an opposite conclusion by suggesting that the decadal variability is internal to the Tropics. Based on model experiments, Xie and Tanimoto (1998) and Tanimoto and Xie (1999) suggest that the tropical low-frequency variability is likely to derive from extratropical forcing.

The key element in resolving any of the issues related to the tropical decadal variability is to identify the atmospheric forcing associated with the decadal SST anomalies. Tanimoto and Xie (1999) show that a NAO-like SLP pattern dominates the North Atlantic when the tropical north–south temperature gradient has extreme values. The heat flux associated with NAO has three centers of action: subpolar gyre, western subtropics (20°–40°N), and eastern North Atlantic (5°–25°N) off the African coast (Cayan 1992), which are also the centers of the leading EOF mode for surface heat flux (Häkkinen 1999). The center off the African coast coincides with the area of the tropical dipole, and thus a natural linkage between the northern Tropics and NAO exists. The role of local heat flux as a source of northern tropical SST anomalies has been discussed by Carton et al. (1996) and Enfield and Mayer (1997). However, the forcing of southern tropical SST anomalies appear to be problematic. Enfield and Mayer (1997) could not find

Corresponding author address: Sirpa Häkkinen, NASA Goddard Space Flight Center, Code 971, Greenbelt, MD 20771.
E-mail: hakkinen@gsfc.nasa.gov

any relationship to heat flux while Chang et al. (1997) could construct empirical modes for joint SST–heat flux variability involving both the southern and northern Tropics.

Since heat flux forcing may not be the leading cause of the southern tropical anomalies, we have to explore the role of ocean circulation changes, either driven by local wind stress or remotely forced. One such candidate is the meridional wind variability that appears to be strongly correlated with southern tropical SST anomalies (Bojariu 1997). The work of Philander and Pacanowski (1981a) shows that southerly winds set up a shallow equatorial cell with southerly flow at the surface and northerly flow at subsurface. This cell is associated with upwelling in the southern side and downwelling in the northern side. They also suggest that the southerly winds are responsible for the temperature distribution of the tropical Atlantic where a cold tongue is found in the southeast (SE) sector of the Tropics in an equilibrium state (in a viscous fluid). The other candidate for tropical SST anomalies is the thermohaline circulation that would mainly influence the subsurface temperatures.

Our objective is to study the relationship between the heat flux, wind stress, SST, and upper-ocean temperature anomalies in the Atlantic Tropics. Furthermore we will examine how the SST anomalies in the tropical Atlantic relate to the extratropical ocean, NAO, and the variability in the equatorial Pacific. Analyses are done for SST and atmospheric data based on the Comprehensive Ocean–Atmosphere Response Experiment (COADS; daSilva et al. 1994), which have been used to simulate the oceanic variability from 1946 to 1993. All results from COADS were cross validated by the 51-yr dataset from the National Centers for Environmental Prediction–National Center for Atmospheric Research (NCEP–NCAR) reanalysis.

We will show that the southern tropical SST anomalies are closely linked to the northern tropical subsurface anomalies even though the SST anomalies on either side of the equator are not correlated. This linkage is achieved through the NAO influence, where the subsurface signal propagates from high latitudes to the Tropics. Secondly we will show that SST in the Atlantic Tropics is influenced by the Pacific low-frequency variability. The Pacific and NAO impact on the southern SST takes place mainly through a dynamic adjustment to meridional wind stress anomalies in the central equatorial region, but in the northern Tropics the SST anomalies are driven by local heat flux. The NAO and Pacific impact are not completely separated seasonally, and since SST anomalies can persist for several months, the influence of the two forcings compete in the surface signal. The contents are divided so that the observational and model-simulated datasets along with the ocean model and its forcing, are discussed in section 2. The comparison of observed and simulated SST is presented in section 3a. The variability of the simulated oceanic anomalies in the upper 200 m are discussed in section 3b. The forcing of the northern and southern SST anomalies are considered in section 4. Section 5 presents a summary of interactions between the northern and southern Tropics in the Atlantic.

6. Discussion

The Atlantic upper-ocean temperature variability is studied from COADS observations and from an ocean model simulation forced by COADS anomalies appended to a monthly climatology. The starting point of this study is the SST–heat flux relationship: we find that in the northern Tropics the heat flux anomalies force the temperature anomalies, but in the southern Tropics the relationship between the heat flux and temperature anomalies is neutral, and closer to the equator a weak damping is evident. A comparison with a model experiment without wind stress anomalies but retaining atmospheric anomalies contributing to surface heat exchange shows that the southern tropical SST anomalies would be forced by the local atmosphere as opposed to being neutral or damped as in the full simulation (also in the COADS data). This behavior is consistent with a strong coupling between the atmosphere and the ocean, where SSTA practically drives the atmospheric temperature anomalies. The difference in the surface heat exchange between the two experiments suggests that the southern anomalies have to arise from other processes such as wind-driven circulation changes. Our study suggests that the initial appearance of SSTA in the southern Tropics is a forced response to ocean circulation changes, but does not exclude the possibility of a subsequent atmospheric response as put forward in Robertson et al. (2000).

Specifically the low-frequency southern tropical SST variability is found to be tied to the cross-equatorial wind stress. Based on Philander and Pacanowski (1981a) the meridional wind stress in the Tropics leads to a shallow overturning cell at the equator and pycnocline changes along the boundaries such that southerly winds would cause a strong cold tongue in the eastern southern Tropics. Analogous to this, the northerly wind stress component would lead to deeper pycnocline and warm SST anomalies in the STA region. The significance of the meridional wind component has been brought up by Bojariu (1997) in search of connections between NAO and the tropical variability. We find a connection between NAO and STA that is quite specific to the boreal winter season and that during spring–early summer the Pacific remote forcing is also associated with STA, again through a meridional wind stress signal at the equator.

This difference in the dynamic origin of the northern and southern variability is limited to the surface. At the subsurface (at 100 m and below) the model results show that temperature anomalies of the same sign exist on both sides of the equator. This in-phase relationship is expected from the studies of oceanic adjustment to high-latitude buoyancy forcing that would give rise to equatorward-propagating boundary waves, transforming into equatorial Kelvin waves along the equator and branching into both hemispheres on the eastern boundary and generating westward-propagating Rossby waves in their wake (Wajsowicz 1986; Kawase 1987). The wave dynamics of the extratropical origin determine that the anomalies at depth on both sides of the equator are of the same sign.

Annals of Glaciology 34 2002
© International Glaciological Society

Assessment of the relative accuracy of hemispheric-scale snow-cover maps

DOROTHY K. HALL,[1] RICHARD E. J. KELLY,[2] GEORGE A. RIGGS,[3] ALFRED T. C. CHANG,[1] JAMES L. FOSTER[1]

[1]*Hydrological Sciences Branch, NASA Goddard Space Flight Center, Code 974, Greenbelt, MD 20771, U.S.A.*
[2]*Goddard Earth Sciences and Technology Center, University of Maryland, Baltimore County, 1000 Hilltop Circle, Baltimore, MD 21250, U.S.A.*
[3]*Science Systems and Applications, Inc., Lanham, MD 20706, U.S.A.*

ABSTRACT. There are several hemispheric-scale satellite-derived snow-cover maps available, but none has been fully validated. For the period 23 October–25 December 2000, we compare snow maps of North America derived from the Moderate Resolution Imaging Spectroradiometer (MODIS) and operational snow maps from the U.S. National Oceanic and Atmospheric Administration (NOAA) National Operational Hydrologic Remote Sensing Center (NOHRSC), both of which rely on satellite data from the visible and near-infrared parts of the spectrum; we also compare MODIS maps with Defense Meteorological Satellite Program (DMSP) Special Sensor Microwave/Imager (SSM/I) passive-microwave snow maps for the same period. The maps derived from visible and near-infrared data are more accurate for mapping snow cover than are the passive-microwave-derived maps, but discrepancies exist as to the location and extent of the snow cover even between operational snow maps. The MODIS snow-cover maps show more snow in each of the 8 day periods than do the NOHRSC maps, in part because MODIS maps the effects of fleeting snowstorms due to its frequent coverage. The large ($\sim$30 km) footprint of the SSM/I pixel, and the difficulty in distinguishing wet and shallow snow from wet or snow-free ground, reveal differences up to 5.33×10^6 km^2 in the amount of snow mapped using MODIS vs SSM/I data. Algorithms that utilize both visible and passive-microwave data, which would take advantage of the all-weather mapping capability of the passive-microwave data, will be refined following the launch of the Advanced Microwave Scanning Radiometer (AMSR) in the fall of 2001.

INTRODUCTION

The areal extent of snow cover has been monitored continuously from satellite observations by the U.S. National Oceanic and Atmospheric Administration (NOAA) since 1966 (Matson and others, 1986). Although several weaknesses have been identified (Robinson 1993) in the long-term operational snow product, it is nevertheless the longest climatological time series of snow cover available. Passive-microwave maps of snow cover have been produced since 1978, providing information on snow extent as well as some information on snow-water equivalent. In order to improve the snow-cover record to optimize future long-term climate studies, and as input to general circulation models, it is important to develop an objective way of mapping snow globally, if trends in snow cover, such as those discussed in Brown (1997), are to be validated. In addition, the accuracy of the snow-cover input data needs to be verified in order to establish the accuracy of the model output (Derksen and LeDrew, 2000).

In December 1999, the Moderate Resolution Imaging Spectroradiometer (MODIS) sensor was launched by the National Aeronautics and Space Administration (NASA), and some daily, global maps of snow cover at a spatial resolution of 500 m began to be available in February 2000. Snow maps have been orderable through the U.S. National Snow and Ice Data Center, Boulder, CO, since 13 September 2000. In this paper, we compare 8 day composite MODIS snow maps, NOAA/National Operational Hydrologic Remote Sensing Center (NOHRSC) operational maps, and passive-microwave-derived maps from the Defense Meteorological Satellite Program (DMSP) Special Sensor Microwave/ Imager (SSM/I). Each map is known to have a unique set of problems or limitations. The 30 m resolution Landsat Enhanced Thematic Mapper Plus (ETM+) and the NOAA operational product, the Interactive Multisensor Snow and Ice Mapping System (IMS), are used as ancillary data and are considered "ground truth" for this work.

BACKGROUND

MODIS-derived snow maps

The MODIS snow-mapping algorithm is fully automated, which makes the results consistent from scene to scene. The algorithm uses reflectances in MODIS bands 4 (0.545–0.565 μm) and 6 (1.628–1.652 μm), uncorrected for atmospheric effects, to calculate the normalized-difference snow index (NDSI) (Hall and others, in press). Snow cover is mapped using a grouped-criteria technique algorithm. A pixel will be mapped as snow if the NDSI is $\geq$0.4 and reflectance in MODIS band 2 (0.841–0.876 μm) is $\geq$11%. However, if the MODIS band 4 reflectance is $<$10%, then the pixel will not be mapped as snow even if the other criteria are met. This prevents pixels containing very dark targets from being

mapped erroneously as snow. MODIS bands 1 (0.620–0.670 μm) and 2 (0.841–0.876 μm) are used to calculate the normalized-difference vegetation index (NDVI). An additional test using the NDSI and NDVI is used to improve the detection of snow in dense forests (Klein and others, 1998). A cloud mask (Ackerman and others, 1998) and a land/water mask are inputs to the MODIS snow-cover maps.

DISCUSSION AND CONCLUSION

Analysis of the eight time periods, beginning on 23 October and ending on 25 December 2000, reveals that the MODIS maps nearly always show more snow cover than do the NOHRSC maps. MODIS, because of its frequent coverage, permits the mapping of some fleeting snowstorms that may be missed (either accidentally or intentionally) in both the NOAA operational products (NOHRSC and IMS). Since the NOHRSC and IMS products are subjective, the analysts who construct the maps may use ground data, in addition to satellite data, to refine the snow maps. Some minor snow events, located at the edges of areas mapped as snow by both maps, may not be deemed significant enough to label as snow if the snow cover is not continuous or persistent, a common occurrence especially at the beginning of the snow season. Or, the mapping techniques will miss the effects of these storms if the maps are not produced on a frequent basis. In general, there were not eight NOHRSC maps for each 8 day period, while the MODIS maps were produced from 8 days of data (except the 1–7 November period). NOAA's IMS product is produced daily. The greater temporal resolution of the MODIS maps is advantageous for mapping maximum snow cover, because several swaths of data may be obtained on the same day.

However, the MODIS maps exaggerate the amount of snow in some locations, as determined from comparisons with NOHRSC, IMS and ETM+ images. This is obvious in the Pacific Northwest (western Washington, Oregon and northern California). While there is snow in these locations — often only scattered snow cover — the MODIS maps show nearly continuous snow cover in some cases. The binning technique to map the 500 m resolution MODIS maps into 1/4° × 1/4° resolution maps may permit overestimation of snow cover in some cases. Where only a small amount of the cell is snow-covered, in these early MODIS products, the entire 1/4° × 1/4° pixel will be mapped as snow. An improved binning technique is under development. Maps will be produced at 1/20° × 1/20°, or 5.6 km resolution, beginning in the fall of 2001, and fractional snow cover will be provided as well. This should enhance the utility of the maps considerably.

A modification of the Chang and others (1987) algorithm, and the Grody and Basist (1996) SSM/I algorithm were studied, and the Grody and Basist (1996) algorithm was found to map even less snow cover in the early part of the snow season than did the Chang and others (1987) modified algorithm. It was therefore decided that the Chang and others (1987) modified algorithm was superior for the purposes of this work.

As the winter progresses, agreement between the MODIS and SSM/I maps improves. This was also noted by Armstrong and Brodzik (1999) in their comparison study using the SSM/I maps and the NESDIS weekly maps. As the snow deepens during winter, and the temperatures are consistently colder, the SSM/I mapping improves, and the agreement between the visible and passive-microwave maps improves. Areas of discrepancy are still present, however, especially in coastal areas where mixed pixels of SSM/I data erroneously map the coastal areas as snow-free when in fact there is snow. An example of this may be seen in northern Quebec on the 18–25 December 2000 MODIS/SSM/I difference map (Fig. 2).

The results herein are specific to the North American continent. There are likely to be circumstances on other continents that affect the results of snow mapping with the MODIS algorithms, and these can only be discovered by performing such studies on other continents.

With the launch of NASA's Aqua satellite in 2001, snow-mapping algorithms will be developed using the Advanced Microwave Scanning Radiometer–EOS (AMSR-E) sensor (Chang and Koike, 2000) that should utilize the superior mapping capabilities of the visible sensors, and the all-weather capabilities of the passive-microwave sensors (Tait and others, 2000). The improved spatial resolution of the AMSR-E data (up to 12.5 km), relative to the coarser resolution of the SSM/I, will facilitate comparison with visible and near-infrared snow maps.

Near-term improvements in the MODIS snow-mapping algorithm include providing the 8 day composite snow-cover maps at 5.6 km resolution, and improving the usage of the cloud mask (Ackerman and others, 1998), so that fewer clouds are mapped erroneously as snow.

While the intent of this work was not to establish which product is the most accurate, it is obvious that the passive-microwave data are less accurate in terms of mapping total snow-covered area. This is due to the relatively low (~30 km) spatial resolution of the data, and the fact that the wet snow and shallow snow may not be mapped by the existing automated passive-microwave algorithms, especially in the early part of the snow season.

Relative errors in snow-cover mapping, using both visible/near-infrared and passive-microwave maps, are easier to ascertain than absolute errors. This is because it is very often impossible, in retrospect, to determine which map is the most accurate, or precisely where the snow was located. A technique that combines ground measurements with determination of snow-mapping accuracy in different land-cover types (e.g. Hall and others, 2001) is an attempt to begin to assess the absolute accuracy of snow-cover maps.

MODIS and NOHRSC maps often agree very well, except that the MODIS nearly always maps more snow cover than does the NOHRSC (Table 1). MODIS maps show more snow than the NOHRSC maps, especially at the beginning of the snow season when the more frequent temporal coverage of MODIS permits mapping of shallow snow deposits from fleeting storms. However, we do not know which map is the more accurate since none of the hemispheric-scale snow maps has been fully validated. We can only study the relative accuracy of the maps at this time, augmented by accuracy assessments in selected locations where we have access to either ground measurements or Landsat ETM+ data.

ELSEVIER

Remote Sensing of Environment 83 (2002)

Remote Sensing of Environment

www.elsevier.com/locate/rse

MODIS snow-cover products

Dorothy K. Hall [a,*], George A. Riggs [b], Vincent V. Salomonson [c], Nicolo E. DiGirolamo [b], Klaus J. Bayr [d]

[a] *Hydrological Sciences Branch, NASA/Goddard Space Flight Center, Code 974, Greenbelt, MD 20771, USA*
[b] *Science Systems and Applications, Inc., Lanham, MD 20706, USA*
[c] *NASA/Goddard Space Flight Center, Code 900, Greenbelt, MD 20771, USA*
[d] *Department of Geography, Keene State College, Keene, NH 03431, USA*

Received 1 April 2001; received in revised form 20 December 2001; accepted 1 February 2002

Abstract

On December 18, 1999, the Terra satellite was launched with a complement of five instruments including the Moderate Resolution Imaging Spectroradiometer (MODIS). Many geophysical products are derived from MODIS data including global snow-cover products. MODIS snow and ice products have been available through the National Snow and Ice Data Center (NSIDC) Distributed Active Archive Center (DAAC) since September 13, 2000. MODIS snow-cover products represent potential improvement to or enhancement of the currently available operational products mainly because the MODIS products are global and 500-m resolution, and have the capability to separate most snow and clouds. The MODIS snow-mapping algorithms are automated, which means that a consistent data set may be generated for long-term climate studies that require snow-cover information. Extensive quality assurance (QA) information is stored with the products. The MODIS snow product suite begins with a 500-m resolution, 2330-km swath snow-cover map, which is then gridded to an integerized sinusoidal grid to produce daily and 8-day composite tile products. The sequence proceeds to a climate-modeling grid (CMG) product at 0.05° resolution, with both daily and 8-day composite products. Each pixel of the daily CMG contains fraction of snow cover from 40% to 100%. Measured errors of commission in the CMG are low, for example, on the continent of Australia in the spring, they vary from 0.02% to 0.10%. Near-term enhancements include daily snow albedo and fractional snow cover. A case study from March 6, 2000, involving MODIS data and field and aircraft measurements, is presented to show some early validation work.
© 2002 Elsevier Science Inc. All rights reserved.

1. Introduction

Snow-cover maps of the Northern Hemisphere have been available since 1966 from the National Oceanic and Atmospheric Administration (NOAA). These maps have continually been improved as new satellite data have become available. These maps, however, are not global and they rely on analysts to fine-tune the maps. For operational use, this is an advantage. However, for long-term climate studies, it is imperative to have a data set that is developed using an objective technique for snow mapping so that the data from the maps can be consistent when used as input to climate models.

On December 18, 1999, the Earth Observing System (EOS) Terra spacecraft was launched with a complement of five instruments, one of which is the Moderate Resolution Imaging Spectroradiometer (MODIS). MODIS data are now being used to produce snow-cover products from automated algorithms at Goddard Space Flight Center in Greenbelt, MD. The products are transferred to the National Snow and Ice Data Center (NSIDC) in Boulder, CO, where they are archived and distributed via the EOS Data Gateway (EDG).

The MODIS snow-cover maps represent a potential improvement relative to hemispheric-scale snow maps that are available today mainly because of the improved spatial resolution and snow/cloud discrimination capabilities of MODIS, and the frequent global coverage. Their accuracy, however, has not yet been established, nor has the accuracy of existing operational maps. The difficulty in establishing the accuracy of any of these maps is that it is not known which map is the "truth" (if any) and the techniques used to map snow cover in the various maps are different, resulting in different products. The improved spatial resolution of the MODIS snow maps (500 m), relative to snow maps derived from other available sensors, e.g. NOAA's Advanced Very High Resolution Radiometer (AVHRR) at 1.1-km resolution, should benefit hydrologists for snow-cover mapping. In this paper, we describe the MODIS snow products, and discuss a case study of early validation efforts from a field and aircraft experiment near Keene, NH, in March 2000, and field measurements in December 2000.

2. Background

2.1. Instrument descriptions

2.1.1. MODIS

MODIS is an imaging spectroradiometer that employs a cross-track scan mirror, collecting optics, and a set of

individual detector elements to provide imagery of the Earth's surface and clouds in 36 discrete, narrow spectral bands from approximately 0.4 to 14.0 μm (Barnes, Pagano, & Salomonson, 1998). Key land-surface objectives are to study global vegetation and land cover, global land-surface change, vegetation properties, surface albedo, surface temperature, and snow and ice cover on a daily or near-daily basis (Justice et al., 1998). The spatial resolution of the MODIS instrument varies with spectral band, and ranges from 250 m to 1 km at nadir.

2.1.2. MODIS Airborne Simulator (MAS)

The MAS is a spectroradiometer designed to acquire calibrated radiances. The spectral coverage and radiometric response of an existing multichannel instrument were modified to approximate the narrow spectral bands of the MODIS for measuring scientific parameters of cloud and terrestrial surface targets (King et al., 1996). The MAS, with 50 spectral bands in the wavelength range from 0.55 to 14.2 μm, is flown aboard a NASA ER-2 research aircraft at an altitude of about 20 km. Data from MAS channels 1–10, in the visible, near-infrared and short-wave-infrared parts of the spectrum, are discussed in this paper. The MAS views 43° on either side of nadir with an Earth swath width of 37.25 km. The 15-cm aperture spatial instantaneous field-of-view is 2.5 mrad, or 50-m spatial resolution at nadir from the nominal aircraft height.

2.1.3. The Landsat Enhanced Thematic Mapper Plus (ETM+)

The ETM+ was launched on April 15, 1999, on the Landsat-7 satellite (http://www.landsat.gsfc.nasa.gov/project/satellite.html). The ETM+ has eight discrete bands ranging from 0.45 to 12.5 μm, and the spatial resolution ranges from 15 m in the panchromatic band, to 60 m in the thermal-infrared band. All of the other bands have 30-m resolution. ETM+ data can be accessed as browse products and ordered from the USGS EROS Data Center in Sioux Falls, SD from the following Web address: http://www.edcsns17.cr.usgs.gov/EarthExplorer/. ETM+ data provide a high-resolution view of snow cover that can be compared with the MODIS and operational snow-cover products. However, ETM+ data are only acquired once every 16 days and are therefore not frequent enough for mapping changing snow-cover conditions operationally.

2.2. Snow maps

2.2.1. NOAA operational snow maps

2.2.1.1. National Environmental Satellite, Data and Information Service (NESDIS). The Satellite Analysis Branch of NOAA's NESDIS began to generate Northern Hemisphere Weekly Snow and Ice Cover analysis charts derived from NOAA's GOES and POES visible satellite imager, in November 1966. Maps were manually constructed and the spatial resolution of the charts was 190 km. However, since 1997, a new Interactive Multi-Sensor Snow and Ice Mapping System (IMS) is used by analysts to produce products daily at a spatial resolution of about 25 km, and utilizes a variety of satellite data to produce the maps (Ramsay, 1998). NOAA also produces a daily product, developed by automated techniques, which uses visible, near-infrared and passive-microwave data to map snow cover, and agrees in 85% of the cases studied, with the IMS product (Romanov, Gutman, & Csiszar, 2000).

2.2.1.2. The National Operational Hydrologic Remote Sensing Center (NOHRSC) maps. NOHRSC snow-cover maps, generated by National Weather Service NOHRSC hydrologists, are distributed electronically in near real time, to local, state and federal users during the snow season (Carroll, 1995). The NOHRSC 1-km maps are generated primarily from the NOAA polar-orbiting satellites and the Geostationary Orbiting Environmental Satellite (GOES) satellites to develop daily digital maps depicting the areal extent of snow cover for the coterminous United States, and Alaska, and portions of southern Canada.

4. Discussion and conclusion

A sequence of MODIS snow-cover products is presented. The swath products are mapped to the integerized sinusoidal grid to create the daily tile product. Eight days of the daily tile products are used to produce the 8-day composite tile product. These products are at 500-m resolution. The CMG product is produced at 0.05° (~ 5.6-km) resolution and consists of daily and 8-day composite products. Examples of the products are shown, focusing on the site of a field and aircraft experiment from March 6, 2000, and fieldwork on December 23, 2000. The MODIS snow map shows patchy snow cover on March 6th, as confirmed by the field measurements. However, nearly complete snow cover is mapped near Keene on December 23rd, which is an overestimation of snow cover as compared to the ETM+-derived map for the same day, as confirmed by field measurements but is likely due to the greater resolution of the MODIS image relative to the ETM^+ image.

Other work shows that the MODIS snow-cover maps compare favorably with current operational maps (Hall et al., in press), and perform better than do passive microwave-derived snow-cover maps during the daytime and in the fall months in the Northern Hemisphere when the snow is still wet.

Future enhancements to the MODIS snow maps include daily snow albedo (Klein et al., 2000), which should be available in the fall of 2002, and fractional snow cover at 500-m spatial resolution. Future re-processing will allow all of the MODIS snow maps to be processed in a consistent manner.

Satellite observation of Chromophoric Dissolved Organic Matter (CDOM) variability in the wake of hurricanes and typhoons

Frank E. Hoge

National Aeronautics and Space Administration, Goddard Space Flight Center, Wallops Flight Facility, Wallops Island, Virginia, USA

Paul E. Lyon

E. G. & G. Inc., Goddard Space Flight Center, Wallops Flight Facility, Wallops Island, Virginia, USA

Received 13 March 2002; accepted 5 June 2002; published 4 October 2002.

[1] Satellite observation of Chromophoric Dissolved Organic Matter (CDOM) absorption coefficient variability in the wake of numerous hurricanes and typhoons is reported here for the first time. Storm-induced vertically-mixed CDOM from deeper depths has a higher absorption coefficient than the photochemically degraded CDOM within the undisturbed pre-storm upper mixed layer. Principal findings are: (1) Little variability is observed prior to storm encounter at which time the CDOM-defined wake rapidly develops a notable right side asymmetry. (2) The more robust right-side CDOM absorption coefficient elevation is visible up to ~30days depending on storm intensity. In a way that is similar to existing sea surface temperature imagery applications, the techniques in this paper are proposed as a complementary new research tool for the study of atmosphere-ocean interactions. *INDEX TERMS:* 4504 Oceanography: Physical: Air/sea interactions (0312); 4572 Oceanography: Physical: Upper ocean processes; 4847 Oceanography: Biological and Chemical: Optics; 4552 Oceanography: Physical: Ocean optics. **Citation:** Hoge, F. E., and P. E. Lyon, Satellite observation of Chromophoric Dissolved Organic Matter (CDOM) variability in the wake of hurricanes and typhoons, *Geophys. Res. Lett.*, *29*(19), 1908, doi:10.1029/2002GL015114, 2002.

1. Introduction

[2] Dissolved organic matter (DOM) in seawater represents one of the largest reservoirs of reduced carbon on the earth's surface [*Hedges and Farrington*, 1993]. There is as much carbon in DOM in the oceans as there is carbon in CO_2 in the atmosphere [*Hansell and Carlson*, 1998]. The absorbing form can be remotely observed and is frequently described as chromophoric or colored dissolved organic matter (CDOM). The CDOM absorption coefficient is quite easily retrieved from satellite observations by inversion of an oceanic radiance model [*Hoge et al.*, 1995; *Hoge et al.*, 2001]. However, this CDOM absorption coefficient varies (1) temporally as downwelling irradiance photodegrades or photo-oxidizes the material in the upper ocean layer and (2) with depth since CDOM molecules receive less irradiance at-depth and thus incur less photodegradation [*Vodacek et al.*, 1997; *Chen and Bada*, 1992; *Siegel and Michaels*, 1996]. Vertical differences in the CDOM absorption coefficient are especially pronounced under stratified conditions where a strong thermocline acts as an effective barrier separating the overlying water mass (which is exposed to high solar radiation) from the underlying water mass (which receives little or no insolation). During the period of maximum hurricane activity (July–September) stratification of the oceans of the northern hemisphere are at a maximum, extending as far north as hurricanes are sustained.

[3] Prior to the work reported herein, the principal satellite-derived observations of hurricane forcing of the upper ocean mixed layer have been via sea surface temperature (SST) [*Bates and Smith*, 1985; *Stramma et al.*, 1986; *Shay et al.*, 1992; *Shay et al.*, 2000]. These observations (and modeling studies) have shown that the maximum SST response generally occurs to the right of the storm track and is known as the rightward bias. This rightward bias of the maximum SST cooling is dominated by vertical mixing processes [*Shay et al.*, 1992; *Price et al.*, 1994]. Sea surface fluxes and upwelling underneath the hurricane track generally contribute less to the SST cooling pattern [*Jacob et al.*, 2000].

[4] The application of satellite-derived inherent optical properties imagery to vertical redistribution of chromophoric dissolved organic matter (CDOM) by hurricanes and typhoons is reported here for the first time. Herein, we hypothesize that CDOM, vertically mixed from deeper depths as a result of storm-forcing, provides the source of the CDOM absorption coefficient increases observed in the SeaWiFS retrievals described in this paper. The techniques in this paper are proposed as a complementary new research tool for the study of atmosphere-ocean interaction in much the same way sea surface temperature imagery has historically been used.

2. Methods

2.1. Retrieval of Oceanic Inherent Optical Properties (IOP) from SeaWiFS Water-Leaving Reflectances

[5] All the SeaWiFS global area coverage (GAC) Level 2 reflectances for the complete September 1997 to December 2001 were processed by linear matrix inversion of an oceanic radiance model [*Hoge and Lyon*, 1996; *Hoge et al.*, 1999a; *Hoge et al.*, 1999b; *Hoge and Lyon*, 1999; *Hoge et al.*, 2001]. The inherent optical properties (IOPs), CDOM absorption coefficient, phytoplankton absorption coefficient, and backscattering coefficient, at each invertible pixel are binned into 0.09 square degree bins. When a bin contains more than one valid pixel for a single day of

orbits, then the pixels are averaged together. Multiple pixels in a single bin typically exist only near the polar regions due to the SeaWiFS global coverage period of ~2 days. The complete global averaged binned data are called daily global maps.

[6] The oceanic CDOM variability images to be discussed later were created from a 25-day sliding mean global IOP map, where 24 previous daily global maps and the current day's global map are averaged together. Thus, for the next day's image, the oldest day's data is dropped and a new day's data is included to constitute the new 25 day mean. The process is progressively repeated as each oldest day is dropped and a new day is added. Due to orbit configurations and cloud cover, each sliding mean bin does not necessarily contain an average of 25 valid pixels, but is usually an average of less than 12 valid pixels. The 25-day sliding mean results in more contiguous imagery by removing the clouds from the images and reduces uncertainty in the retrieved IOPs (effects caused by errors in the atmospheric correction to the reflectance spectra).

[7] Data used in the hurricane and typhoon track line extractions (encounter diagrams to be discussed) were produced with a 3-day sliding mean of the daily global maps to eliminate artifacts in the encounter diagrams that are caused by the global coverage period of SeaWiFS. The 3-day sliding mean also allows better estimates of the duration and rate of the increase seen in the CDOM absorption coefficient than the 25-day sliding mean data.

3. Results

[8] We have observed CDOM wakes in at least 40 hurricanes/typhoons during global survey of the 1997, 1998, 1999, 2000 CDOM signatures derived from SeaWiFS reflectances. Although our studies are continuing, CDOM wakes have been found in ~50% of the hurricanes/typhoons in the North Atlantic Ocean and Eastern Pacific Ocean. In the Western Pacific Ocean the occurrence of CDOM wakes is highly variable ranging from ~10% to 50% of the typhoons depending on the location: typhoons that traverse low CDOM areas were much more likely to leave tracks than the typhoons that mainly traverse very high CDOM absorption waters (the latter providing little visual contrast).

4. Summary and Discussion

[14] It has been shown that wakes from major oceanic storm events can be identified by their CDOM absorption coefficient increases measured relative to (a) pre-storm values, (b) adjacent undisturbed regions, (c) post-storm photochemically degraded surface waters. The right-side asymmetry seen in the CDOM absorption coefficient is consistent with historic sea surface temperature findings from satellites, aircraft, ships, and buoys. CDOM absorption coefficient increases of ~100–200% are common. Non-contemporaneous ship data [*Vodacek et al.*, 1997] strongly suggest that these CDOM absorption coefficient increases are due to vertically-mixed [*Shay et al.*, 1992; *Price et al.*, 1994] water whose CDOM has not yet been photochemically degraded to the lower prevailing values routinely found at the sea surface. No change in the average number of carbon atoms in the water column is inferred from these observations; simply a higher optical activity for those chemical species brought to the surface by the storm [*Siegel and Michaels*, 1996]. While satellites can offer observations over large space and time scales, cloud cover can severely limit timely observations. This is true of SST as well as ocean color measurements. The delay time until the cloud cover clears can induce unwanted diurnal heating in the case of (a) SST and (b) CDOM photodegradation/mixing in the case of ocean color. The photodegradation is however mitigated somewhat by the reduced sunlight due to cloud cover.

[15] The current state of our analysis of the SeaWiFS post hurricane/typhoon imagery permits us to retrieve CDOM absorption changes over oceanic basin wide scales. We have made no attempt to tie these findings to observations made by other investigators using data acquired from satellite SST imagery or to any physical oceanographic data that may have been collected by moorings or drifters (if these even exist for hurricane Gert or super typhoon Keith). These observations were discovered in the course of developing SeaWiFS CDOM absorption imagery to observe its distribution in the world's oceans. One of the goals of this paper is to introduce new observational methods to the physical oceanography and meteorological communities who study coupling of intense storms into the upper ocean. We hope that this new tool will complement the physical oceanographic measurements now in use. The large dynamic range of the change in CDOM absorption coefficient may enable more detailed studies of the effects caused by ocean and atmosphere interactions.

[16] The enhanced CDOM absorption coefficient has been seen in numerous named storms and can possibly be seen in less intense storms but these lesser magnitude storms have not yet been sought nor studied by our group. However, it seems safe to conjecture that their effects may eventually be seen under certain pre-existing/storm-driven wind, wave, and current conditions. The CDOM increases have been seen within the tropical storm portions of Gert and Keith (tropical storm wind speeds of ~17 to ~33 m/s). We have seen, but have not yet reported, significant CDOM increases due to known periodic sustained wind events. Thus, the threshold wind speed for CDOM absorption coefficient increases is yet to be established for specifically defined or pre-existing oceanographic conditions.

[17] The phytoplankton absorption coefficient showed no significant signature within the imagery and therefore are not shown. Absence of a phytoplankton bloom is validated by the concurrent absence of an increase in the backscattering coefficient that would accompany phytoplankton growth.

[18] While outside the scope of this paper, numerous studies can be devised by the reader using this CDOM absorption coefficient signature. First, nutrients have been found to be correlated with CDOM [*Chen and Bada*, 1992] and thus studies of the absence of detectable nutrient-facilitated phytoplankton growth and its associated absorption within the CDOM wake is recommended. Second, assuming a known photobleaching rate and upwelling/vertical mixing coefficients, an estimate of the storm energy transfer rate may be possible. Third, an investigation of the intensity and duration of the signature relative to location may be of interest.

Air and Water Monitoring for Homeland Security

Paul R. Houser[*]

Last year's terrorist attacks on the World Trade Center and on the Pentagon have heightened our awareness of actual and potential threats to our nation's safety and security. Assuring homeland security has become a national priority (Bush, 2001), meaning that we must take decisive actions both to prevent and to mitigate future homeland security threats. On 8 October 2001, President George W. Bush established the Office of Homeland Security with the mission to "…develop and coordinate the implementation of a comprehensive national strategy to secure the United States from terrorist threats or attacks" (Executive Order 13228). Homeland security is a challenge of monumental scale and complexity, requiring a comprehensive, long-term strategy that involves partnership with State and local governments, the private sector, and citizens. The president's strategy will build an emergency management system that is better able to manage not just terrorism but all hazards affecting our nation and its people.

A critical element of homeland security lies in the vitality of our environment, which is primarily defined by the availability and quality of our air and water resources. Homeland security efforts must therefore include advanced understanding, assessment, and prediction of natural and human-induced variations in our environment, enabling retooled policies and planning, allocation of resources, and partnership strategies. Whether the cause is a terrorist, an accident, or a natural disaster, the efforts needed to avoid and to alleviate air- and water-related threats are similar. We must be able to identify and assess the magnitude of current threats, to evaluate various preventative and corrective actions, and to predict future threats.

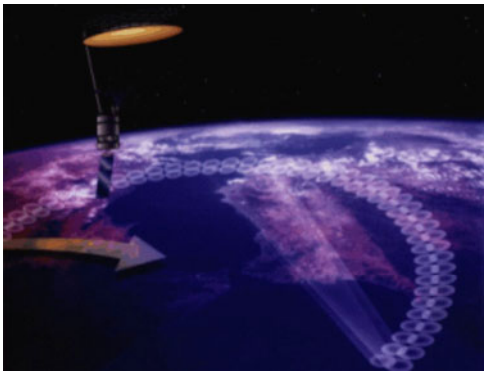

Proposed Hydrospheric State Mission to observe soil moisture and soil freezing.

Over the past few decades, we have made substantial progress in our ability to monitor, assess, and predict air quality and water resources. However, only the scientific community has effectively realized these developments with marginal returns to management and operations. Now, more than ever, we must take action to make the necessary links for improved homeland security through knowledge-added disaster preparation, assessment, and mitigation. We must also view homeland air and water security at the global and multi-national levels, encompassing not only terrorism and vandalism but also natural disasters and potential adversities from human-induced change.

---

[*] Published in August 2002 special NASA Earth Science Enterprise issue of *Earth Observation Magazine*, 11(8):33–36.

Planning, Communication, and Implementation

A traditional disconnect between the environmental management and the scientific research communities has prevented the definition of a mutually beneficial research agenda and the free flow of information to address new threats. As a result, a significant time lag occurs before scientific advancements are implemented to the benefit of society. Environmental management policy is often based on outdated knowledge and technology. Further, scientific research is often performed without understanding stakeholder needs. This paradigm lock has come about because the two main groups have become isolated: scientists by the lack of proven utility of their findings and stakeholders by legal and professional precedence and by disaggregated institutions. For example, global change research is largely focused on mean climate impacts (such as global temperature) of century-scale greenhouse gas changes, while environmental managers need a reliable prediction of extreme event variations (such as floods and droughts) in the seasonal to decadal timeframe.

We must take decisive action to eliminate this paradigm lock. It is essential that we continuously modernize and integrate our air and water observation, assessment, and prediction tools to provide reliable and timely information for homeland security. But this information is meaningless unless accompanied by timely and adequate mitigation action. Communication must be established to transmit information to users quickly, to evaluate various response options in a prediction system, to enable planning, and to take decisive mitigation action. The NOAA weather radio and the network of media resources can deliver hazard emergency messages to the public effectively. We must encourage and demonstrate similar bridge-building dialogue between scientists and policy makers to establish real pathways to define a society-relevant research agenda and to transfer state-of-the-art data and tools to the users who need them.

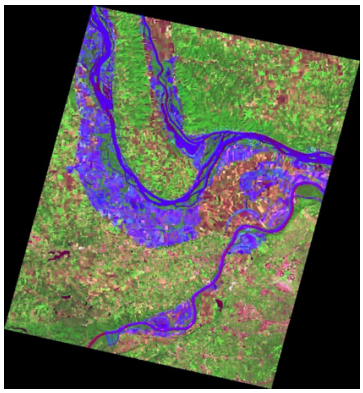

Flood images in the area around St. Louis, Missouri, in July and August 1993 produced by the Institute for Technology Development/Space Remote Sensing Center (ITD/SRSC). The broad blue areas, derived from ERS-1 radar data, show the extent of the flooding and are overlaid on an older SPOT image to delineate the rivers under normal circumstances.

We will likely be surprised by future attacks and by environmental variability, but we do not have to be unprepared. One way to reduce the adverse impact of surprise is to maintain an acceptable level of preparedness at all times. We must improve terrorism and hazard response plans so that when improved warnings become available, decision makers will know how to take action. Improving both air and water monitoring, prediction, and preparation will allow warning and response to work synergistically, providing enhanced homeland security.

Surface Soil Moisture Retrieval and Mapping Using High-Frequency Microwave Satellite Observations in the Southern Great Plains

THOMAS J. JACKSON AND ANN Y. HSU

USDA-ARS Hydrology and Remote Sensing Laboratory, Beltsville, Maryland

PEGGY E. O'NEILL

Hydrological Sciences Branch, Laboratory for Hydrospheric Processes, NASA Goddard Space Flight Center, Greenbelt, Maryland

(Manuscript received 16 November 2001, in final form 10 July 2002)

ABSTRACT

Studies have shown the advantages of low-frequency (<5 GHz) microwave sensors for soil moisture estimation. Although higher frequencies have limited soil moisture retrieval capabilities, there is a vast quantity of systematic global high-frequency microwave data that have been collected for 15 yr by the Special Sensor Microwave Imager (SSM/I). SSM/I soil moisture studies have mostly utilized antecedent precipitation indices as validation, while only a few have employed limited ground observations, which were typically not optimal for this particular type of satellite data. In the Southern Great Plains (SGP) hydrology experiments conducted in 1997 and 1999, ground observations of soil moisture were made over an extended region for developing and validating large-scale mapping techniques. Previous studies have indicated the limitations of both the higher-frequency data and models for soil moisture retrieval. Given these limitations, an alternative retrieval technique that utilizes multipolarization observations was implemented and tested for the SGP region. A technique for extracting algorithm parameters from the observations was developed and tested. The algorithm was then used to produce soil moisture maps of the region for the two study periods.

1. Introduction

The potential of passive microwave remote sensing for measuring surface soil moisture has been demonstrated over a range of microwave frequencies (Choudhury and Golus 1988; Paloscia et al. 1993; Lakshmi et al. 1997; Drusch et al. 2001) and a variety of platforms (Wang 1985; Jackson et al. 1999; Jackson and Hsu 2001). These studies clearly show the advantages of low-frequency (<5 GHz) microwave sensors for this application. Although low-frequency sensors are recognized as the best direction for future soil moisture measurement systems, there is still a good reason in the meantime to consider the use of higher frequencies: the vast quantity of global systematic high-frequency microwave data that have been collected for the past 15 yr by the Special Sensor Microwave Imager (SSM/I).

Despite the fact that high-frequency microwave sensors will have limited retrieval capabilities, there are some conditions under which these observations can provide useful soil moisture information. Most studies using SSM/I and other passive microwave satellite systems to estimate soil moisture have utilized antecedent precipitation indices (APIs) as validation (Choudhury and Golus 1988; Ahmed 1995; Teng et al. 1993; Owe et al. 1992). Morland et al. (2001) compared APIs to soil moisture in estimating SSM/I emissivity. In that study they found APIs to be less correlated to emissivity and concluded that rapid drying of the soil layer, which determines the microwave emission was not adequately reflected in APIs.

A few investigations have employed limited observations from ground networks that were not optimally designed for this particular type of satellite data. The ground networks were either sparse, such as in Koike et al. (2000) (one measurement station per one SSM/I footprint) and in Vinnikov et al. (1999) (17 soil moisture stations for the entire state of Illinois), or the soil moisture layer observed was much deeper than that which determines the microwave response, such as in Owe et al. (1992) (20 cm) and in Vinnikov et al. (1999) (10 cm).

As part of the Southern Great Plains (SGP) hydrology experiments conducted in 1997 (SGP97) and 1999 (SGP99), ground observations of soil moisture were made over an extended region in order to contribute to the validation and demonstration of large-scale mapping of soil moisture using SSM/I data. In a previous investigation the use of a single-channel soil moisture retrieval algorithm was evaluated with limited datasets collected over the region in 1992 and 1994 (Jackson 1997). An investigation by Drusch et al. (2001) used the SGP97 SSM/I data and a more sophisticated radi-

TABLE 1. SSM/I satellite platforms.

Satellite	Dates of operation	Ascending equatorial crossing time (UTC)
F8	Jun 1987–Apr 1994	0612
F10	Dec 1990–Nov 1997	2215
F11	Nov 1991–May 2000	1925
F13	Mar 1995–present	1754
F14	Apr 1997–present	2046
F15	Dec 1999–present	2120
F16	2003 launch	TBD

ative transfer approach that fully considered atmospheric effects to study soil moisture and brightness temperature relationships.

These previous studies have indicated the limitations of both the high-frequency data and the models used for soil moisture retrieval. In the current investigation an alternative retrieval technique utilizing multipolarization observations and based upon the work of Njoku and Li (1999) was implemented and tested for the SGP region. Available information on parameters needed by the soil moisture retrieval algorithm at high frequencies is lacking. As part of the current investigation, a technique for extracting algorithm parameters from the observations was developed and tested. The algorithm was then used to produce soil moisture maps of the region for the two study periods.

2. The SSM/I instrument

The SSM/I is a conical scanning total power microwave radiometer system operating at a look angle of 53° at four frequencies: 19.4, 22.2, 37, and 85.5 GHz. The 22.2-GHz channel operates in V polarization and the other three channels in both V and H polarization. Spatial resolution [effective field of view (EFOV) 3-dB beamwidth] ranges from 69 km by 43 km at 19.4 GHz to 15 km by 13 km at 85.5 GHz. The orbital period is about 102 min, which results in 14.1 orbits per day. For a given satellite, coverage is possible twice a day approximately 12 h apart on the ascending and descending passes. Additional information can be found in Hollinger et al. (1990).

SSM/I instruments have been a component of the Defense Meteorological Satellite Program since 1987. Table 1 summarizes some aspects of the data records available from this series of satellites.

7. Conclusions

Previous studies have suggested that microwave data with frequencies higher than 10 GHz are not appropriate for soil moisture estimation since the vegetation will strongly mask surface information. However, a number of investigations using SSM/I data have presented evidence that there is a usable soil moisture signal under some conditions. Much of this work has been qualitative in nature, relying on indices and not the surface soil moisture for validation.

There are well-established theories describing the microwave emission of the land surface. Vegetation is important in these models but is less significant at low frequencies. At higher frequencies the vegetation is a more dominant feature, and soil moisture retrievals are more sensitive to the representation and parameterization of vegetation effects. Estimating algorithm parameters a priori, as suggested for low frequencies, may not be reliable. For this reason we evaluated a retrieval technique utilizing dual-polarization observations.

Data collected in two field experiments in the Southern Great Plains of the United States were used with SSM/I measurements to better understand the behavior of soil moisture and emissivity at these higher frequencies. The region used for the investigation was well suited to the limitations of using 19-GHz data to estimate soil moisture.

For each of three study areas, a linear relationship was observed between soil moisture and emissivity. Areas with lighter vegetation and the use of H-polarization data produced better linear regression results based on correlation and standard error of estimate values.

An attempt was made to describe the observed linear trends using a radiative transfer model in which the vegetation parameters were optimized. This is essentially the same as using the single-polarization approach described in Jackson (1997). Analysis resulted in values of the vegetation optical depth and the single-scattering albedo that were reasonable based upon published data. The single-channel algorithms had higher SEE than the linear regressions but low bias. These results suggest that there is a limitation on accuracy that is attributed to either the model structure or the quality of the ground observations. Both causes are considered possible.

The dual-polarization algorithm explicitly incorporates parameters that were lumped in the single-channel optimization. It utilizes the same equations but makes assumptions about the effects of polarization on some parameters. If these assumptions on vegetation effects are valid, it is a potentially robust solution. The most significant problem in applying this approach is reducing the number of unknowns to two (i.e., soil moisture and the vegetation parameter b).

The availability of data to perform atmospheric corrections and to estimate effective soil temperature at the time of SSM/I observation may add some restrictions to the application of this approach to areas without meteorological network and radiosonde observations. As an alternative to estimating temperature, van de Griend (2001) demonstrated that effective temperature could be estimated using 37-GHz V-polarization brightness temperature and some climatologic records over semiarid areas. The *Aqua* satellite, recently launched by NASA, includes sensors that can provide atmospheric profile information. With these additional measurements this approach can be extended to other areas with sparse vegetation.

An error analysis of the dual-polarization algorithm revealed that it produced good results for two of the test areas (CF and LW) but poor results at ER. This is attributed to the sources of error identified in previous investigations (Jackson et al. 2002).

Subject to the assumptions made in its implementation, the dual-polarization algorithm worked well in these tests with SSM/I data. We acknowledge that conditions in the SGP region are benign for the frequency used. However, it is anticipated that with lower-frequency channels available with AMSR that the assumptions and limitations imposed by vegetation on soil moisture estimation will be improved.

Remote sensing of subpixel snow cover using 0.66 and 2.1 μm channels

Yoram J. Kaufman,[1] Richard G. Kleidman,[2] Dorothy K. Hall,[1] J. Vanderlei Martins,[3] and Jonathan S. Barton[4]

Received 5 June 2001; revised 8 February 2002; accepted 17 February 2002; published 23 August 2002.

[1] Hydrologic models increasingly require knowledge of the amount of snow cover within a pixel in order to provide accurate estimates of snow covered area. Present methods for remote sensing of subpixel snow cover require knowledge of the spectral reflectance properties of the snow as well as the background material, making these methods difficult to apply globally. Similar problems were encountered in global remote sensing of aerosol particles over varying land terrain. Since both aerosol and snow are dark at 2.1 μm, we suggest a method for sub-pixel snow mapping based on experience with remote sensing of aerosols. Here the pixel reflectance at 2.1 μm is used to estimate the reflectance of the non-snow regions in the pixel at 0.66 μm. The difference between the total pixel brightness at 0.66 μm and the derived brightness of the same pixel without the snow is used to estimate the sub-pixel snow cover with an error usually < ±0.05. *INDEX TERMS:* 1610 Global Change: Atmosphere (0315, 0325); 1827 Hydrology: Glaciology (1863)

1. Introduction

[2] Remote sensing of subpixel snow cover is hindered by the unpredictable variability of the spectral properties of the subpixel non-snow surface cover. To overcome this difficulty, spectral mixing modeling techniques have been applied to the mapping of snow cover [*Rosenthal*, 1993; *Nolin et al.*, 1993]. These techniques represent the mixed pixel spectral properties and composition by combining several classes of surface covers from the image classification. The resultant fraction of snow represents the fraction of snow subpixel cover. This technique is scene based and very difficult to implement on a large scale. Automated techniques to map the subpixel snow cover are reported by *Rosenthal and Dozier* [1996], but are still problematic for use at the global scale because they apply only to a single scene or a set of scenes. In that work, a decision-tree threshold analysis approach using several spectral channels is used. The numeric thresholds were derived from the same remote sensing data sets that are used for snow detection. Though very useful for regional applications, they are not optimal for global applications because of the need to employ spectral end-members that describe the scene parameters. These end-members are unique to a scene or set of scenes, and it is very difficult to derive end-members that are globally applicable due to the extreme variability in spectral reflectance of non-snow features.

[3] We suggest that a method that must be applied globally, on a routine basis, needs to rely on a much simpler algorithm, and properties globally.

[4] Since February 2000, the Moderate Resolution Imaging Spectroradiometer (MODIS) on the Terra satellite [*Kaufman et al.*, 1998] has been acquiring data, globally at 0.25 to 1 km spatial resolution. MODIS data are used to produce operationally, binary snow maps [*Hall et al.*, in press]. Subpixel snow cover is a necessary enhancement of this product. A computationally-frugal technique for subpixel snow cover detection is required for automated, global snow cover mapping.

[5] We find the problem of remote sensing of subpixel snow to be similar to remote sensing of aerosol [*Kaufman et al.*, 1997a]. In both cases the optical properties of the background surface cover, as observed from space, are mixed with the subpixel snow or the aerosol above the surface, each with its own spectral properties. The method to separate the aerosol and surface contribution is based on the fact that fine aerosol is transparent and non-reflective at the long solar wavelengths (e.g. 2.1 μm) and therefore its contribution at 2.1 μm is negligible. Snow is also very dark in this wavelength, in particular if the snow is not fresh, with large grain sizes and therefore its contribution to the pixel reflectance is small. In the case of aerosol the reflectance of the surface under the aerosol at 0.66 μm is estimated using an empirical relationship of surface reflectance in 0.66 and 2.1 μm [*Kaufman et al.*, 1997b; *Karnieli et al.*, 2000]:

$$\rho_{0.66} = [0.5 \pm 0.05]\rho_{2.1} \tag{1}$$

This relationship provides a simple method to estimate the surface reflectance under the aerosol layer over the land. It eliminates the need to generate and update global maps of surface reflectance values. The aerosol optical thickness, a measure of the aerosol column concentration, is determined from the difference in the surface reflectance measured at the top of the atmosphere, $\rho^{a}_{0.66}$ that includes the surface, molecular scattering and aerosol:

$$\Delta\rho_{0.66-2.1} = \rho^{a}_{0.66} - 0.5\rho_{2.1} => \text{ aerosol optical thickness}$$

The technique was validated against ground based measurements around the world and resulted in accurate values of aerosol optical thickness over the land [1998; 2002]. A similar technique is developed here for the subpixel snow cover in the pixel from the difference $\Delta\rho_{0.66-2.1}$, thus avoiding the need for global maps of the surface reflectance.

2. Approach

[6] After applying an atmospheric correction to the Landsat data [e.g., *Vermote et al.*, 1997] the corrected surface reflectance, $\rho^{c}_{0.66}$, is derived from the measured one, $\rho^{a}_{0.66}$. The basic approach to derive the snow fraction from the corrected reflectance is:

$$f_{snow} = (\rho^{c}_{0.66} - 0.5\rho_{2.1})/\rho^{snow}_{0.66} \tag{2}$$

where $\rho_{2.1}$ is the pixel reflectance at 2.1 μm and $\rho^{snow}_{0.66}$ is the reflectance of the snow.

[7] The snow reflectance varies with the direction of observations and age of the snow. It may be determined as the average of the brightest 1–5% of the pixels in a given region with restricted view direction (e.g. ±20°), in the 250 m MODIS resolution. In the present study we found $\rho^{snow}_{0.66} = 0.6$, and estimate the error as ±0.2. Here we assume that the snow reflectance at 2.1 μm is small and does not distort the relationship between the reflectance at 2.1 μm and 0.66 μm used for the background reflectance.

[8] The applicability of the empirical relationship (1) was originally suggested to hold for $\rho_{2.1} < 0.15$. But recently we found in regions with no standing water the relationship can be extended to brighter surfaces ($\rho_{2.1} < 0.25$) [*Kaufman et al.*, 2000; *Karnieli et al.*, 2000]. This finding is also supported by recent modeling study [*Kaufman et al.*, 2002]. Original application of equation 2 to a Landsat-5 Thematic Mapper (TM) scene used by *Rosenthal and Dozier* [1996], and comparison with their validated technique, showed non-linearity in the errors in the fractional snow retrieval. We associated this non-linearity to variability of the snow reflectance, due to variability in the snow thickness, and grain size as a function of the snow fraction and due to multiple scattering between the snow and vegetation or soil. This leads to an empirical correction of the snow fraction obtained from equation 3:

$$f^{c}_{snow} = f_{snow}\rho^{snow}_{0.66}/(\rho^{snow}_{0.66} - 0.09 + 0.07f_{snow}) \tag{3}$$

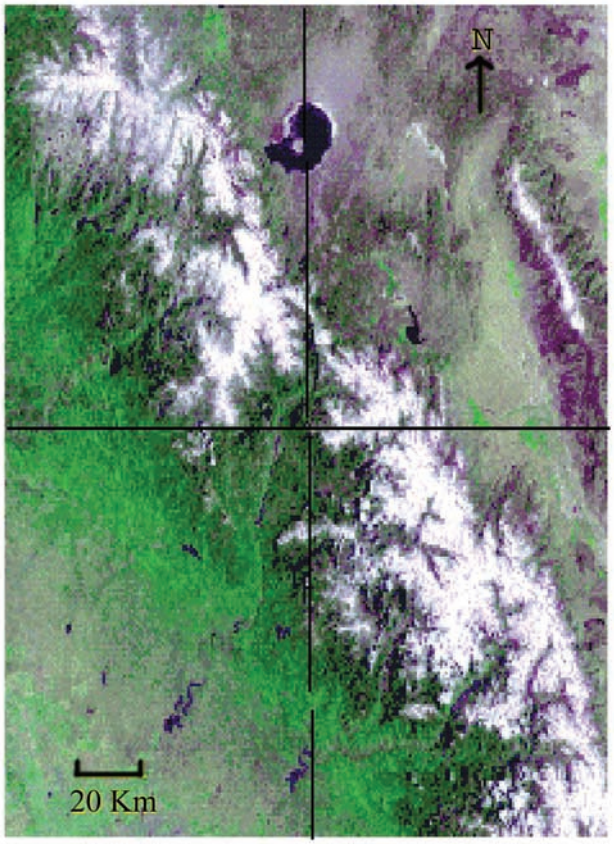

Figure 1. Color composite (red - 0.67 μm, green - 0.87 μm and blue - 0.49 μm) of the Landsat Thematic Mapper image acquired May 10, 1992. The image shows the southern Sierra Nevada range, including Mono Lake, California and the White Mountains to the east. Lines on the image show divisions into the four quadrants discussed in the analysis and in Figure 2. LL-lower left, UL-upper left, LR-lower right, UR-upper right.

3. Application

[9] The method is applied to the same Landsat 5 TM image used by *Rosenthal and Dozier* [1996]. The image, acquired May 10, 1992, shows the southern Sierra Nevada mountain range, including Mono Lake, California (Figure 1).

[10] To reduce the atmospheric effect on the snow retrieval, we applied a simple atmospheric correction to the 0.66 μm channel, by estimating the atmospheric reflectance (for black surface) based on the top-of-atmosphere bidirectional reflectance (BRF) of the darkest water body in the image, in this case Mammoth Lake. The correction then follows *Fraser and Kaufman* [1985], assuming that for surface reflectance of 0.4 the atmospheric effect is zero. The reflectance of the water is assumed to be 0.005. The corrected reflectance at 0.66 μm, $\rho^{c}_{0.66}$ is calculated from the top of the atmosphere BRF $\rho^{a}_{0.66}$ by:

$$\rho^{c}_{0.66} = \left(\rho^{a}_{0.66} - \rho^{atm}_{0.66}\right)\rho^{crit}_{0.66} / \left(\rho^{crit}_{0.66} - \rho^{atm}_{0.66}\right) \quad (4)$$

where $\rho^{atm}_{0.66}$ is the atmospheric path radiance due to aerosol and molecular scattering ($\rho^{atm}_{0.66} = 0.03$) and $\rho^{crit}_{0.66}$ is the critical surface reflectance (0.4), defined as the value of the surface reflectance for which additional aerosol does not change the apparent brightness observed from space. The subpixel snow fractions derived from equation 2 and from the correction in equation 3 are shown in Figure 2. To demonstrate the repeatability of the technique, we divided the Landsat scene into 4 equal quadrants and compared the snow fraction with the validated technique of *Rosenthal and Dozier* [1996], that is used here as the ground truth for each quadrant (called "measured snow cover"). The results show very good agreement, mainly for the empirically corrected data. The detailed errors in the 4 quadrants are plotted as a function of the measured snow cover in Figure 3. The average absolute error is between ±1% and 2% in the snow cover for the 4 quadrants. An image of the spatial distribution of the errors is seen in Figure 4. The positive and negative errors are clustered in regions with similar surface conditions that have a similar error according to the assumptions in equation 3.

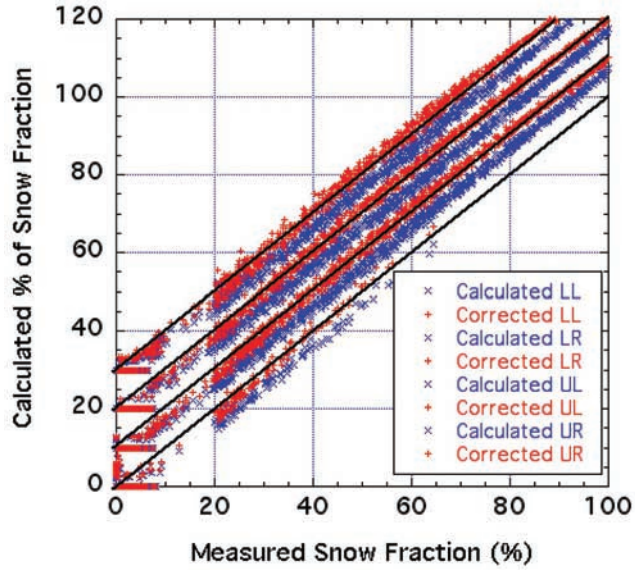

Figure 2. Scatter plot of the calculated snow cover (in %) from equation 2 (blue) and the empirically-corrected snow cover from equation 3 (red) as a function of the snow fraction derived by the validated technique of *Rosenthal and Dozier* [1996]. The results for the 4 quadrants were shifted by 10% on the abscissa, for better viewing of the scatter plots. Therefore all the black lines start in their corresponding zero point.

6. Conclusions

[13] A new technique to measure sub-pixel snow cover is presented. It is based on principles of remote sensing of aerosol over the land. Both aerosol and sub-pixel snow are dark at 2.1 μm and much brighter at 0.66 μm. A relationship between directional reflectance of the non-snow (vegetation and soils) part of the surface, at 0.66 and at 2.1 μm is used to predict the reflectance at 0.66 μm in the absence of snow. Then the excess reflectance at 0.66 μm at the top of the atmosphere measured from the satellite sensor is attributed to snow. The successful application of this relationship to aerosol suggests that the same relationship between the non-snow surface reflectance between 2.1 and 0.66 μm can also be used for snow. The method is expected to be most accurate for snow fractions smaller than 30%. Error analysis shows that this technique can measure snow fractions of 0.1 with an error of ±0.03 while that of 0.3 with an error of ±0.1. Validation using the 4 quadrants of a single Landsat TM image reveal errors of 2–4%. The algorithm was shown to be independent of the spatial scale of the data, at least in the case being studied, and equally accurate for detecting sub-pixel snow in resolutions of 30 m and 500 m. Global validation is yet to be made, however an application to MODIS data collected in the same location of the Landsat data of Figure 1 is shown in Figure 6. MODIS is providing 500-m resolution snow-cover products on a daily basis using a binary snow-detection algorithm. The addition of a subpixel snow-cover algorithm is a planned enhancement, and several algorithms are being tested [*Barton et al.*, 2001]. In Figure 6 we show the subpixel fraction of snow derived from the MODIS data.

Initial Testing of a Massively Parallel Ensemble Kalman Filter with the Poseidon Isopycnal Ocean General Circulation Model

CHRISTIAN L. KEPPENNE

Science Applications International Corporation, Beltsville, Maryland

MICHELE M. RIENECKER

NASA Seasonal-to-Interannual Prediction Project, Laboratory for Hydrospheric Processes, Goddard Space Flight Center, Greenbelt, Maryland

(Manuscript received 24 August 2001, in final form 5 March 2002)

ABSTRACT

A multivariate ensemble Kalman filter (MvEnKF) implemented on a massively parallel computer architecture has been developed for the Poseidon ocean circulation model and tested with a Pacific basin model configuration. There are about 2 million prognostic state-vector variables. Parallelism for the data assimilation step is achieved by regionalization of the background-error covariances that are calculated from the phase–space distribution of the ensemble. Each processing element (PE) collects elements of a matrix measurement functional from nearby PEs. To avoid the introduction of spurious long-range covariances associated with finite ensemble sizes, the background-error covariances are given compact support by means of a Hadamard (element by element) product with a three-dimensional canonical correlation function.

The methodology and the MvEnKF implementation are discussed. To verify the proper functioning of the algorithms, results from an initial experiment with in situ temperature data are presented. Furthermore, it is shown that the regionalization of the background covariances has a negligible impact on the quality of the analyses.

Even though the parallel algorithm is very efficient for large numbers of observations, individual PE memory, rather than speed, dictates how large an ensemble can be used in practice on a platform with distributed memory.

1. Introduction

a. Background and motivation

Many of the early advances in ocean data assimilation have emerged from practical applications in the tropical Pacific. These applications have been driven by the need to initialize the ocean state for coupled atmosphere–ocean forecasts of the El Niño–Southern Oscillation (ENSO) phenomenon. In addition, hindcast estimates of the ocean state have been useful in diagnosing the evolution of El Niño. Over much of the world's oceans, large-scale assimilation is facilitated by the availability of satellite altimetry because of the sparsity of in situ data. However, in the tropical Pacific, the ocean observing system was vastly improved by the deployment of the Tropical Atmosphere Ocean (TAO) array of moored buoys (e.g., McPhaden et al. 1998) to support seasonal-to-interannual (SI) climate studies and prediction. One of the major successes of the Tropical Ocean Global Atmosphere program was the emergence of coupled physical models (as opposed to statistical models) with some prediction skill (e.g., Chen et al. 1995; Ji et al. 1996).

Recently, the NASA Seasonal-to-Interannual Prediction Project (NSIPP) has been established to further the utilization of satellite observations for prediction of short-term climate phenomena. NSIPP undertakes routine experimental forecasts in a research framework with global coupled ocean–atmosphere–land surface models. The initial implementation has used an ocean analysis system employing a simple assimilation methodology—a univariate optimal interpolation (UOI)—with the Poseidon isopycnal ocean general circulation model (OGCM; Schopf and Loughe 1995; Konchady et al. 1998; Yang et al. 1999). Like several other ocean data assimilation systems currently in use at other institutions (e.g., Ji and Leetma 1997), it is based on the assumption that the forecast-error covariances are approximately Gaussian and that the covariances between the temperature-field errors and the salinity-field and current-field errors are negligible.

Largely due to the high-resolution coverage and accuracy of the TAO measurements, the UOI is effective in improving surface and subsurface temperature-field estimates in the equatorial region in comparison with the estimates obtained without temperature assimilation. As a result, its introduction into the NSIPP coupled forecasting system has resulted in significant improvements in the coupled model's hindcast skill of Niño-3 temperature anomalies.

The UOI has the advantage of being inexpensive in terms of computing resources. Nevertheless, it suffers from three major shortcomings: first, it can only be used to assimilate measurements of a model prognostic variable; second, it does not use any statistical information about the expected inhomogeneous distribution of model errors; third, it is based on a steady-state error–covariance model, which gives the same weight to a unit innovation regardless of how accurate the ocean-state estimate has become as a result of previous analyses. Directly linked to this shortcoming is the failure to provide time-dependent estimates of the model errors.

In response to the first two shortcomings, a parallel multivariate OI (MvOI) system has been implemented. The MvOI uses steady-state estimates of the model-error statistics computed from ensemble runs of the OGCM in the presence of stochastic atmospheric forcing from an ensemble integration of the atmospheric general circulation model (AGCM) (Borovikov and Rienecker 2002). Yet, the MvOI cannot adjust to dynamically evolving error statistics. A parallel multivariate ensemble Kalman filter (MvEnKF) has been developed to address this shortcoming. This paper discusses its design, implementation, and initial testing.

b. Overview of the ensemble Kalman filter

Although the Kalman filter (Kalman 1960) and its generalization to nonlinear systems, the extended Kalman filter, are statistically optimal sequential estimation procedures that minimize error variance (e.g., Daley 1991; Ghil and Malanotte-Rizzoli 1991; Bennett 1992), they cannot be used in the context of a high-resolution ocean or atmospheric model because of the prohibitive cost of time stepping the model-error covariance matrix when the model has more than a few thousand state variables. Therefore, reduced-rank (e.g., Cane et al. 1996; Verlaan and Heemink 1997) and asymptotic (e.g., Fukumori and Malanotte-Rizzoli 1995) Kalman filters have been proposed. Evensen (1994) introduced the ensemble Kalman filter (EnKF) as an alternative to the traditional Kalman filter. In the EnKF, an ensemble of model trajectories is integrated and the statistics of the ensemble are used to estimate the model errors. Closely related to the EnKF are the singular evolutive extended Kalman filter (Pham et al. 1998) and the error-subspace statistical estimation algorithms described in Lermusiaux and Robinson (1999).

Evensen (1994) compared the EnKF to the extended Kalman filter in twin assimilation experiments involving a two-layer quasigeostrophic (QG) ocean model on a square 17×17 grid. Evensen and van Leeuwen (1996) used the EnKF to process U.S. Navy Geodesy Satellite (Geosat) altimeter data into a two-layer, regional QG model of the Agulhas current on a 51×65 grid. Houtekamer and Mitchell (1998) and Mitchell and Houtekamer (2000) used the EnKF in identical twin experiments involving a three-level, spectral QG model at triangular truncation T21 and parameterized model errors.

Keppenne (2000, hereafter K00) conducted twin experiments with a parallel MvEnKF algorithm implemented for a two-layer, spectral, T100 primitive equation model with parameterized model errors. With about 2×10^5 model variables, the state-vector size was small enough in this application to justify a parallelization scheme in which each ensemble member resides in the memory of a separate CRAY T3E processor [hereafter, processing element (PE)]. To parallelize the analysis, K00's algorithm transposes the ensemble across PEs at analysis time, so that each PE ends up processing data from a subregion of the model domain. The influence of each observation is weighted according to the distance between that observation and the center of each PE region.

To filter out noise associated with small ensemble sizes, Houtekamer and Mitchell (2001) developed a parallel EnKF analysis algorithm that applies a Hadamard (element by element) product (e.g., Horn and Johnson 1991) of a correlation function having local compact support with the background-error covariances. They tested this analysis scheme on a 128×64 Gaussian grid corresponding to a 50-level QG model using randomly generated ensembles of first-guess fields. The benefits of constraining the covariances between ensemble members using a Hadamard product with a locally supported correlation function has also been investigated by Hamill and Snyder (2000) in the context of an intermediate QG atmospheric model.

5. Summary

This article describes the MvEnKF design and its parallel implementation for the Poseidon OGCM. A domain decomposition whereby the memory of each PE contains the portion of every ensemble member's state vector that corresponds to the PE's position on a 2D horizontal lattice is used. The assimilation is parallelized through a localization of the forecast-error covariance matrix. When data becomes available to assimilate, each PE collects from neighboring PEs the innovations and measurement-functional elements according to the localization strategy. The covariance functions are given compact support by means of a Hadamard product of the background-error covariance matrix with an idealized locally supported correlation function. In EnKF implementations involving low-resolution models, one has the freedom to work with ensemble sizes on the order of hundreds or thousands. Rather, with the state-vector size of approximately 2 million variables considered here, memory, communications between PEs, and operation count limit the ensemble size. In most instances, 40 ensemble members distributed over 256 CRAY T3E PEs are used.

Besides the details of the observing system implementation, the impact of the background-covariance localization on the analysis increments is discussed, as well as performance issues. To confirm that the data assimilation system is working properly, the discussion also includes results from an initial test run in which the MvEnKF is used to assimilate TAO temperature data into Poseidon.

Some issues that must be addressed to improve the MvEnKF are the deficiency of the system-noise model, which only accounts for forcing errors, the problem of ensemble initialization, which can be addressed using a perturbation-breeding approach, and the memory limitations inherent with running the MvEnKF on a MPP with distributed memory. On a machine with globally addressable memory, the memory-imposed constraints would be less severe. Fortunately, the modular, object-oriented approach used to develop the MvEnKF allows an easy port of the implementation from the CRAY T3E to almost every distributed-memory or shared-memory parallel computing architecture.

Evidence and quantification of the correlation between radar backscatter and ocean colour supported by simultaneously acquired in situ sea truth

I-I Lin, Liang-Saw Wen, and Kon-Kee Liu
National Center for Ocean Research, Taipei, Taiwan

Wu-Ting Tsai
National Chiao-Tung University, Taiwan

Antony K. Liu
NASA Goddard Space Flight Center, USA

Received 5 September 2001; accepted 1 April 2002; published 28 May 2002.

[1] Near simultaneously (within 2 hours) acquired ERS-2 Synthetic Aperture Radar (SAR) and Sea-viewing Wide Field-of-view Scanner (SeaWiFS) data over an upwelling region shows remarkable similarity in feature's location, scale, and boundary. Under uniform wind and sea states, reduction of Normalised Radar Cross Section (NRCS) from SAR is found highly correlated with the increase of SeaWiFS Chlorophyll-a (Chl-a) concentration. Typically, 1 mg/m3 of chlorophyll-a is correspondent with a 5 dB reduction of NRCS. This relationship is supported by simultaneously collected in situ sea truth measurements. This work provides a direct evidence and exceptional quantification of the relationship between radar backscatter and ocean colour that has long been speculated. *INDEX TERMS:* 4275 Oceanography: General: Remote sensing and electromagnetic processes (0689); 4279 Oceanography: General: Upwelling and convergences; 4219 Oceanography: General: Continental shelf processes; 4504 Oceanography: Physical: Air/sea interactions (0312)

1. Introduction

[2] The correlation between Synthetic Aperture Radar (SAR) backscatter and ocean colour is a long being speculated issue [*Nilsson and Tildesley*, 1995; *Clemente-Colón and Yan*, 1999; *Gower and Vachon*, 2001]. *Nilsson and Tildesley* [1995] found possible cases in using SAR to discriminate different oceanic water masses and they attributed to the cause being that different water masses carrying different surfactants which results in difference in backscatter.

[3] It is well reported that natural films or surfactants can effectively dampen ocean surface roughness causing attenuation of radar backscatter. Under suitable wind condition, these films can be detected in Synthetic Aperture Radar (SAR) imagery [*Alpers and Hühnerfuss*, 1989; *Espedal et al.*, 1996]. Surfactants are mainly originated from ocean biological activities [*Zutic et al.*, 1981]. *Nilsson and Tildesley* [1995] thus suggested that, under appropriate condition, SAR may be able to discriminate water masses that have different biological activities via difference in the associated surfactants. They further suggested that it may be possible to discriminate different scales, types, and intensity of ocean biological activities by Normalised Radar Cross Section (NRCS). That is, SAR may carry ocean colour information and there is a potential to retrieve ocean colour information from SAR NRCS. Similar example in using SAR to discriminate different water masses was also found by *Hsu et al.* [1997a, 1997b].

[4] However, there are very few co-located/near or co-incident pair of SAR and ocean colour images to confirm the above hypothesis. Clearly the major reason is the lack of operational overlap between SAR (1991 onwards) and ocean colour sensors till the launch of ADEOS-I ocean colour sensor (OCTS) in 1996 and SeaWiFS Sensor in 1997. *Liu et al.* [2000] is one of the rare published evidence of such correlation. They found strong correlation and the matching of boundary between ERS-2 SAR and SeaWiFS data of coccolithophore bloom in the East Bering Sea during the fall of 1997. However, in *Liu et al.* [2000], no quantification nor in situ data to support the correlation between SAR NRCS and SeaWiFS Chlorophyll-a (Chl-a) was provided.

[5] This study attempts to provide another pair of evidence between ERS-2 SAR NRCS and SeaWiFS Chl-a. In addition, correlation of the 2 parameters are quantified and supported by simultaneously acquired in situ sea truth data.

2. Methodology

[6] In order to confirm the above hypothesis, near simultaneously (within 2 hours) acquisition of ERS-2 SAR image and SeaWiFS image was made on 19 August 2000 over our study site, the upwelling region off Northeastern Taiwan. This upwelling system is formed by upwelling of the subsurface Kuroshio water when Kuroshio encounters the continental shelf break of the East China Sea [*Liu et al.*, 1992] and the system is known to be of active biological activities [*Gong et al.*, 1997]. Previous study has also confirmed the presence of surfactants associated with this system [*Hsu et al.*, 1997a, 1997b]. In order to assess the changes of NRCS due to other potential co-existing processes, sea surface temperature (SST) from the Advanced Very High-Resolution Radiometer (AVHRR), and surface synoptic weather charts and digital weather data from the nearest weather station, Penchiayu (122.07°E,25.63°N) were also collected at nearest available acquisition time (within 6 hours) for joint analysis. Sea truth data were collected by Taiwan's Research Vessel R/V Ocean Researcher 2 (OR-2) simultaneously during the satellite data acquisition. Sea truth parameters includes temperature, salinity, and chlorophyll-a concentration. Temperature and salinity data were collected using a Seabird CTD device. Chlorophyll-a samples were collected using ultra-clean sampling protocols [*Wen et al.*, 1999] and analysed using fluoroscence and spectrophotometric methods [*Grasshoff et al.*, 1983]. Cruise track during the in situ campaign was coordinated

Copyright 2002 by the American Geophysical Union.
0094-8276/02/2001GL014039$05.00

according to the SAR image (Figure 1). ERS-2 SAR passed the study area at 02:28 UTC 19 August 2000, and this SAR image was processed in near real-time (within 6 hours) at Taiwan's Ground Receiving Station. The locations of upwelling features were identified and this information was transmitted to OR-2 which was standing-by in neighboring waters by 08:00 UTC for collecting immediate sea truth.

3. Correlation of SAR NRCS and SeaWiFS Chl-a

[7] In Figure 1 a dark feature in the ocean extends northeastward from the northern tip of Taiwan, where upwelling is known to occur [*Liu et al.*, 1992]. Figure 2 illustrates a subscene of the ERS-2 SAR image. In order to compare with the SeaWiFS image (04:37 UTC 19 August 2000), the SAR image was look-averaged from the original 12.5m to 1130m spatial resolution. Prior to look-averaging, antenna pattern correction and 8 × 8 Lee filter (for speckle removal) were applied. This SAR image is displayed in NRCS which was calculated as $NRCS = 20 \times \log DN - K$, where DN is the pixel Digital Number and the K value is 57.3, given by the ERS-2 SAR Ground Receiving Station at the Center for Space and Remote Sensing Research, National Central University, Taiwan. The NRCS was color-coded for easy distinction and reference.

[8] The dark feature shown in Figure 1 is depicted as the coloured region in Figure 2, which is characterized by various degree of lower NRCS (−10.0 to −25.1 dB) in contrast with the uniformly higher NRCS (−7.0 to −10.0 dB) in the white region. In the co-located SeaWiFS image (Figure 3), there exists a similarly southwest to northeast trending feature, which is characterised by higher Chl-a concentration (0.7 to 2.0 mg/m3) in contrast to the ambient Chl-a concentration below 0.7 mg /m3. The features (low NRCS in SAR and high Chl-a in SeaWiFS) found in both images have an almost exact match in their location, scale, and boundary (solid and dashed curves in Figure 3).

[9] To quantify the relationship between NRCS and Chl-a, data from 4 transects in both images are extracted (Figures 2 and 3). Figure 4 illustrates the relationship in one exemplary transect (transect C). The elevated concentration of Chl-a is apparently attributable to the Kuroshio upwelling [*Gong et al.*, 1997]. A clear negative correlation is found between SAR NRCS and Chl-a. It is tantalizing to conclude that the reduction of NRCS within the feature is attributed to the surfactant produced during the active phytoplankton growth, but the reduction may also be caused by other environmental factors, such as wind field or sea surface temperature. To accurately quantifying the NRCS/Chl-a relationship, effects on co-existing factors such as changes in SST and wind must be eliminated [*Clemente-Colón and Yan*, 1999].

4. Wind and SST Effects on NRCS

[10] The effect of the ambient wind field is assessed using the surface synoptic weather charts and digital wind vector time series data of the Penchiayu weather station (data source: Central Weather Bureau, Taiwan) during the study period. It was found that through out the SAR and SeaWiFS data acquisition period, the wind field has been stable and is dominant by a uniformly weak (≤ 5 m/s) southwesterly wind, typical of the southwestern monsoon condition of the study area during summer. Thus the effect of changes in NRCS due to wind is insignificant and can be ignored.

[11] The theory that changes in SST produces changes in NRCS (via changes in air-sea boundary layer stability) is well established [*Friehe et al.*, 1991; *Zheng et al.*, 1997]. However, in the presence of surfactant, the effect of SST becomes secondary [*Clemente-Colón and Yan*, 1999]. To assess and quantify the effect of SST on NRCS, two AVHRR SST images are collected at nearest acquisition time (one at 21:00 UTC 18 August 2000, 5 hours before and one at 08:13 UTC 19 August 2000, 5 hours after) from SAR image acquisition. Figure 5 illustrates the co-located AVHRR SST subscene acquired at 08:13 UTC, around 5 hours after the SAR acquisition. It can be seen that the upwelled cold water pockets are located along the northeastern coast of Taiwan. The corresponding SST is between 27.4°C and 27.9°C in contrast to the ambient warm water in the range of 28.4°C to 30.0°C. The SST image (not shown in this letter) collected before the SAR image acquisition shows similar patterns suggesting that the air-sea system has been stable between these two SST images consistent with the synoptic weather charts (not shown). Thus, Figure 5 is representative of the SST condition during SAR image acquisition. In Figure 5, it can also be seen clearly that the boundary of the cold SST waters deviates greatly from the SAR and SeaWiFS boundaries thus affirming that upwelling features observed in the SAR image (Figure 2) is not dominant by SST effects.

5. Quantification of NRCS and Chl-a Relationship

[12] Though SST is not the primary contributor to NRCS, to accurately quantify the relationship between Chl-a and NRCS, the effect of SST on NRCS is removed before quantification of the NRCS/Chl-a relationship. In recent studies of *Clemente-Colón and Yan* [1999, 2001] over upwelling regions, a $0.66 dB/°C$ NRCS to SST relationship is obtained for ERS-2 SAR. In this study, this relationship is adopted since the same SAR system, the ERS-2 SAR is used. NRCS attenuation is defined as the local NRCS relative to the average ambient NRCS, $\approx -7.7 dB$, outside the upwelling feature. After correction of the effect of SST, NRCS attenuation is plotted against SeaWiFS Chl-a concentration from data along the 4 transects. The number of the total original data pairs from the 4 transects is 1829. As mentioned, to match the spatial resolution of SeaWiFS image, the SAR image was look-averaged. After look-averaging, the data points were then binned into 0.1 mg/m3 chl-a interval and is shown in Figure 6. It can be seen from Figure 6 that higher Chl-a concentration corresponds to higher attenuation of NRCS. In average, 1 mg/m3 Chl-a corresponds to 5 dB attenuation of NRCS. The correlation coefficient is around 0.62. A preliminary linear empirical relationship between ERS-2 SAR NRCS attenuation and Chl-a concentration is derived as $NRCS = 4.64 \times Chl_a + 1.46$. The simultaneously acquired in situ Chl-a measurements (3 coloured points) are also depicted. It can be seen that the derived NRCS versus Chl-a relationship is consistent with the sea truth data in a limited range of parameters.

6. Conclusion

[13] Results from the multi-sensor analysis found that SAR image is characterized by low NRCS (Normalized Radar Cross Section) in the upwelling region off Northeastern Taiwan. In comparison with the ambient waters, the attenuated NRCS is between 0 to 14 dB. In the SeaWiFS image acquired two hours later, the upwelling region is characterized by high Chl-a concentration in the range between 0.7 to 2.0 mg/m3 whereas the ambient Chl-a concentration is below 0.7 mg/m3. It is also found that the upwelling features (low NRCS in SAR and high Chl-a in SeaWiFS) found in both images have an almost perfect match in their locations, scales, and boundaries. Furthermore, it is found that the attenuation of the NRCS is correlated with the increase of Chl-a concentration. Potential misinterpretation due to wind effect is eliminated by comparing with near-simultaneously acquired synoptic weather charts and digital wind vector data. Since changes of SST also affect NRCS, the contribution of SST to NRCS is removed by using the co-located and near-time AVHRR/SST data in an empirical model. The corrected NRCS is then used to derive a preliminary linear empirical relationship with Chl-a concentration. In addition, this relationship is consistent with simultaneously acquired in situ sea truth data. This finding provides a direct evidence of the relationship between SAR NRCS and Chl-a which also confirms and quantifies previous investigations [*Nilsson and Tildesley*, 1995; *Liu et al.*, 2000]. It also supports the hypothesis of the association between the presence of ocean surface slicks and biological activity for global air-sea flux exchange estimation [*Asher*, 1997; *Tsai and Liu*, in press]

Ocean Surface Layer Drift Revealed by Satellite Data

By Antony K. Liu, Yunhe Zhao, Wayne E. Esaias,

Oceans and Ice Branch, NASA Goddard Space Flight Center, Greenbelt, MD

Janet W. Campbell and Timothy S. Moore

Ocean Process Analysis Laboratory, Institute for the Study of Earth, Oceans, and Space

University of New Hampshire, Durham, NH

Historically, from low earth orbits, ocean surface feature tracking analyses have been based on data from a single orbital sensor collected over the revisit interval of a single satellite. In this paper, we report the first time that ocean surface layer currents have been derived by performing feature tracking using data from different sensors on different satellites. Satellite ocean color data provide important insight into the marine biosphere by quantifying certain fundamental properties (e.g. phytoplankton pigment concentration, marine primary production) on a global scale. In addition, satellite ocean color data can also be used as a tracer for measuring ocean surface layer currents, because the ocean color signal comprises information from a deeper water depth (10 to 30 meters) than surface signatures (such as sea surface temperature).

At present, there are two major global ocean color sensors in orbit. The Sea-viewing Wide Field-of-View Scanner (SeaWiFS) was launched onboard the Orbview-2 satellite in August 1997 [McClain et al., 1998], and the Moderate Resolution Imaging Spectroradiometer (MODIS) was launched onboard the Terra (EOS AM-1) satellite on December 18, 1999. Both satellites are in polar orbits at 705 kilometer altitudes, and each sensor views greater than 90% of the Earth's surface in 1-2 days. SeaWiFS acquires data in 8 visible and near-infrared bands, and MODIS acquires data in 36 spectral bands (UV-VIS-IR). Several of the MODIS visual wavelength bands are analogous to the SeaWiFS ocean color bands. These data will provide important new information on the interactions between earth's major climate components and improve our understanding of global physical and biological processes on the land, in the oceans, and in the lower atmosphere [Esaias et al., 1998].

On a daily basis, the global observations of MODIS and SeaWiFS overlap to a large degree, with MODIS currently preceding SeaWiFS by about 70 minutes. The availability of multiple ocean color sensors in orbit allows the production of new data products. One such product, surface layer drift, can be derived when two satellite tracks overlap within a short time (for example, a few hours) without cloud coverage.

In this note, we demonstrate how chlorophyll *a* concentration images provided by MODIS and SeaWiFS can be used to derive surface layer drift. Data from MODIS and SeaWiFS (Figure 1) were collected on May 8, 2000 at 15:45 and 16:52 GMT, respectively, off the east coast of the United States. Major oceanographic features, such as the Gulf Stream boundary and a large cold-core eddy south of the Gulf Stream, can be clearly identified. To validate the results, data from several drifter buoys are compared with the satellite-derived flow field. The qualitative comparison shows a generally consistent pattern.

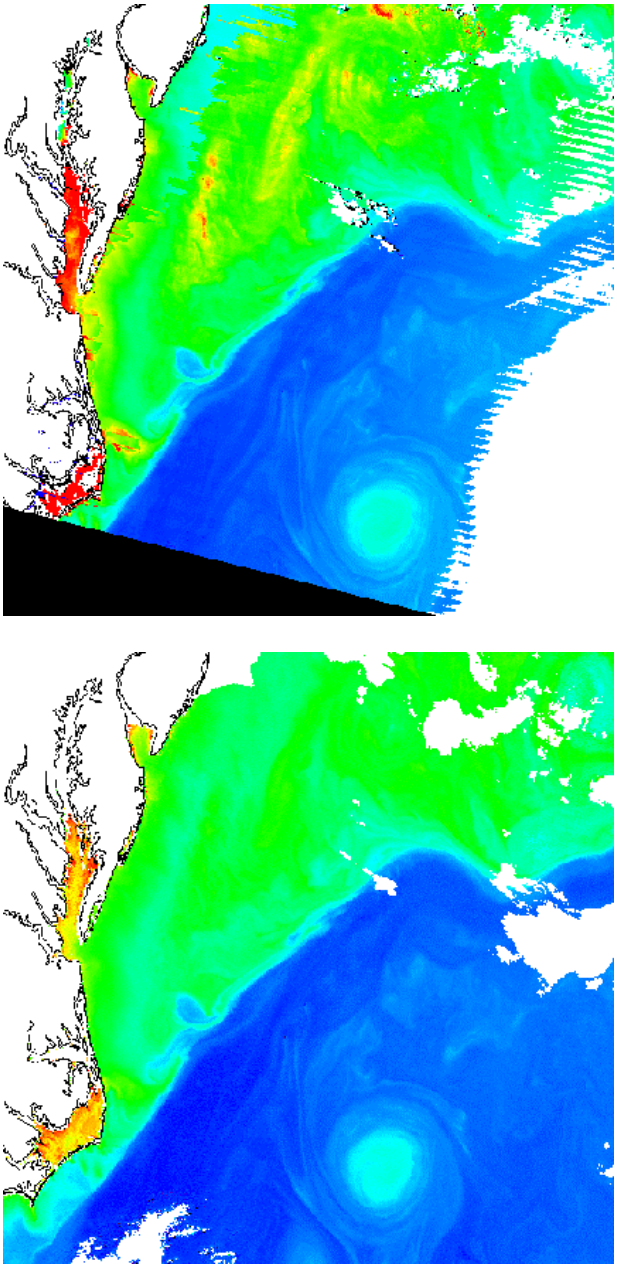

Fig. 1. Chlorophyll-a concentration data collected over US east coast from (a) MODIS, and (b) SeaWiFS on May 8, 2000 separated by 67 minutes.

Comparison of MODIS and SeaWiFS Data

Currently, the comparison between SeaWiFS and MODIS is made with no correction for advection-induced change of chlorophyll values at different times, and is simply a pixel-pixel comparison. Advection between ocean color feature locations will add to the root-mean-square (RMS) errors, especially in high gradient regions. The satellite-derived current field can be used to assess the impact of changing chlorophyll values. Using the derived initial and end pixel numbers of the tracked features or the drift vector, the chlorophyll values at the original and end locations can be compared.

Figure 3 shows the comparison of chlorophyll *a* concentration data from MODIS and SeaWiFS (a) at the same locations, and (b) at the advected locations using the center pixel of a 17 x 17 km box surrounding the vector location. The RMS difference in chlorophyll concentration between these versions of MODIS and SeaWiFS chlorophyll products are 1.0124 mg/m^3 (or 0.1415 in log value) and 0.9701 mg/m^3 (or 0.1358 in log value) at the same locations and at the advected locations, respectively. The linear fit is somewhat improved after including the effects of advection. A reduction of 4 % in RMS error is attributed to correction for surface layer drift which can be derived from satellites. If a simple regression is used to eliminate the bias, the reduction of RMS difference is increased to 6.3%. Most of the points of improvement are at the locations where SeaWiFS predicts higher chlorophyll than the preliminary MODIS algorithm used here. This implies that the low chlorophyll concentration areas near the Gulf Stream were moved into the relatively high concentration locations. Although the improvement is small, it is in the expected direction, and the comparison demonstrates the general first-order accuracy of the drift field derived from satellite data. This comparison also indicates that surface layer drift is generally tangential to chlorophyll concentration gradient, allowing a steady gradient to be maintained. Once advection effects are well constrained, additional nonlinear effects such as biological growth/decay and diffusion processes can be targeted for further investigations.

Annals of Glaciology 34 2002
© International Glaciological Society

The potential of using Landsat 7 ETM+ for the classification of sea-ice surface conditions during summer

THORSTEN MARKUS,[1,2] DONALD J. CAVALIERI,[1] ALVARO IVANOFF[3]
[1]*NASA Goddard Space Flight Center, Code 971, Greenbelt, MD 20771, U.S.A.*
[2]*Joint Center for Earth Systems Technology, University of Maryland, Baltimore County, Baltimore, MD 21250, U.S.A.*
[3]*Science System and Applications Inc., Lanham, MD 20706, U.S.A.*

ABSTRACT. During spring and summer, the surface of the Arctic sea-ice cover undergoes rapid changes that greatly affect the surface albedo and significantly impact the further decay of the sea ice. These changes are primarily the development of a wet snow cover and the development of melt ponds. As melt ponds generally do not exceed a couple of meters in diameter, the spatial resolutions of sensors like the Advanced Very High Resolution Radiometer and Moderate Resolution Imaging Spectroradiometer are too coarse for their identification. Landsat 7, on the other hand, has a spatial resolution of 30 m (15 m for the panchromatic band) and thus offers the best chance to map the distribution of melt ponds from space. The different wavelengths (bands) from blue to near-infrared offer the potential to distinguish among different surface conditions. Landsat 7 data for the Baffin Bay region for June 2000 have been analyzed. The analysis shows that different surface conditions, such as wet snow and melt-ponded areas, have different signatures in the individual Landsat bands. Consistent with in situ albedo measurements, melt ponds show up as blueish, whereas dry and wet ice have a white to gray appearance in the Landsat true-color image. These spectral differences enable areas with high fractions of melt ponds to be distinguished.

INTRODUCTION

Melt ponds and wet snow cover a significant area of the summer Arctic sea ice. Melt features on sea ice can cover more than 50% of the sea-ice area (Derksen and others, 1997; Fetterer and Untersteiner, 1998). As the albedo of wet snow and melt ponds is considerably lower than the albedo of dry ice (down to 0.2 for 30 cm deep ponds (Grenfell and Maykut, 1977)), accurate classification is essential for estimates of the polar summertime energy balance.

Perovich and others (1986) measured the spectral albedos of dry snow, wet snow and melt ponds for several depths. Whereas wet snow reduces the spectral albedo, compared to dry snow, by about the same value over the whole visible range, melt ponds have a greater reduction at longer wavelengths and therefore appear blueish. The spectral albedo of melt ponds for wavelengths greater than 800 nm is about 0.05 independent of melt-pond depth, whereas at 500 nm the albedo decreases from 0.6 for an early-season 0.1 m deep melt pond to 0.25 for a 0.3 m deep old melt pond. Nevertheless, melt ponds can have a range of color tones depending on the underlying ice type and ice thickness. The relative higher blue albedos have also been observed by Morassutti and LeDrew (1996) and Barber and Yackel (1999). Tschudi and others (1997) made use of this spectral difference to identify melt ponds using video data.

For large spatial areas, the Landsat 7 Enhanced Thematic Mapper Plus (ETM+) is an excellent sensor with which to study the surface properties of sea ice during summer. In addition to the different spectral bands, covering the range from 450 nm (blue) to near-infrared and also thermal infrared, the data have a spatial resolution of 30 m (15 m for the panchromatic band) (Table 1). This high spatial resolution is necessary to enable the identification of melt ponds, as these commonly have diameters of a couple of meters, although melt ponds as large as 400 m across have been measured (Fetterer and Untersteiner, 1998). On first-year ice, melt ponds are generally larger in extent and shallower compared to multi-year sea ice. Therefore, areas of first-year ice only are an excellent test site for investigating melt-pond signatures in the Landsat data.

As part of the pre-launch summer Arctic Earth Observing System (EOS) Aqua Advanced Microwave Scanning Radiometer validation aircraft campaign Meltpond 2000 in June/July 2000 (Cavalieri, 2000), four cloud-free Landsat 7

Table 1. Landsat characteristics

Band No.	*Bandwidth* nm	*Field of view* m	*Sample distance* m
1	450–515	30	30
2	525–605	30	30
3	630–690	30	30
4	750–900	30	30
5	1550–1750	30	30
6	10400–12500	30	60
7	2090–2350	30	30
8	520–900	13 × 15	15

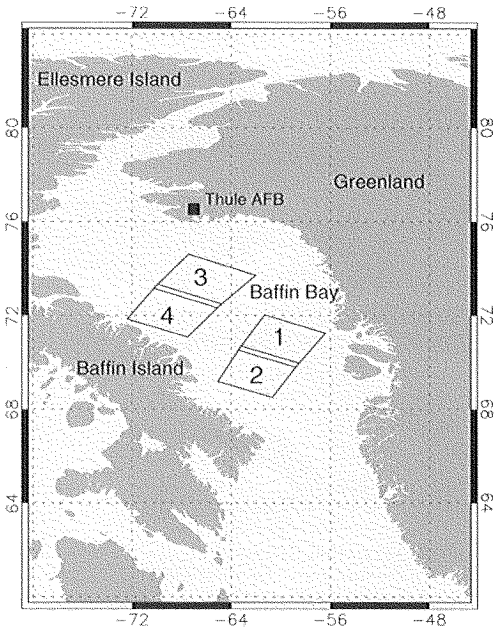

Fig. 1. Overview of the Landsat scenes acquired for 26–27 June 2000 (see Table 2 for details).

scenes over Baffin Bay were acquired (Fig. 1; Table 2). Baffin Bay is a good area for this initial investigation as it does not contain any multi-year ice so that we only have one primary ice type and the observed signatures result from variations in the surface properties only.

ANALYSIS

After the digital numbers of each Landsat band have been scaled into absolute radiances for each wavelength (R_λ), respective reflectivities (α_λ) are calculated following

$$\alpha_\lambda = \frac{\pi R_\lambda}{S_\lambda \cos\theta}, \qquad (1)$$

where S_λ is the respective solar irradiance given in the Landsat 7 Science Data User Handbook and θ is the solar zenith angle.

Spectral analysis of melt features

Figure 2a shows a true-color subset of Landsat scene 2 (Table 2) of Baffin Bay where bands 3, 2, 1 are red, green and blue, respectively. The width of the image is 25 km. One can clearly distinguish between open water and individual ice floes. Whereas open water has a very distinct signature, the summertime reflectivities of sea ice vary significantly. Dry snow is generally seen as white, but with the onset of melt and the consequent wettening of the snow/ice cover, various tones of blue and gray are apparent. Only ridges and hummocks, despite some likely wetness, still appear as white. As mentioned above, melt ponds (at least shallow melt ponds) appear as light blue in the true-color images (point A). Additionally, one can identify different shades of blue (points B–D) that are separate from different shades of gray (points E–H). This is even more distinct in the two-dimensional histograms of band 1 vs band 4 and band 1 vs band 3 (Fig. 3). The majority of pixels fall along the ice–water line from point E (white ice) to point H (open water). Points F and G, which also lie on this line, represent very wet snow or remains of decaying sea ice. The heavy population of pixels with reflectivities of 0.68 in band 1 results from saturation in the high-gain Landsat data. The saturation limits the reflectivities so that expected maximum reflectivities of about 0.9 are not measured. If one continued the H-G-F line until the reflectivity in band 3 was about 0.65, reflectivities of band 1 would reach values of about 0.9. According to Perovich and others (1986), a wet snow cover shifts the albedo by about the same value for the whole visible range. Therefore points F and G lie on the ice–water line. On the other hand, when melt ponds develop, shorter wavelengths remain relatively high compared to the longer wavelengths. Thus, pixels will deviate from the dry-ice–open-water line towards higher band 1 (blue) values, and presumably move from point A to point D as the melt-pond depth increases.

It is noteworthy that points A–D (and similar pixels) lie on the outer margin of the distribution. These pixels have been identified because of their distinct blue signature. We assume that as melt ponds develop and increase in depth, pixels move from point E to A and then to points B, C and D. Pixels between the A–D curve and the E–H line are likely pixels that contain mixtures of melt ponds and ice with different degrees of wetness.

Table 2. Details of the Landsat scenes shown in Figure 1

Scene	Date	Time (GMT)	Sun elevation angle
1	26 June 2000	15:41:21	42.33°
2	26 June 2000	15:41:45	43.54°
3	27 June 2000	16:23:48	39.83°
4	27 June 2000	16:24:12	41.07°

CONCLUSIONS

This study has demonstrated the potential inherent in Landsat 7 ETM+ data for the classification of summertime sea-ice surface conditions. The Baffin Bay area is an ideal region for investigating melt ponds because all the sea ice is first-year ice and melt ponds tend to be shallower and larger in extent compared to multi-year ice. Areas with a high fraction of melt ponds can easily be distinguished from white and wet ice by their blueish appearance and by their greater negative spectral gradients between bands 2 and 3. Although areas with vast amounts of melt ponds are identifiable in the Landsat images, individual melt ponds may be too small to be detected. The distance of a given pixel in band 3 or 4 from the ice–water line (see Fig. 3) may help to estimate the fraction of melt ponds, but higher-resolution data are needed. As part of the Meltpond 2000 experiment, video data have been obtained which are currently being analyzed. We anticipate that these data will help to quantitatively access the accuracy of the algorithm and to address the problem of "mixed pixels" in the Landsat data. Further investigations are needed to develop a broader range of case-studies and to acquire coincident in situ measurements for enabling a detailed analysis of melt-pond signatures (e.g. relationship to melt-pond depth) in the ETM+ data. Whereas clouds can be detected using band 5 or 7, cloud shadows alter the spectral signatures and therefore must be detected visually before large-scale operational analyses can be carried out.

Evaluation of Late Summer Passive Microwave Arctic Sea Ice Retrievals

Thorsten Markus and Sverre T. Dokken

***Abstract*—The melt period of the Arctic sea ice cover is of particular interest in studies of climate change due to the albedo feedback mechanisms associated with meltponds and openings in the ice pack. The traditionally used satellite passive microwave sea ice concentration algorithms have deficiencies during the summer months due to the period's highly variable surface properties. A newly developed ice concentration algorithm overcomes some of these deficiencies. It corrects for low ice concentration biases caused by surface effects through the use of 85 GHz data in addition to the commonly used 19 and 37 GHz data and, thus, the definition of an additional ice type representing layering and inhomogeneities in the snow layer. This new algorithm will be the standard algorithm for Arctic sea ice concentration retrievals with the EOS Aqua advanced microwave scanning radiometer (AMSR-E) instrument. In this paper, we evaluate the performance of this algorithm for the summer period of 1996 using data from the special sensor microwave imager (SSM/I) which has frequencies similar to the AMSR instrument. The temporal evolution of summertime passive microwave sea ice signatures are investigated and sea ice concentration retrievals from the standard NASA team and the new algorithm are compared. The results show that the introduction of the additional sea ice type in the new algorithm leads to improved summertime sea ice concentrations. The SSM/I sea ice retrievals are validated using SAR-derived ice concentrations that have been convolved with the SSM/I antenna pattern to ensure an appropriate comparison. For the marginal ice zone, with ice concentrations ranging from 40% to 100%, the correlation coefficient of SAR and SSM/I retrievals is 0.66 with a bias of 5% toward higher SAR ice concentrations. For the central Arctic, where ice concentrations varied between 60% and 100%, the correlation coefficient is 0.87 with a negligible bias.**

***Index Terms*—Arctic, passive microwave remote sensing, sea ice.**

I. Introduction

DURING spring and summer, the surface of the Arctic sea ice cover undergoes rapid changes that affect the surface albedo and impact the further decay of the sea ice. Later in the summer, the remaining sea ice cover sets the stage for next winter's sea ice growth. Satellite passive microwave data have widely been used to continuously monitor polar sea ice conditions. Unfortunately, summertime is the most difficult season for using passive microwave sensors to estimate accurately sea ice concentrations, i.e., the areal fraction of sea ice within a satellite pixel. The reason for this is that summer sea ice/snow surface conditions are extremely variable in time as well as in space. After the air temperatures reach 0 °C, the snow layer becomes wet, then melts and forms meltponds. These meltponds eventually melt through the sea ice causing a drainage of the pond and/or a flooding of the floes with sea water. Initially a wet snow surface behaves radiometrically as a blackbody resulting generally in overestimates of ice concentration, whereas meltponds appear as open water in the microwave signal causing an underestimate. To increase the complexity further, melt and freeze events frequently intersperse when the air temperature is oscillating about the freezing point. The evolution of summer time passive microwave signatures has been studied by several authors [1], [4], [7]– [9], [11], [14], [15], [19], [20].

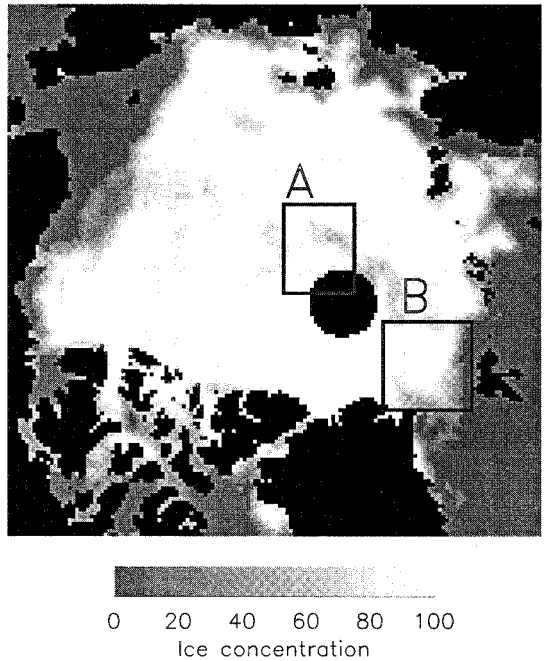

Fig. 1. September 1, 1996 Arctic ice concentration using SSM/I data and the NT2 algorithm as described in section 2. The two black boxes, labeled A and B, indicate the two regions studied in detail in this paper.

A new passive microwave sea ice concentration algorithm has recently been developed [17]. This algorithm, which is briefly described in Section II, overcomes some of the shortcomings of the original NASA Team algorithm [3]; [13] as demonstrated in Comiso *et al.* [7]. In this paper, we are investigating the behavior of the new algorithm during Arctic summer conditions. First, we take ground-based measurements of emissivities of summer sea ice conditions and analyze the resulting ice concentrations for both the NASA Team and the new algorithm (Section III). We also investigate the temporal evolution of SSM/I brightness temperatures and the retrieved sea ice concentrations (Section IV). For validation, we compare the SSM/I ice concentrations with SAR sea ice concentration retrievals during September 1996 (Section V). Fig. 1 shows the two areas investigated (black boxes). In the central Arctic (box A), the SAR data cover the period from September 1, 1996 through September 7, 1996 and for the area closer to the ice edge (box B), SAR data are available for the period September 15,

1996 through September 22, 1996. These areas are coincident with ship-borne measurements. When the cloud cover disappeared, the outgoing thermal radiation often cooled the atmosphere close to the ground forming fog. The average ice thickness varied from 8 cm to 56 cm, with a thin snow cover (8 cm to 15 cm) located at 85 °N, 10 °E and southward to the marginal ice zone. In the eastern high Arctic there were no signs that a summer melt had taken place, since relatively high salinity was found in the surface parts of the second-year ice cores, investigated along the transect 85 °N 149 °E to 160 °E. On the other hand, areas closer to the ice edge i.e., south of 85 °N along 10 cm °E had experienced melting conditions. This conclusion is based on the large number of frozen melt ponds found in this part of the Arctic. Typically, the ponds were covered by 10 to 20 cm of fresh ice above a layer of fresh water on multiyear ice. Preliminary analysis of the scan SAR wide radarsat imagery from 15 and 21 August 1996 indicates that ice concentration in the high Arctic was on average 85%, which was close to visual observations made from the icebreaker bridge.

II. SSM/I Brightness Temperatures and Ice Concentrations

The brightness temperatures (T_B) from the DMSP special sensor microwave imager (SSM/I) are daily averages mapped onto a polar-stereographic projection map (commonly referred to as the SSM/I grid) available at the National Snow and Ice Data Center, Boulder, CO [*NSIDC*, 1992]. Ice concentrations have been derived using an enhanced version of the NASA Team sea ice concentration algorithm [17] (hereafter referred to as the NT2 algorithm). Similar to the original NASA Team (NT) algorithm [3]; [5], [6] it uses ratios of brightness temperatures in order to account for variations in physical temperature, but in addition to the 19 GHz and 37 GHz channels, the enhanced algorithm utilizes also the 85 GHz channels of the SSM/I. The incentive for using the 85 GHz channels was to correct for low concentration biases caused by surface effects primarily in parts of the Antarctic. In the NT algorithm, tiepoints for open water (OW), first-year (FY) ice and multiyear (MY) ice using the polarization at 19 GHz,

$$PR(19) = \frac{T_B(19V) - T_B(19H)}{T_B(19V) + T_B(19H)} \tag{1}$$

and the spectral gradient ratio between 37 GHz and 19 GHz at vertical polarization,

$$GR(37V19V) = \frac{T_B(37V) - T_B(19V)}{T_B(37V) + T_B(19V)} \tag{2}$$

span a triangle in which the fractions for each of the three surface types and thus, ice concentrations are calculated [Fig. 2(a)]. Low ice concentration biases result primarily from the sensitivity of the 19 GHz horizontal polarization channel to inhomogeneities such as layering in the snow cover. These lead to reduced values of $T_B(19H)$ that result in higher $PR(19)$ values and thus, in lower ice concentrations. As this sensitivity is not apparent in the horizontal polarization channel at 85 GHz the ratio difference

$$\Delta GR = GR(85H19H) - GR(85V19V) \tag{3}$$

provides an estimate of the amount of layering with $T_B(19H)$ being the only channel affected. Thus, ΔGR enables the identification of an additional surface type, labeled C. With increasing layering effects ΔGR will also increase. In order to obtain ice concentrations the NT2 algorithm additionally uses the ratios $PR_R(19)$ and $PR_R(85)$. These are polarizations rotated (therefore the subscript R) through an angle, ϕ, which is the angle between the $GR(37V19V)$-axis and the FY-MY line [see Fig. 2(a)] following

$$PR_R(\nu) = -GR(37V19V) \times \sin\phi_\nu + PR(\nu) \times \cos\phi_\nu \tag{4}$$

where ν is either 19 GHz or 85 GHz. The angles ϕ_ν for 19 and 85 GHz and for both hemispheres are given in [17]. This makes the rotated polarizations independent of FY and MY ice type fractions. Because of the increasing sensitivity to atmospheric effects with increasing frequency the new algorithm applies a forward atmospheric radiative transfer model to correct for weather in the ice concentration retrievals. Therefore, we not only have one tiepoint for each surface type but several for each modeled atmospheric state. Fig. 2(b) and 2(c) show scatter plots of the same SSM/I data as in Fig. 2(a) for ΔGR versus $PR_R(19)$ and ΔGR versus $PR_R(85)$, respectively. Modeled ratios (tiepoints) for the pure surface types with different atmospheric conditions are indicated as grey circles. Fig. 3(a) presents a flow chart of the algorithm. The ratios $PR_R(19)$, $PR_R(85)$, and ΔGR are calculated from the measured SSM/I brightness temperatures (this set is labeled $\mathbf{R}$ in Fig. 3(a). We also calculate these ratios from our model data for all ice concentrations (in 1% increments) and various atmospheric conditions ($\langle \mathbf{R} \rangle$) in Fig. 3(a) and then find the best agreement between the measured and modeled ratios for each pixel. It has been demonstrated in [17] that this approach effectively corrects for cloud contamination particularly in areas of lower ice concentrations such as in the marginal sea ice zone.

VI. Conclusions

The evolution of summer time passive microwave signatures and ice concentration are investigated and the results are compared with SAR ice concentration retrievals. This analysis shows that the NT2 sea ice concentration algorithm is better than the traditional NASA Team algorithm during the summer season. The agreement of NT2 results with the SAR retrievals is very good whereas the NT algorithm underestimates ice concentration. The reason for the improvement is based on the utilization of the 85-GHz channels and the definition of an added surface type in addition to the standard first-year and multiyear ice types. This new ice type represents areas with significant amount of inhomogeneities or layering in the snow cover. These inhomogeneities are particularly common during the summer when frequent melt and freeze events alter the snow/ice structure. Nevertheless, this study only gives hints of when and why the NT2 algorithm performs better than the NT algorithm. Dedicated high-resolution passive microwave measurements with coincident in-situ measurements of the snow/ice physical and radiative properties as well as with atmospheric observations are needed to more completely evaluate the algorithm and possibly suggest further improvements.

ELSEVIER

Ecological Modelling 153 (2002) 197–215

ECOLOGICAL MODELLING

www.elsevier.com/locate/ecolmodel

Modelling the effect of temperature on the maximum growth rates of phytoplankton populations

John R. Moisan [a,*], Tiffany A. Moisan [a,1], Mark R. Abbott [b,2]

[a] *Laboratory for Hydrospheric Processes, NASA/GSFC Wallops Flight Facility, Wallops Island, VA 23337-5099, USA*
[b] *College of Oceanic and Atmospheric Science, Oregon State University, Corvallis, OR 97331-5503, USA*

Received 3 January 2001; received in revised form 28 November 2001; accepted 20 December 2001

Abstract

Functional relationships which parameterize growth based on the Eppley temperature relationship for phytoplankton maximal growth rates are increasingly being used in marine and freshwater ecosystem models. In this paper, we demonstrate the effect of using such generalized relationships in modelling studies. Two suites of numerical experiments are carried out to investigate the sensitivity of models to generalized growth relationships. In each experiment, 100 individual species or groups of phytoplankton are allowed to compete under a variety of growth versus temperature relationships. One suite of experiments is carried out within a simple 'chemostat' type model that is forced with seasonally varying temperature and photosynthetically available radiation (PAR) fields. A second suite of experiments is carried out using a biogeochemical mixed-layer model to demonstrate the sensitivity of these models to various temperature versus growth relationships. The key difference in the biogeochemical mixed-layer simulations is in the timing of the ecosystem response to seasonal variability of the mixed-layer depth and temperature. The Eppley growth versus temperature relationship overestimates phytoplankton growth by as much as 80% during the spring when growth rates are crucial to the timing of the spring blooms. This decrease in growth rates causes a delay in the spring phytoplankton bloom which in turn results in significant changes in all other model constituents. The results from both suites of experiments show that it is important to resolve the intrinsic growth dynamics of a population in order to properly resolve the maximum growth rates of phytoplankton populations. The results also present a possible explanation for why phytoplankton are commonly found growing within water colder than their optimal temperature for growth. A dynamic growth versus temperature model is introduced that is capable of resolving the growth dynamics of a population of phytoplankton under a variety of temperature forcing scenarios. This new growth versus temperature model/relationship will be useful in global biogeochemical models and demonstrates the importance of underlying population dynamics in controlling bulk community growth estimates.
© 2002 Elsevier Science B.V. All rights reserved.

Keywords: Phytoplankton; Temperature; Maximum growth rate; Population

1. Introduction

General circulation models (GCM) are currently being coupled to ecosystem models in order to simulate global ocean ecosystems. These circulation models are based on well-understood equations of motion, state, and continuity. Marine ecologists have yet to discern such relationships or 'laws'. The development of ecological theory with applicable equations for use in models has been slow, and the testing of these theories has been difficult due to the complex interactions between organisms and their environment.

Historically, modelling the ocean's ecosystem has been approached from an empirical perspective. Typically, ecosystem modelers develop or assemble a set of empirically-derived functions for

* Corresponding author. Tel.: +1-757-824-1312; fax: +1-757-824-1036.
E-mail addresses: jmoisan@osb.wff.nasa.gov (J.R. Moisan), tmoisan@osb.wff.nasa.gov (T.A. Moisan), abbott@oce.orst.edu (M.R. Abbott).
[1] Tel.: +1-757-824-1046; fax: +1-757-824-1036.
[2] Tel.: +1-541-737-4045; fax: +1-541-737-2064.

each of the specific trophic levels and use these to control the flow of material between the model's components. These functions are then a fixed set of equations that are not allowed to acclimate to changes in the ecosystem that may arise naturally, such as changes in nutrient flux, temperature, light, species succession, competition, food availability, predation, and phenotypic, or on longer time scales, genotypic, changes. There are currently no ecosystem models that are based entirely on first principles (Behrenfeld and Falkowski, 1997a; Evans and Fasham, 1993). Models are generally based upon some level of empirical or bulk parameterizations. The task is to decide upon what level to parameterize the individual processes in order to accurately quantify the observed system response.

Microalgae are capable of carrying out photosynthesis and cellular division over a wide range of temperatures. The effects of temperature on marine algae have been studied extensively for many years (Berry and Bjorkman, 1980; Berry and Raison, 1981; Davison, 1991). It is well-known that phytoplankton have an optimal temperature for growth (Li, 1980). Below the optimal temperature, plant growth rates increase with temperature according to their individual Q_{10} value. The Q_{10} relationship is often parameterized using the Arrhenius function, but in a physical chemistry framework, its shape is controlled by the net effect of the Maxwell–Boltzmann relationships from all of the cellular processes which are linked to Calvin cycle enzymatic activities (Falkowski, 1980). Above the optimal temperature, growth rates decrease due to inactivation or denaturation of proteins or other factors (Ratkowsky et al., 1983).

While a general shape occurs for each growth versus temperature curve, the individual shapes vary widely between different species, and even clones of the same species (Jorgensen, 1968; Falkowski, 1977; Smayda, 1969; Yoder, 1979; Suzuki and Takahashi, 1995). The reasons for this wide range in variability may not be caused solely by temperature variability but also by changes in nutrient and light conditions under which they were grown. The optimal temperature for the curves also varies with changes in the temperature at which the phytoplankton are grown (Li, 1980). However, despite differences in the shapes of the temperature versus growth curves, a general equation can be derived for maximal growth. Eppley (1972) assembled a limited data set of growth curves from phytoplankton batch cultures. From this data set, an empirical equation was derived for estimating the maximum growth rate based on temperature, $\mu_{max} = \log(2)\, 0.851(1.066^T)$, for a given temperature, T. Other growth rate versus temperature relationships have been proposed using data from other laboratory experiments (Ahlgren, 1987).

5. Conclusions

Our results demonstrate the importance of intrinsic population variability on ecosystems. The model results show that phytoplankton population growth rates do not resemble the Eppley (1972) relationship that, to date, all global ecosystem models use, nor many of the other relationships presented in Behrenfeld and Falkowski (1997a), Falkowski et al. (1998). However, the resulting population growth curves (c.f. Fig. 6) are very similar in shape to the growth versus temperature relationship obtained by Behrenfeld and Falkowski (1997b), Balch and Byrne (1994). The major differences in these curves is that the resulting growth relationship presented in this paper does not account for nutrient- and light-limitation. It is hoped that the results from this study will help lead to the development of better primary production models.

A new model for determining the maximum growth rate for a population of phytoplankton is presented that takes into account the general shape of the individual phytoplankton growth versus temperature relationships and the variability of the temperature. This new model is unique in that it is capable of resolving species succession within the global ecosystem and retains the intrinsic variability or dynamics of the population as a whole. At present, this new formulation has yet to be tested within a GCM framework. The results from the new formulation are robust when compared against simulations with 100 plus phytoplankton. Further efforts will focus on the effects of nutrient uptake variability with the hope of establishing a similar global model.

Research Signpost
37/661 (2), Fort P.O., Trivandrum-695 023, Kerala, India

Recent Res. Devel. Geophysics, 4 (2002): 105-117 ISBN: 81-7736-076-0

Recent developments in satellite microwave remote sensing of soil moisture

Manfred Owe
Goddard Space Flight Center, S-54967-G, Receiving/Bldg 16W, Code 239, Soil Conservation Road
Greenbelt, MD 20771-0001, U.S.A

Abstract

Significant research developments in microwave remote sensing of soil moisture have occurred over the last ten years. These developments have been brought about largely through a combination of modelling and field studies. Field studies are usually instrument oriented, and typically consist of ground-based radiometer studies, aircraft missions, and often satellite studies. Modelling studies have been conducted both independently and in support of instrument programs. A number of key modelling studies have been conducted with retrospective satellite data sets. The Scanning Multichannel Microwave Radiometer (SMMR), which was carried on board the Nimbus-7 satellite, has provided an important 9-year (1978-1987) global data set of microwave observations, and has been the basis for a number of important microwave-based soil moisture studies. Results from several of these studies, along with results from some instrument field studies are presented.

Introduction

Surface moisture is an important link between the land surface and the atmosphere. It has direct influence on the exchange of heat and moisture between these two sinks, and as such is an important element in the global circulation process. Surface soil moisture has been identified as a parameter of significant potential for improving the accuracy of large-scale land surface-atmosphere interaction models. However, soil moisture is quite difficult to measure accurately both temporally and spatially, especially at large spatial scales. Soil moisture changes constantly, as a result of precipitation, evaporation processes (which includes extraction by vegetation), and redistribution within the soil. Soil moisture is highly variable at both small and large spatial scales, due largely to the variability of precipitation and the heterogeneity of the land surface (e.g. vegetation, soil physical properties, topography, etc.). While point sampling of soil moisture is generally thought to be the most accurate, the observed value is usually representative only of a relatively small area immediately surrounding the measurement. Subsequent spatial averaging of these measurements, especially at scales up to 10^2 - 10^3 km^2 or larger, will often introduce large errors. Since remotely sensed land surface measurements are already a spatially averaged value, they are a logical input parameter to regional or larger-scale land process models. Regular and improved estimates of soil moisture have been shown to significantly enhance the performance of GCM's and certain mesoscale models, such as flood forecast models [1].

Microwave remote sensing has been used to monitor surface soil moisture with increasing degrees of success. Both ground-based [2-5] and airborne radiometer experiments [6,7] have generally provided good results, largely because of good quality observations of supporting land surface properties such as soil moisture,

Correspondence/Reprint request: Dr. Manfred Owe, Goddard Space Flight Center, S-54967-G, Receiving/Bldg 16W, Code 239, Soil Conservation Road Greenbelt, MD 20771-0001, U.S.A. E-mail: owe@hsb.gsfc.nasa.gov

vegetation, and surface temperature. These experiments are generally supported by intensive soil moisture measuring programs, to ensure optimum spatial representation for comparison. However, satellite-based studies [8-10] have historically been less successful. This is due to a great extent, to a general inadequacy of surface observations at the larger spatial scales. Traditional satellite remote sensing studies have relied heavily on either relatively sparse ground measurements of soil moisture or modelled data, primarily for calibration purposes. These approaches would typically use a radiative transfer model to first solve for the vegetation component, which then would be related to some measurable remote sensing parameter, such as the Normalized Difference Vegetation Index (NDVI).

Recently, however, a number new soil moisture retrieval techniques have been developed. These approaches partition the observed microwave signal into its component parts, and are somewhat unique in that they do not require ground observations of soil moisture or vegetation biophysical properties for calibration purposes. This paper will briefly present some basic microwave theory and then describe the results of several theoretical applied studies which have been conducted during the past several years.

Discussion and conclusions

Efforts to use remote sensing as a more consistent and cost effective method of monitoring the Earth and providing regular observations of various surface and atmospheric parameters has been highly successful. Certain parameters, such as vegetation biomass, snow cover, snow water equivalent, and land use classification, are reported regularly, and often in near real time through operational satellite monitoring programs. In many instances, historical global data-bases have been compiled, and have proven invaluable as validation tools.

Research in the area of microwave remote sensing has lead to important developments in recent years. A combination of field programs and modelling studies have aimed at improving the interpretation of passive microwave observations of the land surface. Developments in inverse modelling techniques have resulted in improved estimates of important land surface parameters such as soil moisture and vegetation canopy properties. Knowledge of vegetation properties such as single scattering albedo and optical depth is important because they tend to mask and distort the microwave signal. Their effect must be removed in order to obtain accurate estimates of soil moisture.

Surface soil moisture is a key factor in the partitioning of incoming radiation at the land surface. It is a common link between the moisture and energy balances, which are the physical bases for land surface modelling. While the importance of soil moisture is largely understood, independent spatial estimates at local to global scales are still largely unavailable. This lack of soil moisture information has had a negative affect on land process modelling efforts.

Passive microwave remote sensing presents the greatest potential for providing this information at regular spatial and temporal scales. Reliable estimates of surface moisture should provide the necessary input for improved predictions of global circulation. Real time estimates should also improve weather and climate modelling efforts, while the development of retrospective data sets will provide necessary information for simulation and validation of long term climate and global change studies. Additional applications of these data include desertification and drought monitoring, agricultural forecasting, and flood potential prediction.

Research results have demonstrated strong potential for deriving soil moisture from C-band microwave systems, and should provide a basis for further development and application of inverse modelling techniques at this frequency. This is especially important, in light of the upcoming launch of the NASA AQUA platform, and since the development of longer wavelength systems is still uncertain for the foreseeable future.

Plans are currently underway, to develop a more than 20-year database of historical global surface soil moisture. Because the Nimbus-7 SMMR data are available only through mid-1987, the data will be extended with Defense Satellite Mapping Program (DSMP) Special Sensor Microwave/Imager (SSM/I) observations from the beginning of August 1987. However, since the lowest frequency on the SSM/I is 19 GHz, which corresponds to a wavelength of only about 1.6 cm. the SSM/I data product will be somewhat degraded. Nevertheless, it should still be useful for hydrological modelling purposes. The dataset will again revert back to C-band, after the launch of the new AQUA satellite, currently scheduled for late 2001. The database will be in the form of daily global maps of soil moisture. Expected errors will be based on the calculated vegetation optical depth. The data product will be made available to the general public, through the Goddard Space Flight Center Distributed Active Archive Center (DAAC).

Hydrologic Data Assimilation with the Ensemble Kalman Filter

ROLF H. REICHLE,* DENNIS B. MCLAUGHLIN, AND DARA ENTEKHABI

Ralph M. Parsons Laboratory, Department of Civil and Environmental Engineering, Massachusetts Institute of Technology, Cambridge, Massachusetts

(Manuscript received 28 December 2000, in final form 22 March 2001)

ABSTRACT

Soil moisture controls the partitioning of moisture and energy fluxes at the land surface and is a key variable in weather and climate prediction. The performance of the ensemble Kalman filter (EnKF) for soil moisture estimation is assessed by assimilating L-band (1.4 GHz) microwave radiobrightness observations into a land surface model. An optimal smoother (a dynamic variational method) is used as a benchmark for evaluating the filter's performance. In a series of synthetic experiments the effect of ensemble size and non-Gaussian forecast errors on the estimation accuracy of the EnKF is investigated. With a state vector dimension of 4608 and a relatively small ensemble size of 30 (or 100; or 500), the actual errors in surface soil moisture at the final update time are reduced by 55% (or 70%; or 80%) from the value obtained without assimilation (as compared to 84% for the optimal smoother). For robust error variance estimates, an ensemble of at least 500 members is needed. The dynamic evolution of the estimation error variances is dominated by wetting and drying events with high variances during drydown and low variances when the soil is either very wet or very dry. Furthermore, the ensemble distribution of soil moisture is typically symmetric except under very dry or wet conditions when the effects of the nonlinearities in the model become significant. As a result, the actual errors are consistently larger than ensemble-derived forecast and analysis error variances. This suggests that the update is suboptimal. However, the degree of suboptimality is relatively small and results presented here indicate that the EnKF is a flexible and robust data assimilation option that gives satisfactory estimates even for moderate ensemble sizes.

1. Introduction

Near-surface soil moisture is a key variable in the atmospheric and hydrologic models that are used to predict weather and climate. Since soil moisture controls the partitioning of moisture and energy fluxes at the land surface, it has an important influence on the hydrologic cycle over timescales ranging from hourly to interannual. Land surface fluxes in turn affect the evolution of vertical buoyancy in the atmospheric column and also affect the baroclinicity that develops in the horizontal plane (Pan et al. 1995; Paegle et al. 1996). The formation and growth of clouds as well as the evolution of precipitating weather systems over land are affected by surface fluxes and surface soil moisture (Shaw et al. 1997). In fact, the timescale of soil moisture anomalies is at least on the order of several days, which is the forecast-lead horizon of operational weather forecasts.

At seasonal to interannual timescales, predictability of climatic variables such as precipitation is dependent on the land surface boundary conditions of the climate system. Koster et al. (2000) show that over the United States and other large continental regions soil moisture rivals sea surface temperature in explaining the variance in seasonal precipitation anomalies. Increasingly soil moisture and the memory associated with it are recognized to have important roles in the feedback mechanisms that intensify and prolong climate anomalies.

Despite the importance of soil moisture in weather and climate prediction there are currently no operational networks of in situ sensors that provide data suitable for these applications. Since such networks are logistically infeasible and prohibitively expensive, the focus has turned to remote sensing techniques that provide additional information about the land surface at large scales. In particular the L-band (1.4 GHz) microwave brightness temperature of the land surface is correlated with surface soil moisture because of the sharp contrast between the dielectric constants of water and soil minerals (Njoku and Entekhabi 1995).

Interpretation of remotely sensed passive and active microwave measurements is complicated by the effects of canopy microwave optical thickness, surface microroughness, and physical temperature. Remote sensing measurements are only one of many data sources that provide valuable information about soil moisture. Precipitation, soil texture, topography, land use, and a variety of meteorological variables influence the spatial distribution and temporal evolution of soil moisture. We can gain additional information from a coupled model of the soil–vegetation–atmosphere system that relates the measured variables to one another and to soil moisture. Yet uncertainties in the forcing data, the heterogeneity of the land surface at various scales, and the nonlinear nature of land–atmosphere interactions limit our ability to accurately model and predict the state of the land surface and the associated fluxes.

Modern data assimilation theory provides methods for optimally merging the information from uncertain remote sensing observations and uncertain land model predictions (Errico 1999; Errico et al. 2000). Among the prior work on large-scale soil moisture assimilation are studies by Bouttier et al. (1993) and Rhodin et al. (1999) who assimilate low-level air temperature and relative humidity to estimate soil moisture. This approach

aims at improving numerical weather prediction and treats soil moisture as a tuning parameter. Houser et al. (1998) focus on the four-dimensional assimilation of in situ observations and soil moisture retrievals. The weak-constraint variational method of Reichle et al. (2001b) yields near-optimal estimates of the land surface states from direct assimilation of microwave observations. Reichle et al. (2001a) prove the concept of optimal downscaling for the case where soil moisture estimates are required at scales smaller than the scale of the microwave observations. They also show that soil moisture can be satisfactorily estimated even if quantitative precipitation estimates are not available.

In this paper we examine the feasibility of using the ensemble Kalman filter (EnKF) for soil moisture data assimilation. The EnKF is an attractive option for land surface applications because (i) its sequential structure is convenient for processing remotely sensed measurements in real time, (ii) it provides information on the accuracy of its estimates, (iii) it is relatively easy to implement even if the land surface model and measurement equations include thresholds and other nonlinearities, and (iv) it is able to account for a wide range of possible model errors. On the other hand, the EnKF relies on a number of assumptions and approximations that may compromise its performance in certain situations.

The EnKF and variants have been successfully applied to meteorological and oceanographic problems of moderate complexity in small- to medium-sized domains (Evensen and van Leeuwen 1996; Houtekamer and Mitchell 1998; Lermusiaux 1999; Madsen and Canizares 1999; Keppenne 2000). Hamill et al. (2000) provide an excellent discussion of the state of the art of ensemble forecasting and assimilation methods in the meteorological and oceanographic context. The models of geophysical flow used in most of these studies are chaotic in nature and typically have dominant modes that can grow rapidly within a certain subspace. Most such models also have an attractor and sample only a small subdomain of their phase space (Anderson and Anderson 1999). This greatly increases the potential to successfully apply ensemble filtering methods. By contrast, typical land surface models are dissipative in nature. Perturbations in the initial conditions tend to die out after a certain time rather than amplify. Consequently, the soil moisture ensemble filtering problem has certain distinctive aspects that merit closer investigation.

This paper evaluates the performance and computational burden of the EnKF for a synthetic experiment. As a benchmark for the EnKF we use a variational method that solves the optimal smoothing problem. We begin in section 2 with a brief review of the EnKF. The benchmark variational method is discussed in the cited references, including (Reichle et al. 2001b). In section 3 we briefly describe the land model and the setup of the synthetic experiments we use to investigate design issues. In section 4 we discuss the results of these experiments and compare the EnKF with the variational method. We conclude in section 5 with a summary of major findings.

5. Summary and conclusions

In this paper, we discuss the application of the ensemble Kalman filter to hydrologic data assimilation and in particular to the estimation of soil moisture from L-band microwave brightness temperature observations. We also compare the performance of the EnKF to an optimal smoother (weak-constraint variational algorithm). Both methods are applied to the same problem and use identical state and measurement equations, error statistics, and synthetically generated measurements. We conclude that with relatively few ensemble members the EnKF yields reasonable soil moisture estimates. For a state vector dimension of 4608 and a relatively small ensemble size of 30 (or 100; or 500), the actual errors in surface soil moisture at the final update time decrease by 55% (or 70%; or 80%) from the value obtained without assimilation (as compared to 84% for the optimal smoother).

The EnKF significantly underestimates the forecast error variances for 100 ensemble members. However, the error variance estimates derived by the filter are reasonably good when the ensemble size is increased to 500 members. Our results indicate that the forecast error variances vary strongly with time and space. This implies that it is very important to account for dynamic error covariance propagation. Assimilation schemes that use static forecast error covariances (e.g., statistical interpolation) are unlikely to produce the desired near-optimal estimates.

More research is required to better understand the EnKF and its variants. In particular, better understanding is needed of the role of nonlinearities and related asymmetries in the conditional forecast probability density function. We have found that nonlinearities in the model and measurement processes contribute to differences in the filtering and smoothing estimates even at the final update. In our application the state (soil moisture) is bounded above and below and its distribution cannot always be well approximated by a Gaussian pdf. For very wet or dry conditions, in particular, the soil moisture pdf exhibits considerable skewness. It is likely that the variational smoother is superior to the EnKF when dealing with nonlinear and non-Gaussian effects. However, it is important to recognize that the variational approach is designed to estimate the mode of the conditional forecast density while the EnKF is designed to estimate the mean. So even if both approaches work as intended their estimates at the end of the smoothing interval can be expected to differ when the density is asymmetric.

In a practical application of the EnKF, it will probably be necessary to model the forecast covariance rather than to compute it in an exact sense. In the EnKF, covariance modeling could include smoothing out the ensemble-derived covariances before the update or applying the update to subregions of the computational domain. Ultimately, a hybrid filter that combines empirical forecast error covariances with dynamic error propagation via the EnKF (Hamill and Snyder 2000) may be the best approach.

Extended versus Ensemble Kalman Filtering for Land Data Assimilation

ROLF H. REICHLE

Goddard Earth Sciences and Technology Center, University of Maryland, Baltimore County, Baltimore, and Hydrological Sciences Branch, NASA Goddard Space Flight Center, Greenbelt, Maryland

JEFFREY P. WALKER

The University of Melbourne, Parkville, Victoria, Australia

RANDAL D. KOSTER AND PAUL R. HOUSER

Hydrological Sciences Branch, NASA Goddard Space Flight Center, Greenbelt, Maryland

(Manuscript received 1 October 2001, in final form 5 April 2002)

ABSTRACT

The performance of the extended Kalman filter (EKF) and the ensemble Kalman filter (EnKF) are assessed for soil moisture estimation. In a twin experiment for the southeastern United States synthetic observations of near-surface soil moisture are assimilated once every 3 days, neglecting horizontal error correlations and treating catchments independently. Both filters provide satisfactory estimates of soil moisture. The average actual estimation error in volumetric moisture content of the soil profile is 2.2% for the EKF and 2.2% (or 2.1%; or 2.0%) for the EnKF with 4 (or 10; or 500) ensemble members. Expected error covariances of both filters generally differ from actual estimation errors. Nevertheless, nonlinearities in soil processes are treated adequately by both filters. In the application presented herein the EKF and the EnKF with four ensemble members are equally accurate at comparable computational cost. Because of its flexibility and its performance in this study, the EnKF is a promising approach for soil moisture initialization problems.

1. Introduction

Climate prediction at seasonal-to-interannual timescales depends on accurate initialization of the slowly varying components of the earth's system, most notably sea surface temperature (SST) and soil moisture. While tropical SST is often the dominant source of predictability, its influence appears to be mostly limited to the Tropics (Koster et al. 2000b). Skill in the prediction of summertime continental precipitation and temperature anomalies in the extratropics may instead depend on the initialization of soil moisture and other land surface states. Since soil moisture controls the partitioning of the latent and sensible heat fluxes to the atmosphere, it can influence precipitation recycling.

The initialization of the land surface states for a seasonal climate forecast can be accomplished by assimilating soil moisture observations into the land model up to the start time of the prediction. With assimilation we attempt to combine the information from the observations and the model in an optimum way. Since for seasonal forecasts we are only interested in the estimates at the start time of the prediction, sequential assimilation methods like Kalman filters are ideally suited to the task. The well-known extended Kalman filter (EKF) can be used for nonlinear applications, but the computational demand resulting from the error covariance integration limits the size of the problem (Gelb 1974). For this reason, the EKF has been used mostly for problems that focus on the estimation of the vertical soil moisture profile (Katul et al. 1993; Entekhabi et al. 1994). More recently, Walker and Houser (2001) have applied the EKF to soil moisture estimation across the North American continent by neglecting all horizontal error correlations and treating surface hydrological units (catchments) independently. This yields an effectively low-dimensional filter.

The ensemble Kalman filter (EnKF) is an alternative to the EKF (Evensen 1994). The EnKF circumvents the expensive integration of the state error covariance matrix by propagating an ensemble of states from which the required covariance information is obtained at the time of the update. Reichle et al. (2002) applied the EnKF to soil moisture estimation and found that it performed well against a variational assimilation method. Since the variational approach generally requires the adjoint of the hydrologic model, which is not usually available and is difficult to derive, the obvious choices for advanced land assimilation algorithms are the EKF and the EnKF. There are many variants of the EKF and the EnKF that have been used in meteorology and oceanography, notably reduced-rank square root algorithms (Verlaan and Heemink 1997), particle filters (Pham 2001), methods that use pairs of ensembles (Houtekamer and Mitchell 1998), and hybrid approaches that combine ensembles with reduced-rank approaches (Heemink et al. 2001; Lermusiaux and Robinson 1999) or with variational methods (Hamill and Snyder 2000). In this paper, we focus on the relative merits of using the traditional EKF and EnKF for soil moisture assimilation.

The major differences between the EKF and the EnKF are (i) the approximation of nonlinearities of the hydrologic model and the measurement process (the EKF uses a linearized equation for the error covariance propagation while the EnKF nonlinearly propagates a finite ensemble of model trajectories), (ii) the range of model errors that can be represented (the EnKF can account for a wider range of model errors), (iii) the ease of implementation (the EKF requires derivatives of the nonlinear hydrologic model, evaluated numerically or from a tangent-linear model), (iv) computational efficiency (it must be determined how many ensemble members are needed in the EnKF to match the performance of the EKF), and (v) the treatment of horizontal correlations in the model or measurement errors (the EKF cannot account for horizontal error correlations in large systems for computational reasons). Insights into many important issues can be gained from low-dimensional versions of both filters.

Although approximate nonlinear filters such as the EKF and the EnKF have been found to work well in some applications, their value in a particular nonlinear problem cannot be assessed a priori but must be determined by simulations (Jazwinski 1970). We investigate the above differences in the context of soil moisture initialization for seasonal prediction using synthetic data in a twin experiment. Since all uncertain inputs are known by design, such experiments are well suited for a first assessment of algorithm performance. Tests with actual observations will be conducted in future studies. For retrospective analysis, surface soil moisture can be retrieved from the Scanning Multifrequency Microwave Radiometer (SMMR) for the period 1979–87 (Owe et al. 2001). These retrievals are derived from the 6.6-GHz (C band) and 37-GHz channels. Similar retrievals should soon be available from the Advanced Microwave Scanning Radiometer for the Earth Observing System (AMSR-E). In the future, passive 1.4-GHz (L band) sensors should also become available (Kerr et al. 2001).

5. Summary and conclusions

In this paper, we compare two promising data assimilation methods for soil moisture initialization in seasonal climate prediction. The extended Kalman filter (EKF) and the ensemble Kalman filter (EnKF) were used to assimilate synthetic surface soil moisture observations into the Catchment Model, with model error parameters calibrated against actual estimation errors. The best results are obtained for both filters when the model error in the root zone excess is large compared to the model errors in the surface excess and the catchment deficit. Using the calibrated filter parameters we find that the EKF and the EnKF produce satisfactory estimates of soil moisture.

The EKF and the EnKF (with four ensemble members) show comparable performance for comparable computational effort. For 10 or more ensemble members, the EnKF outperforms the EKF. This is ascribed to the EnKF's flexibility in representing nonadditive model errors. The actual estimation errors of the EnKF converge quickly with increasing ensemble size, even though the filter-derived (expected) error covariances are noisy for small ensembles. The numerical differentiation scheme used in the EKF requires frequent checks in order to avoid divergent error covariances or loss of positive definiteness. Although these checks interrupt the integration of the error covariances, and information from earlier updates is partially lost, they are not a major source of error.

The normalized innovations are found to be inconsistent with a standard normal distribution. This is because our representation of model errors cannot fully account for the effects of uncertainties in the forcing and imperfectly known model parameters that we use in our twin experiment. Nonlinearities in the land model generate skewness in the distribution of ensemble states. But this skewness information is only very approximately used in the EnKF update and is not available in the EKF. Fortunately, the nonlinearities are not a dominant source of error, because the local linearization strategy of the EKF is for the most part successful and because the nature of the soil moisture bounds limits the actual estimation errors.

Catchment-to-catchment error correlations could arise from large-scale errors in the forcing or from unmodeled lateral fluxes such as river or groundwater flow. Moreover, satellite data are likely to exhibit horizontal error correlations. The present paper compares the EKF and EnKF under the assumption that horizontal error correlations can be neglected. The importance of such correlations is a topic of active research. If horizontal error correlations turn out to be important, information can be spread laterally, in particular from observed to unobserved catchments. When horizontal error correlations are taken into account in the EnKF, small error correlations associated with observations that are far apart must be filtered out (Mitchell and Houtekamer 2000). For computational reasons, the EKF must be approximated using a rank-reduction technique such as the reduced-rank square root method (Verlaan and Heemink 1997).

Before soil moisture assimilation can become a routine tool for seasonal climate prediction, many more questions will need to be addressed. Important areas of research include the investigation of multivariate assimilation using more Catchment Model prognostic variables as states, the direct assimilation of radiances as opposed to soil moisture retrievals, and the assimilation of other types of remote sensing data such as soil temperatures or vegetation parameters. Finally, soil moisture estimates from the assimilation must then be shown to improve the accuracy of seasonal climate forecasts. In summary we can say that the EnKF is more robust and offers more flexibility in covariance modeling (including horizontal error correlations). This leads to its slightly superior performance in our study and makes the EnKF a promising approach for soil moisture initialization of seasonal climate forecasts.

Coastal polynyas in the southern Weddell Sea: Variability of the surface energy budget

Ian A. Renfrew and John C. King
British Antarctic Survey, Cambridge, UK

Thorsten Markus
NASA Goddard Space Flight Center, Greenbelt, Maryland, USA

Received 16 November 2000; revised 13 August 2001; accepted 26 September 2001; published 28 June 2002.

[1] The surface energy budget of coastal polynyas in the southern Weddell Sea has been evaluated for the period 1992–1998 using a combination of satellite observations, meteorological data, and simple physical models. The study focuses on polynyas that habitually form off the Ronne Ice Shelf. The coastal polynya areal data are derived from an advanced multichannel polynya detection algorithm applied to passive microwave brightness temperatures. The surface sensible and latent heat fluxes are calculated via a fetch-dependent model of the convective-thermal internal boundary layer. The radiative fluxes are calculated using well-established empirical formulae and an innovative cloud model. Standard meteorological variables that are required for the flux calculations are taken from automatic weather stations and from the National Centers for Environmental Production/National Center for Atmospheric Research reanalyses. The 7 year surface energy budget shows an overall oceanic warming due to the presence of coastal polynyas. For most of the period the summertime oceanic warming, due to the absorption of shortwave radiation, is approximately in balance with the wintertime oceanic cooling. However, the anomalously large summertime polynya of 1997–1998 allowed a large oceanic warming of the region. Wintertime freezing seasons are characterized by episodes of high heat fluxes interspersed with more quiescent periods and controlled by coastal polynya dynamics. The high heat fluxes are primarily due to the sensible heat flux component, with smaller complementary latent and radiative flux components. The average freezing season area-integrated energy exchange is 3.48×10^{19} J, with contributions of 63, 22, and 15% from the sensible, latent, and radiative components, respectively. The average melting season area-integrated energy exchange is -5.31×10^{19} J, almost entirely due to the radiative component. There is considerable interannual variability in the surface energy budget. The standard deviation of the energy exchange during the freezing (melting) season is 28% (95%) of the mean. During the freezing season, positive surface heat fluxes are equated with ice production rates. The average annual coastal polynya ice production is 1.11×10^{11} m^3 (or 24 m per unit area), with a range from 0.71×10^{11} (in 1994) to 1.55×10^{11} m^3 (in 1995). This can be compared to the estimated total ice production for the entire Weddell Sea: on average the coastal polynya ice production makes up 6.08% of the total, with a range from 3.65 (in 1994) to 9.11% (in 1995). *INDEX TERMS:* 3349 Meteorology and Atmospheric Dynamics: Polar meteorology; 4540 Oceanography: Physical: Ice mechanics and air/sea/ice exchange processes; 4207 Oceanography: General: Arctic and Antarctic oceanography; 4504 Oceanography: Physical: Air/sea interactions (0312); *KEYWORDS:* polynyas, sea ice, Weddell Sea, surface energy budget, surface fluxes, high-salinity shelf water

1. Introduction

[2] Coastal polynyas are regions of open water, or thin ice, formed by offshore winds blowing the sea ice pack out to sea. Their fixed locations provide a focus for wintertime air-sea-ice interactions within the polar regions, as the exposure of belts of relatively warm water to the cold polar atmosphere allows the exchange of vast quantities of heat, cooling the surface ocean and warming the boundary layer of the atmosphere. If the ocean is at freezing point, the cooling results directly in ice production; hence there is a release of latent heat and a rejection of salt as ice is formed. The rejected salt-enriched brine acts as a positive density forcing [e.g., *Curry and Webster*, 1999]. The atmospheric warming leads to changes in boundary layer dynamics, for example, the generation of convective plumes and, in general, an increase in boundary layer winds due to downward momentum transport [e.g., *Dare and Atkinson*, 1999]. The latent heat of fusion released as ice forms within wind-generated polynyas means they are often referred to as "latent heat" polynyas [e.g., *Smith et al.*, 1990].

[3] The impact of coastal polynyas on the ocean is important for several reasons. The fixed location, tied to the coastline and in regions prone to strong wind forcing, means the density forcing of the ocean is also spatially fixed. Indeed, as the air-sea exchange within a polynya is 1 or 2 orders of magnitude greater than through the surrounding sea ice, the local ocean forcing is likely to be dominated by the coastal polynya contribution. In this study we focus

on the coastal polynyas that habitually form off the Ronne Ice Shelf, in the southern Weddell Sea (Figure 1). This is an important region oceanographically as it is in the Weddell Sea that the major portion of Antarctic Bottom Water (the most extensive water mass in the world ocean) is thought to be generated through a number of pathways [e.g., *Foldvik and Gammelsrød*, 1988]. Most of the pathways have as a starting point High Salinity Shelf Water, a dense water mass formed by salinization of Circumpolar Deep Water over the continental shelf. The salinization is caused by the production of sea ice, and as coastal polynyas tend to be located over the continental shelves, they are thought to be the primary production sites of High Salinity Shelf Water.

Figure 1. A map of the southern Weddell Sea region. The study region is marked by the inner rectangle.

6. Conclusions

[51] The surface energy budget of coastal polynyas in the southern Weddell Sea has been investigated through the combination of satellite observations, meteorological data, and simple physical models. The surface energy budget time series are illustrated through Figures 10–15 and Tables 4–7. For coastal polynyas in the freezing season, positive sensible heat fluxes dominate the surface energy budget, with latent and radiative heat fluxes generally augmenting the oceanic cooling. The turbulent heat fluxes are characterized by episodes of high heat fluxes, interspersed with more quiescent periods. Coastal polynya dynamics set the timescales for these changes: strong offshore winds blow open the polynyas, which then refreeze at rates determined by the atmospheric and oceanic conditions. The total wintertime energy exchange is related to the cumulative coastal polynya area (indeed, the turbulent heat fluxes are strongly related); however, the varying atmospheric boundary layer is also important in modifying the fluxes. On average, the total energy exchange is 3.48×10^{19} J, with contributions of 63, 22, and 15% from the sensible, latent, and radiative terms, respectively. The wintertime energy exchange is not related to the length of the freezing season. For coastal polynyas in the melting season the area-integrated fluxes are dominated by the absorption of shortwave radiation. Over the 7 year period from 1992 to 1998 the ocean warms more than it cools through the presence of coastal polynyas. In particular, the anomalous summertime open water area of 1997–1998 allowed an enormous area-integrated warming of the ocean.

[52] During the freezing season, positive surface heat fluxes have been equated with ice production rates. The mean average coastal polynya ice production per unit area is 24.0 m, with a range from 15.6 (in 1998) to 31.7 m (in 1992). In terms of total annual coastal polynya ice production the mean is 1.11×10^{11} m^3 with a range from 0.71×10^{11} (in 1994) to 1.55×10^{11} m^3 (in 1995). The interannual variability is large: the standard deviation is 28% of the annual mean. Ice production has roughly a normal distribution over the freezing season, with strong modifications due to the episodic nature of the time series, for example, coastal polynya opening episodes may span a couple of months. These ice production calculations are compared to estimates of the ice production in the entire Weddell Sea from passive microwave data and an assumed average ice thickness of 0.5 m. The mean coastal polynya ice production is 6.08% of the entire Weddell Sea ice production, although this ratio varies from 3.65 (in 1994) to 9.11% (in 1995). The total annual Weddell Sea ice production does not vary that much: the standard deviation is only 5% of the mean. Hence variability in the ratio is determined primarily by changes in the coastal polynya ice production.

[53] An estimate of the accuracy of these results can be made through a comparison of the 1998 AWS and NCEP surface energy budgets. In the mean the components match remarkably well (to within 10 W m^{-2}). The correlation coefficients are over 0.75, and the linear regression slopes are over 0.8. The differences in mean monthly ice production are 8% over the whole year but only 2% if the anomalous months of February and March 1998 are ignored. This suggests that the use of the NCEP model data is well founded. For example, we would expect the time series to be accurate to within ~5% in terms of annual ice production. In addition to this however, there will be errors associated with (1) the determination of the sea ice cover, (2) the representativeness of the meteorological data, (3) the neglected physical processes in the CIBL model, and (4) the use of simple formulae for the radiative terms. We would estimate absolute errors associated with the above to be of the order 20%, in terms of the annual ice production, for example, but much less than that, of order 10%, when examining the interannual variability within the climatology. We are therefore confident that the interannual variability described here is genuine.

[54] A number of directions for future research have become apparent during this study. The transformation of this surface energy budget into an oceanic buoyancy forcing is one objective of future work. To do this will involve the assessment of a number of physical processes that affect both the heat flux and, in particular, the freshwater flux, for example, precipitation, blowing snow deposition, ice shelf melt, and changes inthe oceanographic conditions. The buoyancy forcing is a key ingredient for ongoing studies of sub–ice shelf oceanography and bottom water formation [*Nicholls and Makinson*, 1998; *Comsio and Gordon*, 1998], and so, a study along these lines is planned.

A Parameterized Surface Reflectivity Model and Estimation of Bare-Surface Soil Moisture With L-Band Radiometer

Jiancheng Shi, *Senior Member, IEEE*, K. S. Chen, *Senior Member, IEEE*, Qin Li, Thomas J. Jackson, *Fellow, IEEE*, Peggy E. O'Neill, and Leung Tsang, *Fellow, IEEE*

***Abstract*—Soil moisture is an important parameter for hydrological and climatic investigations. Future satellite missions with L-band passive microwave radiometers will significantly increase the capability of monitoring earth's soil moisture globally. Understanding the effects of surface roughness on microwave emission and developing quantitative bare-surface soil moisture retrieval algorithms is one of the essential components in many applications of geophysical properties in the complex earth terrain by microwave remote sensing. In this study, we explore the use of the integral equation model (IEM) for modeling microwave emission. This model was validated using a three-dimensional Monte Carlo model. The results indicate that the IEM model can be used to simulate the surface emission quite well for a wide range of surface roughness conditions with high confidence. Several important characteristics of the effects of surface roughness on radiometer emission signals at L-band 1.4 GHz that have not been adequately addressed in the current semiempirical surface effective reflectivity models are demonstrated by using IEM-simulated data. Using an IEM-simulated database for a wide range of surface soil moisture and roughness properties, we developed a parameterized surface effective reflectivity model with three typically used correlation functions and an inversion model that puts different weights on the polarization measurements to minimize surface roughness effects and to estimate the surface dielectric properties directly from dual-polarization measurements. The inversion technique was validated with four years (1979–1982) of ground microwave radiometer experiment data over several bare-surface test sites at Beltsville, MD. The accuracies in random-mean-square error are within or about 3% for incidence angles from 20° to 50°.**

***Index Terms*—L-band radiometer, soil moisture, surface emission.**

I. Introduction

SOIL MOISTURE is a key parameter in numerous environmental studies, including hydrology, meteorology, and agriculture. Previous investigations have established the fundamentals of passive microwave remote sensing as an important tool in determining the physical properties of soils [1]–[8]. The ability to estimate soil moisture in the surface layer to an approximately 5-cm depth by microwave remote sensing at 1.4 GHz has been demonstrated under a variety of topographic and land cover conditions. Application of microwave retrieval of soil moisture to hydrological and meteorological sciences has been influenced by the natural variability and complexity of the vegetation canopy and surface roughness that significantly affect the sensitivity of emission measurements to soil moisture. At high frequencies (C-band or higher), it is well understood that the instrument's ability to monitor soil moisture is limited by vegetation cover. At lower frequencies, this problem can be greatly reduced. Two possible future spaceborne L-band multipolarization passive microwave techniques—two-dimensional synthetic aperture interferometry [5], [8] and filled-aperture mesh deployable reflectors [9]—will significantly increase the capability of monitoring earth's soil moisture globally. In addition to operating at long wavelengths, these multipolarization instruments provide an opportunity to utilize multiple polarization data in the estimation of soil moisture. The full utilization of these data will require a further understanding of surface roughness effects on the emission signals, especially on the relationships of the emission signals at different polarizations, in order to develop a quantitative algorithm for global soil moisture mapping.

The surface reflectivity model is one of the essential components in many applications of microwave remote sensing of geophysical properties in complex earth terrain. It is a direct component in monitoring soil moisture in bare or vegetated surfaces and serves as the boundary condition in studying snow, vegetation, and atmospheric properties. Currently, there are two types of approaches used to model surface reflectivity:

1) *semiempirical approach:* this type of model is generally found to be easy to use without significant computing efforts and is generally easy to implement as an inversion model;
2) *physical modeling approach:* the surface reflectivity can be obtained by integrating the bistatic scattering coefficient over the upper hemisphere [10].

The most commonly used semiempirical model that describes the bare-surface emission as a function of the surface roughness and dielectric properties is the so-called Q/H model [11], [12]. The parameter Q describes the energy emitted in orthogonal polarizations due to surface roughness effects. H is a measure of the effect of surface roughness to increase surface emissivity. However, it has been recognized that there can be a great difference between the direct physical measurements of surface roughness in the field and those derived by fitting the Q/H model with observed soil moisture or dielectric constant measurements [13], [14]. Commonly, the surface roughness parameter in the Q/H model has to be determined empirically from the experiment data and often is called "effective roughness." This is an inconvenient technique to apply in either the forward calculation to relate the soil moisture with microwave radiometer measurements or the inverse calculation, since there are no quantitative relationships between the empirical roughness parameter and the commonly used measurable surface roughness characteristics such as the root-mean-square (rms) height s, the autocorrelation length l, and the autocorrelation function.

Attempts to improve understanding of the effects of surface roughness and how traditional surface roughness parameters can

be directly related to emission signals have resulted in the development of several surface reflectivity models. In comparison with the Q/H model, all of these models determined that the Q parameter is not very important [14]–[17]. Depending on the empirical data sources and the techniques used to develop the reflectivity models, the H parameter can have a variety of different forms.

- Mo and Schmugge [15] simulated the effects of surface roughness on the effective surface reflectivity using the Kirchhoff model and compared L- and C-band measurements from three field sites with different roughness conditions. They found that the H parameter depends on soil moisture and the ratio of s/l and that it varies with the incidence angle and polarization.
- Saatchi *et al.* [16] used the traditional surface scattering models—small perturbation model, physical optical model, and geometric optical model—to simulate the effect of surface roughness for horizontal (H) polarization and compared the results with experimental data over a frequency range of 1–12 GHz. A parameterized reflectivity model was developed with two (coherent and noncoherent) components. Unfortunately, vertical (V) polarization was not studied.
- Wegmüller and Mätzler [14] developed an empirical rough-surface reflectivity model using ground radiometer measurements with frequencies ranging from 1–100 GHz and with incidence angles of 20° to 70°. The reported accuracies of the surface reflectivity in terms of the random-mean-square errors (rmse) were 0.095 and 0.061 for H and V polarizations, respectively. This level of accuracy is about 20% of the dynamic range of the surface emission response to soil moisture.
- Wigneron *et al.* [17] also developed an empirical rough-surface reflectivity model using experimental measurements over seven different roughness conditions at L-band 1.4 GHz and incidence angles $\leq$ 40°. The reported accuracy for the surface reflectivity was 0.031 (rmse). This study concluded that the H parameter is independent of both incidence angle and polarization.

VII. Conclusion

Understanding the effects of surface roughness on microwave emission and developing quantitative bare-surface soil moisture retrieval algorithms are essential to many applications of geophysical properties in complex earth terrain by microwave remote sensing. In this study, we first validated the IEM model with a highly accurate but complex 3-D Monte Carlo model. A comparison showed that the IEM model slightly overestimates the emissivity for V polarization with rmses of 0.008 and 0.013 at 40° and 50° incidence angles, respectively. For H polarization, the errors were more random with rmses of 0.01 and 0.017 at 40° and 50°. The results indicate that the IEM model can be used to simulate the surface emission quite well for a wide range of surface roughness and conditions.

Then, we used an IEM model to simulate a database with a wide range of surface roughness and dielectric conditions. Using the IEM-simulated data, we demonstrated several important characteristics of surface roughness effects on microwave emission signals that were not incorporated in currently used surface effective reflectivity models. It was found that the effects of surface roughness on microwave emission signals at V and H polarization might be different in both magnitude and direction, depending on the incidence angle, surface roughness, and dielectric properties. The overall effect of surface roughness can be explained by the combined effects from two components: the coherent component that decreases as the surface roughness increases and the noncoherent component that increases as the roughness changes. As a result, the total reflected energy may have two outcomes when comparing rough and flat surfaces. If the amount of reduction in the coherent component of the reflected energy is greater than the increase in noncoherent scattering, surface roughness reduces the effective reflectivity. This represents all cases for H polarization at all incidence angles. However, when the amount of the reduction in the coherent component of the reflected energy is less than the increase in the noncoherent scattering, surface roughness actually increases the effective reflectivity. This only occurs in V polarization. As a result, the surface effective reflectivity in V polarization could be greater than its corresponding Fresnel reflectivity depending on the incidence angle, surface roughness, and dielectric properties. This also impacts roughness effects on the polarization ratio V/H measurements. These two important characteristics have been not incorporated in the currently available semiempirical surface effective reflectivity models.

We developed a surface effective reflectivity model for L-band (1.4 GHz) utilizing both V and H polarizations and three typical correlation functions (gaussian, 1.5-power, and exponential) by parameterizing the IEM model simulated data for a wide range of surface soil moisture and roughness properties. When compared to the IEM model simulated data, the parameterized model in (4) has the accuracy (rmse) better than 0.01 for V polarization at all incidence angles with the best accuracy (0.0035) at 40°. For H polarization, the accuracy increases as the incidence angle increases with the worst accuracy (0.011) at 20° and the best accuracy (0.0028) at 60°. These results indicate that the parameterized model can reproduce the IEM model predictions over a wide range of surface roughness conditions.

Using the IEM model simulated database for a wide range of surface soil moisture and roughness properties, we developed an inversion model that uses dual polarization measurements to minimize surface roughness effects and to estimate surface dielectric properties directly. For the IEM model simulated data, the algorithm in (8) has an accuracy of 1.68% at 20°. The accuracy increases as the incidence angle increases. The best accuracy can be seen at 45° with 0.55%. Validation of this inversion technique with ground microwave radiometer experiment data indicated that there was an overall trend for soil moisture underestimation in the algorithm performance. However, all rmses are within or about 3% for incidence angle between 20° and 50°.

Influence of Microphysical Cloud Parameterizations on Microwave Brightness Temperatures

Gail M. Skofronick-Jackson, *Member, IEEE*, Albin J. Gasiewski, *Senior Member, IEEE*, and James R. Wang, *Senior Member, IEEE*

***Abstract*—The microphysical parameterization of clouds and rain cells plays a central role in atmospheric forward radiative transfer models used in calculating microwave brightness temperatures. The absorption and scattering properties of a hydrometeor-laden atmosphere are governed by particle phase, size distribution, aggregate density, shape, and dielectric constant. This study investigates the sensitivity of brightness temperatures with respect to the microphysical cloud parameterization. Calculated wideband (6–410 GHz) brightness temperatures were studied for four evolutionary stages of an oceanic convective storm using a five-phase hydrometeor model in a planar-stratified scattering-based radiative transfer model. Five other microphysical cloud parameterizations were compared to the baseline calculations to evaluate brightness temperature sensitivity to gross changes in the hydrometeor size distributions and the ice–air–water ratios in the frozen or partly frozen phase. The comparison shows that enlarging the raindrop size or adding water to the partly frozen hydrometeor mix warms brightness temperatures by as much as 55 K at 6 GHz. The cooling signature caused by ice scattering intensifies with increasing ice concentrations and at higher frequencies. An additional comparison to measured Convection and Moisture Experiment (CAMEX-3) brightness temperatures shows that in general all but two parameterizations produce calculated T_Bs that fall within the CAMEX-3 observed minima and maxima. The exceptions are for parameterizations that enhance the scattering characteristics of frozen hydrometeors.**

***Index Terms*—Clouds, electromagnetic scattering, millimeter wave radiometry, rain, remote sensing, snow.**

I. Introduction

OVER the past four decades, significant effort has been devoted to understanding the microphysical cloud characteristics of convective storms (e.g., [1]–[3]). The microphysics of clouds is of considerable interest in a wide range of interdisciplinary studies. These studies include improving global climate models for understanding climate variability, investigating the role of hydrometeors in lightning generation, examining chemical interactions and rain evolution in clouds for pollution research, studying radar and lidar remote sensing applications, and developing precipitation parameter retrievals from satellite-based passive microwave imagery.

Of interest here is improving our understanding of the relationships between the microphysics of hydrometeors in a convective storm and the upwelling microwave brightness temperatures for the purposes of rain rate and precipitation parameter retrieval. A comprehensive understanding of these relationships is hindered by the lack of accurate and sufficiently detailed atmospheric microphysical profile truth [4], [5]. Difficulties in obtaining microphysical cloud profile truth for convective systems stem from limitations in remotely sensed measurements, aircraft sampling capabilities, and the extremely inhomogeneous and complex nature of convection [6], [7]. The dynamics of convection complicate the *in situ* measurements of hydrometeor size, shape, total water content and the ice–air–water ratio, and Nyquist spatial and temporal sampling of these quantities remains a formidable challenge.

A microphysical cloud parameterization used in radiative transfer models requires specifying the size distributions and ice–air–water ratios for each hydrometeor type at each atmospheric level along with vertical profiles of temperature, relative humidity, and pressure. Parameterizations have been developed using statistics from physical models of particle growth and coalescence as well as knowledge from limited *in situ*, radar, and lidar observations. Early cloud parameterizations (e.g., [8]) used in radiative transfer models allowed for a uniform rain layer and separate cloud water layer with no ice particles. Later models added an ice layer (e.g., [9]–[12]).

Contemporary microphysical cloud parameterizations allow for multiple liquid and ice phases (e.g., [2], [4], [13], [14]). Several research studies have indicated that five hydrometeor phases adequately represent a convective storm [5], [15] from the standpoint of passive microwave signatures. The five hydrometeor phases are generally classified as cloud water, rain drops, cloud ice, snow (or ice aggregates), and graupel (including hail). The rain drops are commonly modeled by the Marshall–Palmer (MP) [16] size distribution. However there appear to be no universally accepted size distribution parameterizations or ice–air–water ratios for the other four hydrometeor types [6]. In general, the microphysical parameterizations used by radiative transfer modelers are appropriate for only specific storm occurrences.

As satellite passive microwave sensing of rain rate and other precipitation parameters (e.g., cell top altitude, see [17]) matures, it is important to understand the impact of the various common hydrometeor parameterizations on the upwelling microwave brightness. Accordingly, the purpose of this work is to study the sensitivity of computed microwave brightness temperatures to changes in the microphysical parameters. The analysis of these changes is facilitated using wideband microwave aircraft data. Since identifying the best parameterization requires detailed collocated and coincident *in situ*, radar, and radiometer observations, we instead focus on identifying a plausible class of parameterizations. Indeed, cloud parameterizations are case specific. The work of [18] and [19] are two examples where parameterizations that best match case-specific radiometer observations have been determined. Even though an optimal parameterization cannot be identified in this study, inappropriate and unrealistic parameterizations can be identified and avoided in future work.

In studying microphysical cloud parameterizations and their effect on computed brightness temperatures, a planar-stratified atmosphere and a midlatitude oceanic surface are assumed. The simple planar model is adequate for all but the most localized cumuluform convection. The highly reflective oceanic background is more uniform and provides greater sensitivity to hydrometeor scattering and absorption than would a land background, and thus represents the more conservative of the two backgrounds. For comparison purposes, four cloud profiles are selected to represent the early cumulus, evolving, mature, and dissipating stages of a convective storm. Six microphysical cloud parameterizations were selected for use in evaluating brightness temperature sensitivities to the hydrometeor size parameters, and frozen particle ice–air–water ratios. A five-hydrometeor-phase (cloud water, rain, cloud ice, dry snow, and dry graupel) parameterization is considered to be the baseline case. Brightness temperatures at twelve frequencies (6.0, 10.69, 18.7, 23.8, 36.5, 89.0, 150.0, 183.31 + 7.0, 220.0, 325 + 8.0, 340.0, and 410.0 GHz) were computed for each of the four cloud stages and six parameterizations using the planar-stratified scattering-based radiative transfer model of [11]. We discuss herein the variations in brightness temperature values when the microphysical cloud parameterization is changed in the radiative transfer calculations.

While convective storms under different prevailing conditions (e.g., tropical, midlatitude, maritime, or continental) have differing hydrometeor characteristics, this study nonetheless identifies several issues. First, in order to select the proper parameterization for any specific condition, one requires a set of detailed atmospheric truth profiles along with a collocated and coincident set of brightness temperature observations. Second, we show the sensitive relationship between the brightness temperature and the underlying hydrometeor profile. In identifying these issues we first briefly describe the radiative transfer model and calculations, including the ocean surface and top-of-atmosphere conditions. Dielectric mixing theory for heterogeneous snow and graupel particles is outlined. Section III details the six microphysical cloud parameterizations. The comparison among the six parameterizations (Section IV) and to the aircraft data (Section V) is described with a summary in Section VI.

VI. Summary

Brightness temperatures at twelve frequencies between 6.0 and 410.0 GHz were computed for four storm stages obtained from the simulated GCE model set of [36]. The four profiles used in the comparison represent a convective storm in its early cumulus, evolving, mature, and dissipating stages. The investigation illustrates how specific microphysical cloud parameterizations can affect oceanic microwave brightness temperatures.

The densities of the five hydrometeor types of the GCE data were mapped into six different microphysical cloud parameterizations. The parameterizations were designed to evaluate brightness temperature sensitivity to particle size distributions and ice–air–water ratios. A comparison among the six parameterizations, four convective storm stages, and twelve frequencies was performed. A five hydrometeor-phase parameterization [2], [13] was considered as the baseline case.

The comparisons generally showed that increasing the emphasis of water or rain warmed the brightness temperatures. When the size distribution of rain was changed to that of the Joss *et al*. thunderstorm size distribution (which favors larger particle diameters), the T_B values at 6 GHz were warmed by up to 55 K. At 18 and 23.8 GHz the larger-sized Joss particles initiate liquid scattering more so than the smaller-sized MP size distribution, resulting in a small T_B cooling. From 10.69 GHz to 36.5 GHz, a transition from mostly absorptive (characterized by warmer T_B values) to mostly scattering (characterized by cooler T_B values) occurs. At stage C (the early cumulus profile), a change from having the coolest T_B at 10.69 GHz for all parameterizations and pixels (because there is little absorptive warming) to having the warmest T_B values at 36.5 GHz (because there is little scattering) occurs. Above 36.5 GHz changes in the raindrop size distribution initiated no differences in the T_B values with respect to the five-phase model due to the strong scattering signatures of storm-top ice at these higher frequencies. Adding liquid water to the snow and graupel hydrometeors caused absorptive warming at the low and middle frequencies.

From 89 GHz to 220 GHz the scattering signature is stronger than the absorptive warming signature. The comparison showed that the cooling signature due to ice scattering at higher frequencies was increased with larger ice concentrations. The ice concentration rose when additional ice was allocated to the ice–air–water ratio. Above 220 GHz the T_B variability among all six parameterizations and four stages was reduced. The compression was caused by an increasing sensitivity to hydrometeor size as wavelength decreased. This increasing sensitivity caused an increased opacity at the higher frequencies.

Finally, a comparison of the calculated T_B values with available observed T_B values from the CAMEX-3 experiment showed reasonable agreement for most stages and parameterizations. Exceptions occurred for the doubled ice-ratio parameterization and the two-phase parameterization. These two parameterizations consistently yielded T_B values outside the range of the observed minima and maxima, indicating that they are less physically realistic than the others. Another interesting feature is that the 220 and 340 GHz T_B calculations are well within the minima and maxima of the observations, thus providing an argument for increasing the diversity and complexity of frozen hydrometeors in models of convective cloud profiles. (The parameterizations used herein do not provide enough diversity at these frequencies.) Finally, there are a few stages/parameterizations/frequencies whose calculations do not fall within the observed minima and maxima. These few inconsistent cases could mean that the clouds were inadequately categorized into cumulus, evolving, mature, and/or dissipating stages or that the parameterizations are not modeling the true cloud microphysics for all cases. A detailed coincident set of T_B observations and *in situ* PSD measurements might be used to further refine cloud microphysical parameterizations.

Direct estimation of sea state impacts on radar altimeter sea level measurements

D. Vandemark
NASA/Goddard Space Flight Center, Wallops Island, Virginia, USA

N. Tran[1] and B. D. Beckley
Raytheon/ITSS, Greenbelt, Maryland, USA

B. Chapron
IFREMER/Centre de Brest, Plouzané, France

P. Gaspar
Collecte Localisation Satellites, Ramonville, France

Received 1 July 2002; accepted 9 September 2002; published 17 December 2002.

[1] A new sea state bias modeling approach is presented that makes use of altimeter-derived marine geoid estimates. This method contrasts with previous models that require differencing between repeat altimeter passes for SSB isolation, along with complex bivariate inversion, to derive a relation between wind speed, wave height and SSB. Here one directly bin-averages sea height residuals over the wind and wave correlatives. Comparison with the most current nonparametric repeat-pass model shows close agreement and provides a first validation of this simpler and more direct technique. Success is attributed mainly to extensive space and time averaging. Ease in implementation and benefits in working with absolute levels provide much appeal. Further advantages and potential limitations, centered on the need to effectively randomize large sea level anomaly components to expose the bias, are also discussed. *INDEX TERMS:* 1640 Global Change: Remote sensing; 4275 Oceanography: General: Remote sensing and electromagnetic processes (0689); 4504 Oceanography: Physical: Air/sea interactions (0312); 6959 Radio Science: Radio oceanography; 4215 Oceanography: General: Climate and interannual variability (3309). **Citation:** Vandemark, D., N. Tran, B. D. Beckley, B. Chapron, and P. Gaspar, Direct estimation of sea state impacts on radar altimeter sea level measurements, *Geophys. Res. Lett.*, *29*(24), 2148, doi:10.1029/2002GL015776, 2002.

1. Introduction

[2] The SSB in a satellite altimeter's range measurement results in a sea level estimate that falls below the true mean. Modeled SSB correction uncertainty is thought to be 1.5–2 cm on average and can exceed 5 cm in high seas [*Chelton et al.*, 2001].

[3] A location's sea surface height (SSH) measurement, uncorrected for SSB, contains the geoid signal (h_g), the ocean dynamic topography (η), the SSB, and other measurement and correction factors (w):

$$SSH = h_g + \eta + SSB + w. \tag{1}$$

SSB modeling normally begins by eliminating the dominant marine geoid signal from equation (1) by differencing precise repeat measurements either along collinear tracks [*Chelton*, 1994] or at orbit crossover points [*Gaspar et al.*, 1994]. Repeating altimeter measurements typically occur within 3–17 days, thus longer-term variance in the large η term is also removed. Using the two additional radar altimeter products, radar cross section-derived wind speed (U) and significant wave height (SWH), SSB estimation relates time-dependent range differences to corresponding wave height and wind speed differences.

[4] While relatively successful, the development of empirical SSB models based on repeat-pass differences presents several limitations [*Gaspar et al.*, 2002]. Key among these is the need to develop a nonparametric model function to resolve nonlinearities obscurred within standard regression techniques operating on differenced data. In addition, residual error analysis can only be performed in the space of the differenced variables. Further, large amounts of data and complex, numerically-optimized inversions are also required to properly develop such a model.

[5] Another approach is to solve for SSB directly by imposing a constant *a priori* mean sea level at each altimeter observation location thus eliminating the geoid. While substantial errors residing within equation (1) discouraged this approach in the past, the TOPEX/Poseidon mission has now provided ten years of precise measurements along the same 254 ground tracks across the global ocean. This paper provides a preliminary demonstration of this approach using TOPEX data.

2. Methods

[6] Following equation (1), a long-term average for the sea surface at any referenced location k on an altimeter's ground track can be written as:

$$MSS_k = \left(h_g + \langle\eta\rangle + \langle SSB - SSB_{\mathrm{m}}\rangle + \langle w\rangle\right)_k \tag{2}$$

where $\langle\rangle$ denotes the expectation computed over a given time period. SSB_m are the model-derived sea state range corrections employed in this surface determination, and w comprises all other error components (e.g. in sensor range corrections, interpolation errors, orbit, tides, atmospheric terms, etc. . .) built into the mean sea surface MSS_k estimate. Equation (2) assumes independence between source terms.

[7] An individual height residual, $\Delta h_k = SSH_k - MSS_k$, used in SSB estimation is thus:

$$\Delta h_k = (SSB + (\eta - \langle\eta\rangle) - \epsilon_{SSB} + (w - \langle w\rangle))_k \quad (3)$$

where $\epsilon_{SSB} = \langle SSB - SSB_m\rangle$ at any k defines the time-independent SSB modeling error within MSS_k. Note that the many realizations forming every MSS_k and ϵ_{SSB} differ from the arbitrary sample denoted in equation (3). Next, let dynamic sea level variability $(\eta - \langle\eta\rangle)$ be joined with $(w - \langle w\rangle)$ to form a noise term ϵ. By design, the geoid term cancels out to give:

$$\Delta h_k = (SSB + \epsilon_{SSB} + \epsilon)_k \quad (4)$$

Error terms on the right side of the equation depend upon the quality of the estimates used to build MSS_k including, to some extent, the accuracy of the SSB model(s) used.

[8] An empirical bivariate SSB model is readily built by defining MSS_k globally and then computing the mean height bias at discrete bins across the (U, SWH) domain. Each bin holds the average over height residuals for all locations (k, ij), meeting the condition that altimeter-derived wind and wave height estimates fall within a (U_i, SWH_j) bin having width (ΔU, ΔSWH), given as:

$$SSB(U_i, SWH_j) = \langle (SSH_{ij} - MSS)_k \rangle \quad (5)$$

The ϵ terms are dropped in equation (5) under a tentative assumption of weak dependency on sea state effects and assumed convergence of η and w terms towards zero mean values under long-term global averaging.

[9] Implementing this formula using TOPEX NASA altimeter (TOPEX hereafter) data is straightforward. The sea surface height residuals used are interpolated, georeferenced values computed along the TOPEX track using an established mean sea surface [*Wang*, 2001]. This surface merges multiple years and several satellite mission data sets (TOPEX, ERS, and Geosat) along the mean tracks of TOPEX [*Koblinsky et al.*, 1998], spanning a time period from 1986 to 1999. The large time period and number of repeat measurements lead to precise geoid determinations along the TOPEX track. This provides not only a reference mean sea level for oceanic studies, but also a low noise *MSS* along the altimeter's ground track that was not available in past SSB investigations.

[10] Prior to computing Δh_k, TOPEX measurements are corrected for all geophysical and instrumental effects and the original SSB (version 2.0 algorithm [*Gaspar et al.*, 1994]) is removed from each height estimate. These estimates are given at 1-s along-track intervals (~every 6 km) and interpolated to fixed georeferenced track locations. All Poseidon-1 altimeter and any erroneous (using conventional data quality flagging) TOPEX estimates are eliminated. Pairing of the NASA/GSFC Altimeter Pathfinder dataset with both TOPEX radar cross section σ_0 and *SWH* data is accomplished using the same georeferencing interpolation. The 10-m wind speed is calculated from σ_0 using the modified Chelton and Wentz algorithm [*Witter and Chelton*, 1991]. One 10-day TOPEX cycle of pathfinder data prepared in this manner provides 350,000–400,000 samples. For direct comparison to the most current SSB model [*Gaspar et al.*, 2002] (NP02 hereafter), cycles 21–131, April 1993–April 1996, are examined. The number of samples used in this 3-year average exceeds forty million. For demonstrations here, data are not spatially subsampled to insure independence. Data set size would contract by a factor of 7–10 with such sampling. By comparison, the NP02 crossover set contains 633,000 points for the same period.

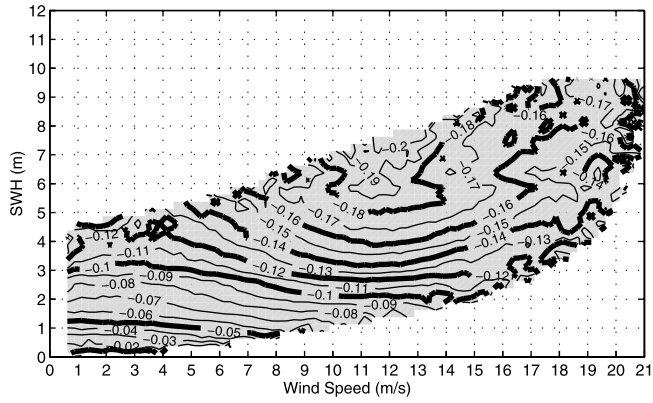

Figure 1. Isolines for the global TOPEX SSB estimate (in meters) obtained from bin-averaging into boxes of width (0.25 m/s, 0.25 m) over the (U, SWH) domain.

4. Conclusion

[18] This is the first reported direct (non-differenced) realization of on-orbit altimeter SSB impacts. The technique relies upon averaging over a numerous realizations to isolate the small SSB signature. Results from a 3-year global average mirror that obtained using satellite crossover differences and subsequent nonparametric model inversion. It is also shown that an accurate SSB estimate can be obtained over most of the altimeter-derived (U, SWH) domain with as little as 100 days of data, a substantial improvement. Direct intercomparison corroborates two separate empirical TOPEX SSB derivations, but observed mm-level offsets and estimate differences for infrequently observed locations in the (U, SWH) domain highlight the need for future refinement.

[19] There is no question that this direct method is simpler to implement from numerous perspectives, foremost the avoidance of complex and numerically-intensive nonparametric inversion. Moreover, one is now working directly with the height residual and its correlatives, rather than time-dependent differences in all terms. These points, among others, suggest the benefit that direct assessment may have in speeding studies to evaluate the relative importance of additional characteristics of sea state beyond altimeter-derived (U, SWH). For instance, direct regression of TOPEX height residuals against global model-derived long wave products, unobtainable using the altimeter, are in progress and may identify remaining SSH variance. Further, the sparse time-sampling approach of Figure 2a can also be applied spatially, where basin-scale evaluation of the sea state impacts now becomes more tractable. It is also likely that this SSB methodology is applicable to altimeters aboard ERS, Envisat, or Geosat Follow-On platforms with use of an appropriate mean surface reference.

Ocean-color optical property data derived from the Japanese Ocean Color and Temperature Scanner and the French Polarization and Directionality of the Earth's Reflectances: a comparison study

Menghua Wang, Alice Isaacman, Bryan A. Franz, and Charles R. McClain

We describe our efforts to study and compare the ocean-color data derived from the Japanese Ocean Color and Temperature Scanner (OCTS) and the French Polarization and Directionality of the Earth's Reflectances (POLDER). OCTS and POLDER were both on board Japan's Sun-synchronous Advanced Earth Observing Satellite from August 1996 to June 1997, collecting approximately 10 months of global ocean-color data. This operation provided a unique opportunity for the development of methods and strategies for the merging of ocean-color data from multiple ocean-color sensors. We describe our approach to the development of consistent data-processing algorithms for both OCTS and POLDER and the use of a common *in situ* data set to calibrate vicariously the two sensors. Therefore the OCTS- and POLDER-measured radiances are bridged effectively through common *in situ* measurements. With this approach to the processing of data from two different sensors, the only differences in the derived products from OCTS and POLDER are the differences that are inherited from the instrument characteristics. Results show that there are no obvious bias differences between the OCTS- and POLDER-derived ocean-color products, whereas the differences due to noise, which stem from variations in sensor characteristics, are difficult to correct at the pixel level. The ocean-color data from OCTS and POLDER therefore can be compared and merged in the sense that there is no significant bias between two.
© 2002 Optical Society of America
OCIS codes: 010.0010, 280.0280, 010.4450.

1. Introduction

The Japanese Ocean Color and Temperature Scanner (OCTS)[1] and French Polarization and Directionality of the Earth's Reflectances (POLDER)[2] were both flown on the Japanese Sun-synchronous Advanced Earth Observing Satellite (ADEOS) from August 1996 to June 1997, collecting about 10 months of global ocean color data. ADEOS was on a polar orbit at an altitude of 800 km with local crossing time (descending node) at around 10:40 am. This was the first time in history that two ocean-color sensors were on board the same platform and viewed the global ocean with the same temporal and similar global spatial coverages. Therefore the operation provides an ideal case for studying and comparing ocean-color data that is derived from two different sensors, hence allowing the development of a strategy for a ocean-color data merger from multiple ocean-color sensors. The primary goal of the National Aeronautics and Space Administration Sensor Intercomparison and Merger for Biological and Interdisciplinary Oceanic Studies (SIMBIOS) project is to develop methods for the meaningful comparison and merging of data products from multiple ocean-color missions.[3] In a recent study, Wang and Franz[4] show that, using a vicarious intercalibration approach between the modular optoelectronic scanner (MOS)[5] and the Sea-viewing Wide Field-of-View Sensor (SeaWiFS)[6,7] (SeaWiFS ocean color data were used as "truth"), one can meaningfully compare the ocean optical property data derived from two sensors. The bias differences

M. Wang (wang@simbios.gsfc.nasa.gov), A. Isaacman, B. A. Franz, and C. R. McClain are with the National Aeronautics and Space Administration Goddard Space Flight Center, Greenbelt, Maryland 20771. M. Wang is also with the University of Maryland—Baltimore County, Baltimore, Maryland 21210. A Isaacman and B. A. Franz are also with the Science Applications International Corporation General Sciences Corporation, Beltsville, Maryland 20705.

Received 7 March 2001; revised manuscript received 19 September 2001.
0003-6935/02/060974-17$15.00/0
© 2002 Optical Society of America

are reduced significantly between the two products. In the Wang–Franz study,[4] measurements from the two sensors had a temporal difference of about 90 min. In this paper, we compare the ocean-color data derived from OCTS and POLDER measurements using consistent data-processing algorithms for both sensors and vicarious calibrations based on a common *in situ* data set from the Marine Optical Bouy (MOBY)[8] in the waters off Hawaii. Therefore differences in the derived ocean-color products from OCTS and POLDER are associated primarily with differences in instrument characteristics. We first give a brief overview of the sensor characteristics of the OCTS and the POLDER and their differences. Detailed algorithm descriptions for processing OCTS and POLDER data are then presented. Next we outline the vicarious calibration scheme in which the OCTS- and POLDER-measured radiances are calibrated with a common *in situ* MOBY data set. Finally, we provide results that compare OCTS and POLDER ocean-color data with global *in situ* measurements and compare a series of OCTS measurements with those of POLDER over the Sargasso Sea and the Bermuda area.

6. Conclusion

We describe a procedure to calibrate vicariously OCTS and POLDER Level-1B data using the MOBY *in situ* measurements. This procedure effectively bridges the OCTS and POLDER Level-1B data through the use of a common set of MOBY *in situ* measurements. The vicarious calibration assumes the band 865-nm gain coefficients are not changed, while the visible bands are adjusted such that the derived normalized water-leaving radiances are forced to be equivalent to the MOBY *in situ* measurements. Using the derived gain coefficients, we can use a consistent atmospheric-correction algorithm to process OCTS and POLDER data from Level-1B to Level-2 products. Therefore the differences in the OCTS and POLDER-derived ocean-color products are mainly from the differences of the sensor characteristics, i.e., with this approach, the retrieved products would be identical if the two sensors were identical.

We demonstrate the efficacy of vicariously recalibrating OCTS and POLDER with a common *in situ* data set and using a consistent atmospheric-correction algorithm for data processing. Both the OCTS- and POLDER-derived normalized water-leaving radiances compare reasonably well with independent *in situ* data. Over the Sargasso Sea and the Bermuda area, the ocean-color products derived from OCTS have a good agreement with data from POLDER measurements. It is particularly important that there are no obvious bias differences between the OCTS- and POLDER-derived ocean-color data, i.e., the overall ratio values between the OCTS- and POLDER-derived normalized water-leaving radiances at 443, 490, and 565 nm are 1.0004, 1.0103, and 0.9840, while the ratio value in the derived chlorophyll-a concentration is 0.9907. However, the noise differences, which are usually inherited from sensor characteristics, are difficult to remove at the pixel level. These noise differences possibly can be reduced with data-averaging schemes (e.g., averaging Level-2 data to Level-3 products). To resolve the noise problem, however, one will generally need improved instruments, e.g., high sensor signal-to-noise performance, good sensor linearity response, and high radiometric stability. It is found that the POLDER-derived $[L_w(\lambda)]_N$ are usually more noisy than those of OCTS, in particular, for the 443-nm band products. This most likely results from the POLDER sensor nonlinearity response problem.[37] On the other hand, effects of the subpixel cloud contamination around cloud edge lead to high sparkling values in the POLDER-retrieved ocean color products.

The OCTS and POLDER data-processing procedures and algorithms are scheduled to be implemented in MSL12 within the SeaDAS software,[12] which is freely available. Therefore interested scientists can process OCTS and POLDER data with the widely distributed SeaDAS software package.

The OCTS and POLDER Level-1B data were provided by National Space Development Agency of Japan and Centre National d'Etudes Spatioles of France. We thank J.-M. Nicolas for his assistance with the POLDER Level-1B data, D. Clark and his research group for providing the MOBY data, J. O'Reilly and S. Maritorena for the modified OC2 algorithm, F. Patt for help in OCTS navigation analyses, S. Bailey and J. Werdell for help for the SeaBASS *in situ* data analyses, and two anonymous reviewers for their helpful comments. This research was supported by funding provided by National Aeronautics and Space Administration under the Sensor Intercomparison and Merger for Biological and Interdisciplinary Oceanic Studies (SIMBIOS) project and partly from NASA SIMBIOS grant NAS5-00203.

SCANNING VOL. 24, 247–256 (2002)
© FAMS, Inc.

Received: February 14, 2002
Accepted with revision: April 29, 2002

Irregular Snow Crystals: Structural Features as Revealed by Low Temperature Scanning Electron Microscopy

WILLIAM P. WERGIN, ALBERT RANGO,* JAMES FOSTER,† ERIC F. ERBE, CHRISTOPHER POOLEY‡

Soybean Genomics and Improvement Laboratory, Agricultural Research Service (ARS), U.S. Department of Agriculture (USDA), Beltsville, Maryland; *Jornada Experimental Range, ARS, USDA, New Mexico State University, Las Cruces, New Mexico; †Laboratory for Hydrological Sciences, NASA Goddard Space Flight Center, Greenbelt; Maryland and ‡Hydrology and Remote Sensing Laboratory, ARS, USDA, Beltsville, Maryland, USA

Summary: For nearly 50 years, investigators using light microscopy have vaguely alluded to a unique type of snow crystal that has become known as an irregular snow crystal. However, the limited resolution and depth-of-field of the light microscope has prevented investigators from characterizing these crystals. In this study, a field-emission scanning electron microscope, equipped with a cold stage, was used to document the structural features, physical associations, and atmospheric metamorphosis of irregular snow crystals. The crystals appear as irregular hexagons, measuring 60 to 90 mm across, when viewed from the a-axis. Their length (c-axis) rarely exceeds the diameter. The irregular crystals are occasionally found as secondary particles on other larger forms of snow crystals; however, they most frequently occur in aggregates consisting of more than 100 irregular crystals. In the aggregates, the irregular crystals have their axes oriented parallel to one another and, collectively, tend to form columnar structures. Occasionally, these columnar structures exhibit rounded faces along one side, suggesting atmospheric metamorphoses during formation and descent. In extreme cases of metamorphoses, the aggregates would be difficult to distinguish from graupel. Frost, consisting of irregular crystals, has also been encountered, suggesting that atmospheric conditions that favor their growth can also occur terrestrially.

Key words: field-emission scanning electron microscopy, low-temperature scanning electron microscopy, snow crystals, irregular crystals, snowflakes, rime, graupel

PACS: 61.16 Bg, 61.66.-f, 81.10.Aj, 92.40.Rm

Address for reprints:

William P. Wergin
Soybean Genomics and Improvement Laboratory
Agricultural Research Service
U.S. Department of Agriculture
Beltsville, MD 20705, USA

Introduction

Snow crystals have been studied with the light microscope for more than 100 years. However, because of their small size, delicate structure, and topography, this instrument has failed to elucidate many of the structural details of the crystals. In addition, snow is difficult to transport, store, image, and photograph without subjecting samples to structural changes resulting from sublimation, melting or recrystallization. Examination of snow crystals with a scanning electron microscope (SEM) would solve problems associated with resolution, topography, and their delicate nature. However, for obvious reasons, frozen samples cannot be imaged at ambient temperatures in a conventional SEM.

In 1970, Echlin *et al.* (1970) solved this problem for biologists by describing a cold stage that could be interfaced with an SEM and operated at temperatures below –130° C. At these temperatures, the vapor pressure of water is not significant and sublimation does not occur at a detectable rate. Furthermore, recrystallization of pure water-ice does not occur (Beckett and Read 1986) and frozen, fully hydrated samples remain stable for several hours while being observed (Wergin and Erbe 1991).

Recently, this procedure, which has become known as low-temperature (LT) SEM, was used to compare frozen, fully hydrated, fractured membranes of yeast in the SEM with the platinum/carbon (Pt/C) replicas of the identical cells in the transmission electron microscope (TEM) (Wergin and Erbe 1990). Results indicated that macromolecular particles, as small as 10 nm in diameter, retained their structure, were stable, and could be imaged and photographed with LTSEM. The images, which were obtained in the LTSEM, were comparable with those of the same cells in the Pt/C replicas, which were photographed in a TEM. Encouraged by these results, identical snow crystals were imaged and photographed with a light microscope, imaged and photographed in the

Contribution of the Agricultural Research Service, U.S. Department of Agriculture; Not subject to copyright.

LTSEM, and then rephotographed with a light microscope. The results further demonstrated that observation in the LTSEM did not alter the structure of the snow crystals (Wergin *et al.* 1998). In addition, techniques were developed to collect, ship, and store fresh and metamorphosed snow crystals for subsequent imaging with an LTSEM. These techniques have been successfully used to record detailed images of thousands of snow crystals that were collected from numerous states including Alaska, Colorado, Montana, Utah, Wyoming, Wisconsin, Maryland, and West Virginia. In previous studies, we have described the detailed structure of snow and ice grains including columns, needles, plates, stellar dendrites, depth hoar, and glacial ice that were collected from several states (Rango *et al.* 1996a, b, 2000; Wergin and Erbe 1994a, b; Wergin *et al.* 1995, 1996a, b, 1998, 1999). The current study uses LTSEM to illustrate the features and distinctive characteristics of the elusive group of crystals recognized by The International Commission on Snow and Ice (Colbeck *et al.* 1990) and simply referred to as "irregular crystals."

Materials and Methods

Collection Procedure

Data illustrated in this study resulted from six different snow collections during 1993–1999 from sites near the following locations: Beltsville, Maryland; Bearden Mt., West Virginia and Greenwood, Wisconsin. The samples, which were obtained when the air temperatures ranged from –5°C to 0°C, consisted of freshly fallen snowflakes. To collect samples, a thin layer of liquid Tissue-Tek, a commonly used cryoadhesive for biological samples, was spread on a flat copper plate (15 × 27 mm). The Tissue-Tek and the plates were precooled to ambient outdoor temperatures (below freezing) before use. Newly fallen snowflakes were either permitted to settle on the surface of the Tissue-Tek or were lightly dislodged from the snow surface and allowed to fall onto the surface of the cryoadhesive. Next, the plate was either rapidly plunged into a Styrofoam vessel containing liquid nitrogen (LN_2) or placed on a brass block that had been precooled with LN_2 to –196°C. This process, which solidified the Tissue-Tek, resulted in firmly attaching the snow crystals to the plate. The frozen plates were inserted diagonally into prefabricated 20 cm segments of square, brass channel tubing, containing an end cap, and lowered into dry shipping dewars that had been previously cooled with LN_2. The dewars containing the samples were conveyed from the collection sites and then either transported by van (from West Virginia) or shipped by air (Wisconsin) to the laboratory in Beltsville, Maryland. Upon reaching the laboratory, the samples were transferred under LN_2 to a LN_2 storage dewar where they remained at –196°C for as long as 9 months before being further prepared for observation with LTSEM.

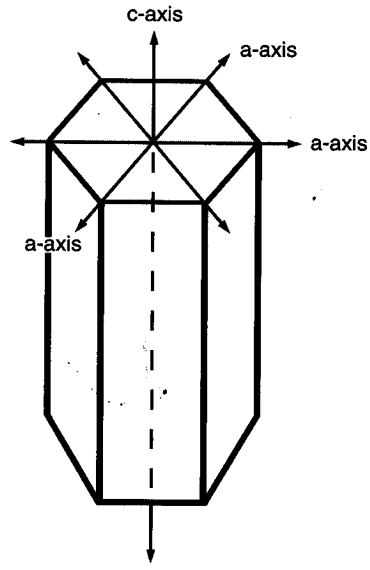

FIG. 1 Diagram illustrating the crystallographic axes of snow crystal growth. Environmental conditions that favor growth along the a-axes result in flat hexagonal plates and stellar dendrites, whereas conditions that favor c-axis growth produce elongated columns and needles. Neither type of growth predominates in the formation of irregular crystals.

Conclusion

This study uses LTSEM to characterize small discrete crystals believed to correspond to the irregular crystals that previous investigators have attempted to describe with the light microscope. These crystals, which appear as irregular hexagons when viewed along their a-axes, generally measure 60 to 90 μm across. Their lengths (c-axis) rarely exceed their diameters. Although the irregular crystals are occasionally found as individual, secondary particles on other larger forms of snow crystals, such as plates and dendrites, they are most frequently encountered in aggregates consisting of more than 100 crystals that tend to form a column. The aggregates are often associated with needles, suggesting that the atmospheric conditions that favor needle growth may be close to those that favor growth of irregular crystals. Furthermore, examples believed to represent atmospheric metamorphoses of irregular crystals are commonly encountered. Metamorphosis can result in aggregates that consist of partially sublimated crystals and droplets that collectively would be difficult to distinguish from graupel when using a light microscope.

Microsc. Microanal. 8 (Suppl. 2), 2002
DOI 10.1017.S1431927602106246

Low Temperature Scanning Electron Microscopy of Irregular Snow Crystals

William P. Wergin,* Albert Rango,** James Foster,*** Eric F. Erbe,* and Christopher Pooley****

*Soybean Genomics and Improvement Laboratory, Agricultural Research Service (ARS), U.S. Department of Agriculture (USDA), Beltsville, MD 20705 USA
**Jornada Experimental Range, ARS, USDA, New Mexico State University, 401 E. College Ave., Las Cruces, NM 88003 USA
***Laboratory for Hydrological Sciences, NASA Goddard Space Flight Center, Greenbelt, MD 20771 USA
****Hydrology and Remote Sensing Laboratory and Soybean Genetics and Improvement Laboratory, ARS, USDA, Beltsville, MD 20705 USA

Snow crystals occur in eight basic types: columns, needles, plates, dendrites, irregular crystals, graupel, hail and ice pellets.[1] Most of these types have been described and photographed.[2] However, our understanding of the "irregular crystals" remains vague because the limited resolution and depth-of-field associated with the light microscope have prevented investigators from fully characterizing and clearly illustrating the features of these crystals. Our study used a field-emission scanning electron microscope (FESEM), equipped with a cold stage, to document the structural features, physical associations and atmospheric metamorphosis of irregular snow crystals.

Snow samples, consisting of freshly fallen snowflakes, were collected from six different locations where air temperatures ranged from -5^0 C to 0^0 C. The collection procedure consisted of spreading a cryo-adhesive on a pre-cooled flat copper plate and allowing newly fallen snowflakes to settle on the surface. Next, the plate was rapidly frozen in LN_2. The frozen plates were placed in a dry shipping dewar and conveyed to the laboratory where they were coated for observation in a Hitachi S-4100 FESEM equipped with an Oxford CT 1500 HF Cryotrans system as previously describe.[3]

Crystals, believed to correspond to irregular crystals, appeared as short, irregular hexagons, measuring 60 to 90 μm across, when viewed from the a-axis (**Fig. 1**). Their length (c-axis) rarely exceeded the diameter. The irregular crystals were occasionally found as secondary particles on other larger forms of snow crystals (**Fig. 2**). However, they most frequently occurred as aggregates consisting of more than 100 irregular crystals (**Fig. 3**). In the aggregates, the irregular crystals had their c-axes oriented parallel to one another and collectively, tended to form columnar structures. Occasionally the aggregates exhibited rounded facets along one side, suggesting atmospheric metamorphoses and unidirectional fall. In extreme cases of metamorphoses, the aggregates would be difficult to distinguish from graupel. Frost, consisting of irregular crystals, was also encountered, suggesting that atmospheric conditions that favor this form of growth also occur terrestrially (**Fig. 4**).

Results obtained with low temperature FESEM suggested that crystals, which were previously designated as "irregular crystals", have distinctive features that can be used to characterize and distinguish them from other types of snow crystals.

[1] S. Colbeck et al., *The International Classification for Seasonal Snow on the Ground*, Univ. of Colorado, Boulder, 1990.
[2] U. Nakaya. *Snow Crystals: Natural and Artificial*, Harvard Univ. Press, Cambridge, MA, 1954.
[3] W.P. Wergin et al., *Scanning*. 17 (1995) 41.

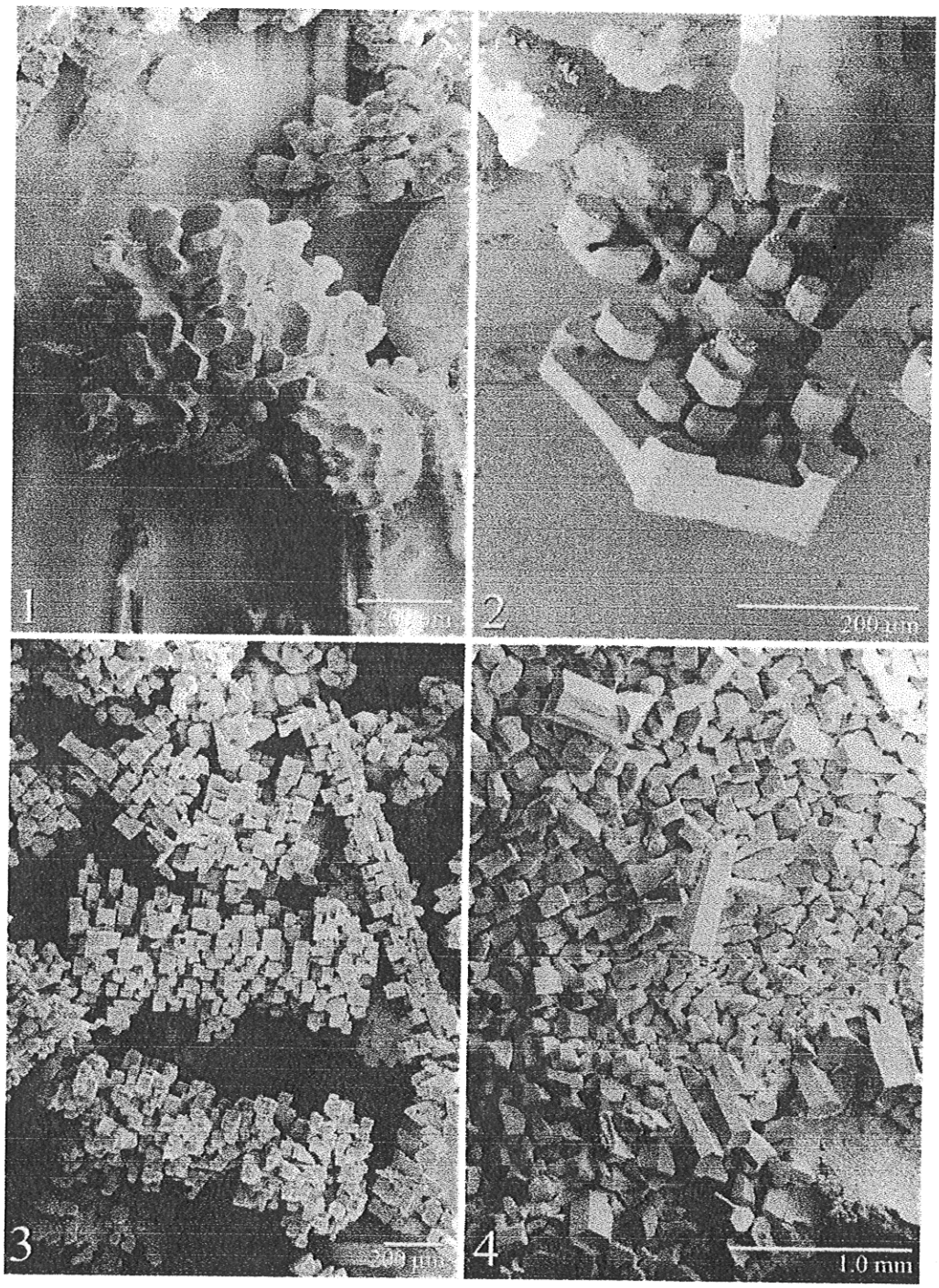

Figure 1. A-axis view of irregular crystals, which appear as asymmetric hexagons.
Figure 2. Irregular crystals, which occur as secondary particles on the surface of a dendritic arm.
Figure 3. Several "snowflakes", each consisting of aggregates of numerous irregular crystals.
Figure 4. Irregular crystals that had formed on the surface of a leaf.

Validation of Sea Ice Motion from QuikSCAT with those from SSM/I and Buoy

Yunhe Zhao, Antony K. Liu, and David G. Long, *Senior Member, IEEE*

***Abstract*—Arctic sea ice motion for the period from October 1999 to March 2000 derived from QuikSCAT and special sensor microwave/imager (SSM/I) data using the wavelet analysis method agrees well with ocean buoy observations. Results from QuikSCAT and SSM/I are compatible when compared with buoy observations and complement each other. Sea ice drift merged from daily results from QuikSCAT, SSM/I, and buoy data gives more complete coverage of sea ice motion. Based on observations of six months of sea ice motion maps, the sea ice motion maps in the Arctic derived from QuikSCAT data appear to have smoother (less noisy) patterns than those from NSCAT, especially in boundary areas, possibly due to constant radar scanning incidence angle. For late summer, QuikSCAT data can provide good sea ice motion information in the Arctic as early as the beginning of September. For early summer, QuikSCAT can provide at least partial sea ice motion information until mid-June. In the Antarctic, a case study shows that sea ice motion derived from QuikSCAT data is consistent with pressure field contours.**

***Index Terms*—QuikSCAT, sea ice motion, special sensor microwave/imager (SSM/I), wavelet transform.**

I. Introduction

QUIKSCAT, a "quick recovery" mission to fill the gap created by the loss of data from the NASA Scatterometer (NSCAT), when the ADEOS-1 satellite lost power in June 1997, was launched on June 19, 1999. QuikSCAT is an active sensor, and the sensor footprint is an ellipse 25 km $\times$ 37 km. In both the Arctic and the Antarctic regions, repeated footprints of the satellite make it possible to construct QuikSCAT images with a 12.5 km grid and finer resolution (e.g., see [1]). In this paper, the daily (estimated over a four-day sliding window for the Arctic and over a one-day sliding window for the Antarctic) sea ice motion derived from QuikSCAT using an ice-tracking algorithm based on wavelet transform is demonstrated, and the applications of the daily sea ice motion are indicated. The uncertainty of QuikSCAT-derived sea ice motion is determined from validation with those from *in situ* buoy data and Defense Meteorological Satellite Program (DMSP) special sensor microwave/imager (SSM/I) observations during the same period of time. The instrument differences between QuikSCAT and NSCAT lead to significantly different spatial and temporal sampling characteristics, and it is for this reason that QuikSCAT ice motion validation is required. NSCAT is a fan-beam scatterometer with fixed azimuth but variable incidence, while QuikSCAT has fixed incidence and variable azimuth.

Satellite observations provide more complete and routine coverage of polar region than observations from any other means, and they have been used by several authors in deriving polar sea ice drift (e.g., see [2] and references cited there). The efficiency and utility of wavelet transform in analyzing nonlinear dynamical ocean systems has also been documented in several papers ([2] and references cited there). In Section II, wavelet analysis for ice feature tracking and sea ice motion from QuikSCAT and SSM/I data are presented. Wavelet analysis results from QuikSCAT and SSM/I are compared with the ice motion derived from buoys for validation in Section III. Section IV deals with the potential application of QuikSCAT data in summer ice tracking. Section V is devoted to a sea-ice-tracking case study for the Antarctic using QuikSCAT data. The results and applications of satellite-derived sea ice motion are discussed and summarized with previous NSCAT and SSM/I data in the final section.

II. Wavelet Analysis of Satellite Images

A sea-ice-tracking procedure based on wavelet transform of satellite data and its error analysis have appeared in [2]–[4]. The effect of wavelet transform is a bandpass filter with a threshold for feature detection. For the details of the procedure, we refer readers to [2]–[4]. In this study, the same procedure is applied to QuikSCAT and SSM/I data with a few modifications. For the Arctic, QuikSCAT images with 12.5 km pixel size are first constructed from QuikSCAT Level 2A data, and SSM/I images are obtained from SSM/I compact discs. QuikSCAT Sigma-0 data has an incidence angle either around 54.24° (v-polarization) or around 46.44° (h-polarization) within $\pm 0.5°$. Only v-polarization Sigma-0 data with an incidence angle around 54.24° are used in the construction of QuikSCAT images because of its better coverage. Areas indicated by sea ice flags in QuikSCAT data as land, open ocean, or no-data areas are masked in the images. For the Antarctic case study, the QuikSCAT data are processed with a scatterometer image reconstruction (SIR) resolution enhancement algorithm to a pixel resolution of 4.45 km from QuikSCAT Level 1B data [1], and sea ice extent is determined using the method of [5]. The QuikSCAT design specifications for location accuracy requirements are 25 km (rms) absolute and 10 km (rms) relative. However, the actual performance is currently estimated to be better than 6 km (rms) absolute and less than 1 km (rms) relative with bias dominating the total error [6]. Thus, QuikSCAT has very high precision measurement locations, far exceeding its design specifications and enabling the application of resolution enhancement algorithms. For both cases, wavelet transform is then applied to the satellite image at various scales to separate various ice textures or features. In the Arctic, two tracking regions are considered: coast/bay for fast ice motion (with a two-day sliding window), and central Arctic for slow ice motion (with a four-day sliding window). Template matching is performed with the results from the wavelet transform of the images between day 1 and day 5 for the central Arctic and between day 2 and day 4 for the coast/bay.

In the Antarctic, template matching is performed with the results from the wavelet transform of the images between day 1 and day 2. For both cases, velocities are estimated by dividing the displacement over the time interval. Finally, the sea ice drift map can be merged by block average with outlier filtering. The outlier filtering after block average is performed as follows: at any location, the mean velocity of nine neighboring ice velocities is computed. If the angle between the mean ice velocity and the ice velocity at the location is bigger than a certain degree, then the ice velocity at the location is discarded.

Fig. 1(a) and (b) show sea ice drift maps of the Arctic Ocean for November 5, 1999, derived from SSM/I and QuikSCAT data, respectively, where thin white arrows indicate velocities derived from satellite data, while thick white arrows indicate velocities derived from buoy data. Two circulation patterns—one in the Beaufort Sea and the other across the Chukchi, Beaufort, and Laptev Seas—are clearly observed in the maps. The ice motion converges in an area between the Chukchi Sea and the Beaufort Sea. Notice that velocities derived from both QuikSCAT and SSM/I data agree well with those from buoy data. Wavelet transform scales used in deriving these images from QuikSCAT and SSM/I data are based on parameter study and testing and are 1.0, 2.42, and 2.828. The resultant ice velocities have been block averaged to a 100 km $\times$ 100 km grid with outlier filtering. The empty areas with no velocity in the map indicate the regions where the tracking procedure cannot be used, since no matching templates between the time periods can be determined. Clearly, the ice motion maps derived from QuikSCAT and SSM/I data for November 5, 1999 are complementary to each other. The regions without ice velocity data from QuikSCAT and SSM/I are generally not colocated, since the QuikSCAT and SSM/I data correspond to different physical features: surface roughness and brightness–temperature anomalies, respectively. For the period from October 1999 to March 2000, based on the observations of sea ice motion maps, the patterns of motion from QuikSCAT appear smoother than those from SSM/I.

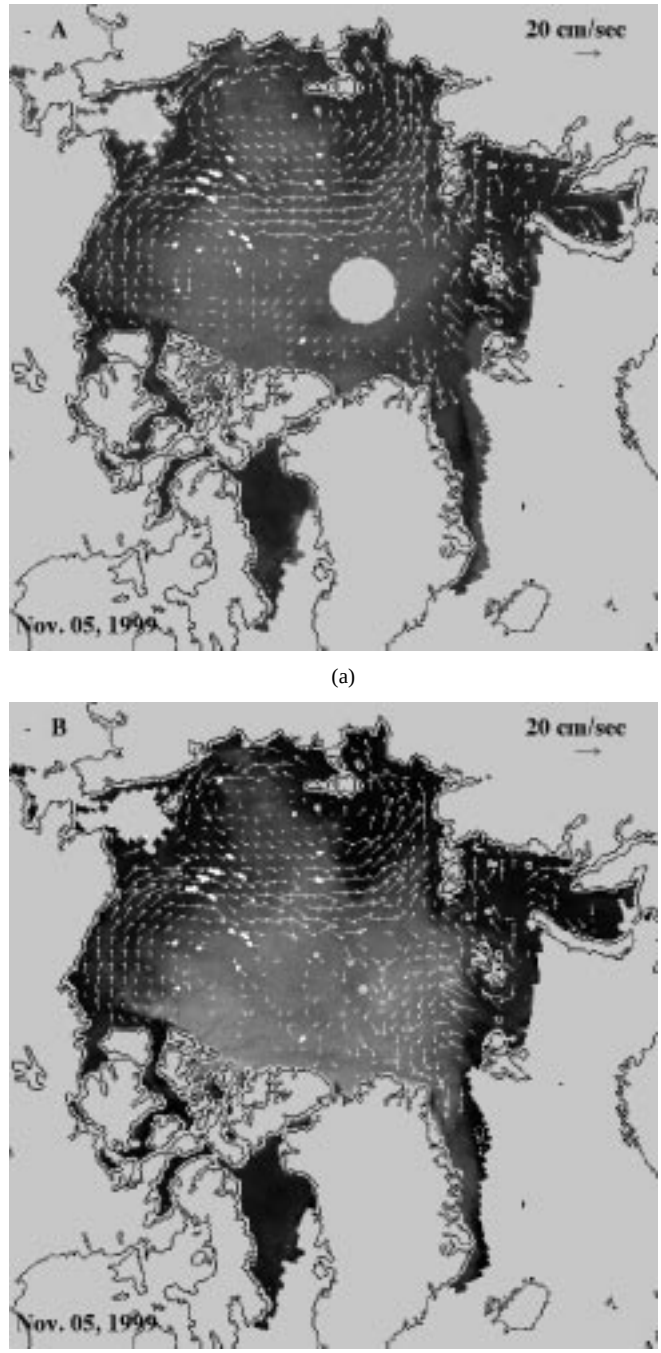

Fig. 1. Arctic sea ice drift maps of the Arctic basin in a grid of 100 $\times$ 100 km derived from (a) SSM/I 85 GHz radiance data and (b) from QuikSCAT data on November 5, 1999. Thin white arrows indicate velocities derived from feature tracking using wavelet analysis, while thick white arrows indicate velocities from buoys.

VI. Discussion

To further examine satellite-data-derived sea ice motion, Table I summarizes some six-month comparison results of sea ice motion derived from SSM/I, NSCAT, and QuikSCAT with those derived from buoy data for different periods. For all comparison periods, the rms of the speed differences between buoy-derived ice velocities and satellite-derived ones are all under 3 cm/s, and the rms of the direction differences between them are around 30°. Moreover, all satellite-derived sea ice motion data sets are consistent and comparable.

It is clear that sea ice motion products derived from SSM/I, NSCAT, and QuikSCAT data have very good quantitative agreements with the ice motion products derived from buoy data. But, the sea ice motion products derived from NSCAT and QuikSCAT data are slightly more accurate than that derived from SSM/I data because both NSCAT and QuikSCAT are active sensors and do not suffer from cloud and atmospheric effects. Also, the results from NSCAT and QuikSCAT are very consistent. The rms of the direction difference between NSCAT-derived and buoy-derived ice drift for the period from October, 1996 to March, 1997 is slightly better than that between QuikSCAT-derived ice velocities and buoy-derived ones for the same winter period in 1999 and 2000. But keep in mind that the rms are for two different periods and that the ice motion in the central Arctic during winter 1999 has a very slow motion, and so the ice-tracking results are less accurate. In fact, based on the observations, the ice motion maps from QuikSCAT data appear to have smoother patterns than those from NSCAT, especially in boundary areas, e.g., in the Kara and Barents Seas where there is no buoy for comparison.

Other Contributions

American Meteorological Society

AMS

2002 Annual Meeting

January 13-17
Orlando, FL

P1.6 MODIS RADIANCES AND REFLECTANCES FOR EARTH SYSTEM SCIENCE STUDIES AND ENVIRONMENTAL APPLICATIONS

S. P. Ahmad *, V. V. Salomonson, W. L. Barnes, X. Xiong, G. G. Leptoukh, and G. N. Serafino

NASA Goddard Space Flight Center, Greenbelt, Maryland

1. Introduction

The Moderate Resolution Imaging Spectroradiometer (MODIS), a major component of NASA's Earth Observing System (EOS), was designed to provide improved long-term global observations of land, ocean and atmosphere features relative to "heritage sensors". MODIS was launched aboard the Terra satellite on December 18, 1999 (10:30 am equator crossing time, descending node, Sun-synchronous near polar orbit). MODIS with its 2330 km viewing swath width provides almost daily global coverage. It acquires data in 36 high spectral resolution bands between 0.415 and 14.235 microns with spatial resolutions of 250 m (2 bands), 500 m (5 bands), and 1000 m (29 bands). This year a similar instrument will be flown on the EOS-Aqua satellite (1:30 pm equator crossing time, ascending node). This will enable studies of the diurnal variation of rapidly varying systems. The radiance data measured by MODIS with some new channels (never used before for remote sensing from space) provides improved information about the physical structure of the Earth system. Measured raw sensor counts, radiometrically calibrated and geolocated radiances along with derived atmosphere and ocean data are archived (Ahmad et al. 2002) at the NASA Goddard Earth Sciences (GES) Distributed Active Archive Center (DAAC). These products and other MODIS derived products archived at other NASA centers are made freely available to the public and scientific community.

The purpose of this presentation is to provide key characteristics of the MODIS radiance and reflectance products (referred to as the Level 1B product) with some examples of applications of the MODIS radiances in detecting human impacts on the earth and its climate and how this data is used in improving the predictions and characterization of natural disasters such as wild fires, volcanoes, floods and drought.

2. MODIS Instrument

MODIS, a cross-track scanning radiometer, provides high spectral resolution data from 36 bands with center wavelengths ranging from 0.412 to 14.235 microns (Barnes et al. 1998). MODIS spectral band passes are shown in Table 1. MODIS carries 490 detectors that are aligned in parallel rows on four separate focal planes (Visible, NIR, SWIR/MWIR, and LWIR).

The number of detectors per band are 10 for 1000 m, 20 for 500 m, and 40 for 250 m spatial resolution bands. In addition, 2 of the 1000 m spatial resolution bands provide measurements for the same scenes at two gains, 13 L and 14L at low gains for measuring bright scenes and 13H and 14H at high gains for measuring dark ocean scenes.

The instrument's 110 degree field of view is swept over the focal planes by the double sided rotating scan mirror. Each mirror rotation provides two scans (one for each mirror side). The scan period is 1.477 sec. During each scan, 5 view sectors (solar diffuser, spectral radiometric calibration assembly, blackbody, space, and earth view) are observed. The 110 degree-wide instrument field of view sweeps out a ground swath approximately 2330 km wide during the 0.451 seconds of earth view. The ground swath (± 55 deg viewing angles relative to nadir) exhibits significant earth curvature effects. The 55 degree scan angle increases to approximately 65 degree due to earth curvature. In addition, ground resolution increases with scan angle.

7. Summary

The strengths of MODIS include its global coverage, high radiometric resolution, appropriate dynamic ranges, and accurate calibration in reflective and thermal infrared bands designed for retrievals of atmospheric, land and sea surface properties. Almost 40 higher level science standard products are being produced from MODIS Level 1B radiance data. Even though data validation activities are still in progress, the provisional radiometrically calibrated radiances and reflectances, and derived products (version-3) show very fine details and exceed the expectations when compared to in-situ observations. Almost one year of consistent data processed with an improved calibration algorithm (version-3), will soon be made available to the public and science user community. These high radiometric accuracy measurements can be used by the scientific community to detect subtle signatures of climate change, study regional and global phenomena, and for prediction and characterization of natural disasters such as wild fires, volcanoes, floods and drought. MODIS radiance counts, calibrated radiance and reflectance, geolocation products, and all derived geophysical atmospheric & ocean products are archived at the Goddard DAAC (http://daac.gsfc.nasa.gov). All land products are archived at Earth Resource Observation System (EROS) Data Center (EDC), and snow & ice products are archived at the National Snow and Ice Data Center (NSIDC). MODIS products, ancillary and related data, documents, and data analysis and visualization tools are freely made available to the public and science user community from these data archive centers via NASA EOS Data Gateway (EDG) at http://eos.nasa.gov/imswelcome.

* Corresponding author address: Dr. Suraiya Ahmad, NASA/GSFC, Code 902, Greenbelt, MD 20771
email: ahmad@daac.gsfc.nasa.gov

NASA/TM-2002-210005

SIMBIOS Project 2001 Annual Report

Giulietta S. Fargion, Science Applications International Corporation, Maryland
Charles R. McClain, Goddard Space Flight Center, Greenbelt, Maryland

National Aeronautics and
Space Administration

Goddard Space Flight Center
Greenbelt, Maryland 20771

March 2002

Chapter 22

Measurements and modeling of apparent optical properties of ocean waters in support to ocean color data calibration, validation, and merging

David Antoine, André Morel, Marcel Babin and Hervé Claustre
Laboratoire d'Océanographie de Villefranche, CNRS-INSU, Villefranche sur Mer, France

Stanford B. Hooker
NASA/GSFC, Greenbelt, Maryland

22.1 INTRODUCTION

This progress report does not show any results in terms of *in situ* data because the buoy' deployment is only planned for late January 2002. The advancement of the buoy development and testing, of the instrument integration and testing, and of all other preparatory activities (in particular monthly cruises to the deployment site) are succinctly described here. The objectives and the analyses that are planned thanks to the data to be collected are also reminded. This project is supported by the European Space Agency (ESA/ESTEC contract N° 14393/00/NL/DC), the French Space Agency "Centre National d'Etudes Spatiales (CNES)", the "Centre National de la Recherche Scientifique (CNRS-INSU)" and the "Observatoire Océanologique de Villefranche sur mer". A prerequisite to building long-term (over decades) archives of ocean color, in response to the need for assessing the response of the oceanic biota to climate changes, is to accurately calibrate the top-of-atmosphere satellite observations, then to validate the surface geophysical parameters derived from these observations. Ensuring coherence between these geophysical products, as derived from different sensors, is also an important aspect to consider. When ocean color observations from different sensors are considered in view of data merging, their cross-calibration and validation might be facilitated if it could be "anchored" on continuous long-term *in situ* stations (IOCCG, 1999). Deploying and maintaining moorings that operate in a continuous way is, however, a difficult task.

In response to these concerns, we propose to carry out match-up analyses and vicarious calibration experiments, based on a data set to be built from a permanent marine optical buoy. This new type of marine optical buoy has been specifically designed for the acquisition of radiometric quantities, and has been already deployed in the Mediterranean sea in July 2000 (a deployment of 3 months for validating the mooring concept), between France and Corsica.

The vicarious calibration experiments should allow the top-of-atmosphere total radiance to be simulated and compared to the satellite measurements, in particular for the European MERIS sensor. By this way, the need for a change of the pre-flight calibration coefficients for a given sensor might be evaluated, and its amount quantified. From this data set, match-up analyses shall be also possible for chlorophyll concentration and water-leaving radiances, as well as algorithm evaluation (atmospheric correction and pigment retrieval). Because of a certain commonality in the band sets of the new-generation ocean color sensors, the data acquired with the buoy might be used for several of these sensors, and then contribute to the international effort of cross-calibrating them and of cross-validating their products, which are amongst the basic goals of SIMBIOS. In addition, some protocol issues (measurements) are specifically linked to the use of buoys, while others, of general concern to marine optics measurements, may find specific answers in the case buoys are used. We propose to examine these aspects, which, to our knowledge, have not been thoroughly investigated up to now.

Description of the planned analyses

Two main "vicarious" calibration paths exist to produce ocean color products of the desired accuracy, *i.e.*, water-leaving radiances within an error of about 5% in the blue for an oligotrophic ocean (Gordon, 1997, Antoine and Morel, 1999). The first one is usually referred to as "vicarious calibration", and consists in forcing the satellite-derived water-leaving radiances to agree with a set of *in situ* water-leaving radiances ("match-up analyses"). A set of "vicarious calibration coefficients" is therefore obtained, which is applied to the Top-of-atmosphere (TOA) total radiances measured by the sensor. The second procedure, which is also an indirect ("vicarious") calibration is sometimes referred to as a "radiometric calibration", and consists in simulating the TOA signal that the sensor should measure under certain conditions, and to compare it to the measured signal.

2002 IEEE International Geoscience and Remote Sensing Symposium and the 24th Canadian Symposium on Remote Sensing

IGARSS 2002

REMOTE SENSING:
Integrating Our View of the Planet

IEEE

June 24-28, 2002
Toronto Canada

Status of Terra MODIS and Aqua MODIS

William L. Barnes, X. (Jack) Xiong, and Vincent V. Salomonson

NASA/Goddard Space Flight Center

Greenbelt, Maryland

Abstract- Launched on December 18, 1999, the MODIS ProtoFlight Model on-board the EOS Terra spacecraft (near sun-synchronous polar orbit, 10:30 am equator crossing time) has been providing the science community global data sets for over two years. The instrument has been performing well on-orbit in terms of its spatial and spectral characterization and radiometric calibration. Many science products have been developed and validated using the MODIS Level 1B calibrated data. To be launched in April 2002, the MODIS Flight Model 1 on the EOS Aqua spacecraft (1:30 pm equator crossing time) will enhance the MODIS products by providing afternoon observations.

I. Introduction

The MODerate Resolution Imaging Spectroradiometer (MODIS) is the key instrument on NASA's Earth Observing System (EOS) Terra and Aqua spacecraft. The MODIS ProtoFlight Model (PFM) was launched on-board the Terra spacecraft on December 18, 1999 in a near sun-synchronous polar orbit (descending southward, 10:30 am equator crossing time). The instrument nadir door was first opened on February 24, 2000. The instrument has been providing the science community global data sets for over two years. Overall, the instrument has been performing well in terms of its spatial and spectral characterization and radiometric calibration based on the on-orbit observations. Most of the land, oceans, and atmosphere science products developed from the Terra MODIS L1B calibrated data sets have been validated and put in use by a broad user community. In April 2002, MODIS Flight Model 1 (FM1) will be launched on the EOS Aqua spacecraft (ascending northward, 1:30 pm equator crossing time). This new mission will complement the Terra MODIS data sets by proving afternoon observations.

II. Instrument Overview

MODIS has 36 spectral bands ranging from 0.4-14.5 μm, distributed on four focal plane assemblies (VIS, NIR, SW/MWIR, and LWIR) with nadir spatial resolutions of 250m (bands 1-2), 500m (bands 3-7), and 1000m (bands 8-36). The operating temperature of the two cold FPAs (SW/MWIR, and LWIR) is controlled by a passive radiatiive cooler. Using a two-sided scan mirror, the instrument provides a 10 km (nadir) along track by 2330 km crosstrack swath every 1.478 seconds. The 20 reflective solar bands (RSB) are spectrally located between 0.4 and 2.1 μm. The wavelengths of 16 thermal emissive bands (TEB) range from 3.75-14.5 μm.

MODIS on-orbit calibrators include a solar diffuser (SD) and a solar diffuser stability monitor (SDSM) for the RSB radiometric calibration, a blackbody (BB) for the TEB radiometric calibration, and a Spectroradiometric Calibration Assembly (SRCA) for spatial and spectral characterization. A detailed description of the MODIS instrument characterization and pre-launch calibration results have been reported by Barnes, Pagano and Salomonson [1].

V. Summary and Conclusions

In summary, the Terra MODIS is an excellent sensor that has already provided more than 400 terrabytes of science data in over 40 global products spanning the period from November 2001 to the present. On-orbit performance has verified the pre-launch tests indicating that the sensor has met all but a very few of the large number of demanding specifications. Test data from the Aqua MODIS promises somewhat better performance than the Terra model. The Aqua satellite is slated for launch in April 2002. The combined data from the AM and PM MODIS should greatly enhance our ability to study the Earth as a system.

16th Conference on Hydrology

13–17 January 2002
Orlando, Florida

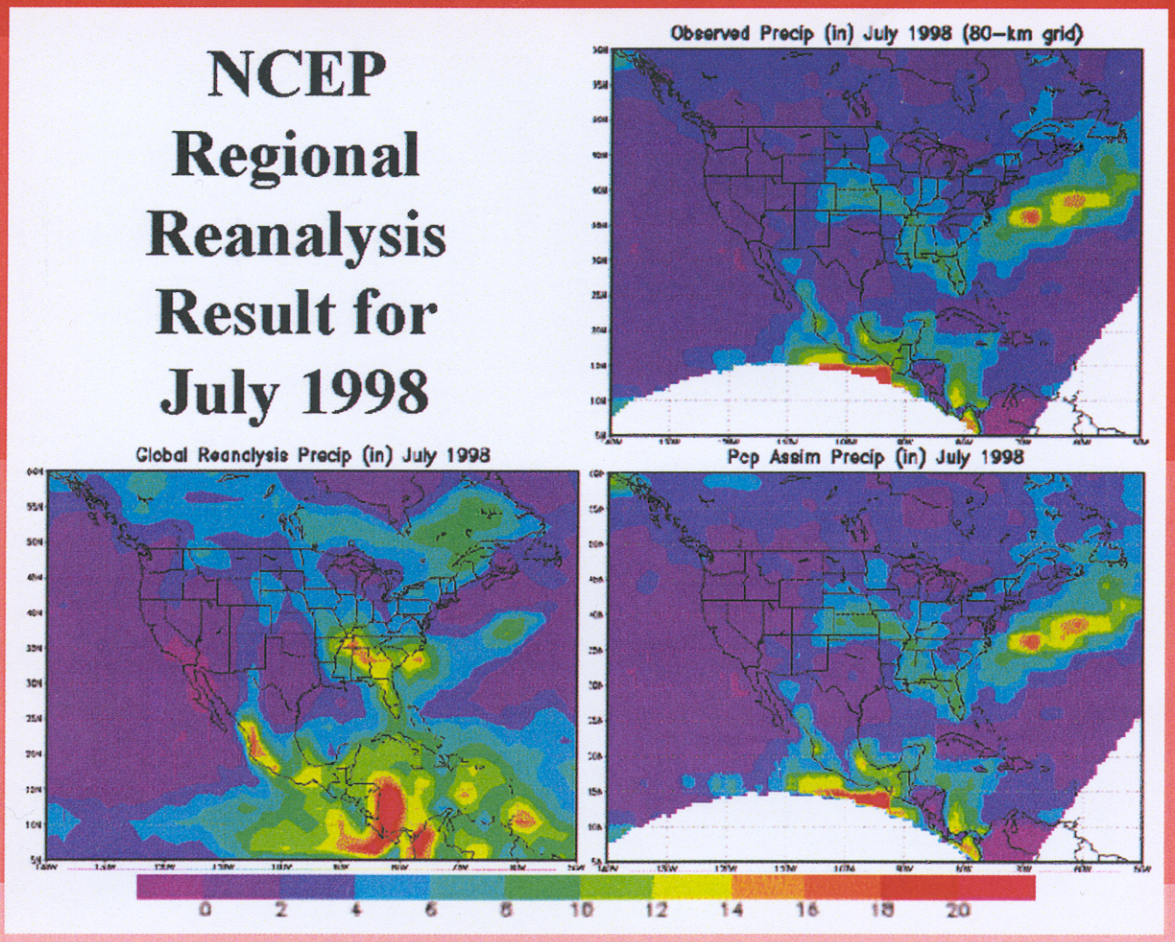

AMERICAN METEOROLOGICAL SOCIETY

J4.5 THE EFFECT OF ERRORS IN SNOW ASSIMILATION ON LAND SURFACE MODELING

Brian A. Cosgrove[1] and Paul R. Houser[2]

[1]SAIC / Hydrological Sciences Branch & Data Assimilation Office
[2]Hydrological Sciences Branch & Data Assimilation Office
NASA Goddard Space Flight Center

1. INTRODUCTION

The accurate portrayal of the hydrological cycle is extremely important in land surface modeling. Central to this effort is the treatment of snow, as errors in the representation of this quantity can impact practically all other modeled quantities through alterations in the water and energy balances. Although land surface model (LSM) simulations can benefit from the assimilation of snow cover and snow depth observations, they can be negatively impacted if such observations contain errors or if a model bias exists in the simulation of surface or soil temperatures. Both cases may lead to excessive melting or growth of snow packs, and to large alterations in both the energy and water balances. Such problems in the snow assimilation process, made evident by the repeated melting and replenishing (without a snowfall event) of snow pack over significant areas of the United States, exists in the Eta Data Assimilation System (EDAS, Rogers et al., 1996) and is a product of the EDAS system's direct insertion assimilation of snow data (Figures 1a-c, 2). Occurring on a 24 hour cycle, the repeated melting infuses the soil column with a large quantity of water that upsets the hydrological cycle.

2. DISCUSSION

In an effort to quantify the impacts of such errors in snow assimilation on water and energy budgets, a series of Mosaic LSM (Koster and Suarez, 1996) simulations were performed over the period covering October 1998 to September 1999. A control run was conducted to provide "perfect" snow observations that were then directly assimilated, once per day, into experimental runs (Figure 3) which featured a range of warm and cold biases created by the manipulation of shortwave and surface temperature forcing data. These experimental simulations show that even a 0.5°C warm bias can interact with assimilated snow data to significantly impact the water budget. After one month of directly inserting snow data into an experimental Mosaic run characterized by this forcing bias, the total column soil moisture changed by up to 3.5%, and changed by up to 11% in a run featuring a 2°C warm bias (Figure 4). The error in the water budget is also substantial in both experimental runs, with the largest residuals of up to 250mm occurring over mountainous regions (Figure 5) in the 2°C bias run.

3. CONCLUSION

These preliminary results demonstrate that while it might be expected that the assimilation of error-free snow observations would lead to improved LSM results, a small LSM temperature bias leads to large-scale errors in the water balance. Even if the snow assimilation system perfectly reconciled modeled and observed snowpack states, the law of mass conservation could still be violated if biases exist in the model. Complicating the issue is the fact that in practice, snow observations are not without error. As such, more research is needed to determine how best to reconcile imperfect snow observations with LSMs that may be characterized by model biases.

*Corresponding Author: Brian A. Cosgrove
NASA Goddard Space Flight Center
Mail Code 974, Greenbelt, MD 20771
Email: Brian.Cosgrove@gsfc.nasa.gov

American Meteorological Society

AMS

2002 Annual Meeting

January 13-17
Orlando, FL

P1.11 AN INTEGRATED AIRBORNE MEASUREMENT SYSTEM FOR THE DETERMINATION OF ATMOSPHERIC TURBULENCE AND OCEAN SURFACE WAVE FIELD PROPERTIES

Gennaro H. Crescenti, Jeffrey R. French, and Timothy L. Crawford
Air Resources Laboratory Field Research Division
National Oceanic and Atmospheric Administration
Idaho Falls, Idaho

Douglas C. Vandemark
Laboratory for Hydrospheric Processes
NASA / Goddard Space Flight Center
Wallops Island, VA

1. INTRODUCTION

A small single-engine research aircraft has been used in numerous air-sea interaction research studies to investigate the spatial variation of both the marine atmospheric boundary layer and the ocean surface wave field. The integrated instrument suite of *in situ* sensors carried by a LongEZ (registration N3R) airplane is used to measure mean properties of the atmosphere as well as turbulent fluxes of heat, moisture, and momentum. These data are coupled with remote sensor measurements of the ocean surface, such as sea surface temperature, wave height, length, slope, and phase. This integrated measurement platform is a powerful tool to directly examine mass, momentum and energy exchange processes occurring across the air-sea interface.

2. AIRCRAFT

Over the last ten years, N3R (Fig. 1) has been used in a number of air-sea interaction research studies (Crawford et al. 1993, Crescenti et al. 1999; Vogel and Crawford 1999; French et al. 2000; Mourad et al. 2000; Vandemark et al. 2001). N3R is set apart from other airborne measurement platforms for a number of reasons.

Fig. 1. N3R in flight during a research mission.

Corresponding author address: Gennaro H. Crescenti, U.S. Dept. Commerce / NOAA, Air Resources Laboratory 1750 Foote Drive, Idaho Falls, ID 83402; e-mail: jerry.crescenti@noaa.gov

The LongEZ was designed in the early 1980's as a high-performance sport aircraft. N3R is a custom-built aircraft licensed by the Federal Aviation Administration (FAA) under an experimental amateur- built airworthiness category. It is a safe and reliable aircraft with exceptional performance characteristics. The differences of N3R from that of other single-engine aircraft are visually apparent. Unlike most aircraft that are constructed with metal, N3R is fabricated from a lighter and stronger fiberglass and foam composite. Another important difference is that the engine is mounted on the rear of the airframe. The large main laminar-flow wing is set back further than that of conventional aircraft. Vertical winglets found on either end of the main wing enhance aircraft lift. A smaller second wing (canard) is found near the nose of the aircraft. This forward lifting surface is designed to increase aircraft stability and to prevent the main wing from stalling.

An important characteristic of an aircraft with a pusher engine and a canard is that it responds to turbulence far less than conventional aircraft with the same wing loading (weight per unit area). Since the canard contributes to both lift and stability, it can be heavily loaded relative to the main wing. For conventional aircraft with a rear-mounted elevator, an upward wind gust will tend to make the aircraft pitch up. This increases the lift generated by the wings and amplifies the aircraft response to an upward wind gust. In contrast, canard aircraft have their elevators forward of their center of gravity. The same upward wind gust will push the canard elevator up which results in a compensating downward pitch response. Aircraft pitch response to either upward or downward wind gusts is opposed to the gust direction, thus giving canard-type aircraft their superior turbulent response characteristics.

A canard aircraft is also stall-resistant. As the angle of attack on the airplane is increased, the canard loses lift before the main wing. This causes the nose to drop, which decreases the angle of attack, thereby providing automatic stall recovery without allowing the main wing to stall.

8. SUMMARY

The N3R integrated airborne measurement system is capable of acquiring high-fidelity atmospheric turbulence and ocean surface wave field data. N3R is a high-utility aircraft that is an ideal platform to carry state-of-the science *in situ* and remote sensors. These data are being used to advance our understanding of air-sea interaction.

NASA/TM-2002-210005

SIMBIOS Project 2001 Annual Report

Giulietta S. Fargion, Science Applications International Corporation, Maryland
Charles R. McClain, Goddard Space Flight Center, Greenbelt, Maryland

National Aeronautics and
Space Administration

Goddard Space Flight Center
Greenbelt, Maryland 20771

March 2002

Chapter 2

SIMBIOS: Science Team and Contracts

Giulietta S. Fargion

Science Applications International Corporation (SAIC), Beltsville, Maryland

2.1 SCIENCE TEAM

The Science Team is selected through a NASA Research Announcement (NRA). Presently, NASA has had two NRA's, in 1996 and 1999. NASA HQ manages the process of team selection, but the Goddard Space Flight Center (GSFC) NASA Procurement Office handles the team contracts, work statements and, if necessary, budget negotiations. The Project funds numerous US investigators and collaborates with several international investigators, space agencies (e.g., NASDA, CNES, KARI, etc.) and international organizations (e.g., IOCCG, JRC). US investigators under contract provide *in situ* atmospheric and bio-optical data sets, and develop algorithms and methodologies for data merger schemes. NASA GSFC Procurement requires formal evaluations for all contracts at the end of each contract year. These evaluations are to go into a database and are shared with the PI's institution or upper management.

The locations of specific SIMBIOS team investigations (i.e., NRA-99) are shown in Figures 2.1. The international ocean color community response for the NRA-99 was overwhelming, with a total of 75 PI's attempting to collaborate with the Project group in twelve proposals. The twelve international proposals cover topics ranging from protocols, calibration-validation activities, atmospheric-biological algorithms, and data merging.

The SIMBIOS Science Team (NRA-96) meetings were held in August 1997 at Solomons Island (Maryland), in September 1998 at La Jolla (California) and in September 1999 at Annapolis (Maryland). Meanwhile, the SIMBIOS Science Team's (NRA-99) meeting will be held in January 2001 at GSFC in Greenbelt, Maryland and in January 2002 at the Mariott (BWI), Baltimore, Maryland.

In general, all Science Team members, US and international, were in attendance or were represented by one of their staff. Also, the IOCCG and MODIS Teams are invited, and most attended or sent representatives. During each year the Project Office has fostered international collaborations by hosting visiting scientists at GSFC. These visits lasted from one week to several months. For international participants, the Project provided partial or as-needed travel support to team meetings or to collaborate with the project on specific topics such as calibration, and product evaluations.

The fifth science team meeting (January 2002) was the most attended, participation reached over 90 scientists (Figure 2.2). The team had a substantial US (SIMBIOS and MODIS PIs) and international participation, with official representation from OCTS, POLDER-I and II, MOS, MERIS, GLI, and VIIRS misssions. During the meeting the team addressed atmospheric correction and bio-optical algorithms, a MODIS data merging plan for 2002, uncertainty budget and sources from in situ observation, SeaWIFS re-processing, protocols updates and international collaborations. The agenda, presentations, minutes and recommendations are posted at http://simbios.gsfc.nasa.gov/Info/

Chapters 4 to 21 contain the individual PI's contributions and describe the funded research topics, field studies activities, and results of concluded research. These chapters are reproduced as submitted with minimal editing by thr Project Office.

2.2 CONTRACT OVERVIEW

The second-year of the SIMBIOS NRA-99 contracts ended on November 30, 2000. The SIMBIOS Project scheduled a telephone conference (telecon), of about 30-45 minutes, with each PI and other appropriate staff during the month of October. Prior to the telecon, the SIMBIOS Project reviewed each contract, the statement of work, and the agreed to deliveries. The Project Office followed the same procedure used in 1999 and coordinated an inside panel with key contract and project personnel to perform an across-the-board evaluation of all funded contracts (Table 2.1).

Table 2.1 Contract evaluation key personnel

Contracting Officer:	Lynne Hoppel
Contracting Assistant:	Kathy Lingerfelt
Resource/Financial Officer:	Patty Clow
Manager , SIMBIOS Project:	Giulietta Fargion
Manager, Office for Global Carbon Studies:	Charles McClain

The four categories to be evaluated are suggested in the "Evaluation of Performance" from the Federal Acquisition Regulation (FAR) 42.15 and NASA FAR Supplement (NSF) 1842.15 or NASA form 1680 used by GSFC.

NASA/TM-2002-210005

SIMBIOS Project 2001 Annual Report

Giulietta S. Fargion, Science Applications International Corporation, Maryland
Charles R. McClain, Goddard Space Flight Center, Greenbelt, Maryland

National Aeronautics and
Space Administration

Goddard Space Flight Center
Greenbelt, Maryland 20771

March 2002

Chapter 3

SIMBIOS Project Data Processing and Analysis Results

Giulietta Fargion, Bryan Franz, Ewa Kwiatkowska-Ainsworth, Christophe Pietras and Paul Smith
Science Applications International Corporation (SAIC), Beltsville, Maryland

Sean Bailey, Joel Gales and Gerhard Meister
FutureTech Corporation, Greenbelt, Maryland

Kirk Knobelspiesse and Jeremy Werdell
Science Systems and Applications Inc., Greenbelt, Maryland

Charles McClain and Gene Feldman
NASA Goddard Space Flight Center, Greenbelt, Maryland

3.1 INTRODUCTION

The SIMBIOS Project is concerned with ocean color satellite sensor data intercomparison and merger for biological and interdisciplinary studies of the global oceans (Barnes et al., 2000). Imagery from different ocean color sensors (OCTS, POLDER, SeaWiFS, MOS and OSMI) can now be processed by a single software package using the same algorithms, adjusted by different sensor spectral characteristics, and the same ancillary meteorological and environmental data. This enables cross-comparison and validation of the data derived from satellite sensors and, consequently, creates continuity in ocean color information on both the temporal and spatial scale. The next step in this process is the integration of *in situ* ocean and atmospheric parameters to enable cross-validation and further refinement of the ocean color methodology. The SIMBIOS Project Office accomplishments during 2001 year are summarized under (a) satellite data processing, (b) data merging (c) SeaBASS database, (d) supporting services, (e) sun photometers and calibration activities and (f) calibration round robins. These accomplishments are described below.

3.2 SATELLITE DATA PROCESSING

3.2.1 Satellite Characterization

The SIMBIOS Project has worked closely with our colleagues in the OSMI Program and with the instrument manufacturer to define and assemble the instrument performance characteristics required for the lookup tables for the algorithms that determine OSMI top-of-the-atmosphere radiances. Of special importance in this regard are the spectral responses of the OSMI bands and the spatial co-registration of the detectors. In addition, the Project has opened a collaboration with the GLI Program.GLI is scheduled for launch nor sooner than November 2002. The GLI/SIMBIOS collaboration has centered on the characteristics of the GLI scan mirror as a function of scan angle and the normalization of detector-to-detector gain differences in the GLI bands. Plans are underway for a cross-calibration of the GLI and SeaWiFS near infrared bands, which are used for the determination of the aerosol type and amount for the atmospheric correction algorithms.

3.2.2 MOS Data Collection, Processing, and Distribution

Since February of 1999, the SIMBIOS project has been operating a receiving station at NASA's Wallops Flight Facility (WFF) to acquire data from the German Modular Optoelectronic Scanner (MOS) onboard the Indian IRS-P3 spacecraft. When a pass is acquired at Wallops, the raw files are transferred to the SIMBIOS project at NASA's Goddard Space Flight Center via an automated FTP process. The raw files are then converted to Level-0 format through a software package provided by the Indian Space Research Organization (ISRO). The resulting Level-0 files are made available to the German Remote Sensing Data Centre (DLR-DFD) for archive and distribution. In addition, the SIMBIOS project is processing the data through Level-1B using the standard software provided by the German Institute for Space Sensor Technology (DLR-ISST) (Neumann et al., 1995). All data processed by the SIMBIOS project is made available through the MOS browse system at http://simbios.gsfc.nasa.gov/oceancolor.html. The Level-1B data can be processed to Level-2 using SIMBIOS-developed software tools distributed through SeaDAS.

NASA/TM-2002-210005

SIMBIOS Project 2001 Annual Report

Giulietta S. Fargion, Science Applications International Corporation, Maryland
Charles R. McClain, Goddard Space Flight Center, Greenbelt, Maryland

National Aeronautics and
Space Administration

Goddard Space Flight Center
Greenbelt, Maryland 20771

March 2002

Preface

The purpose of this technical report is to provide current documentation of the the Sensor Intercomparison and Merger for Biological and Interdisciplinary Oceanic Studies (SIMBIOS) Project activities, NASA Research Announcement (NRA) research status, satellite data processing, data product validation, and field calibration. This documentation is necessary to ensure that critical information is related to the scientific community and NASA management. This critical information includes the technical difficulties and challenges of validating and combining ocean color data from an array of independent satellite systems to form consistent and accurate global bio-optical time series products. This technical report is not meant as a substitute for scientific literature. Instead, it will provide a ready and responsive vehicle for the multitude of technical reports issued by an operational project.

The SIMBIOS Science Team Principal Investigators (PIs) original contributions to this report are in chapters four and above. The purpose of these contributions is to describe the current research status of the SIMBIOS-NRA-96 funded research. The contributions are published as submitted, with the exception of minor edits to correct obvious grammatical or clerical errors.

BUENOS AIRES 2002
29th International
Symposium on Remote
Sensing of
Environment
"Information for
Sustainability and
Development"
April 8 – 12, 2002
Buenos Aires
ARGENTINA
CONAE
29th International
Symposium on
Remote Sensing
of Environment

Seasonal Snow Extent and Snow Mass from 1988 - 2001 in the Patagonia Region of South America Using SSM/I Passive Microwave Data

J. L. Foster, A. T. C. Chang, D. K. Hall, and R. Kelly
NASA/Goddard Space Flight Center
Hydrological Sciences Branch
Greenbelt, MD USA 20771

jfoster@glacier.gsfc.nasa.gov

ABSTRACT - Seasonal snow cover in South America was examined in this study using passive microwave satellite data from the Special Sensor Microwave Imagers (SSM/I) on board Defense Meteorological Satellite Program (DMSP) satellites. For the period from 1988-2001, both snow cover extent and snow depth (snow mass) were investigated during the winter months (May-August) in the Patagonia region of Argentina. Since above normal temperatures in this region are typically above freezing, the coldest winter month was found to be not only the month having the most extensive snow cover but also the month having the deepest snows. For the fourteen-year period of this study, the average snow cover extent (May-August) was about 0.46 million km^2 and the average monthly snow mass was about 1.18 x 10^{13} kg. July 2000 was the month having the greatest snow extent (8.1 million km^2) and snow mass (approximately 2.8 x 10^{13} kg).

I. INTRODUCTION

Using data from the SSM/I on board DMSP satellites, seasonal snow extent and snow depth (snow mass) have been calculated for the period from 1988-2001 in the middle latitudes of South America. It should be noted that in mid winter approximately 99% of the snow cover in the Southern Hemisphere is confined to Antarctica. The data record shows that South America is the only continent in the Southern Hemisphere (other than Antarctica) where an extensive, non-mountainous, winter snow cover may occur. Therefore, the emphasis in this study is on South America. The objectives of this study are to map the seasonal snow cover during the cold months of the year using passive microwave satellite data and to generate a snow record comparable to the record for North America and Eurasia.

II. STUDY AREA

In southern Argentina, snow may accumulate as early as May and as late as October. Each winter, snow is a regular feature south of about 45 degrees latitude, and in the snowiest years, over 1 million square km of snow has been measured (Dewey and Heim, 1983). A single storm may cover the ground with several hundred thousand km^2 of snow. Snow can fall at locations much further north than expected, and it can even lay on the ground for a few days as far north as 27 degrees south latitude. Snow here is usually confined to elevations greater than 1,000 meters above sea level, where as much as 30 cm of snow has been observed in southern Brazil. In July 2000, freezing temperatures and snowfall in southern Brazil and Paraguay damaged coffee crops (Prohaska, 1976).

Typically, snow cover in southern South America results from disturbances embedded in the westerly air streams. East winds and heavy precipitation during the winter in southern South America are caused by quasi-stationary, high-pressure systems at high latitudes over the western South Atlantic Ocean (Kidson, 1988). These anticyclones block the normally zonal air flow in such a way that normal sea level cyclonic systems are steered around the "high" toward Patagonia (the South American states of Rio Negro, Chubut, Santa Cruz and Tierra Del Fuego). In southeastern Brazil, snow can fall when incursions of polar air from the south push northward, coincident with a weakening of the normally dominant sub-tropical high-pressure belt.

Although snow cover may be significant in South America in terms of its effects on weather, especially temperature and agriculture, it is variable from year-to-year. This is to be expected when accumulations generally are shallow. According to Dewey and Heim (1983), over a 7-year period from 1974-1980, snow cover reached a maximum extent of about 1 x 10^6 million km^2 in 1980, but in 1979, the maximum extent was only about 70% of this amount. For comparison, during the 1980 snow season, snow covered an area about the size of the country of Boliva.

VI CONCLUSIONS

Exclusive of Antarctica, seasonal snow in the Southern Hemisphere is, for the most part, confined to South America. Though snow may fall and even persist on the ground for several days in Africa and Australia, on those continents, however, snow is basically a novelty. This study demonstrates that passive microwave radiometry is especially useful in estimating the snow cover extent and snow mass in areas where clouds are a near-constant problem and where the snow is typically ephemeral. The passive microwave observations show that there are sharp year-to-year differences that exist in the seasonal snow extent over the Patagonia region of South America. This agrees with earlier findings in the work of Dewey and Heim (1983).

SPIE Conference on Remote Sensing for Agriculture, Ecosystems, and Hydrology – 2002

September 17-22, 2002
Capsis Sofitel Conference Center
Agia Pelagia
Crete, Greece

Comparison of Relative Errors in Snow Maps in North America and Eurasia in 2001-02

J. L. Foster*, D. K. Hall*, R. E. J. Kelly**, A. T. C. Chang*, J.Y.L. Chien***

*Code 974, NASA/Goddard Space Flight Center
Greenbelt, MD 20771 U.S.A.
email: jfoster@glacier.gsfc.nasa.gov
phone: 301-614-5769, fax: 301-614-5808

**Goddard Earth Sciences and Technology Center
University of Maryland, Baltimore County
Baltimore, MD 21250 U.S.A.

***General Sciences Corporation, Laurel, MD 20707 U.S.A.

ABSTRACT

Results of this investigation confirm previous results by several authors (see Armstrong and Brodzik, 1999; Hall et al., in press) that correspondence between the MODIS and SSM/I-derived snow maps improves as the winter progresses. Early in the season, the SSM/I snow mapping algorithms are unable to identify shallow and wet snow as snow cover, while the MODIS snow maps perform well under those circumstances, but cannot map snow through clouds and cannot provide estimates of SWE. By mid winter when the snowpack is deeper, temperatures are colder, and liquid water in the snowpack is minimal, the agreement between MODIS- and SSM/I-derived snow maps improves. For North America, the difference averaged about 5% for maps examined in February of 2002, and for Eurasia (eastern Asia), the difference was less than 10% in January of 2001.

1. INTRODUCTION

Accurate snow maps are required for hydrological and climatological applications and by operational agencies to monitor snow conditions, and to predict spring water supply and flood conditions. Visible/near-infrared-based snow maps have the advantage of high spatial and temporal resolution (tens of meters and daily coverage) and the ability to measure albedo, while passive-microwave snow maps have a high temporal resolution, the spatial resolution is poor (on the order of tens of km). However, passive microwave data are indifferent to clouds and darkness, but visible data are limited to daytime operation, and clouds limit their mapping efficacy. In this study, Moderate Resolution Imaging Spectroradiometer (MODIS) and Special Sensor Microwave Imager (SSMI) snow data are examined and compared during the winter season in North America and Eurasia.

Since November 1978, the Scanning Multichannel Microwave Radiometer (SMMR) instrument on the Nimbus-7 satellite, and the SSMI on the Defense Meteorological Satellite Program (DMSP) series of satellites have been acquiring passive microwave data that can be used to estimate both snow extent and snow water equivalent (snow depth). In addition, passive-microwave sensors have the capability to estimate snow depth and snow-water equivalent (SWE) as well as snow extent.

NASA's MODIS sensor on-board the Terra and Aqua satellites, and the Advanced Microwave Scanning Radiometer (AMSR) currently all produce snow maps. The Terra satellite, launched in December of 1999, has the MODIS as part of its payload of five instruments, while the Aqua satellite, launched in May of 2002, contains a second MODIS instrument, the AMSR-E and four other instruments. Snow maps have

NASA/TM-2002-210004/Rev3-Vol2

James L. Mueller[1] and Giulietta S. Fargion[2]
Editors

[1] *CHORS, San Diego State University, San Diego, California*
[2]*Science Applications International Corporation, Beltsville, Maryland*

Ocean Optics Protocols For Satellite Ocean Color Sensor Validation, Revision 3, Volume 2

J. L. Mueller, C. Pietras, S. B. Hooker, D. K. Clark, A. Morel, R. Frouin, B.G. Mitchell, R. R. Bidigare, C. Trees, J. Werdell, G. S. Fargion, R. Arnone, R. W. Austin, S. Bailey, W. Broenkow, S. W. Brown, K. Carder, C. Davis, J. Dore, M. Feinholz, S. Flora, Z.P. Lee, B. Holben, B. C. Johnson, M. Kahru, D. M. Karl, Y. S Kim, K. D. Knobelspiesse, C. R. McClain, S. McLean, M. Miller, C. D. Mobley , J. Porter, R.G. Steward, M. Stramska, L. Van Heukelem, K. Voss, J. Wieland, M. A.Yarbrough and M. Yuen.

National Aeronautical and
Space administration

Goddard Space Flight Space Center
Greenbelt, Maryland 20771

February 2002

Chapter 14

Sun and Sky Radiance Measurements and Data Analysis Protocols

Robert Frouin[1], Brent Holben[2], Mark Miller[3], Christophe Pietras[4], Kirk D. Knobelspiesse[5], Giulietta S. Fargion[4], John Porter[6] and Ken Voss[7]

[1]*Scripps Institution of Oceanography, University of California, San Diego, California*
[2]*Biospheric Sciences Branch, NASA Goddard Space Flight Center, Greenbelt, Maryland*
[3]*Department of Applied Science, Brookhaven National Laboratory, Upton, New York*
[4]*SAIC General Sciences Corporation, Beltsville, Maryland*
[5]*Science Systems and Applications, Inc., Greenbelt Maryland*
[6]*School of Ocean & Earth Science & Technology, University of Hawaii, Hawaii*
[7]*Physics Department, University of Miami, Florida*

14.0 INTRODUCTION

This chapter is concerned with two types of radiometric measurements that are required to verify atmospheric correction algorithms and to calibrate vicariously satellite ocean color sensors. The first type is a photometric measurement of the direct solar beam to determine the optical thickness of the atmosphere. The intensity of the solar beam can be measured directly, or obtained indirectly from measurements of diffuse global upper hemispheric irradiance. The second type is a measurement of the solar aureole and sky radiance distribution using a CCD camera, or a scanning radiometer viewing in and perpendicular to the solar principal plane.

From the two types of measurements, the optical properties of aerosols, highly variable in space and time, can be derived. Because of the high variability, the aerosol properties should be known at the time of satellite overpass. Atmospheric optics measurements, however, are not easy to perform at sea, from a ship or any platform. This complicates the measurement protocols and data analysis. Some instrumentation cannot be deployed at sea, and is limited to island and coastal sites. In the following, measurement protocols are described for radiometers commonly used to measure direct atmospheric transmittance and sky radiance, namely standard sun photometers, fast-rotating shadow-band radiometers, automated sky scanning systems, and CCD cameras. Also discussed are methods of data analysis and quality control, as well as proper measurement strategies for evaluating atmospheric correction algorithms and atmospheric parameters derived from satellite ocean color measurements.

14.1 AUTOMATIC SUN PHOTOMETER AND SKY RADIANCE SCANNING SYSTEMS

The technology of ground-based atmospheric aerosol measurements using sun photometry has changed substantially since Volz (1959) introduced the first hand-held analog instrument almost four decades ago. Modern digital units of laboratory quality and field hardiness collect data more accurately and quickly and are often equipped for onboard processing (Schmid et al. 1997; Ehsani 1998, Forgan 1994; and Morys et al. 1998). The method used remains the same, i.e., a detector measures through a spectral filter the extinction of direct beam solar radiation according to the Beer-Lambert-Bouguer law:

$$V(\lambda) = V_o(\lambda)\left(\frac{d_o}{d}\right)^2 \exp\left[-\left(\tau(\lambda)M\right)\right]t_g(\lambda), \tag{14.1}$$

where $V(\lambda)$ is the measured digital voltage, $V_0(\lambda)$ is the extra-terrestrial voltage, M is the optical air mass, $\tau(\lambda)$ is the total optical depth, λ is wavelength, d and d_o are respectively the actual and average earth-sun distances, and $t_g(\lambda)$ is the transmission of absorbing gases. The total optical depth is the sum of the Rayleigh and aerosol optical depth.

16th Conference on Hydrology

13–17 January 2002
Orlando, Florida

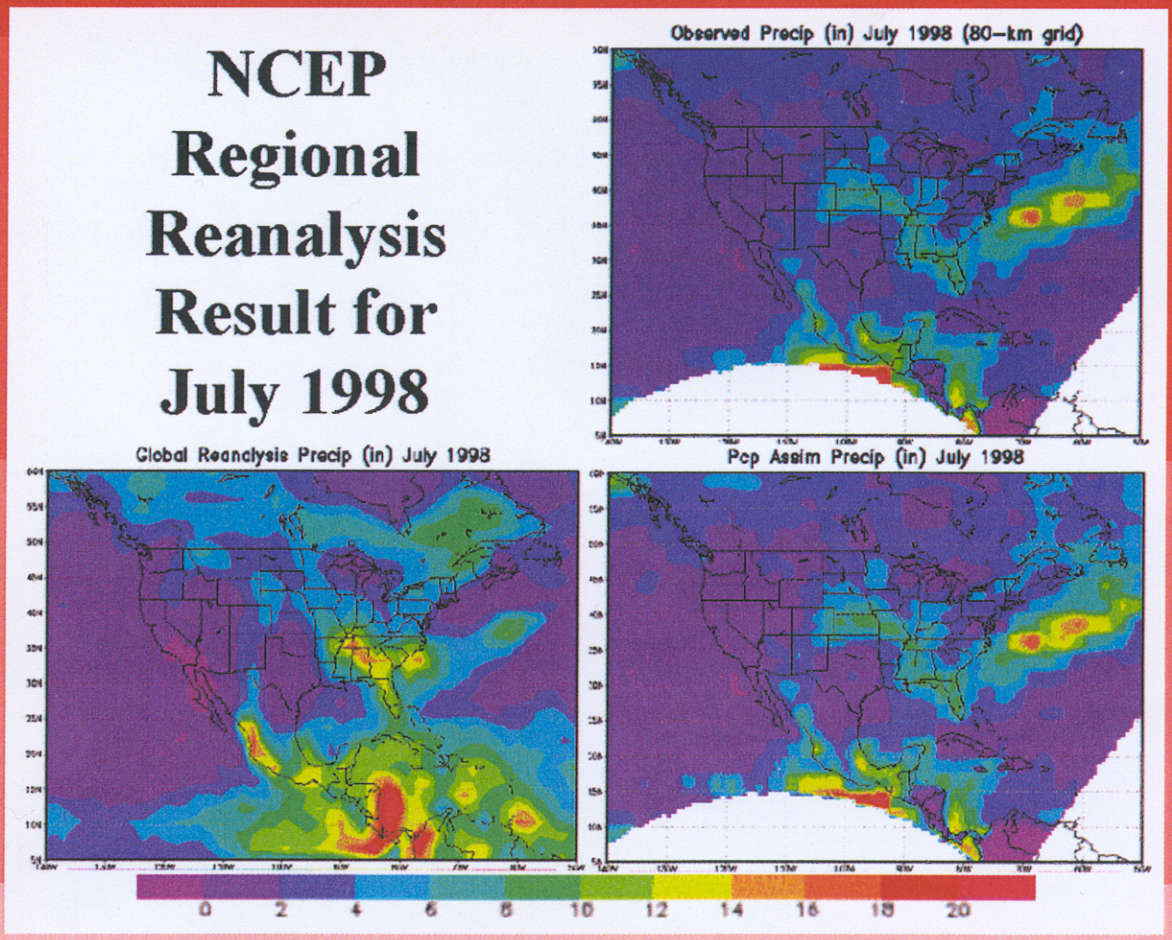

AMERICAN METEOROLOGICAL SOCIETY

J1.15 IMPACT OF REMOTELY SENSED LEAF AREA INDEX ON A GLOBAL LAND DATA ASSIMILATION SYSTEM

Jon C. Gottschalck*[1], Paul R. Houser[1], and Xubin Zeng[2]
[1] NASA / GSFC – UMBC / GEST, Greenbelt, Maryland
[2] University of Arizona, Tucson, Arizona

1. INTRODUCTION

The parameterization of vegetation in land surface models plays a major role in the simulation of the surface energy balance and therefore weather and clim*ate prediction. Historically, parameters in land surface process models have been assigned based on generalized land surface classifications that do not account for local anomalies in phenology. More recently, however, there have been studies that have incorporated satellite remote sensing data in the parameterization of the vegetation used in land surface models (Sellers et al. 1996; Los et al. 2000; Zeng et al. 2001). Satellite data provides better spatial and temporal resolution and so improved sampling of the seasonal variability of critical vegetation parameters such as leaf area index (LAI) and fractional vegetation cover. Our hypothesis is that using these improved remotely-sensed parameters may produce improved land surface simulations and our group is actively working on incorporating satellite remote sensing data into the Global Land Data Assimilation System (GLDAS, http://ldas.gsfc.nasa.gov) currently being developed at NASA's Goddard Space Flight Center and at NOAA's National Center for Environmental Prediction. This paper presents the current state of this work -- our initial methodology and preliminary findings.

3. RESULTS AND DISCUSSION

Differences in the assignment of LAI impact a number of processes and variables in CLM2. In this paper we focus on canopy transpiration, soil surface temperature, and total column soil moisture and focus on North America for the sake of clarity. Figure 2 illustrates the difference in canopy transpiration (original LAI – AVHRR LAI) between the two model simulations after one month. There are some substantial differences mainly over the central and western areas of North America (transpiration lower with the AVHRR LAI) caused by the assignment of much higher values of LAI in the original CLM2 (Figure 1). The vegetation types in these areas include grassland and shrubland that equate to lower LAI values using the radiative transfer algorithm then what other datasets have shown (Sellers et al. 1996; Los et al. 2000). In addition, large areas of cropland in this region are impacted by weather and agricultural changes. The absolute magnitudes in canopy transpiration for the model runs ranged up to 350 Wm^{-2}.

Less canopy transpiration alters the surface energy balance through lower total latent heat flux. Figure 3 illustrates the difference in soil surface temperature and shows a signature very similar to that of Figure 2 with warmer soil surface

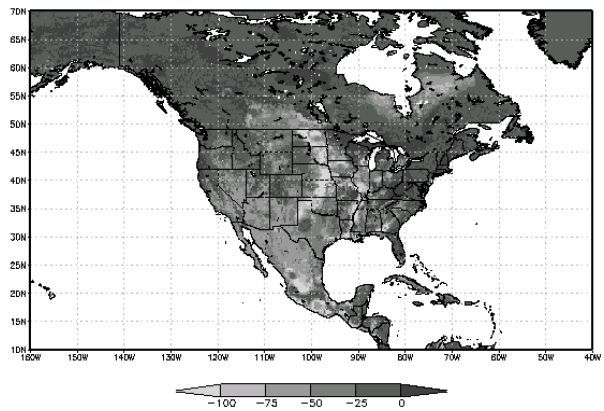

Figure 2: Difference in canopy transpiration (original LAI – AVHRR LAI) in Wm^{-2} valid on 30 June 2001.

temperatures in western North America and in parts of the southeast US and Mississippi River valley where the AVHRR dataset indicates areas of lower LAI. In addition, greater solar radiation enters the soil and allows higher temperatures. The differences are substantial and are range up to and over 10° C warmer for the AVHRR simulation in parts of the central and western US and Mexico. The AVHRR simulation also shows that the soil surface temperature across the whole continent for the most part is warmer than with the original LAI designation. The absolute temperatures in both model runs generally ranged from 260 – 330 °K globally.

The lower transpiration in these areas limits the loss of total soil moisture content for the AVHRR simulation (Figure 4). The soil is significantly moister across Mexico for instance.

* Corresponding author address: Jon C. Gottschalck, Hydrological Sciences Branch – Code 974, NASA / Goddard Space Flight Center, Greenbelt, MD 20771; e-mail: jgottsch@hsb.gsfc.nasa.gov.

NASA/TM-2002-210005

SIMBIOS Project 2001 Annual Report

Giulietta S. Fargion, Science Applications International Corporation, Maryland
Charles R. McClain, Goddard Space Flight Center, Greenbelt, Maryland

National Aeronautics and
Space Administration

Goddard Space Flight Center
Greenbelt, Maryland 20771

March 2002

Chapter 7

Merging Ocean Color Data From Multiple Missions

Watson W. Gregg
NASA Goddard Space Flight Center, Greenbelt, Maryland

7.1 INTRODUCTION

We propose to investigate, develop, and test algorithms for merging ocean color data from multiple missions. We seek general algorithms that are applicable to any retrieved Level-3 (derived geophysical products mapped to an Earth grid) ocean color data products, and that maximize the amount of information available in the combination of data from multiple missions. Most importantly, we will investigate merging methods that produce the most complete coverage in the smallest amount of time, nominally, global daily coverage. We will emphasize 4 primary methods: 1) averaging, 2) subjective analysis, 3) blending, and 4) statistical (optimal) interpolation. We will also assess the ability to produce fuller coverage in larger time increments, including 4-day, 8-day (weekly), monthly, and seasonal. Secondarily, we will investigate the ability of the missions to produce coverage at different times of day, for diel variability and dynamical evaluations, and develop algorithms to produce this information, again on as full a spatial coverage as possible. We intend to develop methods that are not mission-specific, but take advantage of the unique characteristics of the missions as much as possible. However, given the peculiarities of sensor design and performance, and mission characteristics, we acknowledge that individual merging methods may be required to take full advantage of the unique characteristics of the missions as much as possible, and produce the highest quality data set.

7.2 RESEARCH ACTIVITIES

Work has focused on analysis, development, and testing of candidate merger algorithms. We began investigating four possible approaches for merging ocean color satellite data: (1) simple splicing/averaging, where data from two or more satellites are averaged where they coexist at grid points, and use of a single satellite in gaps where only one exists; (2) subjective analysis, where specific dependences and deficiencies are identified using knowledge about sensor environmental conditions and co-located observations are merged using different weighting functions for the sensors; (3) the Conditional Relaxation Analysis Method (CRAM), where the best data are selected as interior boundary conditions into a merged set using Poisson's equation; and (4) optimal interpolation, where merging occurs by weighting individual sensor data to minimize spatial covariance function. The latter two algorithms were developed under separate funding. The algorithms have been characterized and implemented in software; their capabilities and limitations are known, as well as their ability to be modified. The application of algorithms and potential modifications depends on a characterization of the merged data sets.

Significant progress has been made on each of these techniques with the majority of analysis this year focusing on blending. The blended analysis has traditionally been applied to merging satellite and in situ data. Also known as the Conditional Relaxation Analysis Method (CRAM), this analysis assumes that in situ data are valid and uses these data directly in the final product. To blend multiple satellite ocean color data sets, one sensor's data would replace the role of the in situ data as the internal boundary condition (IBC). In January 2001, initial results of the application of blended analysis using SeaWiFS and early MODIS data were presented at the SIMBIOS Science Team Meeting in Greenbelt, Maryland. SeaWiFS chlorophyll data were used as the IBC. The radiometric calibration of the MODIS data was insufficient for scientific use but served the purpose of algorithm investigation. For this preliminary analysis, six weeks of daily Level-3 globally mapped MODIS and SeaWiFS data were obtained from the Goddard DAAC. Routines were written in IDL (Interactive Data Language) to extract the MODIS and SeaWiFS chlorophyll images from their native HDF (Hierarchical Data Format), to scale and orient the images properly, to retrieve the accompanying quality flags for MODIS, and to save the resulting images as FORTRAN binary. Global equal-area mapped MODIS data is available at 4-km, 36-km, and 1-degree; SeaWiFS standard mapped images are at 9-km resolution. Both are available daily, weekly, monthly and yearly. For testing, the blend code was modified to run at different spatial resolutions and several weeks of blended results were obtained using daily 36-km and 1-degree data. Running the blend code at a higher spatial resolution on a global data set is possible, but time consuming.

NASA/TM---2002-104606, Vol. 22

Technical Report Series on Global Modeling and Data Assimilation

Max Suarez, Editor

Volume 22

A Coupled Ocean-Atmosphere Radiative Model for Global Ocean Biogeochemical Models

Watson W. Gregg
Goddard Space Flight Center, Greenbelt, Maryland

National Aeronautics and Space Administration

Goddard Space Flight Center
Greenbelt, Maryland 20771

August 2002

Abstract. An ocean-atmosphere radiative model (OARM) evaluates irradiance availability and quality in the water column to support phytoplankton growth and drive ocean thermodynamics. An atmospheric component incorporates spectral and directional effects of clear and cloudy skies as a function of atmospheric optical constituents, and spectral reflectance across the air-sea interface. An oceanic component evaluates the propagation of spectral and directional irradiance through the water column as a function of water, five phytoplankton groups, and chromophoric dissolved organic matter. It tracks the direct and diffuse streams from the atmospheric component, and a third stream, upwelling diffuse irradiance. The atmospheric component of OARM was compared to data sources at the ocean surface with a coefficient of determination (r^2) of 0.97 and a root mean square of 12.1%.

1 Introduction

Knowledge of oceanic irradiance is critical for realistic simulation of ocean biogeochemistry. Since irradiance affects ocean thermodynamics and physiological processes of biota in the oceans, it may affect the abundances and distributions of phytoplankton, and potentially affect the uptake of carbon dioxide.

In order to understand the effects of irradiance on phytoplankton abundances and primary production in the global oceans, we require a reasonably realistic simulation of the irradiance reaching the ocean surface, and propagating through the water column. The simulation must explicitly include the effects of atmospheric optical constituents on surface irradiance, processes occurring at the air-sea interface, and the results of these effects in the water column taking into account the optical properties of the water, phytoplankton, and dissolved detrital materials. In this paper we describe atmospheric and oceanic radiative transfer models, combined as the Ocean-Atmosphere Radiative Model (OARM) that provide a reasonably complex and realistic representation of atmospheric radiative processes and the irradiance availability in the oceans.

2 Ocean-Atmosphere Radiative Model (OARM)

2.1 Atmospheric Component.

The atmospheric radiative model is based on the Gregg and Carder (1990) spectral model for clear skies, and relies on Slingo (1989) for spectral cloud transmittance. The clear sky model of Gregg and Carder (1990) was derived from Bird and Riordan (1986), but was limited to the spectral range of photosynthetically available radiation (PAR), defined as 350-700 nm. It also contained increased spectral resolution and marine atmospheric and surface reflectance conditions. It compared within $\pm$6.6% root mean square (RMS) with surface observations of spectral irradiance and $\pm$5.1% RMS with integrated PAR (Gregg and Carder, 1990). This model is extended for OARM from the PAR spectral domain to the entire solar spectrum, from 200 nm to 4 um, representing >99% of the total solar irradiance impinging on the top of the atmosphere. For computational efficiency, the spectral resolution is degraded from 1 nm used in Gregg and Carder (1990) to a variable resolution appropriate for the spectral absorbing properties of the major atmospheric optically active gases, specifically ozone, water vapor, oxygen, and carbon dioxide (Table 1). The spectral resolution is fixed at 25 nm for the PAR range, which is the region of interest for phytoplankton photosynthesis.

2002 IEEE International Geoscience and Remote Sensing Symposium and the 24th Canadian Symposium on Remote Sensing

IGARSS 2002

REMOTE SENSING:
Integrating Our View of the Planet

IEEE

June 24-28, 2002
Toronto Canada

Frequency Dependence of Scattering by Dense Media of Small Particles Based on Monte Carlo Simulation of Maxwell's Equations

Jianjun Guo*, Leung Tsang*[§], Alfred T.C. Chang**, Kung-Hau Ding[+], Chi-Te Chen*

*Department of Electrical Engineering, University of Washington, Box 352500, Seattle, WA 98195-2500
Tel: (206)221-6513 Fax: (206)543-3842
[§]Department of Electronic Engineering, City University of Hong Kong, Hong Kong
[+] Air Force Research Lab, Sensors Directorate/SNHE, 80 Scott Road, Hanscom AFB, MA 01731-2909
** Hydrological Sciences Branch, NASA/Goddard Space Flight Center, Greenbelt, MD 20771-0001
Email: jguo@u.washington.edu

Abstract The frequency dependence of scattering by geophysical media at microwave frequencies is an important issue because multi-frequency measurements are useful for remote sensing applications. Classically, the independent scattering theory states that if the particles are small, scattering is proportional to the fourth power in 3-D scattering and the third power in 2-D scattering. In this paper, we study rigorously the frequency dependence of scattering by dense media by Monte Carlo simulations of the solutions of both 2- and 3-dimensional Maxwell's equations. The particle positions are generated by deposition and bonding techniques. The Sparse-Matrix Canonical-Grid method has been applied to speed up the simulation of scattering by 2D small particles. Numerical solutions of Maxwell's equations indicate that the frequency dependence of densely packed sticky small particles is much weaker than that of independent scattering. The results are illustrated using parameters of snow in microwave remote sensing.

I Introduction

Wave propagation and scattering in the densely packed media are important issues in the volume scattering problem of geophysical media [1][2]. The frequency dependence of emission and scattering of snow at microwave remote sensing frequencies (e.g. 19GHz, and 37GHz) is a quantity that must be studied rigorously because multi-frequency measurements are useful for remote sensing applications. When the particles are much smaller than a wavelength, the frequency dependence is to the fourth power for 3-D particles and the third power for the 2-D particles, based on the conventional independent scattering model. Physically, in densely packed media, the particles can adhere to form aggregates. The correlation between particles has to be taken into account. To better understand such a scattering property, we study the frequency dependence of scattering by sticky and non-sticky particles rigorously. In this rigorous approach, we generate the positions of particles rigorously using bonding technique; and then solve the Maxwell's equations that include all the multiple scattering based on Monte Carlo simulation. For the sticky particles, the frequency variation is dependent on a "sticky" parameter representing the degree of adhesiveness of the cylinders. The extinction, scattering and absorption properties of dense media are calculated for dense media of sticky and non-sticky particles. The T-matrix method is used. It has been shown that the internal field formulation of Foldy-Lax equations have much better condition numbers for the matrix equations [2]. Thus the use of internal field formulation is advantageous for iterative solution of the Foldy-Lax matrix equation. Various numerical parameters are tested to show that the results are accurate. Convergence tests are performed for these numerical parameters. A sufficient number of realizations of the Monte Carlo simulations is performed to ensure the convergence. Up to 50 realizations are used in this paper. For most of the cases, the results converge within 20 to 30 realizations. The number of particles used in this study is between 100 and 2000 depending on the fractional volume and frequency.

IV Simulation Results and Discussions

We use the internal field formulation and conjugate gradient (CG) method in computing the numerical results. In the following, we present results for dielectric cylinders with ε_p=3.2 based on Monte Carlo simulations for non-sticky and sticky cylinders (2D problem) and spherical particles (3D problem). In Table 1, we tabulate the results of normalized scattering coefficients κ_s/k for the 2-D scattering problem.

For 3D scattering problem, we tabulate the frequency dependence of scattering rates in Table II. The scattering rate at 18 GHz is used as reference. Assuming the scattering rates and frequencies has the relationship of

$$\frac{\kappa_s(at\ f_2)}{\kappa_s(at\ f_1)} = \left(\frac{f_2}{f_1}\right)^n \tag{9}$$

where f_1 and f_2 are the frequencies, κ_s is the scattering rate at a specific frequency, and n is the index of frequency dependence.

NASA/TM-2002-210004/Rev3-Vol1

James L. Mueller[1] and Giulietta S. Fargion[2]
Editors

[1] *CHORS, San Diego State University, San Diego, California*
[2]*Science Applications International Corporation, Beltsville, Maryland*

Ocean Optics Protocols For Satellite Ocean Color Sensor Validation, Revision 3, Volume 1

J. L. Mueller, C. Pietras, S. B. Hooker, D. K. Clark, A. Morel, R. Frouin, B.G. Mitchell, R. R. Bidigare, C. Trees, J. Werdell, G. S. Fargion, R. Arnone, R. W. Austin, S. Bailey, W. Broenkow, S. W. Brown, K. Carder, C. Davis, J. Dore, M. Feinholz, S. Flora, Z.P. Lee, B. Holben, B. C. Johnson, M. Kahru, D. M. Karl, Y. S Kim, K. D. Knobelspiesse, C. R. McClain, S. McLean, M. Miller, C. D. Mobley , J. Porter, R.G. Steward, M. Stramska, L. Van Heukelem, K. Voss, J. Wieland, M. A.Yarbrough and M. Yuen.

National Aeronautical and
Space administration

Goddard Space Flight Space Center
Greenbelt, Maryland 20771

February 2002

Chapter 8

Stability Monitoring of Field Radiometers Using Portable Sources

Stanford B. Hooker

NASA Goddard Space Flight Center, Greenbelt, Maryland

8.1 INTRODUCTION

Mueller and Austin (1995) included a discussion on tracking instrument performance in between calibration activities with stable lamp sources in rugged, fixed geometric configurations. The recommended specifications of the device included the stability of the lamp output and the repeatability of measurement must be sufficient to detect 2 % variations in an instrument's performance. In terms of the protocols for using the source, it was recommended that an instrument should be connected to the portable standard and its response recorded daily, keeping a record of instrument responsivity throughout an experiment. Furthermore, these sources would provide an essential warning of problems if they appear.

One of the more important requirements in the use of the portable source was it must be available when the complete radiometric calibrations are performed, so a baseline may be established and maintained for each sensor channel, but recognizing that the source cannot be a substitute for complete calibrations. The temporal record they provide will, however, be invaluable in cases where the pre-and post-cruise calibrations disagree or if the instrument is disturbed, e.g., opened between calibrations, subjected to harsh treatment during deployment or transport, or if the data quality are otherwise suspect. These portable standards are an important part of the recommended instrument package.

8.2 The SQM

Although Mueller and Austin (1995) specified the need for, and described some of the requirements of, a portable source, no such device was then commercially available. In response to the need for a portable source, NASA and NIST developed the SQM. The engineering design and characteristics of the SQM are described by Johnson et al. (1998), so only a brief description is given here. A separate rack of electronic equipment, composed principally of two computer controlled power supplies and a multiplexed, digital voltmeter (DVM), are an essential part of producing the stable light field. All of the external components are controlled by a computer program over a general purpose interface bus (GPIB).

The SQM has two sets of halogen lamps with eight lamps in each set; both lamp sets are arranged symmetrically on a ring and operate in series, so if one lamp fails, the entire set goes off. The lamps in one set are rated for 1.05 A (4.2 V) and are operated at 0.95 A, and the lamps in the other set are rated for 3.45 A (5.0 V) and are operated at 3.1 A; the lamp sets are hereafter referred to as the 1 A and 3 A lamps, respectively. The lamps are operated at approximately 95 % of their full amperage rating to maximize the lifetime of the lamps.

A low, medium, and high intensity flux level is provided when the 1 A, 3 A, and both lamp sets are used, respectively. Each lamp set was aged for approximately 50 hours before deploying the SQM to the field. The interior light chamber has bead-blasted aluminum walls, so the diffuse component of the reflectance is significant. The lamps illuminate a circular plastic diffuser protected by safety glass and sealed from the environment by o-rings. The diffuser is resilient to ultraviolet yellowing, but can age nonetheless. The exit aperture is 20 cm in diameter and has a spatial uniformity of 98 % or more over the interior 15 cm circle. The SQM does not have, nor does it require, an absolute calibration, but it has design objectives of better than 2 % stability during field deployments.

A faceplate or *shadow collar* provides a mounting assembly, so the device under test (DUT), usually a radiance or irradiance sensor, can be positioned in the shadow collar. The DUT has a D-shaped collar fitted to it at a set distance, 3.81 cm (1.5 inch), from the front of the DUT. This distance was chosen based on the most restrictive clearance requirement of the radiometers used in the different deployment rigs. The D-shaped collar ensures the DUT can be mounted to the SQM at a reproducible location and orientation with respect to the exit aperture each time the DUT is used.

NASA Technical Memorandum 2002–206892, Volume 19

SeaWiFS Postlaunch Technical Report Series

Stanford B. Hooker, Editor
NASA Goddard Space Flight Center
Greenbelt, Maryland

Elaine R. Firestone, Senior Scientific Technical Editor
Science Applications International Corporation
Beltsville, Maryland

Volume 19, Coastal Atmosphere and Sea Time Series (CoASTS), Part 1: A Tower-Based, Long-Term Measurement Program

Giuseppe Zibordi
Jean-François Berthon
John P. Doyle
Stefania Grossi
Dirk van der Linde
Cristina Targa
JRC Space Applications Institute
Ispra, Italy

Luigi Alberotanza
CNR Institute for the Study of Dynamics of Large Masses
Venice, Italy

ABSTRACT

The Coastal Atmosphere and Sea Time Series (CoASTS) Project, aimed at supporting ocean color research and applications, from 1995 up to the time of publication of this document, has ensured the collection of a comprehensive atmospheric and marine data set from an oceanographic tower located in the northern Adriatic Sea. The instruments and the measurement methodologies used to gather quantities relevant for bio-optical modeling and for the calibration and validation of ocean color sensors, are described. Particular emphasis is placed on four items: 1) the evaluation of perturbation effects in radiometric data (i.e., tower-shading, instrument self-shading, and bottom effects); 2) the intercomparison of seawater absorption coefficients from *in situ* measurements and from laboratory spectrometric analysis on discrete samples; 3) the intercomparison of two filter techniques for *in vivo* measurement of particulate absorption coefficients; and 4) the analysis of repeatability and reproducibility of the most relevant laboratory measurements carried out on seawater samples (i.e., particulate and yellow substance absorption coefficients, and pigment and total suspended matter concentrations). Sample data are also presented and discussed to illustrate the typical features characterizing the CoASTS measurement site in view of supporting the suitability of the CoASTS data set for bio-optical modeling and ocean color calibration and validation.

1. INTRODUCTION

Optical measurements from space enable estimates of the concentration of materials suspended or dissolved in seawater (i.e., pigment, sediment, and colored dissolved organic matter) which are of great relevance in environmental and climate-related studies. Because of this, a number of new advanced ocean color sensors were designed to support oceanographic studies and applications including the Modular Opto-electronic Sensor (MOS), the Ocean Color and Temperature Scanner (OCTS), the Polarization and Directionality of the Earth's Reflectance (POLDER) sensor, the Sea-viewing Wide Field-of-view Sensor (SeaWiFS), the Moderate Resolution Imaging Spectroradiometer (MODIS), and the Medium Resolution Imaging Spectrometer (MERIS). All of these sensors were successfully launched and have contributed significantly to the general problem of inverting optical measurements to derive concentration estimates of biogeochemical parameters; several continue to provide regular coverage of the global biosphere.

To ensure a better exploitation of the data supplied by spaceborne sensors, national and international calibration and validation projects have been started. Their major objectives are the development of the bio-optical algorithms required for extracting quantitative information from space data; the validation of products obtained from satellite imagery; and the indirect absolute calibration (i.e., vicarious calibration) of the radiometers in space. All of these activities require comprehensive *in situ* atmospheric and marine measurements. In agreement with this requirement, the Coastal Atmosphere and Sea Time Series (CoASTS) Project was set up at the Joint Research Centre (JRC) in Ispra, Italy to support bio-optical modeling and ocean color calibration and validation exercises at a coastal site in the northern Adriatic Sea.

In order to provide a comprehensive overview of the CoASTS measurement activities, this report has three primary objectives:

1) Present the instrumentation and the measurement methodologies,
2) Assess the accuracy of the most relevant measurements needed for bio-optical modeling as well as ocean color vicarious calibration and algorithm validation activities; and
3) Discuss sample data that display the relevant features of the measurement site.

10. CONCLUSIONS

This report presented the measurement program used within the CoASTS Project (at the AAOT site) and extensively discussed the applied methods with a particular emphasis on those more relevant for bio-optical modeling and the calibration and validation of ocean color sensors. The methods discussed for the analysis of radiometric measurements highlighted the importance of correcting in-water radiance and irradiance data from superstructure (tower-shading) effects, instrument self-shading, and bottom effects. These perturbations for the specific measurement conditions analyzed in this study, may induce an overall spectral uncertainty in $L_u(0^-\lambda)$ ranging from 4–18% at 412 nm, −2 to +10% at 490 nm, −9 to +10% at 555 nm, and 6–16% at 665 nm.

The intercomparison of seawater absorption coefficients from AC-9 *in situ* measurements and from laboratory spectrometric analysis of discrete seawater samples, showed the best agreement when the scattering correction—for perturbation effects induced in AC-9 data by the finite acceptance angle of the optics and the non-ideal reflective surface of the absorption chamber—is performed removing a variable percentage of the scattering coefficient. In this case, the scatterplots of the absorption coefficients from spectrometric analysis of seawater samples and AC-9 measurements showed average absolute percentage differences of −2, −19, −18, and −18% at 412, 488, 555, and 676 nm, respectively.

NASA Technical Memorandum 2002–206892, Volume 20

SeaWiFS Postlaunch Technical Report Series

Stanford B. Hooker, Editor
NASA Goddard Space Flight Center
Greenbelt, Maryland

Elaine R. Firestone, Senior Scientific Technical Editor
Science Applications International Corporation
Beltsville, Maryland

Volume 20, Coastal Atmosphere and Sea Time Series (CoASTS), Part 2: Data Analysis

Jean-François Berthon
Giuseppe Zibordi
John P. Doyle
Stefania Grossi
Dirk van der Linde
Cristina Targa
JRC Space Applications Institute
Ispra, Italy

ABSTRACT

In this document, the first three years of a time series of bio-optical marine and atmospheric measurements are presented and analyzed. These measurements were performed from an oceanographic tower in the northern Adriatic Sea within the framework of the Coastal Atmosphere and Sea Time Series (CoASTS) project, an ocean color calibration and validation activity. The data set collected includes spectral measurements of the in-water apparent (diffuse attenuation coefficient, reflectance, Q-factor, etc.) and inherent (absorption and scattering coefficients) optical properties, as well as the concentrations of the main optical components (pigment and suspended matter concentrations). Clear seasonal patterns are exhibited by the marine quantities on which an appreciable short-term variability (on the order of a half day to one day) is superimposed. This short-term variability is well correlated with the changes in salinity at the surface resulting from the southward transport of freshwater coming from the northern rivers. Concentrations of chlorophyll a and total suspended matter span more than two orders of magnitude. The bio-optical characteristics of the measurement site pertain to both Case-1 (about 64%) and Case-2 (about 36%) waters, based on a relationship between the beam attenuation coefficient at 660 nm and the chlorophyll a concentration. Empirical algorithms relating in-water remote sensing reflectance ratios and optical components or properties of interest (chlorophyll a, total suspended matter, and the diffuse attenuation coefficient) are presented.

1. INTRODUCTION

The use of remotely-sensed ocean color data has increased considerably over the last years, since several new sensors were put in orbit more than 10 years after the Coastal Zone Color Scanner (CZCS) ceased its activity. These sensors, specifically, the Sea-viewing Wide Field-of-view Sensor (SeaWiFS), the Ocean Color and Temperature Scanner (OCTS), the Marine Optical Spectroradiometer (MOS), the Moderate Resolution Imaging Spectroradiometer (MODIS), and the Medium Resolution Imaging Spectrometer (MERIS), present advanced characteristics compared to CZCS, in the addition of a certain number of channels, and an increased signal-to-noise ratio and dynamic range (IOCCG 1998). These increased capacities are intended, in particular, to improve the retrieval of chlorophyll a concentration in the open ocean (Hooker et al. 1992 and O'Reilly et al. 1998), as well as eventually allowing the retrieval of additional marine quantities such as total suspended matter or colored dissolved organic matter (Carder et al. 1999).

For the open ocean, the possibility of retrieving chlorophyll a and additional water components from remotely-sensed data is presumably simplified, because in most cases, they all co-vary (but see Carder et al. 1991). In coastal waters (where most of the so-called optical "Case-2" waters can be found), however, this retrieval is less successful. In effect, because of the diversity of the sources (rivers, atmospheric input, bottom resuspension, etc.) the simplifying assumption of co-variation may not be verified. Consequently, by contributing—often antagonistically—to the total marine signal, the occurrence of these different components makes their separation much more difficult on an optical basis.

As a consequence of the number of sensors now operational, there is an increasing demand for *in situ* bio-optical data (water and atmosphere) in order to address two main topics:

1) The development of models and algorithms allowing the retrieval of marine and atmospheric quantities from the signal at the top of the atmosphere; and
2) The vicarious calibration of the sensors, and the validation of their different products.

Programs including time-series of measurements on specific sites such as the Marine Optical Buoy (MOBY, Clark et al. 1997), the Yamato Bank Optical Mooring (YBOM, Kishino et al. 1997), and the Plymouth Marine Bio-Optical Data Buoy (PlyMBODy, Pinkerton and Aiken 1999), or repetitive ship cruises such as the Atlantic Meridional Transect (AMT) program (Aiken et al. 2000) were developed considerably in the past years. Basing the investigation of the environment on a long time or space scale, one of their objectives was, in particular, to encompass a wide range of optical properties and concentration of optically significant components.

In this context, a program of extensive *in situ* measurements called the Coastal Atmosphere and Sea Time Series (CoASTS), was set up (Zibordi et al. 2002). Within this program, a series of marine and atmospheric measurements are performed from an oceanographic tower located in the northern Adriatic Sea, off the Venice Lagoon. As of this writing, the project has provided more than six years of data (with a frequency of 1–2 campaigns per month) including water apparent and inherent optical properties and the corresponding optically significant components, as well as atmospheric measurements, which allows for the estimation of aerosol properties. The resulting data set was

NASA Technical Memorandum 2002–206892, Volume 17

SeaWiFS Postlaunch Technical Report Series

Stanford B. Hooker, Editor
NASA/Goddard Space Flight Center
Greenbelt, Maryland

Elaine R. Firestone, Senior Scientific Technical Editor
Science Applications International Corporation
Beltsville, Maryland

Volume 17, The Seventh SeaWiFS Intercalibration Round-Robin Experiment (SIRREX-7), March 1999

Stanford B. Hooker
NASA/Goddard Space Flight Center
Greenbelt, Maryland

Scott McLean
Jennifer Sherman
Mark Small
Gordana Lazin
Satlantic, Inc.
Halifax, Canada

Giuseppe Zibordi
JRC/SAI/Marine Environment Unit
Ispra, Italy

James W. Brown
RSMAS/University of Miami
Miami, Florida

Abstract

This report documents the scientific activities during the seventh SeaWiFS Intercalibration Round-Robin Experiment (SIRREX-7) held at Satlantic, Inc. (Halifax, Canada). The overall objective of SIRREX-7 was to determine the uncertainties of radiometric calibrations and measurements at a single calibration facility. Specifically, this involved the estimation of the uncertainties in a) lamp standards, b) plaque standards (including the uncertainties associated with plaque illumination non-uniformity), c) radiance calibrations, and d) irradiance calibrations. The investigation of the uncertainties in lamp standards included a comparison between a calibration of a new FEL by the National Institute of Standards and Technology (NIST) and Optronic Laboratories, Inc. In addition, the rotation and polarization sensitivity of radiometers were determined, and a procedure for transferring an absolute calibration to portable light sources was defined and executed.

Prologue

The Sea-viewing Wide Field-of-view Sensor (SeaWiFS) Project at the National Aeronautics and Space Administration (NASA) Goddard Space Flight Center (GSFC) has two important goals with respect to the spaceborne radiance measurements (Hooker and Esaias 1993): a) normalized water-leaving radiance with an uncertainty to within 5%, and b) chlorophyll *a* concentration with an uncertainty to within 35%. These goals are very ambitious, and can only be achieved by augmenting the SeaWiFS measurements with a program of ongoing validation measurements to a) verify the radiometric uncertainty and long-term stability of the SeaWiFS instrument's radiance responsivities, and b) validate the atmospheric correction models and algorithms used to convert SeaWiFS radiances to water-leaving radiances, $L_W(\lambda)$. One of the principal approaches to this critical aspect of the SeaWiFS mission are frequent direct comparisons between spaceborne and *in situ* measurements of $L_W(\lambda)$. Because there are many sources of uncertainty contributing to the final uncertainty objective (5%), each source must be minimized and kept at the lowest level possible. The goal for the calibration of the field instruments has always been to have reproducible calibrations from 400–850 nm as close to 1% as possible (with 2% as a hoped for upper limit).

The calibration goal for SeaWiFS field instruments is not only driven by a simple argument of sums. Given the myriad objectives associated with SeaWiFS validation, the only economically feasible approach for acquiring a large and globally distributed database of *in situ* radiometric measurements, is to solicit contributions of data from the oceanographic community at large. Such an approach demands an assurance that the aggregate data set will be of uniform quality, and one of the first points of quality control is maintaining a high standard for instrument calibration (Hooker and McClain 2000).

The entire process is more complicated than a careful scrutiny of calibration facilities, and the SeaWiFS Project is addressing this problem through the SeaWiFS Calibration and Validation Program (McClain et al. 1992). At the outset, the Project sponsored a workshop to draft protocols for ocean optics measurements to support SeaWiFS validation (Mueller and Austin 1992), which included instrument performance specifications, and requirements for instrument characterization and calibration. The importance of the protocols to the community was established by the considerable expansion of the original document to accommodate a broader range of measurements, techniques, and sampling considerations (Mueller and Austin 1995).

The strategy adopted for the validation of the SeaWiFS remote sensing data is to calibrate all of the field instruments within a network consisting of the instrument manufacturers plus a few additional laboratories that have recurringly provided instrument calibrations. In recognition of the need to maintain internal consistency between calibrations of *in situ* instruments and that of the SeaWiFS instrument itself, the SeaWiFS Project, under the Calibration and Validation Program, implemented an ongoing series of SeaWiFS Intercalibration Round-Robin Experiments (SIRREXs). The objectives of the SIRREX activity, at each separate event and over time, are to accomplish the following:

1. Intercalibrate FEL lamp working standards of spectral irradiance and to reference each to the National Institute of Standards and Technology (NIST) scale of spectral irradiance via a secondary or tertiary standard;
2. Intercalibrate the integrating sphere sources of spectral radiance;
3. Intercompare the plaques used to transfer the scale of spectral irradiance from an FEL lamp to a scale of spectral radiance, as well as the support electronics involved (most critically shunts and voltmeters);
4. Evaluate the suitability of the equipment and laboratory methods being employed for radiometric calibrations at each institution; and
5. Intercompare radiometers in the field while evaluating the measurement protocols being used.

NASA Technical Memorandum 2002–206892, Volume 17

SeaWiFS Postlaunch Technical Report Series

Stanford B. Hooker, Editor
NASA/Goddard Space Flight Center
Greenbelt, Maryland

Elaine R. Firestone, Senior Scientific Technical Editor
Science Applications International Corporation
Beltsville, Maryland

Volume 17, The Seventh SeaWiFS Intercalibration Round-Robin Experiment (SIRREX-7), March 1999

Stanford B. Hooker
NASA/Goddard Space Flight Center
Greenbelt, Maryland

Scott McLean
Jennifer Sherman
Mark Small
Gordana Lazin
Satlantic, Inc.
Halifax, Canada

Giuseppe Zibordi
JRC/SAI/Marine Environment Unit
Ispra, Italy

James W. Brown
RSMAS/University of Miami
Miami, Florida

Chapter 2

SIRREX-7 Instrumentation

Stanford B. Hooker
NASA/Goddard Space Flight Center
Greenbelt, Maryland

Scott McLean
Satlantic, Inc.
Halifax, Canada

Abstract

The highest priority for the instrumentation used for SIRREX-7 was to bring together as wide a diversity of equipment used in the laboratory calibration and field measurement process as possible, so the agreed upon minimum number of replicates for a particular equipment type was three. Each participating group contributed more than one example of a particular equipment type, which ensured equipment with a wide range of ages, calibration histories, sensitivities, flux levels, etc. Equipment that was used as part of the digitization or control process, like voltmeters and shunts, were calibrated as close to the SIRREX-7 activity as possible; all other types of equipment were reviewed to ensure their calibration histories were within the guidelines prescribed by the manufacturer or the protocols governing their use (like lamps and plaques). In some cases, equipment that did not meet the recency of calibration requirements were used, so the effect of ignoring this practice (regardless of the reason) could be quantified. In addition, some equipment with known problems were included to see if the outer range of variance in the results was defined by substandard equipment or if other factors (like operator error) were more important.

2.1 INTRODUCTION

The equipment used during SIRREX-7 was representative of the instrumentation used on a regular basis by the ocean color community either for laboratory calibration or field measurements. Although several manufacturers were not represented in the suite of instruments used, the functionality of the missing devices was represented, so individual groups using nonrepresentative equipment can still derive lessons and conclusions from SIRREX-7. With a small number of participants, it was not feasible to accept the added complexity of differing instruments; by using predominantly one manufacturer, it was possible to maximize the number of experiments or the number of replicate samplings within an experiment over the relatively short time period of the activity.

2.2 LAMPS

Many laboratories base their absolute calibrations of irradiance and radiance responsivities on the NIST scale of spectral irradiance, which is available to the wider community through calibrated tungsten–halogen FEL lamps (Walker et al. 1987). Some laboratories acquire a calibrated FEL lamp standard of spectral irradiance directly from NIST, but more typically, a laboratory bases its irradiance scale on a lamp which was calibrated and certified as traceable to the NIST scale by a commercial standardizing laboratory. The former are usually referred to as *secondary* standards, and the latter as *tertiary* standards. In some cases, a laboratory will purchase additional seasoned, but uncalibrated lamps, and transfer the spectral irradiance scale from their primary calibrated lamp using a transfer radiometer (the JRC was experimenting with this approach using L005). The use of less expensive standards for calibration experiments is a common practice in most cases, because it avoids a shortening in the useful lifetime of the primary reference lamp. One of the questions addressed here is what extra uncertainty is associated with this cost-effective practice.

Another type of lamp is the so-called *working lamp*. This lamp is used for illumination requirements in keeping with FEL light levels wherein it would not be prudent or cost effective to reduce the lifetime of a standard lamp. Detailed information about the standard and working lamps used during SIRREX-7 is presented in Table 5. The former are indicated by the "L" codes and the latter by the "W" codes.

NASA Technical Memorandum 2002–206892, Volume 17

SeaWiFS Postlaunch Technical Report Series

Stanford B. Hooker, Editor
NASA/Goddard Space Flight Center
Greenbelt, Maryland

Elaine R. Firestone, Senior Scientific Technical Editor
Science Applications International Corporation
Beltsville, Maryland

Volume 17, The Seventh SeaWiFS Intercalibration Round-Robin Experiment (SIRREX-7), March 1999

Stanford B. Hooker
NASA/Goddard Space Flight Center
Greenbelt, Maryland

Scott McLean
Jennifer Sherman
Mark Small
Gordana Lazin
Satlantic, Inc.
Halifax, Canada

Giuseppe Zibordi
JRC/SAI/Marine Environment Unit
Ispra, Italy

James W. Brown
RSMAS/University of Miami
Miami, Florida

Chapter 1

SIRREX-7 Overview

Stanford B. Hooker
NASA/Goddard Space Flight Center
Greenbelt, Maryland

Scott McLean
Satlantic, Inc.
Halifax, Canada

Abstract

The primary objective of SIRREX-7 was a thorough inquiry into the absolute capability of a single calibration facility. A small team of investigators was assembled to address this question at Satlantic, Inc. The experimental group was kept small, because the entire activity had to take place in a single room with a small number of experimental stations. Because this required a substantial commitment in time and resources, there was a strong desire to learn as much as possible about the equipment and methods normally used in the calibration process. Consequently, a wide diversity of each equipment type was assembled: 10 FEL lamps, 7 reflectance plaques, 10 fixed wavelength radiometers, 1 hyperspectral radiometer, the SXR, 1 single-channel mapping (narrow field-of-view) radiometer, plus the original SQM and 4 SQM-IIs. The instrumentation came from three different organizations with differing calibration and measurement objectives, so the assembled equipment had a diverse range of calibration histories, ages, sizes, intended uses, sensitivities, flux levels, etc. Although SIRREX-7 was conducted at only one facility, the diversity in equipment ensures that a significant subset of the results achieved will have a wider applicability to the larger community.

1.1 INTRODUCTION

The determination of the absolute radiometric response of an irradiance or radiance sensor requires a properly staffed and equipped calibration facility. For SeaWiFS calibration and validation activities, the latter must include stable sources and sensors with defined spectral radiometric characteristics traceable to NIST. The calibration facility must also have a variety of specialized radiometric and electronic equipment, including reflectance plaques, spectral filters, integrating spheres, and highly regulated power supplies for the operation of the lamps. Precision electronic measurement capabilities are also required, both for setting and monitoring lamp current and voltage, and for measuring the output of the radiometer.

Although there have been six previous SIRREXs and significant progress was made at each one, in terms of understanding the sources of uncertainties in radiometric calibrations, a thorough inquiry into the absolute capability of a calibration facility regularly used by the ocean color community was not investigated. This was an important task, because, as already mentioned, the goal of a calibration facility used for SeaWiFS validation is to provide reproducible calibrations from 400–850 nm to within ±1%. SIRREX-7 was convened with a small team of investigators to estimate calibration uncertainties at Satlantic, Inc. The experimental group was kept small, because the entire activity had to take place in a single room. Satlantic agreed to be the hosting organization, because:

1. Many SeaWiFS and SIMBIOS investigators rely on Satlantic equipment and calibrations;
2. They have a state-of-the-art facility (all calibrations are done in a clean room with exceptional baffling and optical alignment equipment);
3. They commercialized the original SQM (so several units were available for an absolute intercomparison experiment); and
4. They have the interest and commitment (having participated in all of the previous SIRREXs) to underwrite the significant financial requirements for the hosting organization.

A final uncertainty budget for any instrument requires a thorough understanding of laboratory and field performance. The SeaWiFS Project participated to provide expertise and unique equipment (the original SQM and SXR), a variety of sources and targets (plaques, FEL lamps, etc.),

NASA Technical Memorandum 2002–206892, Volume 17

SeaWiFS Postlaunch Technical Report Series

Stanford B. Hooker, Editor
NASA/Goddard Space Flight Center
Greenbelt, Maryland

Elaine R. Firestone, Senior Scientific Technical Editor
Science Applications International Corporation
Beltsville, Maryland

Volume 17, The Seventh SeaWiFS Intercalibration Round-Robin Experiment (SIRREX-7), March 1999

Stanford B. Hooker
NASA/Goddard Space Flight Center
Greenbelt, Maryland

Scott McLean
Jennifer Sherman
Mark Small
Gordana Lazin
Satlantic, Inc.
Halifax, Canada

Giuseppe Zibordi
JRC/SAI/Marine Environment Unit
Ispra, Italy

James W. Brown
RSMAS/University of Miami
Miami, Florida

Chapter 8

Absolute Calibration of the SQM and SQM-II

Stanford B. Hooker
NASA/Goddard Space Flight Center
Greenbelt, Maryland

Scott McLean
Gordana Lazin
Satlantic, Inc.
Halifax, Canada

Abstract

To better understand the capability of portable sources, a series of experiments were conducted to transfer an absolute calibration to the original SQM and four SQM-IIs, and to map the homogeneity of an SQM-II exit aperture. Approximately 25% of the central portion of the exit aperture was within 2% of the maximum signal, and about 40% was to within 5%. The decay in SQM flux over a 500 day time period, which included one shipping event, was estimated to be approximately 0.9% every 100 days. The decay for an SQM-II (S/N 004) over the same time period, but encompassing four shipping events, was approximately 2.2% every 100 days. The average and standard deviations in the coefficient of variation was used as a stability parameter for the SQM and SQM-II. Both sources showed a spectral dependence with the greatest stability in the red part of the spectrum, and the least stability in the blue. The standard deviation in the coefficient of variation was independent of wavelength for the SQM, but the SQM-II had a noticeable spectral dependence—the reddest wavelength (775 nm) had a standard deviation approximately half that of the blue wavelengths. Using the overall averages as generalized metrics for stability, the SQM was more stable than the SQM-II: the overall average was a factor of three smaller, and the overall standard deviation was an order of magnitude smaller.

8.1 INTRODUCTION

Most SeaWiFS validation campaigns have been on Atlantic Meridional Transect (AMT) cruises (Aiken et al. 2000), which occur twice a year and involve a transit of the Atlantic Ocean between Grimsby (UK) and Stanley (Falkland Islands) with a port call in Montevideo (Uruguay). In all of the AMT cruises the SQM was a part of, it was shipped long distances between the US, the UK, and the Falkland Islands or Uruguay (also once to South Africa) with no negative effects on performance both during the cruise time period and between cruises.

The SQM lamps were changed after its commissioning to produce a flux level more in keeping with the radiometers being deployed on AMT cruises, but the same lamp set was used during AMT-5 through AMT-7 (another lamp change was made after AMT-7 to fine tune the flux levels). During the design stage of the SQM, there was some controversy about running the lamps below their rated current (approximately 95% of rating), but there has been no observable degradation in the performance of the lamps as a result of this—indeed, they have survived long shipment routes using a variety of transportation vehicles (trucks, planes, etc.) on repeated occasions, as well as, the high vibration environment of a ship.

Figure 30 is a summary of SQM performance during the AMT-5 through AMT-7 time period (spanning 460 days). It shows the internal blue monitor signal, measured with the glass fiducial, as a function of time, but presented as the percent difference with respect to the mean value for the entire time period. A confirmation of the signal is given by the R035 radiometer for the 443 nm channel (which is very similar to the blue internal monitor), and it very nearly mirrors the internal monitor signal. The two detectors yield similar decay rates of approximately 0.007% per day, or approximately 0.25% for a 35-day cruise. This is an underestimate, however, because the degradation is due mostly to lamp usage, and this is most significant during use, and not during shipping and storage. This is best seen by looking at the individual cruises, and comparing them to the laboratory work after AMT-7.

NASA Technical Memorandum 2002–206892, Volume 17

SeaWiFS Postlaunch Technical Report Series

Stanford B. Hooker, Editor
NASA/Goddard Space Flight Center
Greenbelt, Maryland

Elaine R. Firestone, Senior Scientific Technical Editor
Science Applications International Corporation
Beltsville, Maryland

Volume 17, The Seventh SeaWiFS Intercalibration Round-Robin Experiment (SIRREX-7), March 1999

Stanford B. Hooker
NASA/Goddard Space Flight Center
Greenbelt, Maryland

Scott McLean
Jennifer Sherman
Mark Small
Gordana Lazin
Satlantic, Inc.
Halifax, Canada

Giuseppe Zibordi
JRC/SAI/Marine Environment Unit
Ispra, Italy

James W. Brown
RSMAS/University of Miami
Miami, Florida

Chapter 5

Uncertainties in Radiance Calibrations

Stanford B. Hooker
NASA/Goddard Space Flight Center
Greenbelt, Maryland

Scott McLean
Jennifer Sherman
Satlantic, Inc.
Halifax, Canada

Abstract

Three types of experiments were conducted to estimate the uncertainties in radiance calibrations using a plaque and FEL lamp: a) The average repeatability uncertainty (based on one plaque and one FEL used with 11 trials for three different radiometers) was less than 0.1% (0.06% in the blue–green part of the spectrum and 0.09% in the red); b) the uncertainty that can be removed from radiance calibrations if ambient rather than dark measurements are used was 0.13% (0.11% in the blue–green and 0.17% in the red); and c) the overall uncertainty from secondary reflections, (for example, originating from an alignment laser) was 0.11% (0.06% in the blue–green wavelength domain and 0.19% in the red).

5.1 INTRODUCTION

The calibration coefficient for a radiance sensor (identified by S_{ID}) is computed using a plaque (identified by T_{ID}) with a calibrated reflectance, $R^{\mathrm{cal}}_{T_{\mathrm{ID}}}$, plus a standard lamp (identified by L_{ID}) with a calibrated irradiance, $E^{\mathrm{cal}}_{L_{\mathrm{ID}}}$. The general procedures require the lamp to be positioned a distance d on axis and normal to the center of the plaque (specific details for each step are given in Sect. 1.5). The radiance sensor is capped, and dark voltage levels for the sensor are recorded. An average dark level for each channel, $\bar{D}_{S_{\mathrm{ID}}}(\lambda)$, is calculated from the dark samples.

The radiance sensor is positioned to view the plaque at 45° with respect to the lamp illumination axis†. The lamp is powered on, and the voltage levels of the individual sensor channels are recorded, from which an average calibration voltage for each channel, $\bar{V}_{S_{\mathrm{ID}}}(\lambda)$, is obtained. The calibration coefficient is calculated as:

$$C^{\mathrm{Rad}}_{S_{\mathrm{ID}}}(\lambda) \;=\; \frac{\frac{1}{\pi}\, R^{\mathrm{cal}}_{T_{\mathrm{ID}}}(\lambda)\, E^{\mathrm{cal}}_{L_{\mathrm{ID}}}(\lambda, 50)}{\bar{V}_{S_{\mathrm{ID}}}(\lambda) - \bar{D}_{S_{\mathrm{ID}}}(\lambda)} \left[\frac{50\ \mathrm{cm}}{d}\right]^2, \qquad (10)$$

where d is given in centimeters.

† An alternative angle for which the reflectance of the plaque is known is also acceptable, but for all of the SIRREX-7 experiments, 45° was the calibrated reflectance angle of the plaque and the corresponding sensor viewing angle.

Three types of experiments were conducted to explore the uncertainties associated with radiance calibrations: a) one plaque and one FEL were used with three OCR-200 radiometers to estimate the repeatability uncertainty in radiance calibrations (based on 11 trials for each sensor); b) three OCR-200 sensors and the SXR were used to explore the uncertainties in ambient versus dark measurements; and c) the uncertainty from secondary reflections used in the calibration process (in this case, an alignment laser) was measured with the SXR and three OCR-200 sensors.

5.2 RADIANCE REPEATABILITY

The uncertainties in radiance calibrations were estimated by independently calibrating three OCR-200 sensors (R035, R036, and R067) 11 times each (following the usual procedures). The trials were all with the same plaque and FEL, but the lamp was not powered on and off each time; it was left on to minimize lamp usage time (standard FEL lamps are too expensive to include the warm-up time for each trial in the experiment).

5.2.1 Equipment

The equipment used for the radiance repeatability trials was as follows:

- Satlantic Optronic lamp F-547 (L008);
- Satlantic white (18 in) plaque 05816 (T001);

NASA Technical Memorandum 2002–206892, Volume 17

SeaWiFS Postlaunch Technical Report Series

Stanford B. Hooker, Editor
NASA/Goddard Space Flight Center
Greenbelt, Maryland

Elaine R. Firestone, Senior Scientific Technical Editor
Science Applications International Corporation
Beltsville, Maryland

Volume 17, The Seventh SeaWiFS Intercalibration Round-Robin Experiment (SIRREX-7), March 1999

Stanford B. Hooker
NASA/Goddard Space Flight Center
Greenbelt, Maryland

Scott McLean
Jennifer Sherman
Mark Small
Gordana Lazin
Satlantic, Inc.
Halifax, Canada

Giuseppe Zibordi
JRC/SAI/Marine Environment Unit
Ispra, Italy

James W. Brown
RSMAS/University of Miami
Miami, Florida

Chapter 7

Rotation and Polarization Uncertainties

Stanford B. Hooker
NASA/Goddard Space Flight Center
Greenbelt, Maryland

Scott McLean
Mark Small
Satlantic, Inc.
Halifax, Canada

Abstract

Separate experiments were conducted during SIRREX-7 to estimate the rotation and polarization uncertainties of radiometers during the calibration process. Rotational uncertainties for radiance sensors were usually less than 1%, with single and multiple aperture systems having average rotational uncertainties of 0.2–0.3% and 0.4–0.9%, respectively. Rotational uncertainties for a multiple aperture irradiance sensor was 0.7% on average, which was in close agreement with multiple aperture radiance sensors. The only significant spectral dependence was with an OCR-2000 (hyperspectral) sensor which had maximal effects in the bluest and reddest wavelengths and minimal effects in the green domain. The average polarization parameter, in percent, varied between 0.6–4.6%. The Satlantic instruments had an average polarization below 2.0%, but the OCR-200 sensors showed maximum polarization sensitivity in the blue part of the spectrum (1.4–2.4%), while the OCR-2000 instrument had maximum sensitivity in the red wavelength domain (2.1–2.6%).

7.1 INTRODUCTION

Two different experiments were designed to estimate the rotation and polarization effects on the calibration process. Although the former can be considered as a mechanical positioning problem, there are practical aspects of the problem which are more associated with the usual methods used during instrument calibration. For example, the angular positioning of the sensor during the calibration process is usually not maintained from one calibration to the next (in fact, many commercial radiometers are cylindrical and are not explicitly indexed), and the mounting hardware used is not always the best for reproducing an indexing scheme. The D-shaped collar was designed to overcome this limitation, and when used with a V-block is much easier to use for repositioning requirements than a ring carrier. In comparison, polarization is mostly an instrument design problem, with a design objective that is set by the optical protocols being used.

7.2 ROTATION EFFECTS

Two experiments were conducted to estimate the rotation sensitivity of radiance and irradiance sensors during the calibration process. Most Satlantic radiometers (e.g., the OCR-200 and OCR-1000 series of instruments) have separate apertures for each channel organized in one or more circular arrays around a central channel (Fig. 3), so changes in the orientation of the sensor in a V-block or ring mount will necessarily cause a change in what part of the plaque is viewed during the calibration process. The objective of the rotation experiments was to determine the level of uncertainty that can be associated with this part of the sensor positioning process.

Custom rotator mount adapters, which took advantage of the D-shaped collars, were built for the OCI-200 and OCR-200 series of radiometers. Separate custom adapters were also built for the SXR and the OCR-2000 instruments. The latter two also required a mechanical support (a V-block) to stabilize the large housings of these instruments during the rotation process. Although this helped maintain the stability of the large mass of these instruments during rotation, it did not ensure an axial symmetry for all trials, and some data were not used, because of unbalanced rotation.

7.2.1 Rotation of Radiance Sensors

Four types of radiance sensors were used for the rotation sensitivity experiments: R035, R064, P002, and X001.

NASA Technical Memorandum 2002–206892, Volume 21

SeaWiFS Postlaunch Technical Report Series

Stanford B. Hooker, Editor
NASA Goddard Space Flight Center
Greenbelt, Maryland

Elaine R. Firestone, Senior Scientific Technical Editor
Science Applications International Corporation
Beltsville, Maryland

Volume 21, The Eighth SeaWiFS Intercalibration Round-Robin Experiment (SIRREX-8), September–December 2001

Giuseppe Zibordi
Davide D'Alimonte
Dirk van der Linde
Jean-François Berthon
JRC/Institute for Environment and Sustainability
Ispra, Italy

Stanford B. Hooker
NASA/Goddard Space Flight Center
Greenbelt, Maryland

James L. Mueller
SDSU/Center for Hydro-Optics and Remote Sensing
San Diego, California

Gordana Lazin
Scott McLean
Satlantic, Inc.
Halifax, Canada

Chapter 2

The CHORS Immersion Factor Method

Stanford B. Hooker
NASA/Goddard Space Flight Center
Greenbelt, Maryland

James L. Mueller
SDSU/Center for Hydro-Optics and Remote Sensing
San Diego, California

Giuseppe Zibordi
JRC/IES/Inland and Marine Waters Unit
Ispra, Italy

Abstract

The CHORS method for experimentally determining the immersion factor for irradiance sensors is based on the method developed at the Visibility Laboratory for this measurement. It uses tap water and has the following major features: a) it uses a large covered tank with a sensor support system, which places the radiometer well above the turbulence associated with filling and emptying the tank (the volume of water below the sensor is greater than the amount above the sensor) or any perturbations from the bottom of the tank, so the interior of the tank (when covered) is especially *black*; b) it uses a 400 W lamp with a very small filament, so the light source very nearly approximates a point source; and c) it uses an adjustable final baffle to ensure the cone of light illuminating the in-water sensor is as small as possible.

2.1 INTRODUCTION

The CHORS laboratory procedure for characterizing immersion coefficients for an irradiance sensor was first described in Petzold and Austin (1988). The apparatus used was designed to accept a large variety of sensor types, both large and small, from different manufacturers. Although measurement accuracy was an important objective of the method, another priority was to be able to execute the measurement process in a time-efficient manner.

2.2 LABORATORY SETUP

The characterization of immersion factors at CHORS took place in a *high-bay* facility adjacent to the room used for radiometric calibrations. The walls and ceiling of the facility were painted flat black to remove any significant sources of reflected or secondary illumination.

A schematic of the CHORS measurement system for measuring $I_f(\lambda)$ for cosine collectors, is shown in Fig. 2. It consisted primarily of a large fiberglass tank in which the radiometer to be characterized could be immersed, a screened 400 W tungsten-halogen lamp with a power supply (PS) and multiple baffles, a reference radiometer to monitor the lamp, and a ducted fan to keep the lamp and reference cooled. The in-water sensor was placed in a support frame on top of a grated platform. The platform was covered with a fine black mesh and provided two functions:

1. It significantly reduced any water turbulance during the filling (and, to a lesser extent, the draining) of the tank; and
2. It provided a horizontal surface which allowed the sensor support frame to be accurately leveled and positioned within the baffled light field.

To reduce light reflections within the tank, the interior was painted with an exterior flat black paint, and the metal surfaces of the grated platform plus the sensor support frame were covered with black tape or black paint. The inside of the tank lid was painted black, and a large opening in the lid was fitted with a black curtain which could be drawn back to permit easy access to the inside of the tank.

The sensor support frame was composed primarily of a tube with an inner diameter just a little larger than the outer diameter of the in-water radiometer. A D-shaped collar was fitted to each in-water sensor which leveled the radiometer against the top of the tube. The flat side of the D-shaped collar (Fig. 1) was used as a coarse alignment reference to ensure the radiometer was positioned in a reproducible fashion within the light field.

NASA/TM-2002-210005

SIMBIOS Project 2001 Annual Report

Giulietta S. Fargion, Science Applications International Corporation, Maryland
Charles R. McClain, Goddard Space Flight Center, Greenbelt, Maryland

National Aeronautics and
Space Administration

Goddard Space Flight Center
Greenbelt, Maryland 20771

March 2002

Chapter 9

Refinement of Protocols for Measuring the Apparent Optical Properties of Seawater

Stanford B. Hooker
NASA/GSFC/SeaWiFS Project, Greenbelt, Maryland

Giuseppe Zibordi and Jean-François Berthon
JRC/IES/Inland and Marine Waters, Ispra, Italy

André Morel and David Antoine
CNRS/UPMC/Laboratoire d'Océanographie de Villefranche, Villefranche-sur-Mer, France

9.1 INTRODUCTION

Ocean color satellite missions, like the Sea-viewing Wide Field-of-view Sensor (SeaWiFS) or the Moderate Resolution Imaging Spectroradiometer (MODIS) projects, are tasked with acquiring a global ocean color data set, validating and monitoring the accuracy and quality of the data, processing the radiometric data into geophysical units using a set of atmospheric and bio-optical algorithms, and distributing the final products to the scientific community. The long-standing objective of the SeaWiFS Project, for example, is to produce water-leaving radiances to within 5% absolute (Hooker and Esaias 1993). The accurate determination of upper ocean apparent optical properties (AOPs) is essential for the vicarious calibration of ocean color data and the validation of the derived data products, because the sea-truth measurements are the reference data to which the satellite are compared (Hooker and McClain 2000). The uncertainties associated with *in situ* AOP measurements have various sources, such as, the deployment and measurement protocols used in the field, the absolute calibration of the radiometers, the environmental conditions encountered during data collection, the conversion of the light signals to geophysical units in a data processing scheme, and the stability of the radiometers in the harsh environment they are subjected to during transport and use.

In recent years, progress has been made in estimating the magnitude of some of these uncertainties and in defining procedures for minimizing them. For the SeaWiFS Project, the first step was to convene a workshop to draft the SeaWiFS Ocean Optics Protocols. The protocols adhere to the Joint Global Ocean Flux Study (JGOFS) sampling procedures (Joint Global Ocean Flux Study 1991) and define the standards for optical measurements to be used in SeaWiFS radiometric validation and algorithm development (Mueller and Austin 1992). The protocols are periodically updated as deficiencies are identified and outstanding issues are resolved (Mueller and Austin 1995, and Mueller 2000). The follow-on inquiries into controlling uncertainties investigated a variety of topics. The SeaWiFS Intercalibration Round-Robin Experiment (SIRREX) activity demonstrated that the uncertainties in the traceability between the spectral irradiance of calibration lamps were approximately 1.0%, and the intercomparisons of sphere radiance was approximately 1.5% in absolute spectral radiance and 0.3% in stability (Mueller et al. 1996). The first SeaWiFS Data Analysis Round Robin (DARR-94) showed differences in commonly used data processing methods were about 3–4% of the aggregate mean estimate (Siegel et al. 1995). Hooker and Aiken (1998) made estimates of radiometer stability using the SeaWiFS Quality Monitor (SQM), a portable and stablelight source, and showed the stability of radiometers in the field during a 36-day deployment was on average to within 1.0% (although some channels occasionally performed much worse). More recently, Hooker and Maritorena (2000) quantified differences in the in-water methods and techniques employed for making radiometric measurements and demonstrated a total uncertainty in the measurement of in-water AOPs at approximately the 3% level.

9.2 RESULTS

Open Ocean

The SeaWiFS Field Team has combined the collection of ground-truth observations with specific experiments to investigate the sources of uncertainties in AOP measurements.

NASA Technical Memorandum 2002–206892, Volume 21

SeaWiFS Postlaunch Technical Report Series

Stanford B. Hooker, Editor
NASA Goddard Space Flight Center
Greenbelt, Maryland

Elaine R. Firestone, Senior Scientific Technical Editor
Science Applications International Corporation
Beltsville, Maryland

Volume 21, The Eighth SeaWiFS Intercalibration Round-Robin Experiment (SIRREX-8), September–December 2001

Giuseppe Zibordi
Davide D'Alimonte
Dirk van der Linde
Jean-François Berthon
JRC/Institute for Environment and Sustainability
Ispra, Italy

Stanford B. Hooker
NASA/Goddard Space Flight Center
Greenbelt, Maryland

James L. Mueller
SDSU/Center for Hydro-Optics and Remote Sensing
San Diego, California

Gordana Lazin
Scott McLean
Satlantic, Inc.
Halifax, Canada

Chapter 1

SIRREX-8 Overview

Stanford B. Hooker
NASA/Goddard Space Flight Center
Greenbelt, Maryland

Giuseppe Zibordi
JRC/IES/Inland and Marine Waters Unit
Ispra, Italy

Abstract

The primary objective of SIRREX-8 was a thorough inquiry into the uncertainties associated with the general problem of determining the immersion factors for marine radiometers, and restricting the analysis to Satlantic in-water Ocean Color Irradiance 200-series sensors (the so-called OCI-200 instruments). A small team of investigators was assembled to address these points at three different facilities (the diversity in participants assured no one peculiarity in one of the methods could bias the results). The secondary SIRREX-8 objective was to measure the cosine response of one sensor at two of the participating facilities. Although up to 12 sensors were measured, 9 were rotated through all three facilities. The instrumentation came primarily from two different organizations with differing measurement objectives, so the assembled sensors had a diverse range of calibration histories, ages, intended uses, sensitivities, saturation levels, etc. The diversity in sensors means a significant subset of the results will have a wider applicability to the larger community.

1.1 INTRODUCTION

When a cosine collector is immersed in water, its light transmissivity is less than it was in air. Irradiance sensors are calibrated in air, however, so a correction for this change in collector transmissivity must be applied when the in-water raw data are converted to physical units. The correction term is called the immersion factor, and it must be determined experimentally, using a laboratory protocol, for each sensor wavelength, λ.

When the sensor is illuminated, the raw optical data samples at each wavelength are recorded as digitized voltages, $V(\lambda)$, usually in counts. Each sample is recorded at a particular time, t_i, which also sets the depth, z. Raw irradiance data are typically converted to physical units using a calibration equation of the following form:

$$E(\lambda, t_i) \;=\; C_c(\lambda)\, I_f(\lambda)\, \big[V(\lambda, t_i) \;-\; \bar{D}(\lambda)\big], \qquad (1)$$

where $E(\lambda, t_i)$ is the calibrated irradiance, $C_c(\lambda)$ is the calibration coefficient (determined during the radiometric calibration of the sensor), $I_f(\lambda)$ is the immersion factor†, and $\bar{D}(\lambda)$ is the average bias or dark voltage measured during a special *dark cast* with the caps on the radiometer. The difference between $V(\lambda, t_i)$ and $\bar{D}(\lambda)$ is the net signal level detected by the radiometer while exposed to light.

In some cases, dark voltages are replaced by so-called *background* or *ambient* measurements, so illumination biases can be removed along with the dark correction. For the purposes of SIRREX-8, background data were collected with the direct illumination of the target by the source occulted by an intervening *on-axis baffle*, so only indirect light (from the source and any other light emissions from equipment in the room) reached the sensor aperture. Ambient data were collected with the source off, so only illumination from other light-emitting devices in the room reached the sensor aperture.

In the formulation given in (1), the irradiances measured during ocean color field campaigns are usually the in-water downward irradiance, $E_d(z, \lambda)$, the in-water upwelled irradiance, $E_u(z, \lambda)$, and the above-water total solar irradiance, $E_d(0^+, \lambda)$. In some data processing schemes (Hooker et al. 2001), there is an explicit attempt to try and get the extrapolated in-water downward irradiance to agree with the measured above-water total solar irradiance over the time period associated with the extrapolation interval, so the application of the immersion factor to the former must be accurate.

† For the purposes of the calibration equation, the immersion factor for an above-water irradiance sensor is always equal to unity.

NASA Technical Memorandum 2002–206892, Volume 17

SeaWiFS Postlaunch Technical Report Series

Stanford B. Hooker, Editor
NASA/Goddard Space Flight Center
Greenbelt, Maryland

Elaine R. Firestone, Senior Scientific Technical Editor
Science Applications International Corporation
Beltsville, Maryland

Volume 17, The Seventh SeaWiFS Intercalibration Round-Robin Experiment (SIRREX-7), March 1999

Stanford B. Hooker
NASA/Goddard Space Flight Center
Greenbelt, Maryland

Scott McLean
Jennifer Sherman
Mark Small
Gordana Lazin
Satlantic, Inc.
Halifax, Canada

Giuseppe Zibordi
JRC/SAI/Marine Environment Unit
Ispra, Italy

James W. Brown
RSMAS/University of Miami
Miami, Florida

Chapter 9

SIRREX-7 Synthesis, Discussion, and Conclusions

Stanford B. Hooker
NASA/Goddard Space Flight Center
Greenbelt, Maryland

Giuseppe Zibordi
JRC/SAI/Marine Environment Unit
Ispra, Italy

Scott McLean
Satlantic, Inc.
Halifax, Canada

Abstract

A combined uncertainty budget for radiometric calibrations can be constructed from the SIRREX-7 data set. Although it is comprehensive, it does not address every source of uncertainty at the same level of detail and some must be considered as approximate. Nonetheless, the care taken in each experiment ensures the uncertainty estimates are representative of what can be expected if careful metrology and practices are used. Perhaps just as importantly, the consequences of discrepancies are also well estimated. To provide a range of possible outcomes in the calibration process, minimum, typical, and maximum uncertainties are computed from the various entries, which range from 1.1–3.4% and 1.5–6.7% for irradiance and radiance calibrations, respectively. The Satlantic facility falls somewhere between the minimum and typical values. If an additional (average) 1.0% is included to account for an unknown bias detected with the lamp and plaque uncertainty experiments (described in Sects. 3.2 and 4.2, and discussed in Sects. 9.2 and 9.5), the uncertainty for Satlantic irradiance calibrations is 1.8%, and the uncertainty for radiance calibrations is 2.3%.

9.1 INTRODUCTION

This chapter synthesizes the results from the various SIRREX-7 experiments and discusses the conclusions that can be drawn from them. The lessons learned are separated according to irradiance or radiance calibrations, and those applicable to both. Not all types of Satlantic sensor were included in SIRREX-7, in fact, the most common instrument was the model 200 series of radiance and irradiance sensors (Table 7). Most Satlantic instruments share design commonalities, however, so the results have some applicability to most instrument classes. An obvious exception is the difference between single- and multiple-aperture sensors: the latter have more complicated alignment effects, because they have multiple viewing axes.

A summary of the various experiments executed during SIRREX-7 is presented in Table 13. Although it was not possible to replicate all the experiments the same number of times, the primary experiments were executed as many times as economically feasible to ensure statistical reliability. Most of the experiments involved the use of all three principle components of radiometry, source, target, and detector, so most have results applicable to other objectives. The material presented here is organized primarily according to the order the experiments were presented in Chapters 3–8 (some information originally presented in different chapters was combined into one section).

9.2 LAMP UNCERTAINTIES

The results from the investigations into lamp uncertainties (Sect. 3.2.3) showed a deterministic bias when the irradiance of the lamps calculated from the SXR measurements of the NIST plaque were compared to the values supplied with the lamp (Fig. 5). Each component of the experiment has an uncertainty on the order of 1%, and given another (maximum) 1% from mechanical setup uncertainties, the range of uncertainty seen with the so-called *trusted* lamps is within the quadrature sum of these components, that is, the approximately 2% uncertainty in the blue part of the spectrum is very close to $\sqrt{4}$.

The spectral dependence in SXR uncertainties is approximately 0.5% (Johnson et al. 1998a), with maximal un-

NASA Technical Memorandum 2002–206892, Volume 17

SeaWiFS Postlaunch Technical Report Series

Stanford B. Hooker, Editor
NASA/Goddard Space Flight Center
Greenbelt, Maryland

Elaine R. Firestone, Senior Scientific Technical Editor
Science Applications International Corporation
Beltsville, Maryland

Volume 17, The Seventh SeaWiFS Intercalibration Round-Robin Experiment (SIRREX-7), March 1999

Stanford B. Hooker
NASA/Goddard Space Flight Center
Greenbelt, Maryland

Scott McLean
Jennifer Sherman
Mark Small
Gordana Lazin
Satlantic, Inc.
Halifax, Canada

Giuseppe Zibordi
JRC/SAI/Marine Environment Unit
Ispra, Italy

James W. Brown
RSMAS/University of Miami
Miami, Florida

Chapter 6

Uncertainties in Irradiance Calibrations

Stanford B. Hooker
NASA/Goddard Space Flight Center
Greenbelt, Maryland

Giuseppe Zibordi
JRC/SAI/Marine Environment Unit
Ispra, Italy

Scott McLean
Jennifer Sherman
Satlantic, Inc.
Halifax, Canada

Abstract

Three types of experiments were conducted to estimate the uncertainties associated with irradiance calibrations using an FEL standard lamp: a) the repeatability uncertainty (based on one FEL standard lamp used during 11 trials with three different irradiance sensors) was less than 0.5% (0.2% on average, with usually larger uncertainties in the blue part of the spectrum and smaller uncertainties in the red); b) the additional uncertainty that can be removed from radiance calibrations if ambient rather than dark measurements are used was 0.05% (0.05% in the blue, 0.04% in the green, and 0.06% in the red); and c) the overall uncertainty from secondary reflections, originating from ancillary equipment used during the calibration process (in this case, an alignment laser) was 0.06% (0.03% in the blue–green wavelength domain and 0.12% in the red).

6.1 INTRODUCTION

Typically, the calibration coefficients for an irradiance sensor (identified by S_{ID}) are computed using an FEL standard lamp (L_{ID}) with a calibrated irradiance, $E^{\mathrm{cal}}_{L_{\mathrm{ID}}}(\lambda, 50)$. The general procedures require the lamp to be positioned a distance d on axis and normal to the faceplate of the irradiance sensor (Sect. 1.5.7). The irradiance sensor is capped, and dark (digital voltage) levels for the sensor are recorded from which average dark levels, $\bar{D}_{S_{\mathrm{ID}}}(\lambda)$, are calculated.

The lamp is powered on, and the voltage levels of the individual sensor channels are recorded, from which an average calibration voltage for each channel, $\bar{V}_{S_{\mathrm{ID}}}(\lambda)$, is obtained. The calibration coefficient is calculated using:

$$C^{\mathrm{Irr}}_{S_{\mathrm{ID}}}(\lambda) \;=\; \frac{E^{\mathrm{cal}}_{L_{\mathrm{ID}}}(\lambda, 50)}{\bar{V}_{S_{\mathrm{ID}}}(\lambda) - \bar{D}_{S_{\mathrm{ID}}}(\lambda)} \left[\frac{50\ \mathrm{cm}}{d}\right]^2, \qquad (14)$$

where d is given in centimeters.

Three types of experiments were conducted to explore the uncertainties associated with irradiance calibrations:

a) The same FEL standard lamp was used with three OCI-200 radiometers to estimate the repeatability uncertainty in irradiance calibrations (based on 11 trials for each sensor);

b) The importance of ambient versus dark measurements was explored with three OCI-200 sensors; and

c) The uncertainty associated with reflections from improperly baffled ancillary equipment used in the calibration process (in this case, an alignment laser) was measured with three OCI-200 sensors.

6.2 IRRADIANCE REPEATABILITY

This experiment was designed to estimate the uncertainties in irradiance calibrations (set up and executed following the usual procedures). Three OCI-200 sensors (I040, I050, and I097) were calibrated independently 11 times each. Although the trials were all executed with the same FEL standard lamp, the lamp was not powered on and off for each trial; it was left on to minimize the amount of time used with the lamp (standard FEL lamps are too expensive to include the warm-up time for each trial in the experiment).

NASA Technical Memorandum 2002–206892, Volume 17

SeaWiFS Postlaunch Technical Report Series

Stanford B. Hooker, Editor
NASA/Goddard Space Flight Center
Greenbelt, Maryland

Elaine R. Firestone, Senior Scientific Technical Editor
Science Applications International Corporation
Beltsville, Maryland

Volume 17, The Seventh SeaWiFS Intercalibration Round-Robin Experiment (SIRREX-7), March 1999

Stanford B. Hooker
NASA/Goddard Space Flight Center
Greenbelt, Maryland

Scott McLean
Jennifer Sherman
Mark Small
Gordana Lazin
Satlantic, Inc.
Halifax, Canada

Giuseppe Zibordi
JRC/SAI/Marine Environment Unit
Ispra, Italy

James W. Brown
RSMAS/University of Miami
Miami, Florida

Chapter 3

Uncertainties in Lamp Standards

Stanford B. Hooker
NASA/Goddard Space Flight Center
Greenbelt, Maryland

Giuseppe Zibordi
JRC/SAI/Marine Environment Unit
Ispra, Italy

Scott McLean
Jennifer Sherman
Satlantic, Inc.
Halifax, Canada

Abstract

The uncertainties associated with the use of lamp standards was estimated by using several lamps with different calibration histories to illuminate a NIST reflectance standard (T005), and then comparing the calibrated radiance from the plaque (calculated from the calibrated reflectance of the plaque and the calibrated irradiance from the lamp), with that measured by the SXR. The average uncertainty of the most *trusted* lamps, those with no known problems and established good performance capabilities, was approximately 1.2%. All of the lamps had a calibration repeatability less than 0.5%, and all of the lamps except one had a repeatability less than 0.2%. A comparison of an Optronic calibration of an FEL lamp with a NIST calibration of the same lamp showed an overall average agreement to within approximately 1.3%. A similar comparison exercise executed as a part of SIRREX-5 showed the Optronic calibration of FEL F-409 differed from the NIST calibration by an average of approximately 2.6%, whereas a second calibration by Optronic differed from the NIST calibration by about 0.8%.

3.1 INTRODUCTION

Three experiments were conducted to examine the uncertainties associated with using lamps during calibrations. The first involved using a NIST reflectance standard and the SXR to estimate the uncertainties in using Labsphere (Spectralon) plaques, the second quantified how much of the variability in calibrations is due to changes in the lamp from one calibration session to the next, and the third compared the NIST and Optronic calibrations for a newly purchased lamp.

3.2 LAMP UNCERTAINTIES

The uncertainties associated with the use of lamp standards was estimated by using several lamps with different calibration histories to illuminate a NIST reflectance standard (T005), and then comparing the calibrated radiance from the plaque (calculated from the calibrated reflectance of the plaque and the calibrated irradiance from the lamp), with that measured by the SXR. A monitoring sensor (R035) was mounted on the rail opposite the SXR to provide an independent measure of the illumination stability of the plaque.

3.2.1 Equipment

The equipment used for determining the uncertainties in lamp standards involved the following:

- Satlantic NIST lamp F-409 (L007), and SeaWiFS NIST lamps F-182 (L002) and F-137 (L001);
- JRC Hoffman Lamps H97505 (L004) and H96551 (L005);
- Satlantic Optronic lamps F-539, F-536, and F-516 (L003, L006, and L000, respectively), plus two new Satlantic Optronic lamps F-547 (L008) and F-548 (L009);
- NIST plaque K299 (T005);
- The SXR (X001) with custom mount and digital voltmeter (V003);

NASA Technical Memorandum 2002–206892, Volume 17

SeaWiFS Postlaunch Technical Report Series

Stanford B. Hooker, Editor
NASA/Goddard Space Flight Center
Greenbelt, Maryland

Elaine R. Firestone, Senior Scientific Technical Editor
Science Applications International Corporation
Beltsville, Maryland

Volume 17, The Seventh SeaWiFS Intercalibration Round-Robin Experiment (SIRREX-7), March 1999

Stanford B. Hooker
NASA/Goddard Space Flight Center
Greenbelt, Maryland

Scott McLean
Jennifer Sherman
Mark Small
Gordana Lazin
Satlantic, Inc.
Halifax, Canada

Giuseppe Zibordi
JRC/SAI/Marine Environment Unit
Ispra, Italy

James W. Brown
RSMAS/University of Miami
Miami, Florida

Chapter 4

Uncertainties in Plaque Standards

Stanford B. Hooker
NASA/Goddard Space Flight Center
Greenbelt, Maryland

Giuseppe Zibordi
JRC/SAI/Marine Environment Unit
Ispra, Italy

Scott McLean
Jennifer Sherman
Gordana Lazin
Satlantic, Inc.
Halifax, Canada

Abstract

The experiments conducted to estimate the uncertainties associated with the use of plaque standards involved calculating the reflectances of seven plaques using SXR measurements and the calibrated irradiance provided with the lamp standard, which were then compared to the reflectances provided with each plaque. The average uncertainties between the calculated and calibrated reflectances showed a range of 1.0–3.2%. With the exception of the gray plaque (T007), maximum uncertainties occurred in the blue part of the spectrum, and minimum uncertainties in the red. The importance of bidirectional effects was determined by comparing the SXR plaque measurements made from two different sides of a plaque, but with the same viewing geometry. The smallest uncertainties were associated with T005 (the NIST PTFE plaque), and the largest with T007 (the gray plaque), 0.3 and 2.1%, respectively. All of the other plaques had RPD vlaues which fell into a narrow range with the same spectral dependence and an overall average RPD of approximately 1.0%. Plaque uniformity improved with all increases in the lamp-to-plaque distance. Regardless of the lamp-to-plaque distance, there was a constant offset of aproximately 20 mm in the vertical (z) direction between the maximum signal and the center of the plaque for all the lamps; some of the lamps also showed offsets in the horizontal (x) direction.

4.1 INTRODUCTION

Three experiments were conducted to examine the uncertainties associated with using plaques during calibrations. The first involved using a NIST reflectance standard and the SXR to estimate the uncertainties in using Labsphere (Spectralon) plaques, the second estimated the importance of bidirectional effects by comparing calibrations from two different sides of a plaque, but with the same viewing geometry, and the third used a mapping radiometer to estimate the uniformity of Labsphere plaques illuminated with the same FEL lamp.

4.2 PLAQUE UNCERTAINTIES

This experiment was designed to estimate the uncertainties in plaque standards by comparing the calculated reflectance of a number of different plaques illuminated with a single NIST standard lamp. The reflectance of each plaque was calculated using the SXR measurements and the calibrated irradiance provided with the lamp. The calculated reflectances were then compared to the reflectances provided with each plaque.

4.2.1 Equipment

The equipment used for determining the uncertainties in plaque standards involved the following:

- Satlantic Optronic Lamp F-539 (L003);
- NIST plaque K299 (T005);
- The SeaWiFS gray (10 in) plaque 24328 (T007), the JRC white (18 in) plaque 22463 (T004), the new Satlantic white (18 in) plaque 05816 (T001), and the two old Satlantic white (18 in) plaques 13172 (T002) and 01873 (T003);

GLDAS: AN IMPORTANT CONTRIBUTION TO CEOP

Paul R. Houser and Matthew Rodell

Hydrological Sciences Branch
NASA Goddard Space Flight Center

Scientists at NASA's Goddard Space Flight Center (GSFC) have developed a high-resolution Global Land Data Assimilation System (GLDAS) in cooperation with researchers at NOAA's National Centers for Environmental Prediction (NCEP). The goal of GLDAS is to produce optimal output fields of land surface states and fluxes by making use of data from advanced observing systems (See figure on back page). Errors in land surface forcing and parameterization tend to accumulate in modeled land stores of water and energy, leading to incorrect surface water and energy partitioning. GLDAS aims to minimize this effect by constraining the models in two ways. First, by forcing the land surface, primarily by observations (such as precipitation and radiation), the biases in atmospheric model-derived forcing are avoided. Second, by employing land surface data assimilation techniques, observations of land surface storages (soil temperature, soil moisture, and snow depth/cover) can be used to steer unrealistic simulated storages towards reality. These techniques also enable identification and mitigation of observational errors and minimization of the impact of simplified land parameterizations. **The value-added data produced by GLDAS will improve land surface, weather, and climate predictions by providing global fields of land surface energy and moisture stores for initialization.**

Drivers have been installed in GLDAS for three land surface models (LSMs): Mosaic; the Community Land Model (CLM); and the NCEP, Oregon State University, United States Air Force, and Office of Hydrology model (NOAH). GLDAS runs globally with a 15-minute time step at 0.25° (soon to be 0.125°) and coarser resolutions. A vegetation-based "tiling" approach is used to simulate sub-grid scale variability, with the University of Maryland's 1 km global vegetation data set as its basis. Soil parameters are derived from 5-minute global soils information produced by USDA Agricultural Research Service. GLDAS uses the GTOPO30 global digital elevation model as its standard and corrects input fields accordingly. In addition to an operational, near-real time simulation using the standard parameterization and forcing data, several parallel simulations run with varying combinations of models, forcing data, and advanced options. Forcing options include the global atmospheric forecast model output (from GSFC's Data Assimilation Office, NCEP, and the Euro-observation-based precipitation and radiation fields. Advanced options, which are in various stages of planning, implementation, and testing, include a routine for satellite-based updates of leaf area index, canopy greenness and albedo, soil moisture and temperature data assimilation, observation-based snow corrections, simulation of the atmospheric boundary layer, and runoff routing.

The Coordinated Enhanced Observation Period (CEOP) was initiated by the international efforts of GEWEX and is focused on the measurement, understanding and modeling of water and energy cycles within the climate system. It is motivated by the synchronism of the new generation of Earth observing satellites and GEWEX Continental Scale Experiments (CSEs). Its primary goal is to develop a consistent data set for 2003-2004 to support research objectives in climate prediction and monsoon system studies. The requirements of the international climate research community at large have been taken fully into account in planning the assembly of the data set. CEOP also will assist studies of global atmospheric circulation and water resources availability. CEOP has gained the interest of a broad range of international organizations, as evidenced by the proposal for an Integrated Global Water Cycle Observations (IGWCO) theme within the framework of the International Global Observing Strategy Partnership (IGOS-P), which has re-affirmed CEOP as "the first element of the IGWCO." The CEOP implementation plan can be viewed at: http://www.gewex.org/ceop/ceop_ip.pdf.

CEOP aims to integrate the many streams of data coming from new space-based observation systems into a coherent database relevant to CEOP science issues, which will facilitate analytical investigations.

GLDAS is a valuable tool for CEOP because it assimilates the information from multiple models and observation platforms to provide the best available assessment of the current state of the land surface. The international GEWEX and CEOP communities have recognized that GLDAS can be leveraged and further developed to address the needs of CEOP. CEOP is specifically interested in the generation and application of GLDAS results in regional climate analysis, model initialization, and comparison with results from field campaigns and modeling experiments. The use of GLDAS model location time series (MOLTS), which are time series of land surface model output for points of interest, will be one of the primary tools to enable this globally-consistent intercomparison. Each GLDAS MOLTS will be particularly relevant because it will be generated based on a GLDAS subgrid "tile" with a vegetation class that matches that of the observation. Furthermore,

land surface models that GLDAS drives (currently three; five planned). These comparison exercises and the data produced by the continental scale experiments also will provide much-needed validation for the GLDAS project.

CEOP has requested that NASA further develop GLDAS as a central "CEOP data integration center", including the following aspects:

- A test bed for evaluating multiple land surface models.
- Long term land model baseline experiments and intercomparisons.
- Linking and inclusion of reference site observations with globally consistent observation and modeling to enable GEWEX-CSE land transferability studies.
- Land initialization for seasonal-to-interannual coupled predictions.
- Evaluation of numerical weather and climate predictions for land.
- Integration of remotely sensed land observations in land/atmospheric modeling for use in CEOP and higher level understanding.
- A quality control check on observations.
- 4DDA "value-added" GLDAS-CEOP data sets.
- The production of GLDAS MOLTS.
- The expansion of GLDAS to include selected atmosphere and ocean observations.
- The development of a long-term archive function.

The GLDAS contribution to CEOP is expected to have the following timeline:

- Data Integration Period (2002-2005): Compile the forcing data (observations and analyses) and assimilation data including radiance observations (level 1), high-level satellite data products, *in situ* observations, and NWP land analyses into a long term archive. Produce MLDAS (Molts LDAS) by reconfiguring GLDAS to run only MOLTS points for explicit linkages to CEOP reference sites.
- Reanalysis Period (2006-2007 work activity): Reprocess CEOP data in a globally consistent 1/8 degree resolution; global land reanalysis including multiple land model products (NOAH, CLM, VIC, etc.) and data assimilated value-added analysis.

For more information on GLDAS, please visit http://ldas.gsfc.nasa.gov.

GLDAS: AN IMPORTANT CONTRIBUTION TO CEOP

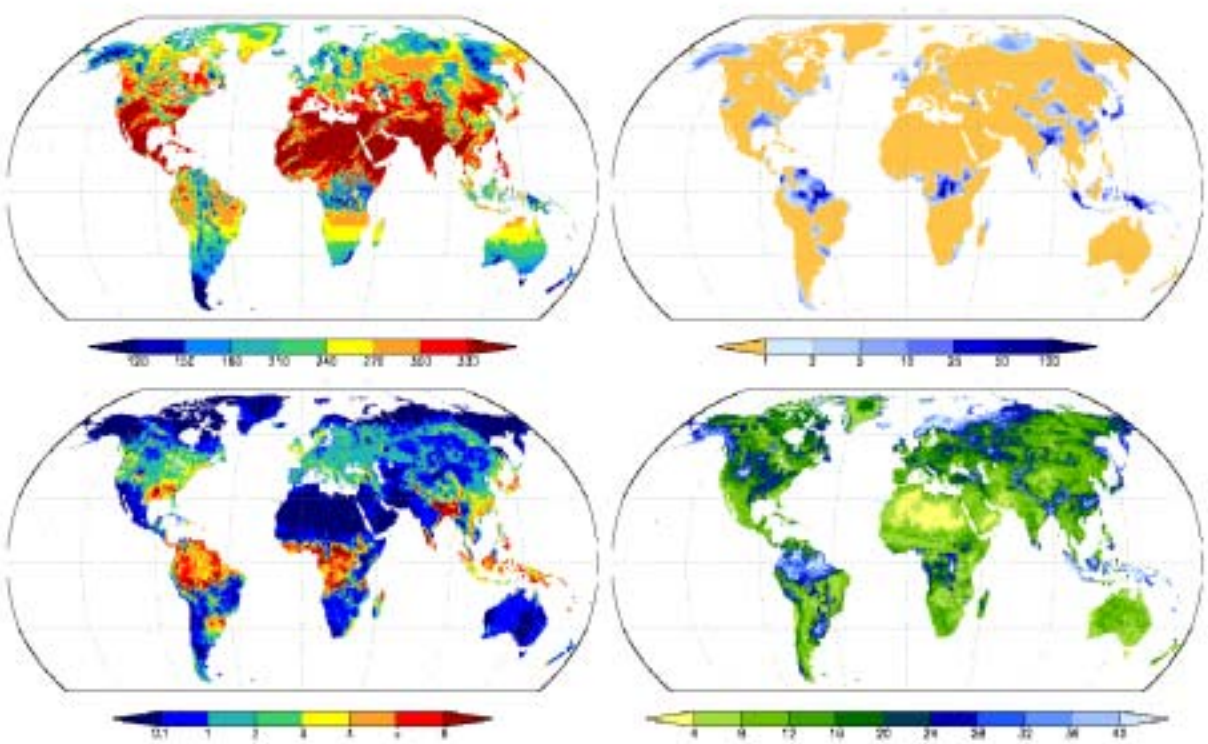

GLDAS forcing and output, 30 April 2002. Mean observation-based downward shortwave radiation [W/m^2] (top left); total precipitation [mm] (top right); total evapotranspiration [mm] (bottom left); mean

2002 IEEE International Geoscience and Remote Sensing Symposium and the 24th Canadian Symposium on Remote Sensing

IGARSS 2002

REMOTE SENSING:
Integrating Our View of the Planet

IEEE

June 24-28, 2002
Toronto Canada

Remotely Sensed Forcing Data and the Global Land Data Assimilation System

U. Jambor[1], P. R. Houser[2], M. Rodell[2], J. Gottschalck[1], C.-J. Meng[1,3], B. Cosgrove[4], and J. K. Entin[5]

[1]*Goddard Earth Science and Technology Center, University of Maryland, Baltimore County / NASA GSFC Hydrological Sciences Branch, Greenbelt, MD 20771*
[2] *NASA GSFC Hydrological Sciences Branch, Greenbelt, MD 20771*
[3]*NOAA National Centers for Environmental Prediction, Camp Springs, MD 20746*
[4]*SAIC / NASA GSFC Hydrological Sciences Branch, Greenbelt, MD 20771*
[5]*Now at NASA Headquarters, Washington, DC 20546*

***Abstract*—A high-resolution, near-real-time Global Land Data Assimilation System (GLDAS) that integrates information from relevant satellite- and ground-based observations within a land data assimilation framework is being developed at NASA's Goddard Space Flight Center and NOAA's National Centers for Environmental Prediction (NCEP). The GLDAS framework enables it to serve as a powerful tool for various types of research and applications. Here, we examine the impact of replacing model-based forcing fields with observation-derived fields on Mosaic land surface model (LSM) simulations. Due to a paucity of recent land surface state observations over large domains, GLDAS-forced Mosaic LSM simulations will be evaluated against finer-resolution North American LDAS-forced results.**

I. INTRODUCTION

Accurate initialization of land surface moisture and energy stores is critical in weather and climate prediction because of their regulation of surface water and energy fluxes between the surface and atmosphere over a variety of time scales. Since these are integrated states, errors in land surface forcing and parameterization accumulate in land stores, leading to incorrect surface water and energy partitioning. The purpose of the Global Land Data Assimilation System (GLDAS) is to integrate satellite- and ground-based observational data products, using advanced land surface modeling and data assimilation techniques, in order to produce optimal fields of land surface states and fluxes [1]. GLDAS drives multiple land surface models (LSMs) globally at 0.25° and lower spatial resolutions on a sub-hourly timestep. A vegetation-based "tiling" approach is used to simulate sub-grid scale variability, with a 1 km global vegetation dataset as its basis. Soil and elevation parameters are based on high-resolution global information. The system runs in near-real time using a combination of observation-based precipitation and radiation fields and the best available global coupled weather forecast model output (Fig. 1). The global land surface fields that GLDAS provides will be used for initialization of coupled weather and climate prediction models and subsequent research and applications. Furthermore, the 2001-forward GLDAS archive of modeled and observed, global, surface meteorological data will be unparalleled in scope.

The GLDAS project has its basis in the North American Land Data Assimilation System (NLDAS) project [2]. The study region for the NLDAS encompasses the continental United States and parts of Mexico and Canada, and LSMs are run at 0.125° resolution. By choosing to compare the GLDAS forcing and output fields with those of the NLDAS over a concurrent, common domain, the underlying assumption is that the NLDAS simulation is a better representation of the true atmospheric and land surface states. This study is a step towards understanding the GLDAS product over the global domain by first focusing on a region that is heavily observed and modeled.

II. METHODOLOGY

Three types of operational Mosaic LSM [3] runs were performed over July 2001. The two GLDAS simulations were run at 0.25° resolution, with each vegetation-based tile included per grid cell accounting for at least 10% of the grid cell area. The NLDAS simulation was run at 0.125° resolution, allowing for up to 10 vegetation-based tiles per grid cell, each accounting for at least 5% of the grid area.

For both GLDAS experiments the baseline forcing was 1° global grid output from the Goddard Earth Observing System Data Assimilation System (GEOS) model [4]. The second

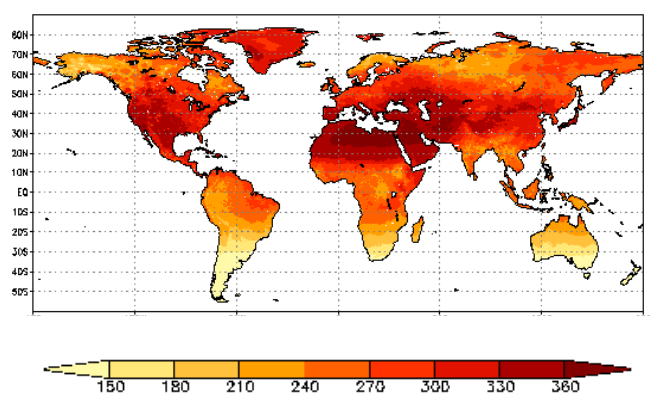

Fig. 1. Mean downward shortwave flux (W m^{-2}) for July 2001. This forcing field was assembled by GLDAS, using satellite-derived radiation data to replace baseline model forcing values whenever possible.

IV. CONCLUSION

Accurate representation of atmospheric forcing inputs in land surface simulations is fundamental. As such, it is important to identify which types of forcing data are most appropriate for such use, and the limitations associated with them. The GLDAS and NLDAS frameworks are well suited to perform such evaluations.

Recognizing the differences in model resolution, land surface parameters, and initial conditions among these discussed GLDAS and NLDAS simulations, we plan to minimize their effect on an LSM outcome by constraining such differences in future experiments.

2002 IEEE International Geoscience and Remote Sensing Symposium and the 24th Canadian Symposium on Remote Sensing

IGARSS 2002

REMOTE SENSING:
Integrating Our View of the Planet

IEEE

June 24-28, 2002
Toronto Canada

Parameterization of snowpack grain size for global satellite microwave estimates of snow depth

R.E.J. Kelly[1], A.T.C. Chang[2], L. Tsang[3], and C.T. Chen[3]
[1]Goddard Earth Sciences and Technology Center, University of Maryland Baltimore County, MD 21250 USA
[2]Hydrological Sciences Branch/Code 974, NASA/Goddard Space Flight Center, Greenbelt, MD 20771, USA
[3]Department of Electrical Engineering, University of Seattle, Washington, WA 98195-2500

Abstract- For accurate estimation of global snow depth or snow water equivalent on the Earth's surface using passive microwave instruments, knowledge of the snow pack's physical properties is important. It is known that the bulk snow grain size distribution exerts an important control over the microwave response from snow between 3mm and 300 mm wavelengths. In the absence of high quality snowpack data at a global scale, we show how the grain size distribution can be estimated using a general empirical model of grain growth. This information is used to parameterize a dense media radiative transfer model (DMRT) to estimate the radiometric response from a snow pack as a function of changing grain size distribution. The DMRT equations are based on the quasi-crystalline approximation (QCA) for densely distributed moderate sized particles in a medium such as a snow pack. The model snow depth estimates from the DMRT are used to calibrate a Special Sensor Microwave Imager (SSM/I) snow depth retrieval algorithm which is based on the brightness temperature difference between 19 and 37 GHz with the SWE. The method is tested using meteorological data from the WMO global network. Results show that using the DMRT model coupled with a grain size model improved estimates of snow depth are obtained.

I. Introduction

Remote sensing has been used to monitor continental-scale snow cover area in the northern hemisphere for almost 25 years [1]. With the improvement in satellite microwave instrumentation, regional and local scales can now be mapped effectively. However, passive microwave (PM) retrieval methods of snow water equivalent (SWE) and/or snow depth (SD) are less mature with large errors often resulting from retrievals at the global scale. One of the key reasons for these large errors is because instantaneous parameterization of snowpack properties at the global scale is not straightforward. Studies have shown that snowpack models can be used successfully to quantify changes in propereties of the pack (e.g. average grain size) [2]. These models often require intensive-scale observations of meteorological surface conditions that are usually not available in a high quality globally distributed form. Thus, to overcome this problem, we implement a simple statistical model of snow pack grain growth and couple it to a microwave emission model and passive microwave observations to estimate snow depth.

III. Testing of the model and Conclusions

The model is tested on snow depth time series (1992-1993, 1993-1994 and 1994-1995) for two locations, one in north Sweden (67° 13' N, 23° 24' E) and the other in north America (56° 39' N, 111° 13' W). The original algorithm of

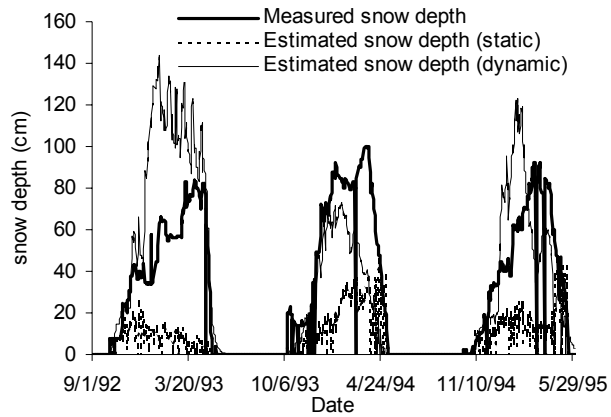

Fig. 2 Comparison of measured snow depth with estimated snow depth from the static and dynamic algorithms for north Sweden.

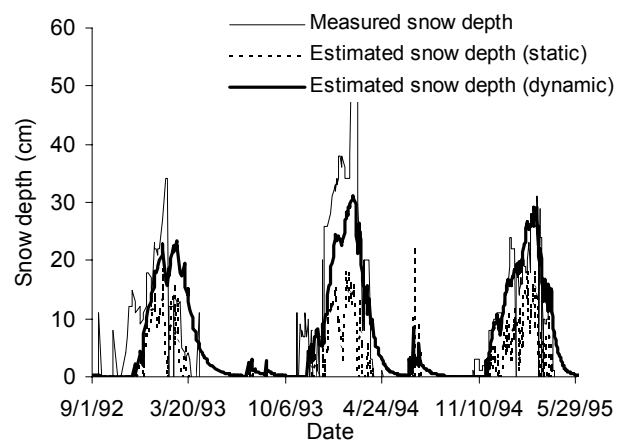

Fig. 3 Comparison of measured snow depth with estimated snow depth from the static and dynamic algorithms for north America.

[1] is compared with the newer algorithm and the results are shown in Figs. 2 and 3 for Sweden and north America respectively. Generally, the original static algorithm underestimates snow depth systematically for both sites. For the north Sweden site, however, there is overestimation in the 1992-1993 winter season but for the other two years the results are good. Overall, the correlation between the static algorithm and measured snow depth over the accumulated three winter seasons for north Sweden is 0.61 and for the dynamic model it is 0.77. For the north American site, the correlation for the static model is 0.71 while for the dynamic model it is 0.87. Thus, the dynamic model shows improvement over the original static algorithm.

Special Report

CEOP Satellite Data Integration

Figure 1. 500Tera-byte data archive system at the Institute Industrial Sciences, University of Tokyo

Toshio Koike, University of Tokyo
Paul Houser and Matthew Rodell, NASA GSFC

Special Report

CEOP Satellite Data Integration

Toshio Koike, University of Tokyo
Paul Houser and Matthew Rodell, NASA GSFC

Figure 1. 500Tera-byte data archive system at the Institute Industrial Sciences, University of Tokyo

To provide satellite data integration products including 4DDA "value-added" Global Land Data Assimilation System (GLDAS) datasets, of water cycle variables, two CEOP Satellite Data Integration Centers (CSDICs) are to be established, one at the University of Tokyo (UT) in cooperation with NASDA and the other at NASA's Goddard Space Flight Center (GSFC).

The CSDIC at UT will receive CEOP customized levels 1b and 2 and standard level 3 earth observation satellite data from space agencies and archive them by using a 500 tera-byte data archival system at the Institute of Industrial Sciences of UT as shown in Figure 1. The Committee on Earth Observation Satellite (CEOS) Working Group on Information Systems and Services (WGISS) Test Facility for CEOP (CEOP-WTF) advanced by NASDA and NASA will be developed for providing catalogue interoperability with CEOS agencies' systems by using CEOS' protocols and exchanging data and information with CEOS agencies and affiliates as well as users through automated links. Integrated CEOP satellite products overlaid with in-situ data and model output will be delivered to users by Web Mapping Technology and other visual technologies through networks. UT and NASDA propose a three phased approach for production and archiving of satellite data products; Phase I, for all reference sites, started in June, 2002, Phase II, for the monsoonal regions, begin in June, 2003, and Phase III, fully operational, beginning in September, 2005. To support phenomena detection, knowledge discovery and coincident search capabilities across a huge amount of very heterogeneous datasets, "Visual Data Mining" combined with the artificial intelligence approach in the computer sciences is now being developed as an important function of the CSDIC at UT.

Scientists at GSFC have developed a high-resolution GLDAS in cooperation with researchers at NOAA's National Centers for Environmental Prediction (NCEP). The goal of GLDAS is to produce optimal output fields of land surface states and fluxes by making use of data from advanced observing systems (see GEWEX News May 2002 and http://ldas.gsfc.nasa.gov/ for further details). GLDAS uses various new satellite and ground based observation systems within a land data assimilation framework to produce optimal output fields of land surface states and fluxes. GLDAS includes four components implemented globally at 1/4 degree resolution (higher resolutions are planned) in near real time: land modeling, land surface observation, land surface data assimilation and calibration and validation. The core advantage of GLDAS is its use of satellite-derived observations (including precipitation, solar radiation, snow cover, surface temperature, and soil moisture) to realistically constrain the system dynamics. This allows it to avoid the biases that exist in near-surface atmosphere fields produced by atmospheric forecast models, minimize the impact of simplified land parameterizations, and to identify and mitigate errors satellite observations used in data assimilation procedures (Figure 2 shows the GLDAS system). These value-added GLDAS data will improve land surface, weather, and climate predictions by providing global fields of land surface energy and moisture stores for initialization. GLDAS is a valuable tool for CEOP because it assimilates the information from multiple models and observation platforms to provide the best available assessment of the current state of the land surface. In addition, an interface to access data from the near-real time GLDAS operational model runs is provided through the web site (http://ldas.gsfc.nasa.gov/map/webout.html). A region can be specified by either manually entering the coordinates in the text boxes or automatically by creating a rectangle on the map. Users can subset the data by time period as well as parameter type. The international GEWEX and CEOP communities have recognized that GLDAS can be leveraged and further developed to address the needs of CEOP. The CSDIC at NASA GSFC is working with the CEOP-GLDAS products in cooperation with NASA Data Assimilation Office (DAO).

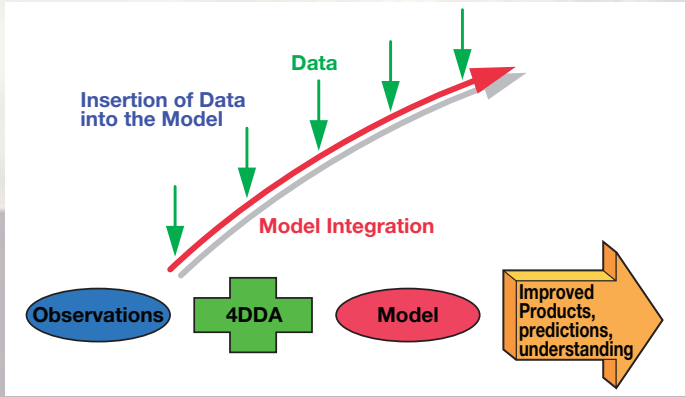

Concept of the Land Data Assimilation System

Genetic and Evolutionary Computation COnference

2002 GECCO

New York

July 9-13, 2002

Comparison of Multiobjective Optimization Evolutionary Algorithms for a Three-objective Problem

Sujay V. Kumar
Goddard Earth Science Technology Center
UMBC, NASA GSFC
Greenbelt, MD 20771

Ranji Ranjithan
Department of Civil Engineering,
North Carolina State University
Raleigh, NC 27695.

Abstract

This paper presents a systematic comparative study of CMEA (constraint method-based evolutionary algorithm) with several other commonly reported mulitobjective evolutionary algorithms (MOEAs) in solving a three-objective optimization problem. The best estimate of the noninferior space was also obtained by solving this MO problem using a binary linear programming procedure. Several quantitative metrics are used in this study to compare the noninferior solutions with respect to relative accuracy, as well as spread and distribution of solutions in the noninferior space. Results based on multiple random trials of the MOEAs indicate that overall CMEA performs better than the other MOEAs for this three-objective problem.

1 Introduction

With the recent emergence of interest in solving realistic multiobjective (MO) problems, numerous multiobjective evolutionary algorithms (MOEAs) have been reported in the literature. While most of them have been successfully tested and evaluated for an array of two-objective test problems, little work is reported on solving MO problems with more than two objectives. Building upon the study reported by Zitzler et al. (2001) for a three-objective problem, this paper reports a comparison of performance of the constraint method-based evolutionary algorithm (CMEA) (Ranjithan et al. 2001, Kumar 2002) with those of SPEA-II (Zitzler et al. 2001), NSGA-II (Deb et al. 2000), and PESA (Corne et al. 2000). These results are also compared with the noninferior set obtained using a MO analysis with a binary linear programming procedure. An array of quantitative metrics is used to conduct a systematic performance comparison among the solutions generated by these MOEAs. In addition to several existing metrics that are extended from the original definitions for two objectives, a new one is defined to evaluate the relative degree of dominance of one set of noninferior solutions over another. As computational needs associated with each MOEA scale up differently with the increase in the number of objectives, the total number of evaluations required to generate the noninferior sets used in this comparative study are kept to be similar. Thus the comparisons represent the quality of the noninferior solutions obtained with similar computational effort.

The next section provides a brief background on CMEA. The subsequent section describes the performance metrics used in this study. Section 4 defines the test problem and a comparison of the results, followed by conclusions.

5 Conclusions

Comparing the noninferior solutions obtained using the MOEAs with those obtained using BLP (which is the best estimate available), CMEA performs relatively well in finding noninferior solutions that are close to the best available estimation, as well as in covering most of the noninferior surface for the thee-objective extended knapsack problem. When comparing the solutions obtained by the different MOEAs tested in this study, CMEA performs better than all others with respect to the spread of solutions in the noninferior space. While CMEA is able to generate a good distribution of solutions in a wider range of the noninferior space, the other MOEAs generate a high density of solutions in the central portion of the noninferior space. In the context of accuracy or degree of dominance, the CMEA solutions dominate those generated by the other MOEAs relatively more frequently. As the total number of function evaluations were kept similar for the different MOEAs, all the comparisons reflect the quality of the resulting noninferior solutions obtained using each MOEA.

While this study provides a systematic comparison of several MOEAs for a three-objective MO problem, further testing and evaluation studies are needed. Similar to the large array of test problems used in two-objective MO optimization, additional three-objective test problems reflecting different problem complexities need to be defined and be used in further comparative studies of these MOEAs. Also, the implications of MO problem scale up on the computational needs of the different MOEAs need to be investigated.

2002 IEEE International Geoscience and Remote Sensing Symposium and the 24th Canadian Symposium on Remote Sensing

IGARSS 2002

REMOTE SENSING:
Integrating Our View of the Planet

IEEE

June 24-28, 2002
Toronto Canada

ESTAR Experience with RFI at L-band and Implications for Future Passive Microwave Remote Sensing from Space

David M. Le Vine
Code 975 Goddard Space Flight Center, Greenbelt, MD 20771
Tel: 301-614-5640; FAX: 301-614-5558; email: dmlevine@priam.gsfc.nasa.gov

Abstract-Although the spectral window at 1.413 GHz (L-band) is protected for passive use, radiometers for remote sensing commonly encounter problems with RFI. Experience with the synthetic aperture radiometer, ESTAR, suggests that airports are one source of this RFI. The existence of RFI at L-band could be a problem for future remote sensing from space.

1. INTRODUCTION

The spectral window at 1.413 GHz (L-band), set aside for passive use only, is critical for remote sensing from space [1]. It is the largest spectral window available at the long wavelength end of the microwave spectrum, and long wavelengths are needed for monitoring parameters such as soil moisture and sea surface salinity. The importance of soil moisture and sea surface salinity for understanding the global hydrologic cycle and ocean circulation, is reflected in the new sensors and remote sensing missions that recently have been proposed to make measurements at L-band from space (e.g. Aquarius [2], Hydros [3] and SMOS [4,5]).

Although the window at 1.413 GHz is protected for passive use, RFI is a common problem. For example, during the Southern Great Plains experiments [6,7], the ESTAR radiometer [5,8] experienced RFI significant enough to warrant changes in flight lines. Noise levels frequently were sufficient to saturate the total power channel. RFI has been a sufficiently common problem for ESTAR, that the first step in processing data is to screen for RFI (a filter is used in data processing to detect rapid changes in brightness temperature).

RFI is a serious concern for future passive remote sensing missions in space. This is especially true for synthetic aperture radiometers because they employ small antennas with a wide field-of-view. The measurement of salinity is particularly vulnerable to RFI because of the extreme radiometric sensitivity (better than 0.2 K) needed to detect small changes in salinity in the open ocean [2]. Studies done during the design of the synthetic aperture radiometer, HYDROSTAR [5], suggest that spurious radiation from air traffic control radar can not be ignored by future L-band sensors in space. (See Section III below.)

II. EXPERIENCE WITH ESTAR

ESTAR is a hybrid synthetic-and-real aperture radiometer. It employs long, "stick" antennas to achieve resolution along track and uses aperture synthesis to achieve resolution across track [8,9]. The use of aperture synthesis across track permits substantial thinning of the array, reducing the number of sticks needed. Thinning could also be done in the along track dimension to further reduce the real aperture. This is being done in Europe for the SMOS mission to measure soil moisture and ocean salinity [5]. Aperture synthesis works well with antennas that have broad beams in the dimension where resolution is to be synthesized. However, broad antennas are particularly sensitive to RFI since radiation is received from a wide field-of-view. In the case of ESTAR, the field-of-view is restricted (about ± 8 degrees) in the along track dimension by the antenna aperture. However, in the across track dimension incoming signals from all angles are received.

Fig. 1 is an ESTAR image made in 1997 in the vicinity of Richmond, VA. The image has been superimposed on a map of land-water boundaries to help identify features. At the far right is the Chesapeake Bay, and the York and James Rivers are visible in the image. This image is the composite of several east-west lines flown at 25 kft with ESTAR aboard the Orion P-3B aircraft based at NASA's Wallops Flight Facility. In this image, the RFI filtering normally done in software was not performed in order to illustrate the problem. The small, vertical, white dashes are strong signals associated with RFI. To get an idea of the temporal structure of these signals, the raw data from the zero spacing channel (total power radiometer) is shown in Fig. 2. The data shown is the uncalibrated output from a noise injection radiometer. This data was collected at about 77 WLong at the location of the arrow in Fig. 1. The periodic spikes are RFI. The undulating signal on which they ride is the slow variation in total power one normally associates with changes in surface features (e.g. soil moisture and vegetation canopy) at L-band. The period (10 s) is reasonable for air traffic control radar (e.g. with a rotation rate of about 5 rpm).

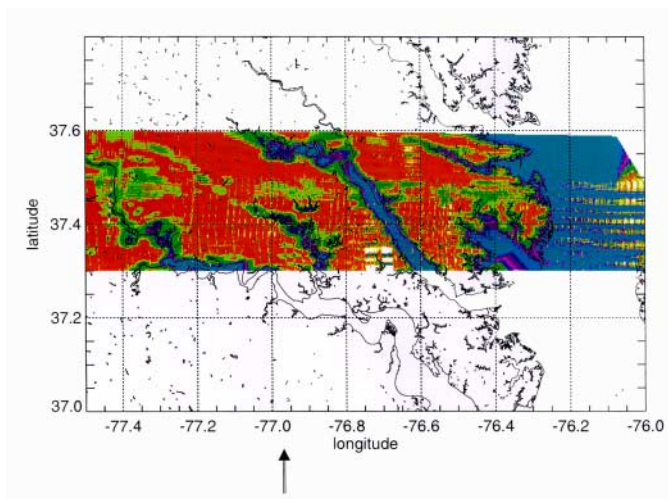

Fig. 1. ESTAR image showing the effects of RFI in the vicinity of Richmond, VA The small vertical stripes are artifacts in the image due to large RFI.

2002 IEEE International Geoscience and Remote Sensing Symposium and the 24th Canadian Symposium on Remote Sensing

IGARSS 2002

REMOTE SENSING:
Integrating Our View of the Planet

IEEE

June 24-28, 2002
Toronto Canada

Bright-Band Modeling of Air/Space-Borne Microwave Radars

Liang Liao[1], Robert Meneghini[2] and Toshio Iguchi[3]
[1]Caelum Research Corp., Code 975, NASA/GSFC, Greenbelt, MD 20771
[2]Code 975, NASA/GSFC, Greenbelt, MD 20771
[3]Applied Research and Standards Division, CRL, Tokyo, 184-8795, Japan

***Abstract*- In simulating the radar echo in the melting layer of stratiform rain, a melting snowflake is modeled as a spherical non-uniform mixture, prescribed as a stratified-sphere in that the fractional water content is given as a function of the radius of sphere. Combined with the melting layer model that depicts the melting fractions and fall velocities of hydrometeors, the radar profiles are produced and then compared with the measurements of TRMM PR and the dual-wavelength airborne radar.**

I. Introduction

The bright band of enhanced radar reflectivity is often observed in the layer where the melting of snow takes place. Understanding the effect of melting hydrometeors on the electric wave propagation is important for algorithms that are used to retrieve rain rates from spaceborne sensors, such as the Tropical Rainfall Measuring Mission (TRMM) Precipitation Radar (PR) and the TRMM Microwave Imager (TMI). Aside from the bright band model needed for simulations of the radar profiles in the melting region, correctly modeling snowflake melting process is also important in the simulation of the radar bright-band profile. The bright band, or melting layer model that describes the complex dynamical and thermodynamical processes within the melting layer, provides the data of the water fractions and fall velocities of the melting snow as a function of the particle size and the distance from the 0^0C isotherm. The melting snow model, on the other hand, describes how the melting process takes place. Two melting models often appear in the literatures: One is the uniformly-mixed model where the water fraction is constant throughout the particle, and another is concentric-sphere model where the water is confined to the outer shell and snow to the inner core. However, many observations [1] suggest that melting of the snowflake starts at its surface and gradually develops towards the center. It therefore becomes more realistic to model a melting snowflake as non-uniform mixture. To compute the scattering properties of such non-uniform melting particles, the stratified-sphere (or multi-layer sphere) scattering model is used, in which a uniform mixture is assumed within each layer with a water fraction that varies with radius. The advantage of using the stratified-sphere model is not only that the melting snowflake can be more realistically prescribed, but its analytical solution exists [2][3]. Having described the stratified-sphere model in Section II, the simulations of the radar bright-band profiles for the cases of TRMM PR and dual-wavelength airborne radar are made in Section III. The results reveal that the simulated profiles agree reasonably well with the measurements.

II. Melting snowflakes

As mentioned previously, the stratified sphere provides a great flexibility to model non-uniform snow-water mixtures in which the fractional water content is given as a function of the radius. The stratified-sphere melting model, used in this study, is composed of 100 equal-thickness layers, and an exponential equation is employed to describe the distribution of the fractional water content of melting snow. In Fig.1 examples are shown of melting particles with the water fractions of 0.2 (left) and 0.4 (right). The gray levels represent the values of water fractions within the particle. The effective dielectric constant of the uniform mixture, applied in each layer of the stratified sphere, is derived from the internal electric fields of the mixture by use of a conjugate gradient-fast Fourier transform (CGFFT) numerical method [4]. The snow density used is uniform within the particle, whereas some measurements indicate that the snow density decreases with increase of radius. However, studies have demonstrated that the difference of the effective dielectric constants between the uniform snow density and non-uniform snow density with the same average density as the uniform case are negligible small [5].

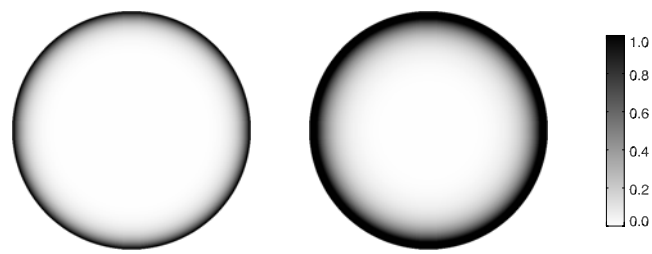

Fig.1. Examples of stratified-sphere model for the melting snowflakes for the overall water fractions of 0.2 (left) and 0.4 (right). The gray levels represents the fractional water contents.

IV. Summary

To use a more realistic melting model, the melting snowflake is modeled as a stratified sphere where the fractional water content is given as a function of the radius. Using this model the simulations of the radar reflectivity profiles associated with the melting layer are made for the cases of the TRMM PR and the dual-wavelength airborne radar. The raindrop size distributions, as input parameters of the melting model, are determined by matching the simulated and measured reflectivity in rain. For TRMM PR the Marshall-Palmer drop size distribution is used, while the 2-parameter exponential form of size distribution is applied for the airborne radar. In the simulations the same melting model is applied for TRMM PR and dual-wavelength airborne radar in the sense that the distributions of the fractional water contents within the melting snowflakes are treated the exactly same. The simulated bright-band profiles are in good agreement with the measured ones.

NASA/TM-2002-210005

SIMBIOS Project 2001 Annual Report

Giulietta S. Fargion, Science Applications International Corporation, Maryland
Charles R. McClain, Goddard Space Flight Center, Greenbelt, Maryland

National Aeronautics and
Space Administration

Goddard Space Flight Center
Greenbelt, Maryland 20771

March 2002

Chapter 1

An Overview of SIMBIOS Project Activities and Accomplishments During FY01

Charles R. McClain
NASA Goddard Space Flight Center, Greenbelt, Maryland

Giulietta S. Fargion
Science Applications International Corporation (SAIC), Beltsville, Maryland

In FY01, the SIMBIOS Project brought a number of activities to fruition and laid the groundwork for FY02 initiatives. With SeaWiFS continuing to perform well, the Terra platform and MODIS launched in December 1999, and several other global missions scheduled for launch (e.g., the Aqua platform with MODIS in 2002, the ENVISAT mission with MERIS in 2002, and ADEOS-II with GLI and POLDER in 2002), the first real opportunties to merge global data sets can be pursued. NASA HQ approved a three-year continuation of the science team (2001-2003) under an NRA and the Project Office. As it is taking some time for the MODIS team to work through the initial on-orbit processing issues, data merger-related activities within the Project Office have been in the development of data merging algorithms and software to read MODIS, development of capabilities for working with multiple global data sets in the future (i.e., OCTS-GAC reprocessing) and supporting the characterization of OSMI. These activities and accomplishments are described below.

SIMBIOS Science Team Support

a. The fifth science team meeting was held in Baltimore in January 2002 with a substantial US (SIMBIOS and MODIS PIs) and international participation, with official representation from OCTS, POLDER-I and II, MOS, MERIS, GLI, and VIIRS misssions. During the meeting the team addressed atmospheric correction and bio-optical algorithms, a MODIS data merging plan for 2002, uncertainty budget and sources from in situ observation, SeaWIFS re-processing, protocols updates and international collaborations. The agenda, presentations, minutes and recommendations are posted at http://simbios.gsfc.nasa.gov/Info/
b. Under a SIMBIOS NRA released in late 1999, a new science team was selected and has been funded under contracts or interagency agreements (2000-2003). The initial team consists of 19 U.S. and 12 international investigations with additional international investigations to be added as post-NRA proposals are received and accepted (i.e., Australian and Korean proposals). Agreements with the international team members were initiated by NASA/HQ in Fall 2000 and most of them have now been signed.
c. In October 2001 the SIMBIOS Project management conducted team performance evaluations on all investigations. Formal evaluations of investigations funded through contracts are required by the NASA Procurement Office. All investigations, with the exclusion of one, where renewed for the second year (2002).

Satellite Data Characterization

a. KOMPSAT/OSMI characterization work was done in collaboration with KARI. Joint scientific papers were presented at the Fall AGU meeting in San Francisco (Franz and Kim, 2002; Kim et al. 2002). In addition, KARI requested assistance from the Project to identify a schedule to record onboard OSMI data. Our recommendation is now implemented.
b. The Project is hosting a NASDA representative (Mr. Tanaka) for one year (June 2001-June 2002) at NASA Goddard Space Flight Center to assist in the GLI preparations. The Project worked on a document entitled ”Instrument characterization of the GLI”, delivered at the GLI science team meeting in Tokyo (November 2001).

Satellite Data Analyses

a. OCTS GAC data reprocessing was completed. This was a very productive collaboration effort with NASDA and Japanese scientists. A scientific presentation was given at the Fall 2001 AGU meeting in San Francisco (Tanaka et al. 2001). OCTS-GAC data is available through the GSFC DAAC, the SIMBIOS Project and NASDA.

American Geophysical Union (AGU)

2002 Spring Meeting Washington Convention Center Washington, DC

May 28-31, 2002
(Tuesday – Friday)

Monitoring the Radiometric Stability of the SeaWiFS Transfer Radiometer II

Authors: Gerhard Meister[1], Giulietta Fargion[2], Charles McClain[3]

[1]: Futuretech Corp., SIMBIOS Project, Goddard Space Flight Center,Greenbelt,MD,USA
[2]: Science Applications International Corporation, SIMBIOS Project, Goddard Space Flight Center, Greenbelt, MD, USA
[3]: NASA, Goddard Space Flight Center, Greenbelt, MD, USA

The SIMBIOS (Sensor Intercomparison and Merger for Biological and Interdisciplinary Oceanic Studies) Project Office conducts calibration round-robin intercomparison experiments on a yearly basis. The core instrument is the SeaWiFS Transfer Radiometer II (SXR-II) designed by the National Institute of Standards and Technology (NIST). This filter radiometer measures the radiances produced in the participating laboratories in six wavelength channels from 411 nm to 777 nm. These measured radiances are compared to the radiances expected by the laboratories. The SXR-II is calibrated once a year at the SIRCUS (Spectral Irradiance and Radiance Calibration with Uniform Sources) facility at the NIST.

The radiometric stability of the SXR-II is one of the largest contributions to the combined standard uncertainty of the SXR-II. The later is estimated to be about 0.8 %. The calibration coefficients of the six SXR-II channels between the NIST calibrations from December 2000 and December 2001 changed between 0.3 % and 1.6 %. The SIMBIOS Project monitors the radiometric stability of the SXR-II with commercially available portable light sources called SeaWiFS Quality Monitors (SQM) on a monthly basis. This contribution discusses the monitoring results from 2001, which were done with an SQM-II from Satlantic Inc. These results showed that a linear interpolation between the two NIST calibrations describes the evolution of the SXR-II calibration coefficients to within +/- 0.5 %, except for channel 1. We also present preliminary results from 2002 with an SQM (OCS-5002) from Yankee Environmental Systems, Inc.

2002 IEEE International Geoscience and Remote Sensing Symposium and the 24th Canadian Symposium on Remote Sensing

IGARSS 2002

REMOTE SENSING:
Integrating Our View of the Planet

IEEE

June 24-28, 2002
Toronto Canada

Integral Equations for a dual-wavelength radar

Robert Meneghini, Code 975, NASA/GSFC, Greenbelt, MD, 20071
Liang Liao, Caelum Research Corp, Code 975
Toshio Iguchi, Communications Research Laboratory, Tokyo, 184-8795, Japan

I. INTRODUCTION

A dual-wavelength spaceborne weather radar is expected to be one of the primary instruments on the proposed Global Precipitation Mission, GPM, satellite. In addition, airborne dual-wavelength weather radar data at (13.6, 35 GHz), (10, 35 GHz), (10, 94 GHz) have been or will be acquired within the next several years. The objective of the paper is to outline some of the techniques for analyzing such data with a focus on an approach that uses integral equations that describe the change in the DSD parameters with radar range.

II. DUAL-WAVELENGTH METHODS

Although dual-wavelength radar techniques for ground-based weather radars have been superseded by polarimetric methods, the dual-wavelength radar offers perhaps the best opportunity for accurate measurements of rain and drop size distribution parameters from airborne and spaceborne platforms. From space, a near-nadir viewing geometry for weather radar is dictated by the need to obtain precipitation measurements uncontaminated by the surface. However, at near-nadir incidence, polarimetric techniques such as Z_{DR} or κ_{DP} that depend on the oblate shape of the raindrops and near-vertical alignment can no longer be used.

Dual-wavelength techniques for rain estimation can be classified into two types. The first comprises methods that estimate the attenuation or differential attenuation followed by a conversion of attenuation into meteorological quantities such as rain rate, R, or liquid water content, M. An advantage of using the specific attenuation, k, rather than the radar reflectivity factor, Z, to infer R and M is that k, M, and R are approximately equal to the third or fourth moment of the drop size distribution. As a consequence, the estimation of M or R from k is fairly insensitive to the exact form of the drop size distribution, DSD.

The best-known approach of this first type is the standard dual-wavelength method where the frequency difference in radar return powers at range r_2 is subtracted from the same frequency difference at range r_1. It can be shown from the radar equation that if the scattering is Rayleigh at r_1 and r_2 (i.e., the individual backscattering cross sections of the raindrops within the scattering volumes are proportional to diameter^6 and frequency^4) this difference of differences is proportional to differential path attenuation in the interval [r_1, r_2]. The technique is simple to apply. Moreover, if differential attenuation can be estimated accurately, it serves as an accurate estimator of M and R because of the insensitivity of the k-R, k-M relations to the DSD. However, the assumption of Rayleigh scattering used in the method is problematic at higher frequencies and higher rain rates where significant non-Rayleigh scattering can occur. Another disadvantage is that the fractional standard deviation, FSD, in the estimate tends to be large because of the finite sampling of the radar and the relatively small differential signal. Although the FSD can be decreased by choosing a larger interval over which the technique is applied, this degrades the resolution. Although the standard dual-wavelength technique is questionable for high resolution estimates for the (13.6, 35 GHz) combination proposed for GPM, it may be well suited for estimating the differential attenuation over the full path, thereby serving as a constraint for the backward recursion solution described below.

In the second approach, the radar reflectivity factors are corrected for attenuation and the information on the size distribution is inferred from the non-Rayleigh backscattering characteristics of the hydrometeors. The equations can take the form either of two coupled Volterra integral equations or two coupled non-linear first order differential equations for the parameters of the DSD [1-3]. Only the first formulation will be considered here. Note that in the standard method, Rayleigh scattering is assumed whereas in this approach, the signal that we wish to extract is the non-Rayleigh scattering signal. Moreover, the objective of the second approach is to estimate parameters of the DSD and then proceed to the R and M estimates whereas the first approach proceeds from the attenuation directly to R and M. The solution to the integral or differential equations, however, is unstable if it is carried out in the forward direction from the storm top toward the surface. This is similar to the instability in the Hitschfeld-Bordan solution in the presence of moderate attenuation in the case of single attenuating-wavelength radar data. The solution can be made more stable by reformulating the equations so that the solution proceeds from the surface to the storm top. This can be done, however, only if estimates of the path integrated attenuation, PIA, at both frequencies can be obtained. We discuss several possibilities below.

In the surface reference technique, SRT, the 2-way PIA is approximated by the difference in the radar return powers from the surface in the presence and absence of rain. The technique can be applied at each frequency so the path attenuations at frequencies 1 and 2 are available. We denote the specific attenuations (dB/km) at f_1 and f_2 by $k(f_1)$ and $k(f_2)$. An alternative is to estimate the differential path attenuation by forming the frequency difference of the surface return powers outside and inside the rain and then taking a difference of these differences. To obtain $k(f_1)$ and $k(f_2)$ from the specific differential attenuation, k_{f1-f2}, we can use measured DSD data and Mie scattering calculations to obtain linear fits of the form: $k(f_i) = \alpha_i + \beta_i k_{f1-f2}$, $f_i = f_1$ or f_2. For example, at T = 10 C, with f_1 = 35 GHz and f_2 = 13.6 GHz we obtain $\alpha_1 = 0.117$, $\beta_1 = 1.04$, $\alpha_2 = 0.117$, $\beta_2 = 0.042$.

16th Conference on Hydrology

13–17 January 2002
Orlando, Florida

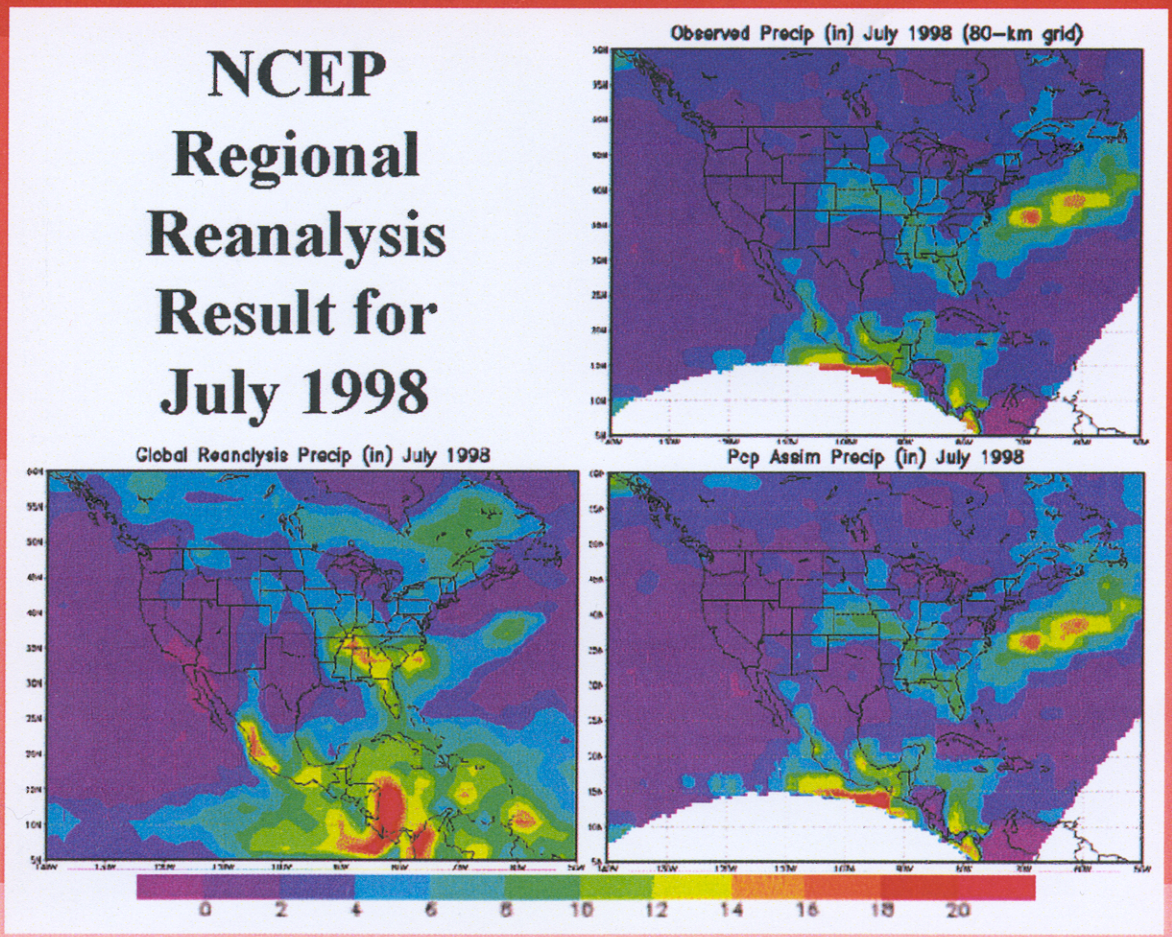

AMERICAN METEOROLOGICAL SOCIETY

J1.1 REDUCING NEAR-SURFACE COOL/MOIST BIASES OVER SNOWPACK AND EARLY SPRING WET SOILS IN NCEP ETA MODEL FORECASTS VIA LAND SURFACE MODEL UPGRADES

K. Mitchell[1], M. Ek[1,2], D. Lohmann[1, 2], V. Koren[3], J. Schaake[3],
Q. Duan[3], P. Grunmann[1,2], G. Gayno[5], Y. Lin[1], E. Rogers[1], D. Tarpley[4], C. Peters-Lidard[6]

[1]NOAA/NWS/National Centers for Environmental Prediction/Environmental Modeling Center
[2]University Corporation for Atmospheric Research/Visiting Scientist Program
[3]NOAA/NWS/Office of Hydrologic Development
[4]NOAA/National Environmental Satellite, Data, and Information Service/Office of Res. & Applications
[5]USAF Air Force Weather Agency
[6]NASA/GSFC Hydrological Sciences Branch

1. INTRODUCTION

Since 1996, a series of NOAA GAPP/GCIP-sponsored land-surface related advances have been implemented in the NCEP mesoscale Eta model and its Eta-based data assimilation system (EDAS). This began with the introduction in January 1996 of a multi-layer soil-vegetation-snow land-surface model originally developed at Oregon State University (Mahrt and Pan, 1984), and modified for use in the Eta model (Chen et al 1996). At that time, the Eta model used initial soil moisture and temperature from the NCEP global model data assimilation system (GDAS), which employs soil moisture nudging to a fixed, annual-cycle soil moisture climatology.

Over the following 2-3 years, subsequent advances to the Eta model land-surface treatment included the use of the NESDIS, high-resolution, NDVI-based vegetation greenness fraction database, adjustments to the initial global model soil moisture, an increase from two to four soil layers, and the use of the NESDIS operational daily 23-km North American snow cover and sea ice analysis. This late 90's period of Eta land-surface improvements culminated in June 1998 with the introduction of continuous self-cycling of Eta soil moisture and soil temperature in the Eta 4-D Data Assimilation System (EDAS). The latter employs no soil moisture nudging. Since then and up to the present (over three years), the Eta model's initial soil moisture and soil temperature have been sole products of the continuous cycling of these two land states in the coupled land-atmosphere EDAS.

Between June 1998 and July 2001, no further significant changes were implemented to the operational Eta/EDAS land-surface package. Section 2 presents examples of the validation of Eta model performance during that period. Simultaneously during that period, off-line development focused on our next generation of land-surface improvements, to include frozen soil processes, plus substantial advances to the snowpack physics and ground heat flux physics. This phase of significant upgrades, in collaboration with our GAPP/GCIP and other partners, led us to coin the name "NOAH" to designate our new LSM. Section 3 describes these LSM upgrades and Section 4 presents some results from the successful testing of these upgrades in the coupled Eta/EDAS, which culminated in their operational implementation on 24 July 2001.

4. COUPLED ETA MODEL TESTING

Pre-implementation testing of the upgraded NOAH LSM in the coupled Eta model spanned 1) a summer month (12 Aug - 12 Sep 2000), 2) a winter month (01 Feb - 01 Mar 2001), and a spring month (24 Apr - 24 May 2001). Over these three periods we continuously executed the cycled EDAS and launched twice-daily 60-h Eta forecasts (one each from the 00Z and 12Z initial times) for both A) the control configuration (then operational suite) and B) the test configuration with the NOAH LSM encompassing the land-surface changes summarized in the previous section. The next two sub-sections present two examples of model bias reduction in the test case.

4.1 *Spring case*

The Eta model control case (i.e. as operational prior to the 24 Jul 2001) exhibits a near-surface cool (moist) bias in forecasts of air temperature (dewpoint) throughout the U.S. north central plains in spring, when the near-surface soil is typically moist from spring rains and the recent snowmelt season, and before substantial green vegetation has emerged. Inspection of Fig. 4 of the 60-h Eta forecast, valid at 00Z on 30 Apr 2001, of the dew point temperature in the lower boundary layer reveals that the test (right frame) is substantially less moist than the control (left frame).

NASA/TM-2002-210004/Rev3-Vol1

James L. Mueller[1] and Giulietta S. Fargion[2]
Editors

[1] *CHORS, San Diego State University, San Diego, California*
[2]*Science Applications International Corporation, Beltsville, Maryland*

Ocean Optics Protocols For Satellite Ocean Color Sensor Validation, Revision 3, Volume 1

J. L. Mueller, C. Pietras, S. B. Hooker, D. K. Clark, A. Morel, R. Frouin, B.G. Mitchell, R. R. Bidigare, C. Trees, J. Werdell, G. S. Fargion, R. Arnone, R. W. Austin, S. Bailey, W. Broenkow, S. W. Brown, K. Carder, C. Davis, J. Dore, M. Feinholz, S. Flora, Z.P. Lee, B. Holben, B. C. Johnson, M. Kahru, D. M. Karl, Y. S Kim, K. D. Knobelspiesse, C. R. McClain, S. McLean, M. Miller, C. D. Mobley , J. Porter, R.G. Steward, M. Stramska, L. Van Heukelem, K. Voss, J. Wieland, M. A.Yarbrough and M. Yuen.

National Aeronautical and
Space administration

Goddard Space Flight Space Center
Greenbelt, Maryland 20771

February 2002

Chapter 1

Ocean Color Radiometry and Bio-Optics

James L. Mueller[1], Roswell W. Austin[1], Giulietta S. Fargion[2] and Charles R. McClain[3]
[1]*Center for Hydro-Optics and Remote Sensing, San Diego State University, California*
[2]*Science Applications International Corporation, Beltsville, Maryland*
[3]*NASA, Goddard Space Flight Center, Greenbelt, Maryland*

1.1 INTRODUCTION

During the period from *circa* 1985 to 1991, the National Aeronautics and Space Administration (NASA) charged a series of successive science working groups with the task of recommending guidelines, goals and mission design criteria for future satellite ocean color remote sensors. The deliberations of these working groups were based on the ocean color science community's experiences with the Nimbus-7 Coastal Zone Color Scanner (CZCS). On the one hand, the highly successful CZCS mission firmly established ocean color remote sensing as a powerful tool for monitoring and studying the bio-optical properties of the global ocean. On the other hand, the radiometric responsivities of the CZCS channels declined progressively with time throughout its 8-year operating life, which just as firmly established the need to independently verify a satellite sensor's performance using *in situ* measurements of the ocean and atmosphere. From those two general perspectives, the principal recommendations of these NASA Ocean Color Science Working Groups (collectively) included:

1. ***Baseline satellite ocean color products*** should include
    a. Normalized water-leaving radiances $L_{\mathrm{WN}}(\lambda)$ (Gordon and Clark, 1981),
    b. Aerosol radiances $L_{\mathrm{a}}(\lambda)$,
    c. Chlorophyll *a* concentration *Chl* $\left[\mathrm{mg\ m^{-3}}\right]$,
    d. The diffuse attenuation coefficient $K(490)$ at a wavelength of 490 nm, and
    e. Calibrated radiances $L_{\mathrm{t}}(\lambda)$ observed at the satellite.
2. ***Principal goals for product uncertainties*** should be
    a. Less than ***5 % uncertainty*** in $\boldsymbol{L_{\mathrm{WN}}(\lambda)}$ and
    b. Less than ***35 % uncertainty*** in ***Chl***.
3. An ***ongoing satellite ocean color sensor system validation program*** is necessary, using *in situ* measurements of ocean radiometric and bio-optical properties, and of atmospheric optical properties, to verify system performance - including algorithms - immediately after launch and throughout a satellite ocean color sensor's operating lifetime.

These and other recommendations of the earlier working groups were endorsed by the Sea-viewing Wide Field-of-view Sensor (SeaWiFS) Science Team and accepted by NASA. Of particular significance in the present context, the SeaWiFS Project Office moved immediately to implement a SeaWiFS Validation Plan designed to assure a best effort to achieve the above product uncertainty goals (McClain *et al.* 1992). A critical aspect of the validation plan was that *in situ* radiometric, optical and bio-optical measurements of uniformly high quality and accuracy be obtained for verifying SeaWiFS system performance and product uncertainties. Therefore, in 1991 the SeaWiFS Project Office sponsored a workshop to recommend appropriate measurements, instrument specifications, and protocols specifying methods of calibration, field measurements, and data analysis necessary to support SeaWiFS validation, leading to the first publication of *Ocean Optics Protocols for SeaWiFS Validation* (Mueller and Austin 1992). Continued discourse within the ocean color research community led to Revisions 1 (Mueller and Austin 1995) and 2 (Fargion and Mueller 2000) of these protocols.

NASA/TM-2002-210004/Rev3-Vol1

James L. Mueller[1] and Giulietta S. Fargion[2]
Editors

[1] *CHORS, San Diego State University, San Diego, California*
[2]*Science Applications International Corporation, Beltsville, Maryland*

Ocean Optics Protocols For Satellite Ocean Color Sensor Validation, Revision 3, Volume 1

J. L. Mueller, C. Pietras, S. B. Hooker, D. K. Clark, A. Morel, R. Frouin, B.G. Mitchell, R. R. Bidigare, C. Trees, J. Werdell, G. S. Fargion, R. Arnone, R. W. Austin, S. Bailey, W. Broenkow, S. W. Brown, K. Carder, C. Davis, J. Dore, M. Feinholz, S. Flora, Z.P. Lee, B. Holben, B. C. Johnson, M. Kahru, D. M. Karl, Y. S Kim, K. D. Knobelspiesse, C. R. McClain, S. McLean, M. Miller, C. D. Mobley , J. Porter, R.G. Steward, M. Stramska, L. Van Heukelem, K. Voss, J. Wieland, M. A.Yarbrough and M. Yuen.

National Aeronautical and
Space administration

Goddard Space Flight Space Center
Greenbelt, Maryland 20771

February 2002

Chapter 3

Data Requirements for Ocean Color Algorithms and Validation

James L. Mueller[1], Giulietta S. Fargion[2] and Charles R. McClain[3]

[1]*Center for Hydro-Optics and Remote Sensing, San Diego State University, California*
[2]*Science Applications International Corporation, Beltsville, Maryland*
[3]*NASA, Goddard Space Flight Center, Greenbelt, Maryland*

3.1 INTRODUCTION

The principal *in situ* variables to be measured, or derived from measurements, for satellite ocean color sensor validation, and algorithm development and validation, are listed in Table 3.1. The variables are grouped, in Table 3.1, into four related groups: Radiometric Quantities (both oceanic and atmospheric), Inherent Optical Properties (IOP) of sea water, Biogeochemical and Bio-Optical Properties of sea water, and Ancillary Data and Metadata required to support the use, analysis, interpretation, and quality assessment of the other data. Those *in situ* variables that are measured are classified into three categories of descending priority.

The first category of measurements, flagged "Required" in Table 3.1, is the minimum subset required for validating a satellite sensor's radiometric performance, exact normalized water-leaving radiances (Chapter 13), and fundamental derived products, including chlorophyll a concentration, aerosol optical thickness, and K(490), and for associated algorithm development and validation.

The second category, flagged "Highly Desired" in Table 3.1, are measurements that supplement the minimum subset and are needed for investigations focused on atmospheric correction algorithms and aerosols, relationships between IOP and remote sensing reflectance, and/or Case 3 algorithms.

The third category, flagged "Specialized Measurement" in Table 3.1, are measurements which either address aspects of ocean bio-optics that are secondary to satellite remote sensing, or require highly specialized equipment that is not readily available to the community at large.

A fourth category, flagged as "Derived", comprises key quantities that are either calculated from the *in situ* measurements, or are derived from models. The above set of variables is also listed in Table 3.2, to identify the satellite ocean color sensor application for which each measurement is needed. Table 3.2 also provides an index of the protocol chapters addressing each *in situ* measurement.

3.2 RADIOMETRIC QUANTITIES

Surface incident spectral irradiance in air, $E_S(\lambda) \equiv E_d(0^+,\lambda)$, downwelled spectral irradiance, $E_d(z,\lambda)$, and upwelled spectral radiance, $L_u(z,\lambda)$, are the fundamental measurable quantities needed to derive normalized water-leaving radiances (or equivalently remote sensing reflectance) in most circumstances. Other radiometric properties listed in Table 3.1, including sky radiance and normal solar irradiance, are also important *in situ* measurements in the SIMBIOS ocean color validation program. Also listed are critical radiometric quantities that are calculated, or derived, from *in situ* measurements. In some cases, listed radiometric quantities may be derived, wholly or in part, from other non-radiometric measurements listed in the table. For example, remote sensing reflectance may either be calculated directly as the ratio of water-leaving radiance $L_W(\lambda)$ to incident irradiance, $L_W(\lambda):E_S(\lambda)$, or it may be modeled as a function of the IOP ratio of the backscattering to absorption coefficients, $b_b(\lambda):a(\lambda)$, and the Bidirectional Reflectance Distribution Function (BRDF) (Chapter 13).

NASA/TM-2002-210004/Rev3-Vol1

James L. Mueller[1] and Giulietta S. Fargion[2]
Editors

[1] *CHORS, San Diego State University, San Diego, California*
[2]*Science Applications International Corporation, Beltsville, Maryland*

Ocean Optics Protocols For Satellite Ocean Color Sensor Validation, Revision 3, Volume 1

J. L. Mueller, C. Pietras, S. B. Hooker, D. K. Clark, A. Morel, R. Frouin, B.G. Mitchell, R. R. Bidigare, C. Trees, J. Werdell, G. S. Fargion, R. Arnone, R. W. Austin, S. Bailey, W. Broenkow, S. W. Brown, K. Carder, C. Davis, J. Dore, M. Feinholz, S. Flora, Z.P. Lee, B. Holben, B. C. Johnson, M. Kahru, D. M. Karl, Y. S Kim, K. D. Knobelspiesse, C. R. McClain, S. McLean, M. Miller, C. D. Mobley , J. Porter, R.G. Steward, M. Stramska, L. Van Heukelem, K. Voss, J. Wieland, M. A.Yarbrough and M. Yuen.

National Aeronautical and
Space administration

Goddard Space Flight Space Center
Greenbelt, Maryland 20771

February 2002

Preface

This document stipulates protocols for measuring bio-optical and radiometric data for the Sensor Intercomparison and Merger for Biological and Interdisciplinary Oceanic Studies (SIMBIOS) Project activities and algorithm development. This document supersedes the earlier version (Fargion and Mueller 2000) and is organized into four parts:

- *Introductory Background*: The initial part covers perspectives on ocean color research and validation (Chapter 1), fundamental definitions, terminology, relationships and conventions used throughout the protocol document (Chapter 2), and requirements for specific *in situ* observations (Chapter 3).
- *Instrument Characteristics*: This group of chapters begins with a review of instrument performance characteristics required for *in situ* observations to support validation (Chapter 4), and the subsequent chapters cover detailed instrument specifications and underlying rationale (Chapter 5) and protocols for instrument calibration and characterization standards and methods (Chapters 6 through 8).
- *Field Measurements and Data Analysis*: The methods used in the field to make the *in situ* measurements needed for ocean color validation, together with methods of analyzing the data, are briefly, but comprehensively, reviewed in Chapter 9. The remaining chapters of this part provide detailed measurement and data analysis protocols for in-water radiometric profiles (Chapter 10), the Marine Optical Buoy (MOBY) radiometric observatory for vicarious calibration of satellite ocean color sensors (Chapter 11), above water measurements of remote sensing reflectance (Chapter 12), determinations of exact normalized water-leaving radiance (Chapter 13), atmospheric radiometric measurements to determine aerosol optical thickness and sky radiance distributions (Chapter 14), determination of absorption spectra from water samples (Chapter 15), and determination of phytoplankton pigment concentrations using HPLC (Chapter 16) and fluorometric (Chapter 17) methods.
- *Data Reporting and Archival*: Chapter 18 describes the methods and procedures for data archival, data synthesis and merging, and quality control applicable to the SeaWiFS Bio-optical Archive and Storage System (SeaBASS), which is maintained to support ocean color validation for the SeaWiFS, SIMBIOS and other cooperating satellite sensor projects. Current SeaBASS file content and formatting requirements are given in Appendix B.

What is new in Revision 3 to the ocean optics protocol document, as compared to Revision 2 (Fargion and Mueller 2000). The most obvious changes are the insertion of 3 new chapters into the document, and the renumbering of the other chapters to accommodate them. The new chapters are:

1. Chapter 2, *Fundamental Definitions, Relationships and Conventions*, introduces the radiometric quantities, inherent optical properties, fundamental concepts and terminology underlying the *in situ* measurement and analysis protocols discussed throughout the document. The chapter also discusses the scales adopted in these protocols for such quantities as extraterrestrial solar irradiance, and the absorption and scattering coefficients of pure water.
2. Chapter 11, *MOBY, A Radiometric Buoy for Performance Monitoring and Vicarious Calibration of Satellite Ocean Color Sensors: Measurement and Data Analysis Protocols*, documents the specific measurement and data analysis protocols used in the operation of this critical radiometric observatory. The MOBY normalized water-leaving radiance time series has provided the principal, common basis for vicarious calibration of every satellite ocean color sensor in operation since 1996.
3. Chapter 13, *Normalized Water-Leaving Radiance and Remote Sensing Reflectance: Bidirectional Reflectance and Other Factors*, develops the physical basis underlying the bidirectional aspects of the ocean's reflectance, and presents methods for removing this effect to determine *exact normalized water-leaving radiance*, the only form of water-leaving radiance suitable for comparisons between determinations based on satellite and *in situ* measurements.

Aside from renumbering, several of the chapters carried over from Revision 2 have been revisited and significantly revised, while others have been modified only slightly. The two chapters providing overviews of Instrument Characteristics (Chapter 4) and Field Measurements and Data Analysis (Chapter 9) have been revised to reflect the changed content of those two major parts of the document.

NASA/TM-2002-210004/Rev3-Vol2

James L. Mueller[1] and Giulietta S. Fargion[2]
Editors

[1] *CHORS, San Diego State University, San Diego, California*
[2]*Science Applications International Corporation, Beltsville, Maryland*

Ocean Optics Protocols For Satellite Ocean Color Sensor Validation, Revision 3, Volume 2

J. L. Mueller, C. Pietras, S. B. Hooker, D. K. Clark, A. Morel, R. Frouin, B.G. Mitchell, R. R. Bidigare, C. Trees, J. Werdell, G. S. Fargion, R. Arnone, R. W. Austin, S. Bailey, W. Broenkow, S. W. Brown, K. Carder, C. Davis, J. Dore, M. Feinholz, S. Flora, Z.P. Lee, B. Holben, B. C. Johnson, M. Kahru, D. M. Karl, Y. S Kim, K. D. Knobelspiesse, C. R. McClain, S. McLean, M. Miller, C. D. Mobley , J. Porter, R.G. Steward, M. Stramska, L. Van Heukelem, K. Voss, J. Wieland, M. A.Yarbrough and M. Yuen.

National Aeronautical and
Space administration

Goddard Space Flight Space Center
Greenbelt, Maryland 20771

February 2002

Chapter 12

Above-Water Radiance and Remote Sensing Reflectance Measurement and Analysis Protocols

James L. Mueller[1], Curtiss Davis[2], Robert Arnone[3], Robert Frouin[4], Kendall Carder[5], Z.P. Lee[5], R.G. Steward[5], Stanford Hooker[6], Curtis D. Mobley[7] and Scott McLean[8]

[1]*Center for Hydro-Optics and Remote Sensing, San Diego State University, California*
[2]*Naval Research Laboratory, Washington, District of Columbia*
[3]*Naval Research Laboratory, Stennis Space Center, Mississippi*
[4]*Scripps Institution of Oceanography, University of California, San Diego, California*
[5]*University of South Florida, St. Petersburg, Florida*
[6]*NASA, Goddard Space Flight Center, Greenbelt, Maryland*
[7]*Sequoia Scientific Inc., Redmond, Washington*
[8]*Satlantic Inc., Halifax, Nova Scotia, Canada*

12.1 INTRODUCTION

As an alternative to the in-water methods of Chapters 10 and 11, water-leaving radiance can be measured from the deck of a ship. A shipboard radiometer is used to measure radiance $L_{\mathrm{sfc}}\left(\lambda,\theta,\phi\in\Omega_{\mathrm{FOV}};\theta_{\mathrm{o}}\right)$ emanating from the sea surface at zenith angle θ (usually chosen between 30° and 50°) and azimuth angle ϕ (usually chosen between 90° and 180° away the sun's azimuth ϕ_{o}). In the convention used here, azimuth angles ϕ are measured relative to the sun's azimuth, *i.e.* $\phi_{\mathrm{o}} = 0$.

The surface radiance measured with a radiometer having a solid-angle field of view (FOV) of Ω_{FOV} sr may be expressed, following Mobley (1999), as

$$L_{\mathrm{sfc}}\left(\lambda,\theta,\phi\in\Omega_{\mathrm{FOV}};\theta_{\mathrm{o}}\right)=L_{\mathrm{W}}\left(\lambda,\theta,\phi\in\Omega_{\mathrm{FOV}};\theta_{\mathrm{o}}\right)+\rho L_{\mathrm{sky}}\left(\lambda,\theta_{\mathrm{sky}},\phi_{\mathrm{sky}}\in\Omega'_{\mathrm{FOV}};\theta_{\mathrm{o}}\right). \quad (12.1)$$

$L_{\mathrm{W}}\left(\lambda,\theta,\phi\in\Omega_{\mathrm{FOV}};\theta_{\mathrm{o}}\right)$ is water-leaving radiance centered at angles (θ, ϕ) and averaged over Ω_{FOV} [as weighted by the radiometer's directional response function (see Chapter 5)]. $L_{\mathrm{sky}}\left(\lambda,\theta_{\mathrm{sky}},\phi_{\mathrm{sky}}\in\Omega'_{\mathrm{FOV}};\theta_{\mathrm{o}}\right)$ is sky radiance measured with the radiometer looking upward at angles (θ_{sky}, ϕ_{sky}). In practice, θ and θ_{sky} are numerically equal angles in the nadir and zenith directions, respectively, and the sea and sky viewing azimuths $\phi = \phi_{\mathrm{sky}}$. The reflectance factor ρ is operationally defined as the total skylight actually reflected from the wave-roughened sea surface into direction (θ,ϕ) divided by sky radiance measured with the radiometer from direction ($\theta_{\mathrm{sky}},\phi_{\mathrm{sky}}$), both quantities being averaged over Ω_{FOV} (Mobley 1999). Remote sensing reflectance is then determined, using water-leaving radiance calculated from (12.1), as

$$R_{\mathrm{RS}}\left(\lambda,\theta,\phi\in\Omega_{\mathrm{FOV}};\theta_{o}\right)=\frac{L_{\mathrm{W}}\left(\lambda,\theta,\phi\in\Omega_{\mathrm{FOV}};\theta_{\mathrm{o}}\right)}{E_{\mathrm{S}}\left(\lambda;\theta_{\mathrm{o}}\right)}, \quad (12.2)$$

where $E_S(\lambda;\theta_o)$ is incident spectral irradiance measured above the sea surface. All of the above variables vary with solar zenith angle θ_o.

A simplified notation is used in Chapters 10 and 11 (and elsewhere in the protocols) when discussing water leaving radiance $L_W(\lambda)$ and remote sensing reflectance $R_{RS}(\lambda)$ derived from in-water profile measurements of $L_u(z,\lambda)$. Because $L_u(z,\lambda)$ is measured viewing the nadir direction, $L_W(\lambda)$ represents radiance leaving the surface in the zenith direction (θ, ϕ) = (0°, 0°). Therefore, $L_W(\lambda)$ in Chapter 11 corresponds to $L\left(\lambda,0,0\in\Omega;\theta\right)$, and $R_{RS}(\lambda)$ to $R\left(\lambda,0,0\in\Omega;\theta\right)$, in the present notation .

NASA/TM-2002-210004/Rev3-Vol2

James L. Mueller[1] and Giulietta S. Fargion[2]
Editors

[1] *CHORS, San Diego State University, San Diego, California*
[2]*Science Applications International Corporation, Beltsville, Maryland*

Ocean Optics Protocols For Satellite Ocean Color Sensor Validation, Revision 3, Volume 2

J. L. Mueller, C. Pietras, S. B. Hooker, D. K. Clark, A. Morel, R. Frouin, B.G. Mitchell, R. R. Bidigare, C. Trees, J. Werdell, G. S. Fargion, R. Arnone, R. W. Austin, S. Bailey, W. Broenkow, S. W. Brown, K. Carder, C. Davis, J. Dore, M. Feinholz, S. Flora, Z.P. Lee, B. Holben, B. C. Johnson, M. Kahru, D. M. Karl, Y. S Kim, K. D. Knobelspiesse, C. R. McClain, S. McLean, M. Miller, C. D. Mobley , J. Porter, R.G. Steward, M. Stramska, L. Van Heukelem, K. Voss, J. Wieland, M. A.Yarbrough and M. Yuen.

National Aeronautical and
Space administration

Goddard Space Flight Space Center
Greenbelt, Maryland 20771

February 2002

Preface

This document stipulates protocols for measuring bio-optical and radiometric data for the Sensor Intercomparison and Merger for Biological and Interdisciplinary Oceanic Studies (SIMBIOS) Project activities and algorithm development. This document supersedes the earlier version (Fargion and Mueller 2000) and is organized into four parts:

- *Introductory Background*: The initial part covers perspectives on ocean color research and validation (Chapter 1), fundamental definitions, terminology, relationships and conventions used throughout the protocol document (Chapter 2), and requirements for specific *in situ* observations (Chapter 3).
- *Instrument Characteristics*: This group of chapters begins with a review of instrument performance characteristics required for *in situ* observations to support validation (Chapter 4), and the subsequent chapters cover detailed instrument specifications and underlying rationale (Chapter 5) and protocols for instrument calibration and characterization standards and methods (Chapters 6 through 8).
- *Field Measurements and Data Analysis*: The methods used in the field to make the *in situ* measurements needed for ocean color validation, together with methods of analyzing the data, are briefly, but comprehensively, reviewed in Chapter 9. The remaining chapters of this part provide detailed measurement and data analysis protocols for in-water radiometric profiles (Chapter 10), the Marine Optical Buoy (MOBY) radiometric observatory for vicarious calibration of satellite ocean color sensors (Chapter 11), above water measurements of remote sensing reflectance (Chapter 12), determinations of exact normalized water-leaving radiance (Chapter 13), atmospheric radiometric measurements to determine aerosol optical thickness and sky radiance distributions (Chapter 14), determination of absorption spectra from water samples (Chapter 15), and determination of phytoplankton pigment concentrations using HPLC (Chapter 16) and fluorometric (Chapter 17) methods.
- *Data Reporting and Archival*: Chapter 18 describes the methods and procedures for data archival, data synthesis and merging, and quality control applicable to the SeaWiFS Bio-optical Archive and Storage System (SeaBASS), which is maintained to support ocean color validation for the SeaWiFS, SIMBIOS and other cooperating satellite sensor projects. Current SeaBASS file content and formatting requirements are given in Appendix B.

What is new in Revision 3 to the ocean optics protocol document, as compared to Revision 2 (Fargion and Mueller 2000). The most obvious changes are the insertion of 3 new chapters into the document, and the renumbering of the other chapters to accommodate them. The new chapters are:

1. Chapter 2, *Fundamental Definitions, Relationships and Conventions*, introduces the radiometric quantities, inherent optical properties, fundamental concepts and terminology underlying the *in situ* measurement and analysis protocols discussed throughout the document. The chapter also discusses the scales adopted in these protocols for such quantities as extraterrestrial solar irradiance, and the absorption and scattering coefficients of pure water.
2. Chapter 11, *MOBY, A Radiometric Buoy for Performance Monitoring and Vicarious Calibration of Satellite Ocean Color Sensors: Measurement and Data Analysis Protocols*, documents the specific measurement and data analysis protocols used in the operation of this critical radiometric observatory. The MOBY normalized water-leaving radiance time series has provided the principal, common basis for vicarious calibration of every satellite ocean color sensor in operation since 1996.
3. Chapter 13, *Normalized Water-Leaving Radiance and Remote Sensing Reflectance: Bidirectional Reflectance and Other Factors*, develops the physical basis underlying the bidirectional aspects of the ocean's reflectance, and presents methods for removing this effect to determine *exact normalized water-leaving radiance*, the only form of water-leaving radiance suitable for comparisons between determinations based on satellite and *in situ* measurements.

Aside from renumbering, several of the chapters carried over from Revision 2 have been revisited and significantly revised, while others have been modified only slightly.

PROCEEDINGS OF SPIE
SPIE—The International Society for Optical Engineering

Remote Sensing for Agriculture, Ecosystems, and Hydrology III

Manfred Owe
Guido D'Urso
Chairs/Editors

17–19 September 2001
Toulouse, France

Sponsored and Published by
SPIE—The International Society for Optical Engineering

Cooperating Organizations
EOS—European Optical Society
CNES—Centre National d'Etudes Spatiales (France)
NASA—National Aeronautic and Space Administration (USA)

Volume 4542

SPIE is an international technical society dedicated to advancing engineering and scientific applications of optical, photonic, imaging, electronic, and optoelectronic technologies.

Recent advances in microwave sensing of soil moisture

Manfred Owe[a], Richard A.M. de Jeu[b]
[a]NASA/Goddard Space Flight Center, Greenbelt, MD 20771;
[b]Faculty of Earth Sciences, Vrije Universiteit Amsterdam, The Netherlands

ABSTRACT

A new approach for retrieving surface soil moisture from satellite microwave brightness temperature is described. The approach uses radiative transfer theory together with a non-linear optimization routine to partition the observed microwave signal into its soil and vegetation components. Vegetation optical depth is derived directly from the microwave polarization difference index, while the soil component is solved in terms of the soil dielectric constant. A global data base of soil physical properties is then used to derive soil moisture from the soil dielectric constant. The approach is tested with historical SMMR data to produce time series of surface soil moisture over several global test sites. Comparisons with ground observations of soil moisture are made. Preliminary results over several global test sites are provided.

Keywords: Remote sensing, microwave brightness temperature, soil moisture, radiative transfer

1. INTRODUCTION

Satellite remote sensing offers potentially the greatest single contribution to large-scale monitoring of the Earth's surface. While ground measurements typically provide the greatest accuracy, they are manpower-intensive, costly, and time consuming. In addition, they are still point measurements, and are usually difficult to aggregate to provide reliable spatial averages. Satellite systems can offer the spatial, temporal, and spectral resolution necessary for consistent and continuous uninterrupted coverage of the whole Earth environment and its surrounding atmosphere. Such detailed observations are necessary in order to detect often-subtle environmental changes. Microwave remote sensing is unique, in that it is the only technology which responds directly to the absolute volume of water which is present in the environment. Radiometric temperature readings in the microwave region have been shown to yield information on soil moisture, precipitable water in clouds, precipitation, and snow. Remote sensing technology is central to the integration of the many interrelated but highly variable point scale phenomena to more useful, regionally-oriented land surface processes. Soil moisture retrieval by microwave is the only remote sensing technique that provides a direct measure of the absolute volume of water in the top soil layer. While the physics of modelling soil emission is relatively straight-forward, accounting for the effects of the overlying vegetation has always presented a more difficult challenge. The signal which emanates from the soil, results from the natural thermal emission in the microwave region, the magnitude of which is determined by the dielectric properties of the combined soil water mixture. However, a vegetation canopy will influence this signal, both by attenuating the soil emission, and by contributing a signal of its own. Emission characteristics of the vegetation are a function of the vegetation dielectric properties. The signal that is subsequently observed by a microwave sensor is highly complex, and must be partitioned into its source components before any soil moisture information can be extracted. Several new approaches for retrieving surface soil moisture from satellite radiometer data have been developed recently [1]. The approach presented here uses radiative transfer theory to solve for surface moisture and the vegetation optical depth. The methodology is somewhat unique, in that it does not require any field observations of soil moisture or canopy biophysical properties for calibration purposes and may be applied at any wavelength. The procedure is being tested with historical 6.6 GHz brightness temperature observations from the Scanning Multichannel Microwave Radiometer (SMMR) [2]. Some microwave theory is presented, along with some preliminary results from several validation studies. Comparisons are made to in-situ observations of soil moisture from several global test sites.

Remote Sensing for Agriculture, Ecosystems, and Hydrology III, Manfred Owe,
Guido D'Urso, Editors, Proceedings of SPIE Vol. 4542 (2002) © 2002 SPIE · 0277-786X/02/$15.00

PROCEEDINGS OF SPIE
SPIE—The International Society for Optical Engineering

Remote Sensing for Agriculture, Ecosystems, and Hydrology III

Manfred Owe
Guido D'Urso
Chairs/Editors

17–19 September 2001
Toulouse, France

Sponsored and Published by
SPIE—The International Society for Optical Engineering

Cooperating Organizations
EOS—European Optical Society
CNES—Centre National d'Etudes Spatiales (France)
NASA—National Aeronautic and Space Administration (USA)

Volume 4542

SPIE is an international technical society dedicated to advancing engineering and scientific applications of optical, photonic, imaging, electronic, and optoelectronic technologies.

Aqua

MONITORING THE EARTH'S WATER CYCLE AND ASSOCIATED VARIABLES FROM THE VANTAGE OF SPACE

Photos of the Aqua spacecraft at TRW in Redondo Beach, California, with all instruments on board. After launch, the solar array will be unfurled, instrument doors will be opened, and antennas will be deployed, with the resulting configuration indicated in the line drawing on p. 2. (Photos courtesy of TRW.)

Aqua Overview

Issues of climate and climate change have considerable relevance to all species of life on Earth. Furthermore, they have received much publicity over the past many years, particularly because of the realization that humans could be having unintended and perhaps detrimental impacts. Nonetheless, the understanding of the Earth / atmosphere system remains inadequate to sort out with certainty human from non-human impacts on long-term climate or to predict with high confidence the likely course of climate changes over the next several decades.

Aqua is a satellite mission aimed at improving our understanding of the Earth / atmosphere system, along with changes occurring within it, through the monitoring and analysis of dozens of Earth variables from a space-based platform orbiting the Earth. Aqua is part of the Earth Observing System (EOS), an international Earth-focused satellite program centered at the United States (U.S.) National Aeronautics and Space Administration (NASA).

"Aqua" being Latin for "water", the Aqua mission is named for the large amount of information it will collect about the Earth's water cycle, including ocean surface water, evaporation from the oceans, water vapor in the atmosphere, clouds, precipitation, soil moisture, sea ice, land ice, and snow cover on the land and ice. Additional variables also being measured by Aqua include radiative energy fluxes, atmospheric aerosols, vegetation cover on the land, phytoplankton and dissolved organic matter in the oceans, and air, land, and water temperatures. One particularly exciting benefit anticipated from Aqua is an improvement in weather forecasting resulting from the Aqua atmospheric temperature and water vapor profiles.

Brochure credits:

Author: Claire L. Parkinson

Designer: Winnie Humberson

Reviewers: Moustafa Chahine
Mike Gunson
Michael D. King
Elena Lobl
Vincent Salomonson
Akira Shibata
Roy Spencer
Bruce A. Wielicki

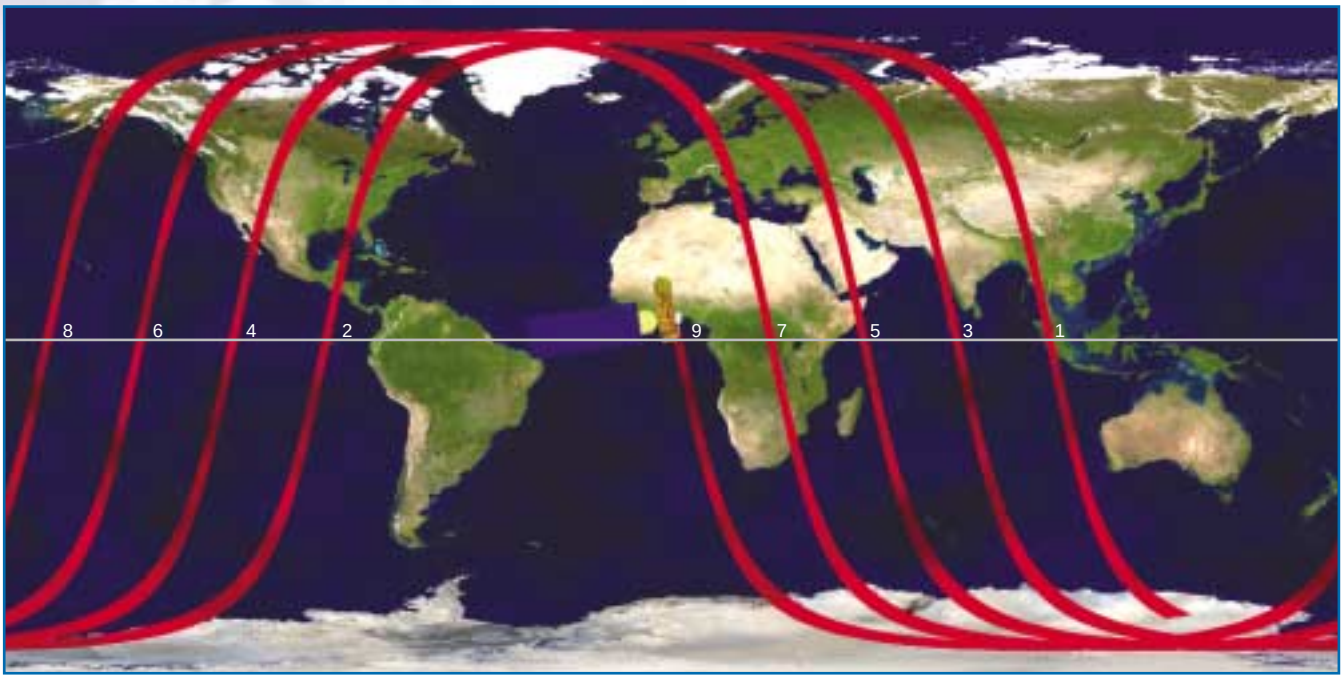

Schematic of the Aqua orbit, with nine consecutive passes over the equator labeled sequentially. Aqua will orbit the Earth at an altitude of 705 km and will approach but not pass directly over the North and South Poles. As the satellite passes northward across the equator, it will do so at 1:30 p.m. local time, then, 49.4 minutes later, as it passes southward across the equator on the opposite side of the Earth, it will do so at 1:30 a.m. local time. (Schematic by Jesse Allen.)

The Aqua spacecraft will carry six major Earth-observing instruments and will be launched from Vandenberg Air Force Base in California, on board a Delta II 7920 - 10L launch vehicle. The launch is scheduled for no earlier than April 18, 2002. Once the spacecraft is launched, it will be maneuvered into a near-polar orbit at an altitude of 705 kilometers, with the satellite orbiting the Earth every 98.8 minutes and crossing the equator on its northward journey at 1:30 p.m. local time and on its southward journey at 1:30 a.m. local time. This will allow collection of afternoon data (as well as 1:30 a.m. data), complementary to the collection of morning data (about 10:30 a.m.) by the EOS Terra satellite launched in December 1999. In order to emphasize the afternoon / morning contrast, the Aqua and Terra missions were originally named EOS-PM and EOS-AM, respectively.

The six Earth-observing instruments on Aqua are:

- Atmospheric Infrared Sounder (AIRS)
- Advanced Microwave Scanning Radiometer for EOS (AMSR-E)
- Advanced Microwave Sounding Unit (AMSU)
- Clouds and the Earth's Radiant Energy System (CERES)
- Humidity Sounder for Brazil (HSB)
- Moderate Resolution Imaging Spectroradiometer (MODIS)

Technically, the spacecraft will be carrying eight Earth-observing instruments, as it has two identical copies of the CERES and the AMSU consists of two physically separate units, the AMSU-A1 and AMSU-A2. Also, Aqua carries several additional instruments, to run the spacecraft, format and store the data, and send the data to the ground. Using standard satellite terminology, however, the Aqua spacecraft is generally said to have six instruments, as listed above. Of these, the AMSR-E is provided by Japan, the HSB is provided by Brazil, and the other four instruments plus the spacecraft, the launch vehicle, and the launch are provided by the United States.

Satellite Imagery for Environment Reporting

Journalists can use these images and data to report and illustrate stories.

By Claire Parkinson

During the past several decades, satellite technology has provided an amazing new ability to observe the earth-atmosphere system. With satellites, the most remote regions of the globe can be viewed as readily as the least remote regions, and data can be collected globally within a few days. Some instruments can obtain surface data even in the presence of a substantial cloud cover, while other instruments can provide the data to produce three-dimensional visualizations of the structure of such atmospheric phenomena as hurricanes and thunderstorms.

Satellites collect data relevant to a wide range of environmental topics, from the ozone hole and low-level pollution in the atmosphere, to deforestation and glacier retreats on the land, to algae blooms and El Niño-signaling temperature patterns in the oceans, to biomass burning and shrinking lakes or eroding coastlines. In each of these cases, and many others, the amount of information that the satellites can provide is enormous. By carefully selecting satellite imagery, these pictures can be used quite effectively by reporters to illustrate many points. For example, journalists who might be reporting on the shrinking of the Aral Sea (caused largely by the diversion of inflowing waters for such purposes as irrigation) can vividly portray this shrinkage by presenting side-by-side, identically geolocated images from different decades.

Types of Satellite Data

Satellite data come in different types, but a common factor is that all satellite instruments measure radiation and only radiation. Some sensors measure various wavelengths of visible radiation, all of which our eyes can see, and other sensors measure ultraviolet, infrared, microwave or other types of radiation, none of which our eyes can

see. In any event, no matter what the topic of ultimate application, what's measured directly is exclusively radiation.

Satellite images constructed from visible data have one inherent gigantic advantage, which is that the images are generally readily understood just by looking at them: Clouds look like clouds, sea ice floes look like sea ice floes, land/sea boundaries are readily identified, etc. Furthermore, the value of some visible imagery has been clear since the first earth-observing satellites were launched decades ago. A prime example of this utility is provided by the visible imagery of hurricanes. Hurricanes form over warm ocean areas, fed by evaporation from the ocean beneath. In view of their oceanic origin, prior to satellites hurricanes were often not observed until just hours before landfall. Now they are readily recognizable in satellite visible images, often days before landfall, thereby enabling what can be lifesaving warnings to the communities along their paths.

Visible radiation is often ideal for observing hurricanes, clouds or, under clear conditions, many phenomena at the earth's surface. Satellite instruments measuring only visible radiation, however, have the same limitations that our eyes have.

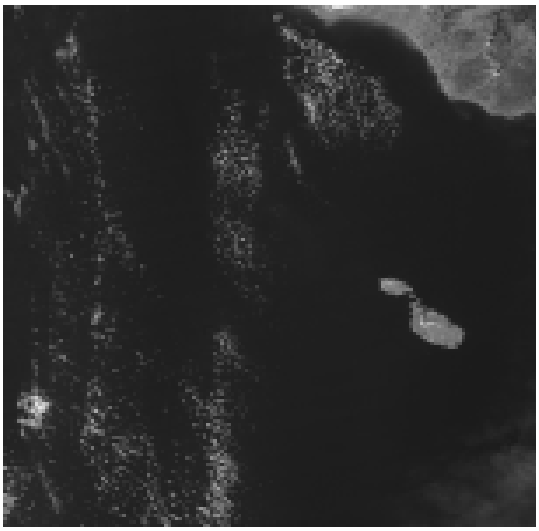

Eruption of Mount Etna, in Sicily, as viewed from NASA's Aqua satellite on October 30, 2002, using data from the Moderate Resolution Imaging Spectroradiometer (MODIS) instrument. ***Original image in color, courtesy of the MODIS Science Team.***

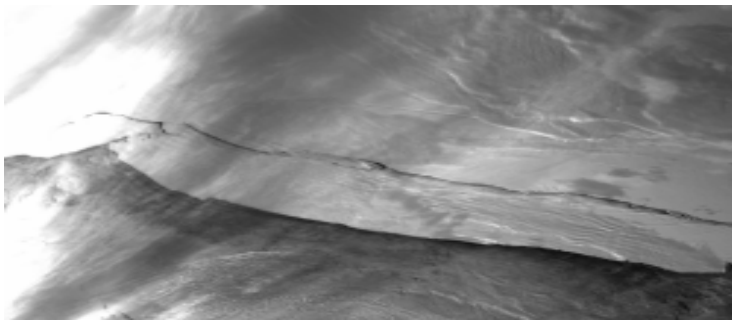

Calving of a major iceberg off the coast of Antarctica, as viewed from NASA's Terra satellite on March 28, 2000, using data from the MODIS instrument. This iceberg is twice the size of Delaware and broke off from Antarctica's Ross Ice Shelf, necessitating remapping of the coastal boundaries. ***Original image in color, courtesy of Jacques Descloitres and the MODIS Science Team.***

NASA Facts

National Aeronautics and
Space Administration

Goddard Space Flight Center
Greenbelt, Maryland 20771
http://www.gsfc.nasa.gov

February 2002

FS-2002-1-028-GSFC

The Earth Observing System Aqua Series

Claire Parkinson

These articles focus on the overarching science priorities of the EOS Aqua mission.
http://aqua.nasa.gov

Weather Forecasting Through the Ages

Introduction

Imagine a rotating sphere that is 12,800 kilometers (8000 miles) in diameter, has a bumpy surface, is surrounded by a 40-kilometer-deep mixture of different gases whose concentrations vary both spatially and over time, and is heated, along with its surrounding gases, by a nuclear reactor 150 million kilometers (93 million miles) away. Imagine also that this sphere is revolving around the nuclear reactor and that some locations are heated more during one part of the revolution and others during another part of the revolution. And imagine that this mixture of gases continually receives inputs from the surface below, generally calmly but sometimes through violent and highly localized injections. Then, imagine that after watching the gaseous mixture, you are expected to predict its state at one location on the sphere one, two, or more days into the future. This is essentially the task encountered day by day by a weather forecaster (Ryan, Bulletin of the American Meteorological Society,1982).

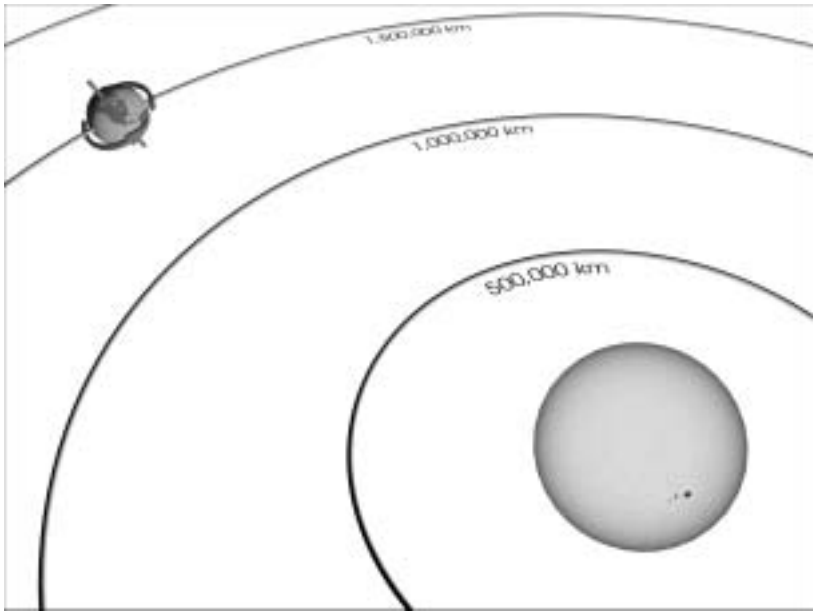

Earth rotates on its axis once every 23 hours, 56 minutes, and completes one revolution around the sun every 365.25 days.

Early History

The art of weather forecasting began with early civilizations using reoccurring astronomical and meteorological events to help them monitor seasonal changes in the weather. Around 650 B.C., the Babylonians tried to predict short-term weather changes based on the appearance of clouds and optical phenomena such as haloes. By 300 B.C., Chinese astronomers had developed a calendar that divided the year into 24 festivals, each festival associated with a different type of weather.

Around 340 B.C., the Greek philosopher Aristotle wrote *Meteorologica*, a philosophical treatise that included theories about the formation of rain, clouds, hail, wind, thunder, lightning, and hurricanes. In addition, topics such

Aristotle, as sculpted by the Greek sculptor Lysippos.

as astronomy, geography and chemistry were also addressed. Aristotle made some remarkably acute observations concerning the weather, along with some significant errors, and his four-volume text was considered by many to be the authority on weather theory for almost 2000 years. Although many of Aristotle's claims were erroneous, it was not until about the 17th century that many of his ideas were overthrown.

Throughout the centuries, attempts have been made to produce forecasts based on weather lore and personal observations. However, by the end of the Renaissance, it had become increasingly evident that the speculations of the natural philosophers were inadequate and that greater knowledge was necessary to further our understanding of the atmosphere. In order to do this, instruments were needed to measure the properties of the atmosphere, such as moisture, temperature, and pressure. The first known design in western civilization for a hygrometer, an instrument to measure the humidity of air, was described by Nicholas Cusa (c.1401-1464, German) in the mid-fifteenth century. Galileo Galilei (1564-1642, Italian) invented an early thermometer in 1592 or shortly thereafter; and Evangelista Torricelli (1608-1647, Italian) invented the barometer for measuring atmospheric pressure in 1643.

While these meteorological instruments were being refined during the seventeenth through nineteenth centuries, other related observational, theoretical, and technological developments also contributed to our knowledge of the atmosphere; and individuals at scattered locations began to make and record atmospheric measurements. The invention of the telegraph and the emergence of telegraph networks in the mid-nineteenth century allowed the routine transmission of weather observations to and from observers and compilers. Using these data, crude weather maps were drawn and surface wind patterns and storm systems could be identified and studied. Weather-observing stations began appearing all across the globe, eventually spawning the birth of synoptic weather forecasting, based on the compilation and analysis of many observations taken simultaneously over a wide area, in the 1860s.

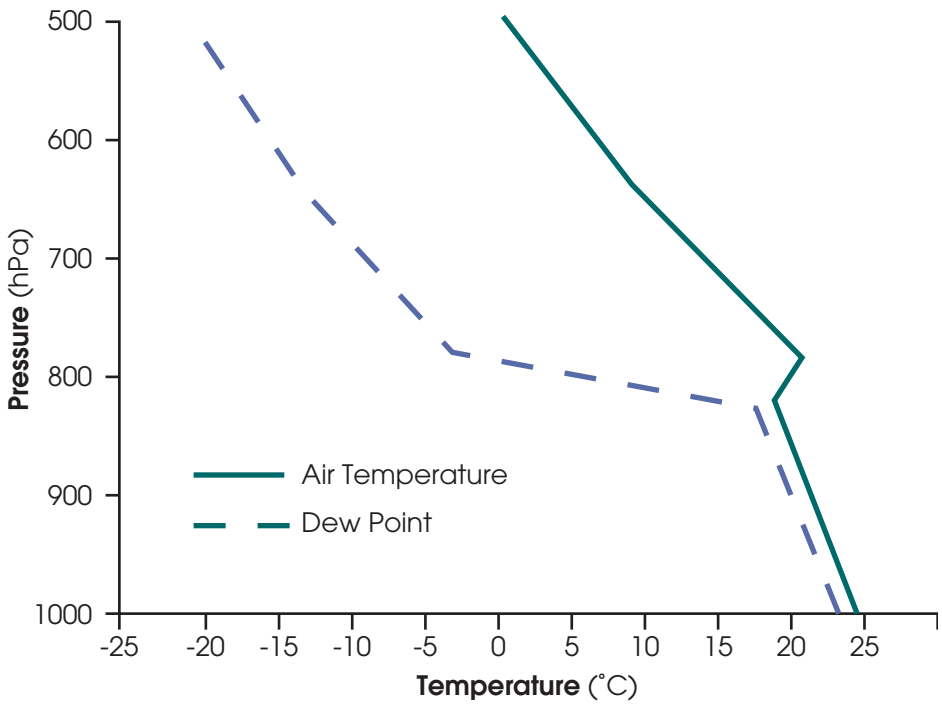

A schematic sounding of air temperature and dewpoint derived from radiosonde data. This sample schematic sounding includes a temperature "inversion" (temperatures increasing with height) at about 800 hPa and reflects atmospheric conditions that frequently precede the development of severe thunderstorms and possibly tornadoes. [1 hectoPascal (hPa) = 1 millibar (mb).]

Closing

Only fifty years ago, weather forecasting was an art, derived from the inspired interpretation of data from a loose array of land-based observing stations, balloons, and aircraft. Since then it has evolved substantially, based on an array of satellite and other observations and sophisticated computer models simulating the atmosphere and sometimes additional elements of the Earth's climate system. All this has been made possible by advances in satellite technology, a sweeping acceleration in worldwide communications, and overwhelming increases in computing power. Aqua's AIRS/AMSU/HSB combination should further these advances, enabling more accurate predictions over longer periods.

Report to NASA on a Workshop on Sea Ice Data Assimilation

Held at the

Naval Academy, Annapolis, MD

On

July 23-24, 2002

Report Edited by
Kim Partington, Ronald Lindsay, Jinro Ukita

September 2002

1 Executive Summary

NASA's Earth Science Enterprise (ESE) aims to understand the Earth system including the effects of humans on the environment. The value of data assimilation (DA) to operational weather forecasting is well recognized, but it has only been comparatively recently that its application to climate research has been initiated. Within this context, a number of DA projects with specific application to sea ice are now under way. This workshop on sea ice DA was organized to assess overall progress made by these projects and to help to address recommendations in a joint effort to enhance the productivity of this area of research.

The workshop objectives, key strategic areas, priority recommendations, and metrics are summarized below. This is followed by background section. The main body of this report consists of three sections: issues and strategies, recommendations and metrics. Information on the agenda of the meeting, the list of attendees and the summary of presentations may be found in the appendices.

The following objectives were set out for this meeting:

- To provide recommendations to NASA on how to improve the collective productivity of data assimilation projects both current and future, including:
  - Collaborations and links between projects and expert groups
  - Generic and specific improvements to NASA datasets
- To generate informal links between related projects that can help to address the complexities of data assimilation. This community is one in which mutual support may be particularly useful given that that the projects are pilot projects.
- To agree on the key technical issues that need to be addressed to make progress with data assimilation. In particular, to agree on a consensus approach, if appropriate (building on, or modifying the approach recommended by NSIDC at their workshop as reported in Weaver et al., 2000).
- To consider how progress may be assessed with data assimilation: milestones, evaluation criteria, and priorities.

In order to build sound strategies the workshop identified five essential areas in the DA procedures as:

- Formulating science questions to be answered,
- Preparation for assimilation
  - Selecting and constructing a model and DA methods and determining their error charateristics,
  - Selecting forcing and assimilation data and determining their errors,
- Performing model simulations with DA, and
- Evaluating the model results with respect to the questions posed.

NASA Technical Memorandum 2002–206892, Volume 16

SeaWiFS Postlaunch Technical Report Series

Stanford B. Hooker, Editor
NASA Goddard Space Flight Center
Greenbelt, Maryland

Elaine R. Firestone, Senior Scientific Technical Editor
Science Applications International Corporation
Beltsville, Maryland

Volume 16, Navigation Algorithms for the SeaWiFS Mission

Frederick S. Patt
Science Applications International Corporation
Beltsville, Maryland

Abstract

The navigation algorithms for the Sea-viewing Wide Field-of-view Sensor (SeaWiFS were designed to meet the requirement of 1-pixel accuracy—a standard deviation (σ) of 2. The objective has been to extract the best possible accuracy from the spacecraft telemetry and avoid the need for costly manual renavigation or geometric rectification. The requirement is addressed by postprocessing of both the Global Positioning System (GPS) receiver and Attitude Control System (ACS) data in the spacecraft telemetry stream. The navigation algorithms described are separated into four areas: orbit processing, attitude sensor processing, attitude determination, and final navigation processing. There has been substantial modification during the mission of the attitude determination and attitude sensor processing algorithms. For the former, the basic approach was completely changed during the first year of the mission, from a single-frame deterministic method to a Kalman smoother. This was done for several reasons: a) to improve the overall accuracy of the attitude determination, particularly near the sub-solar point; b) to reduce discontinuities; c) to support the single-ACS-string spacecraft operation that was started after the first mission year, which causes gaps in attitude sensor coverage; and d) to handle data quality problems (which became evident after launch) in the direct-broadcast data. The changes to the attitude sensor processing algorithms primarily involved the development of a model for the Earth horizon height, also needed for single-string operation; the incorporation of improved sensor calibration data; and improved data quality checking and smoothing to handle the data quality issues. The attitude sensor alignments have also been revised multiple times, generally in conjunction with the other changes. The orbit and final navigation processing algorithms have remained largely unchanged during the mission, aside from refinements to data quality checking. Although further improvements are certainly possible, future evolution of the algorithms is expected to be limited to refinements of the methods presented here, and no substantial changes are anticipated.

1. INTRODUCTION

The navigation processing for the Sea-viewing Wide Field-of-view Sensor (SeaWiFS) data is performed as part of the level-0 to -1a conversion. The level-0 to -1a software extracts and converts the required telemetry from the data stream and passes it to the navigation code, which produces per-scan-line spacecraft position and instrument pointing information. The output of navigation is stored in the level-1a data products for use by downstream processing.

The navigation code is composed of two, largely independent subsystems: orbit processing, which filters the data from the onboard global positioning system (GPS) receiver to produce orbit vectors; and attitude processing, which filters the spacecraft attitude control system (ACS) telemetry and instrument tilt telemetry to determine the SeaWiFS sensor orientation.

The remainder of this section defines constants, reference frames, and transformations which are used in the algorithm descriptions.

1.1 Constants

The following constants are defined here for later use:

- R_E, Earth equatorial radius (6,378.137 km);
- R_M, Earth mean radius (6,371 km);
- f, dimensionless Earth flattening factor (1/298.257);
- ω_E, Earth rotation rate ($7.29211585494\times10^{-5}\,\mathrm{s}^{-1}$);
- ω_O, nominal Orbit angular rate ($2\pi/5940$);
- G_m, Earth gravitational constant ($398600.5\,\mathrm{km}^3\,\mathrm{s}^{-2}$); and
- J_2, dimensionless Earth gravity field perturbation term (1.08263×10^{-3}).

1.2 Reference Frames

In order to describe the navigation algorithms, several basic reference frames (all frames have orthonormal axes) are defined below.

a. *Earth-Centered Inertial (ECI):* This reference frame has its origin at the Earth's center and is inertially fixed. The axes are defined as: x on the equator at the vernal equinox; z at the North Pole; y orthogonal to z and x in the right-hand sense.

b. *Earth-Centered Earth-Fixed (ECEF):* This reference frame also has its origin at the Earth's center and rotates with the Earth. The axes are defined as: x at 0° latitude and longitude (Greenwich meridian at the equator); y at 0° latitude and 90° longitude; and z at the North Pole (also known as Earth-Centered Rotating, or ECR).

c. *Orbital:* This frame has its origin at the spacecraft position and is defined as: x-axis along the geodetic nadir vector; y-axis perpendicular to x and opposite the spacecraft velocity vector; and z-axis toward the orbit normal.

16th Conference on Hydrology

13–17 January 2002
Orlando, Florida

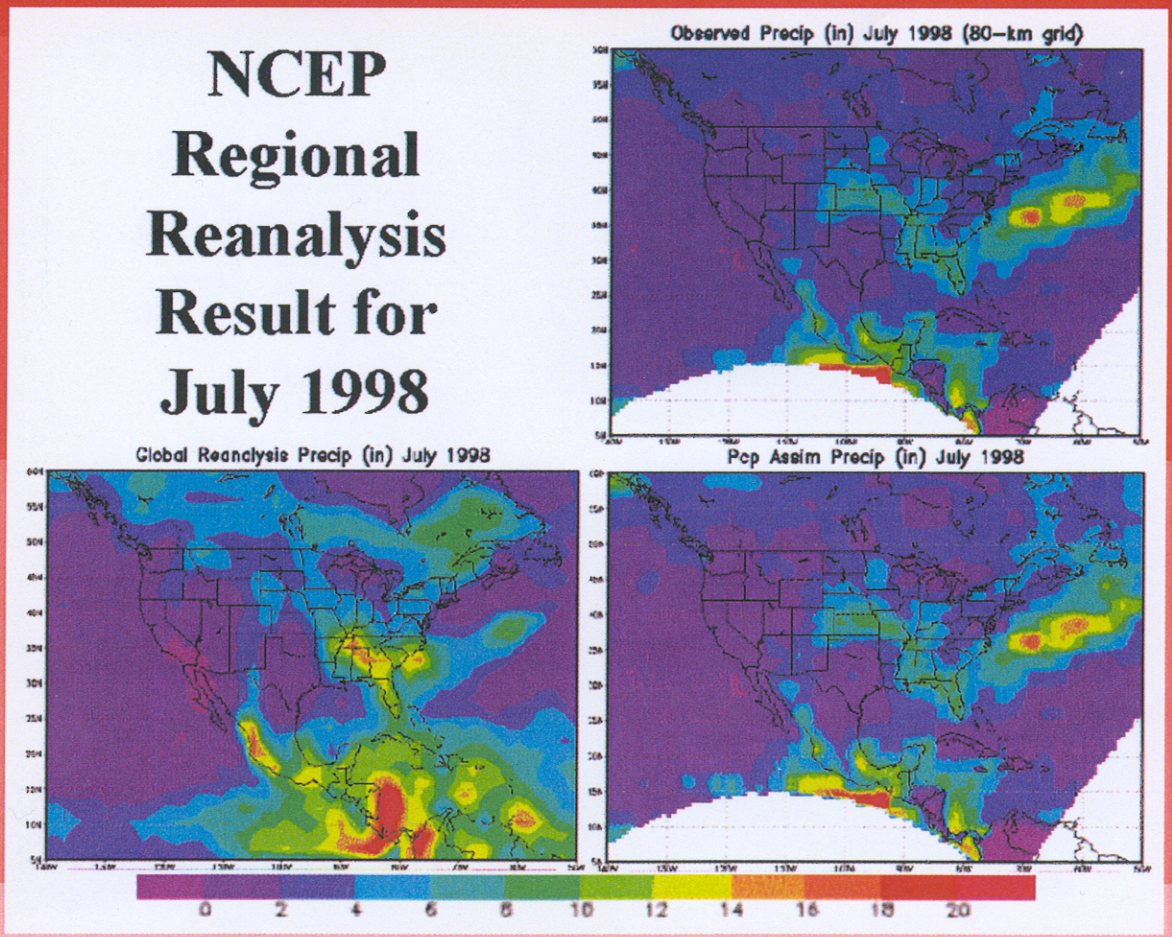

AMERICAN METEOROLOGICAL SOCIETY

J4.4 THE EFFECTS OF IMPLEMENTING TOPMODEL CONCEPTS IN THE NOAH MODEL

C. D. Peters-Lidard*[1]
Hydrological Sciences Branch, Code 974
NASA/Goddard Space Flight Center
Greenbelt, MD 20771

1. INTRODUCTION

Topographic effects on runoff generation have been documented observationally (e.g., Dunne and Black, 1970) and are the subject of the physically based rainfall-runoff model TOPMODEL (Beven and Kirkby, 1979; Beven, 1986a;b) and its extensions, which incorporate variable soil transmissivity effects (Sivapalan et al, 1987, Wood et al., 1988; 1990). These effects have been shown to exert significant control over the spatial distribution of runoff, soil moisture and evapotranspiration, and by extension, the latent and sensible heat fluxes (Famiglietti et al., 1992; Famiglietti and Wood, 1994a; b; Peters-Lidard et al, 1999).

The objective of this research is to investigate and demonstrate the impact of topographic control of runoff production and lateral soil water redistribution on the water and energy balance as simulated by the NCEP NOAH land surface model (Mahrt and Ek, 1984; Mahrt and Pan, 1984; Pan and Mahrt, 1987; Chen et al., 1996; Schaake et al, 1996; Chen et al., 1997; Mitchell, 1999). Currently, the NOAH model solves the Richards equation for 1-D vertical soil water transport in each land surface model grid, which corresponds to the atmospheric model horizontal grid. There is no provision for lateral soil water redistribution or for explicit subgrid soil moisture heterogeneity. Several modifications to NOAH have been incorporated which parameterize the effects of subgrid variability in topography and/or soil moisture, including:

- infiltration/runoff generation parameter "REFKDT" (Schaake et al., 1996). REFKDT is a tuneable parameter that significantly impacts surface infiltration and hence the partitioning of total runoff into surface and subsurface runoff. Increasing REFKDT decreases surface runoff.
- non-linear soil moisture stress function for stomatal resistance (Chen et al., 1996). The non-linearity in this function represents the ability of wetter portions of the grid to transpire even when the grid-averaged soil moisture is near the wilting point, as well as the dryer portions of the grid which may be stressed when the grid-averaged soil moisture is near field capacity.
- drainage parameter "SLOPE" (Schaake et al., 1996). SLOPE is a coefficient between 0.1-1.0 that modifies the drainage out the bottom of the bottom soil layer. A larger surface slope implies larger drainage.

TOPMODEL provides a physically-based approach to represent subgrid topography and soil effects on the runoff production, the soil moisture distribution and drainage, via a drainage index which can be estimated directly from digital topographic and soils data. In the current project, the three parameterizations above are being replaced with a subgrid distribution of the TOPMODEL drainage index to explicitly represent the subgrid distribution of water table depth and soil moisture. The effect of this subgrid distribution on lateral soil water redistribution, runoff generation and surface fluxes will be modeled statistically in the manner of Famiglietti and Wood (1994a) and Peters-Lidard et al. (1997). We are demonstrating the NOAH model in both its original and new forms in the Arkansas-Red River basin using all other input parameters as specified in the LDAS project. By incorporating topographic effects into the existing NOAH model while all other processes remain the same, the effects of this representation on runoff, soil moisture and energy fluxes can be isolated. All simulations are being run off-line and in a retrospective mode for this test period.

4. CONCLUSIONS

The work to date suggests the following three conclusions:

TO 1. The baseflow predicted by the PMODEL equation seems to behave more smoothly and realistically than the original formulation, which has a peak in the summertime.

2. The baseflow predictions, as with other aspects of TOPMODEL, are highly sensitive to parameters related to the Topographic index distribution and the decay of saturated hydraulic conductivity with depth.

3. In order to be useful as an LDAS model, the TOPMODEL parameters must be available for the CONUS and beyond, and therefore, an understanding of the effects of DEM resolution on the parameter estimation is essential.

More results and detailed discussion will be presented at the conference.

Proceedings of the Twelfth

PSU/NCAR Mesocale Model Users' Workshop

June 24-25, 2002
Boulder, CO

Design and evaluation of the coupled MM5/TOPLATS modeling system for a Texas air quality exceedance episode

C. D. Peters-Lidard[*1], J. N. McHenry[2] C. J. Coats[2]

[1*] NASA's Goddard Space Flight Center
Hydrological Sciences Branch, Code 974
Greenbelt, MD

[2]Environmental Modeling Center
MCNC-North Carolina Supercomputing Center
Research Triangle Park, NC

1. INTRODUCTION

Phase II of the Advanced Texas Air Quality Model (ATAQM) has been implemented for the Texas Natural Resources Conservation Commission (TNRCC) to support simulations of the August 25-31, 1998 ozone-exceedance episode in the 8-county Houston-Galveston Non-Attainment Area. ATAQM is a new, state-of-science modeling system that should significantly improve upon recognized deficiencies in current meteorological modeling systems used to drive air quality models in support of State Implementation Planning. ATAQM Phase II consists of the Fifth-Generation PSU/NCAR Mesoscale Model Version 3 (MM5v3); the TOPMODEL-based Land Atmosphere Transfer Scheme (TOPLATS; Famiglietti and Wood, 1994; Peters-Lidard et al, 1997) land surface hydrology model; and a Sea-Surface Atmosphere Transfer Scheme (SSATS). The TOPLATS model is driven with both in situ and remotely sensed estimates of key meteorological variables, including solar radiation and precipitation, and the SSATS model is driven with observed Sea Surface Temperature (SST) data from a combination of in situ (NOAA PORTS) and remotely sensed (CoastWatch AVHRR products) sources.This modeling system is fully documented at http://www.emc.mcnc.org/projects/TNRCC-projects/tnrcc_public.html. Below, we discuss the model configuration and results for the episode.

2. APPROACH

2.1. *TOPLATS Configuration*

The TOPLATS Study Domain (TSD) for this project was set by mosaicking 8-Digit Hydrologic Unit Code watersheds provided by the National Hydrography Dataset (NHD) (USGS, 2001). This domain was chosen to include all watersheds that contain areas of Harris County (Houston), Texas as well as all counties that border Harris. Using this one-county buffer region as a guideline, the domain to model for TOPLATS was set as a large portion of the Eastern Coastal Plains of Texas with an area of approximately 96,000 square kilometers. The region covers an expanse from Matagorda Bay in the most southern point (28.07 N) to near Waco, Texas in the north (31.81 N), and from Lake Charles, Louisiana in the east (93.01 W) to the suburbs of Austin, Texas at the westernmost location (97.37 W)(Figure 1).

The region chosen for this project is much larger than those typically used in previous TOPLATS studies, and is only possible due to the parallel techniques and high performance I/O that have been implemented as part of this research (Coats et al., 1999; Peters-Lidard et al., 1999). The TOPMODEL concept assumes that base flow is the same throughout the watershed of interest, and when the watershed is much larger than 500 square kilometers in area, this assumption may be invalid. Therefore for a large region such as the HGA study requires, the domain is subdivided into smaller watersheds suitable for TOPLATS. In total the region has been divided into 173 watersheds (Figure 2), each of which has watershed-specific parameters required for TOPLATS.

Parameters for TOPLATS were estimated using readily available Digital Elevation Model (DEM), landcover and soils databases. TOPLATS was then "spun-up" for the period January 1-August 24, prior to coupling, using observed forcing data, including NEXRAD WSR88D precipitation, observed solar radiation, and observed surface-station meteorology including wind-speed, temperature, relative humidity, etc. More details about the TOPLATS databases and spin-up are available online at:
http://www.emc.mcnc.org/projects/TNRCC-projects/ATAQM/ataqmII_report1.pdf

Figure 1. Houston-Galveston study region.

Second Annual Earth Science Technology Conference (ESTC-2)

Pasadena, CA
June 11-13, 2002

Synthetic Thinned Aperture Radiometry (STAR) Technologies Enabling 10-km Soil Moisture Remote Sensing from Space

J.R. Piepmeier[1], F.A. Pellerano[1], P. O'Neill[2], D. LeVine[3], E. Kim[3], T. Doiron[1]
NASA's Goddard Space Flight Center
[1]Microwave Instrument Technology Branch/555
[2]Hydrological Sciences Branch/974
[3]Microwave Sensors Branch/975
Greenbelt, MD 20771

Abstract - **Remote sensing of soil moisture at 1.4 GHz at 10-km spatial resolution from space requires the use of very large radiometer apertures (>20 m). Synthetic thinned aperture radiometry (STAR) is a viable solution to the large aperture problem, and several technologies are being developed to enable a spaceflight STAR instrument. The primary motivation for the development is a reduction in power and size, which is achieved by using low power microelectronics, including silicon germanium (SiGe) and ultra low power (ULP) CMOS. STAR system architecture, SiGe microwave radiometer receivers, ULP digital correlators, and calibration are discussed.**

I. INTRODUCTION

NASA's Earth Science Enterprise and the hydrology community are focused on achieving a 10-km spatial resolution global soil moisture mission towards the end of the decade. This type of resolution represents a significant technological challenge. Observation of soil moisture is based on relatively low frequency thermal microwave emission at L-band (1.4 GHz). The long wavelengths at this frequency coupled with the high spatial and radiometric resolutions required necessitates the use of very large apertures (>20 m) [1, 2].

An engineering trade study was completed by NASA Goddard Space Flight Center (GSFC) to determine alternative system configurations that could achieve the science requirements and to identify the most appropriate technology investments and development path for NASA to pursue in order to bring about such a mission [1]. The conclusion of this study was that Synthetic Thinned Aperture Radiometry (STAR) is the most promising technology to enable these very large non-rotating apertures in space. In this technique, the coherent product (correlation) of the signal from pairs of antennas is measured at different antenna-pair spacings (baselines). These products yield sample points in the Fourier transform of the brightness temperature map of the scene, and the scene itself is reconstructed by inverting the sampled transform [3]. The reconstructed image includes all of the pixels in the entire field-of-view of the antennas.

The main advantage of the STAR architecture is that it requires no mechanical scanning of the antenna. Using a static antenna simplifies the spacecraft dynamics and improves the time-bandwidth product of the radiometer. Furthermore, aperture thinning reduces the overall volume and mass of the instrument. A disadvantage is the reduction of radiometric sensitivity (or increase in rms noise) of the image due to a decrease in signal-to-noise for each measurement compared to a filled aperture. Pixel averaging is required for good radiometric sensitivity.

In essence, we are trading a nearly intractable mechanical problem for a tractable electrical one. Because a large STAR radiometer uses many receivers and correlators, the primary objective of our technology development has been to drive down electrical power dissipation, volume and mass. We accomplish this goal through the innovative use of low power microelectronics, including silicon germanium (SiGe) and ultra low power CMOS (ULP CMOS), for microwave receivers, analog-to-digital converters, and digital correlators. In addition, we are studying system architecture issues such as correlated calibration sources and signal distribution.

II. SYSTEM TECHNOLOGY

Technology development for the 10-km soil moisture remote sensing problem began with two investigations. First, a concept was developed for a space-based instrument through a science-driven architecture study [1]. From this study, engineering constraints were derived that motivated several component technology developments. Second, an aircraft instrument was developed to validate the two-dimensional STAR technique for soil moisture remote sensing [4]. The instrument is a research tool that will be used to address remote sensing and instrument systems engineering issues associated with development of a spaceflight STAR instrument.

IV. FUTURE TECHNOLOGY AND SUMMARY

Several technologies motivated by science-driven system studies for 10-km soil moisture remote sensing from space have been presented. The primary developmental drivers are low power and size requirements, which are met using state-of-the-art microelectronics and sensible system design. The next steps needed to advance towards a flight instrument have been proposed and include an integrated panel of SiGe receivers and antennas, the study of a fully integrated SiGe RF-digital receiver-on-a-chip, and the appropriate demonstration of a deployable STAR arm either on the ground or in space. These developments are on-track for a soil moisture mission launch in ~2008.

2002 IEEE International Geoscience and Remote Sensing Symposium and the 24th Canadian Symposium on Remote Sensing

IGARSS 2002

REMOTE SENSING:
Integrating Our View of the Planet

IEEE

June 24-28, 2002
Toronto Canada

The Airborne Conical Scanning Millimeter-wave Imaging Radiometer (CoSMIR)

J.R. Piepmeier, P. Racette, W. Manning[1], J.R. Wang
NASA's Goddard Space Flight Center
Greenbelt, MD 20771
[1]Joint Center for Earth Systems Technology
Baltimore, MD 21250

Abstract - **Results of the first science flight of the airborne Conical Scanning Millimeter-wave Imaging Radiometer (CoSMIR) for high-altitude observations from the NASA ER-2 is discussed. Imagery collected from the flight demonstrates CoSMIR's unique conical/cross-track imaging mode and provides comparison of CoSMIR measurements to those of the SSM/T-2 satellite radiometer.**

INTRODUCTION

The airborne Conical Scanning Millimeter-wave Imaging Radiometer (CoSMIR) will provide measurements useful for atmospheric studies and satellite calibration and validation. Designed to match the tropospheric sounding channels of the Defense Meteorological Satellite Program (DMSP) Special Sensor Microwave Imager/Sounder (SSMIS), the CoSMIR consists of four radiometers operating at 50-54 (3 channels - 50.3, 52.8, and 53.6), 91.655 (dual polarization), 150.0, and 183.31 (3 channels - ±1, ±3, and ±6.6) GHz. For a detailed description of the instrument see [1]. In February, 2002, CoSMIR successfully completed an engineering check flight and its first science flight on the NASA ER-2 high-altitude research aircraft. Imagery was collected using CoSMIR's unique combined conical and cross-track scan mode. Results from this flight are discussed below.

COSMIR IMAGERY

Demonstration of CoSMIR's unique combined conical/cross-track imaging mode can be seen in Fig. 1 for the 50.3 GHz channel. The top two maps contain the forward-conical and aft-conical images over and near the San Francisco Bay area of California; the Bay itself is located slightly above and left of the center of the map. The Pacific coast is seen in the top left portion of the map and the wetland areas contained within and near the San Luis National Wildlife Refuge are located in the lower right section of the maps. The increase in atmospheric path length is noticeable between the conical and cross-track images at 50.3 GHz, which is located near the molecular oxygen 60 GHz absorption complex. An increase in path length leads to an increase in molecular oxygen within the path. This increase produces the higher brightness temperature values seen in the conical-scan images, with incidence angles of 53.6°, compared to the cross-track image with incidence angles less than those of the conically scanned images.

A comparison between the three double-sideband CoSMIR and Special Sensor Microwave/Temperature-2 (SSM/T-2) channel frequencies centered on the 183.31 GHz water vapor band is shown in Fig. 2. The map area is located over the Pacific Ocean southwest of San Francsico. The aircraft flight line followed the sub-satellite track so the CoSMIR cross-track brightness temperatures near nadir (at the center of the swath) are comparable to the underlying cross-track SSM/T-2 brightness temperatures. Comparisons of the 183.31 ± 1.0 GHz channels and the 183.31 ± 3.0 GHz channels are shown in the top-left and middle-left images, respectively. Excellent agreement can be seen in the imagery. The bottom-left image is a comparison of the CoSMIR 183.31 ± 6.6 GHz channel and the SSM/T-2 183.31 ± 7.0 GHz channel. Precipitable water amounts increase along the descending flight line in the southwest direction. Observed brightness temperature differences at $183\pm6.6/7.0$ GHz between the CoSMIR and the SSM/T-2 can be attributed to differences in the passband characteristics of the two instruments. The CoSMIR forward and aft viewing conical scans are shown in the middle and right column, respectively. The channel frequencies and color bars are applicable for the three images contained in each row. The small (+) symbols signify the center beam locations for the SSM/T-2 brightness temperature data.

This development was supported by the Defense Meteorological Satellite Program and the NASA Goddard Space Flight Center.

NASA/TM-2002-21004/Rev3-Vol1

James L. Mueller[1] and Giulietta S. Fargion[2]
Editors

[1] *CHORS, San Diego State University, San Diego, California*
[2]*Science Applications International Corporation, Beltsville, Maryland*

Ocean Optics Protocols For Satellite Ocean Color Sensor Validation, Revision 3, Volume 1

J. L. Mueller, C. Pietras, S. B. Hooker, D. K. Clark, A. Morel, R. Frouin, B.G. Mitchell, R. R. Bidigare, C. Trees, J. Werdell, G. S. Fargion, R. Arnone, R. W. Austin, S. Bailey, W. Broenkow, S. W. Brown, K. Carder, C. Davis, J. Dore, M. Feinholz, S. Flora, Z.P. Lee, B. Holben, B. C. Johnson, M. Kahru, D. M. Karl, Y. S Kim, K. D. Knobelspiesse, C. R. McClain, S. McLean, M. Miller, C. D. Mobley , J. Porter, R.G. Steward, M. Stramska, L. Van Heukelem, K. Voss, J. Wieland, M. A.Yarbrough and M. Yuen.

National Aeronautical and
Space administration

Goddard Space Flight Space Center
Greenbelt, Maryland 20771

February 2002

Chapter 7

Calibration of Sun Photometers and Sky Radiance Sensors

Christophe Pietras[1], Mark Miller[2], Kirk D. Knobelspiesse[3], Robert Frouin[4], Brent Holben[5] and Ken Voss[6]

[1]*Science Applications International Corporation, Beltsville, Maryland*
[2]*Department of Applied Science, Brookhaven National Laboratory, Upton, New York*
[3]*Science Systems and Applications, Inc., Greenbelt, Maryland*
[4]*Scripps Institution of Oceanography, University of California, San Diego, California*
[5]*Biospheric Sciences Branch, NASA Goddard Space Flight Center, Greenbelt, Maryland*
[6]*Physics Department, University of Miami, Florida*

7.1 INTRODUCTION

Atmospheric sensors are designed to measure direct solar signals and sky radiances in order to retrieve the radiative properties of the atmosphere. There are two major types of instruments in use to perform these measurements: sun photometers and sky radiance scanning systems including fast rotating shadow-band radiometers.

Sun photometers capture photometric intensity of the direct solar beam. Their fields of view are small, typically between 1° and 3°, in order to minimize contamination of the transmitted solar signal by scattered skylight. Some photometers are manually aimed at the sun using sun-sighting optics, while other types of photometers are fixed in place and are equipped with automatic sun-tracking mechanisms.

MicroTops II (Morys *et al.* 1998; Porter et al 1999) and SIMBAD (Deschamps *et al.* 2000; Fougnie *et al.* 1999a, 1999b) are two examples of hand-held sun photometers. The fields of view (FOV) of hand-held sun photometers are typically between 2° and 3°, which is generally larger than the FOVs of the automatic sun-tracking photometers (Table 7.1). The wider FOV allows the user to manually aim the instrument at the sun from the rolling deck of a ship. The even wider field of view of SIMBAD (Table 7.1) is intended to measure marine reflectance as well as the solar signal. An improved version, called SIMBADA, has been recently developed and is available since 2001. SIMBADA new features are an integrated GPS and 11 channels.

Examples of fixed, automated tracking sun photometers include the CIMEL (Holben *et al.*, 1998) and the PREDE (Nakajima *et al.*, 1996). The design of a particular sun tracking mechanism is dependent on whether it is to be used on a moving platform (e.g., PREDE POM-01 Mark II), or on a stable station (e.g., CIMEL, PREDE POM-01L). CIMEL and PREDE instruments perform both sun photometric and sky radiance measurements. In sky radiance mode, these instruments measure sky radiances within 3° of the sun in the aureole, and also scan the sky radiance distribution in the principal solar plane. The FOV of the CIMEL and PREDE instruments are less than 1.5° and the instruments are equipped with collimators for stray light rejection (O'Neill *et al.*, 1984; Holben *et al.* 1998; Nakajima *et al.* 1996).

Fast rotating shadow-band radiometers measure solar intensity values indirectly from diffuse and global upper hemispheric irradiance. They have a 2π FOV and are equipped with a solar occulting apparatus. Finally, electronic camera systems equipped with "fisheye" lenses may be used to measure the full sky radiance distribution (Voss *et al.* 1989).

Sun photometers and sky radiometers commonly have several channels from 300 nm to 1020 nm and narrow bandwidths (approximately 10 nm). Their characteristics are summarized in Table 7.1. This chapter will describe calibration techniques, and uncertainties of the sun photometers and sky radiometers. Measurement and data analysis protocols and procedures are discussed in Chapter 14.

2002 IEEE International Geoscience and Remote Sensing Symposium and the 24th Canadian Symposium on Remote Sensing

IGARSS 2002

REMOTE SENSING:
Integrating Our View of the Planet

IEEE

June 24-28, 2002
Toronto Canada

STUDY OF THE VARIABILITY IN THE RAIN DROP SIZE DISTRIBUTION OVER A 2.3 KM PATH

Rafael F. Rincon*[1], Roger Lang[1], Robert Meneghini[2], Steven Bidwell[2], and Ali Tokay[3]

[1]The George Washington University, Washington, DC
[2]NASA/GSFC, Greenbelt, MD
[3] JCET, UMBC, Baltimore, MD

Abstract- In an effort to study the drop size distribution (DSD) a state-of-the-art instrument arrangement was deployed on Wallops Island, VA. The instrumentation consisted of a 2.3-km multi-frequency microwave link, three impact disdrometers, and a network of optical and tipping bucket raingauges. A dual-frequency inversion technique was implemented with the link measurements of attenuations at 25 GHz and 38 GHz to estimate the path-average DSD. Concurrently, an X-band, dual-polarization radar, located in the vicinity, collected polarization and reflectivity measurements over the link path. The evaluation of the estimates and measurements generated some preliminary results.

I. INTRODUCTION

An accurate estimation of the drop size distribution (DSD) is essential in the retrieval of rainfall parameters from microwave measurements and in the modeling of microwave propagation through rain. The DSD is characterized by a high temporal and spatial variability that affects both microwave measurements and ground validation. To study the temporal and spatial variation of drop size distributions a state-of-the-art instrument arrangement was deployed on Wallops Island, VA. The instrumentation consisted of a 2.3-km multi-frequency microwave link, three impact (Joss-Waldvogel) disdrometers, and a network of optical and tipping bucket raingauges. Concurrently, NOAA's ground base X-band radar, located in the vicinity of the link during the March 2001 rain event, collected polarization and reflectivity measurements. The radar operates at 9.34 GHz at horizontal and vertical polarizations.

In this work inversion techniques implemented with the link measurements provided DSD estimates over the path for a highly convective event on March 21, 2001. The estimates were evaluated in conjunction with the measurements from the three disdrometers located directly under the microwave path. The results were evaluated with the radar measurements aloft. Additionally, the estimated DSD and the disdrometer measurements were used to compute path-average rain rates and rainfall accumulation. These results were compared to path-average measurements from the network of optical and tipping bucket rain gauges.

III. CONCLUSION

The link attenuation measurements at 25 and 38 GHz and the implementation of dual-frequency inversion technique yielded a path average DSDs based on an analytical Gamma model. The technique was applied during a highly convective rain event with maximum rain rates of nearly 120 mm/hr. The results showed the potential of the link DSD estimates as a validation tool as well as an accurate estimator of microwave and rainfall parameters.

The rain event presented exhibited high DSD variability over the path, affecting the agreement between the averaged point measurements. The underestimation observed with the disdrometer may also be attributed to the limited measurable drop range from 0.3 to 5 mm.

A more detailed study of the DSD variability and its effects on the rainfall retrievals is under way. The results will be presented at the conference.

* NASA/GSFC/ 975, Bldg. 33, Rm. B409
Greenbelt, MD 20771
Phone: (301) 614-5725, Fax: (301) 614-5558
E-mail: rafael@priam.gsfc.nasa.gov

16th Conference on Hydrology

13–17 January 2002
Orlando, Florida

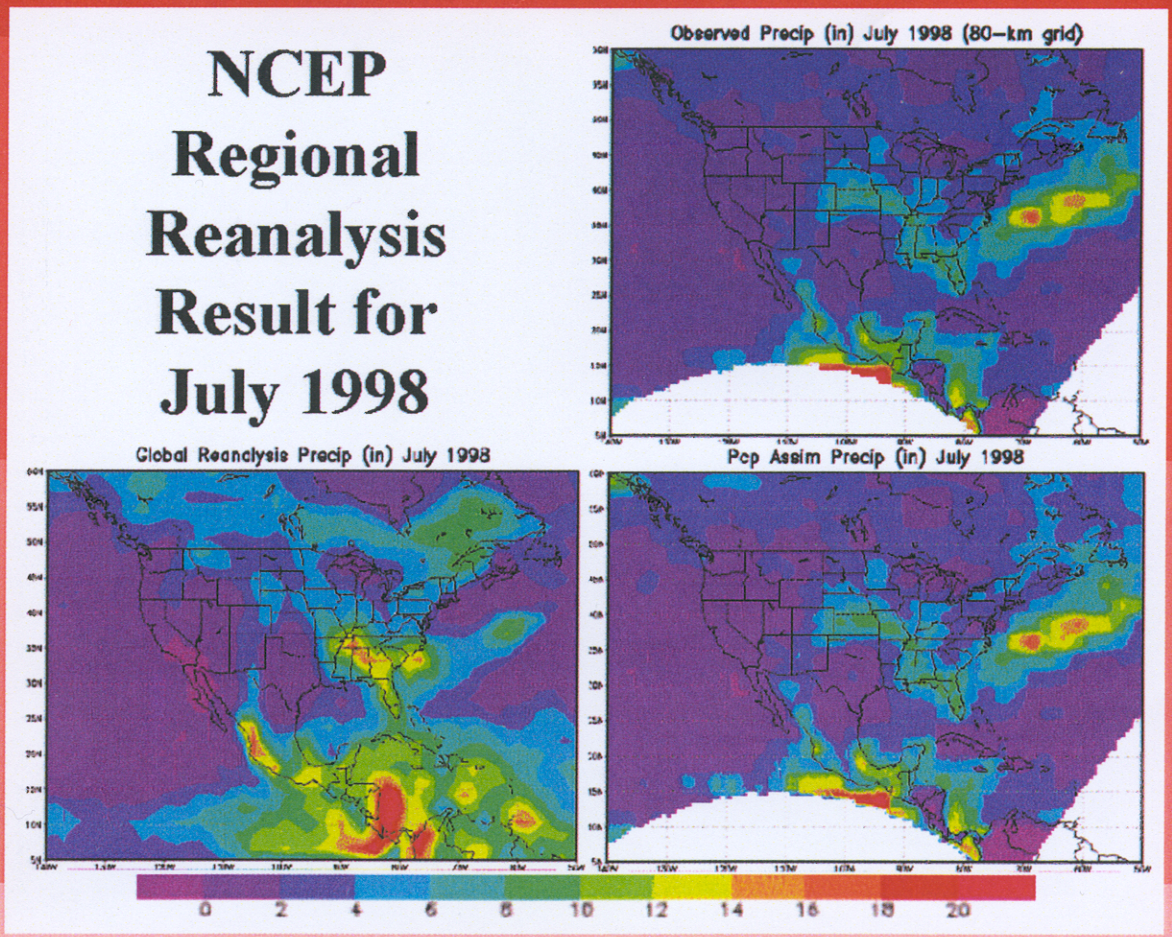

AMERICAN METEOROLOGICAL SOCIETY

J1.5 FORCING A GLOBAL, OFFLINE LAND SURFACE MODELING SYSTEM WITH OBSERVATION-BASED FIELDS

Matthew Rodell[1]*, P. R. Houser[1], U. Jambor[1], J. Gottschalck[1], J. Radakovich[1], K. Arsenault[1], C.-J. Meng[2], and K. E. Mitchell[2]
[1]NASA GSFC, Greenbelt, Maryland [2]NOAA NCEP, Camp Springs, Maryland

1. Introduction

Satellite remote sensing of hydrometeorological states and fluxes has improved steadily over the past two decades. At the same time, increases in supercomputing power and affordability have allowed atmospheric and land surface models to gain complexity and resolution. These models have the ability to fill in observational gaps, so that incorporating data from advanced observing systems into models as forcings and constraints maximizes our knowledge of the processes and resulting states of the Earth system.

The Global Land Data Assimilation System (GLDAS), which is being developed jointly at NASA's Goddard Space Flight Center and NOAA's National Centers for Environmental Prediction, enables users to run multiple, state-of-the-art land surface models (LSMs) using a combination of modeled and observation-based forcing fields (Houser et al., 2001). Drivers have been installed for Mosaic (Koster and Suarez, 1992), the Common Land Model (Dai et al., 2001), the Catchment LSM (Koster, et al., 2000), and NOAA's NOAH LSM. The primary goal of GLDAS is to produce global, high resolution (0.25^o), near-real time fields of land surface states and fluxes. These will be used to initialize weather and climate prediction models and to facilitate flood and drought prediction, agricultural productivity forecasting, water resources decision-making, and a variety of studies in the Earth sciences.

By utilizing data from advanced observing systems, GLDAS can avoid systematic biases which arise in atmospheric model-based precipitation and radiation forcing fields and accumulate in land surface moisture and temperature states. GLDAS is enhanced further by the capability of running the one dimensional LSMs on subgrid tiles, which are based on a 1 *km* global vegetation dataset, an elevation correction based on the GTOPO30 global digital elevation model, and a soil parameterization based on Reynolds, Jackson, and Rawls (1999) 5' global soils information. Future enhancements will include satellite observation-based vegetation updates, a runoff routing scheme, and assimilation of satellite-derived snow (MODIS), soil temperature and moisture (AMSR), and terrestrial water storage (GRACE) observations.

2. Methods

GLDAS began running in near-real time on 1 March 2001, with Mosaic as the operational LSM. The spatial resolution was set to 0.25^o, with one vegetation tile per grid square, 30 minutes was the length of each time step, and Mosaic's original soil scheme was used. Surface state variables were initialized based on fields from NOAA's global, 4DDA, real time meteorological modeling system (GDAS). GDAS also provided all of the forcing data. By 30 July 2001 the time step had been shortened to 15 minutes and the primary source of forcing data had been changed to NASA's GEOS 3.24 global, 4DDA, real time meteorological modeling system. Temporal and spatial interpolation has been required to derive forcing from the GDAS and GEOS files, which are produced every three hours at 0.7^o and 1.0^o resolutions, respectively.

Since 31 July 2001, geostationary satellite infrared (IR) and TRMM / SSM/I microwave-based, 0.25^o, 6-hourly mean rain rate fields from the U.S. Naval Research Laboratory (NRL) have been incorporated into the forcing. NRL does not generate precipitation estimates poleward of 60°, and TRMM / SSM/I coverage is incomplete at 6-hourly resolution. Therefore GLDAS uses GEOS precipitation as a base, overlays NRL IR-based rain, and overlays the result with NRL microwave-based rain.

A restart file was used to initiate a run of GLDAS which paralleled the operational run between 31 July and 31 August 2001. All parameters were identical in the two runs, except that NRL observation-based rain was not used in the test run. The hypothesis was that using observation-based precipitation forcing has a positive effect on the modeled state of the land surface.

4. Discussion

A major theme of the GLDAS project is the utilization of observation-based fields for forcing and constraining land surface models. The results of this investigation support the feasibility of that approach by demonstrating that 1) observation-based develop similar large scale patterns of precipitation accumulation over the course of a month, and 2) believable patterns of soil moisture develop when the observation-based precipitation fields are used as forcing. Furthermore, the small scale heterogeneity seen in the observation-based precipitation fields and resultant soil moisture output fields is likely to be more realistic than the spatial uniformity produced by the modeled forcing. When GLDAS output fields of land surface states are used to reinitialize global coupled meteorological models, the small scale heterogeneity in soil moisture, to which the atmosphere is sensitive, may feed back to have a positive effect on those model simulations.

During the period of study, TRMM / SSM/I rain was not available for 108 non-consecutive hours and IR rain was not available for 114 non-consecutive hours. These data gaps overlapped for 90 hours, during which time GLDAS relied on GEOS forcing exclusively. Therefore the observed precipitation field in Figure 1 (and likewise the output in Figure 2) might be slightly more similar to GEOS field than it otherwise would be. Data gaps are likely to be unavoidable when modeling in near-real time, so the results shown here can be considered representative of GLDAS.

For more results and a detailed description of the GLDAS project, please visit http://ldas.gsfc.nasa.gov.

*** Corresponding author address:** Matthew Rodell, Hydrological Sciences Branch, Code 974.1, NASA Goddard Space Flight Center, Greenbelt, MD 20771; e-mail: mattro@dao.gsfc.nasa.gov.

2002 IEEE International Geoscience and Remote Sensing Symposium and the 24th Canadian Symposium on Remote Sensing

IGARSS 2002

REMOTE SENSING:
Integrating Our View of the Planet

IEEE

June 24-28, 2002
Toronto Canada

An Overview of the Earth Observing System MODIS Instrument and Associated Data Systems Performance

by

Vincent V. Salomonson, William Barnes, Jack Xiong, Steve Kempler and Ed Masuoka

NASA/Goddard Space Flight Center

Greenbelt, Maryland

***Abstract*- The MODIS instrument on the EOS Terra Mission has completed over 2 years of successful operation. Excellent data products have been developed and a full year or more of these products are now available. Validation of these products is continuing and efforts to improve product availability and access are underway. The MODIS on the EOS Aqua satellite is projected to become operational in the late spring/early summer of 2002.**

I. INTRODUCTION

The Moderate Resolution Imaging Spectroradiometer (MODIS) on the Earth Observing System (EOS) Terra Mission began to produce data in February 2000. Now a little over 2 years from that time, the instrument continues to produce good data. Nearly 40 land, oceans, and atmospheres products are achieving maturity for science and applications studies. This paper summarizes the status of the instrumentand the status of processing, archiving and dissemination of MODIS products

II. MODIS INSTRUMENT STATUS

The MODIS instrument has performed well overall. The first several months from launch to October 31, 2000 saw a lot of different adjustments in instrument parameters to reduce electronic noise, striping in some bands, band-to-band crosstalk, etc. On October 31, 2000 a stable configuration, including the operation of the instrument on the "B-side" electronics, was finalized. The instrument operated in that configuration from November 1, 2000 to June 15, 2001. On June 15, 2001 the instrument went out of operation due to a high energy proton event and stayed out of operation until July 2, 2001. Instrument operations were resumed operating on the "A-side" electronics. It was decided, based on performance, that the instrument would remain in that configuration until other factors indicated differently. Up through early March of 2002, the instrument continues to operate on the A-side. Furthermore, this configuration shows no significant differences relative to instrument performance on the B-side during November 2000 to June 2001.

During the period November 2000 to the present, the instrument shows performance at or above specifications in terms of signal-to-noise in all reflected solar bands (1-19, and 26) [1]. The noise-equivalent-delta-temperature (NEDT) performance in thermal infrared bands (20-25, 27-35) also show at or better than specification performance except for occasional channels within a band. Some striping, electronic noise, crosstalk, etc. can still be observed, particularly in short-wave infrared bands and the 1.38 micrometer band (band 26). For the most part, however, all bands provide scientifically useful performance and the Level 1 data from the instrument is considered to be validated for scientific use for the period November 2000 to the present (early March 2002 when this paper was written).

VI.SUMMARY AND CONCLUSIONS

The Terra MODIS instrument is performing well. Over 40 data products have been developed by the MODIS Science Team that are scientifically useful. These data products have been processed and a relatively complete time series completed extending from November 1, 2000 to the present. These products are distributed among the three DAAC's handing MODIS products. Substantial efforts are on-going at the Earth Sciences Data and Information System (ESDIS) Project and DAAC's to improve the user access and interfaces to make the acquisition of MODIS products as user-friendly as possible. The launch of the EOS Aqua spacecraft with a second MODIS on it is eagerly anticipated because it will complement the Terra MODIS by providing afternoon (1:30 P.M. local equator crossing time) observations. The launch date planned at the writing of this paper is April 18, 2002.

2002 IEEE International Geoscience and Remote Sensing Symposium and the 24th Canadian Symposium on Remote Sensing

IGARSS 2002

REMOTE SENSING:
Integrating Our View of the Planet

IEEE

June 24-28, 2002
Toronto Canada

Estimation of Soil Moisture change with PALS's L-band Radiometer

Jiancheng Shi[1], E. G. Njoku[2] , K. S. Chen[3], T. Jackson[4], , P. O'neill[5]

[1]Institute for Computational Earth System Science

University of California, Santa Barbara
Tel: 805-893-2309, Fax: 805-893-2578, E-mail: shi@icess.ucsb.edu

[2]NASA/JPL, [3]National Central University Taiwan, [4]USDA/ARS, [5]NASA/GSFC

Abstract – This study demonstrates the capability of estimating the relative soil moisture change using repeat-pass L-band radiometer. It shows 1) evaluation of the effects of the surface roughness and vegetation in the repeat-pass measurements, 2) development of a technique to estimate the relative soil moisture change, and 3) validation with the ground soil moisture measurements from SGP99 experiment.

I. Introduction

It is understood that the emission from vegetated areas is a function of water content and its spatial distribution as determined by vegetation structure and underlying surface conditions – roughness and soil moisture. Even through these effects can be modeled if the ground measurements are available, it is quite difficult to take into account these effects in the inversion process for soil moisture estimation.

One of the advantages in the satellite passive microwave measurements is the quick repeat-time. They are capable to re-visit or measure surface conditions within a few days. The general characteristics of temporal variability of nature surfaces – the properties that affect the emission signals are:

- Surface soil moisture varies constantly over the time and has a significant diurnal circle during a day until it reaches a very dry condition.
- Vegetation water content has also diurnal variability but it may have no significant change at the same time during a day unless there is a precipitation event. Most of vegetation growth or microstructure in terms of scatter size, shape, and orientation has a longer time scale (days – week) to be considered having a significant change.
- Surface roughness, in general, can be considered as a constant for a long time period (weeks) except some man-made or weather events such as rainfall and agriculture activities.

Therefore, some variables such as surface roughness and vegetation can be considered as a constant between two or three data acquisitions. The changes between the data acquisitions will be mainly resulted from surface soil moisture change. These characteristics make it possible to develop a technique to estimate surface soil moisture change with vegetated surfaces.

In this study, we evaluate the effect of the surface roughness and vegetation cover on estimating the relative soil moisture change. Based on these characteristics, we demonstrate a technique that uses L-band radiometer to estimate the relative soil moisture change from repeat-pass measurements and its validation of PALS instrument derived soil moisture change with the ground measurements from SGP99 experiment.

II. Effects of the Surface Roughness in Repeat-Pass Measurements

To evaluate the effect of the surface roughness on estimating the relative soil moisture change, we first simulated a bare surface emissivity database at 1.41 GHz. This database covers the most possible soil moisture and roughness conditions and the incidence angle from 20° to 70°. Then, we developed a simplified model using this database. It is written as:

$$R_p^e = 1 - E_p = A_p \cdot r_p^{B_p} \qquad (1)$$

where E_p is emissivity and p indicates the polarization. R^e is the effective reflectance that includes the effect of the surface roughness. A_p and B_p are the roughness parameters depending on the polarization, incidence angle, surface RMS height, correlation length and the type of the correlation function. They represent an overall effect of the surface roughness. r_p is the flat surface reflectivity.

Under change detection concept, the relationships in terms of the ratio between any two measurements are evaluated with assumption of no surface roughness change. The signal change between two measurements is resulted only from surface soil moisture change. By varying all possible combination of soil moistures, we simulated the effective reflectivity ratio. That is:

$$R_{p2}^e / R_{p1}^e = (1 - E_{p2}) / (1 - E_{p1}) \qquad (2)$$

V. Summary

One advantage of the passive microwave sensors is the quick repeat-time within a few days. Except soil moisture, most of natural surface characteristics, such as surface roughness and vegetation properties, can be reasonable assumed that there is no-change between the repeat measurements (same time during a day) between the data acquisitions. Based on this concept, we demonstrated the relative soil moisture change in terms of the ratio can be directly estimated from the repeat-pass measurements for both bare and vegetated surfaces when the small albedo assumption is valid. The advantage of this technique is that it does not require the surface information – we do not need to know if the pixel is a bare, vegetated, or fractionally vegetated, and vegetation information as long as the small albedo assumption is valid.

2002 IEEE International Geoscience and Remote Sensing Symposium and the 24th Canadian Symposium on Remote Sensing

IGARSS 2002

REMOTE SENSING:
Integrating Our View of the Planet

IEEE

June 24-28, 2002
Toronto Canada

Observation of Snowfall over Land by Microwave Radiometry from Space

G. M. Skofronick-Jackson
University of Maryland, Baltimore County, GEST Center
NASA Goddard/Code 975
Greenbelt, MD 20771
301-614-5720, FAX 301-614-5558, gailsjackson@ieee.org

J. A. Weinman
NASA Goddard/Code 975
Greenbelt, MD 20771

D.-E. Chang
Forecast Research Laboratory, Meteorological Research Institute
Korea Meteorological Administration,
Seoul, 156-720, Korea

***Abstract* - High frequency (ν > 100 GHz) observations from AMSU-B during the March 5-6, 2001 New England blizzard are used to investigate the detection of snowfall over land. The AMSU-B data are compared to NEXRAD reflectivities. The radiative effects of a snow model are compared with observations. Low altitude water vapor is shown to obscure emission from the underlying ground at high frequencies, but at high altitudes water vapor also reduces the impact of scattering by snow particles.**

1. Introduction

Although most global precipitation occurs as rainfall, snowfall plays a significant role in the extra-tropical hydrological cycle. Snow serves as a reservoir of water that can be released later in the year to support agriculture and hydroelectric activities. Beside the economic and recreational value of snow, snow storms can be hazardous for transportation and other economic activities. One of the important challenges for future satellites is to detect these snow storms from space.

Because snow accumulation on land affects the emission properties of the surface, the measurement of snowfall within the atmosphere has been difficult with radiometers that operate at frequencies less than 100 GHz. Water vapor absorption at frequencies greater than 100 GHz can screen the emission from snow covered surfaces. The Advanced Microwave Sounding Units (AMSU-B) radiometers on the NOAA 15 and 16 spacecraft [1] provide observations at 89, 150 and 183±1, ±3, ±7 GHz. This study will demonstrate that radiation at those higher frequencies can be used to measure snowfall over land because water vapor screening obscures the underlying snow-covered surface.

The AMSU-B radiometer on NOAA-15 initially encountered radio frequency interference from on-board transmitters that were ultimately shut down in the autumn of 1999. Modifications were implemented on the NOAA-16 AMSU-B so that reliable spaceborne data at frequencies greater 100 GHz were available by the winter of 2000-01.

2. Case Study

The Nor'easter of March 5-6, 2001 presented a unique opportunity to observe intense snowfall over land with the NOAA-16 AMSU-B. That blizzard was one of the more intense snow storms of the season, depositing on the order of 50 cm of snow on much of VT, NH and northeastern NY with several stations reporting deposits of 75 cm. Wet snow and sleet were reported along the New England coast, but the mean temperatures encountered in NH and VT remained around –5 C, and reported maxima were only –2 C, so that melting could be disregarded over inland regions throughout the entire day.

Fig. 1 shows a composite of the National Weather Service (NWS) operational weather radar reflectivity, Z_{eff} (dBZ) obtained over the Northeastern U.S. on March 5, 2001 at 23:00 UTC. The snowfall was greatest over CT, MA, VT, and NH. Although the NWS operational radar data have well known limitations, in the absence of a preplanned field observation campaign, they provide readily available data to compare to snowfall derived from microwave brightness temperatures.

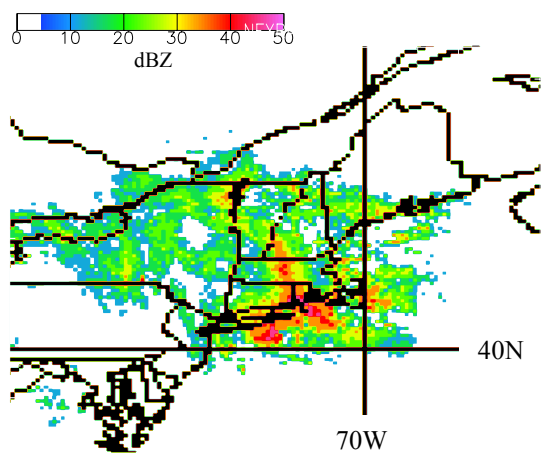

Figure 1: NWS NEXRAD reflectivities for March 5, 2001 2300 UTC.

4. Summary

In summary, the NEXRAD and AMSU-B 150 and 183 GHz channels were found to be qualitatively related to the coincident NEXRAD radar data. Furthermore, an appropriate snow particle model was found to match attenuation measurements of snow and the issues surrounding surface emissivity were addressed. A process is underway to more fully characterize the relationships between the higher frequency brightness temperatures and the snow in the cloud profile.

Report to NASA on a Workshop on Sea Ice Data Assimilation

Held at the

Naval Academy, Annapolis, MD

On

July 23-24, 2002

Report Edited by
Kim Partington, Ronald Lindsay, Jinro Ukita

September 2002

9.7 Representation of Antarctic Coastal Polynyas in Ocean Climate Models: A Justification for Assimilation of Ice Concentration?

Achim Stoessel

Department of Oceanography
Texas A&M University, College Station

Thorsten Markus

NASA Goddard Space Flight Center
Greenbelt, Maryland

Abstract

The representation of Antarctic coastal polynyas in global ocean general circulation models (OGCMs) have a profound impact on long-term deep-ocean properties. Compared to maximum ranges in magnitude of ambient conditions such as wind velocity and air temperature, the extent of coastal polynyas play the most decisive role in determining the rate of Antarctic Bottom Water formation, through the process of sea-ice formation, brine release, and formation of High Salinity Shelf Water. This study investigates the local, regional and high-frequency behaviour of the model representation of coastal polynyas with the aid of daily ice concentration derived from satellite passive microwave data using the "NASA Team 2" algorithm. Large regional and temporal discrepancies arise that are primarily related to the type of convection parameterization used in the model. Arguing that the empirical "thermodynamic lead closing" parameter is the weakest part in the sea-ice component of the OGCM, ice is being redistributed within a model grid cell by assimilating NT2 ice concentration. This measure yields potentially more reliable estimates on the impact of critical high-latitude processes on long-term deep-ocean properties. On the other hand, there are still various issues to be solved, e.g. whether the presented assimilation strategy is useful for the entire ice pack, how to properly deal with coastline mismatch between data and model, and how much assimilation of daily data interferes with daily winds that drive the sea-ice model. Besides the assimilation, this paper has revealed major short-time scale discrepancies between modelled and satellite-derived ice concentration, suggesting that much work is still needed to improve subgrid-scale high-latitude processes in global OGCMs.

Report to NASA on a Workshop on Sea Ice Data Assimilation

Held at the

Naval Academy, Annapolis, MD

On

July 23-24, 2002

Report Edited by
Kim Partington, Ronald Lindsay, Jinro Ukita

September 2002

9.8 Spatial and Temporal Characteristics of Arctic Sea-ice Deformation and its Implication in Data Assimilation

Jinro Ukita, Antony Liu, and Yunhe Zhao

NASA-Goddard Flight Space Center
Code 971
Greenbelt, MD 20771

On interannual to decadal timescales atmospheric circulation exhibits strong modal structures, in which coherent and recursive patterns such as ones defined by NAO and AO emerge. These modes and their associated phases have Arctic manifestations as evidenced by different modes in ice motion. Given this background questions arise as to how these variations in ice motion lead to varying modes of ice deformation, how these modes in deformation modify the way in which sea ice mass is redistributed, how this is compared to possible influence on the mass balance by other oceanic and thermodynamic processes, e.g. more oceanic heat flux, higher air temperature, or more snow precipitation etc., and how this ultimately modifies the sea ice mass balance and eventually the regional freshwater balance. These questions can be more effectively answered through an optimal use of model outputs and data – data assimilation. The first and important step in this effort is to make a critical assessment on data so as to identify relevant spatial and temporal scales for assimilation analysis.

The process most directly responsible for the redistribution of sea-ice mass is uniaxial closing (contraction), e.g. a ice flow against the coast. Yet it is a rare class of events as on the average Arctic ice motion is close to being non-divergent. This requires a careful analysis on how to extract information characterizing this process. Our results based on merged ice motion data constructed from satellite and buoy observations indicate that the relevant timescale for this process likely falls in the range of month to season. Over this temporal scale the emerged spatial pattern on the frequency of uniaxial-contraction events resembles to observed and simulated patterns in ice thickness. These results suggest that within this framework roughly speaking daily to synoptic timescale is a required temporal resolution for assimilation analysis to be both valid and meaningful. They also suggest an effectiveness of a 100 km resolution.

On the basis of this assessment work is under way to construct a simple forward and adjoint ice dynamic model.

2002 IEEE International Geoscience and Remote Sensing Symposium and the 24th Canadian Symposium on Remote Sensing

IGARSS 2002

REMOTE SENSING:
Integrating Our View of the Planet

IEEE

June 24-28, 2002
Toronto Canada

Rain Rate Measurement with an Airborne Scanning Radar Altimeter

E. J. Walsh*, C. W. Wright, D. Vandemark, L. F. Bliven
NASA/GSFC/Wallops Flight Facility, Wallops Island, VA 23337

E. Uhlhorn, P. G. Black, F. D. Marks, Jr.
NOAA/AOML/Hurricane Research Division, Miami, FL 33149-1097

I. Introduction

The NASA Scanning Radar Altimeter (SRA) sweeps a radar beam of 1° half-power width (two-way) across the aircraft ground track within ±22° of nadir, simultaneously measuring the backscattered power at its 36 GHz (8.3 mm) operating frequency and the range to the sea surface at 64 points spaced across the swath at 0.7° incidence angle intervals. The measurement geometry is shown in Fig. 1 with the specific numbers referring to the flights made into Hurricane Humberto on 23 and 24 September 2001, aboard a WP-3D hurricane research aircraft of the NOAA Aircraft Operations Center. The ranges produce raster lines of sea surface topography at a 10 Hz rate. The SRA was primarily designed to produce sea surface directional wave spectra, but the backscattered power measurements can be used to determine path integrated rain rate below the aircraft.

II. Hurricane Humberto

Hurricane Humberto strengthened to Category 2 during the first flight, then diminished to Category 1 for the second flight. The SRA aircraft flight pattern, shown in Fig. 2 for 24 September 2001, was the same on both days. It featured three radial passes through the eye, connected by downwind legs, and was coordinated with three other aircraft in the Coordinated Observations of Vortex Evolution and Structure (COVES) experiment.

The surface wind speed measured by the NOAA AOML Hurricane Research Division (HRD) Stepped Frequency Microwave Radiometer (SFMR) along the flight track is shown in top panel of Fig. 3. The closest approach to the center of the eye on the three radial passes is indicated by the wind speed minimums at 2124 and 2254 UTC on 24 September and 0032 UTC on 25 September 2001. Rain rate measured by the SFMR along the aircraft ground track is shown in the bottom panel.

III. SRA Rain Measurement Technique

Calculations based on the Marshall-Palmer distribution indicate that the attenuation (dB/km) of a 36 GHz radar signal is approximately linearly related to rain rate [1]. At 1.8 km height, the SRA signal suffers a 1dBattenuation for each mm/hr of rain rate. If the sea surface radar backscatter coefficient is constant as one transitions into a region of rain, the loss of signal will determine the rain rate to an accuracy of a fraction of a mm/hr. In general, changes in the backscatter coefficient at nadir are small compared to the rain absorption in the hurricane high wind environment and can be differentiated from changes in rain absorption by examining the variation of backscattered power with incidence angle.

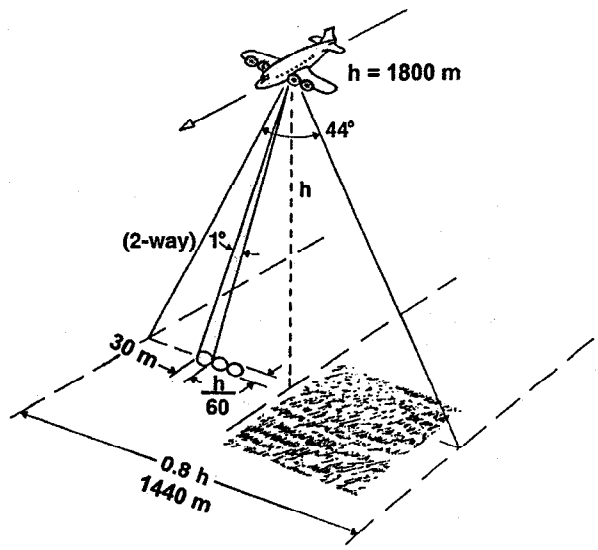

Fig. 1. Scanning Radar Altimeter measurement geometry.

Figure 4 shows the variation of the backscattered power at (a) 37.43°N, 66.69°W, near the beginning of the southeast pass through the eye, and at (b) 37.04°N, 65.71°W. The first observation was during a SFMR data gap, but the SRA data

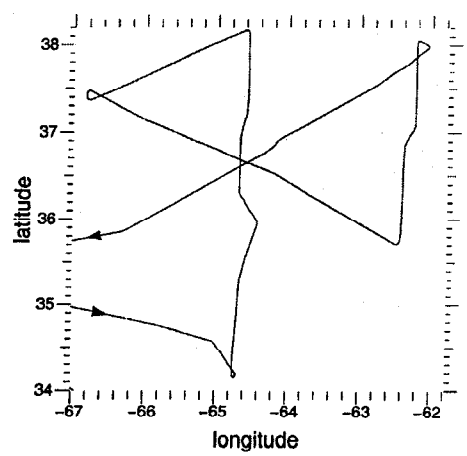

Fig. 2. NOAA aircraft flight track on 24 September 2001.

*presently on assignment at NOAA Environmental Technology Laboratory, 325 Broadway, Boulder, CO 80305-3328.

NASA/TM-2002-210005

SIMBIOS Project 2001 Annual Report

Giulietta S. Fargion, Science Applications International Corporation, Maryland
Charles R. McClain, Goddard Space Flight Center, Greenbelt, Maryland

National Aeronautics and
Space Administration

Goddard Space Flight Center
Greenbelt, Maryland 20771

March 2002

Chapter 20

Assessment, Validation, and Refinement of the Atmospheric Correction Algorithm for the Ocean Color Sensors

Menghua Wang

University of Maryland, Baltimore County, Baltimore, Maryland

20.1 INTRODUCTION

The primary focus of this proposed research is for the *atmospheric correction algorithms evaluation and development* and *satellite sensor calibration and characterization*. It is well known that the atmospheric correction, which removes more than 90% of sensor-measured signals contributed from atmosphere in the visible, is the key procedure in the ocean color remote sensing (Gordon and Wang, 1994). The accuracy and effectiveness of the atmospheric correction directly affect the remotely retrieved ocean bio-optical products. On the other hand, for ocean color remote sensing, in order to obtain the required accuracy in the derived water-leaving signals from satellite measurements, an on-orbit vicarious calibration of the whole system, i.e., sensor and algorithms, is necessary. In addition, it is important to address issues of (i) cross-calibration of two or more sensors and (ii) in-orbit vicarious calibration of the sensor-atmosphere system. The goal of these researches is to develop methods for meaningful comparison and possible merging of data products from multiple ocean color missions. With support and collaboration from the SIMBIOS project office, much efforts have been on studying and comparing the ocean color data derived from the Japanese Ocean Color and Temperature Scanner (OCTS) and the French Polarization and Directionality of the Earth's Reflectances (POLDER). OCTS and POLDER were both on board Japan's Sun-synchronous Advanced Earth Observing Satellite (ADEOS) from August 1996 to June 1997, collecting about 10 months of global ocean color data.

This provides a unique opportunity for developing methods and strategies for the merging of ocean color data from multiple ocean color sensors. In this report, I will very briefly discuss other research activities, but mainly focus on describe collective efforts (with SIMBIOS project office) in the OCTS and POLDER comparison study.

20.2 RESEARCH ACTIVITIES

(a) Studies have been carried out to understand various effects on the performance of the SeaWiFS atmospheric correction algorithm for the ocean color and atmospheric aerosols: (i) the solar and viewing geometry effects, in particular, for cases of the large solar and viewing zenith angles; (ii) the Earth curvature effects, i.e., the spherical-shell atmosphere (SSA) vs. the plane-parallel atmosphere (PPA) (Ding and Gordon, 1994); (iii) effects of the sun glint contaminations on the derived SeaWiFS ocean and atmospheric products (Wang and Bailey, 2001); (iv) the effects of ocean surface wind speed on the SeaWiFS derived aerosol optical thickness; and (v) the effects of polarization in the aerosol lookup tables on the SeaWiFS derived ocean color and atmosphere products. These research works (except item (iii)) are still on going. Some preliminary results, however, show importance and necessary to account for some of these effects.

(b) I have been working on activities for the International Ocean-Color Coordinating Group (IOCCG) atmospheric correction working group. The main objective of the working group is to quantify the performance of the various exiting atmospheric correction algorithms used for the various ocean color missions. Therefore, the derived ocean color products from various ocean color missions can be meaningfully compared and possibly merged. As the atmospheric correction is a key procedure in the ocean color remote sensing, we want to answer question such as how can derived ocean color products from one sensor be best compared with those from others. We want to quantify the differences among the performance of the atmospheric correction algorithms. The core working group members are from OCTS/GLI (Japan), SeaWiFS (US), MODIS (US), POLDER (France), and MERIS (Europe). I am currently serving as the working group leader.

(c) In collaboration with A. Isaacman, B. Franz, and C. McClain and the SIMBIOS project office, we have studied and compared the ocean color data derived the OCTS and POLDER.

NASA/TM-2002-211617

The SeaWiFS Bio-Optical Archive and Storage System (SeaBASS): Current Architecture and Implementation

Editors

Giulietta S. Fargion, Science Applications International Corporation, Beltsville, Maryland
Charles R. McClain, Goddard Space Flight Center, Greenbelt, Maryland

Authors
P. Jeremy Werdell, Science System and Applications Inc., Lanham, Maryland
Sean W. Bailey, Futuretech Corporation, Greenbelt, Maryland

National Aeronautics and
Space Administration

Goddard Space Flight Center
Greenbelt, Maryland 20771

September 2002

Chapter 1

Introduction

1.1 Motivation and Philosophy

Experiences with past and present satellite ocean color missions, such as the Coastal Zone Color Scanner (CZCS) and Sea-viewing Wide Field-of-view Sensor (SeaWiFS), demonstrate the need for high quality *in situ* measurements for bio-optical algorithm development and satellite data product validation (Gordon et al. 1983, Evans and Gordon 1994, McClain et al. 1998, Hooker and McClain 2000). The National Aeronautics and Space Administration (NASA) SeaWiFS Project, for example, is tasked with producing normalized water-leaving radiances with an absolute accuracy of 5% (Hooker and Esaias 1993), which requires comparative, globally distributed *in situ* radiometric measurements with accuracy finer than 5%. The advent of additional missions, such as the Moderate Resolution Imaging Spectroradiometer (MODIS) and the Medium Resolution Imaging Spectrometer (MERIS), and the approach of future missions, including the Global Imager (GLI) and the second Polarization and Directionality of the Earth's Reflectances (POLDER-2) instrument, further underline the need for accurate, temporally and geographically diverse samples of oceanographic and atmospheric data.

Historically, the amount of data suitable for algorithm development and satellite validation activities has been limited due to a paucity of simultaneous observations and the difficulty associated with obtaining globally distributed sampling (O'Reilly et al. 1998, Bailey et al. 2000). With regards to the latter, spatial biases are often undesirable for satellite missions with continuous global coverage. Due to their required accuracy, these data are additionally limited by biases introduced by varying measurement and data processing techniques (Hooker and Maritorena 2000, Hooker et al. 2001). As such, global, high quality, *in situ* data sets are invaluable and prerequisite to advance the field of ocean color.

To facilitate the assembly of a global bio-optical data set, the SeaWiFS Project developed the SeaWiFS Bio-optical Archive and Storage System (SeaBASS), a local repository for *in situ* radiometric and phytoplankton pigment data used regularly in their scientific analyses (Hooker et al. 1994). The system has since been expanded to contain oceanographic and atmospheric data sets collected by the NASA Sensor Intercomparison and Merger for Interdisciplinary Biological and Oceanic Studies (SIMBIOS) Project (McClain et al. 2002), as part of NASA Research Announcements (NRA) NRA-96-MTPE-04 and NRA-99-OES-99, which has aided considerably in minimizing spatial bias and maximizing data acquisition rates (McClain and Fargion 1999a and 1999b, Fargion and McClain 2001 and 2002). The SeaWiFS and SIMBIOS Project Offices (SPO) currently share responsibility for the maintenance of SeaBASS, including all design modification and construction.

To develop consistency across multiple data contributors and institutions, the SPO has defined and documented a series of *in situ* data requirements and sampling strategies that ensure that any particular set of measurements will be acceptable for bio-optical and atmospheric correction algorithm development and ocean color sensor validation (Mueller and Austin 1995, Fargion et al. 2001, Mueller et al. 2002a and 2002b). In addition, the SPO has sponsored a series of round-robin activities to establish and advance the state of instrument calibration, protocols, and traceability to radiometric standards (Mueller 1993, Meister et al. 2002). Data prepared using these techniques are suitable for both verifying the radiometric precision and stability of satellite-borne ocean color sensors and validating the algorithms used to relate the radiances to other geophysical parameters.

NASA/TM-2002-210004/Rev3-Vol2

James L. Mueller[1] and Giulietta S. Fargion[2]
Editors

[1] *CHORS, San Diego State University, San Diego, California*
[2]*Science Applications International Corporation, Beltsville, Maryland*

Ocean Optics Protocols For Satellite Ocean Color Sensor Validation, Revision 3, Volume 2

J. L. Mueller, C. Pietras, S. B. Hooker, D. K. Clark, A. Morel, R. Frouin, B.G. Mitchell, R. R. Bidigare, C. Trees, J. Werdell, G. S. Fargion, R. Arnone, R. W. Austin, S. Bailey, W. Broenkow, S. W. Brown, K. Carder, C. Davis, J. Dore, M. Feinholz, S. Flora, Z.P. Lee, B. Holben, B. C. Johnson, M. Kahru, D. M. Karl, Y. S Kim, K. D. Knobelspiesse, C. R. McClain, S. McLean, M. Miller, C. D. Mobley , J. Porter, R.G. Steward, M. Stramska, L. Van Heukelem, K. Voss, J. Wieland, M. A.Yarbrough and M. Yuen.

National Aeronautical and
Space administration

Goddard Space Flight Space Center
Greenbelt, Maryland 20771

February 2002

Chapter 18

SeaBASS Data Protocols and Policy

P. Jeremy Werdell[1], Sean Bailey[2], and Giulietta S. Fargion[3]

[1]*Science Systems and Applications Inc., Lanham, Maryland*
[2]*Futuretech Corporation, Greenbelt, Maryland*
[3]*Science Applications International Corporation, Beltsville, Maryland*

18.1 INTRODUCTION

The SeaWiFS Project developed the SeaWiFS Bio-optical Archive and Storage System (SeaBASS) to be a local repository for *in situ* optical and pigment data products regularly used in a variety of scientific analyses. Information on the original SeaBASS design is provided in Hooker et al. (1994), and has since been expanded to contain data sets collected by participants of the SIMBIOS Project. A detailed description of the SeaBASS system is available via the World Wide Web:

<http://seabass.gsfc.nasa.gov>.

Both the SeaWiFS and SIMBIOS Projects use *in situ* bio-optical data for the validation of SeaWiFS and other satellite (e.g., OCTS and POLDER) data products, and for the development of new ocean color algorithms. In addition, SeaBASS supports international protocol workshops, data merger studies, and time-series studies. Archived data include measurements of water-leaving radiance, chlorophyll *a*, and other related optical and pigment parameters. When available, additional oceanographic and atmospheric data (given in Table 2.1) are also archived in SeaBASS. Data are collected by a number of different instrument packages, such as profilers, buoys, and above-water measurement devices, on a variety of platforms, including ships, moorings, and drifters. The contents of SeaBASS are made readily available to the SIMBIOS and MODIS Science Team Members, and to other approved individuals (e.g., members of other ocean color instrument teams, volunteer-contributing researchers, etc.) on a case-by-case basis. Access to the database and data archive is available to authorized users through the SeaBASS Web page.

As SIMBIOS US Science Team members are contractually obligated to provide data to SeaBASS, the volume of archived data is rapidly increasing (McClain and Fargion 1999a and 1999b). With the launch of MODIS, as well as a number of present and upcoming international missions (e.g., GLI, POLDER-2, MERIS, OCI, OCM, etc.), the use of the SeaBASS data archive is expected to increase dramatically as these missions begin to require validation data.

18.2 SeaBASS DATA FORMAT

SeaBASS presently contains over 22,000 bio-optical data files, encompassing more than 650 separate experiments. In addition, its historical pigment database holds over 286,000 records of phytoplankton pigment data. To account for the continuous growth of the data archive, the Project believed it essential to develop efficient data ingestion and storage techniques. Such ingestion procedures and protocols were designed to be as straightforward and effortless as possible on the part of the contributing investigators, while still offering a useful format for internal analysis efforts. The Project considered the following to be the most important in the design of the system:

1. Simple data format, easily read and updated;
2. Global portability across multiple computer platforms; and
3. Web accessible data holdings.

2002 IEEE International Geoscience and Remote Sensing Symposium and the 24th Canadian Symposium on Remote Sensing

REMOTE SENSING: Integrating Our View of the Planet

IGARSS 2002

IEEE

June 24-28, 2002
Toronto Canada

Realtime Storm Surge Measurement with a Scanning Radar Altimeter

C. W. Wright, E. J. Walsh[1], W. B. Krabill, D. Vandemark
NASA/Goddard Space Flight Center, Code 972, Wallops Flight Facility, Wallops Island, VA 23337

A. W. Garcia
U.S. Army Engineer Research and Development Center, 3909 Halls Ferry Road, Vicksburg, MS 39180-6199

P. G. Black, F. D. Marks, Jr.
NOAA/AOML/Hurricane Research Division, 4301 Rickenbacker Causeway, Miami, FL 33149-1097

R. A. Luettich, Jr.
University of North Carolina at Chapel Hill, Institute of Marine Sciences, 3431 Arendell Street, Morehead City, NC 28557

[1]presently on assignment at NOAA Environmental Technology Laboratory, 325 Broadway, Boulder, CO 80305-3328

I. Introduction

The NASA Scanning Radar Altimeter (SRA) was designed primarily to measure the energetic portion of the directional wave spectrum by generating a topographic map of the sea surface [1]. The SRA measurement geometry is shown in Fig. 1. The specific numbers refer to the Hurricane Bonnie landfall flight to be described shortly.

The SRA sweeps a radar beam of 1° (two-way) half-power width across the aircraft ground track over a swath equal to 0.8 of the aircraft height, simultaneously measuring the backscattered power at its 36 GHz (8.3 mm) operating frequency and the range to the sea surface at 64 positions at 0.7° incidence angle intervals. The maximum scan rate was 8 Hz during the Hurricane Bonnie flights, but it is presently 10 Hz. In realtime, the slant ranges are multiplied by the cosine of the off-nadir incidence angles (including the effect of aircraft roll attitude) to determine the vertical distances from the aircraft to the sea surface. These distances are subtracted from the aircraft height to produce a sea-surface elevation map which is displayed on a monitor in the aircraft to enable realtime assessments of data quality and wave properties.

On 24 August 1998, the SRA, aboard a NOAA hurricane research aircraft, provided the first documentation of the directional wave spectrum throughout a hurricane in open water when Hurricane Bonnie was about 400 km east of Abaco Island, Bahamas [2]. On 26 August 1998, the SRA provided the first documentation of the directional wave spectrum throughout a hurricane making landfall as Bonnie was approaching Wilmington, NC [3].

II. SRA Wave Topography Measurements

Figure 2 shows a gray-scale-coded topographic map produced from about 700 SRA scan lines as the aircraft crossed Cape Lookout (34.58°N, 76.53°W) during the landfall flight. The aircraft flight direction was from right to left in Fig. 3. The wave topography shows a dramatic spatial variation in the wave field with the waves propagating toward the northwest on the east side of Cape Lookout, and toward the north on the west side.

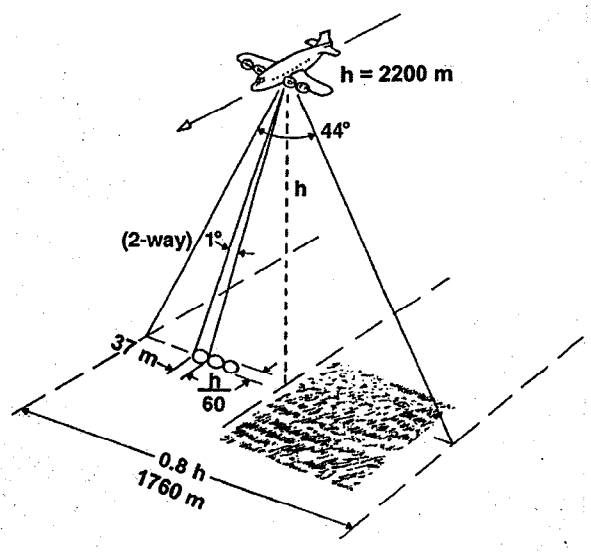

Fig. 1. Scanning Radar Altimeter measurement geometry.

Figure 3 shows five contiguous 10-km segments of SRA gray-scale coded topography on a different flight line as the NOAA aircraft headed north toward Cape Hatteras (35.27°N, 75.44°W). The waves were just starting to "feel" the ocean floor at the beginning of this data set, and the water depth decreased along the track. The waves were initially propagating toward about 335°. As the waves approached the shore, the wavelength shortened, the amplitude decreased, and the propagation direction turned toward the north and finally northeast. The surf zone began at about 6.3 km up from the bottom of the right 10 km segment. The tip of Cape Hatteras is apparent at the top of the same segment.

All the analysis described so far does not require an absolute determination of the height of the aircraft. The swath is wide enough that each scan line can be processed independently and its mean elevation set to zero.

NASA Technical Memorandum 2002–206892, Volume 21

SeaWiFS Postlaunch Technical Report Series

Stanford B. Hooker, Editor
NASA Goddard Space Flight Center
Greenbelt, Maryland

Elaine R. Firestone, Senior Scientific Technical Editor
Science Applications International Corporation
Beltsville, Maryland

Volume 21, The Eighth SeaWiFS Intercalibration Round-Robin Experiment (SIRREX-8), September–December 2001

Giuseppe Zibordi
Davide D'Alimonte
Dirk van der Linde
Jean-François Berthon
JRC/Institute for Environment and Sustainability
Ispra, Italy

Stanford B. Hooker
NASA/Goddard Space Flight Center
Greenbelt, Maryland

James L. Mueller
SDSU/Center for Hydro-Optics and Remote Sensing
San Diego, California

Gordana Lazin
Scott McLean
Satlantic, Inc.
Halifax, Canada

Abstract

This report documents the scientific activities during the eighth SeaWiFS Intercalibration Round-Robin Experiment (SIRREX-8) held at the Center for Hydro-Optics and Remote Sensing (CHORS), the Joint Research Centre (JRC), and Satlantic, Inc. The objectives of SIRREX-8 were to a) quantify the uncertainties associated with measuring the immersion factor with a standard protocol, b) establish if instrument-to-instrument variability prevents the assignment of a set of immersion factors for an entire series of sensors, c) compare average immersion factors obtained from sample OCI-200 radiometers with those provided by Satlantic for the same series of instruments, and d) measure the cosine response of one sensor at CHORS and Satlantic. An overview of SIRREX-8 is given in Chapt. 1, the immersion factor methods used by the participating laboratories are presented in Chapts. 2–4, and the data processing code is documented in Chapt. 5. The cosine response methods and results are presented in Chapt. 6, along with an analysis of the data. A synthesis of the immersion factor results is presented in Chapt. 7 and includes a discussion and conclusion of the effort with respect to the objectives.

Prologue

The purpose of the Sea-viewing Wide Field-of-view Sensor (SeaWiFS) Project at the National Aeronautics and Space Administration (NASA) Goddard Space Flight Center (GSFC) is to obtain valid ocean color data of the world ocean for a five-year period, to process that data in conjunction with ancillary data to meaningful biological parameters, and to make that data readily available to researchers (Hooker et al. 1992). The success of the SeaWiFS mission will be determined by the quality of the ocean color data set and its availability. The culmination of properly executing this responsibility is achieving a radiometric accuracy to within 5% absolute and 1% relative, water-leaving radiances to within 5% absolute, and chlorophyll *a* concentration to within 35% over a range of 0.05–50.0 $\mathrm{mg\,m^{-3}}$ (Hooker and Esaias 1993).

The type and quality of supporting *in situ* optical measurements and analytical protocols for SeaWiFS calibration and validation were drafted at a SeaWiFS workshop in 1990. A central perspective of the workshop was that the significant expense of field work dictates *in situ* observations will accrue over several years from a variety of sources, using different instruments and approaches. These data must be internally consistent, of known and documented accuracy (but within SeaWiFS requirements), and in a form readily accessible for analysis by ocean color scientists. The findings and recommendations of the workshop were presented by Mueller and Austin (1992) and were immediately adopted as the SeaWiFS Ocean Optics Protocols (SOOP).

Although the immediate concerns of the SOOP were the SeaWiFS mission, the capabilities of other potential ocean color sensors were also recognized, with the intent of developing databases that are relevant to long-term future needs. The importance of the SOOP and the accuracy requirements contained therein is well recognized by the broader scientific and commercial ocean color community, as evidenced by the considerable expansion of the original document to accommodate a broader range of measurements, techniques, and sampling considerations (Mueller and Austin 1995, Mueller 2000, and Mueller et al. 2001).

Ensuring the SeaWiFS calibration and validation field data sets are of uniform quality and have an uncertainty less than 5% requires a continuing commitment to quantifying the uncertainties associated with the spaceborne and *in situ* instrumentation. The uncertainties associated with the satellite sensor are not considered here, although it is important to remember that half of the total uncertainty budget is apportioned to the satellite sensor. Assuming the uncertainties combine in quadrature (the square root of the sum of the squares), the allowed uncertainty in the remote and *in situ* optical data is approximately 3.5% for each ($\sqrt{5^2/2}$).

The sources of uncertainty for the ground truth part of the total uncertainty budget have a variety of sources:

1. The measurement protocols used in the field;
2. The environmental conditions encountered during data collection;
3. The absolute calibration of the field radiometers, which must also be traceable to the National Institute of Standards and Technology (NIST);
4. The conversion of the light signals to geophysical units in a data processing scheme; and
5. The stability of the radiometers in the harsh environment they are subjected to during transport and use.

The first step in the process of controlling uncertainties in field data was establishing and publishing the SOOP. The proper application of the SOOP also reduces any unnecessary contributions from environmental effects, but it does not completely remove them—as environmental conditions worsen, which may be unavoidable, uncertainties inexorably increase.

NASA Technical Memorandum 2002–206892, Volume 21

SeaWiFS Postlaunch Technical Report Series

Stanford B. Hooker, Editor
NASA Goddard Space Flight Center
Greenbelt, Maryland

Elaine R. Firestone, Senior Scientific Technical Editor
Science Applications International Corporation
Beltsville, Maryland

Volume 21, The Eighth SeaWiFS Intercalibration Round-Robin Experiment (SIRREX-8), September–December 2001

Giuseppe Zibordi
Davide D'Alimonte
Dirk van der Linde
Jean-François Berthon
JRC/Institute for Environment and Sustainability
Ispra, Italy

Stanford B. Hooker
NASA/Goddard Space Flight Center
Greenbelt, Maryland

James L. Mueller
SDSU/Center for Hydro-Optics and Remote Sensing
San Diego, California

Gordana Lazin
Scott McLean
Satlantic, Inc.
Halifax, Canada

Chapter 7

SIRREX-8 Results, Discussion, and Conclusions

Giuseppe Zibordi
Davide D'Alimonte
JRC/IES/Inland and Marine Waters
Ispra, Italy

Stanford B. Hooker
NASA/Goddard Space Flight Center
Greenbelt, Maryland

James L. Mueller
SDSU/Center for Hydro-Optics and Remote Sensing
San Diego, California

Scott McLean
Gordana Lazin
Satlantic, Inc.
Halifax, Canada

Abstract

The SIRREX-8 experiment for comparing immersion factors involved nine OCI-200 sensors which were all characterized at three different facilities—CHORS, JRC, and Satlantic—using similar laboratory protocols. One of the radiometers, E_u S/N 130, was selected as a so-called *reference* sensor and was measured more frequently than the other eight. The analysis of the SIRREX-8 data showed intralaboratory measurement uncertainties, evaluated through multiple characterizations of the reference radiometer and defined by two standard deviations, ranging from 0.28% for Satlantic, and up to 0.49% and 0.60% for JRC and CHORS, respectively. Interlaboratory uncertainties, evaluated with data from the nine common radiometers, showed average UPDs lower than ±0.6%. The analysis of $I_f(\lambda)$ variability across radiometers of the same series showed average values of approximately 2%, with maximum values of up to 5%, for all three laboratories. Typical $I_f(\lambda)$ values for the OCI-200 series of radiometers were produced with $I_f(\lambda)$ data from measurements taken from the three laboratories.

7.1 INTRODUCTION

The data collected at the three laboratories involved in the SIRREX-8 immersion coefficient intercomparison experiment were analyzed (after quality assurance) to investigate the following:

1. Intralaboratory uncertainties derived from the multiple measurements of the reference radiometer, and
2. Interlaboratory uncertainties derived from the common set of nine radiometers.

Additional objectives of the data analysis were: a) determining the average immersion factors; b) quantifying the variability across the OCI-200 series of radiometers (widely used in ocean color calibration and validation activities); and c) proposing a set of so-called *typical* spectral values for the considered series of radiometers.

7.2 THE DATA SET

The SIRREX-8 data set included the measurements made at CHORS, JRC, and Satlantic for nine OCI-200 radiometers. The methods used at each laboratory followed the protocol described in Mueller and Austin (1995) for the characterization of immersion factors, although there were differences between the published and practiced procedures. Table 12 presents the number of measurement sequences included in the data set. Filtering of measurement sequences affected by perturbations, like poor water quality or radiometer-to-source misalignment, was implemented in near-real time just after each measurement sequence by processing the data with the code described in Chapt. 5. One quality-assured measurement sequence per instrument per laboratory was considered acceptable for comparing data among the three different laboratories.

NASA Technical Memorandum 2002–206892, Volume 21

SeaWiFS Postlaunch Technical Report Series

Stanford B. Hooker, Editor
NASA Goddard Space Flight Center
Greenbelt, Maryland

Elaine R. Firestone, Senior Scientific Technical Editor
Science Applications International Corporation
Beltsville, Maryland

Volume 21, The Eighth SeaWiFS Intercalibration Round-Robin Experiment (SIRREX-8), September–December 2001

Giuseppe Zibordi
Davide D'Alimonte
Dirk van der Linde
Jean-François Berthon
JRC/Institute for Environment and Sustainability
Ispra, Italy

Stanford B. Hooker
NASA/Goddard Space Flight Center
Greenbelt, Maryland

James L. Mueller
SDSU/Center for Hydro-Optics and Remote Sensing
San Diego, California

Gordana Lazin
Scott McLean
Satlantic, Inc.
Halifax, Canada

Chapter 6

Cosine Response Measurements

Giuseppe Zibordi
JRC/IES/Inland and Marine Waters Unit
Ispra, Italy

Stanford B. Hooker
NASA/Goddard Space Flight Center
Greenbelt, Maryland

James L. Mueller
SDSU/Center for Hydro-Optics and Remote Sensing
San Diego, California

Scott McLean
Gordana Lazin
Satlantic, Inc.
Halifax, Canada

Abstract

In addition to the immersion factor characterizations, the cosine response was measured for one irradiance sensor at CHORS and Satlantic (motivated by some preliminary measurements at the JRC). The angular response of an OCI-200 in-water radiometer was characterized by CHORS and by Satlantic using a similar methodology, although the former relied on a point source with a horizontal rotation of the sensor, and the latter relied on a collimated source and a vertical rotation. Results from the analysis of the data from Satlantic show deviations from the ideal cosine response for most of the collectors within, or very close to, the limits suggested by the SeaWiFS Ocean Optics Protocols (i.e., 2% between 0–65° and 10% above 65°). Results obtained from the analysis of the CHORS data show deviations from the ideal cosine response within the suggested limits for the OCI-200 central collector, but consistently higher deviations for the six collectors symmetrically located around the centermost one. The latter result is primarily explained by the use of different sources at the two laboratories (i.e., a lamp at CHORS and a lamp plus a collimator at Satlantic).

6.1 INTRODUCTION

The calibration of irradiance sensors takes place in air with light arriving normal to the plane of the cosine collector faceplate. To properly measure all irradiance arriving at the collector plane, the response should follow a cosine function, such that

$$E_\theta = E_0 \cos\theta, \tag{7}$$

where E_θ is the measured irradiance in response to the light flux arriving at angle θ with respect to the normal of the collector plane, and E_0 is the measured irradiance the same light flux would produce if it were measured normal to the collector plane. Irradiance sensors have a field of view that extends over the hemisphere normal to the sensor faceplate, which is usually separated into two 90° halves, i.e., during a characterization, $-90° < \theta < +90°$.

If (7) is satisfied, an on-axis calibration can be used, and the device will correctly measure the irradiance arriving at the collector plane (regardless of the directional origin of the light). Of course, for an in-water sensor to correctly measure irradiance, there is the added requirement that the immersion factor must be correctly characterized. For in-water irradiance sensors, which were the only ones considered in SIRREX-8, the cosine response must be made with the radiometer under water.

6.2 PRELIMINARY INQUIRIES

A continuing philosophy of the entire SIRREX activity has been to incrementally investigate the sources of uncertainty in radiometric calibrations and measurements. The primary reason for this approach has been the difficulty of assembling the needed resources (personnel, equipment,